S-N/99205--076

Groundwater Flow Model of Corrective Action Units 101 and 102: Central and Western Pahute Mesa, Nevada Test Site, Nye County, Nevada

Revision No.: 0

June 2006

Prepared for U.S. Department of Energy under Contract No. DE-AC52-03NA99205.

Approved for public release; further dissemination unlimited.

Uncontrolled When Printed

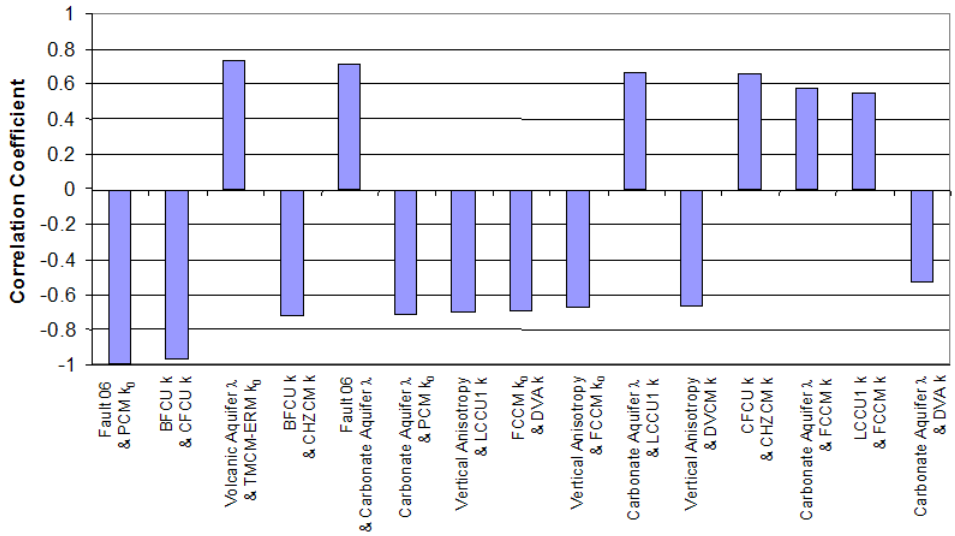

Figure 6-4
Correlation Coefficients from PEST for BN-MME-SDA

decay, only in the reverse sense of the correlation with PCM, the fault and LCA depth decay act similarly to control flow (recall that southern boundary flow was one of the most sensitive observations); the inverse correlation of PCM permeability and LCA depth decay further demonstrates this effect. The permeability of the BFCU and CFCU are also show a high inverse correlation, which, considering their location and role as major confining units in Areas 19 and 20, is a reasonable outcome.

6.2.1.2 Base HFM - All HSU Depth-Decay and Anisotropy (BN-MME-ADA) Model Parameter Sensitivity and Correlations

For this model, k_0, fault permeability multiplier, vertical anisotropy, and depth-decay coefficient parameters were varied individually by HSU or fault. This replicates the more detailed approach inherited from the UGTA regional model (DOE/NV, 1997) where depth decay and anisotropy were ubiquitously used. This resulted in a total of approximately 200 parameters for which sensitivity coefficients were calculated.

Uncontrolled When Printed

The 15 largest sensitivity coefficients calculated for this model using PEST are shown in Figure 6-5 and are all depth-decay parameters. The LCA3a is the LCA3 under Oasis Valley; the LCA Zone 1 (LCAr1) is the LCA along the southeastern edge of the model inherited from the UGTA regional model (DOE/NV, 1997) (see Figure 5-7). The PCM depth-decay parameter (λ) is also a sensitive parameter in this model and acts, as noted in the selected HSU depth-decay and anisotropy case, to control outflow on the south and the influence of the southern boundary. The PBRCM is one of the most extensive units in the Pahute Mesa CAU model and exists at a large range of depths, and it is the λ for the portion that lies under the Silent Canyon Caldera (and Areas 19 and 20) that is the fourth most sensitive parameter. The PBRCM λ is also sensitive in the selected HSU depth-decay and anisotropy case described in Section 6.2.1.1, but not to the same degree. The YMCFCM, like the PCM, lies along the southern boundary and is in position to control the effects of the southern boundary. The BRA, North Timber Mountain subdivision of the TMCM, and TCA are all extensive permeable units in the model. The IA and CHZCM are not so extensive, but CHZCM has 23 calibration wells in it. The DVA λ, as described in Section 6.2.1.1, is also a sensitive parameter. Clearly, with this parameterization approach, the volcanic units' depth decay is a dominant parameter as is depth decay in general.

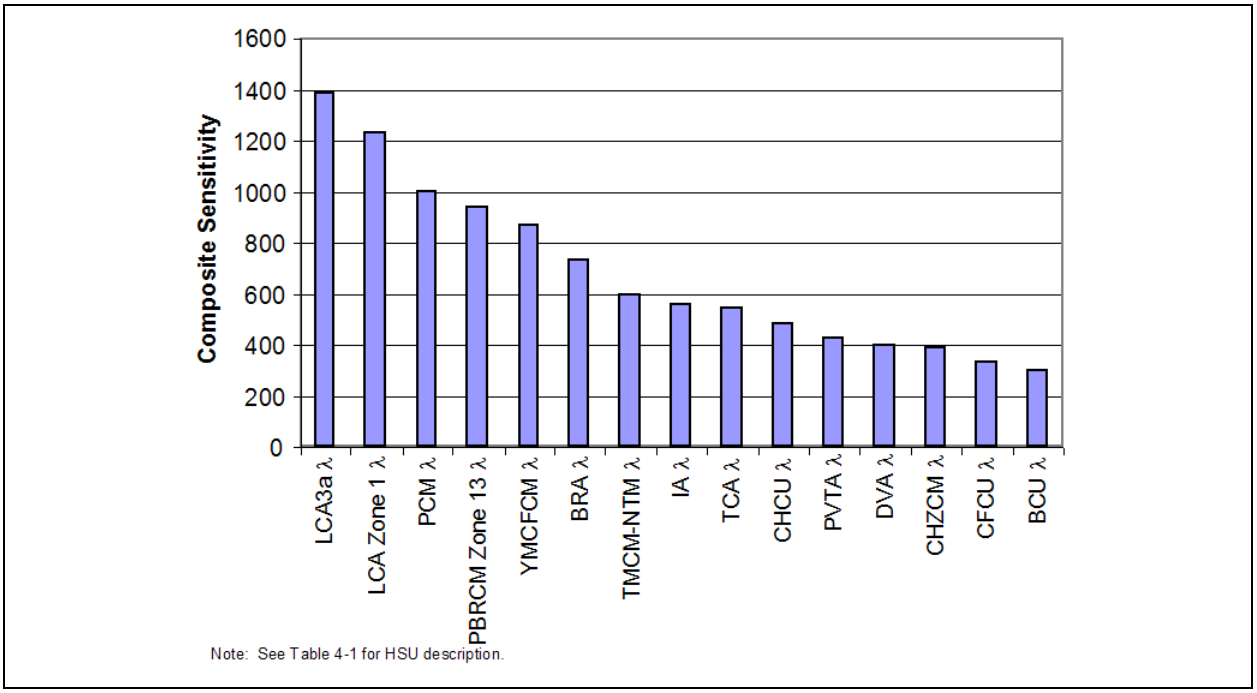

Figure 6-5
Largest Sensitivity Coefficients from PEST for BN-MME-ADA

Uncontrolled When Printed

The 15 most sensitive targets calculated using PEST are depicted in Figure 6-6. This figure shows that Oasis Valley discharge Zone 1, the northernmost target, is the most sensitive observation (unlike the selected HSU depth-decay and anisotropy case) followed by the lateral boundary flux targets for the southern and eastern model boundaries (like the selected HSU depth-decay and anisotropy case). Following these three observations, the observation sensitivity coefficients tend to drop off quickly.

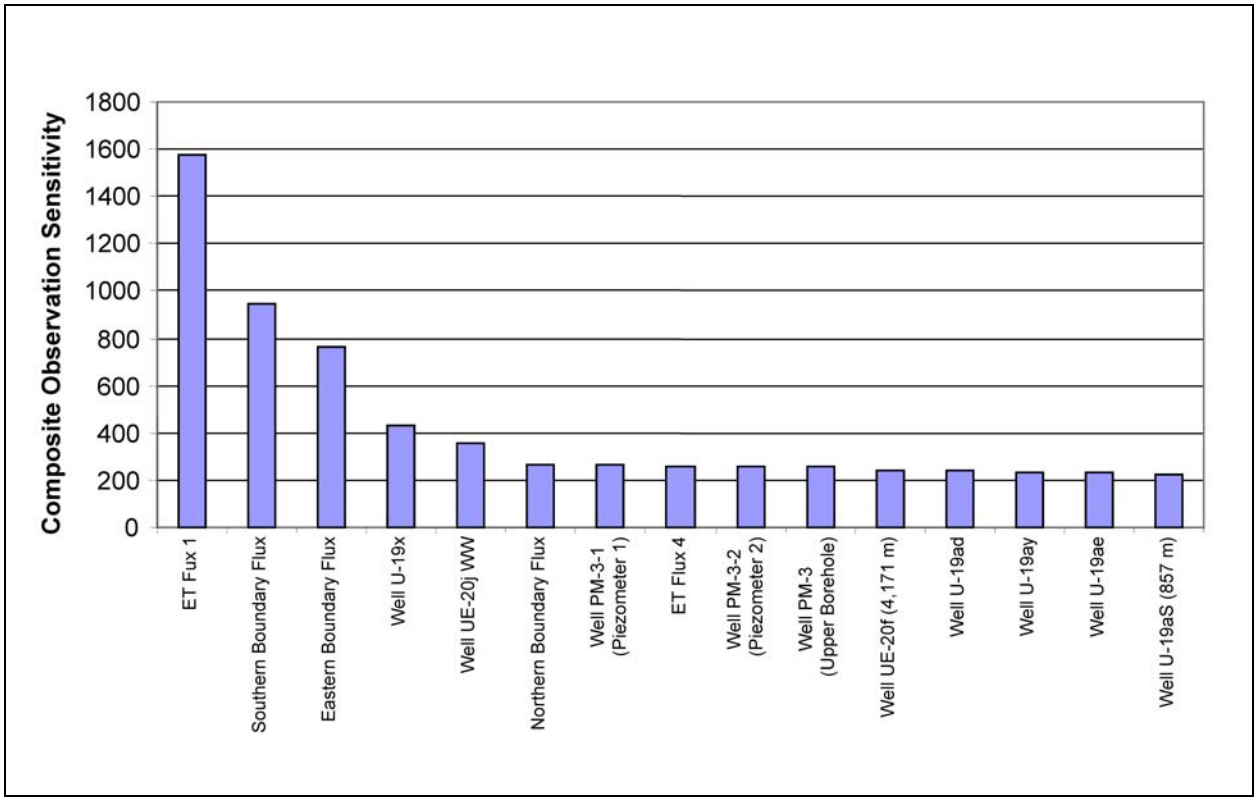

Figure 6-6
Composite Observation Sensitivity from PEST for BN-MME-ADA

The effect of consolidating the depth decay and anisotropy to affect all volcanic aquifers at once was also considered to investigate the representation of the shallower volcanic rocks as a package (the ICUs were not considered in this grouping). The 15 most highly correlated pairs of parameters from the PEST correlation coefficient matrix are shown in Figure 6-7. This figure shows that many parameters appear to be highly correlated (correlation coefficients greater than 0.90 [Hill, 1998]). The first relationship on Figure 6-7 shows that the reference permeability and depth-decay parameter for the UCCU are nearly perfectly (0.99) correlated (the LCCU also shows this behavior, as does the volcanic units to the grouped volcanic depth-decay parameter). Review of the formulation of depth

Uncontrolled When Printed

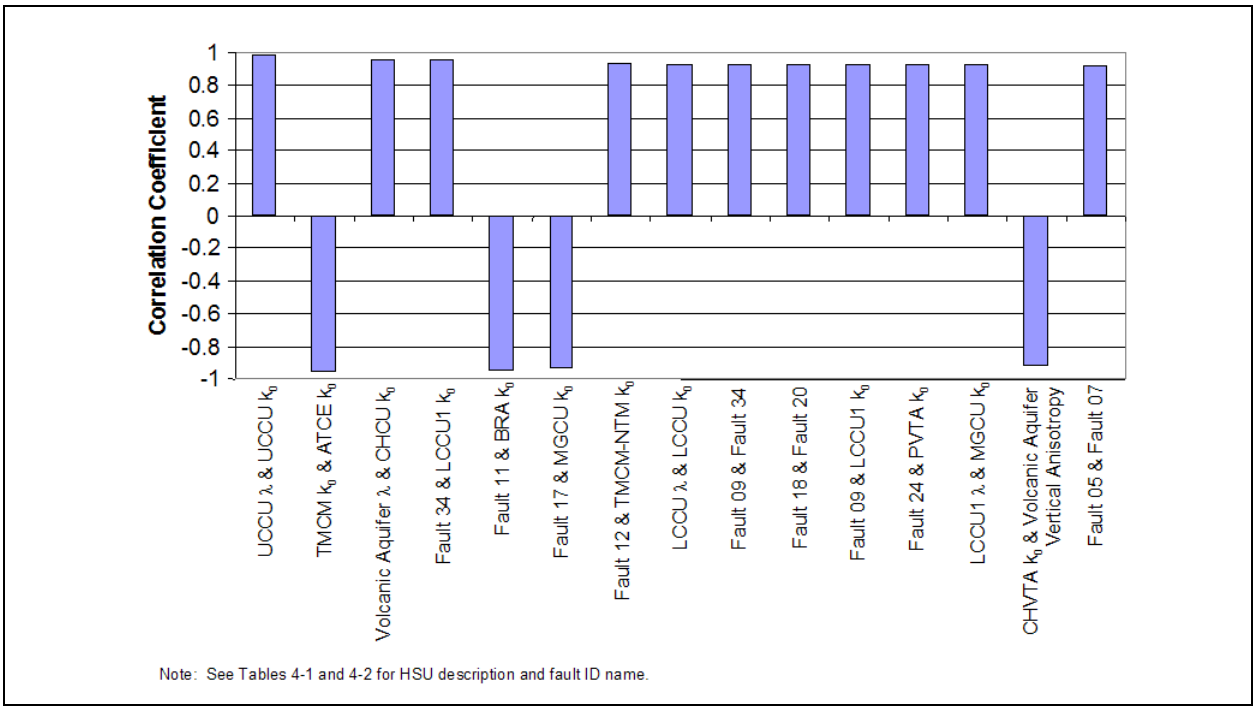

Figure 6-7
Correlation Coefficients from PEST for BN-MME-ADA

decay $k(z) = k_0[10^{(-\lambda d)}]$ shows that as λ gets larger (i.e., depth decay increases), k(z) can be maintained by increasing k_0 proportionally. Oddly, the MGCU k_0 appears as a parameter correlated with LCCU1 k_0. This is interpreted as arising from both units connection along the central-eastern boundary to high regional heads; permeability can be raised in concert to achieve the same effect. The effects of the MGCU in the ADA case were also noted in Section 5.8.2.

Of the faults shown in Figure 6-7, fault 09 is the only one that appears with any consistency (only twice at that). Fault 09 is East Estuary, which is indicated as being correlated with West Estuary and LCCU1 k_0. Like the Boxcar Faults, the Estuary Faults (which have reduced fault permeability in the BN-ADA case) may act in concert, but the reason why East Estuary Fault would be correlated with the LCCU1 permeability is unknown. Hill (1998) states that nonlinear and slight precision effects can make correlation coefficients unreliable. Section 6.2.2.2 shows that the model response to parameter changes is noticeably nonlinear; thus, these results (as all results from local analysis) should be considered approximate and are valid inasmuch as the conceptual model can be used to understand the cause and effect implied by the statistical analysis. Overall, this parameterization approach shows many more extremely correlated parameters than the selected HSU depth-decay and

Uncontrolled When Printed

anisotropy approach described in Section 6.2.1.1. This should not be entirely surprising considering that more than 200 adjustable parameters exist in this model with only 191 observations.

6.2.1.3 SCCC HFM - Selected Depth-Decay and Anisotropy (SCCC-MME-SDA) Model Parameter Sensitivity and Correlations

For this model, permeability, k_0, and fault permeability multiplier parameters were varied individually by HSU or fault, as appropriate. Two HSUs (Calico Hills and BA) were assigned individual vertical anisotropy parameters, and the others were grouped into a single parameter. A single depth-decay coefficient for the volcanic HSUs and another for carbonate HSUs were used. This resulted in approximately 100 parameters for which sensitivity coefficients were calculated using PEST.

The 15 largest sensitivity coefficients calculated for this model using PEST are shown in Figure 6-8. This figure shows that, like the selected HSU depth-decay and anisotropy parameterization of the base HFM, the two depth-decay parameters have much greater sensitivity coefficients than any of the other parameters (note the log-scale used for the y-axis). Other HSUs shown in Figure 6-8 include the FCA, YVCM (a patchy unit near the northern end of Oasis Valley), and THLFA. None of these appear, at least in a similar rank, in the base HFM model sensitivities shown in previous sections. The sensitivity of the Calico Hills anisotropy (recall that the five Calico Hills HSUs in the base HFM were grouped into one for the SCCC HFM, and that about 23 calibration wells exist in it) is attributed to the greater influence that the lumped unit exercises, although vertical anisotropy (as applied to selected volcanic HSUs) still ranks similarly in sensitivity to the base HFM. Unlike the BN-MME-SDA case the model has many sensitive faults. Indeed, seven of the 15 largest sensitivity coefficients belong to permeability multipliers for faults that are scattered throughout the model domain. The three most sensitive are the Timber Mountain Structural Margin (fault 11), the Gold Meadows Structural Zone/Big Burn Valley (fault 22), and the Hot Springs extension to the Timber Mountain Structural Margin (fault 19). Faults 11 and 22 are located such that they can control flow out of Timber Mountain and along the eastern edge of the model, and their sensitivity is easily interpreted as consistent with the conceptual model. It seems odd that the relatively short fault 19 has much impact, but it is located in Oasis Valley where there are discharge, spring, and head data.

The 15 most sensitive targets calculated using PEST are depicted in Figure 6-9. This figure shows that the northernmost Oasis Valley discharge target (Zone 1) is the most sensitive observation,

Uncontrolled When Printed

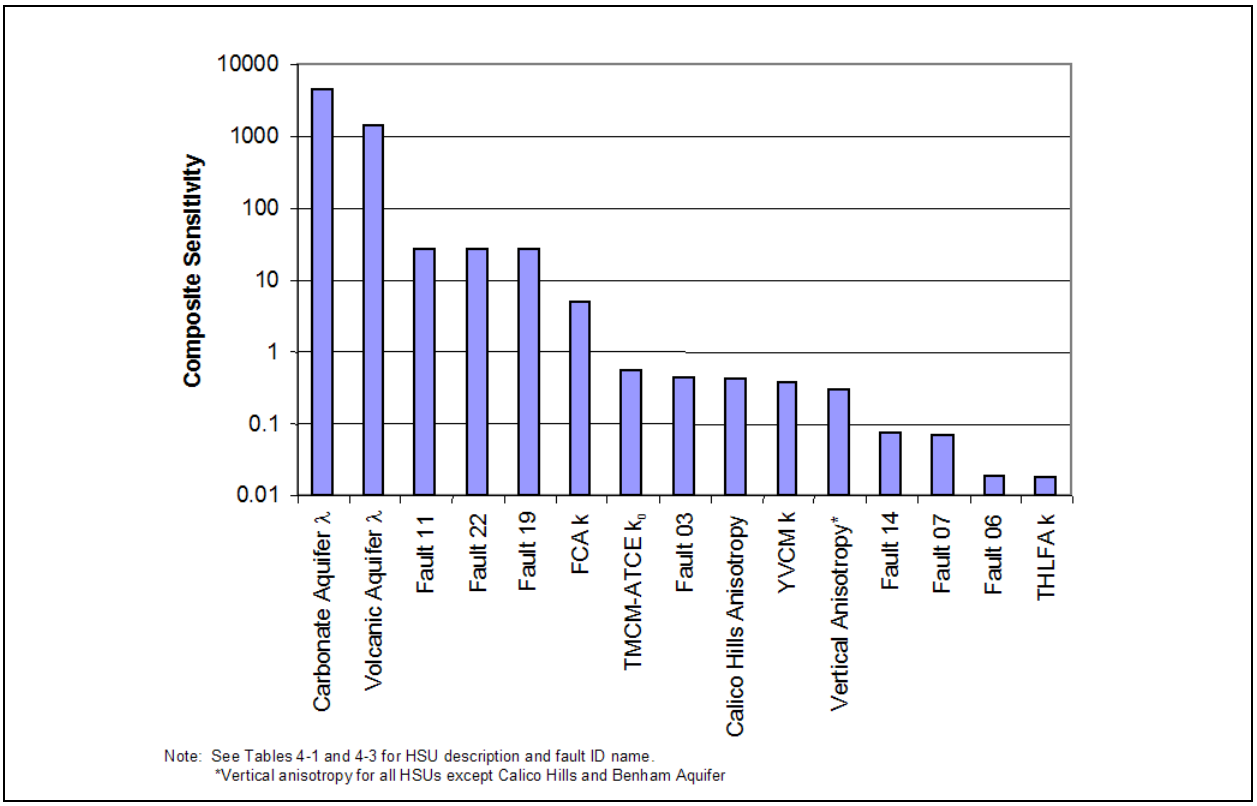

Figure 6-8
Largest Sensitivity Coefficients from PEST for SCCC-MME-SDA

followed by UE-19i, and the southern boundary flux. This may indicate that many parameters impact the flow out ET Zone 1. Following this observation, a series of head observations in wells and the southern boundary flux have very comparable observation sensitivity coefficients but less than half the magnitude of that for discharge Zone 1.

The 15 most highly correlated pairs of parameters (from the correlation coefficient matrix) are shown in Figure 6-10. This figure shows that the carbonate depth-decay coefficient and the permeability of the YVCM are almost perfectly (-0.994) inversely correlated. That the YVCM displays much sensitivity at all is surprising considering its patchy nature, but it lies near ER-EC-4 and ER-18-2. There is no obvious reason as to why the permeability of the YVCM and carbonate depth decay should be so highly correlated. This may be an instance of less-reliable correlation coefficients as noted by Hill (1998). Taken as a group, the depth decay applied to the selected volcanic HSUs is inversely correlated to carbonate depth decay; as depth decay, increases in one group of units it can be counterbalanced by a reduction in depth decay in the other. Considering that the southern boundary

Uncontrolled When Printed

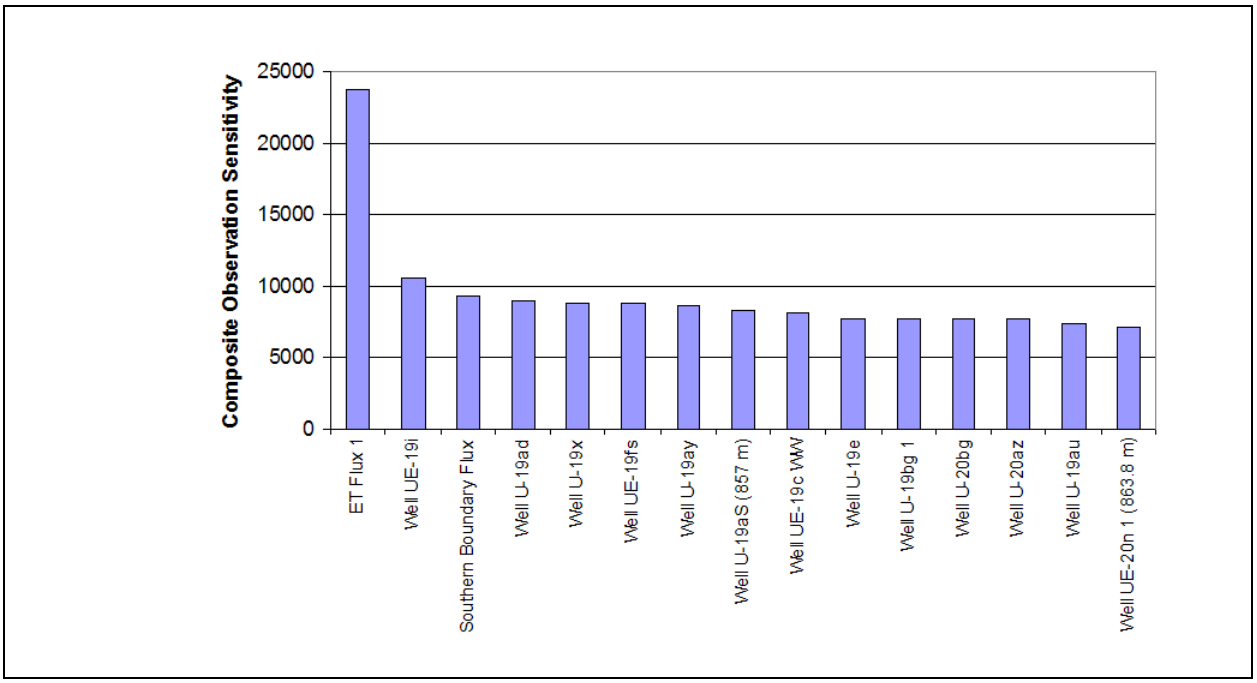

Figure 6-9
Composite Observation Sensitivity from PEST for SCCC-MME-SDA

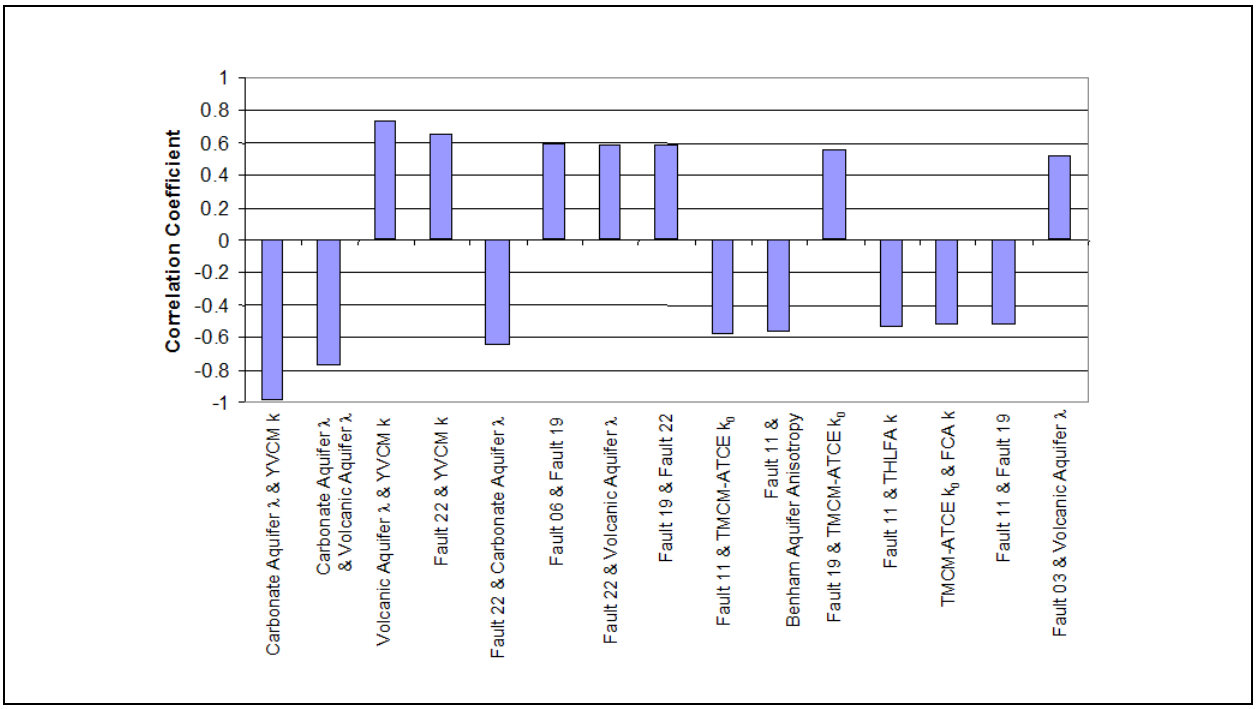

Figure 6-10
Correlation Coefficients from PEST for SCCC-MME-SDA

Uncontrolled When Printed

flow is a strongly sensitive observation and there are no head observations in the LCA, this effect must arise from trying to match boundary flows. In this case, it makes sense that as T in one type (e.g., LCA) of HSU drops from increased depth decay, it can be compensated for by lessening the effect of depth decay in the other type of HSU (e.g., volcanics with depth decay). This relationship is not noticed in the BN-MME-ADA or BN-MME-SDA cases. A number of other parameter pairs exhibit moderately high correlation, more like the selected HSU depth decay and anisotropy parameterization of the base HFM than the all HSU depth-decay and anisotropy case.

6.2.2 Parameter Perturbation Analysis

In the perturbation analysis, input parameters were systematically increased and decreased while changes in the objective function, heads, and various fluxes were recorded. Estimated standard deviations in HSU permeability (SNJV, 2004a; Section 2.0 of this report) and depth decay were available (IT, 1996a through f; IT, 1997a and b; Section 5.0 of this report). It was assumed that these standard deviations were applicable in describing the uncertainty in the calibrated values of these parameters. For each HSU permeability and depth decay, six simulations were completed where the input value was perturbed up and down one-half, one, and two standard deviations from the calibrated value. Vertical anisotropy and fault permeability multipliers were assumed to have log-uniform distributions and were perturbed over several orders of magnitude with ranges depending on assumptions about the uncertainty in the individual parameters.

The same components of the objective function that were used for calibration were also computed for perturbation analysis. An additional metric for the output heads was also computed; the mean difference (*MD*) between the sensitivity simulated output and the calibrated simulated output heads at each of the target wells was calculated as:

$$MD = \frac{1}{n}\sum_{i=1}^{n}(h_{sens,\,i} - h_{cal,\,i}) \tag{6-12}$$

where $h_{sens,i}$ is the perturbation simulation head at well i, $h_{cal,i}$ is the calibrated simulation head at well i, and n is the number of wells. This metric describes more than the objective function components;

the direction of the head change can also be assessed. A positive value indicates that the sensitivity simulation has overall higher heads and a negative value has overall lower heads.

6.2.2.1 Base HFM - Selected HSU Depth-Decay and Anisotropy (BN-MME-SDA) Model Parameter Perturbation Analysis

For perturbation analysis, each HSU's permeability (including k_0), depth decay (if assigned,), and anisotropy (if assigned) were varied. Thus, the detailed effects of each parameter with each HSU were investigated. This resulted in 61 permeability and k_0 parameters, 11 vertical anisotropy parameters, 15 depth-decay parameters, and 11 fault permeability multiplier parameters being varied. In addition, vertical anisotropy was varied as single grouped parameter, the fault permeability multiplier for the Purse Fault was varied as a group, and depth decay was varied as two groups – one for the carbonates and one for the volcanics (the list of HSUs with depth decay and anisotropy is shown in Section 5.6.2) as well as for each HSU. This resulted in approximately 100 parameters that were varied. Approximately 600 simulations were conducted during the analysis shown in this section.

Plots of mean difference in heads, change in the objective function and its constituents, and change in boundary flows were generated for perturbation of each of the approximately 100 parameters in the BN-MME-SDA perturbation analysis. While all of these plots are shown in Appendix D, Figures 6-11 through 6-18 demonstrate selected sensitivity relationships.

Figures 6-11 through 6-14 show plots of the mean difference in heads at the target locations. Figures 6-11 through 6-13 indicate that the permeability (including k_0) and depth-decay parameters exhibit a classical, albeit nonlinear in some cases, sensitivity relationship where an increase in a parameter value is accompanied by a consistent trend of either an increase or decrease in the simulated head. It is also interesting that increases in the permeability (i.e., higher k_0 or lower depth-decay coefficient) for some HSUs result in higher heads while the opposite is true for other HSUs, and that permeability (including k_0) has a larger effect than the depth-decay parameter itself. This may simply be because the range of uncertainty for k_0 is smaller than that for λ (which spans multiple orders of magnitude). The TMCM is by far the most sensitive of all the HSUs with depth decay, followed by the PBRCM under Pahute Mesa. The TMCM has a very large areal coverage, and its properties affect flow in a large part of the domain, hence its sensitivity. The PBRCM under

Uncontrolled When Printed

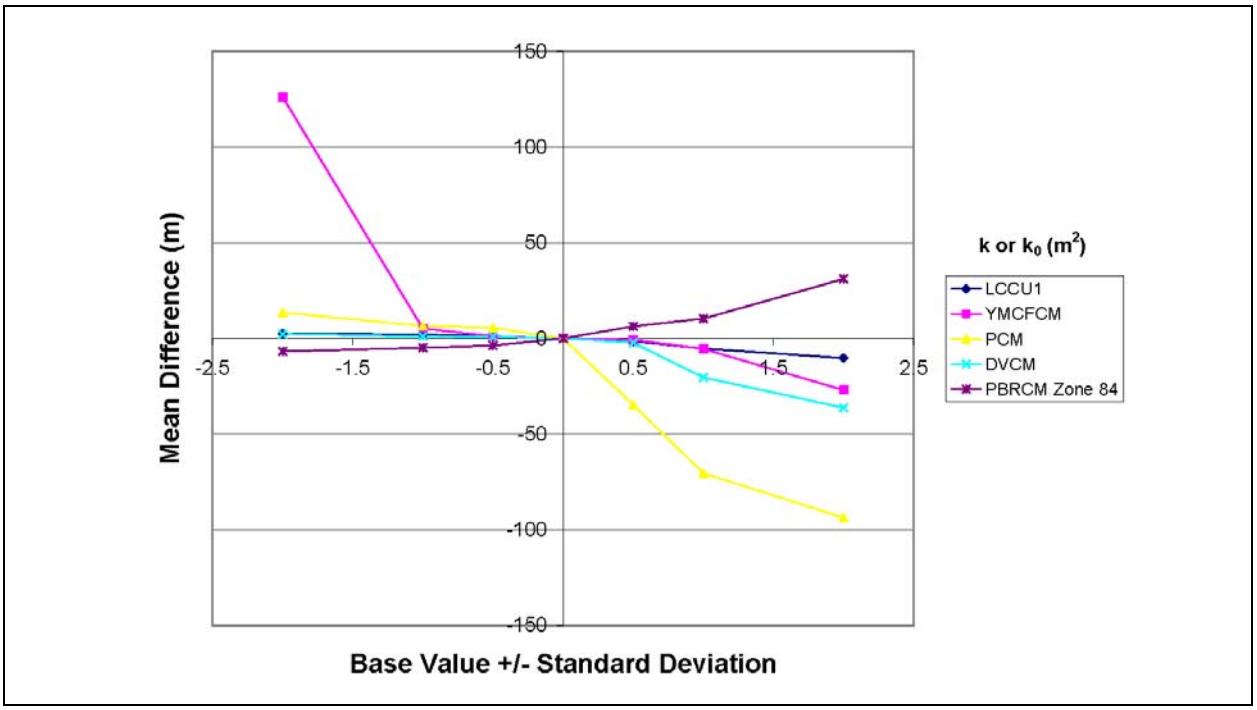

Figure 6-11
Mean Head Difference for BN-MME-SDA

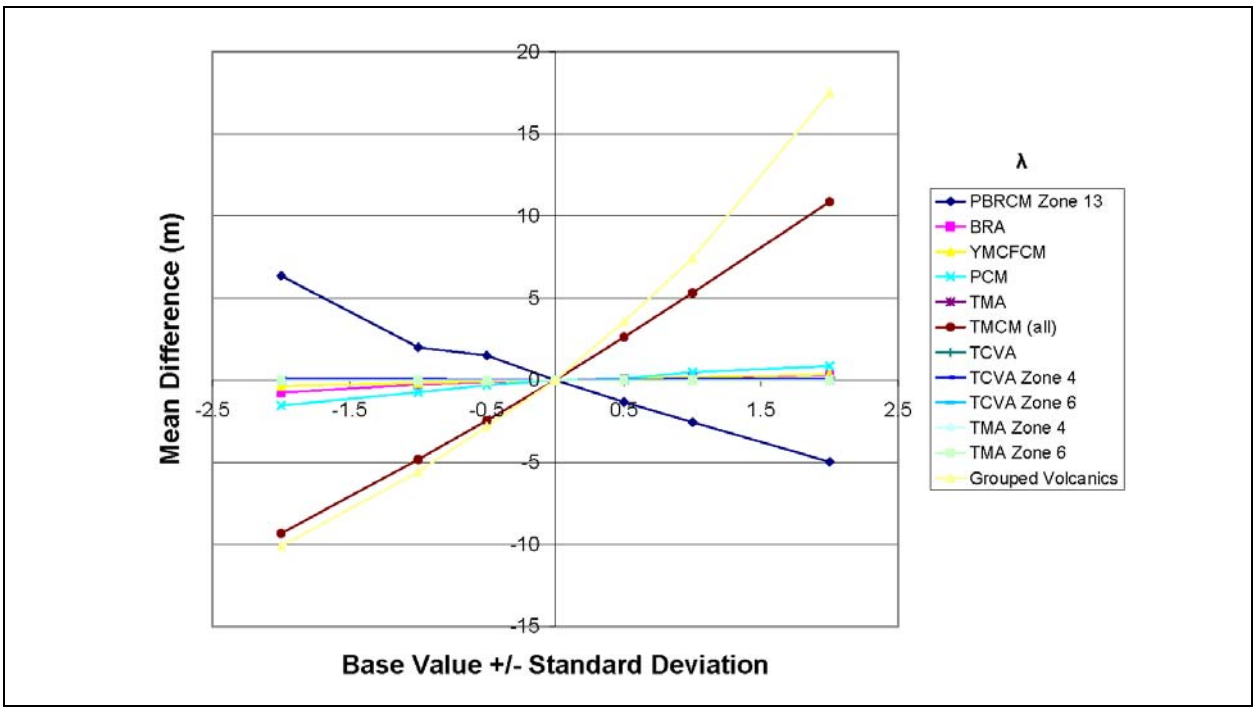

Figure 6-12
Mean Head Difference for Volcanic HSU Depth Decay for BN-MME-SDA

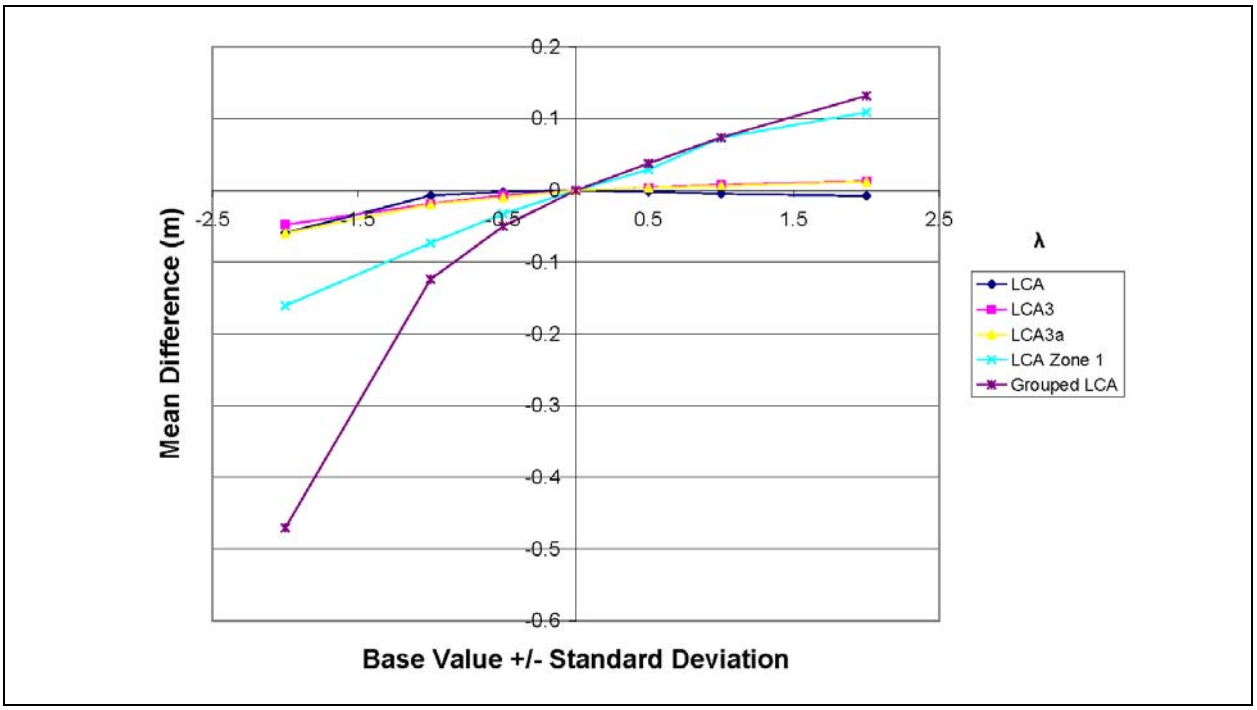

Figure 6-13
Mean Head Difference for Carbonate HSU Depth Decay for BN-MME-SDA

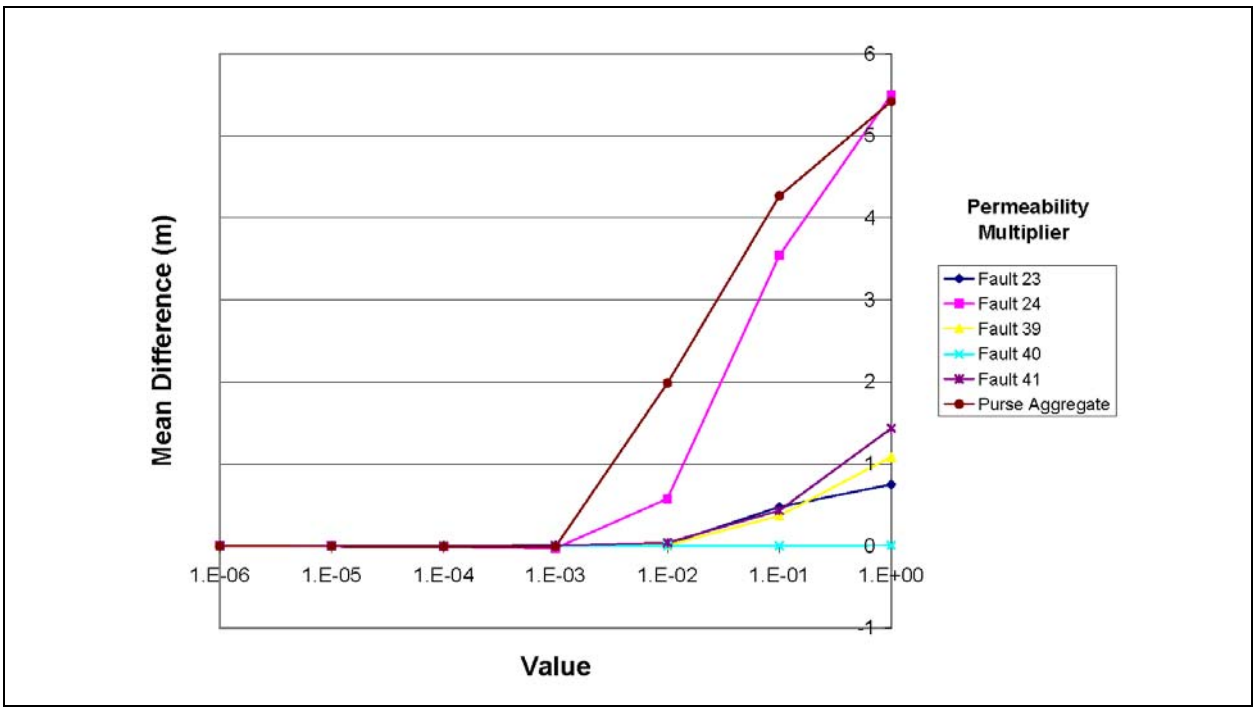

Figure 6-14
Mean Head Difference for Purse Fault Permeability Multipliers for BN-MME-SDA

Uncontrolled When Printed

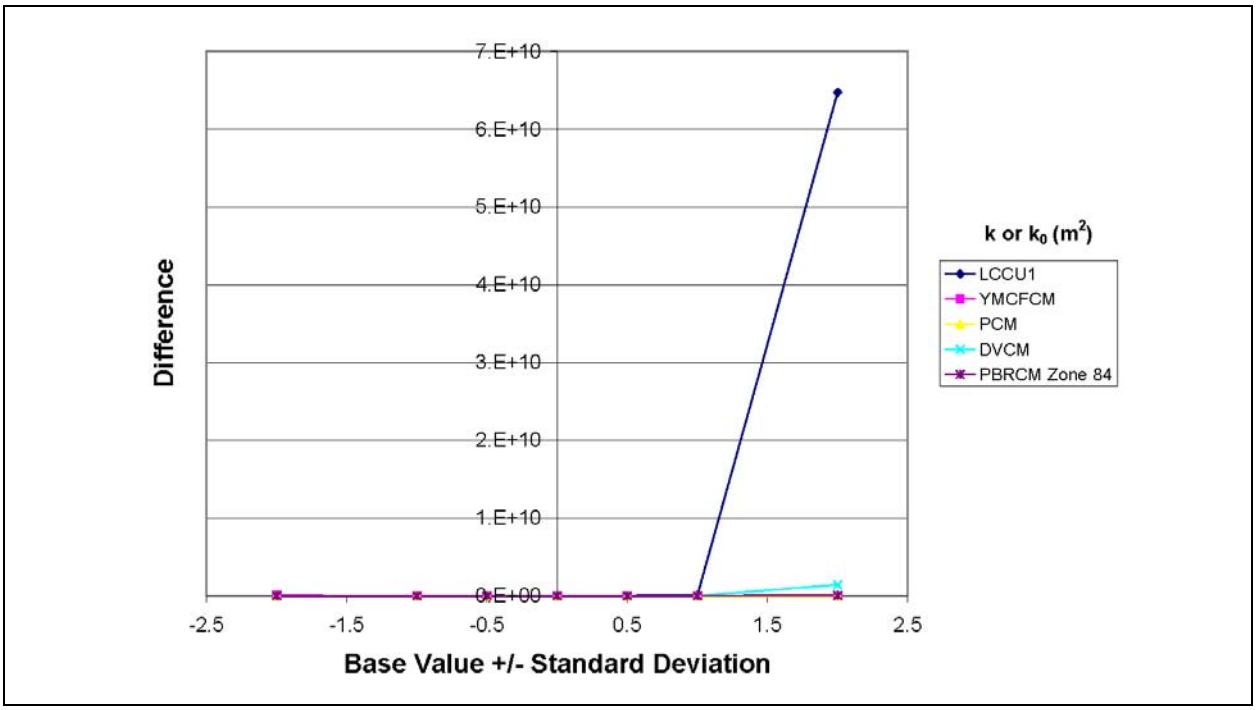

Figure 6-15
PHI Perturbation Plot for BN-MME-SDA

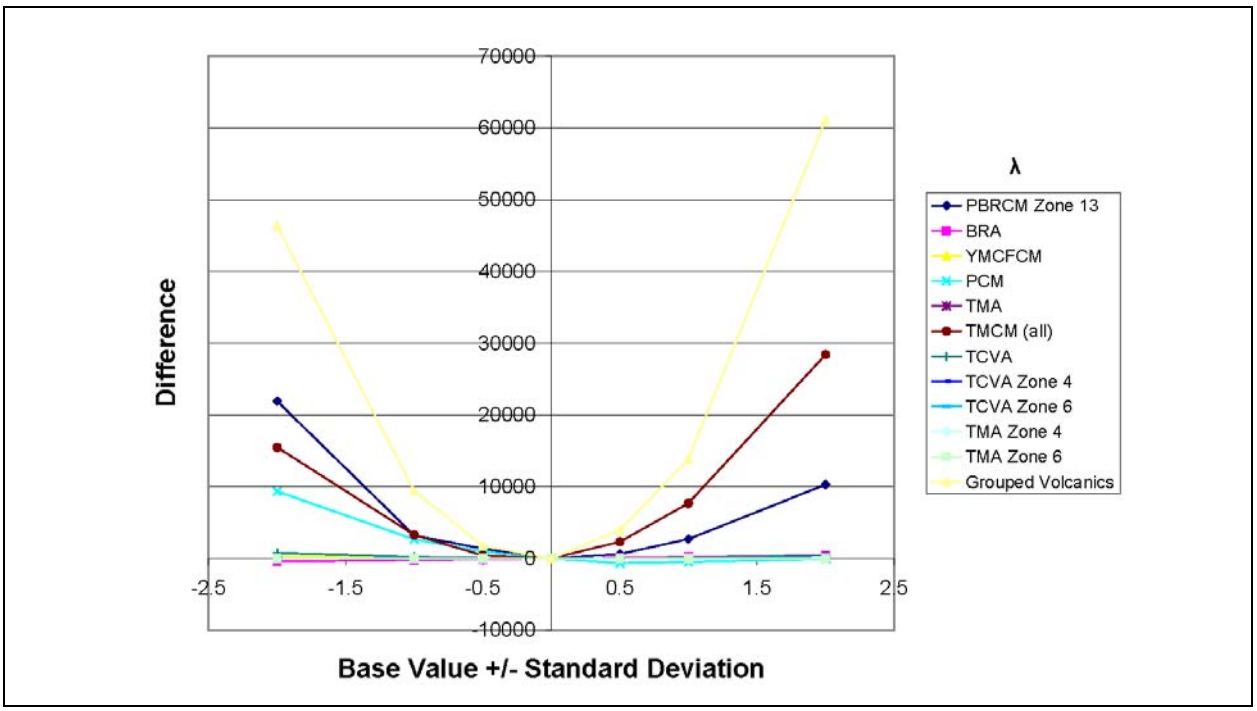

Figure 6-16
PHI Perturbation Plot for Volcanic HSU Depth Decay for BN-MME-SDA

Uncontrolled When Printed

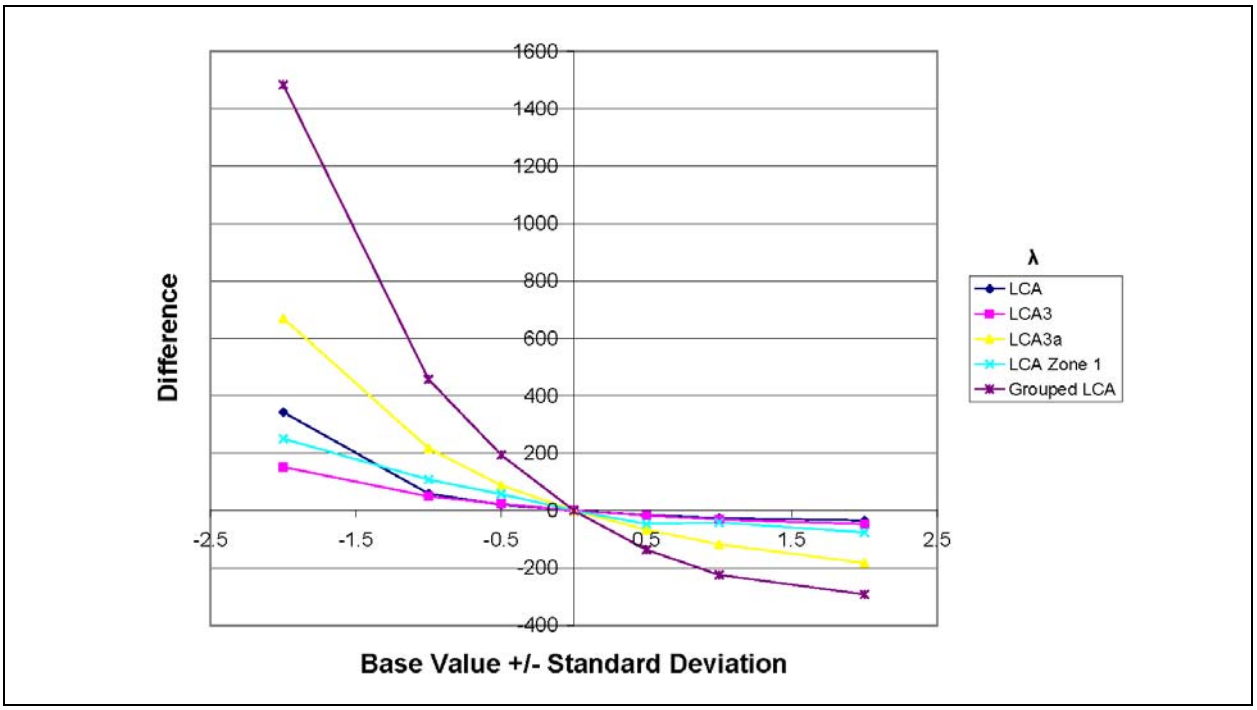

Figure 6-17
PHI Perturbation Plot for Carbonate HSU Depth Decay for BN-MME-SDA

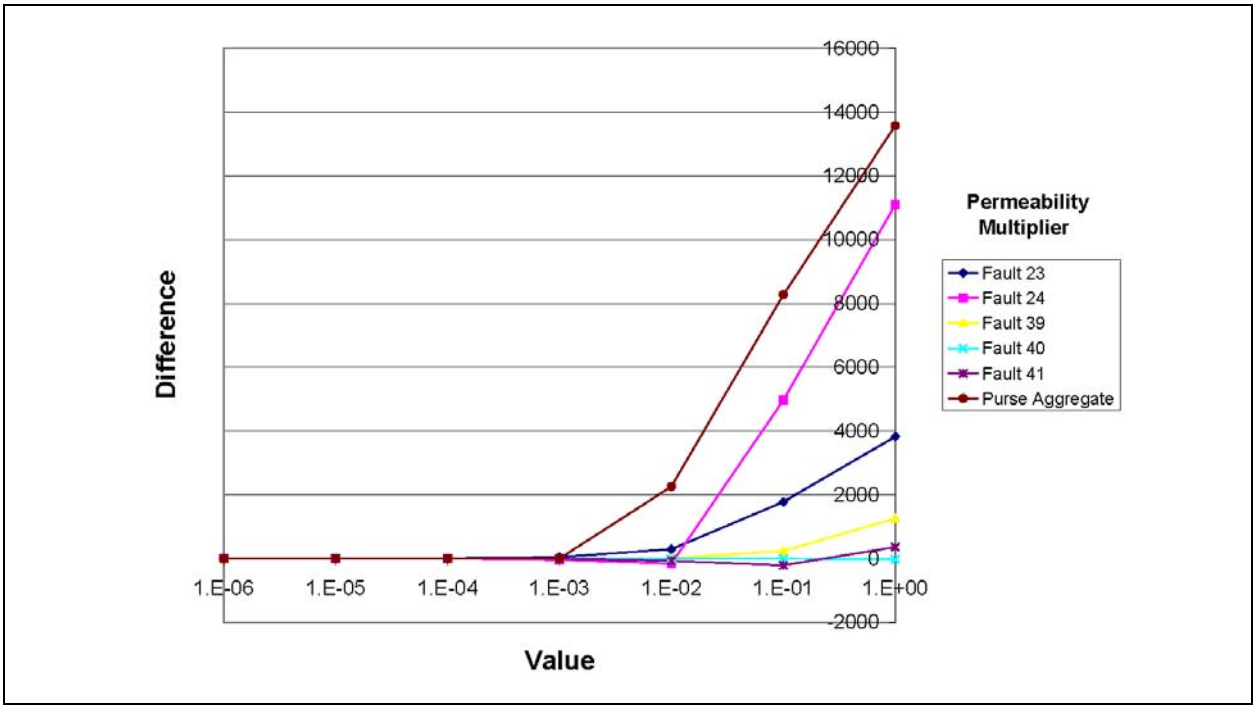

Figure 6-18
PHI Perturbation Plot for Purse Fault Permeability Multipliers for BN-MME-SDA

Uncontrolled When Printed

Pahute Mesa is located where a large part of the calibration data exists, and is connected, like the BRA, to the northern boundary of the model. The PBRCM is also distributed over most of the domain. The BRA is also areally extensive under Pahute Mesa, but is not present much outside Pahute Mesa. Thus, it is concluded that it is this larger connection to the flow system that accounts for the different behavior of the PBRCM and BRA. The TMA and TCVA only had minor influence. The carbonate aquifer (LCA, LCA3, LCA3a, and LCA Zone 1) λ has almost no effect on mean head (Figure 6-13); its primary function seems to be to control the overall water balance with respect to the estimated regional flows.

In contrast, Figure 6-14 shows that the fault permeability multipliers of the Purse Fault system and its individual components exhibit a threshold sensitivity relationship where heads increase with an increase in the fault permeability above a multiplier of 0.001 but heads do not decrease for lower fault permeabilities. As previously discussed, the Purse Fault is comprised of segments of other faults as well as the main fault. Figure 6-14 shows that it is the main part of the fault (fault 24) that has the largest influence on model results, which is reasonable because it comprises most of the length of the fault.

Figure 6-11 indicates that YMCFCM and PCM have the greatest effect on the simulated heads. The PCM and YMCFCM, by the virtue of their location along the southern edge of the model, can affect mean heads in the model by tens of meters. It is probably not depth decay *per se* that drives these sensitivities, but the HSU positions on the southern edge; if they did not have depth decay, their permeability would still be expected to be a sensitive parameter. The DVCM, because of its role in controlling what water is allowed to discharge in Oasis Valley from the west, also has a noticeable, and one-sided, control on lowering heads as its permeability is raised. The western portion of the PBRCM has some control on raising heads, presumably via its connection to the northern edge of the model (and higher) heads down to northern Oasis Valley.

Figures 6-15 through 6-18 show select perturbation plots for the objective function (PHI). Note that these include the same parameters shown in Figures 6-11 through 6-14. Because the PEST sensitivity coefficients and the global sensitivity analysis both focus primarily on the objective function as the model output metric, these plots are most pertinent in comparing the perturbation results to those of the other analysis types. It is immediately apparent that most of the parameters shown in Figures 6-15

Uncontrolled When Printed

through 6-18 exhibit highly nonlinear sensitivity relationships over the range through which they were perturbed. This indicates that the sensitivity coefficients calculated by PEST are, in most cases, valid only locally in the vicinity of the calibration point.

Several other observations can also be made with respect to the perturbation plots of the objective function. Figure 6-15 shows that high values of permeability for LCCU1 have a very large effect on PHI, the permeability of which is unknown, and other diagnostic results such as parameter correlations. Figure 6-16 indicates that the minimum PHI with respect to the volcanic depth-decay parameters is generally centered on the calibration point; it would be difficult to further improve calibration by adjusting k_0 in the volcanic HSUs with depth decay. Depth decay has the largest influence in TMCM and PBRCM (as also noted in the composite head in Figure 6-13), two HSUs that have a large areal extent. In contrast, the minimum PHI with respect to the carbonate depth-decay parameter occurs at values higher than the calibrated value as seen in Figure 6-17, although the change in the objective function is minor. Figure 6-18 indicates that the fault permeability multipliers for the Purse Fault system and its individual components exhibit a threshold sensitivity with low PHI values occurring for multipliers below approximately 0.001, consistent with the threshold value noticed in the mean head difference metric.

There are clearly differences in the sensitivity relationships for mean heads and for the objective function, particularly with respect to the parameters with the highest sensitivity. This is because the large differences in the objective function are dominated by the contribution from the lateral boundary fluxes rather than from the head-based targets. This is also demonstrated in the global sensitivity analysis (see Section 6.2.3), where parameters governing the highest 10 percent of PHI typically coincide with parameters driving the highest 10 percent of boundary flux.

6.2.2.2 Base HFM - All HSU Depth-Decay and Anisotropy (BN-MME-ADA) Model Parameter Perturbation Analysis

For the base HFM - all HSU depth-decay and anisotropy model (BN-MME-ADA), 57 k_0 parameters, 64 vertical anisotropy parameters, 64 depth-decay parameters, and 41 fault parameters were varied. In addition, the fault permeability multiplier for the Purse Fault was varied as a group and for each fault segment, and both vertical anisotropy and depth decay were varied as three groups – one for each of the carbonates, the volcanic units, and the intrusive confining units as well as by HSU. This

Uncontrolled When Printed

resulted in approximately 200 parameters that were varied. Generating results for this perturbation analysis required approximately 1,400 simulations.

Plots of mean difference in heads, difference in the objective function and its constituents, and difference in boundary fluxes were generated for each of the approximately 200 parameters in the base HFM - all HSU depth-decay and anisotropy model perturbation analysis. While all of these plots are shown in Appendix D, Figures 6-19 though 6-24 describe selected sensitivity relationships.

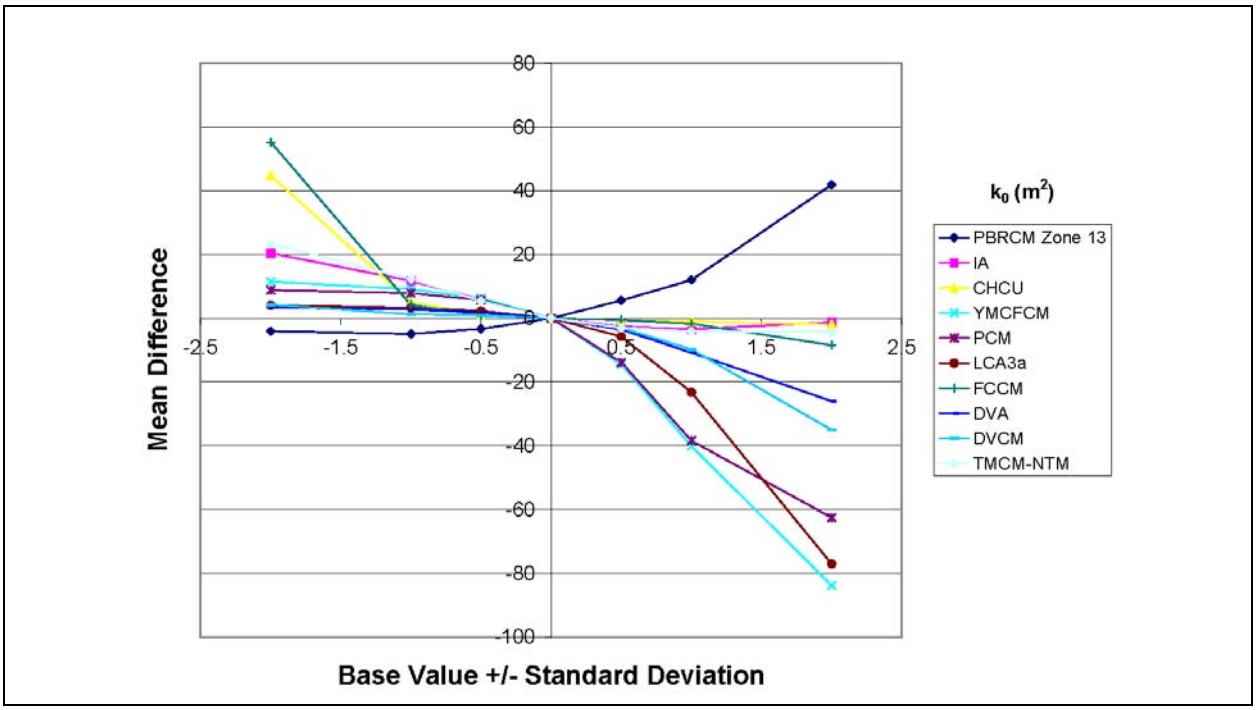

Figure 6-19
Mean Head Difference for BN-MME-ADA

Figures 6-19 through 6-21 depict select perturbation plots for the mean difference in heads at target locations. Figures 6-19 and 6-20 show that the k_0 and depth-decay parameters exhibit a nonlinear sensitivity relationship. It is also interesting that increases in the permeability for some HSUs results in higher heads while the opposite is true for other HSUs. Figure 6-19 indicates that the reference permeability of YMCFCM, LCA3a, and PCM have the greatest effect on simulated heads, although the DVCM, DVA, and PBRCM under Pahute Mesa also have noticeable influence. The YMCFCM and PCM are likely sensitive because (as discussed in the previous section) they lie along the southern edge of the model and can control both flow and head in the model. The PBRCM under

Uncontrolled When Printed

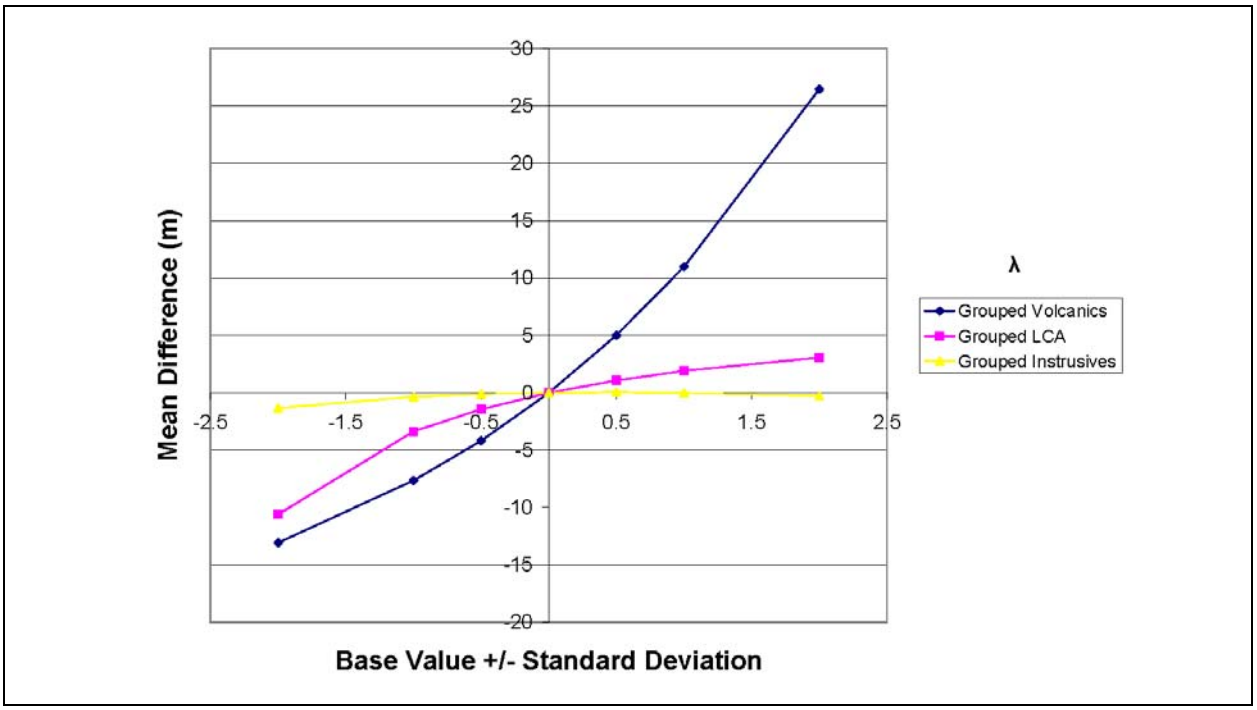

Figure 6-20
Mean Head Difference for Depth-Decay Parameters for BN-MME-ADA

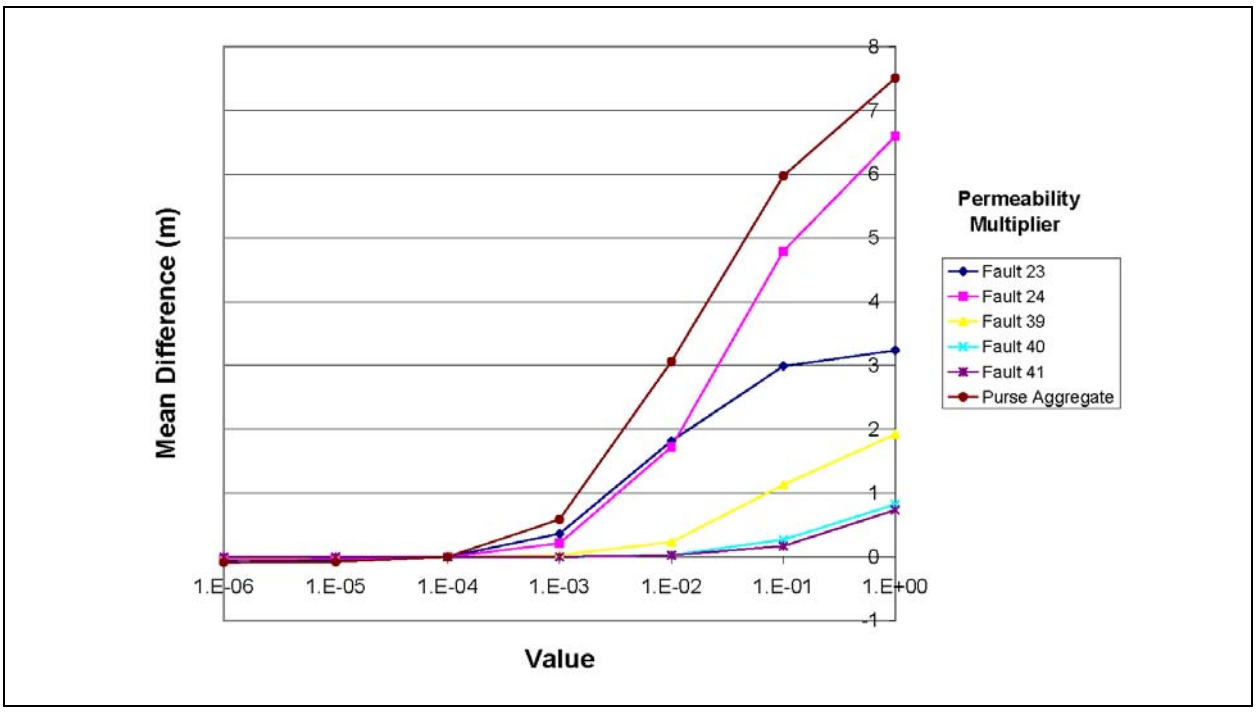

Figure 6-21
Mean Head Difference for Purse Fault Permeability Multipliers for BN-MME-ADA

Uncontrolled When Printed

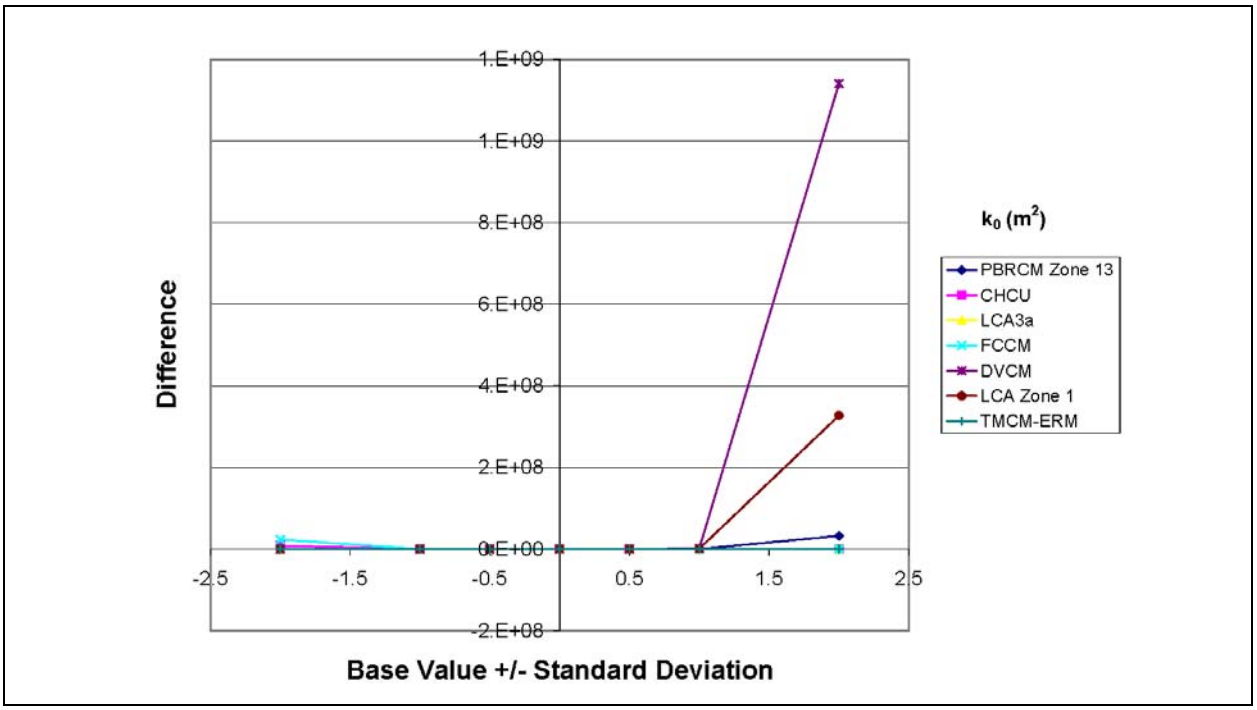

Figure 6-22
PHI Perturbation Plot for BN-MME-ADA

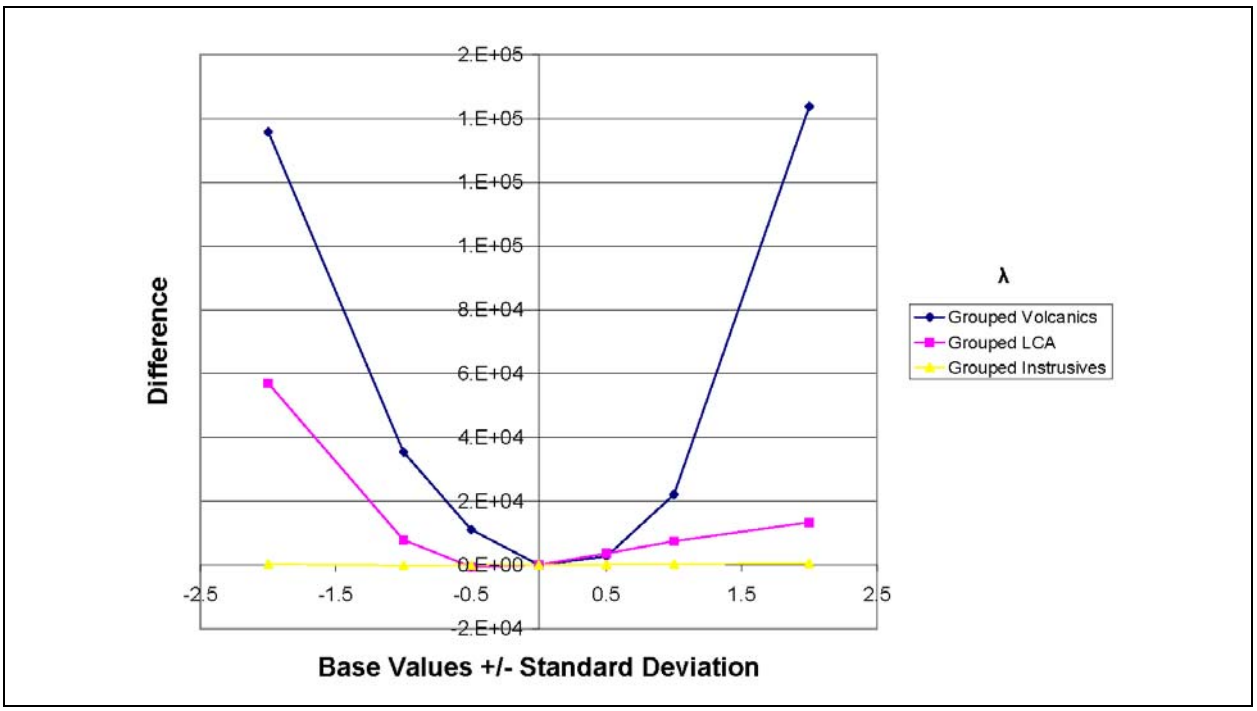

Figure 6-23
PHI Perturbation Plot for Depth Decay for BN-MME-ADA

Uncontrolled When Printed

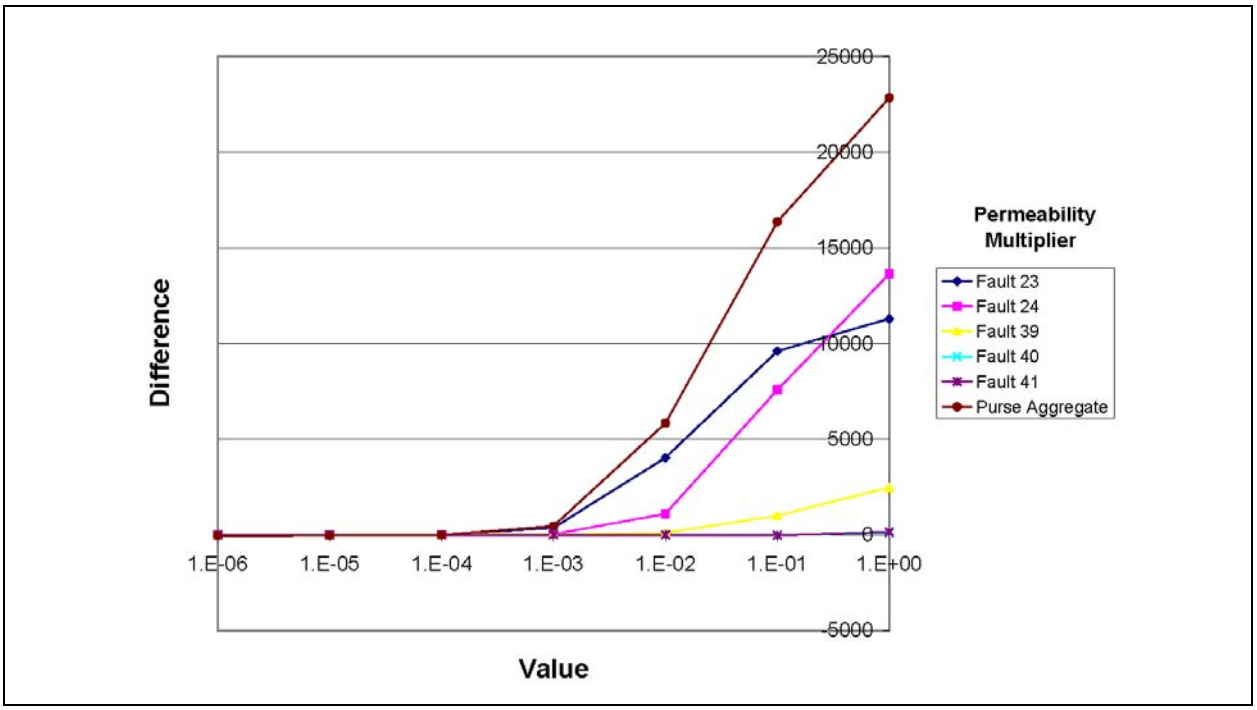

Figure 6-24
PHI Perturbation Plot for Purse Fault Permeability Multipliers for BN-MME-ADA

Pahute Mesa maintains its sensitivity in this model, although the BRA (sensitive in the selected HSU case) drops out. Thus, it seems that the interpretation of the cause of PBRCM sensitivity (presence throughout the CAU model, connection to northern boundary, and presence proximal to a large amount of calibration data) is valid. The sensitivity of the DVCM also suggests that it has a role that is independent of depth decay. In contrast, the IA k_0 appears as a mild influence on mean head, which is not like the selected HSU case.

The impact of the depth-decay parameter (Figure 6-20) of the volcanic HSUs dominates in comparison to the impact for those assigned to the LCA and the ICU; although the overall effect is not as strong as for the reference permeability, it is not negligible. This suggests that uncertainty in the depth-decay parameter (λ) is not, by itself, as critical as the reference permeability and the ICU properties matter very little (at least over the range investigated). Figure 6-21 shows that the fault permeability multipliers of the Purse Fault system and its individual components exhibit a threshold sensitivity relationship where heads increase with an increase in the fault permeability above a multiplier of 0.0001 but heads do not decrease for lower fault permeabilities. The Purse Fault permeability multiplier threshold is 10 times less than that observed for the base HFM - selected HSU

Uncontrolled When Printed

depth-decay and anisotropy parameterization. This may be because in order to maintain the same transmissivity with depth decay as without the permeability, the shallower parts of the HSU must be higher than the average value applied uniformly over the HSU thickness. Thus, a stronger fault to HSU contrast is required to achieve the same sealing effect. The main segment of the fault controls average head the most (it is also the longest individual segment of the Purse Fault system).

Figures 6-22 through 6-24 depict the perturbation plots for the objective function (PHI). Because the PEST sensitivity coefficients and the global sensitivity analysis both focus primarily on the objective function as the model output metric, these plots are most pertinent in comparing the results to those of the other analysis types. It is immediately apparent that most of the parameters shown in Figures 6-22 through 6-24 exhibit highly nonlinear sensitivity relationships over the range through which they were perturbed. This indicates that the sensitivity coefficients calculated by PEST are, in most cases, valid only locally (within a one-half standard deviation of parameter uncertainty or less).

Several other observations can also be made with respect to the perturbation plots of the objective function. Figure 6-22 shows that high values of k_0 for DVCM and LCA Zone 1 (zone along the southeastern edge from the UGTA regional model [DOE/NV, 1997]) have a very large effect on PHI while the large values distort the scale, within about ±1 standard deviation the effects of these parameters are minimal. In contrast, the depth-decay and fault permeability multiplier parameters have a significantly lower impact on PHI at the ends of the range of uncertainty. Figure 6-23 indicates that the minimum PHI with respect to the depth-decay parameters is generally centered (implying that it would be hard to improve the calibration by adjusting k_0) on the calibration point. The largest impact on PHI is coming from the volcanic HSU depth decay and the lowest impact from the depth decay of ICUs. The effects of carbonate HSU depth decay is more similar to ICUs than volcanic HSUs, but non-negligible. Figure 6-24 indicates that the fault permeability multipliers for the Purse Fault and its individual components exhibit a threshold sensitivity with low PHI values occurring for multipliers below approximately 0.0001 (consistent with the mean head behavior). Also, while the main segment of the Purse Fault (fault 24) has the greatest control on mean heads, it is the combined effects of the North Purse Fault (fault 24) and West Purse Fault (fault 23) that contribute to model calibration.

Uncontrolled When Printed

The most sensitive parameters with respect to the objective function are different than for the selected HSU depth-decay and anisotropy parameterization approach. Notably, the IA k_0 has some control on mean heads. Some parameters are sensitive in both this parameterization approach and in the BN-MME-SDA case (see Section 6.2.2.1), including the PCM, YMCFCM, and DVCM. The PCM and YMCFCM have depth decay in the all HSU and selected HSU decay cases, but DVCM does not, and yet it is still sensitive. On the other hand, the LCCU1 permeability was very sensitive without depth decay, but much less so with depth decay (this is explored further in Section 6.2.4.2).

6.2.2.3 SCCC HFM - Selected Depth-Decay and Anisotropy (SCCC-MME-SDA) Model Parameter Perturbation Analysis

For the SCCC HFM – selected depth-decay and anisotropy model (SCCC-MME-SDA), 45 permeability (including k_0) parameters, 10 vertical anisotropy parameters, 15 depth-decay parameters, and 29 fault permeability multiplier parameters were varied. In addition, vertical anisotropy was varied as a single grouped parameter and depth decay was varied as two groups – one for the carbonates and one for the volcanics as well as by HSU. This resulted in approximately 100 parameters that were varied. To generate results for each perturbation case required approximately 600 model runs.

Plots of mean difference in heads, difference in the objective function and its constituents, and difference in boundary fluxes were generated for each of the approximately 100 parameters in the SCCC-MME-SDA model perturbation analysis. All of these plots are shown in Appendix D, but Figures 6-25 through 6-28 describe selected sensitivity relationships.

Figures 6-25 through 6-28 show selected perturbation plots for the mean difference in heads at target locations. These figures indicate that the permeability, k_0, depth decay, and fault permeability multiplier parameters generally exhibit the same type of sensitivity relationships as observed in the base HFM where an increase in a parameter value is accompanied by a consistent trend of either an increase or decrease in the simulated head. In particular, PCM k_0 and DVCM permeability have the same one-sided behavior for all three models analyzed, where average head drops with increasing value; PCM much less so for this HFM. This is reasonable because outside the Silent Canyon Caldera all the HFMs are the same. The PBRCM k_0 also affects heads in the same one-sided fashion in all three models with head rising at higher values. The CHCU permeability, which in the SCCC

Uncontrolled When Printed

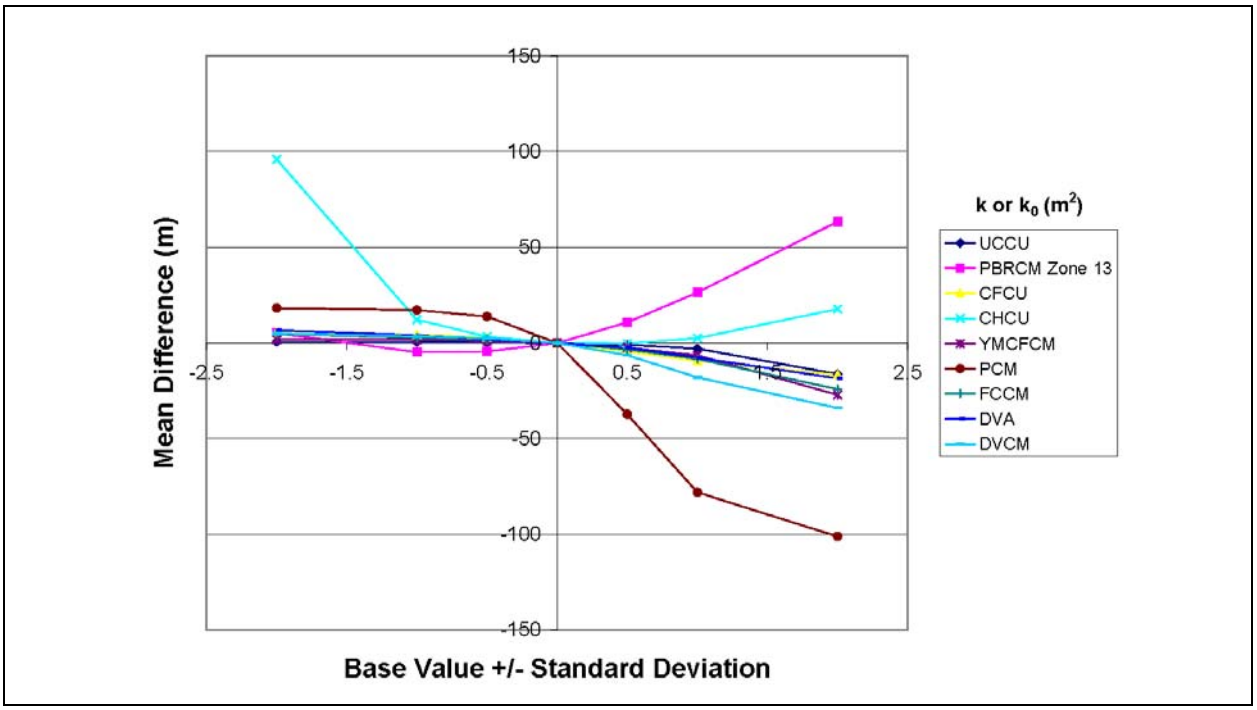

Figure 6-25
Mean Head Difference for SCCC-MME-SDA

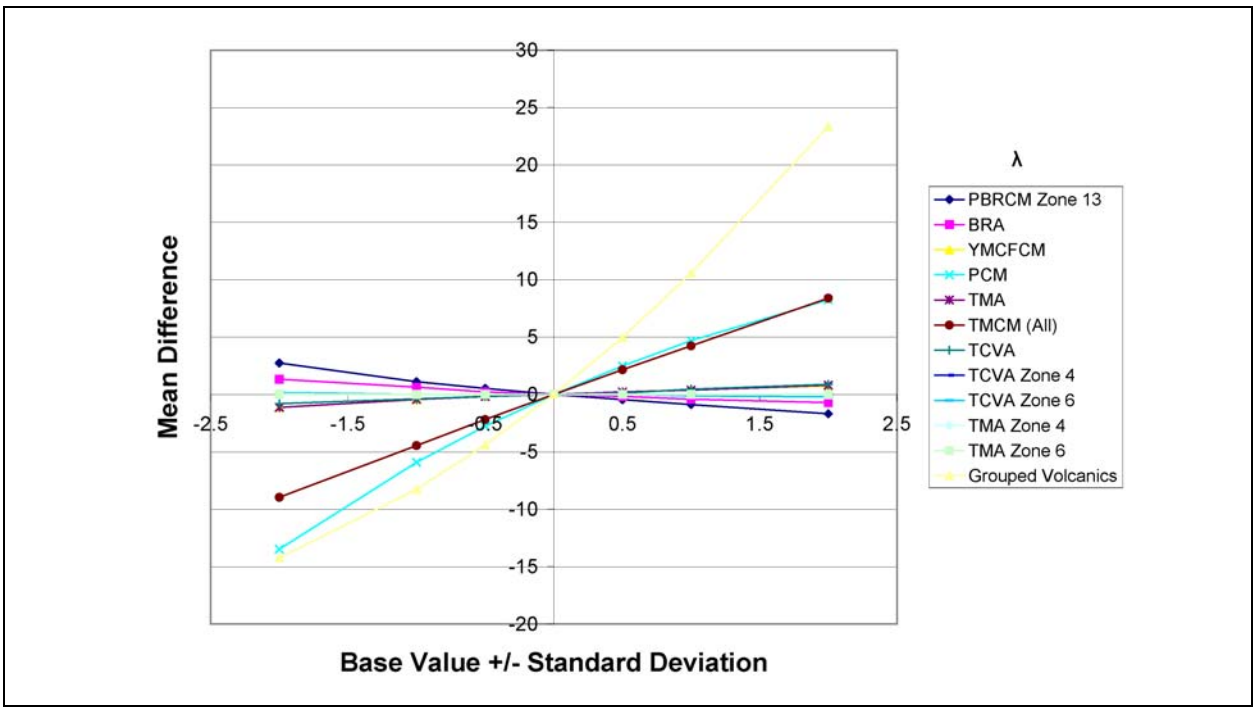

Figure 6-26
Mean Head Difference for Volcanic HSU Depth Decay for SCCC-MME-SDA

Uncontrolled When Printed

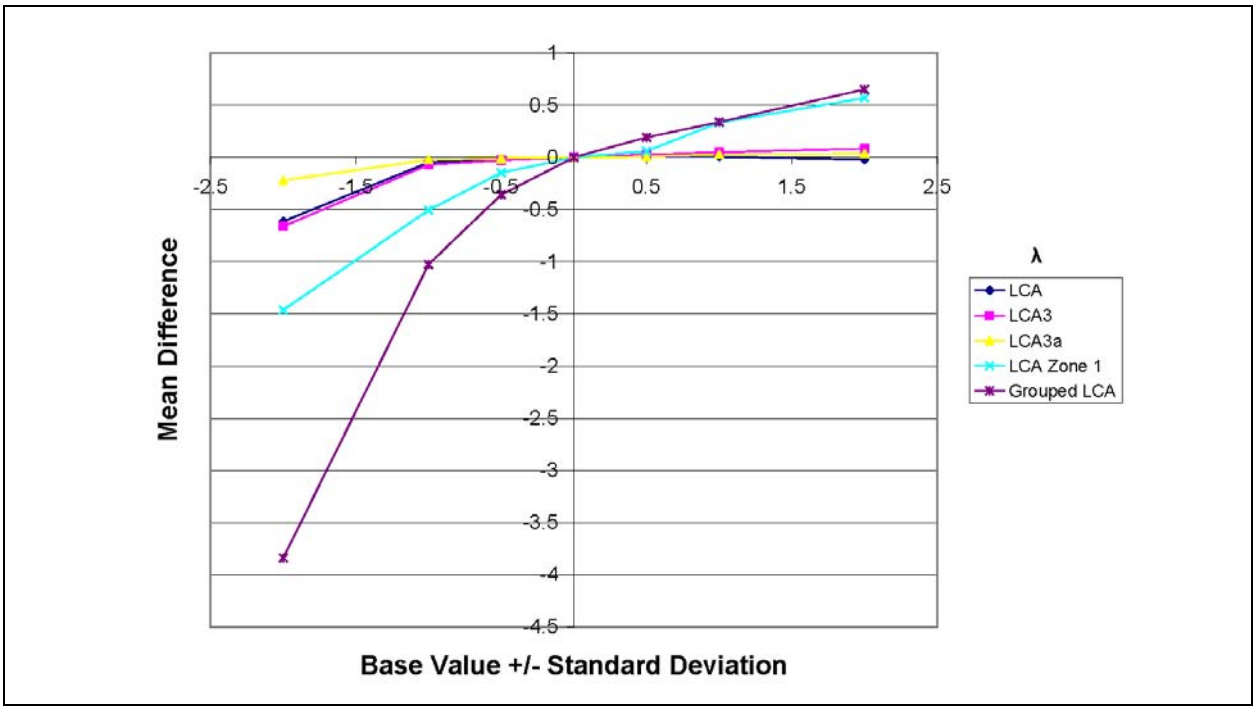

Figure 6-27
Mean Head Difference for Carbonate HSU Depth Decay for SCCC-MME-SDA

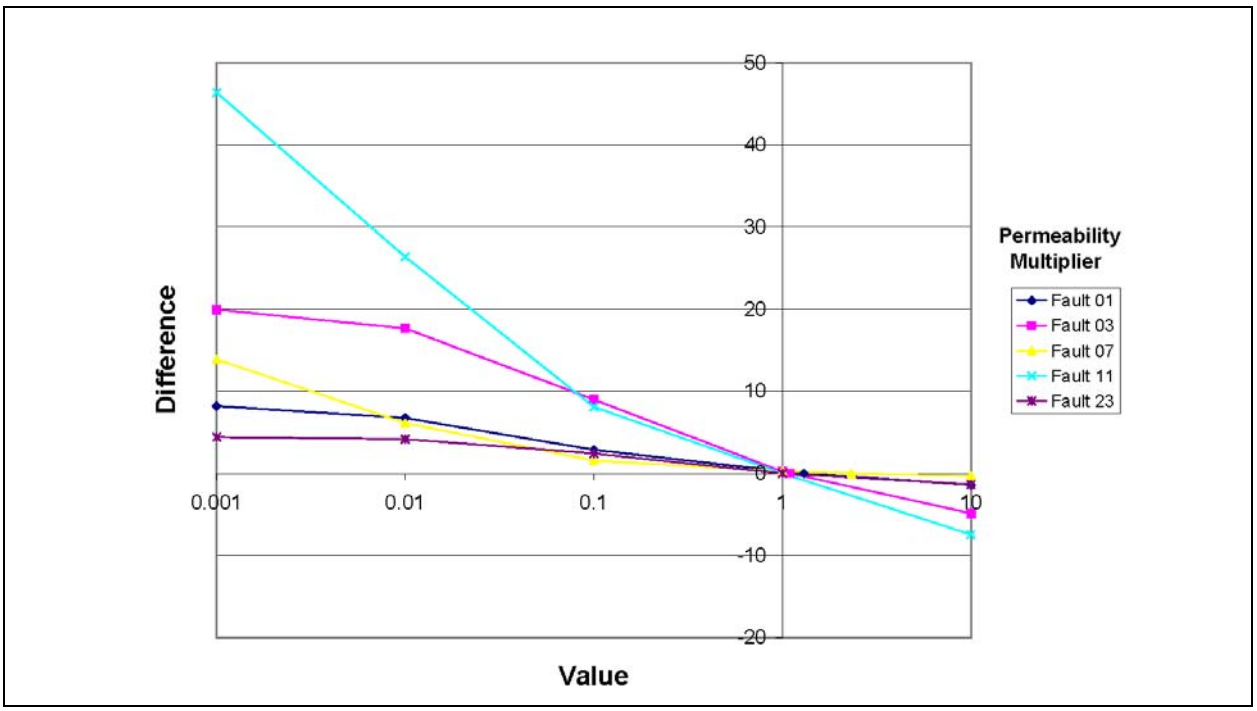

Figure 6-28
Mean Head Difference for Sensitive Fault Permeability Multipliers for SCCC-MME-SDA

Uncontrolled When Printed

HFM represents all the Calico Hills units (represented as five HSUs in the base HFM) affects mean heads the same (always higher) at either the lowest or highest values, and appears as a sensitive parameter because its lumping makes it a relatively large unit with many calibration targets. Physically, the interpretation of the effect of the YMCFCM and PCM to lower heads at increased permeability is to allow water to exit out of and head to drop lower on the southern boundary. The PBRCM effect at higher permeabilities is to increase the influence of areas of higher head to the northeast and east.

The effect of depth decay (Figures 6-26 and 6-27) is larger for the volcanic HSUs than the LCA, most likely because all the head calibration data exist in the volcanic HSUs, with the LCA deriving its sensitivity from the boundary flows. Figure 6-26 shows that it is cumulative effect of depth decay, rather than depth decay of any single unit, that gives depth decay control on mean head, although the PCM (followed closely by the TMCM) is the single most important HSU.

The effects of the faults, shown in Figure 6-28, is similar to the base HFM in that an approximate one-sided behavior is noticed. The faults shown in Figure 6-28, in order of influence on mean head difference, are the Ammonia Tanks Caldera Structural Margin (fault 11), the Claim Canyon Caldera Structural Margin (fault 03), West Greeley (fault 07), Silent Canyon Caldera Margin (fault 01), and the Hogback (fault 23) (see Figure 4-9 for locations). Fault 11 rings Timber Mountain, and as its permeability multiplier is dropped, recharge that occurs there due to orographic effects accumulates and increases heads. The Claim Canyon Caldera Structural Margin is interesting because it was identified in the BN-MME-SDA sensitivity coefficient analysis (see Section 6.2.1.1) as a sensitive feature. The West Greeley Fault, as shown in Figure 4-10, is one of the deepest and most continuous faults in the SCCC HFM, hence its sensitivity. Fault 01 rings most of Areas 19 and 20, and while it is sensitive conceptually, it would be thought that it would have a stronger influence. Finally, the Hogback Fault runs north-south through Oasis Valley, and is thought to exercise some kind of control on heads and flows in that region.

Figures 6-29 through 6-32 present the perturbation plots for the objective function (PHI). Because the PEST sensitivity coefficients and the global sensitivity analysis both focus primarily on the objective function as the model output metric, these plots are most pertinent in comparing the results to those of the other analysis types. It is immediately apparent that most of the parameters shown in

Uncontrolled When Printed

Figures 6-29 through 6-32 exhibit highly nonlinear sensitivity relationships over the range through which they were perturbed. This indicates that the sensitivity coefficients and other statistical diagnostics calculated by PEST are, in most cases, valid only locally in the vicinity of the calibration point.

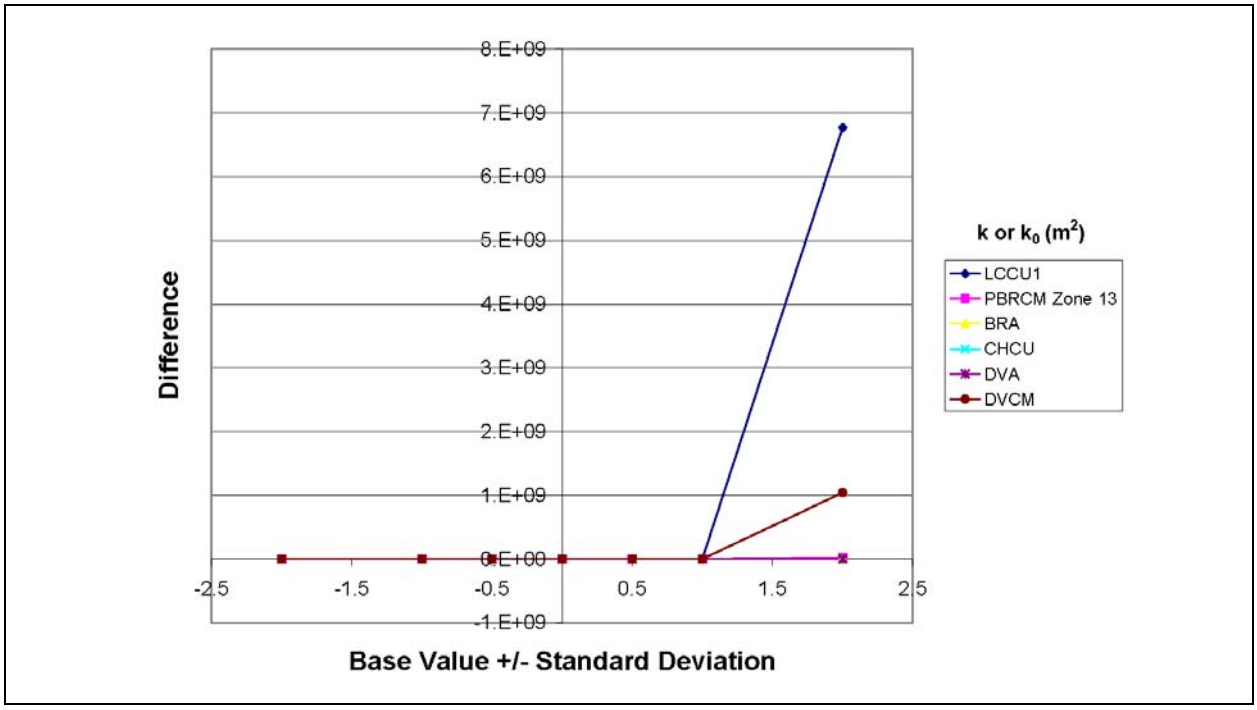

Figure 6-29
PHI Perturbation Plot for SCCC-MME-SDA

Several other observations can also be made with respect to the perturbation plots of the objective function. Like the selected HSU depth-decay and anisotropy base HFM, Figure 6-29 shows that higher permeability for LCCU1 and DVCM have a very large effect on PHI. The role of the LCCU1 in the base HFM selected HSU depth decay and anisotropy is the same as in the SCCC HFM, and it is concluded that adding depth decay to the LCCU1 causes a fundamental change in how the unit acts in the model. It was noted in Section 5.6.3 that WW-8 had the largest misfit in the all HSU depth-decay case, but is reasonably fit in the selected HSU approach even with two different HFMs (although outside the Silent Canyon Caldera the HFMs are the same). The depth-decay and fault permeability multiplier parameters have a significantly lower impact on PHI, although relative to the calibration, the PCM depth decay almost completely dominates the volcanic HSU depth-decay parameter sensitivity on PHI. Figure 6-30 indicates that the minimum PHI with respect to the volcanic

Uncontrolled When Printed

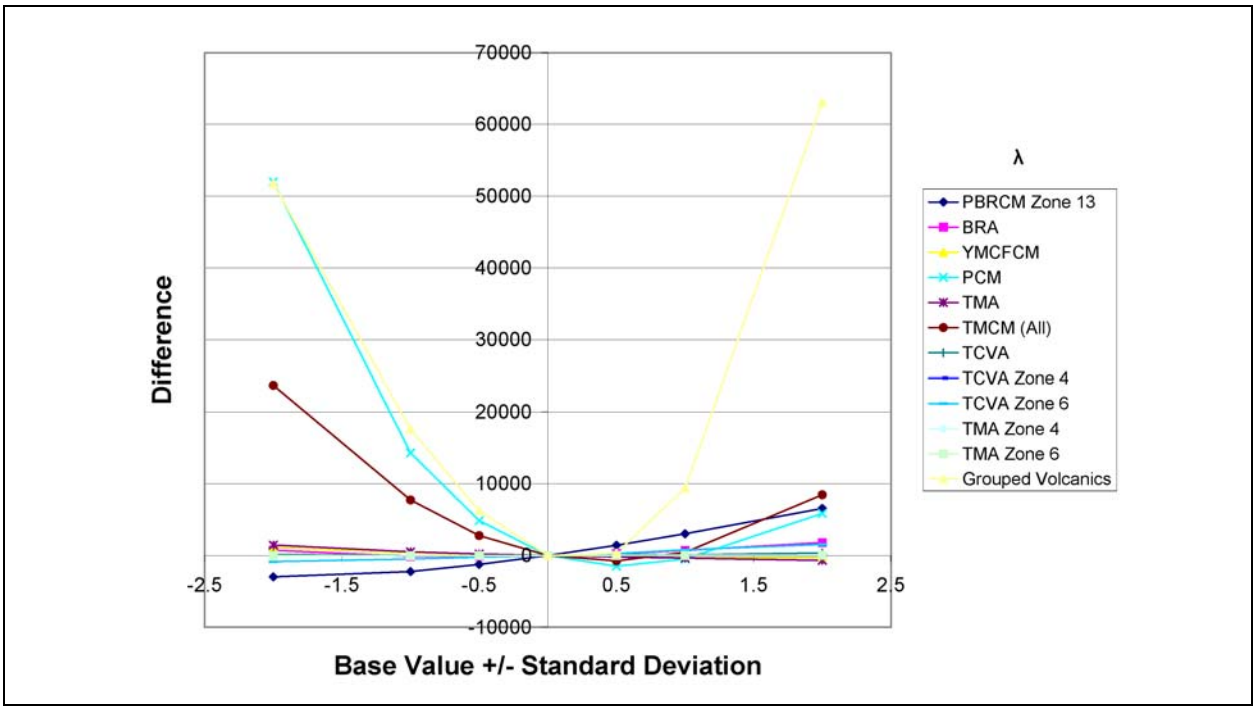

Figure 6-30
PHI Perturbation Plot for Volcanic HSU Depth Decay for SCCC-MME-SDA

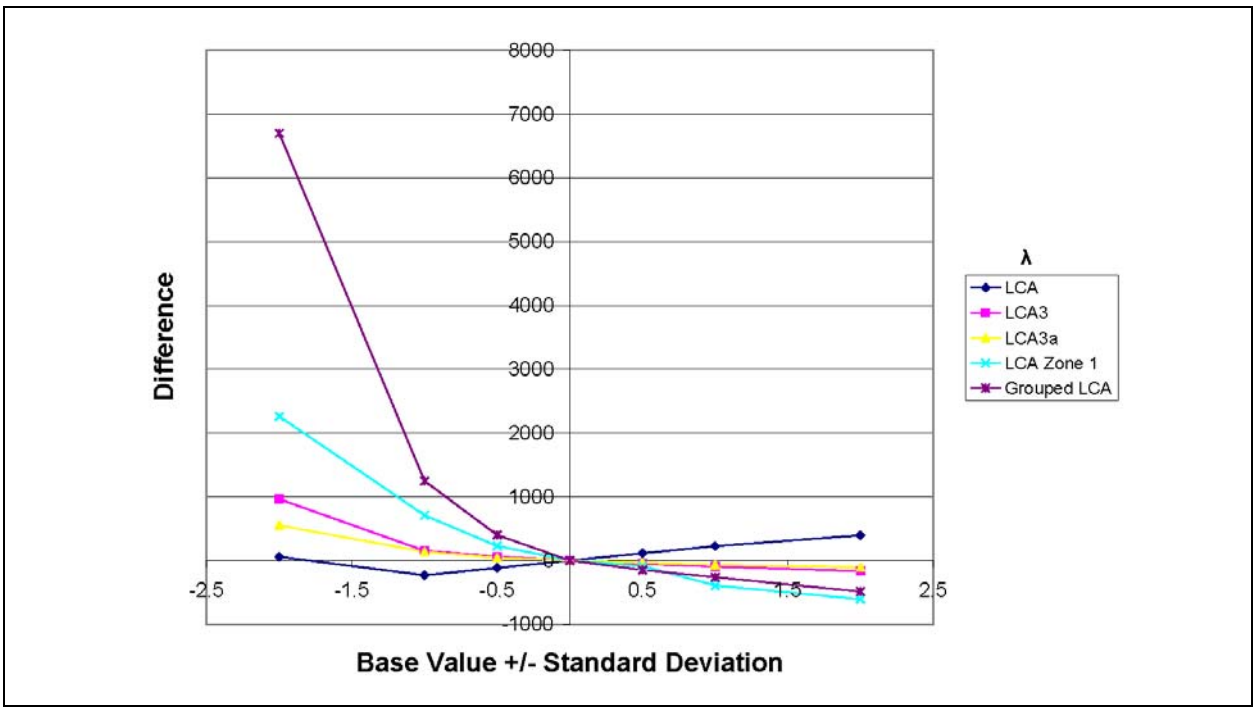

Figure 6-31
PHI Perturbation Plot for Carbonate HSU Depth Decay for SCCC-MME-SDA

Uncontrolled When Printed

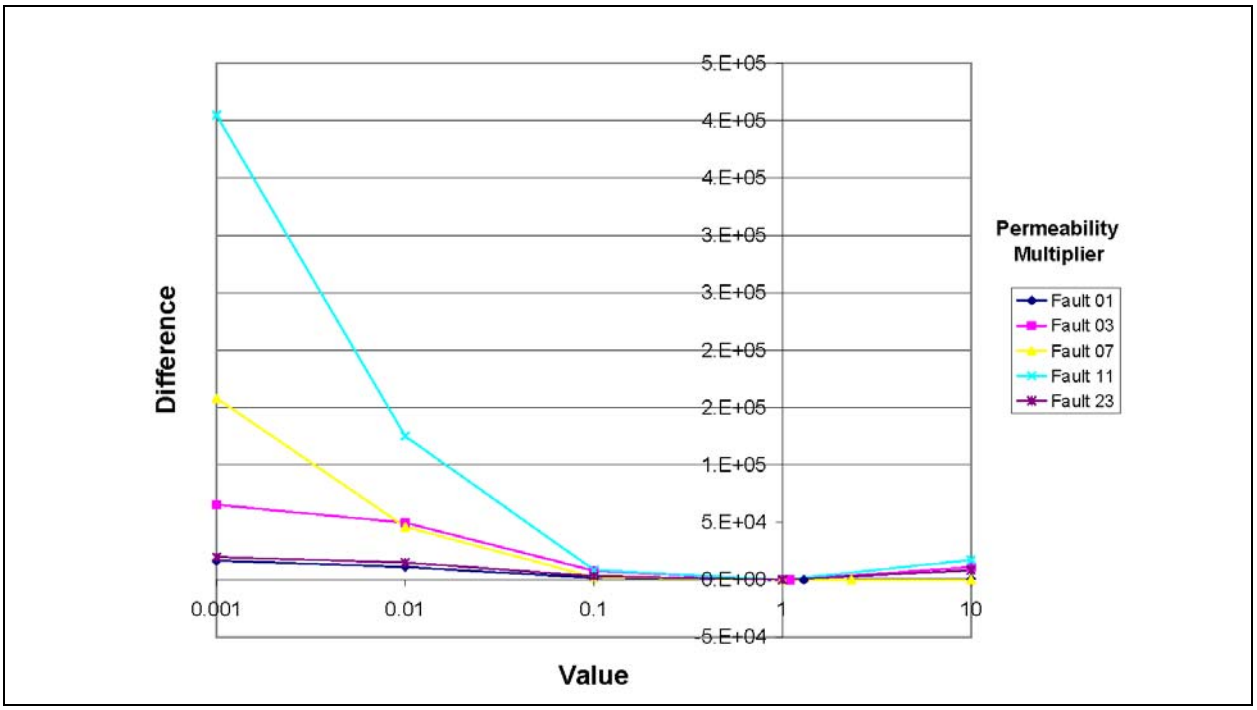

Figure 6-32
PHI Perturbation Plot for Sensitive Fault Permeability Multipliers for SCCC-MME-SDA

depth-decay parameters is generally centered on the calibration point. In contrast, the minimum PHI with respect to the carbonate depth-decay parameter occurs at values higher than the calibrated value as seen in Figure 6-31, although the effect is minor. Figure 6-32 shows the perturbation plots for the most sensitive faults in the SCCC HFM - selected depth-decay and anisotropy model. Dropping the fault permeability multiplier for the Silent Canyon Caldera Margin causes degradation in model fit, while enhancing the fault causes no improvement. Again, there is little sensitivity to the Purse and Boxcar Faults because their limited depth does not give a strong model response. The most sensitive fault is the Ammonia Tanks Caldera Structural Margin (fault 11) ringing Timber Mountain. The West Greeley Fault (fault 07) is also sensitive in controlling calibration on Pahute Mesa, at least in part because it extends to a greater depth on Pahute Mesa than most other faults in the SCCC HFM (see Figure 4-11).

Uncontrolled When Printed

6.2.3 Global Parameter Sensitivity

The motivation for this analysis is described in Section 6.1.1.2. The work flow for the global sensitivity analysis was as follows:

1. Identify adjustable parameters and their ranges.
2. Determine form and components of objective function used for model calibration.
3. Create an experimental design that uniformly samples parameter space.
4. Run forward model for each design point and compute the objective function.
5. Analyze variable importance with respect to objective function.

The adjustable model parameters can be broadly divided into three categories: (a) permeability (including k_0) of the HSUs and the faults (permeability multiplier), (b) anisotropy ratios for a limited number of HSUs, and (c) depth-decay parameters for HSU groups. The parameters were assigned log-normal/normal or log-uniform/uniform distributions to capture the expected range over which they are realistically expected to vary. The central tendency value for each distribution was taken to be the best estimate from the calibrated models.

The objective function is the standard weighted sum-of-squares form, and has four components including: (1) measured heads at observation wells, (2) estimated model boundary flows, (3) spring heads, and (4) Oasis Valley flow. Each observation was assigned a unique weight as described in Section 5.2. Weights were chosen to reflect measurement error and/or reliability of the individual measurement, as well as judgment of the relative importance of different kinds of measurements.

Sampling of the adjustable parameters over the assigned range was carried out using Latin Hypercube sampling, an efficient modification of Monte Carlo random sampling. In order to ensure that this stratified sampling approach does not produce any spurious correlation between any two arbitrary parameters, the restricted pairing technique (Iman and Conover, 1979) was used to force zero correlation between all variable pairs. This strategy produces a “space-filling” design such that all regions of an input-input scatter plot would appear to be equally filled by the sampling scheme. A sample size of 1,000 was chosen as a compromise between sampling density and computational overhead. Forward simulations were carried out for each of the 1,000 sample sets of parameters, and the components of the objective function computed.

Uncontrolled When Printed

After eliminating the non-convergent realizations, classification tree analyses were completed using the lowest 10 percent and the highest 10 percent values of each metric. The rationale for using the 10 percent cutoff is to generate a subset with about 100 realizations so that statistical sensitivity analysis techniques can be applied to produce results with a reasonable degree of reliability. The R-statistical software (Gentleman and Ihaka, 2005) was used for the classification tree analysis. Entropy analyses were completed on the entire dataset for each metric. Model-specific details are given in the results section for each model.

In interpreting classification tree results, it is important to remember that the category "low" refers to the smallest 10 percent PHI values and the category "high" refers to the largest 10 percent PHI values. Each node of a classification tree is labeled with the number of each category that has cascaded to that node, with the number of "high" values comprising the first and the number of "low" values comprising the second. For example, "68/0" indicates that 68 from the "high" category have cascaded to the node. A perfect categorization can be obtained with just two splits. Also, some judgment of the importance of the variables can be made from the structure of the tree itself.

6.2.3.1 Base HFM - Selected HSU Depth-Decay and Anisotropy (BN-MME-SDA) Model

Of the 1,000 Monte Carlo realizations performed to identify key parameters for the base HFM - selected HSU depth-decay and anisotropy (BN-MME-SDA) model, approximately 17 percent did not converge. Global sensitivity analyses of the 83 percent remaining simulations are presented below.

Figure 6-33 shows a line plot of the best 100 percent simulations ranked in terms of PHI. Also shown are the components of PHI based on head measurements (WELL), boundary fluxes (FLUX), spring elevations (SPRING) and Oasis Valley discharge (ETF). It is clear that the primary contributors to PHI are WELL and FLUX, with lesser contributions from ETF and SPRING. Another interesting observation is that simulations where WELL is the dominant contributor to PHI are distinct from simulations where FLUX is the dominant contributor. This suggests that these two components of the objective function are controlled by different groups of model parameters.

Table 6-2 shows the Spearman rank correlation matrix for PHI, WELL, SPRING, FLUX and ETF for the simulations with the lowest 10 percent PHI values (the data shown in Figure 6-34). The strong correlation between PHI and WELL and PHI and FLUX noticed in Figure 6-34 can be clearly

Uncontrolled When Printed

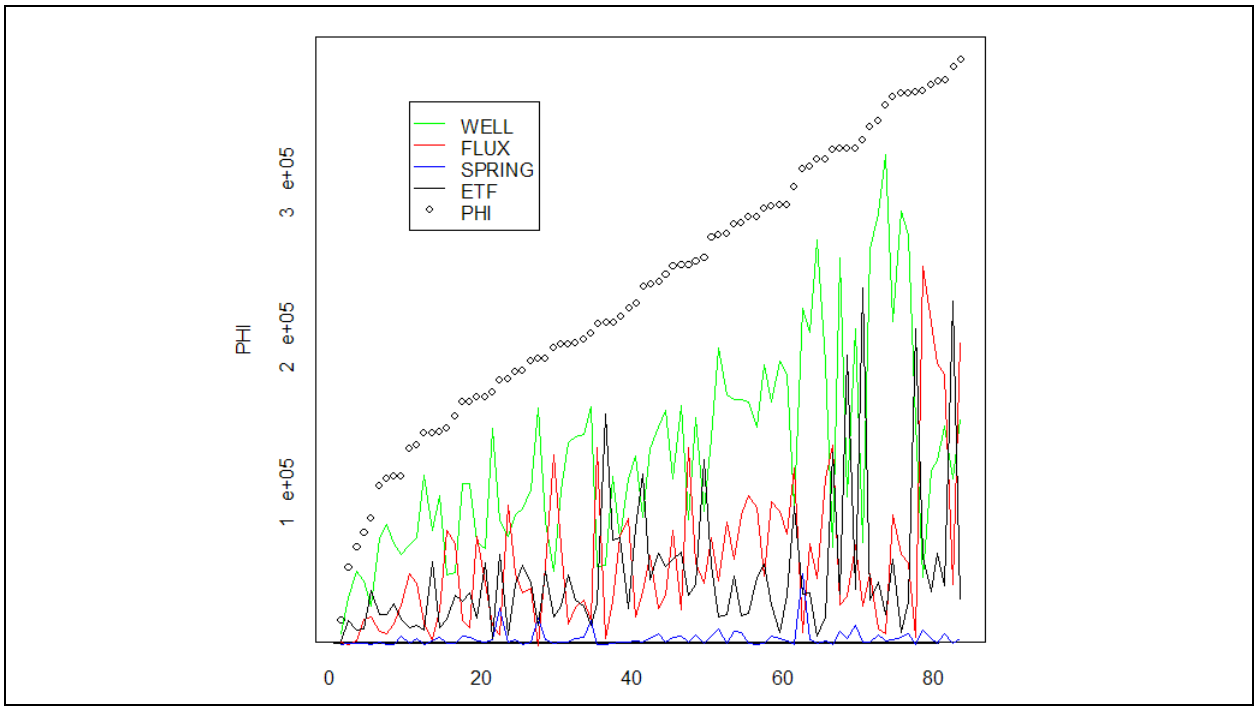

Figure 6-33
100 Best Simulations Ranked by PHI for BN-MME-SDA

Table 6-2
Spearman Rank Correlation Matrix for BN-MME-SDA

	PHI	WELL	SPRING	FLUX	ETF
PHI	1	0.66	0.26	0.49	0.39
WELL	0.66	1	0.46	0.11	-0.03
SPRING	0.26	0.46	1	0.03	-0.04
FLUX	0.49	0.11	0.03	1	0.05
ETF	0.39	-0.03	-0.04	0.05	1

discerned in this table. Also note the strong correlation between WELL and SPRING, suggesting a common set of controlling parameters for these two components of the objective function.

In the following classification tree analyses, the logarithm of permeability will be presented; all other variables will be untransformed. This results in negative numbers because permeability units are m^2, which nearly always has a negative exponent.

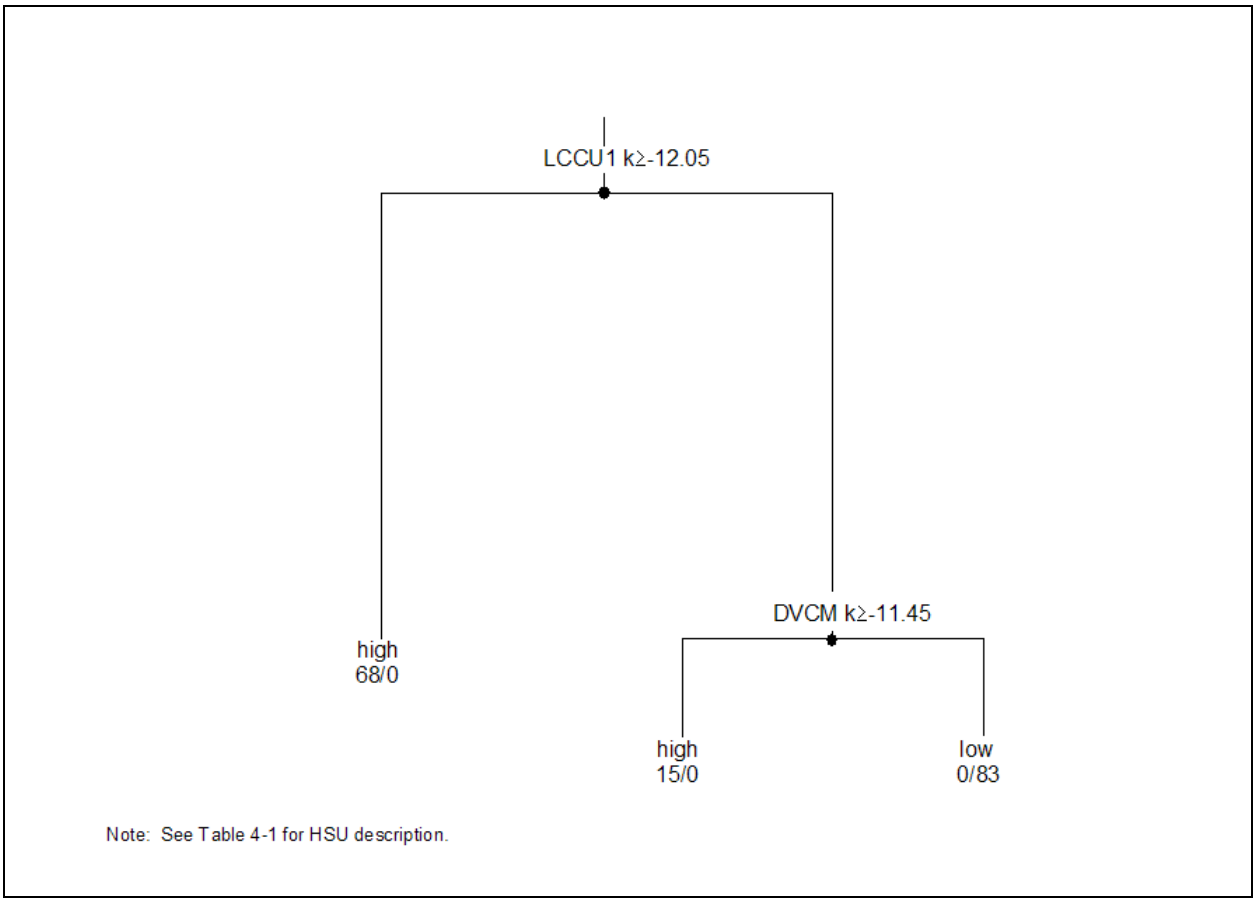

Figure 6-34
Classification Tree on PHI for BN-MME-SDA

A classification tree analysis to determine the decision rules separating the smallest and largest 10 percent of PHI values in Figure 6-33 is shown in Figure 6-34. Here, LCCU1 permeability is the most important because it was chosen for the first split, followed by DVCM permeability. Recall that these parameters were also identified in the sensitivity coefficient and parameter perturbation analyses. The fact that they are identified in the global sensitivity analysis means that their sensitivity is not just a local effect, and that they exercise control on PHI over the full range of possible model outcomes and parameter uncertainty.

The next set of analyses deal with the individual components of PHI. Figure 6-35 shows a classification tree analysis for WELL. Note that the important variables for this case, YMCFCM and PCM reference permeability, are different from those identified earlier for the total objective function (PHI). Also note that the two-variable classification does not produce two pure groups, because the

Uncontrolled When Printed

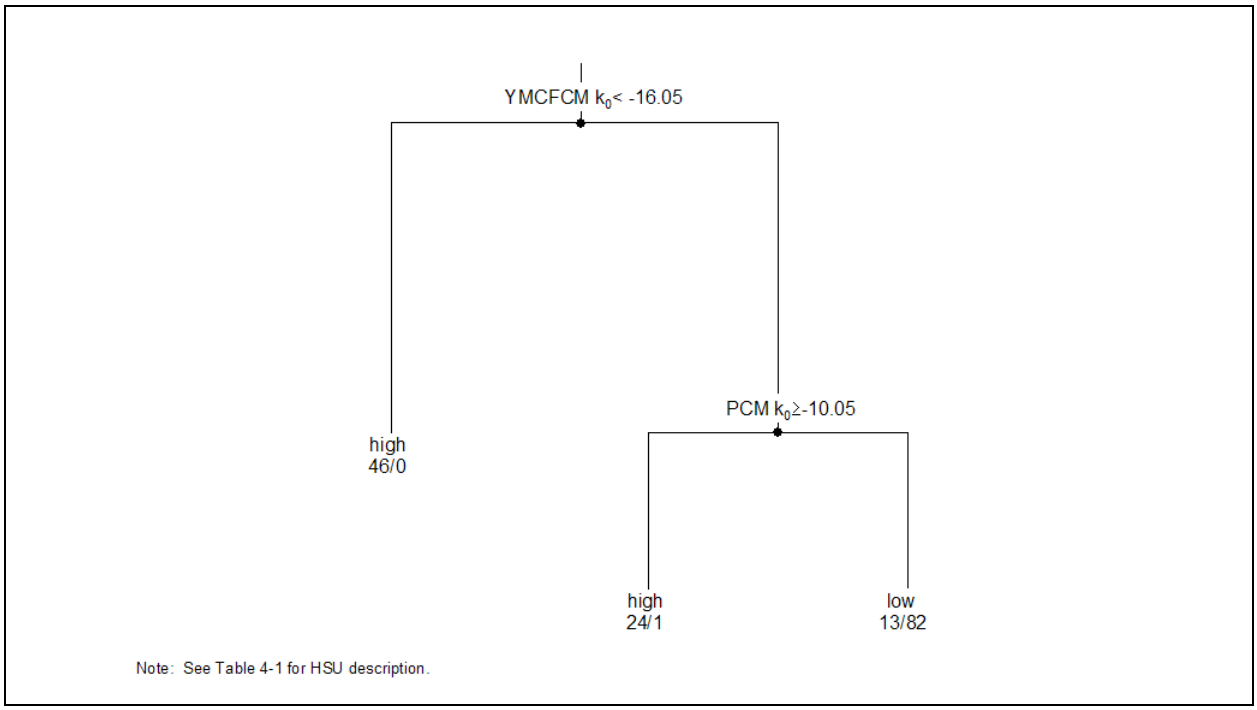

Figure 6-35
Classification Tree on WELL for BN-MME-SDA

node at the far right-hand side of the tree contains 13 high and 82 low values. Thus, the isolation of the group corresponding to the smallest 10 percent of WELL values is not as straightforward as in the case of PHI. Again, the reference permeabilities of YMCFCM and PCM have been previously identified as having an important role in controlling mean head in the model domain and the goodness-of-model calibration.

A similar situation can be seen in the classification tree analysis for SPRING. Figure 6-36 shows the classification tree for SPRING. The lowest 10 percent SPRING values cannot be perfectly explained using two or three variables. Also, the key variables controlling the "low" SPRING values (i.e., PCM k_0 and YMCFCM k_0) are the same as those controlling the lowest 10 percent WELL values (hence the correlation in model output shown in Table 6-2).

Figure 6-37 presents the classification tree separating the subset of FLUX values. The main parameter that influences this model output, almost exclusively by the purity of the split, is LCCU1 permeability. These are very similar to those presented earlier for the total objective function PHI, and primarily reflect the strong correlation between high PHI and high FLUX values. The conclusion

Uncontrolled When Printed

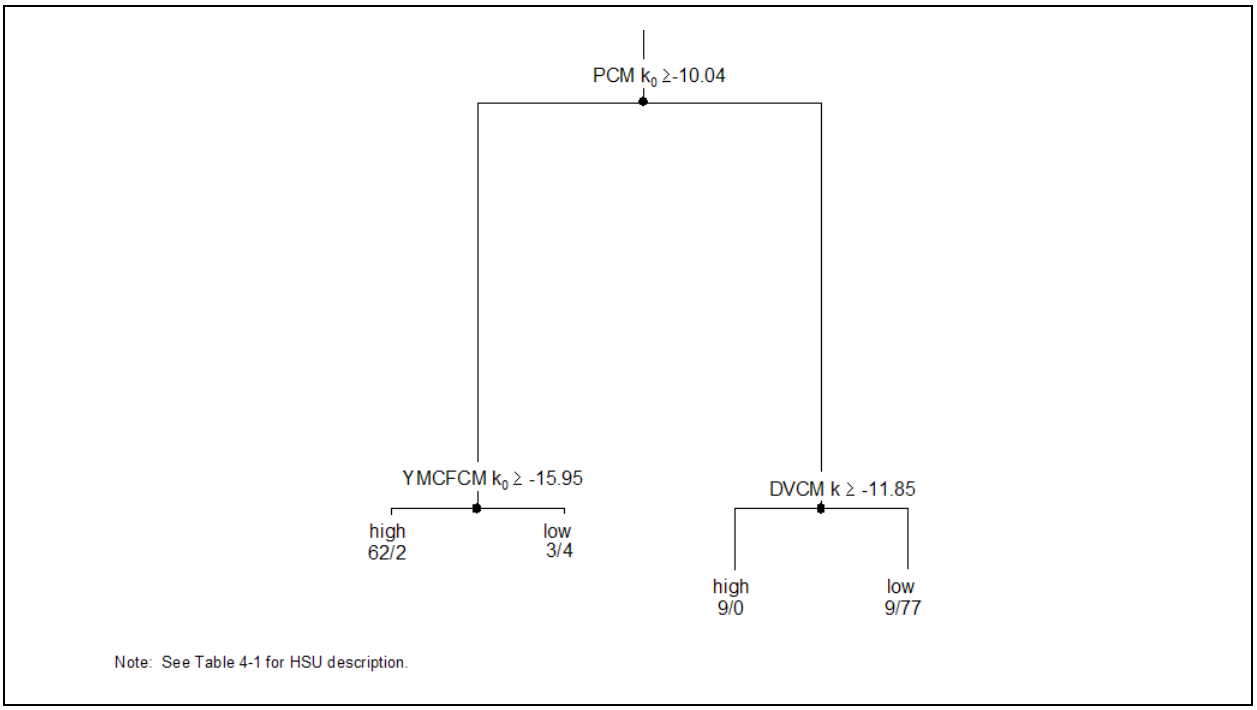

Figure 6-36
Classification Tree on SPRING for BN-MME-SDA

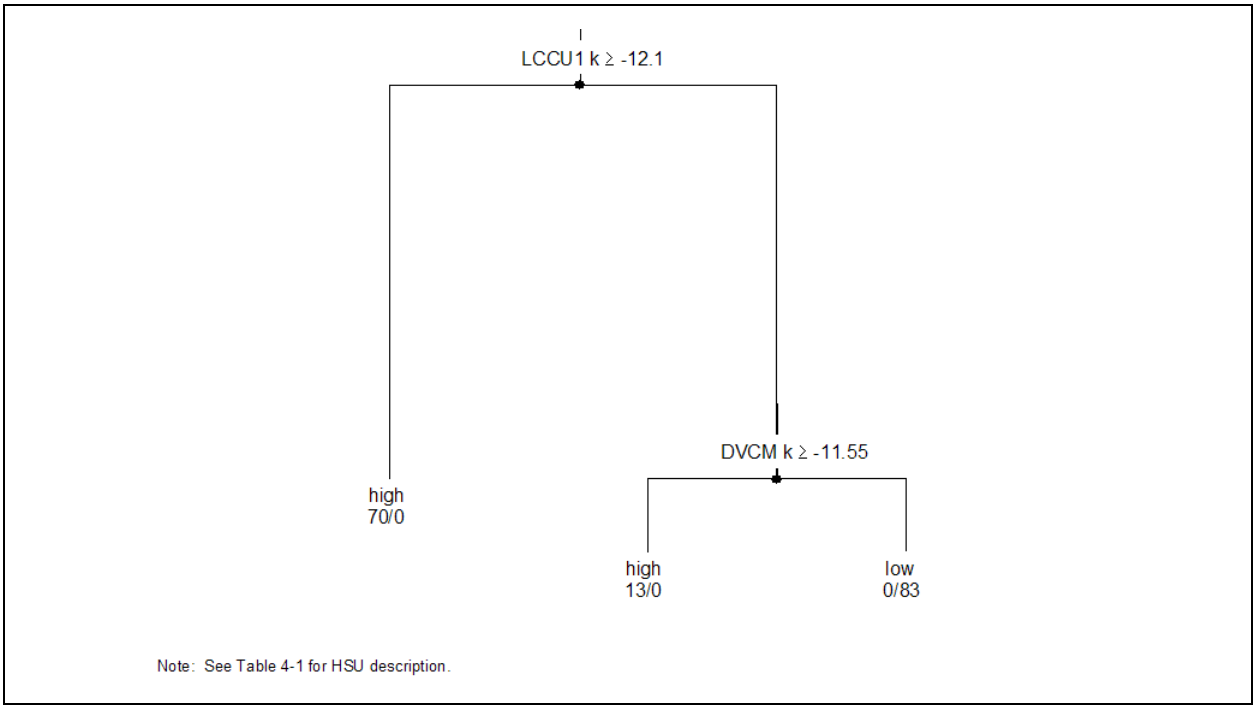

Figure 6-37
Classification Tree on FLUX for BN-MME-SDA

Uncontrolled When Printed

to be drawn from this observation is that combinations of parameter values that produce high FLUX (e.g., high LCCU1 permeability) values are incompatible with low PHI values.

Finally, the classification tree for Oasis Valley discharge is presented in Figure 6-38. Here, a two-variable split is almost perfectly capable of separating the ETF values. Also of interest is the fact that one of the important variables (DVCM permeability) was also identified as important in isolating low values for FLUX and SPRING.

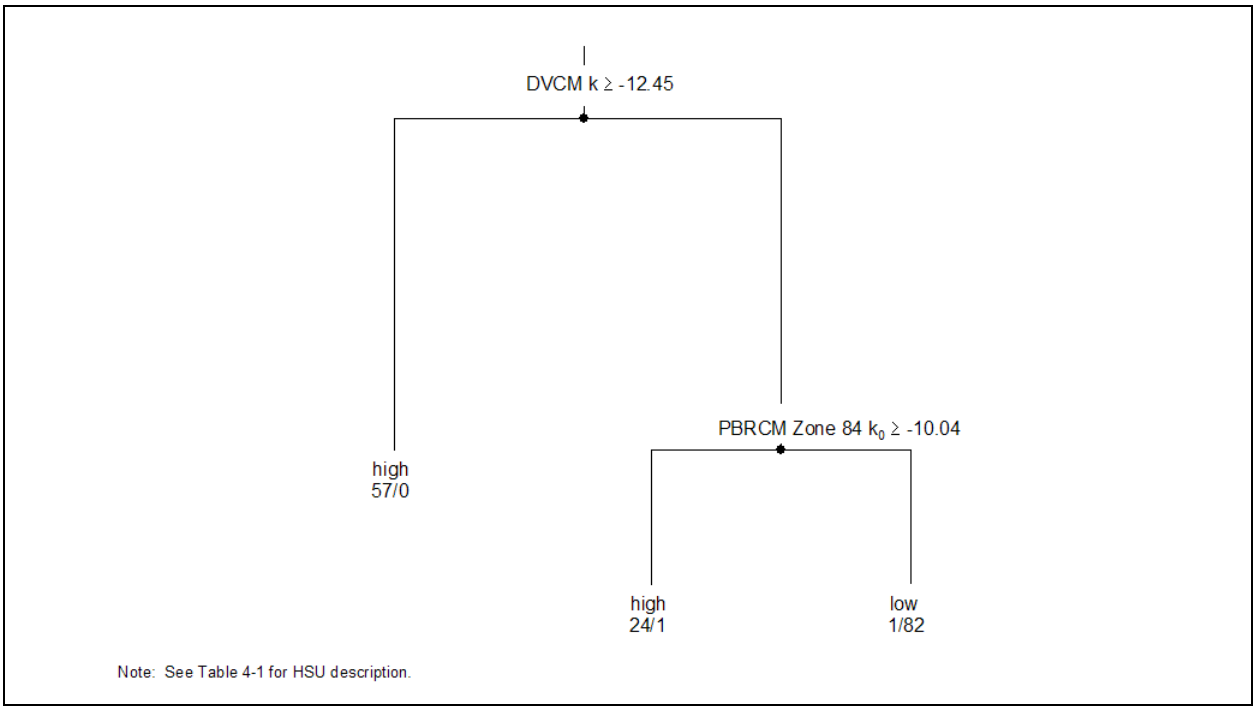

Figure 6-38
Classification Tree on ETF for BN-MME-SDA

The entropy analysis for PHI is shown in Table 6-3. Based on the R-statistic, the top two variables have distinct patterns of association with PHI, and also happen to be the same in order of importance as the top two variables identified from classification tree analysis in Figure 6-34. The other variables appear to have less definitive association.

Figure 6-39 shows bubble plots for the top four variables, where the entries of the contingency table are shown as bubbles of varying sizes. Here, the contingency table is organized such that the quintiles (0-20 percentile, 20-40 percentile, 40-60 percentile, 60-80 percentile, 80-100 percentile) of the

Uncontrolled When Printed

Table 6-3
Results of Entropy Analysis on PHI for BN-MME-SDA

Rank	Variable	R-Statistic
1	LCCU1 k	0.68
2	DVCM k	0.46
3	PBRCM Zone 84 k_0	0.30
4	PCM k_0	0.22
5	TCVA λ	0.19

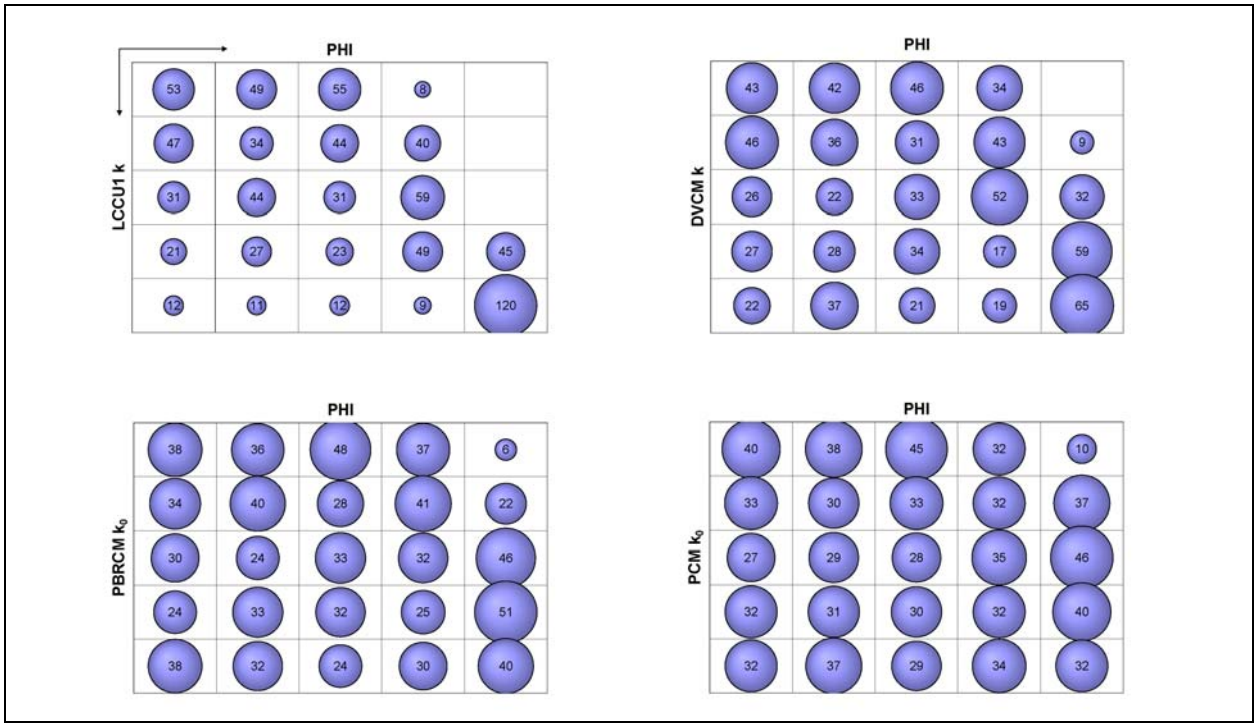

Figure 6-39
Bubble Plots from Entropy Analysis on PHI for BN-MME-SDA

independent variable (input) increase from left to right, and that of the dependent variable (output) increase from top to bottom. The size of the bubble indicates how many observations fall in each quintile-quintile box. The relative importance of the top two variables, LCCU1 and DVCM, is clearly seen through the distinctive patterns in the upper panels. On the other hand, the near-uniform size of the bubbles in the bottom charts indicates the marginal relevance of the other two top-ranked variables.

Results for the entropy analysis of WELL are shown in Table 6-4. Based on the R-statistic, the top two variables are not as dominant or as distinctive as those corresponding to PHI. Also, the order of importance is reversed as compared to the importance ranking from classification tree analysis shown in Figure 6-35. The effects of PCM k_0 and YMCFM k_0 are also opposite; many good results are associated with high values of YMCFCM k_0 and many good results are associated with lower PCM k_0. This effect was also noticed in the perturbation analysis. Because the perturbation analysis sampled for the same distribution types and parameters, the results are similar. However, the global analysis would allow any compensating effects to manifest themselves, and either there are not any or the sample set is too small. The absence of distinctive input-output patterns can also be seen in the bubble plots presented in Figure 6-40, where even the top two variables (top panel) do not appear to be significantly different from the next two variables (bottom panel) in terms of exhibiting distinctive trends.

Results for the entropy analysis for FLUX are given in Table 6-5, with the corresponding bubble plots presented in Figure 6-41. The top two variables (LCCU1 and DVCM permeability) are the same as those identified by the classification tree analysis for FLUX in Figure 6-37 and were noted as sensitive in the sensitivity coefficient and perturbation analyses. As noted earlier, the top-ranked variables for PHI and FLUX are identical, suggesting that a strong correlation between high PHI and high FLUX values may be influencing these results. As mentioned previously, the thrusted LCCU (LCCU1) permeability is unknown, and it seems odd conceptually that it should have an important role in the flow model. It is possible to generate reasonable results at lower LCCU permeability as shown in Figure 6-41, but poor results are strongly associated with the highest values. Thus, while a great deal of uncertainty exists in LCCU1 permeability, at least the upper limit is implausible, and lower values may be more appropriate. Section 6.2.4.2 and Section 7.0 explore this further.

Uncontrolled When Printed

Table 6-4
Results of Entropy Analysis on WELL for BN-MME-SDA

Rank	Variable	R-Statistic
1	PCM k_0	0.34
2	YMCFCM k_0	0.32
3	PBRCM Zone 84 k_0	0.22
4	CFCU k	0.20
5	DVCM k	0.20

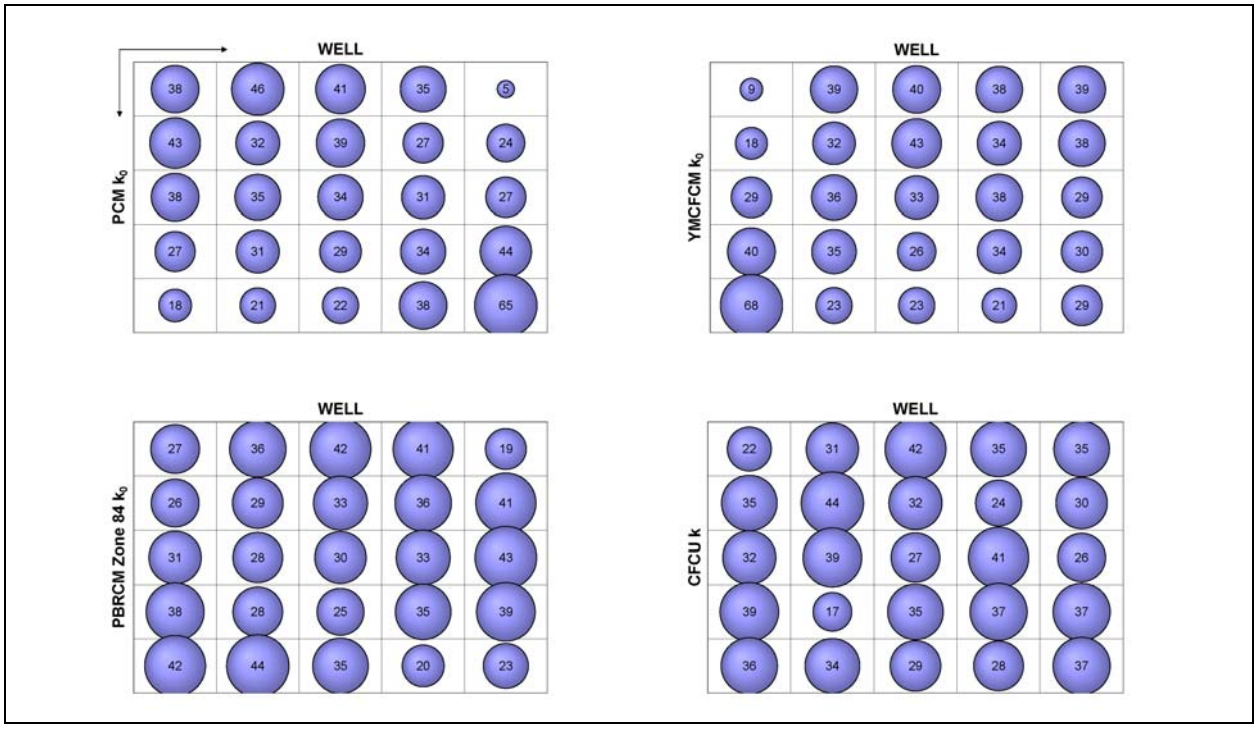

Figure 6-40
Bubble Plots from Entropy Analysis on WELL for BN-MME-SDA

Uncontrolled When Printed

Table 6-5
Results of Entropy Analysis for FLUX for BN-MME-SDA

Rank	Variable	R-Statistic
1	LCCU1 k	0.72
2	DVCM k	0.53
3	PBRCM k_0	0.24
4	PCM k_0	0.24
5	PBRCM k_0	0.23

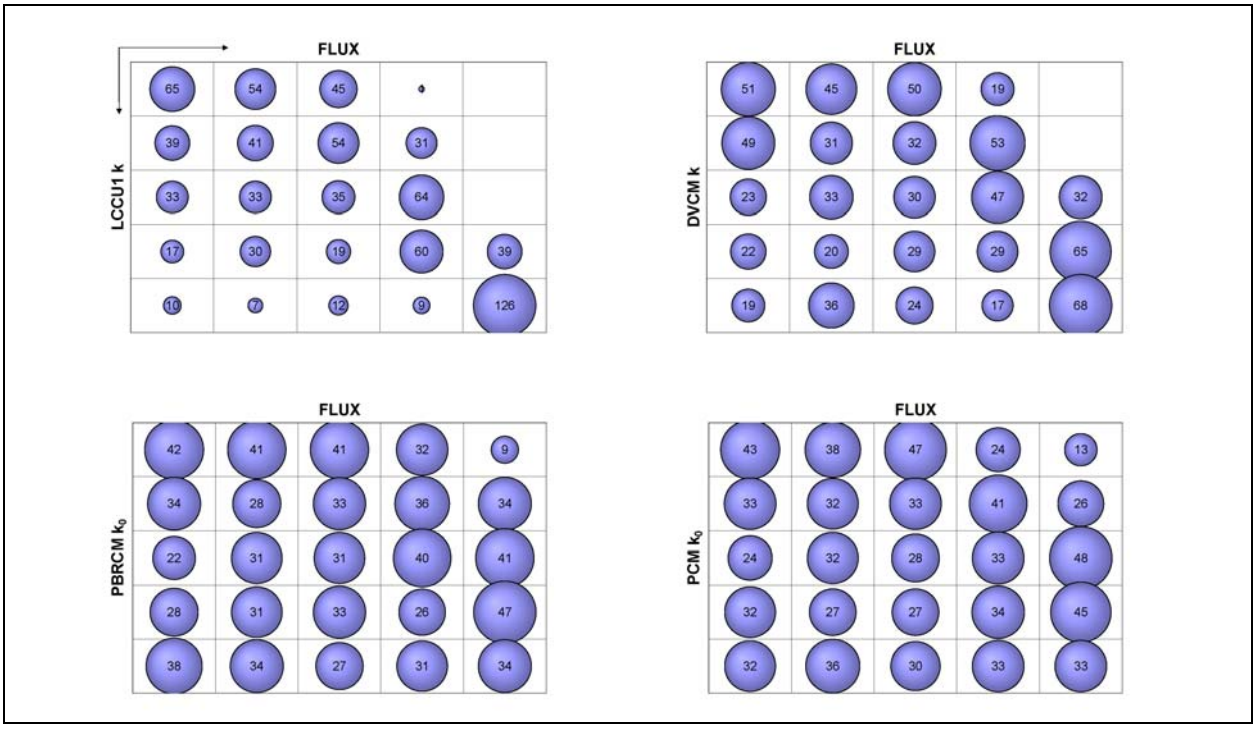

Figure 6-41
Bubble Plots from Entropy Analysis on FLUX for BN-MME-SDA

Uncontrolled When Printed

6.2.3.2 Base HFM - All HSU Depth-Decay and Anisotropy (BN-MME-ADA)

Global sensitivity analysis using Monte Carlo simulation to identify key parameters for the base HFM - all HSU depth-decay and anisotropy case required about 200 parameters to be varied over the 1,000 realizations generated. Approximately 29 percent of the simulations did not converge. Figure 6-42 shows a line plot of the best 10 percent of simulations ranked in terms of PHI, along with its various components. The most consistent and largest contributor to PHI is WELL, with some intermittent contribution by FLUX and ETF and a marginal contribution from SPRING. This is by design through the choice of calibration target weights as described in Section 5.2. This figure also shows that when FLUX and ETF have a significant contribution, WELL does not. This suggests that these two components of the objective function are controlled by different groups of input parameters. This behavior is also noticed in the selected HSU depth-decay and anisotropy parameterization of the base HFM; thus, the effect of parameterization approach does not broadly change model performance.

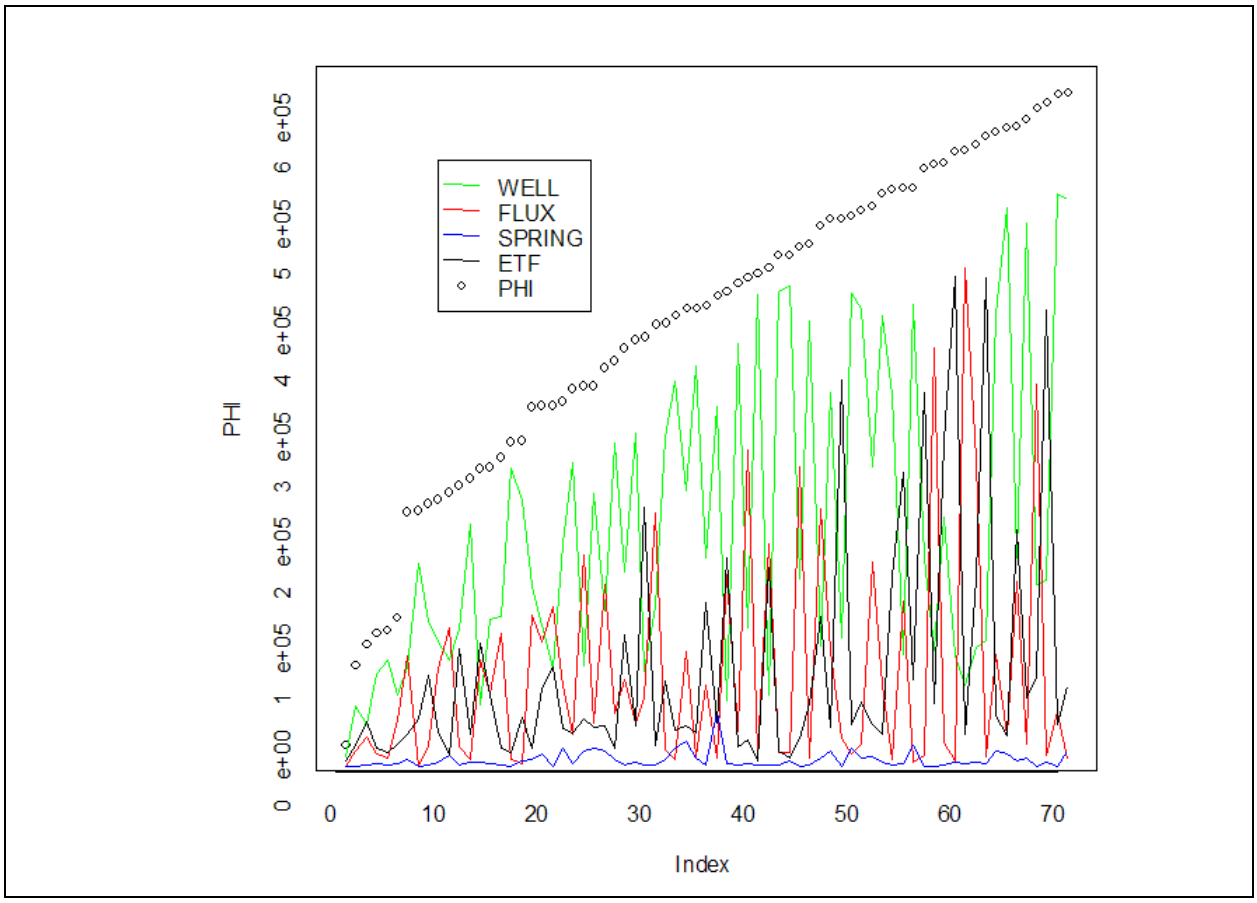

Figure 6-42
100 Best Simulations Ranked by PHI for BN-MME-ADA

Uncontrolled When Printed

Table 6-6 shows the Spearman rank correlation matrix for the best 10 percent of simulations ranked by objective function. WELL has the highest correlation with PHI at 0.47. ETF and PHI also have a relatively high correlation at 0.44. Also note the relatively high correlation between WELL and SPRING at 0.37, and the negative correlation (-0.35) between WELL and FLUX. The correlation of PHI and WELL is also noticed in the selected HSU depth-decay and anisotropy case, as is the correlation between WELL and SPRING. However, the correlation between FLUX and WELL is positive in the aforementioned case, but is negative in Table 6-6. The parameter dominating FLUX in the selected HSU case is the LCCU1 permeability. Thus, as noted in the sensitivity coefficient and perturbation analysis for this parameterization, there is something distinctly different about the behavior of LCCU1 in the selected HSU depth-decay and anisotropy case.

Table 6-6
Spearman Rank Correlation Matrix for BN-MME-ADA

	PHI	WELL	SPRING	FLUX	ETF
PHI	1	0.47	0.14	0.13	0.44
WELL	0.47	1	0.37	-0.35	-0.15
SPRING	0.14	0.37	1	0.02	-0.05
FLUX	0.13	-0.35	0.02	1	0.05
ETF	0.44	-0.15	-0.05	0.05	1

In the following classification tree analyses, the logarithm of permeability will be presented; all other variables will be untransformed.

Figure 6-43 shows a classification tree plot for PHI. The tree has a misclassification rate of only 6 percent [(1+7)/(44+21+77)] after two splits. Based on the order of the splits, variable LCA Zone 1 (the subdivision of the LCA along the southeastern edge of the CAU model propagated from UGTA regional model [DOE/NV, 1997] Zone 1) is the most important followed by DVCM. This also is different from the results shown in Section 6.2.3.1 for base HFM - selected HSU depth decay and anisotropy, although the DVCM is still the second best explanatory variable for both parameterization approaches.

Figure 6-44 shows a classification tree analysis for WELL. Note that the important variables for this case, FCCM and CHCU permeability, are different from those identified earlier for the total objective function (PHI). This classification tree has a misclassification rate of 9 percent after two splits.

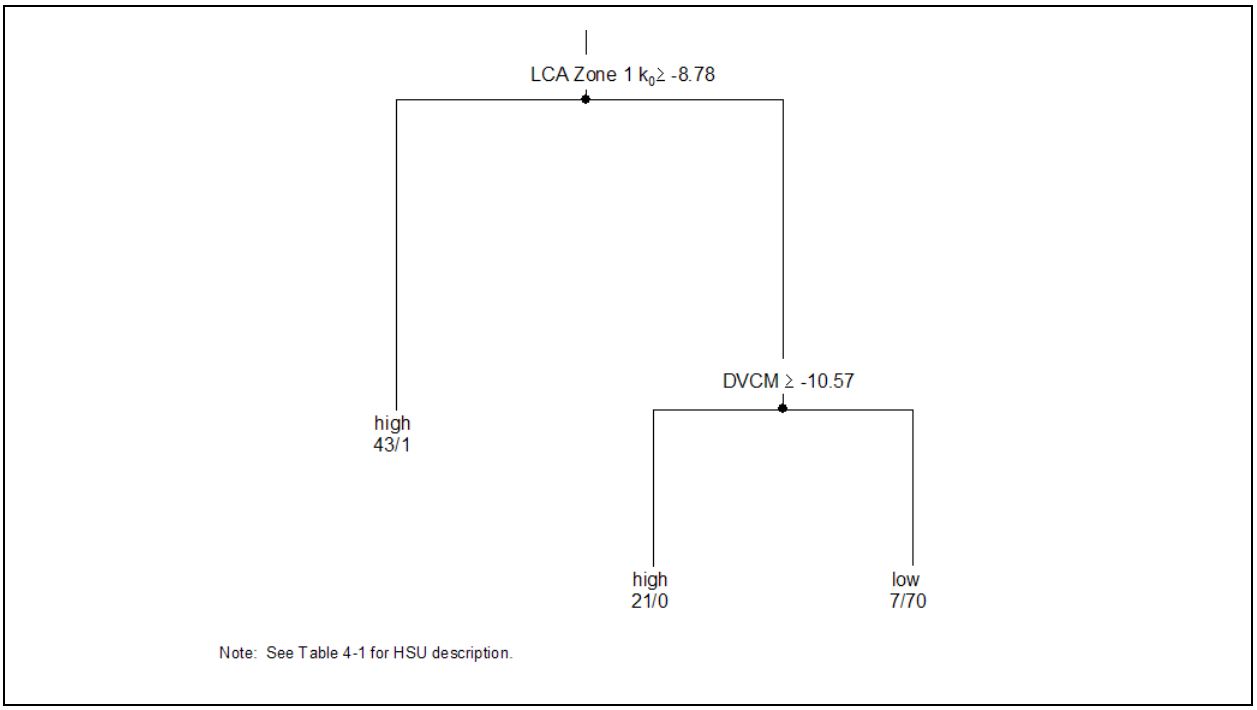

Figure 6-43
Classification Tree on PHI for BN-MME-ADA

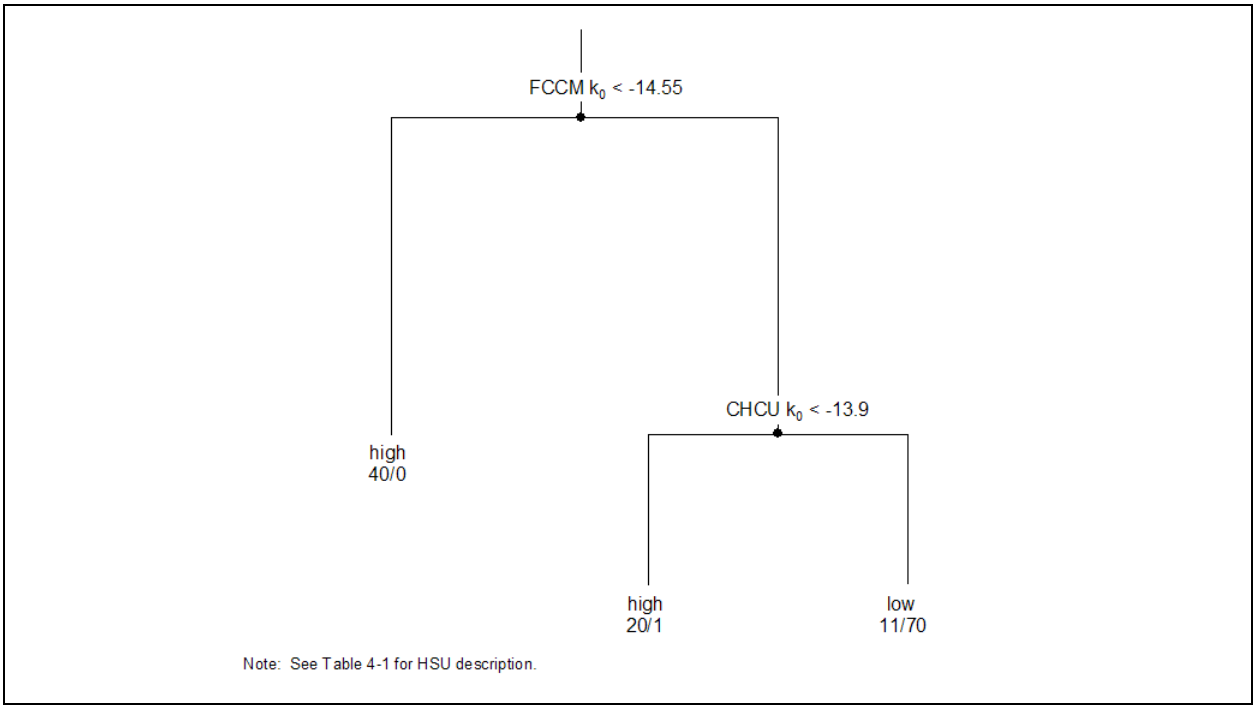

Figure 6-44
Classification Tree on WELL for BN-MME-ADA

Uncontrolled When Printed

When CHCU is less than 1.2 x 10^{-14} m^2, the model results are poorer than when it is larger. Stoller-Navarro Joint Venture (2004a) estimated the mean permeability of the CHCU at about 1 x 10^{-13} m^2 with a standard deviation of about one order of magnitude (see Table 2-19). Thus, the estimated value and its uncertainty appear reasonable in light of model performance.

Figure 6-45 shows the classification tree for SPRING. The lowest 10 percent SPRING values cannot be perfectly explained using three variables, with a misclassification rate of 16 percent. Note that one of the key variables, FCCM k_0, is shared with the set of key variables for WELL. The thrusted LCA (LCA3a) k_0 under Oasis Valley is the primary explanatory variable, most probably because it can drain water under the valley. A depth-decay parameter, that of the East Rainier Mesa subdivision of the TMCM, is also important in explaining misfit for less obvious reasons, although it may be that at lower depth decay more water drains down Fortymile Canyon than is needed to maintain spring heads. Both SNJV (2004a) and Kwicklis et al. (2005) show that some flow from north of the TMCM-ERM area occurs to Oasis Valley, so while peculiar, this explanation is possible.

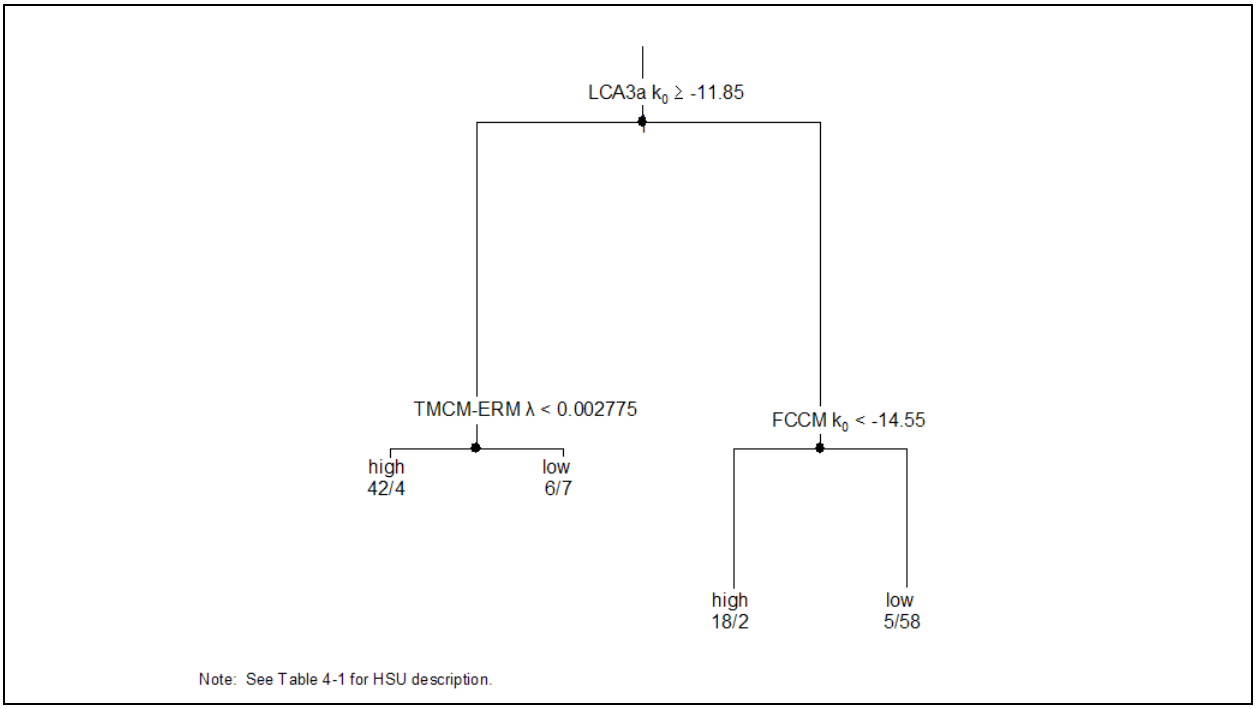

Figure 6-45
Classification Tree on SPRING for BN-MME-ADA

Uncontrolled When Printed

Figure 6-46 presents the classification tree for FLUX. These results appear to be very similar to those presented earlier for the total objective function PHI, and primarily reflect the strong correlation between high PHI and high FLUX values. LCA Zone 1 replaces LCCU1 as the major controlling factor in this parameterization of the base HFM. The LCA Zone 1 was also noted as sensitive in previous all HSU depth-decay and anisotropy case analyses (see Sections 6.2.1.2 and 6.2.2.2), and here is identified explicitly as being associated with southern boundary flow.

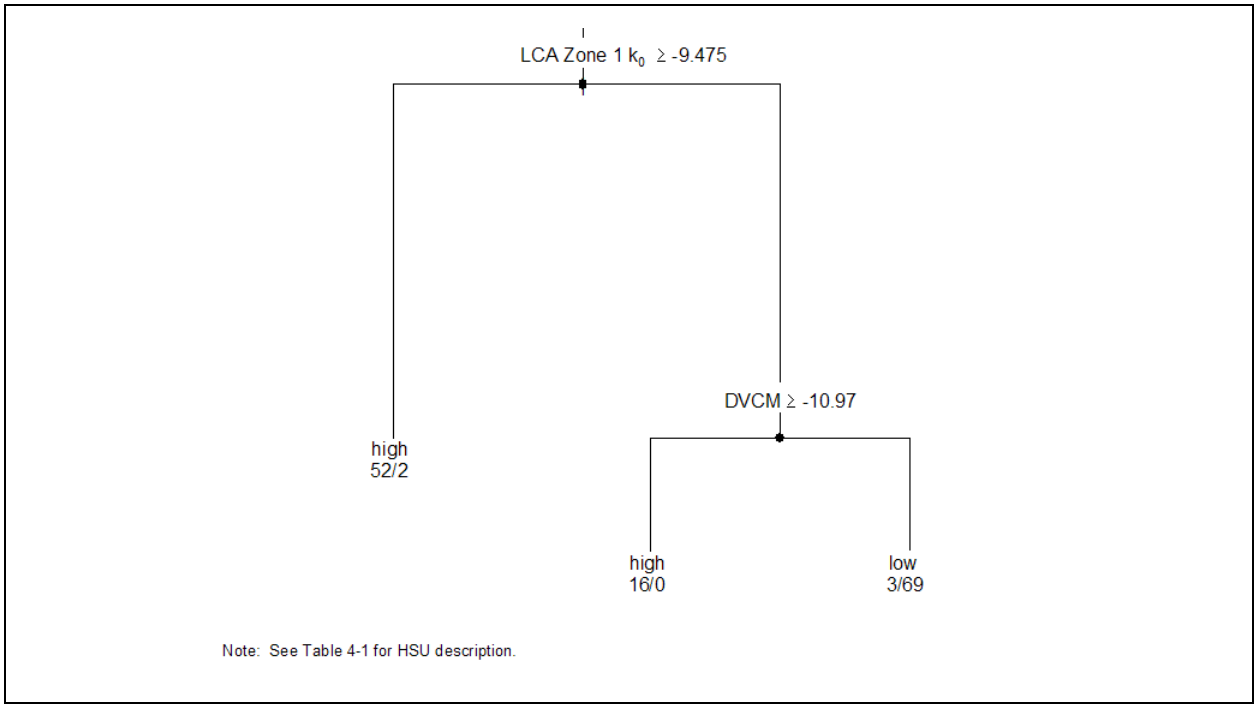

Figure 6-46
Classification Tree on FLUX for BN-MME-ADA

Finally, the classification tree for Oasis Valley discharge is presented in Figure 6-47. Here, a two-variable split perfectly separates the lowest 10 percent of ETF values from the highest 10 percent. Also of interest is the fact that one of the important variables (DVCM) was also identified as important in isolating low values for WELL and SPRING. Both with and without depth decay, the DVCM is important in controlling Oasis Valley discharge. The PBRCM is key in both the selected and all HSU depth-decay cases, but in Section 6.2.3.1, the western zone of the PBRCM versus the PBRCM under Pahute Mesa/Silent Canyon is identified as being an important control.

Uncontrolled When Printed

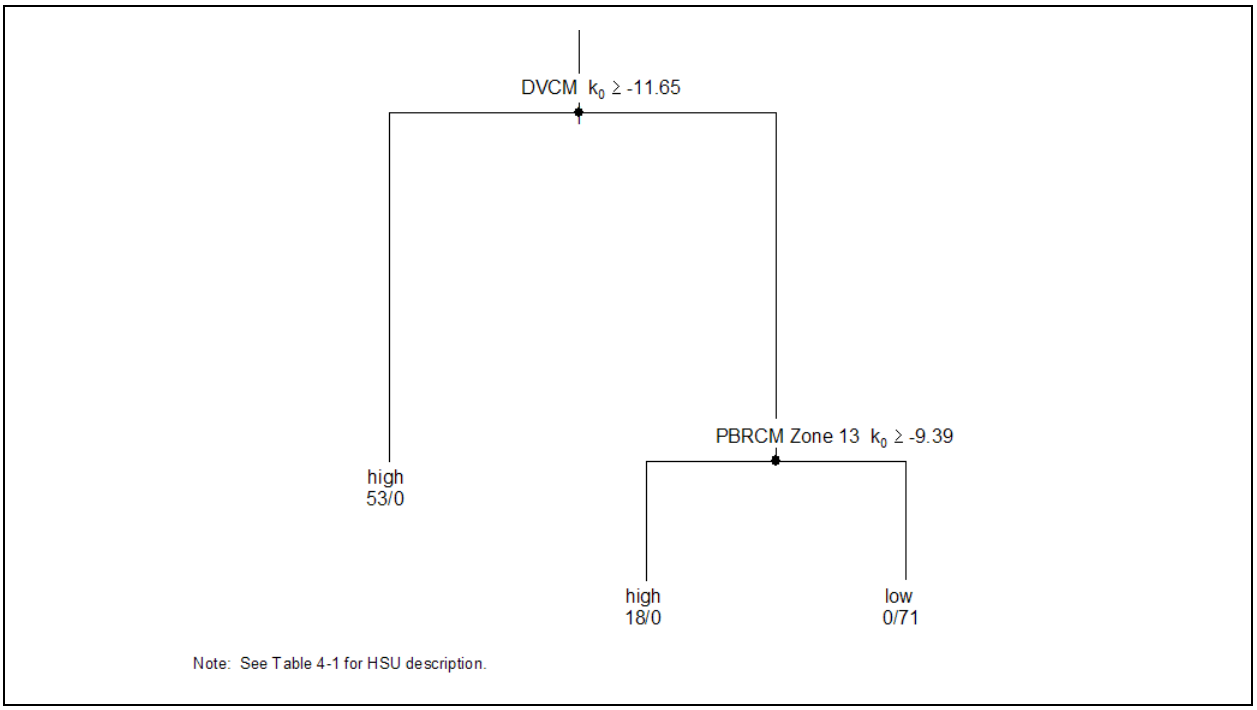

Figure 6-47
Classification Tree on ETF for BN-MME-ADA

Entropy analysis for PHI is shown Table 6-7. Based on the R-statistic, the top two variables have distinct patterns of association with PHI and also happen to be the same in order of importance as the top two variables identified from classification tree analysis in Figure 6-43. The other variables appear to have less definitive association. The second most important variable, DVCM k_0, was also identified in Section 6.2.3.1 for selected depth decay and anisotropy. Figure 6-48 shows bubble plots for the top four variables for PHI, where the entries of the contingency table are shown as bubbles of varying sizes. The relative importance of the top two variables, LCA Zone 1 and DVCM, is clearly seen through the distinctive patterns in the upper panels. On the other hand, the near-uniform size of the bubbles in the bottom panels indicates the marginal relevance of the other two top-ranked variables.

Results for the entropy analysis of WELL are shown in Table 6-8. Based on the R-statistic, the top two variables are not as dominant or as distinctive as those corresponding to PHI. The order of importance is the same as the importance ranking from classification tree analysis shown in Figure 6-44. The absence of distinctive input-output patterns can also be seen in the bubble plots

Uncontrolled When Printed

Table 6-7
Results of Entropy Analysis on PHI for BN-MME-ADA

Rank	Variable	R-Statistic
1	LCA Zone 1 k_0	0.45
2	DVCM k_0	0.43
3	PBRCM Zone 13 k_0	0.26
4	LCA Zone 1 Vertical Anisotropy	0.22
5	CHZCM k_0	0.21

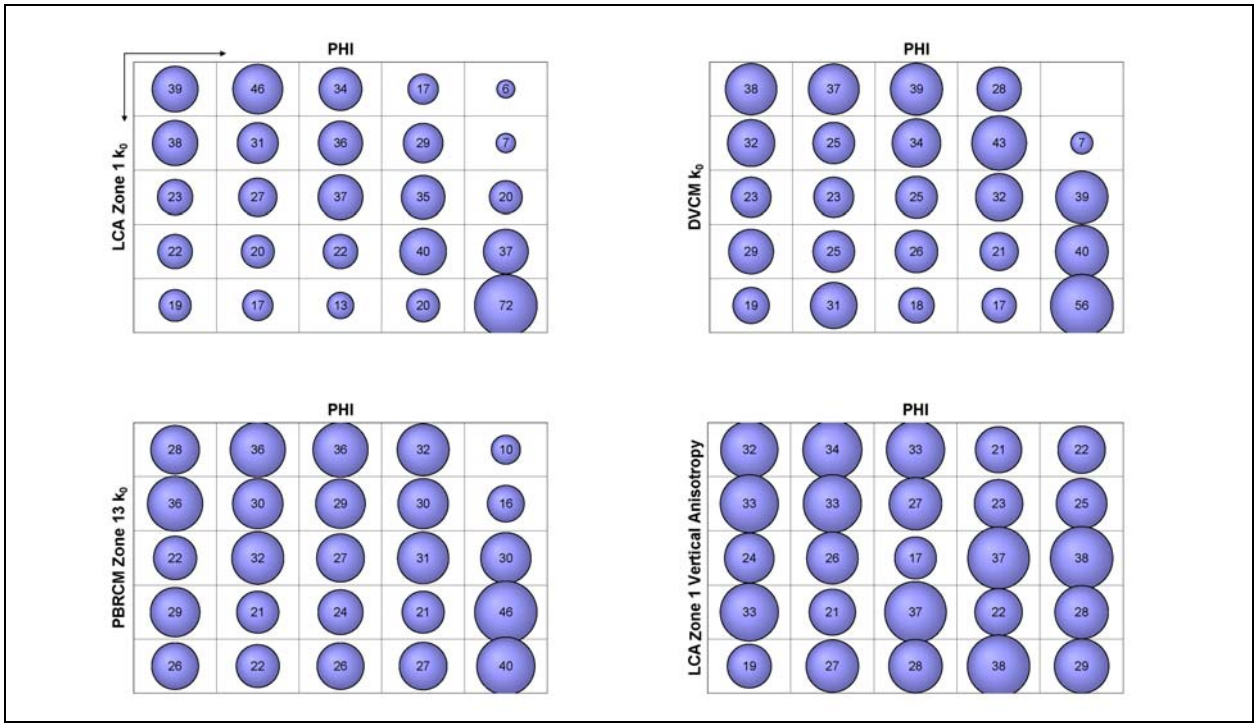

Figure 6-48
Bubble Plots from Entropy Analysis on PHI for BN-MME-ADA

presented in Figure 6-49, where even the top two variables (top panels) do not appear to significantly different from the next two variables (bottom panels) in terms of exhibiting distinctive trends.

Interestingly, this is the first occasion where a fault (West Greeley, in this case) and a volcanic aquifer (IA) on Pahute Mesa are identified as a potentially important factor, although PEST sensitivity and perturbation analyses suggested these variables were important (see Sections 6.2.1.2 and 6.2.2.2).

Table 6-8
Results of Entropy Analysis on WELL for BN-MME-ADA

Rank	Variable	R-Statistic
1	FCCM k_0	0.36
2	CHCU k_0	0.28
3	IA k_0	0.24
4	West Greeley Fault	0.23
5	PBRCM Zone 13 k_0	0.22

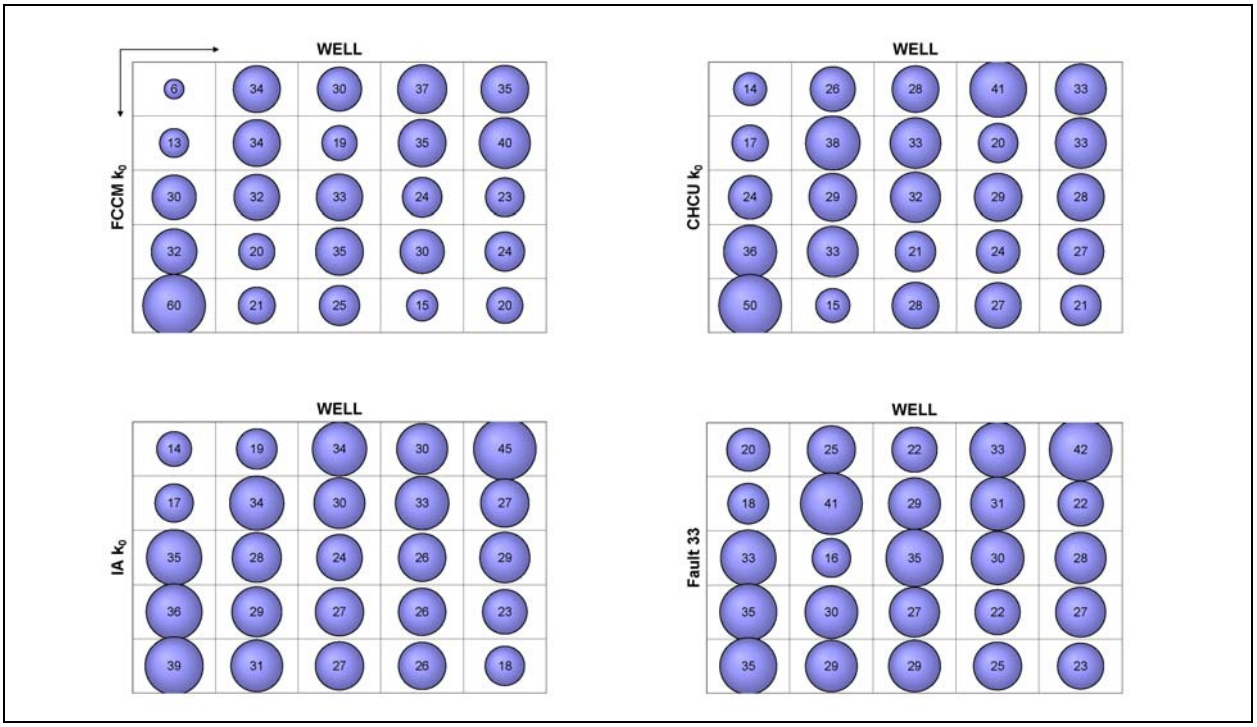

Figure 6-49
Bubble Plots from Entropy Analysis on WELL for BN-MME-ADA

Results for the entropy analysis for FLUX are given in Table 6-9, and the corresponding bubble plots are presented in Figure 6-50. The top two variables are the same as those identified by the classification tree analysis for FLUX. As noted earlier, the top-ranked variables for PHI and FLUX are identical, suggesting that a strong correlation between high PHI and high FLUX values may be influencing these results.

Uncontrolled When Printed

Table 6-9
Results of Entropy Analysis on FLUX for BN-MME-ADA

Rank	Variable	R-Statistic
1	LCA Zone 1 k_0	0.53
2	DVCM k_0	0.50
3	PBRCM k_0	0.30
4	TMCM-ATCE Vertical Anisotropy	0.22
5	UPCU West of Purse Fault k_0	0.22

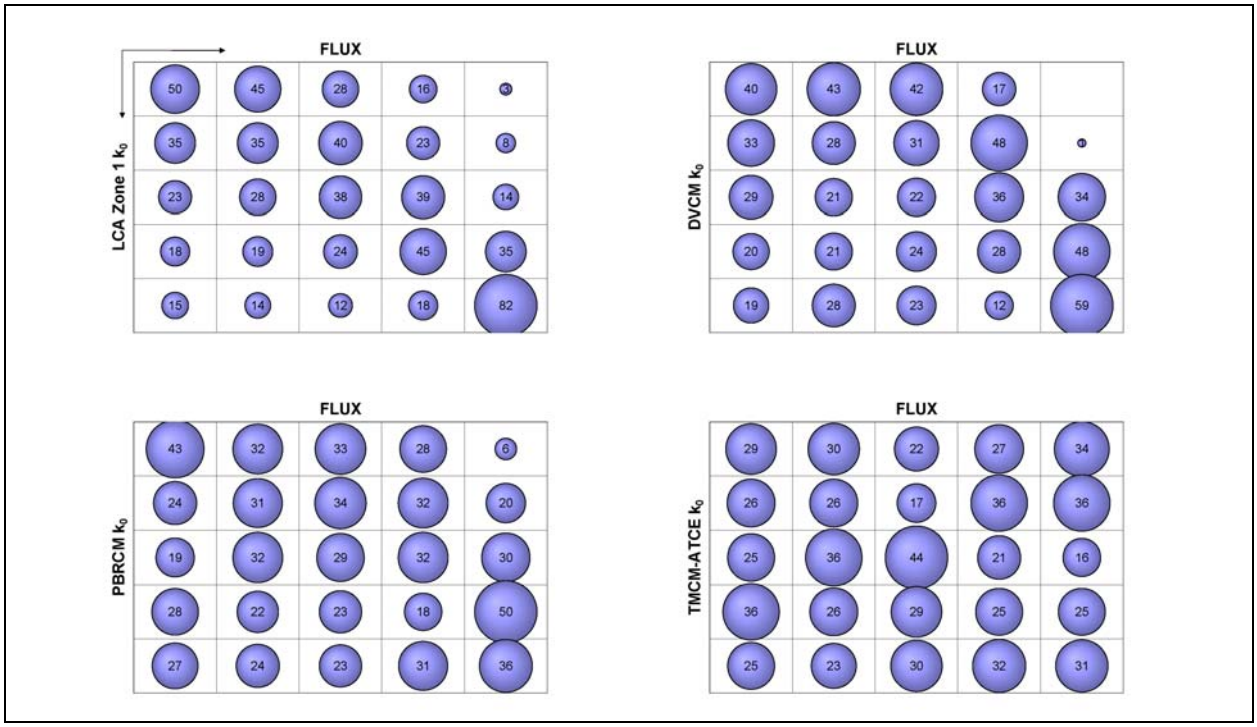

Figure 6-50
Bubble Plots from Entropy Analysis on FLUX for BN-MME-ADA

6.2.3.3 SCCC HFM - Selected HSU Depth Decay and Anisotropy (SCCC-MME-SDA)

Approximately 100 parameters were varied to investigate the global sensitivity using Monte Carlo simulation for the SCCC HFM. Approximately 26 percent of the simulations did not converge.

Figure 6-51 shows a line plot of the best 10 percent of simulations ranked in terms of PHI, along with its various components. The most consistent contributor to PHI is WELL, with some contribution by FLUX, occasional contribution by ETF and a marginal contribution from SPRING. This figure also

Uncontrolled When Printed

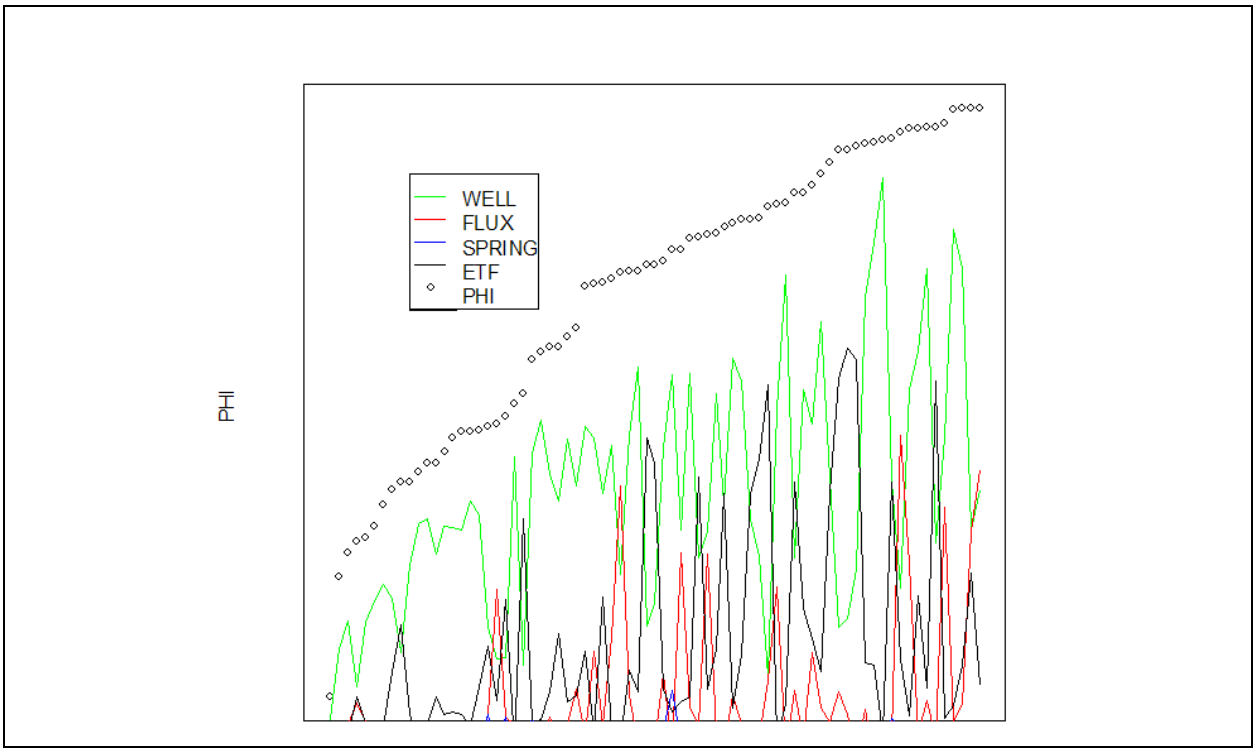

Figure 6-51
100 Best Simulations Ranked by PHI for SCCC-MME-SDA

shows that when FLUX and ETF have a significant contribution, WELL does not. This suggests that these two components of the objective function are controlled by different groups of input parameters.

Table 6-10 shows the Spearman rank correlation matrix for the best 10 percent of simulations ranked by objective function. WELL has the highest correlation with PHI at 0.53. ETF and PHI also have a relatively high correlation at 0.47. Unlike the base HFM - selected HSU depth-decay and anisotropy flow model and the base HFM - all HSU depth-decay and anisotropy case, which both showed correlation between WELL and SPRING, there is little evidence of inter-component metric correlation. Thus, the SCCC HFM is distinctly different than the base HFM in this regard, even though the HFM is the same outside Silent Canyon.

Classification tree analysis to determine the decision rules separating the smallest and largest 10 percent of PHI values is shown in Figure 6-52. The tree has a misclassification rate of less than 1 percent after two splits. Based on the order of the splits, LCCU1 permeability (all permeabilities in log space) is the most important followed by DVCM. While the SCCC HFM shows some differences

Uncontrolled When Printed

Table 6-10
Spearman Rank Correlation Matrix for SCCC-MME-SDA

	PHI	WELL	SPRING	FLUX	ETF
PHI	1	0.53	0.11	0.26	0.47
WELL	0.53	1	-0.06	-0.01	-0.16
SPRING	0.11	-0.06	1	0.19	0.11
FLUX	0.26	-0.01	0.19	1	-0.02
ETF	0.47	-0.16	0.11	-0.02	1

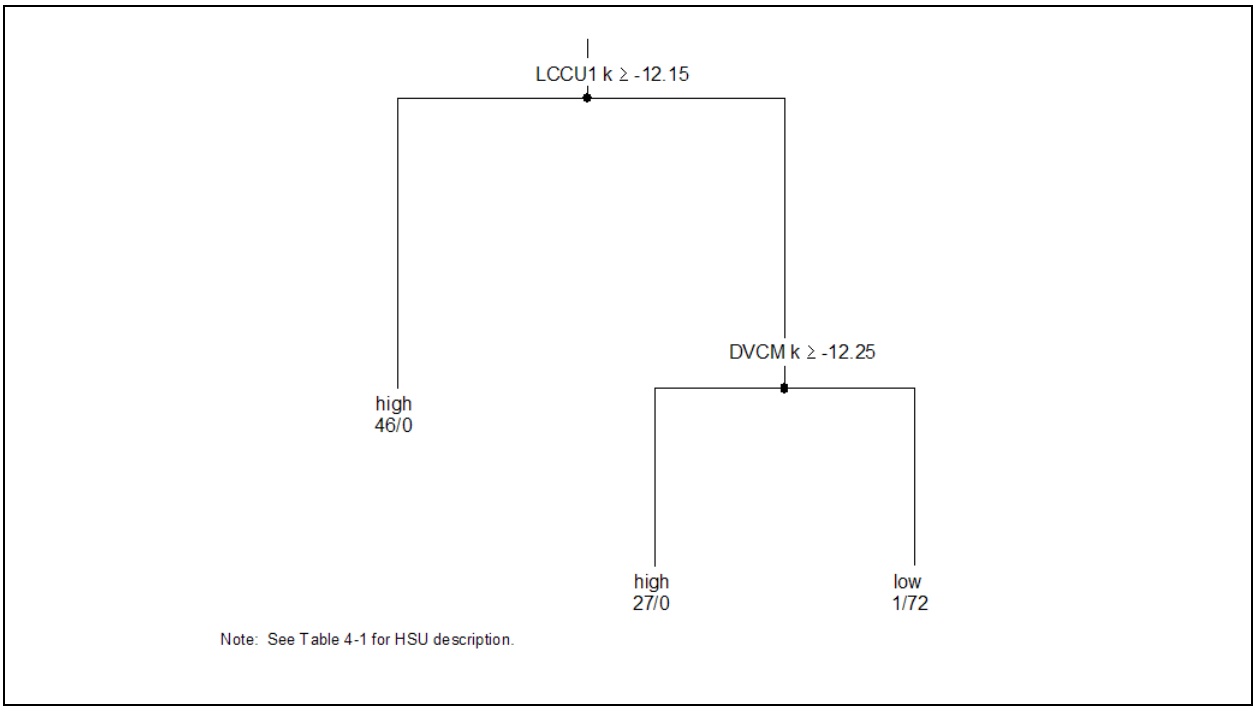

Figure 6-52
Classification Tree on PHI for SCCC-MME-SDA

from the base HFM, the classification tree clearly shows the same parameters as identified in Section 6.2.3.1 for BN-MME-SDA having control on PHI. Thus, because the only difference in how the LCCU1 is handled between the base HFM/SCCC HFM combination and the base HFM - all HSU depth decay and anisotropy is the assignment of depth decay, it is concluded that it is the permeability of the LCCU1, not the HFM, that causes its different roles in model calibration. This is investigated further in Section 6.2.4.2 and Section 7.0.

Uncontrolled When Printed

The next set of analyses deals with the individual components of PHI. Figure 6-53 shows a classification tree analysis for WELL. Note that the important variables for this case, BRA and PBRCM permeability, are different from those identified earlier for the total objective function (PHI). Recall that all Calico Hills HSUs in the base HFM are grouped in the SCCC HFM into the CHCU. This classification tree has a misclassification rate of 16 percent after three splits. The CHCU was also a sensitive parameter for BN-MME-SDA (see Sections 6.2.1.3 and 6.2.2.3).

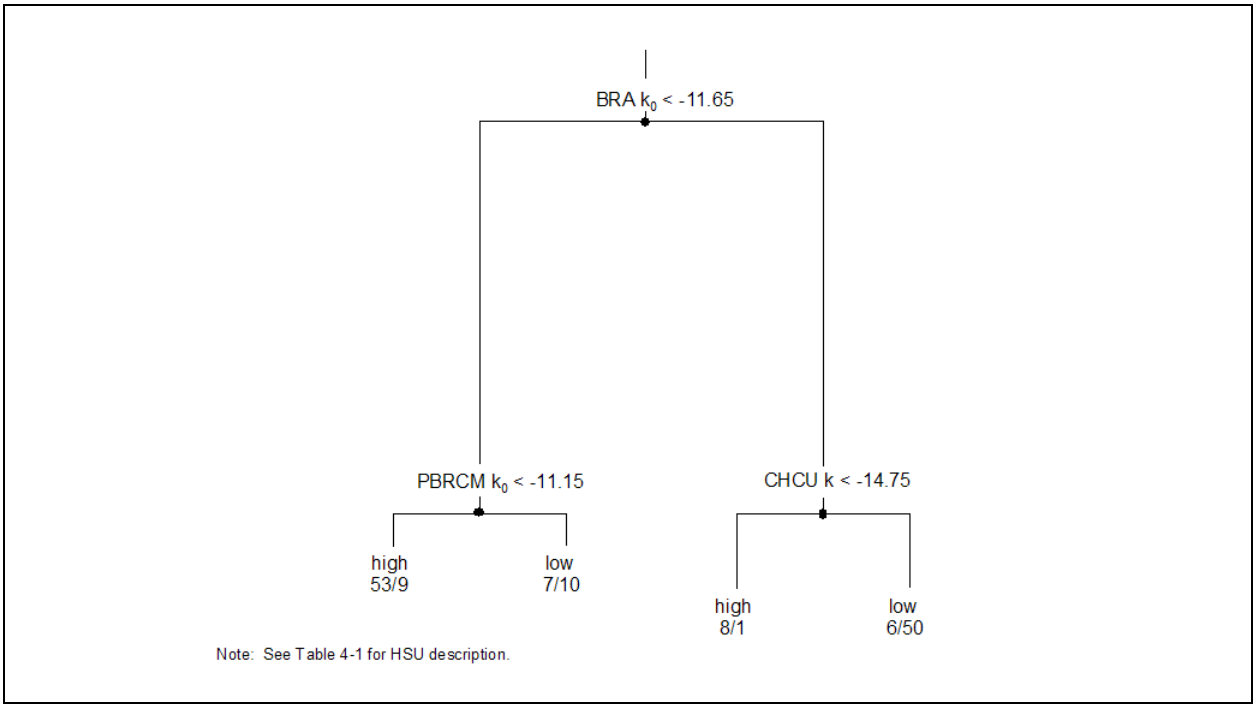

Figure 6-53
Classification Tree on WELL for SCCC-MME-SDA

Figure 6-54 shows the classification tree for SPRING. The lowest 10 percent SPRING values cannot be perfectly explained using two variables, with a misclassification rate of 16 percent. In contrast to the base HFM - selected HSU depth-decay and anisotropy flow model and the base HFM - all HSU depth-decay and anisotropy flow model, no key variables are shared with key variables for WELL. This is expected given the lack of correlation between SPRING and any of the other component variables. This is also the only case where a fault, the Hogback Fault, influences springs. This is not unreasonable, because the Hogback Fault runs north-south through Oasis Valley, and could physically be expected to exert some control on springs, although the other HFMs do not show the Hogback Fault to be especially sensitive. Moreover, the split to low values requires a fault permeability

Uncontrolled When Printed

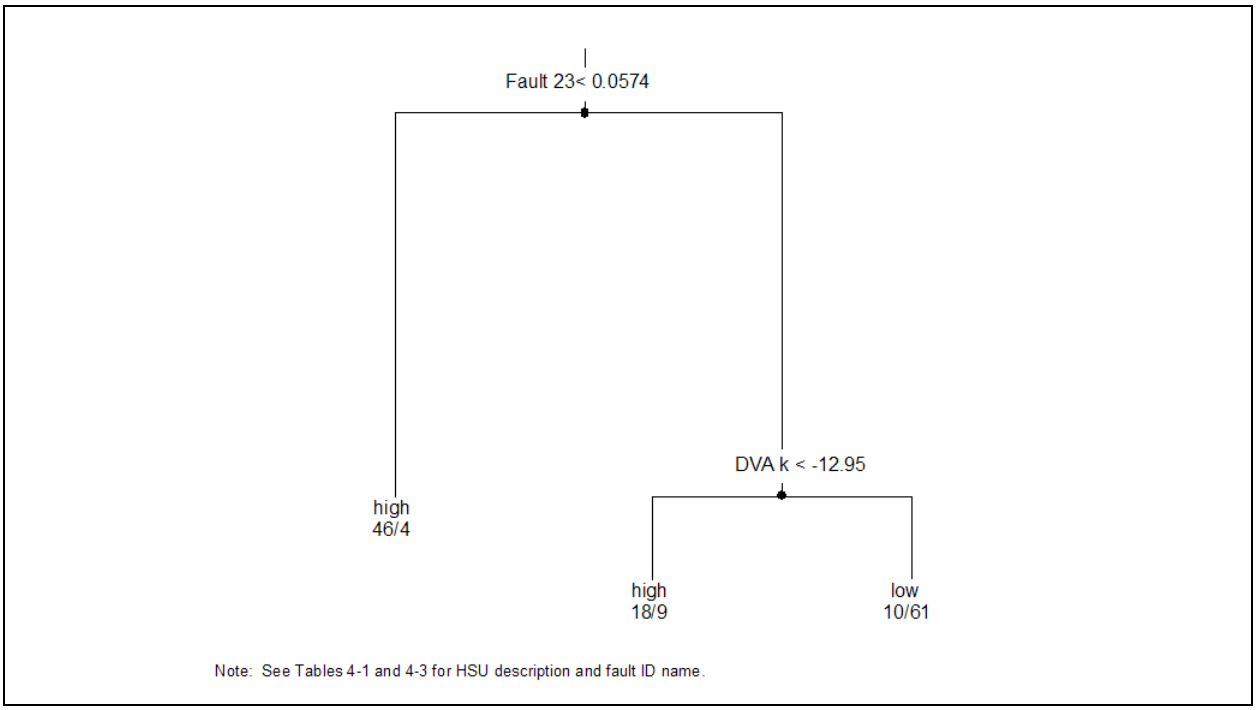

Figure 6-54
Classification Tree on SPRING for SCCC-MME-SDA

multiplier to be greater than about 0.05. Thus, this fault in the SCCC HFM cannot be greatly sealing (as the Purse Fault is in the base HFM).

Figure 6-55 presents the classification tree for FLUX. These results appear to be very similar to those presented earlier for the total objective function PHI, and primarily reflect the strong correlation between high PHI and high FLUX values. These results are also similar to those in Section 6.2.3.1, which is the base HFM parameterized the same way (selected HSU depth decay and anisotropy), but dissimilar to those in Section 6.2.3.2 (the base HFM with all HSU depth decay and anisotropy). Thus, it appears that the difference in how permeability is assigned to the LCCU1 is an important factor.

Finally, the classification tree plot for ETF is presented in Figure 6-56. Here, a two-variable split perfectly separates the ETF values. Also of interest is the fact that one of the important variables, DVCM permeability, was also identified as important in isolating low values for PHI and FLUX, while PBRCM is also identified as key to isolating low values for WELL.

Uncontrolled When Printed

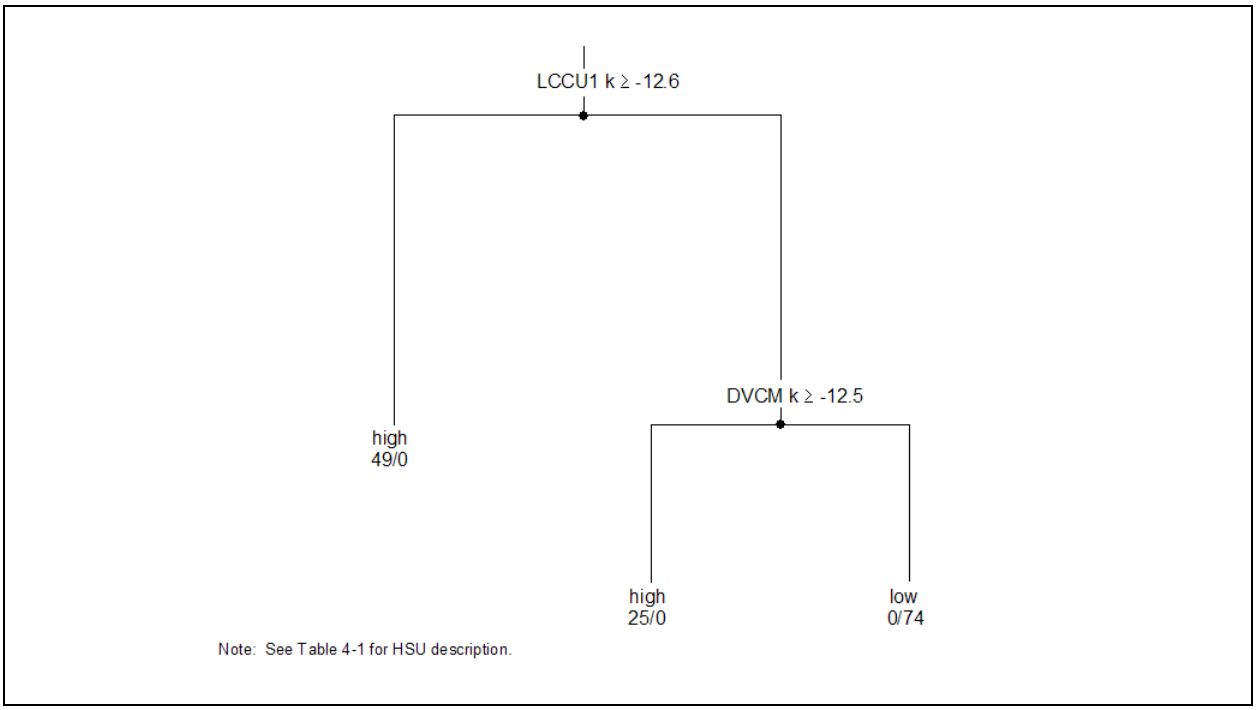

Figure 6-55
Classification Tree on FLUX for SCCC-MME-SDA

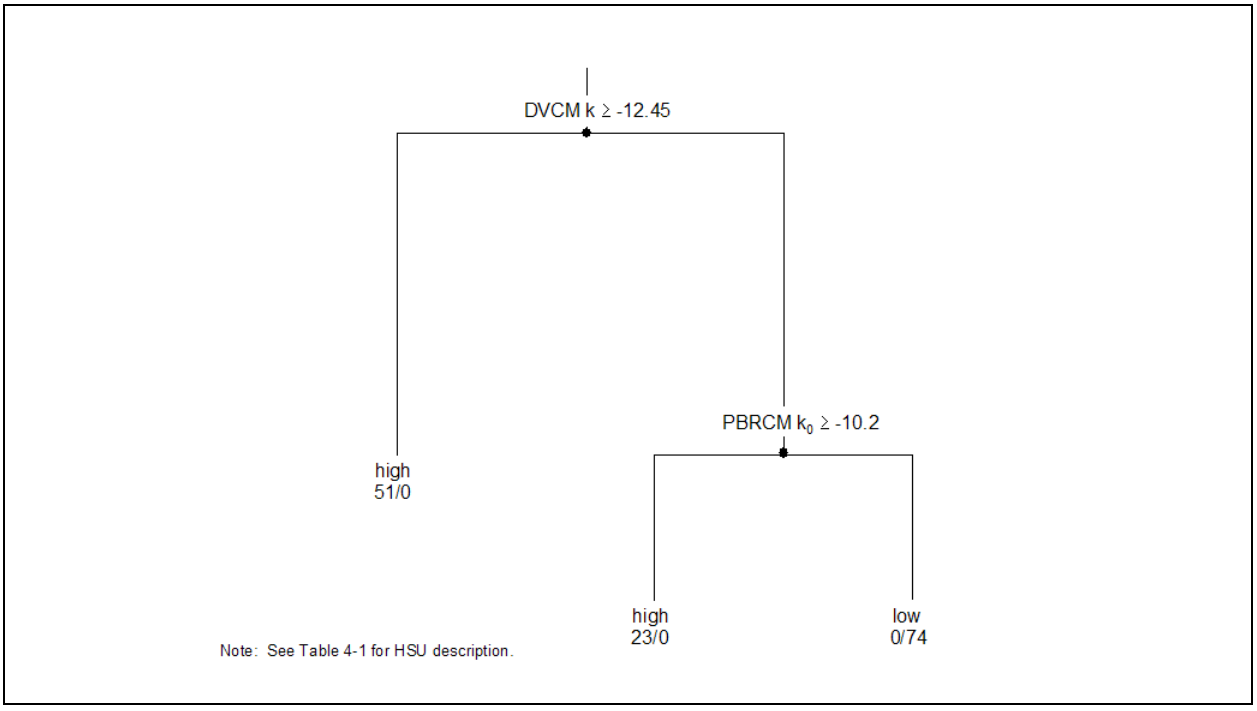

Figure 6-56
Classification Tree on ETF for SCCC-MME-SDA

Uncontrolled When Printed

Entropy analysis for PHI is shown in Table 6-11. Based on the R-statistic, the top two variables have distinct patterns of association with PHI, and also happen to be the same in order of importance as the top two variables identified from classification tree analysis in Figure 6-52. The other variables appear to have less definitive association. The top two variables are the same as found in Section 6.2.3.1 for BN-MME-SDA, and all the models found DVCM permeability as the second most important variable.

Figure 6-57 shows bubble plots for the top four variables, where the entries of the contingency table are shown as bubbles of varying sizes. The relative importance of the top two variables, LCCU1 and DVCM, is clearly seen through the distinctive patterns in the upper panels. On the other hand, the near-uniform size of the bubbles in the bottom panels indicates the marginal relevance of the other two top-ranked variables.

Results for the entropy analysis of WELL are shown in Table 6-12. Based on the R-statistic, the top two variables are not as dominant or as distinctive as those corresponding to PHI. Also, the order of importance is reversed for the first two parameters, compared to the classification tree shown in Figure 6-53. The absence of distinctive input parameter correlation to model performance patterns can also be seen in the bubble plots presented in Figure 6-58, where even the top two variables (top panels) do not appear to be significantly different from the next two variables (bottom panels).

Results for the entropy analysis for FLUX are given in Table 6-13, with the corresponding bubble plots presented in Figure 6-59. The top two variables are the same as those identified by the classification tree analysis for FLUX in Figure 6-55. As noted earlier, the top-ranked variables for PHI and FLUX are identical, suggesting that a strong correlation between high PHI and high FLUX values may be influencing these results.

Uncontrolled When Printed

Table 6-11
Results of Entropy Analysis on PHI for SCCC-MME-SDA

Rank	Variable	R-Statistic
1	LCCU1 k	0.55
2	DVCM k	0.49
3	PBRCM k_0	0.31
4	Fault 05	0.21
5	LCA3 k_0	0.20

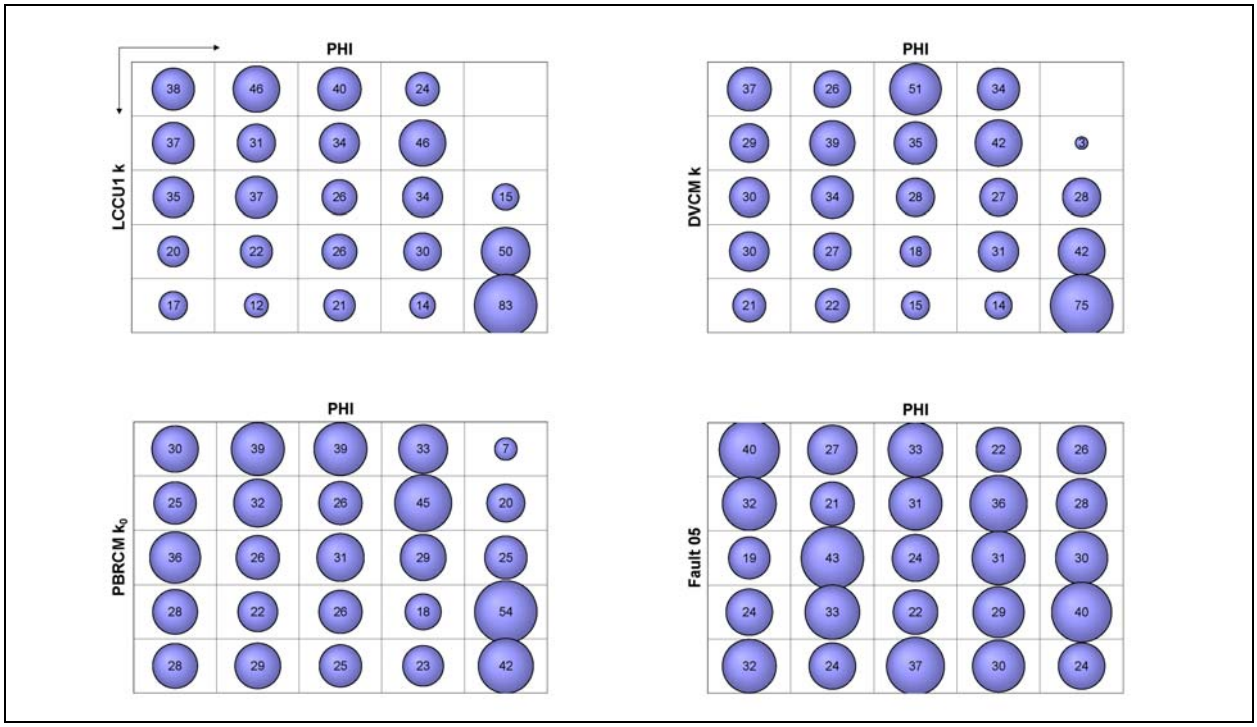

Figure 6-57
Bubble Plots from Entropy Analysis on PHI for SCCC-MME-SDA

Uncontrolled When Printed

Table 6-12
Results of Entropy Analysis on WELL for SCCC-MME-SDA

Rank	Variable	R-Statistic
1	PBRCM k_0	0.31
2	BRA k_0	0.31
3	CHCU k	0.28
4	Fault 11	0.26
5	LCA3 k_0	0.22

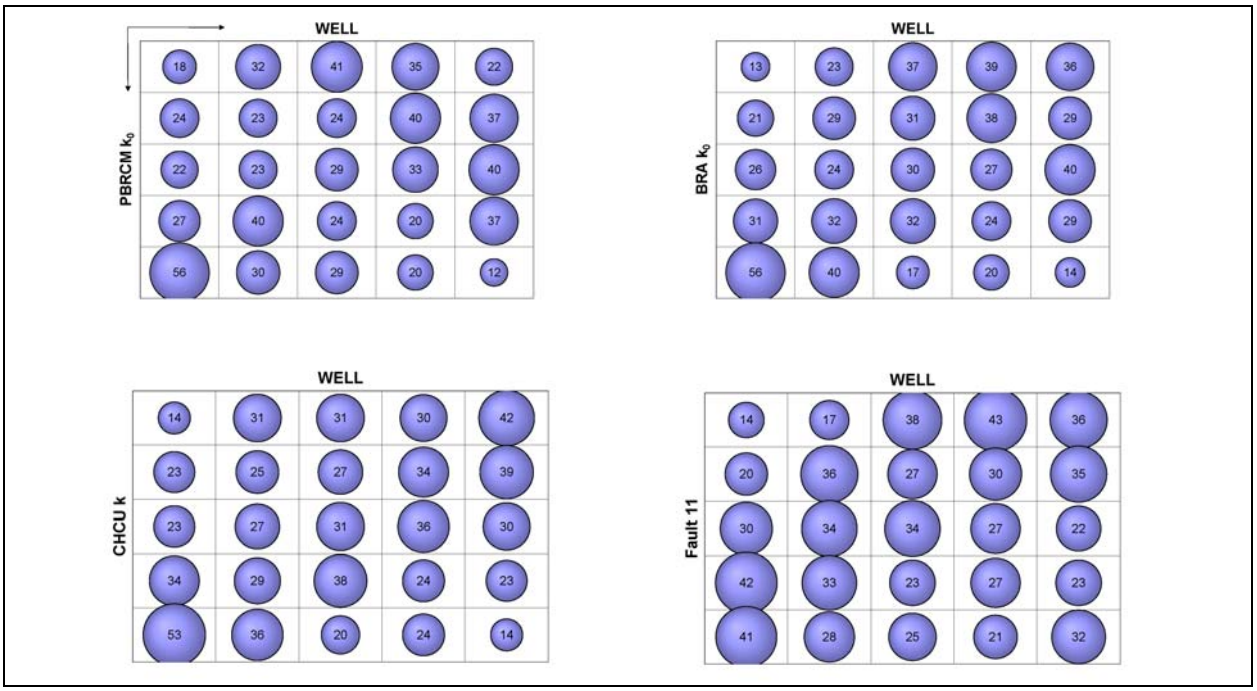

Figure 6-58
Bubble Plots from Entropy Analysis on WELL for SCCC-MME-SDA

Uncontrolled When Printed

Table 6-13
Results of Entropy Analysis on FLUX for SCCC-MME-SDA

Rank	Variable	R-Statistic
1	LCCU1 k	0.70
2	DVCM k	0.61
3	PBRCM k_0	0.26
4	LCA3 k_0	0.21
5	PCM k_0	0.20

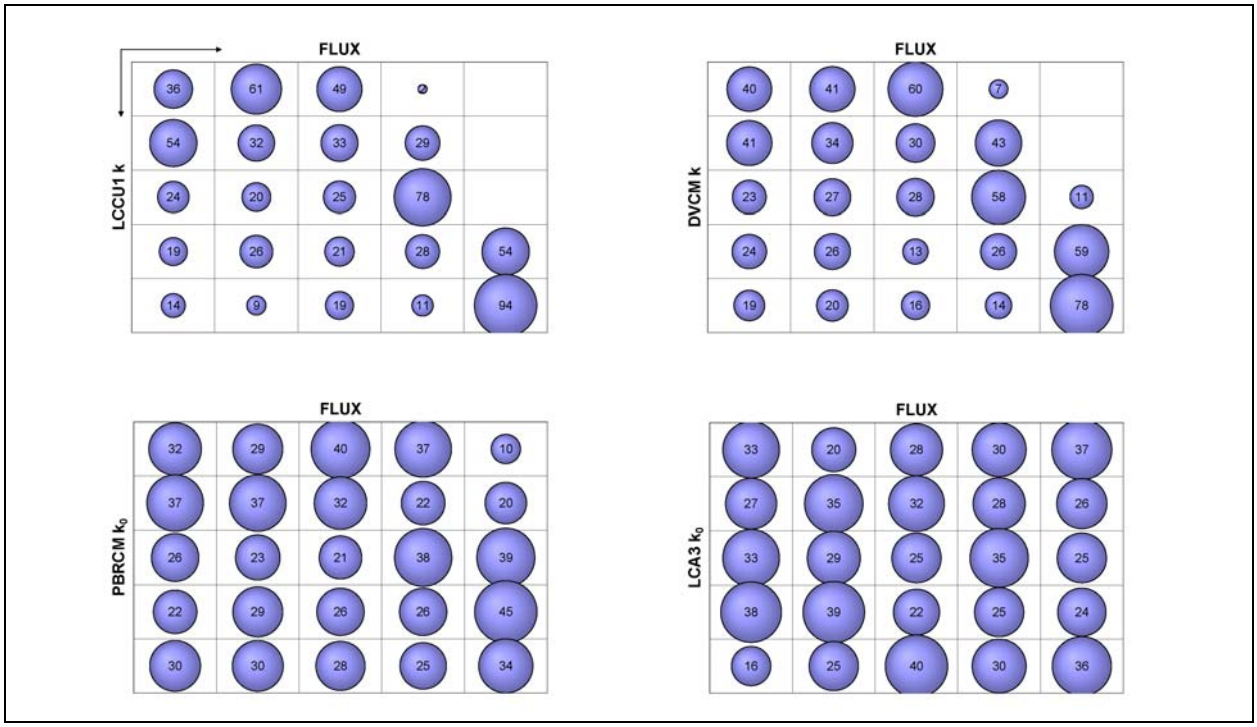

Figure 6-59
Bubble Plots from Entropy Analysis on FLUX for SCCC-MME-SDA

Uncontrolled When Printed

6.2.3.4 Boundary Flux Sensitivity

The CAU model water-balance uncertainty must be considered in the flow model analysis (IT, 1997a). It has been presumed in the Pahute Mesa CAIP (DOE/NV, 1999) that recharge and other high-level uncertainties are the major issue with respect to water-balance uncertainty. However, the global sensitivity analysis suggested that there may be strong variations in water balance from parametric uncertainty, and the following analysis explores this further.

As a subset of the global sensitivity analysis, a classification tree analysis was completed on the base HFM selected HSU depth-decay and anisotropy case to determine the important variables governing the model boundary fluxes. For each of the four model boundaries, there is a specified range of fluxes derived from regional model results. The stochastic simulations completed for the global sensitivity analysis resulted in a distribution of fluxes that spanned beyond these specified ranges. The goal of the classification tree analysis was to attempt to determine what variables were important in determining whether the boundary flux stayed within the specified range.

As an example, Figure 6-60 shows a histogram of the fluxes from the northern boundary, along with the flux range estimated from UGTA regional model analysis (SNJV, 2004a). The x-axis is a log scale, where flux (χ) values have been transformed by:

$$\left\{ \begin{array}{ll} \chi < 0, & -\log10\ (-\chi) \\ \chi > 0, & \log10\ (\chi) \\ \chi = 0 & 0 \end{array} \right\} \tag{6-13}$$

The bimodal look of the transformed distribution is expected, because the tail of the untransformed distribution crosses from negative to positive (from inflow to outflow), and the transformation has the effect of creating two log-normal distributions. Note that a large percentage of the resulting fluxes fall outside the prescribed range just as a consequence of parameter uncertainty.

Classification tree analysis requires binning the data into two classes. In this case, “pass” and “fail” classes were created, where the “pass” class consists of those realizations that fall within flux range and the “fail” class consists of those realizations that fall outside flux range. The histogram in

Uncontrolled When Printed

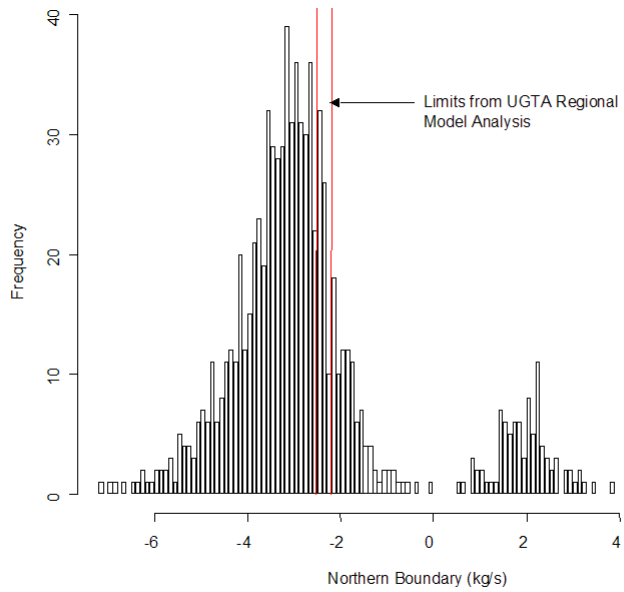

Figure 6-60
Histogram of Log-Transformed Northern Boundary Flux for BN-MME-SDA

Figure 6-60 shows that the classes are highly unbalanced (i.e., there are only 83 passing realizations compared to some 751 failing realizations). The classification tree analysis will be ineffective unless the classes are more balanced. So we will randomly sample twice the number of "pass" realizations from the "fail" class to compare against the passing realizations. For the northern boundary, this means there will be 166 samples in the "fail" class.

Figure 6-61 shows the histogram from the above sampling procedure for the northern boundary flux. Figure 6-62 shows the resulting classification tree. Note that the misclassification rate for this tree is quite high, at about 26 percent. However, the first split (LCCU1 permeability greater than or equal to -12.25) does produce a pure "fail" (i.e., flux outside the UGTA regional model [DOE/NV, 1997] analysis) node, and the second split (LPCU west of Purse Fault 58 less than -16.85) also produces a nearly pure "fail" node. So although the analysis cannot separate the "fail" realizations where the flux falls very near the specified range, a large number (about 92 of the 183) of the "fail" realizations can be separated with just two splits. The physical reasons for the classification tree results is that the LCCU1, which is connected to the highest boundary heads along the northeastern quadrant of the model, moves excessive water at higher permeabilities. The parameter LPCU west of Purse Fault is

Uncontrolled When Printed

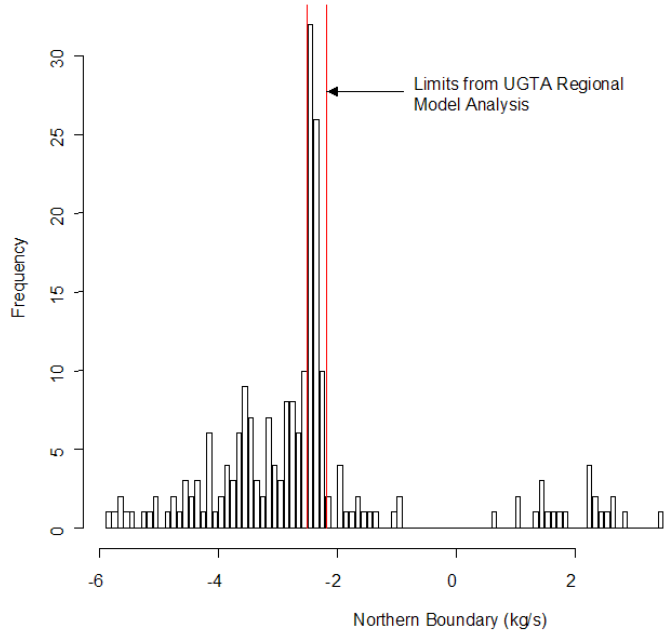

Figure 6-61
Histogram of Log-Transformed Resampled Northern Boundary Flux for BN-MME-SDA

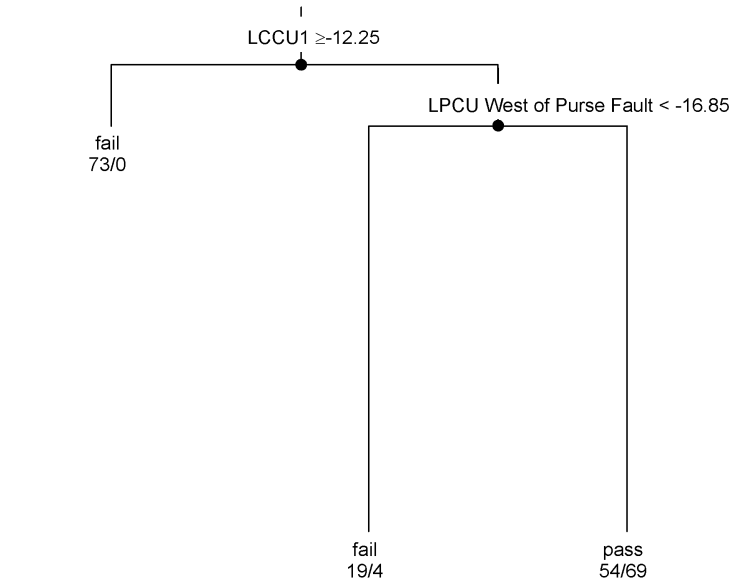

Note: See Table 4-1 for HSU description.

Figure 6-62
Classification Tree for Northern Boundary Flux for BN-MME-SDA

Uncontrolled When Printed

only the portion in the "throat" between Black Mountain and the Purse Fault where PM-3 lies, and acts to check flow through the area, which can be high given the upstream boundary condition was raised over 100 m (see Section 5.3).

Figure 6-63 shows the histogram result for the southern boundary flux. Because all of these fluxes are positive, the transformation process does not produce the bimodal distribution. Also, even in log space, the distribution tails toward the values that are larger in magnitude. Figure 6-64 shows the classification tree for the southern boundary flux. Again, the overall misclassification rate for this tree is high, at about 31 percent. The first split (DVCM permeability greater than or equal to -12.75) does produce a nearly pure "fail" node. The second split, PBRCM anisotropy, is less successful, with both classes rather well represented in the nodes. In this case, only the first parameter in the tree, DVCM, would be considered important for separating the "fail" realizations. Physically, the importance of these two parameters is interpreted as follows: the DVCM permeability controls inflow from Sarcobatus Flat from the west into Oasis Valley that is a relatively short and direct flow path. If the DVCM permeability is too high, flow from the west easily satisfies Oasis Valley discharge, thus increasing flow out of the model across the southern boundary and model misfit with respect to this flow. The PBRCM permeability moves water all across the domain, although substantial faulting breaks its continuity. The PBRCM has previously been shown to be a very sensitive parameter in controlling Oasis Valley discharge because it exists near the water table over much of the western domain (BN, 2002). High horizontal-to-vertical permeability contrast results in a more horizontal character of groundwater flow. The classification tree analysis shows that at vertical-to-horizontal permeability ratios of greater than 0.03, the southern boundary flow "passes" (i.e., falls within the estimated range). Thus, excessive horizontal-to-vertical permeability contrast tends to hold head up and move water to the south with more continuity than more reasonable values. This analysis qualitatively suggests that with the current HFM structure and parameterization, PBRCM vertical-to-horizontal permeability ratio should be greater than 0.03.

Figure 6-65 shows the histogram result for the eastern boundary flux. Figure 6-66 shows the classification tree for the eastern boundary flux. The misclassification rate is lower than the previously discussed flux analyses, at about 18 percent. The first split (PBRCM permeability greater than or equal to -13.15) does a good job of separating the "fail" realizations from the "pass" realizations. The second level splits are less consequential. In this case, the first parameter in the

Uncontrolled When Printed

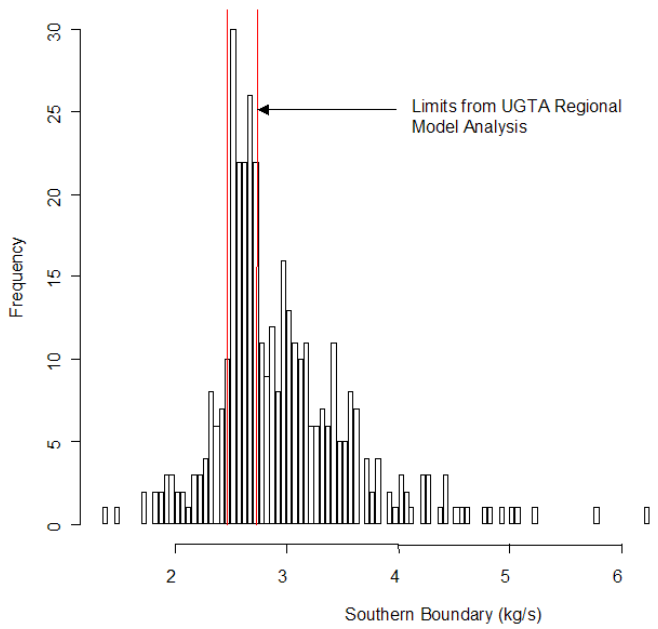

Figure 6-63
Histogram of Log-Transformed Resampled Southern Boundary Flux for BN-MME-SDA

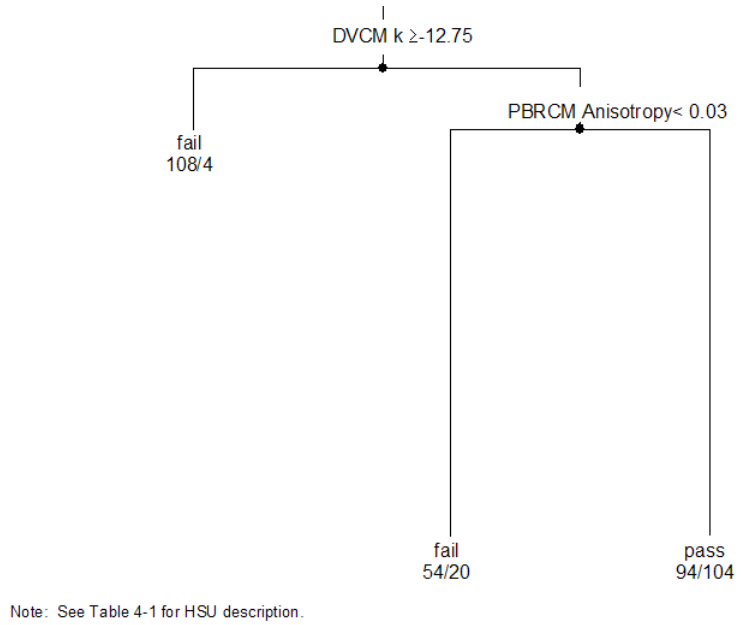

Figure 6-64
Classification Tree for Southern Boundary Flux for BN-MME-SDA

Uncontrolled When Printed

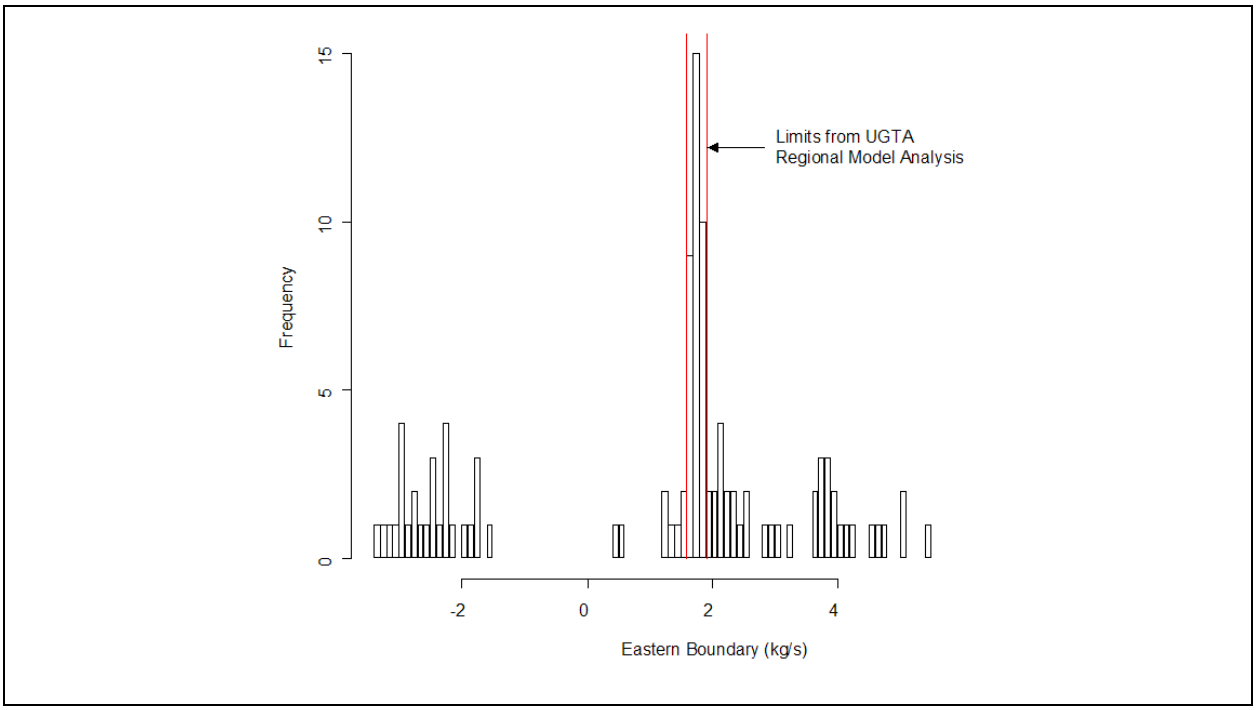

Figure 6-65
Histogram of Log-Transformed Resampled Eastern Boundary Flux for BN-MME-SDA

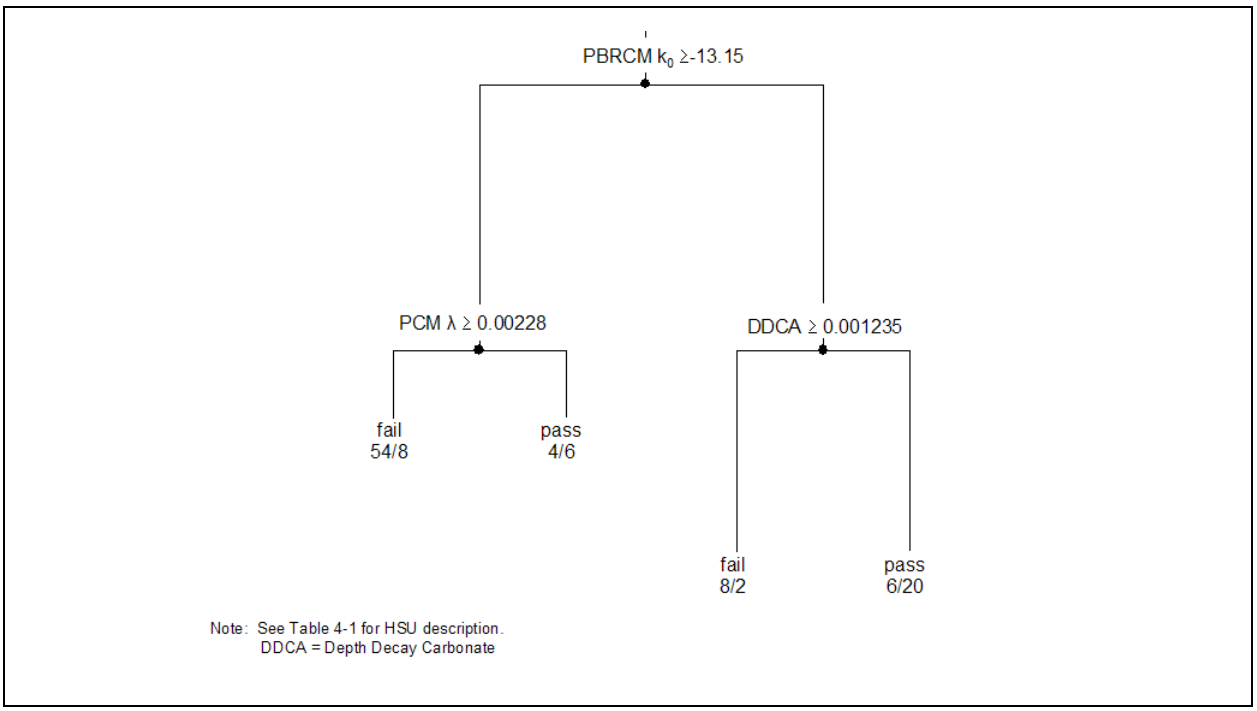

Figure 6-66
Classification Tree for Eastern Boundary Flux for BN-MME-SDA

Uncontrolled When Printed

tree, PBRCM, would be considered most important for separating the "fail" realizations, with a lesser emphasis on PCM depth decay and carbonate aquifer depth decay. The PBRCM is connected to the high hydraulic head near Gold Meadows, which allows it to control eastern boundary flow. The PCM and LCA both lie along (and are the major permeable units) the southern part of the eastern edge, and depth decay in these units helps control flow along this boundary.

Figure 6-67 shows the histogram result for the western boundary flux. The histogram shows a symmetrical lognormal distribution. Figure 6-68 shows the classification tree for the western boundary flux. This classification tree is different from the others in that the first two splits involve the same variable, DVCM. Also, the first two splits are of roughly equal importance, in that they both do a good job of separating "fail" from "pass." Log permeability is between -13.15 and -13.75. This single parameter is controlling the simulated western boundary flux result, and DVCM permeability must lie within the range between 1.7×10^{-14} and 7.1×10^{-14} m^2 in order to give a satisfactory western boundary flux. This is an illustration of the constraint that the strategy of using regional-model water-balance estimates provides and is also a consequence of having a no-flow boundary along much of the western model edge.

It is clear from this analysis that parameter uncertainty can have a large impact on CAU water-balance uncertainty, and that some sort of flow constraint is needed.

Uncontrolled When Printed

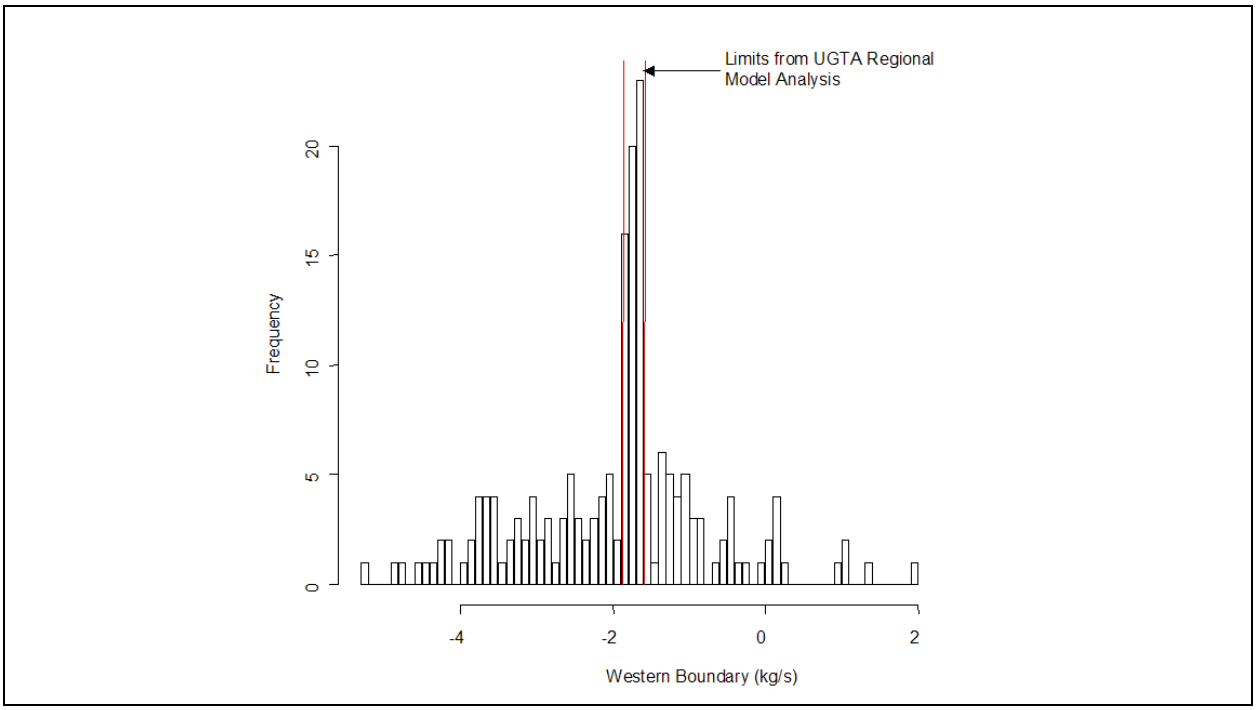

Figure 6-67
Histogram of Log-Transformed Resampled Western Boundary Flux for BN-MME-SDA

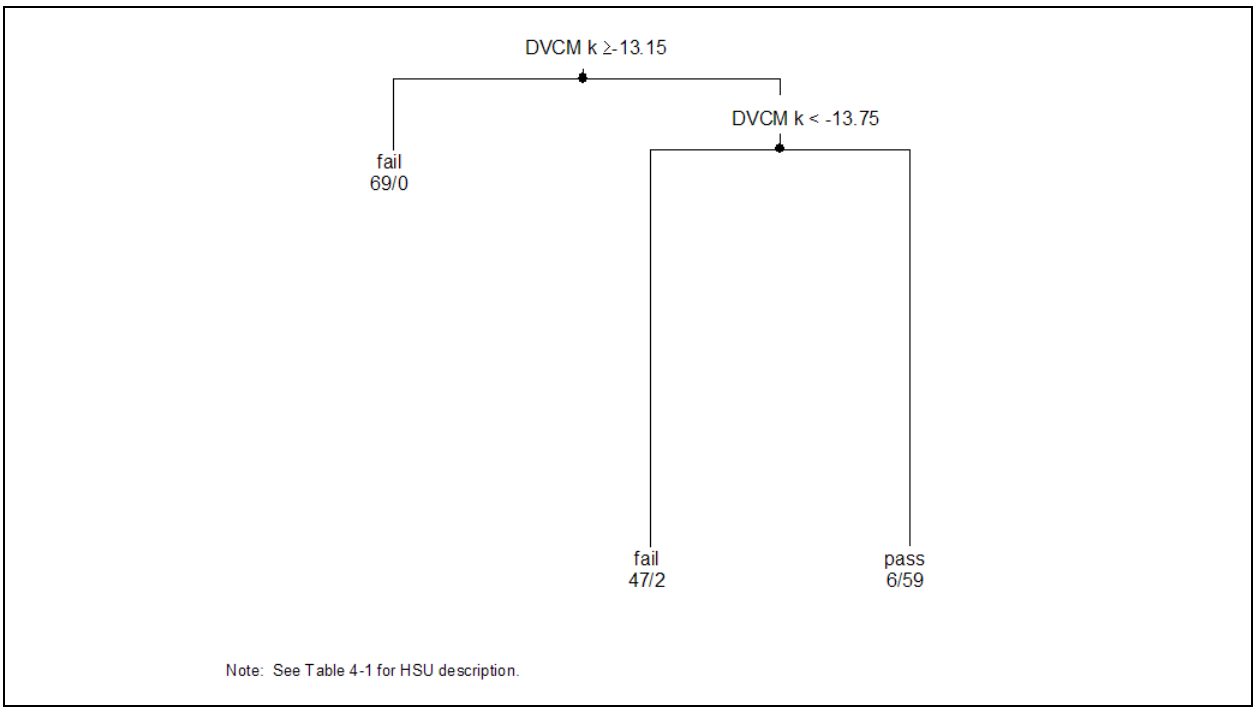

Figure 6-68
Classification Tree for Western Boundary Flux for BN-MME-SDA

Uncontrolled When Printed

6.2.4 Other Model Sensitivities

6.2.4.1 Sensitivity to Evapotranspiration Extinction Depth in Oasis Valley

The DVRFS model (Faunt et al., 2004), the UGTA regional model (DOE/NV, 1997, IT, 1996a through f; IT, 1997a and b), and the CAU flow model all treat ET discharge in Oasis Valley with a third-type boundary condition, where head is set at a value below ground surface representative of the maximum depth that plants can draw water from the water table (the extinction depth). When the simulated head drops below this value, discharge no longer occurs. In the UGTA regional flow model (DOE/NV, 1997), this head was determined by locating the lowest land surface elevation in the cell that encompassed all or part of the Oasis Valley discharge area and assigning a head 10 m below that point. A similar approach was used in the DVRFS. Both these regional models had grid blocks up to 1.5 km on a side in the Oasis Valley region. The Pahute Mesa CAU model has much smaller elements (down to 67.5 m) in Oasis Valley. The land surface elevation at the node was estimated from a digital elevation model, and then a head 3 m below that was assigned from depth to water considerations described in Section 4.3.2.

The sensitivity of the flow model to assumed extinction depth was tested by changing the head at nodes where Oasis Valley ET was simulated for 5 and 10 m less than land surface, the latter value being consistent with the regional models. Increasing the extinction depth to 5 m only increased the model goodness of fit by 0.6 percent, changing the simulated Oasis Valley discharge from 209 to 215 kg/s. Increasing the extinction depth to 10 m increased the objective function by 8 percent (to 18,032) and discharge to 228 kg/s. Thus, it is concluded that over the range deemed reasonable extinction depth is not a greatly sensitive parameter.

6.2.4.2 Reduced LCCU1 Permeability Alternative

The PEST sensitivity, perturbation, and global analyses all ranked the LCCU1 for both the base and SCCC HFM as sensitive. This result is unexpected, because the unthrusted LCCU has such low permeability that it can be considered the bottom of the UGTA regional flow system. The mean permeability estimated for the LCCU1 is relatively high (3×10^{-13} thrusted versus 3×10^{-19} m^2 unthrusted) based on assumed fracturing from thrusting, but is unknown. This discrete sensitivity analysis investigates how the model behaves when the LCCU1 permeability is decreased from

Uncontrolled When Printed

3.7×10^{-13} to 2.9×10^{-14} m^2 and recalibrated. This analysis was done only on the base HFM - selected HSU depth-decay and anisotropy case (BN-MME-SDA).

Figures 6-69 through 6-72 show the observed and unweighted simulated values for the calibration wells, springs, Oasis Valley discharge, and boundary flows. On Figures 6-69 and 6-70, the line of perfect agreement is shown [LCCU1 wells and LCCU1 springs], and ideally the data would plot exactly onto this line. At the very highest observed observation well heads, the model has a tendency toward undersimulation. These plots are not significantly different than those shown in Section 5.6.2.

Calibration summary statistics are shown in Table 6-14, and again are not appreciably different from those in Section 5.6.2. WW-8 is the well with the highest undersimulation in this case, which is a change from the base HFM. It is concluded that the LCCU1 was acting to support heads in the far east-central part of the model domain. It is not known whether this is reasonable, but there are geochemical consequences as further shown in Section 7.0. The objective function for these results is 16,623, which is nearly identical to the value of 16,651 shown in Section 5.6.2.

Figure 6-73 shows the simulated water table, and Figure 6-74 shows the particle tracks from NTS wells. The overall sense of the water table and flow paths do not change appreciably from Section 5.6.2. Some tracks on the eastern part of the domain go much deeper than before, presumably because less flow is routed into the LCCU1 to drive particles horizontally.

Compensating changes in permeability to maintain model calibration resulted in an increase of almost four orders of magnitude in the LCA3 (the thrusted eastern portion of the LCA) reference permeability. Lesser changes were noted in the CHZCM (about an order of magnitude drop), and an order of magnitude drop in the PRBCM Zone 87 (the wedge that separates the SCCC and Timber Mountain).

Uncontrolled When Printed

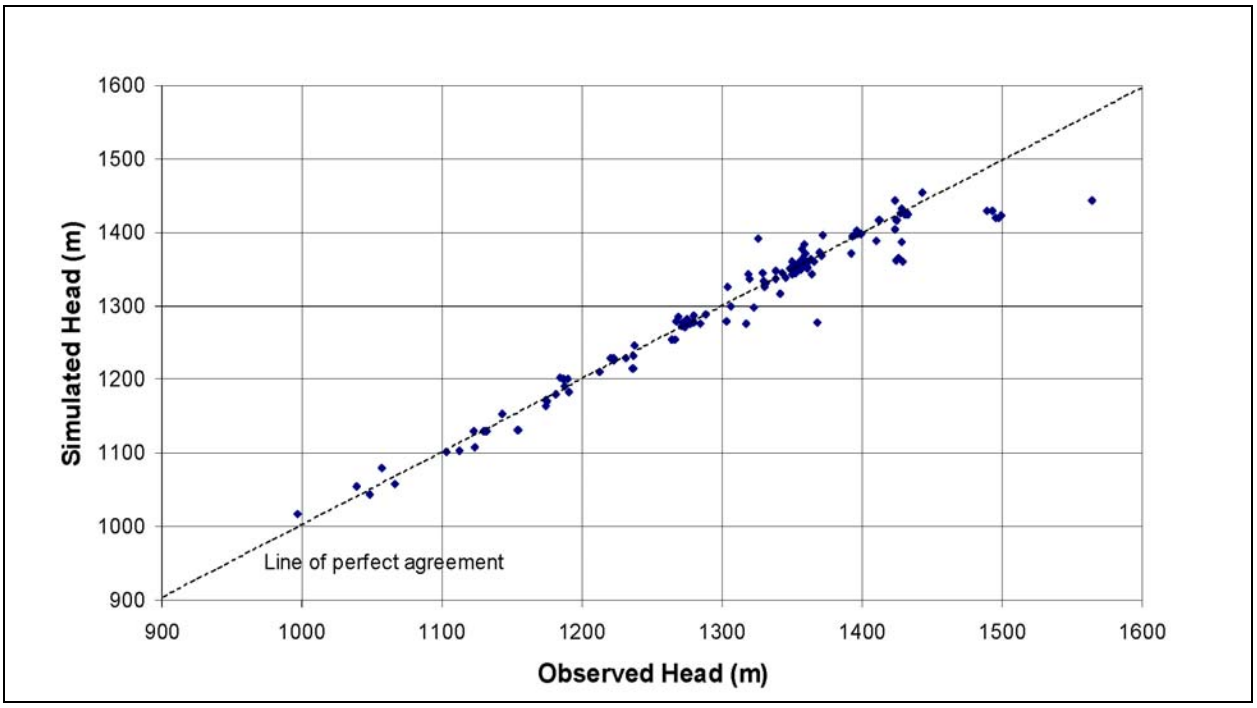

Figure 6-69
Observed Versus Simulated Observation Well Head for BN-MME-SDA Reduced LCCU1 Permeability Alternative

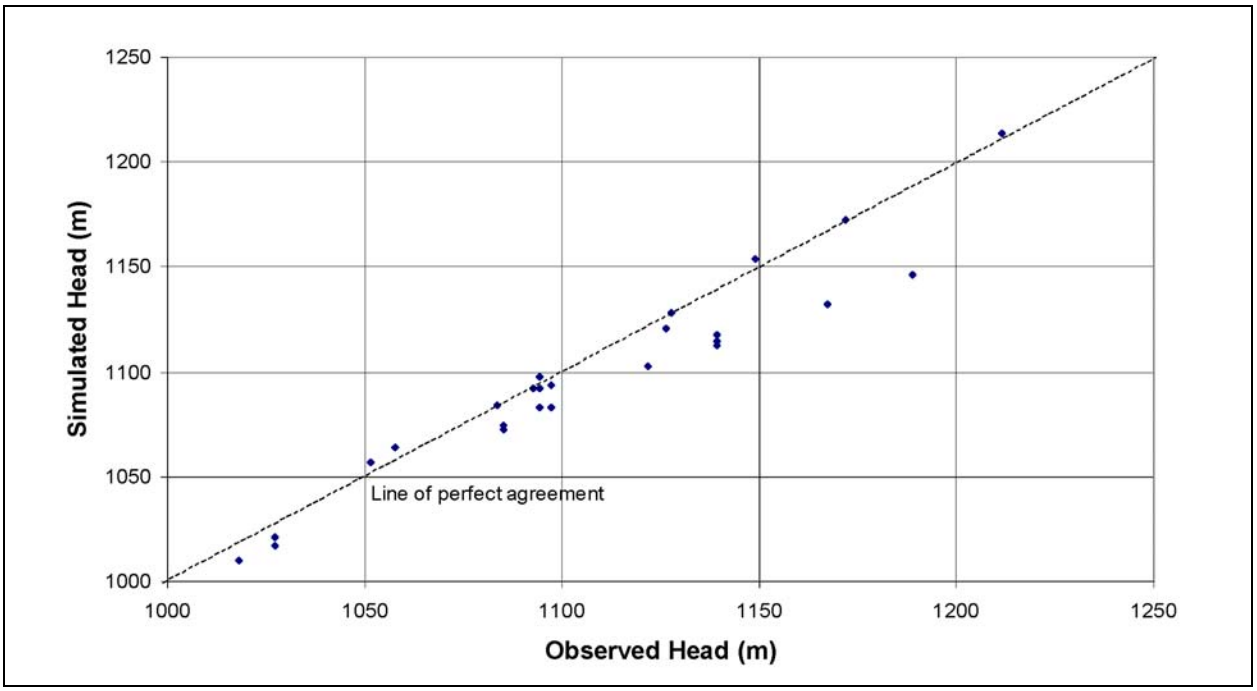

Figure 6-70
Observed Versus Simulated Spring Head for BN-MME-SDA Reduced LCCU1 Permeability Alternative

Uncontrolled When Printed

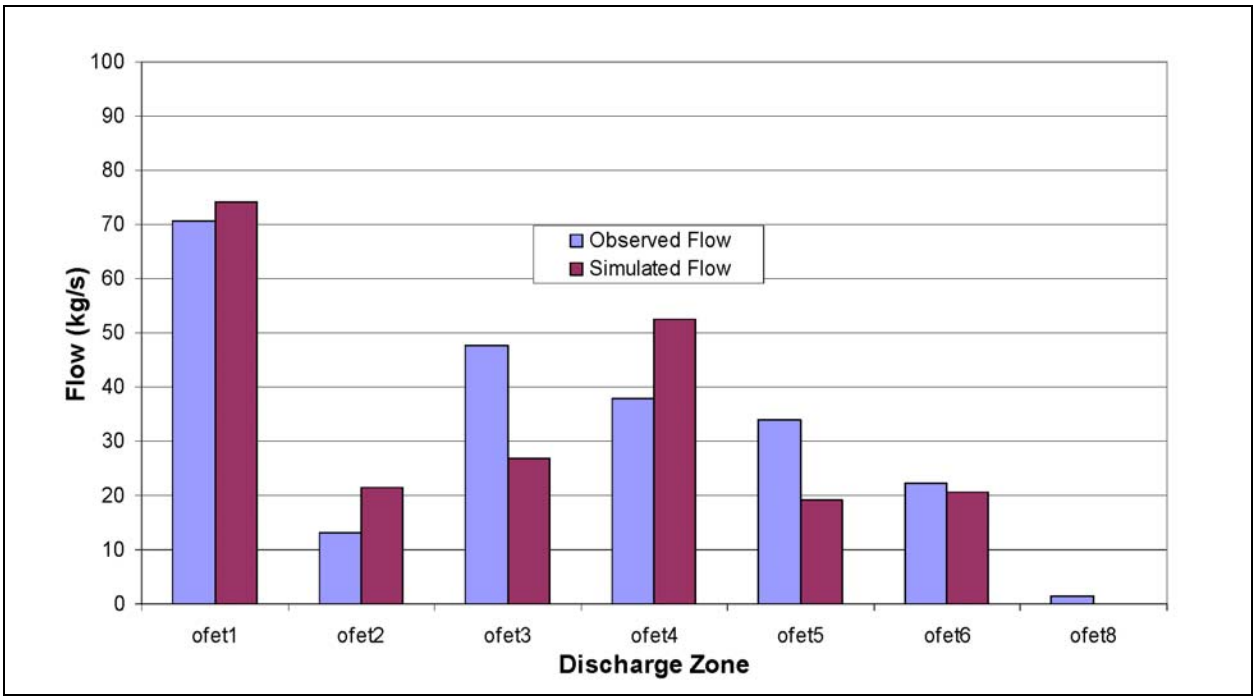

Figure 6-71
Observed and Simulated Oasis Valley Discharge for BN-MME-SDA Reduced LCCU1 Permeability Alternative

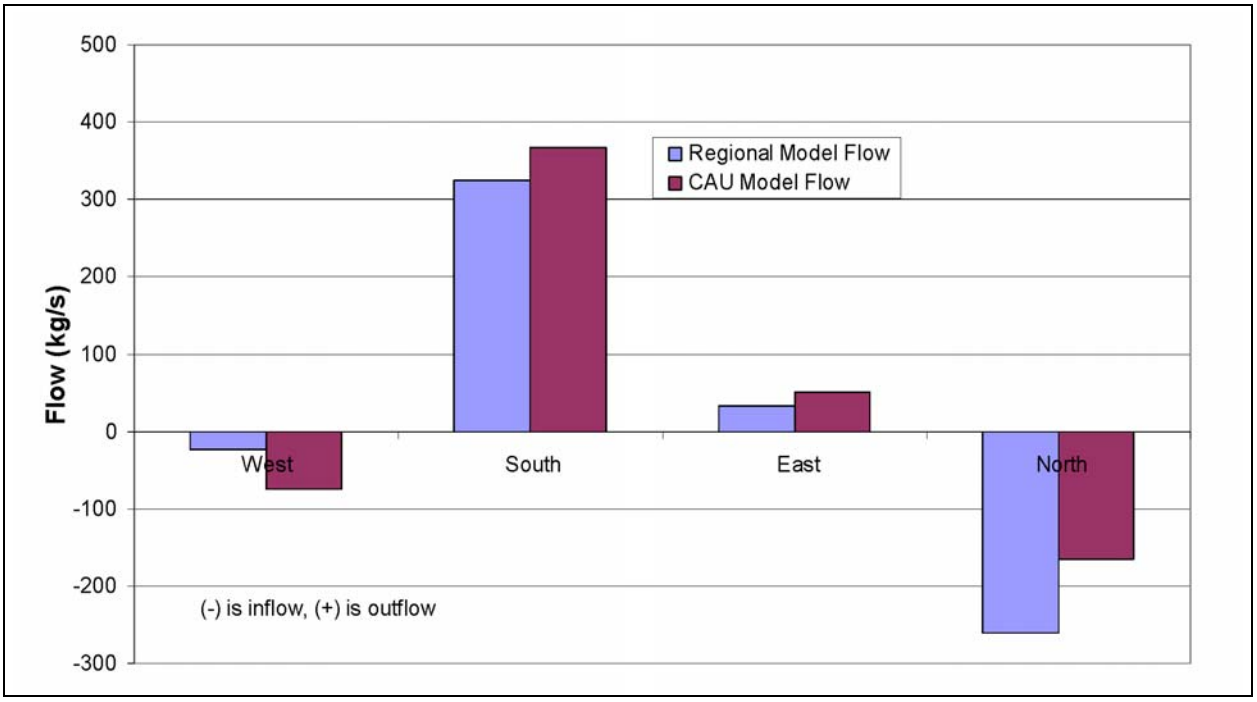

Figure 6-72
Observed and Simulated Boundary Flows for BN-MME-SDA Reduced LCCU1 Permeability Alternative

Uncontrolled When Printed

Table 6-14
Calibration Summary Statistics for BN-MME-SDA Reduced LCCU1 Permeability Alternative

Calibration Data	Number of Data	Mean Weighted Error (m or kg/s)[a]	Maximum Weighted Residual	Minimum Weighted Residual	Error Standard Deviation (m or kg/s)
Well Head	152	-0.056	21 (WW-8)	-24 (U-19ad)	7.3
Spring Head	28	2.6	19 (Torrance Spring)	-6.3 (Spring id 159)	6.8
Oasis Valley Discharge	7	3.4	41 (Zone 3)	-29 (Zone 4)	23
Boundary Flow	4	-13	26 (West)	-47 (North)	29

[a]Positive sign is simulated less than target, negative is larger.

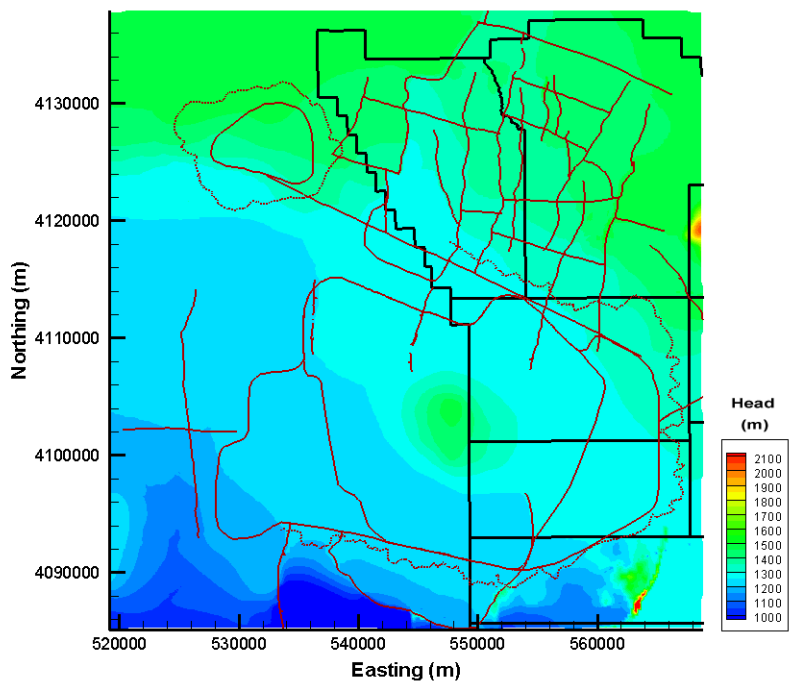

Figure 6-73
Simulated Water Table for BN-MME-SDA Reduced LCCU1 Permeability Alternative

Uncontrolled When Printed

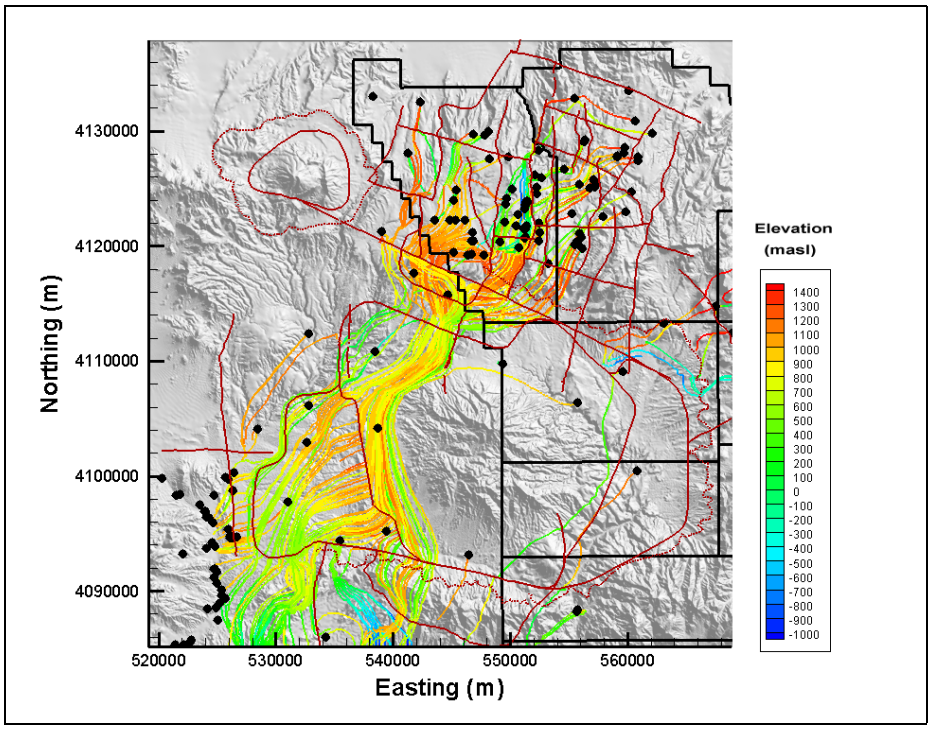

Figure 6-74
Particle Tracks for BN-MME-SDA
Reduced LCCU1 Permeability Alternative

6.2.4.3 Chimney Permeability Enhancement

Pawloski et al. (2001) used chimney permeability values that were at least 70 times higher than the native rock to simulate groundwater flow near CHESHIRE. The chimneys were incorporated in the CAU flow model mesh where the tests were below the water table, and their effect on the flow model was investigated by applying a permeability multiplier of 70 for the chimney nodes. Table 6-15 summarizes the calibration statistics. The objective function changed slightly to 16,609 from 16,651 in the base HFM. Figure 6-75 shows the simulated flow paths, which are very similar to the base HFM - selected HSU depth-decay and anisotropy results. It is concluded that there is very little flow model sensitivity to chimney permeability alteration.

Conceptually this is correct, because the overall scale of alteration is relatively small and any observation well close enough to a test to detect the chimney permeability alteration would be so affected by the test that it would be difficult to use in the calibration.

Uncontrolled When Printed

Table 6-15
Calibration Summary Statistics for Chimney Permeability Enhancement

Calibration Data	Number of Data	Mean Weighted Error (m or kg/s)[a]	Maximum Weighted Residual	Minimum Weighted Residual	Error Standard Deviation (m or kg/s)
Well Head	152	-0.4	19 (ER-OV-06a)	-27 (UE-20n #1 1,005.84 m)	7.5
Spring Head	28	2.8	19 (Torrance Spring)	-5.5 (Ute Springs Culvert)	6.7
Oasis Valley Discharge	7	4.9	41 (Zone 3)	-26 (Zone 4)	24
Boundary Flow	4	-14	26 (West)	-36 (South)	27

[a]Positive sign is simulated less than target, negative is larger.

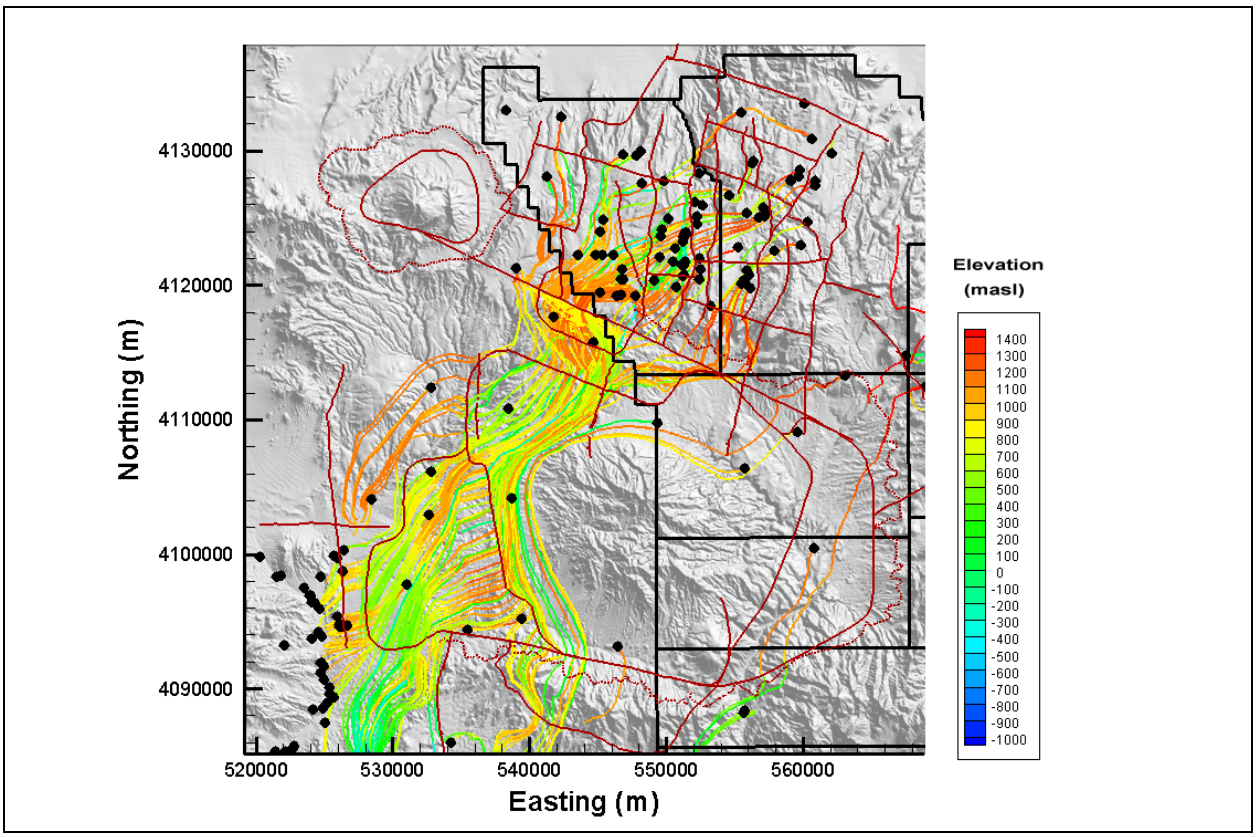

Figure 6-75
Particle Tracks for Chimney Permeability Enhancement

Uncontrolled When Printed

6.2.4.4 Fortymile Canyon Alternative

This variation was designed to test the model sensitivity to flow down Fortymile Canyon. The TMCM Northern Timber Mountain eastern subdivision, Timber Mountain Dome, and Ammonia Tanks eastern subdivision permeabilities were all raised an order of magnitude to try to direct more flow down Fortymile Canyon. The LCCU1 permeability was dropped an order of magnitude to remove its influence and test the ability of recharge in the canyon to support the flow field. This analysis was done only on the base HFM selected HSU depth-decay and anisotropy parameterization, with the USGSD recharge model (which generally tends to give the best calibration results).

Calibration summary statistics are shown in Table 6-16, with simulated Oasis Valley (179 simulated versus 227 kg/s observed) discharge is noticeably lower as the mean observation well error with respect to Table 5-9 in Section 5.6.2. The simulated Oasis Valley discharge is about two standard deviations (about 30 kg/s) away from the estimated value; thus, this model has a lower plausibility than others that agree better with Oasis Valley discharge data. WW-8 is the well with the highest undersimulation in this case, which is consistent with the effects of dropping the LCCU1 permeability. The objective simulation for these results is 19,588, which is slightly worse than the value of 16,651 shown in Section 5.6.2, but still better than the SCCC-MME-SDA and BN-MME-ADA cases.

Table 6-16
Calibration Summary Statistics for BN-MME-SDA Fortymile Canyon Alternative

Calibration Data	Number of Data	Mean Weighted Error (m or kg/s)	Maximum Weighted Residual	Minimum Weighted Residual	Error Standard Deviation (m or kg/s)
Well Head	152	1.3	52 (WW-8)	-23 (U-19ad)	8.7
Spring Head	28	3.1	19 (Torrance Spring)	-5.3 (Spring id 159)	6.8
Oasis Valley Discharge	7	14	47 (Zone 2)	-11 (Zone 3)	26
Boundary Flow	4	2.8	30 (East)	-32 (North)	24

[a]Positive sign is simulated less than target, negative is larger.

Uncontrolled When Printed

Figure 6-76 shows weighted residuals, and Figure 6-77 shows the particle tracks. There is clearly a bias in Fortymile Canyon from the changes that is not easily compensated for with other parameters. This is interpreted as arising from the draining off of water along the canyon from the higher permeabilities. Many more particle tracks exit Areas 19 and 20 and flow down Fortymile Canyon than in the BN-MME-SDA case, which is consistent with the bias to undersimulate Oasis Valley discharge noted in Table 6-16.

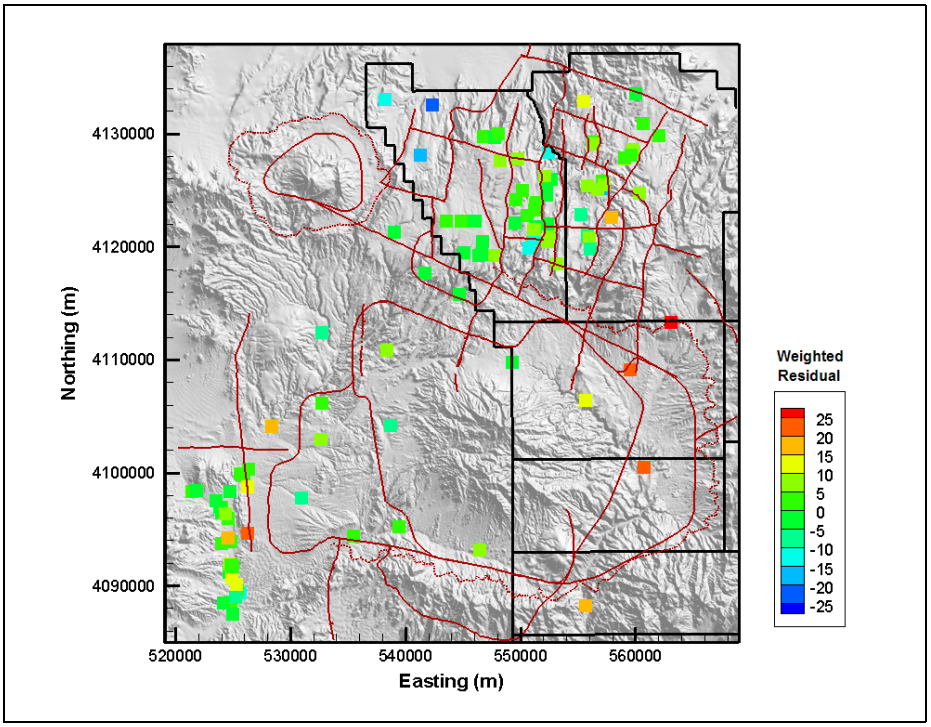

Figure 6-76
Post Plot of Weighted Well and Spring Head Residuals for BN-MME-SDA Fortymile Canyon Alternative

6.2.4.5 Selected Hydrostratigraphic Horizontal Anisotropy

Anisotropy, or directional dependency, in permeability is a characteristic property of fractured rocks (NRC, 1996). Hydraulic anisotropy is commonly determined from multiwell hydraulic test analysis, such as that performed during the BULLION FGE in Area 20 (IT, 1998a) that estimated an average major-to-minor direction permeability ratio of 8 striking about N30°E. These are the only data available for Pahute Mesa. However, fracture analysis as observed in borehole logs can be used as a qualitative tool to assess possible anisotropy. Analysis of composite data for fractures identified in

Uncontrolled When Printed

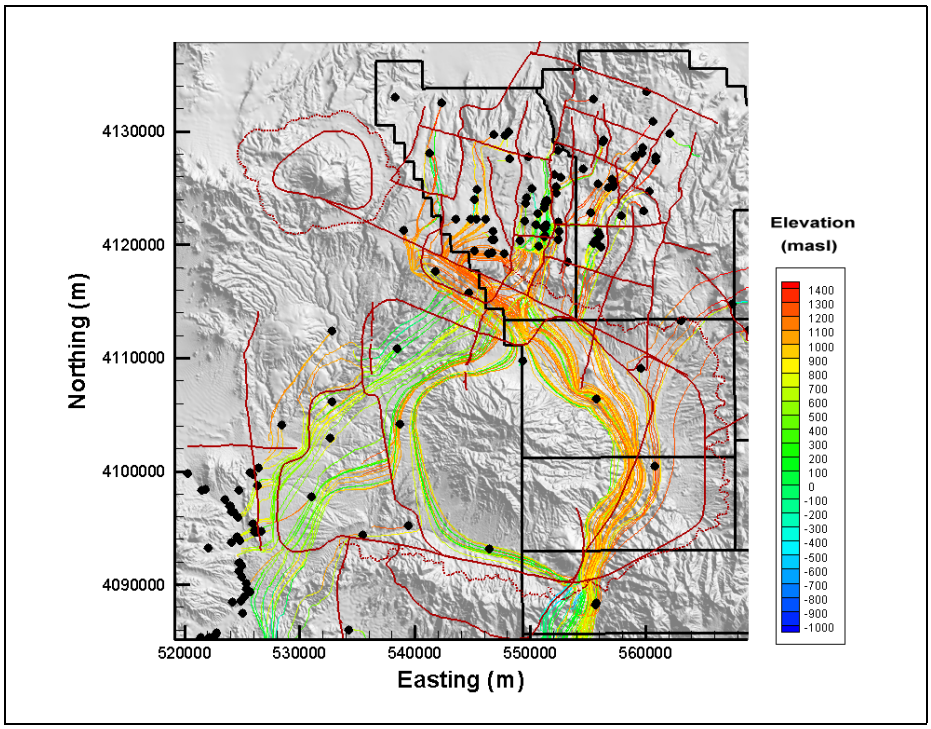

Figure 6-77
Particle Tracks for BN-MME-SDA Fortymile Canyon Alternative

Pahute Mesa and Oasis Valley wells completed in volcanic rocks (LFA, WTA, VTA, and TCU HGUs) reveals four mean fracture populations (IT, 2001). The two predominant populations trend roughly north, and dip west and east. The two secondary populations trend roughly northeast and northwest, and dip northwest and northeast, respectively. The difficulty in utilizing fracture data is illustrated by comparing the BULLION FGE results to the fracture analysis; the hydraulic test is within the range of directions, but the range in direction is very wide (essentially 90°). Horizontal anisotropy was not used in the model because the sparseness of the data were felt to be prohibitive. In addition, the computational demands of using an arbitrary permeability tensor with FEHM make it computationally infeasible. However, the FEHM mesh for the Pahute Mesa flow model is aligned north-south, which allows testing of anisotropy aligned with the strike of the mesh.

Increasing the permeability by a factor of 5 in the y, or north-south, direction for the reduced LCCU1 permeability case (see Section 6.2.4.2) for selected HSUs and recalibrating the model investigated the effects of horizontal anisotropy. Pawloski et al. (2001) used the same value of horizontal anisotropy in their analysis of the CHESHIRE test. Conceptually not all HSUs should have anisotropy, and the ones that were included were lavas and units that had welded tuff present. Thus, all the composite

Uncontrolled When Printed

HSUs were changed, as well as lava-flow aquifers. The changed HSUs are as follows: PBRCM, DVCM, YMCFCM, PCM, TMA, KA, BA, PLFA, CHZCM, TSA, TCA, TMCM, THLFA, THCM, FCA, FCCM, DVA, and TCVA.

Figures 6-78 through 6-81 show the observed and unweighted simulated values for the calibration wells, springs, Oasis Valley discharge, and boundary flows. The Oasis Valley discharge is much too high for Zone 4, which results in the downstream flows being too low. The spring heads also show a bias toward undersimulation that is related to the discharge imbalance. The FCCM and, to a lesser degree, TMCM control shallow flow in that area, and thus the effects on discharge are attributed to the impact anisotropy has on these units.

Table 6-17 summarizes the calibration statistics. The objective function is 32,011. Relative to the LCCU1-MME-SDA calibration, this calibration is distinctly worse and is one of the poorest models evaluated. The degradation in model calibration primarily occurred because of Oasis Valley discharge misfit, although the bias to underpredict spring heads is also increased relative to LCCU1-MME-SDA.

Figure 6-82 shows the posted weighted residuals; there is a slight bias to undersimulate water levels in Oasis Valley that is also suggested by the spring head mean error. There is a pattern of oversimulation through the Thirsty Canyon area down to Oasis Valley that probably causes the oversimulation of discharge in the northern part of the valley. Simulated Oasis Valley discharge is 244 kg/s, which is within 10 percent of the estimated only because of the averaging of errors. Figure 6-83 shows the simulated water table, and Figure 6-84 shows the simulated flow paths. The water table and flow paths have the same general character seen in all the simulation. Thus, including horizontal anisotropy does not create completely implausible results, although the oversimulation of Oasis Valley discharge is probably related to horizontal anisotropy because it is harder to move water east-west into Oasis Valley and it is ringed with composite units that, for this test, had horizontal anisotropy. This effect may also be related to the north-south orientation dictated by the mesh, conceptually if a more easterly strike is used the concentration of flow into northern Oasis Valley might not be so severe. A spatially variable anisotropy would also offset the north-south effects, but no data exist to define such patterns.

Uncontrolled When Printed

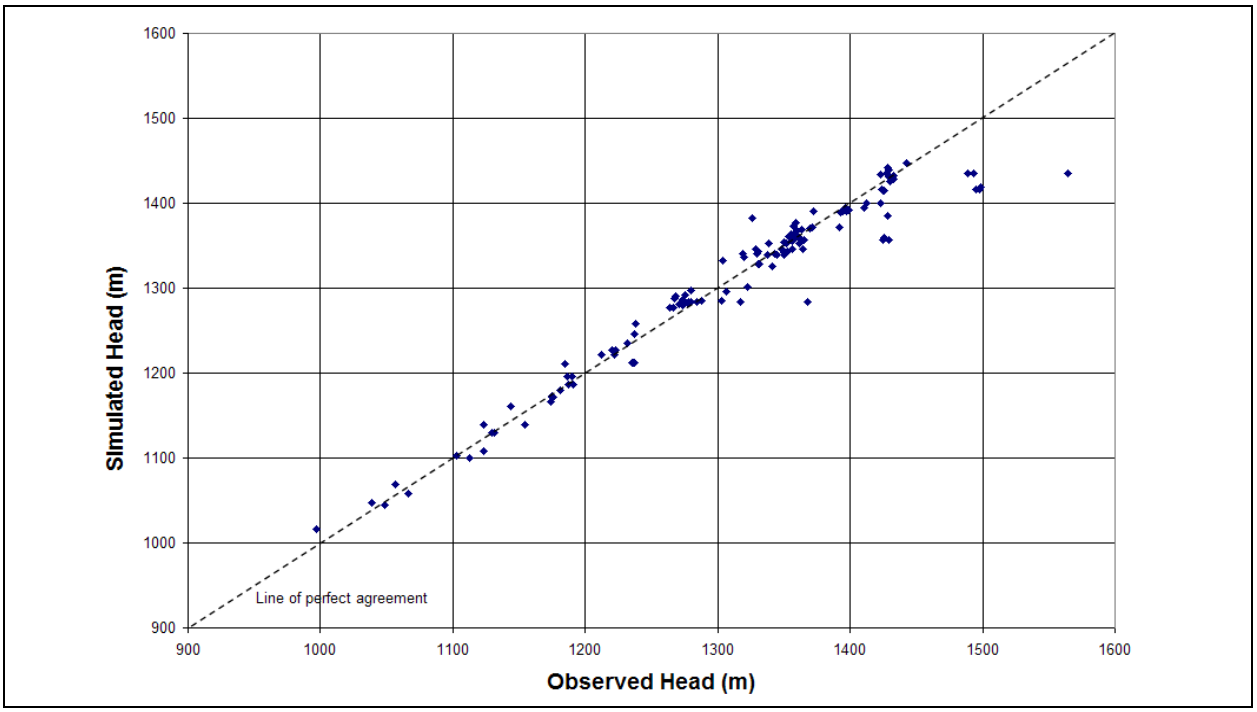

Figure 6-78
Observed Versus Simulated Observation Well Head for BN-MME-SDA Reduced LCCU1 Permeability Alternative with 5:1 North-South Anisotropy

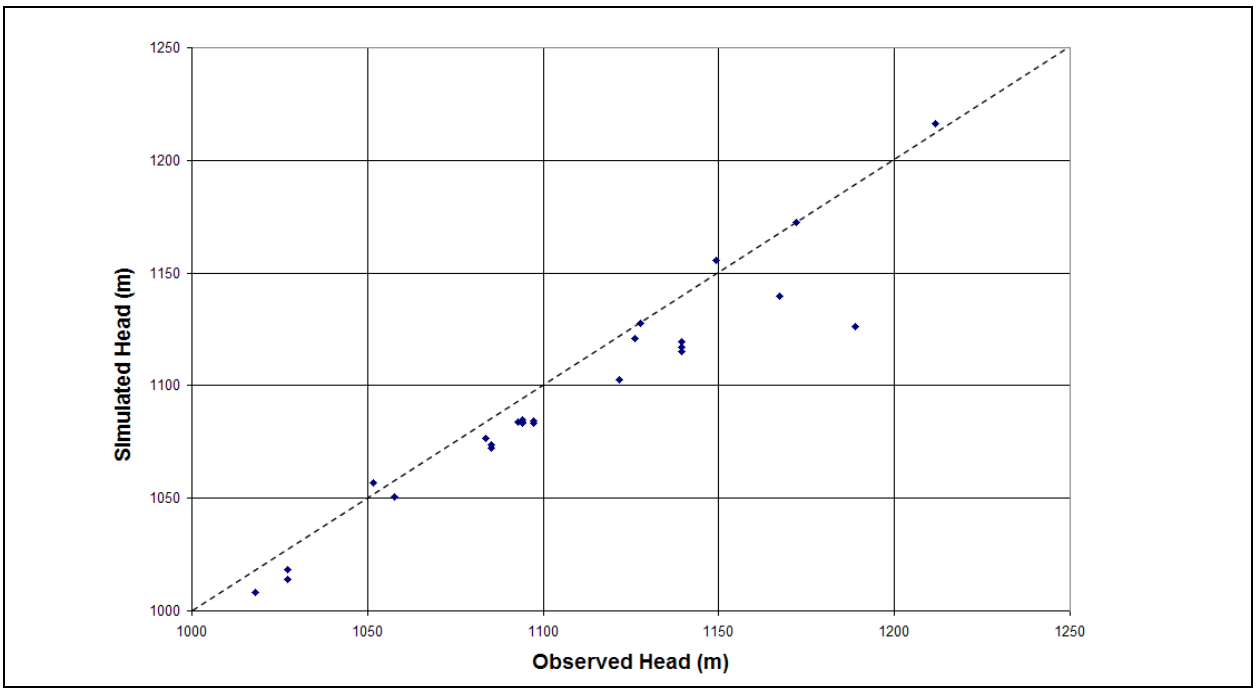

Figure 6-79
Observed Versus Simulated Spring Head for BN-MME-SDA Reduced LCCU1 Permeability Alternative with 5:1 North-South Anisotropy

Uncontrolled When Printed

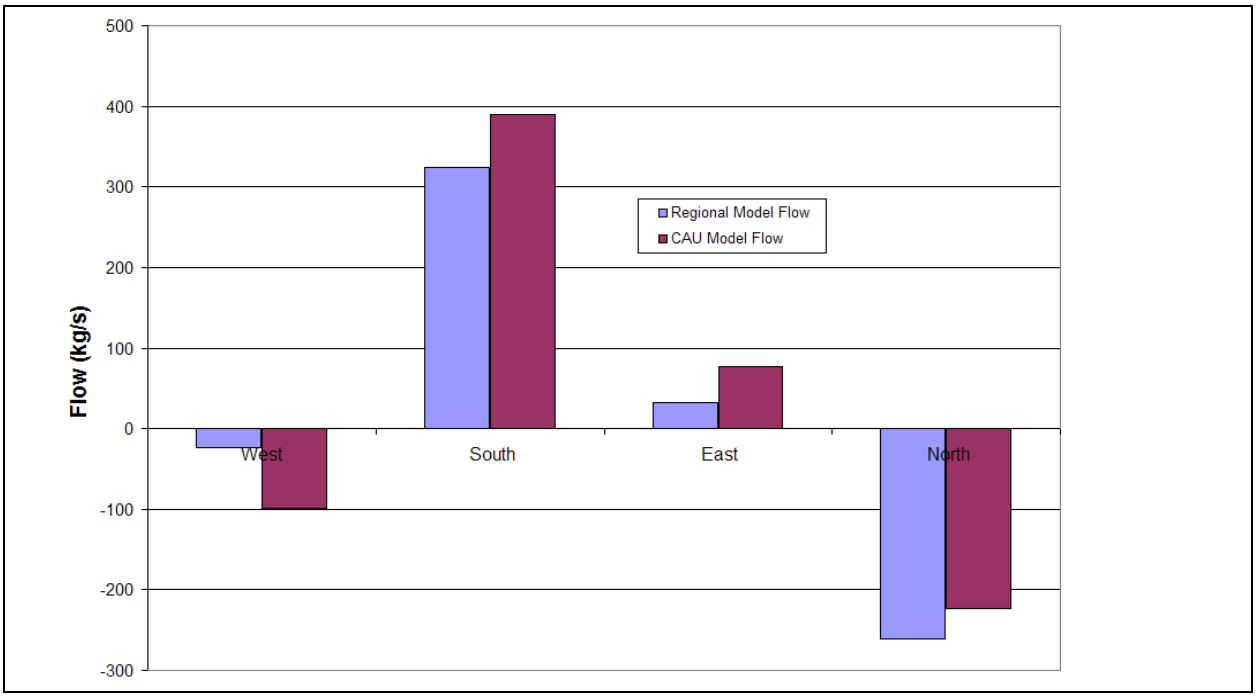

Figure 6-80
Observed and Simulated Oasis Valley Discharge for BN-MME-SDA Reduced LCCU1 Permeability Alternative with 5:1 North-South Anisotropy

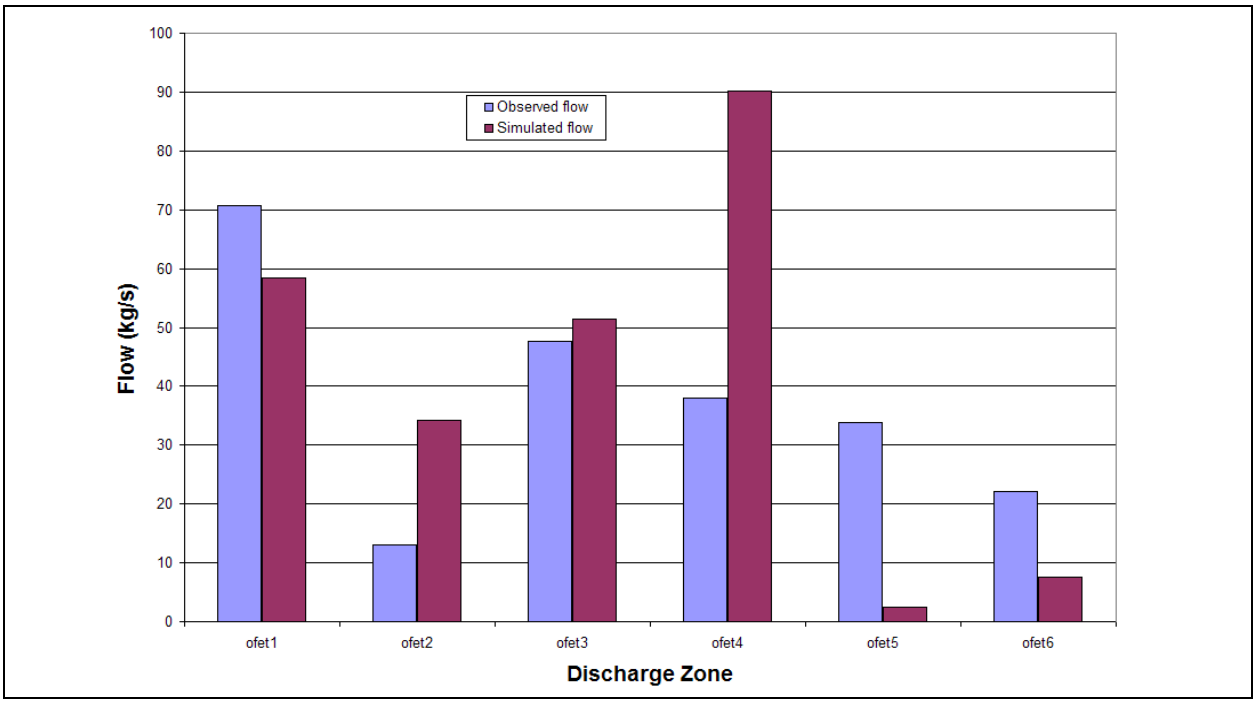

Figure 6-81
Observed and Simulated Boundary Flows for BN-MME-SDA Reduced LCCU1 Permeability Alternative with 5:1 North-South Anisotropy

Uncontrolled When Printed

Table 6-17
Calibration Summary Statistics for LCCU1-MME-SDA with Selected HSU Horizontal Anisotropy of 5:1

Calibration Data	Number of Data	Mean Weighted Error (m or kg/s)	Maximum Weighted Residual	Minimum Weighted Residual	Error Standard Deviation (m or kg/s)
Wells	152	-0.74	20 (ER-OV-06a)	-21 (UE-20n #1) (1,005.84 m)	7.4
Springs	28	5.2	19 (Torrance Spring)	-6.5 (Spring id 159)	8.5
Oasis Valley Discharge	7	-5.0	62 (Zone 5)	-104 (Zone 4)	51
Boundary Flow	4	-9.1	38 (West)	-33 (South)	29

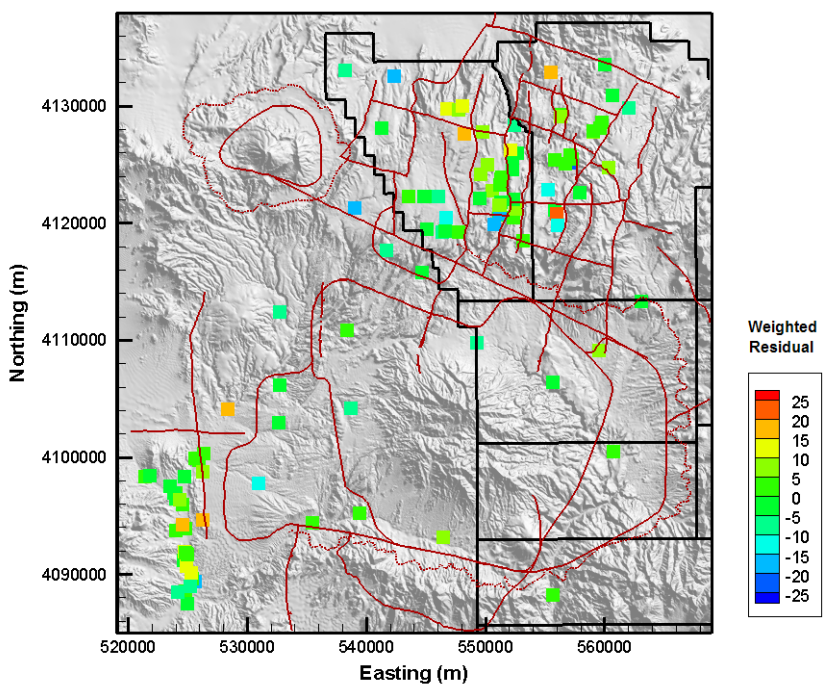

Figure 6-82
Post Plot of Weighted Well and Spring Head Residuals for BN-MME-SDA Reduced LCCU1 Permeability Alternative with 5:1 North-South Anisotropy

Uncontrolled When Printed

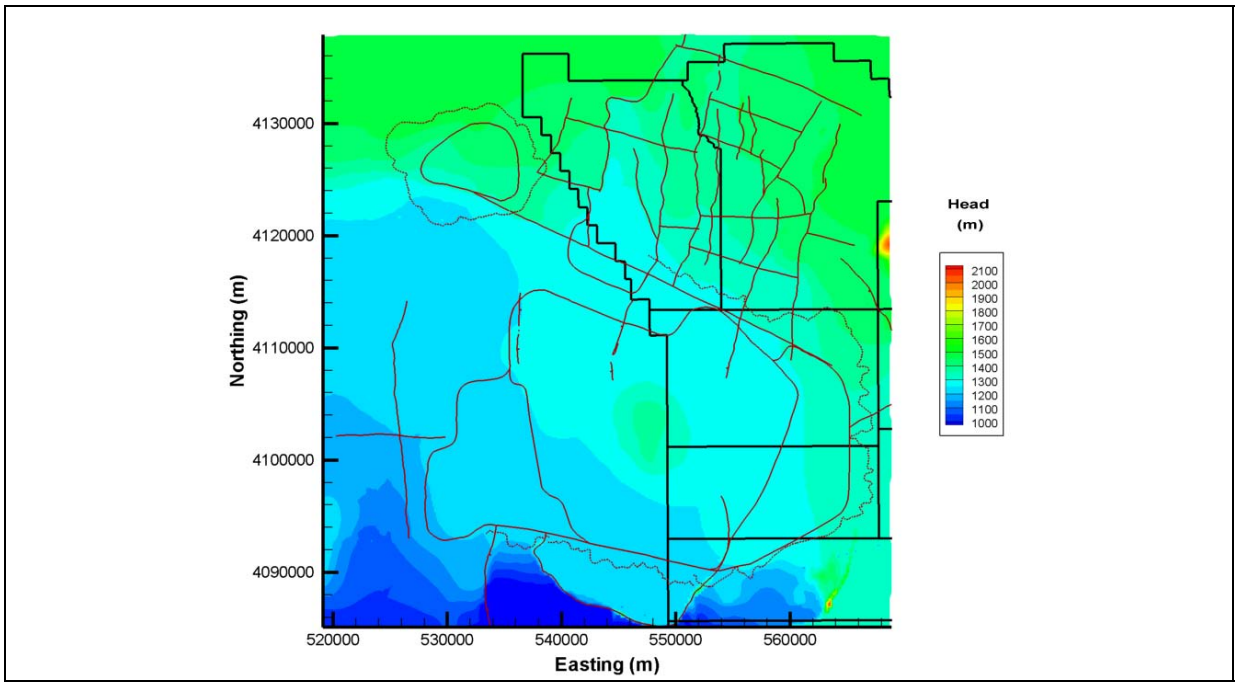

Figure 6-83
Simulated Water Table for BN-MME-SDA Reduced LCCU1 Permeability Alternative with 5:1 North-South Anisotropy

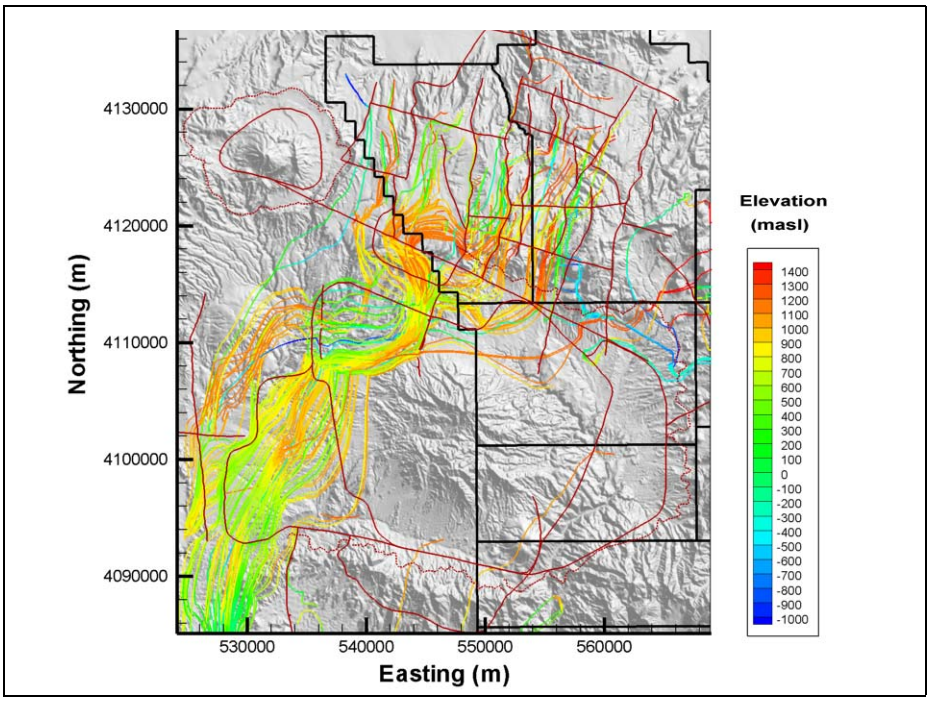

Figure 6-84
Particle Tracks for BN-MME-SDA Reduced LCCU1 Permeability with 5:1 North-South Anisotropy

Uncontrolled When Printed

The HSUs with changed permeability are shown in Figure 6-85. The geometric mean permeability (including reference permeability for HSUs with depth decay) was computed for the anisotropy case and subtracted from the LCCU1-MME-SDA permeability. The display is in log space; thus, a difference of 1.0 is an order of magnitude, and a negative value is an increase from the isotropic case. Figure 6-85 shows that there is a ubiquitous increase in effective permeability when north-south anisotropy is added. This is interpreted to arise because the flow system in the area, while showing a distinct north-south trend, is not strictly north-south like the anisotropy and higher effective permeabilities are required to move water in off-strike directions.

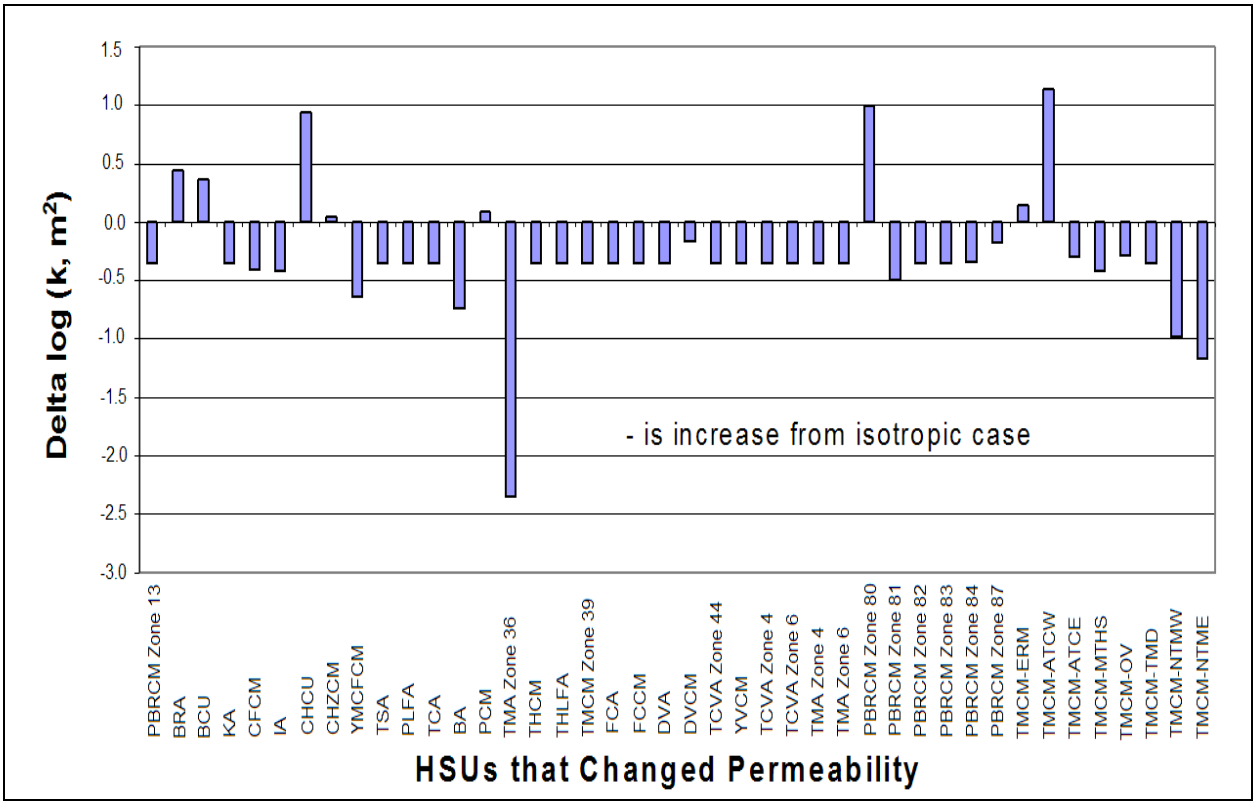

Figure 6-85
HSU Permeability Changes for BN-MME Reduced LCCU1 Permeability with 5:1 North-South Anisotropy

Uncontrolled When Printed

6.2.4.6 Timber Mountain Hydraulic Effects

All of the Pahute Mesa flow models, to some degree and by design, show the effect of a recharge mound under Timber Mountain. This feature is inferred from first principles and only suggested by the observation well data. Because the mound is an interpreted feature, it is important to understand its impact on the flow model. In addition, the Timber Mountain Composite (TMCM) HSU was subdivided during calibration, and the final impact of the subdivision should be investigated (individual parameter sensitivity is described earlier in Section 6.0). Three cases were investigated: 1) material 74, which represents the Timber Mountain Dome area (the area with the highest recharge in Timber Mountain) in Figure 5-6 and is used to control the height of the mound, reference permeability was increased 10 times; 2) the Timber Mountain Dome subdivision of the TMCM reference permeability was increased 100 times; and 3) a single value of the TMCM reference permeability was used.

In each case, the parameter change was made (and stayed fixed in the first two cases) and the model recalibrated. The reduced LCCU1 permeability alternative with MME recharge and selected depth decay as described in Section 6.2.4.2 was used as the starting point for these analyses.

Figures 6-86 through 6-89 show the observed and unweighted simulated values for the calibration wells, springs, Oasis Valley discharge, and boundary flows for all three cases. In general, the differences are mild, and the single TMCM-material case shows the largest errors.

Table 6-18 summarizes the calibration statistics. The objective functions are 16,690, 18,156, and 24,180 (recall the calibration of the case from which these analyses were derived was 16,623) for cases 1 through 3, respectively. The impact of adjusting Timber Mountain Dome and TMCM is generally the same for all cases; model agreement at WW-8 degrades, Torrance Spring is misfit, west and north boundary flows are misfit, as is ET Zone 3 in Oasis Valley.

Uncontrolled When Printed

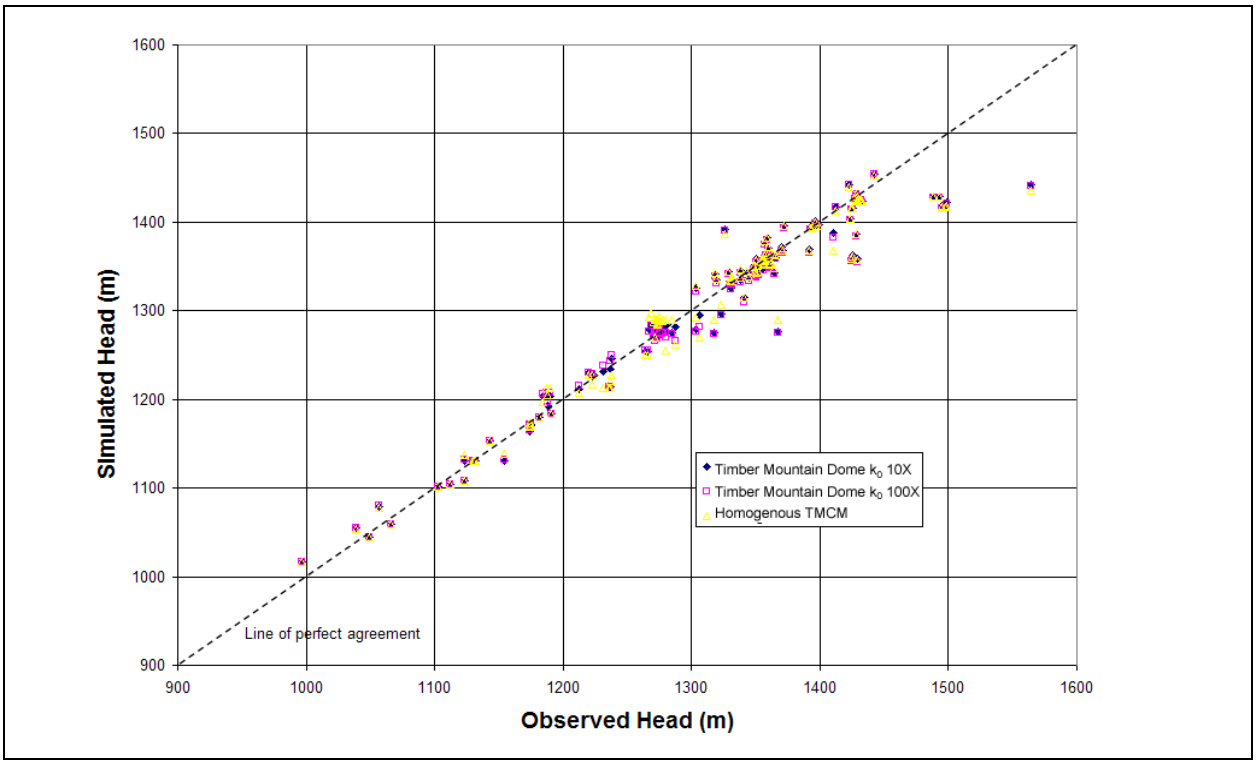

Figure 6-86
Observed Versus Simulated Observation Well Head for TMCM-MME-SDA

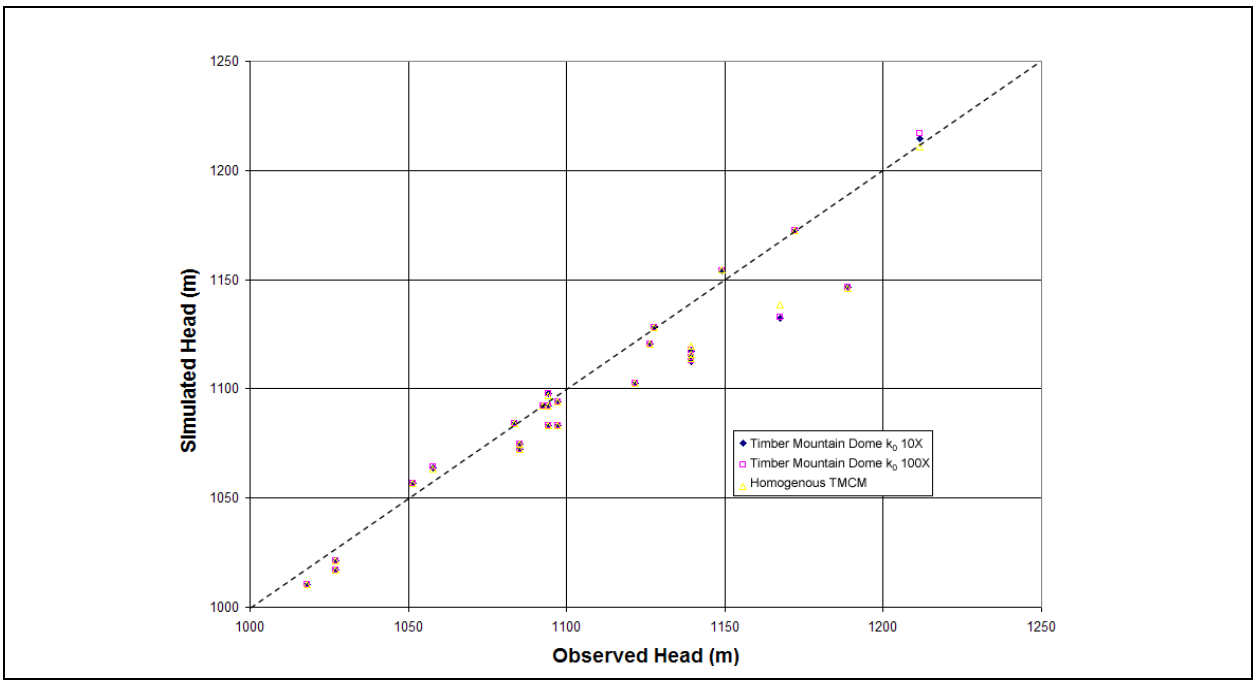

Figure 6-87
Observed Versus Simulated Spring Head for TMCM-MME-SDA

Uncontrolled When Printed

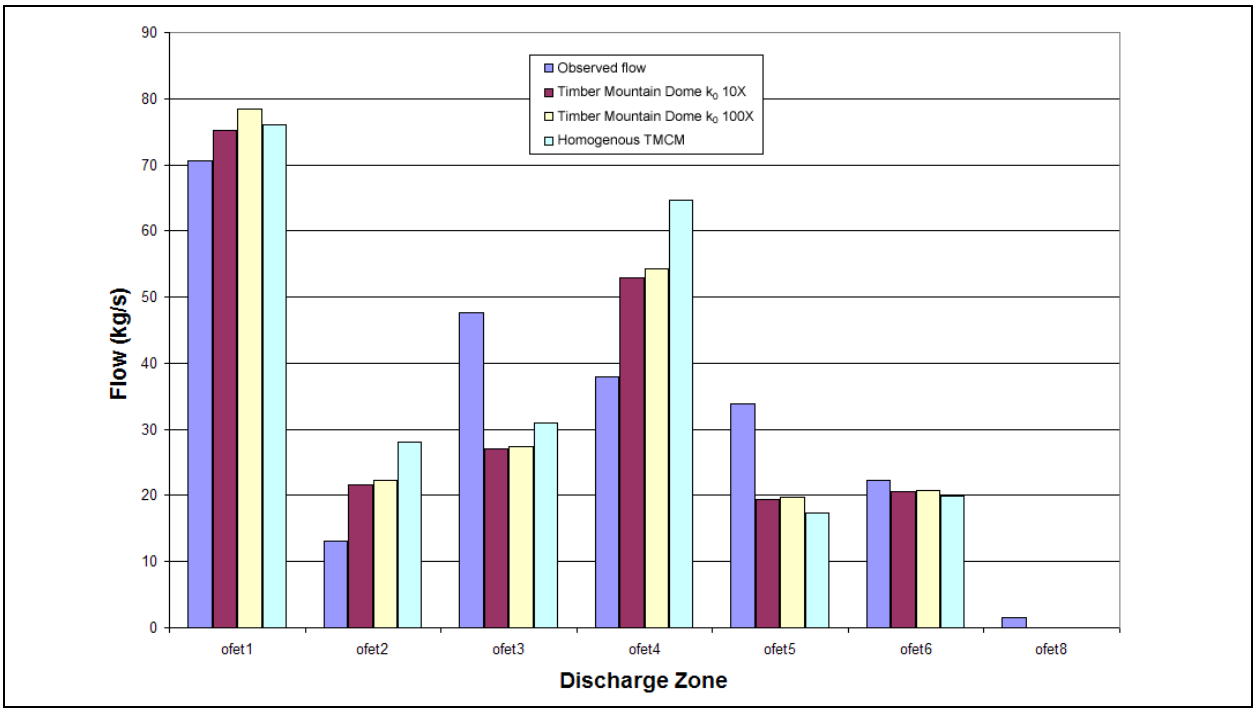

Figure 6-88
Observed and Simulated Oasis Valley Discharge for TMCM-MME-SDA

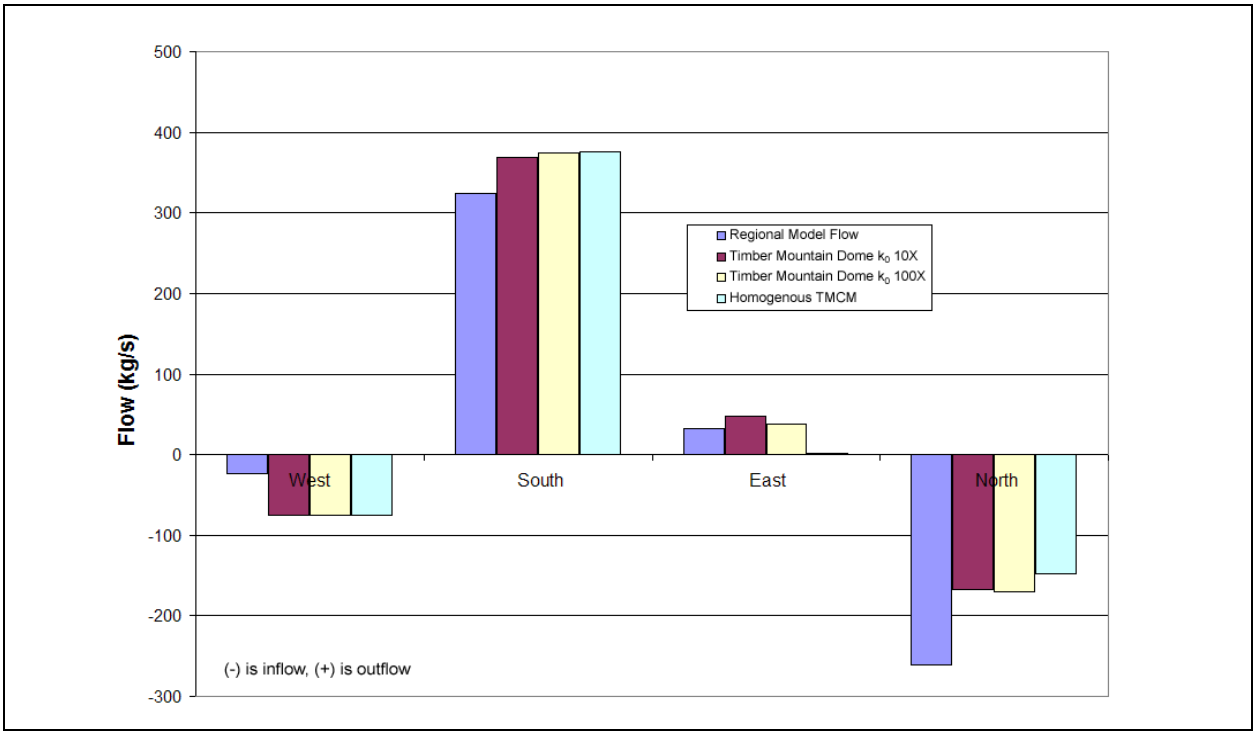

Figure 6-89
Observed and Simulated Boundary Flows for TMCM-MME-SDA

Uncontrolled When Printed

Table 6-18
Calibration Summary Statistics for Timber Mountain Dome Sensitivity

Calibration Data	Number of Data	Mean Weighted Error (m or kg/s)	Maximum Weighted Residual	Minimum Weighted Residual	Error Standard Deviation (m or kg/s)
Wells	152	0.44[a] 1.4[b] 0.12[c]	23 (WW-8) 27 (WW-8) 41 (WW-8)	-23 (U-19ad) -21 (U-19ad) -24 (UE-20n #1 1,005.84 m)	7.3 7.8 8.8
Springs	28	2.6 2.5 2.7	19 (Torrance Spring) 19 (Torrance Spring) 19 (Torrance Spring)	-6.4 (Spring id 159) -6.3 (Spring id 159) -5.5 (Spring id 159)	6.8 6.9 6.8
Oasis Valley Discharge	7	2.8 1.1 -2.9	41 (Zone 3) 40 (Zone 3) 33 (Zone 3)	-30 (Zone 4) -33 (Zone 4) -53 (Zone 4)	23 24 29
Boundary Flow	4	-12.7 -11.9 -10.3	26 (West) 26 (West) 26 (West)	-47 (North) -45 (North) -57 (North)	29 29 35

[a] Material 74 Timber Mountain Dome x 10
[b] Material 74 Timber Mountain Dome x 100
[c] Homogenous TMCM

Figure 6-90 shows the posted weighted residuals. The most notable change is the increasing underprediction in the area of WW-8 as the Timber Mountain Dome reference permeability increases, and in the homogenous case. Forming the mound under Timber Mountain clearly has an effect in this area, although less so elsewhere. Figure 6-91 shows the simulated water table, and Figure 6-92 shows the simulated flow paths. As the Timber Mountain Dome reference permeability increases, decreasing the simulated mound, the potentiometric surface grows flatter (as it conceptually should). The flow paths become more diffuse through the Timber Mountain area as the mound diminishes and no longer focuses flow on its northwest and northeast shoulders.

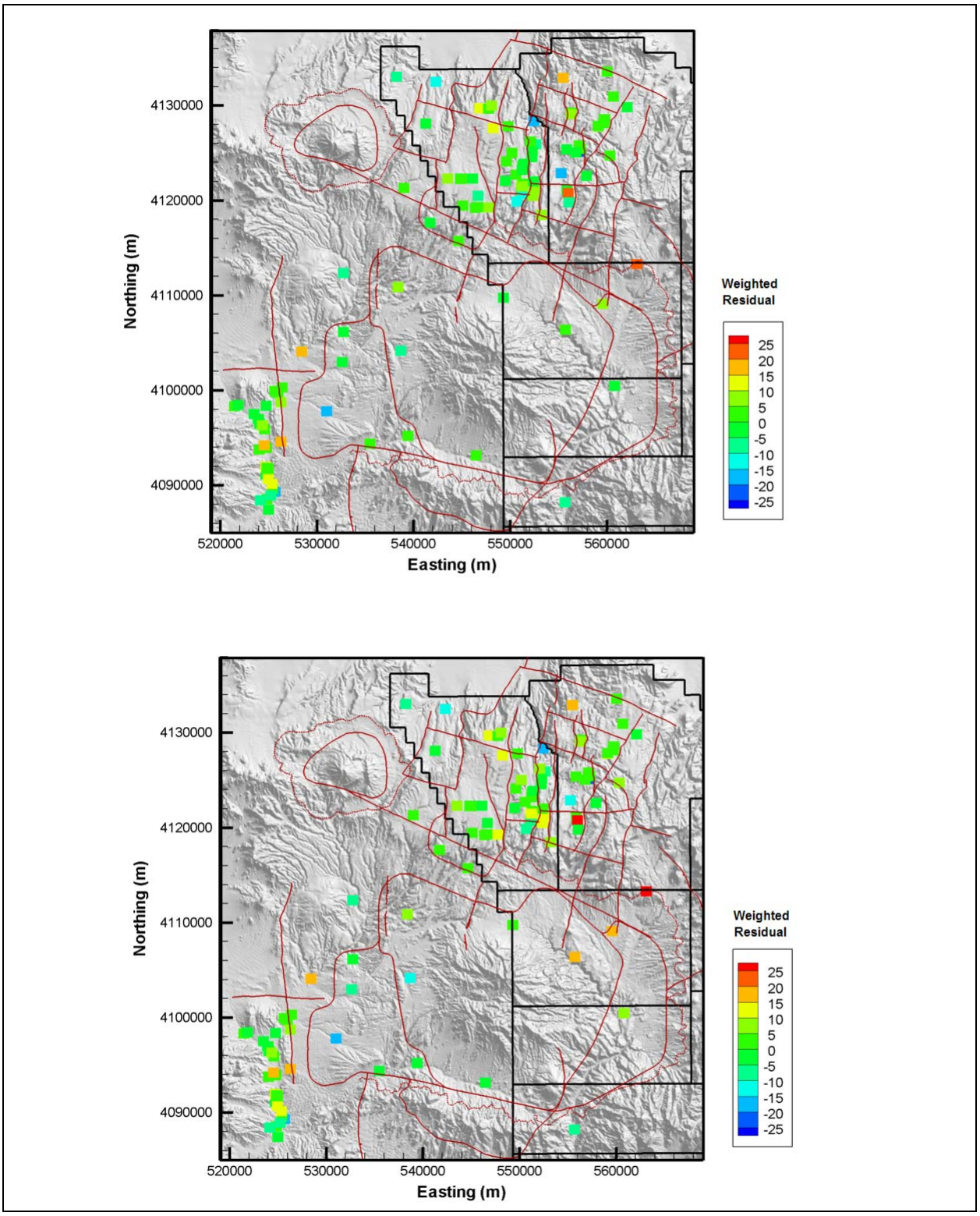

Figure 6-90
Post Plots of Weighted Well and Spring Head Residuals for Timber Mountain Dome k_0 10x (Upper) and 100x (Lower)

Uncontrolled When Printed

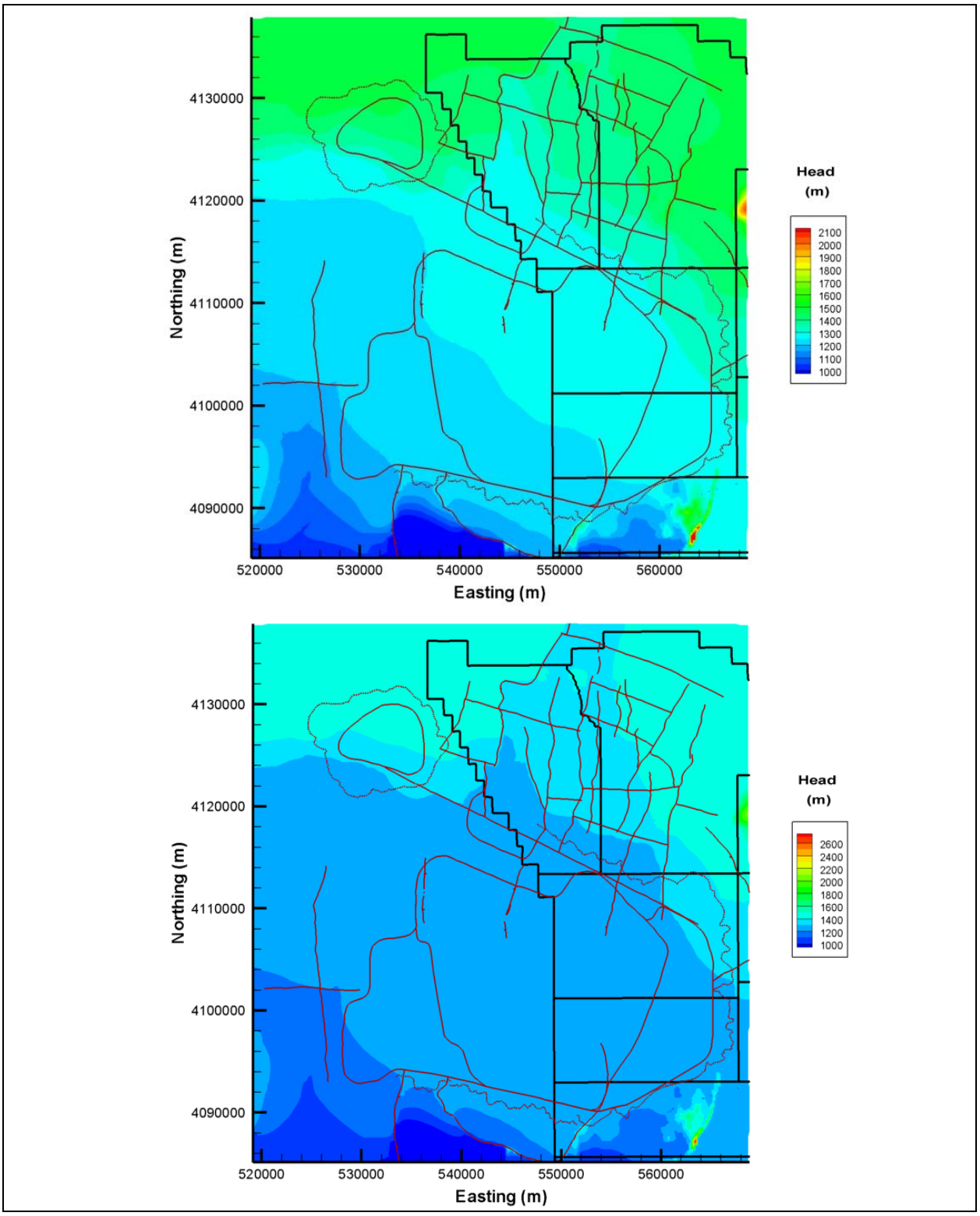

Figure 6-91
Simulated Water Tables for Timber Mountain Dome k_0 10x (Upper) and 100x (Lower)

Uncontrolled When Printed

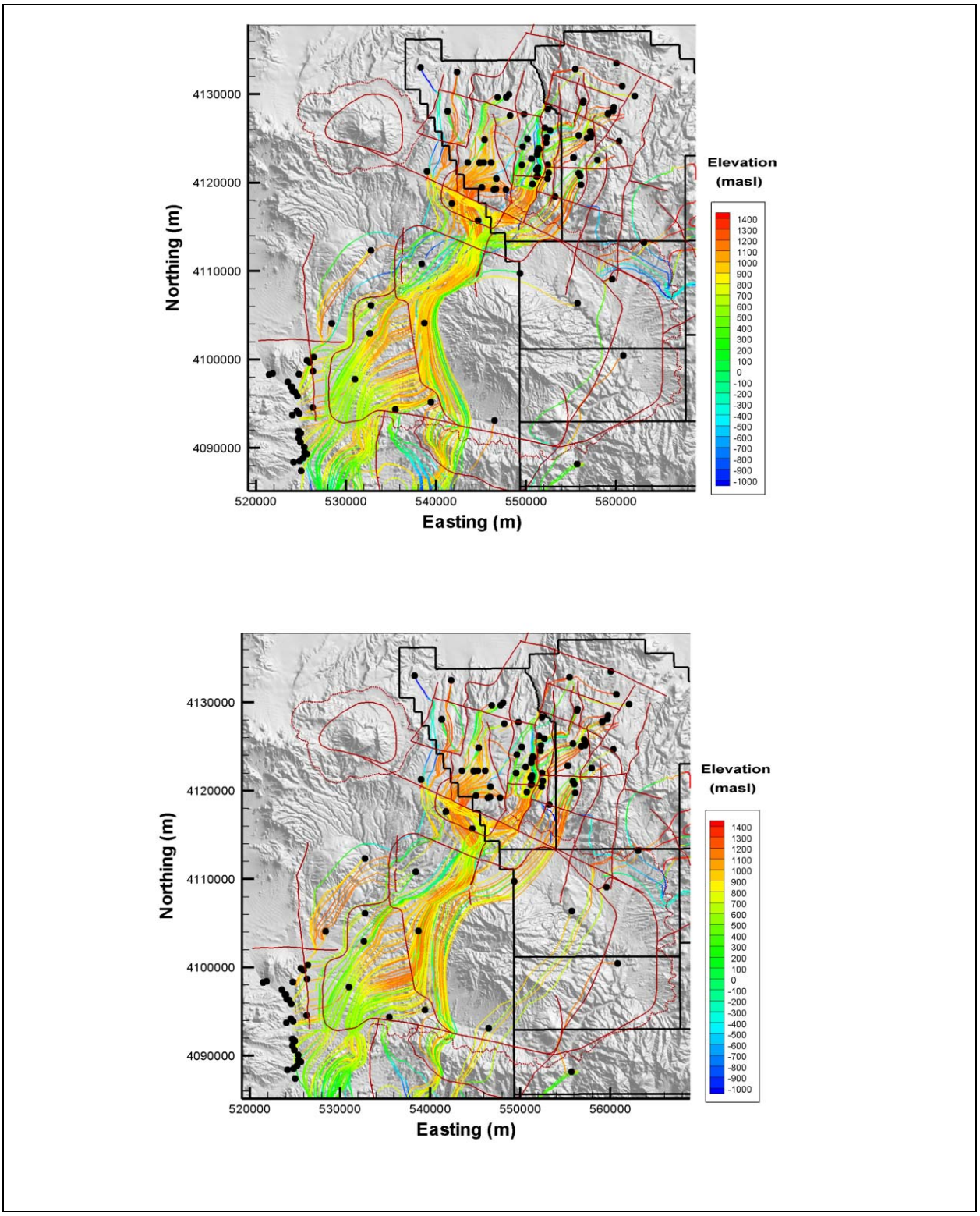

Figure 6-92
Particle Tracks for Timber Mountain Dome k_0 10x (Upper) and 100x (Lower)

6.2.5 Summary of Parameter Sensitivity Analysis

Parameter sensitivity analysis, as is customary practice and specified in the Pahute Mesa CAIP (DOE/NV, 1999), was performed on the two major HFMs in the Pahute Mesa CAU-scale groundwater model using a complementary suite of techniques. Two different approaches to parameterizing the base HFM (selected and all HSU depth decay and anisotropy) were further considered in order to investigate the consequences of choosing one approach or the other. Local sensitivity analyses were carried out using sensitivity coefficients computed by PEST and perturbation analysis around the calibration point. In addition, global sensitivity analyses were carried out using classification tree and entropy analysis to determine parameter importance conditioned over the entire range of parameter variations. For the global sensitivity analysis, a Monte Carlo simulation-based sampling methodology was used to generate multiple parameter combinations to evaluate each model.

The analysis combining a more conventional local sensitivity analysis with a global approach provided important insights about model input/output relationships, with each technique adding information to the overall perspective. In the local sensitivity analysis, the PEST sensitivity coefficients provided a look at relationships very near the point of calibration. This information is somewhat limited because it does not consider the model parameter uncertainty ranges; however, these coefficients provide some of the best insight into what is happening in the final stages of calibration. The perturbation analysis provided an intuitive visualization of the effects of varying individual parameters, with the caveat that combined parameter effects are not captured. In the global sensitivity analysis, the classification tree provided insight into what parameters affect the output over the entire parameter space. The classification tree also showed how particular combinations of parameters interact to produce a particular result. The entropy analysis not only served to corroborate results from the classification tree analysis, but also quantified the relative importance of particular parameters. Also, these global analyses provided information not only about the sensitivity of the objective function (the overall measure of how well the flow model is calibrated) to the input parameters, but also insight into what parameters are most important to the individual components of the objective function. An additional benefit of the Monte Carlo analysis is that it also provides information about which components of the objective function are most important to the total behavior.

Uncontrolled When Printed

The key findings from this analysis are summarized in Table 6-19. Importance rankings are presented with respect to the total objective function, head measurements, and Oasis Valley discharge. Note that the perturbation analyses used the mean difference between heads at target locations as a surrogate for the observation well component of the objective function. The results from the classification tree analysis and entropy analysis are integrated because of their general consistency across all model versions.

Table 6-19
Summary of Key Sensitivity Analysis Findings

Model Case	Sensitivity Analysis Technique	Key Parameters[a]			Comments
		PHI	Oasis Valley Discharge[b]	WELL	
Base HFM – Selected HSU depth decay and anisotropy (BN-MME-SDA)	Global	LCCU1 DVCM	DVCM PBRCM Zone 84[c]	YMCFCM PCM	
	Perturbation	LCCU1 DVCM	DVCM TMA	YMCFCM PCM	
	PEST	Depth decay assigned to selected volcanic HSUs Carbonate depth decay	N/A	N/A	PEST results only for PHI
Base HFM – All HSU depth decay and anisotropy (BN-MME-ADA)	Global	LCA Zone 1 DVCM	PBRCM Zone 13[d] DVCM	FCCM CHCU	
	Perturbation	DVCM LCA Zone 1	DVCM PBRCM Zone 13[d]	YMCFCM LCA3a	
	PEST	LCA3a LCA Zone 1	N/A	N/A	PEST results only for PHI
SCCC HFM – Selected HSU depth decay and anisotropy (SCCC-MME-SDA)	Global	LCCU1 DVCM	DVCM PBRCM	BRA PBRCM CHCU[e]	
	Perturbation	LCCU1 DVCM	DVCM PBRCM	PCM CHCU[e]	
	PEST	Depth decay assigned to selected volcanic HSUs Carbonate depth decay	N/A	N/A	PEST results only for PHI

[a]The top two parameters influencing model calibration
[b]Parameters most important in replicating Oasis Valley discharge
[c]Western PBRCM, see Figure 5-5
[d]PBRCM under Areas 19 and 20, see Figure 5-5
[e]CHCU is all Calico Hills units found in base HFM lumped together in SCCC HFM

Uncontrolled When Printed

The sensitivity analysis confirmed what was observed during flow model calibration: that the major controls on the groundwater flow system are not necessarily all the HSUs on Pahute Mesa. For instance, while it appears that the PBRCM, and to a lesser extent the BRA, have noticeable role in calibration, the fact that the DVCM, PCM, YMCFCM, and LCCU1 dominate (and that the TMCM had any role at all) calibration was unexpected. The underground nuclear tests were all conducted in Areas 19 and 20; hence, the observation well data tend to be clustered there, and the base HFM is also relatively complex in this area. Figure 6-93 shows the PHI perturbation results for the BN-MME-SDA case from 15 HSUs found only on Pahute Mesa: CFCU, CFCM, KA, BFCU, IA, CHCU, CHZCM, CHVCM, CHVTA, TSA, LPCU, PLFA, TCA, UPCU, and BA (see Table 4-1 for HSU descriptions). Remembering that the BN-MME-SDA case had a final objective function of about 17,000 (to the nearest thousand), it is seen that the BFCU, IA, CFCU, and CHZCM have a noticeable effect on calibration over their range of uncertainty. The TCA and CHVTA have a modest effect on model calibration, and the remaining nine HSUs (KA, CFCM, CHCU, TSA, LPCU, PLFA, UPCU, BA, and PVTA) are, practically speaking, of no consequence for model calibration.

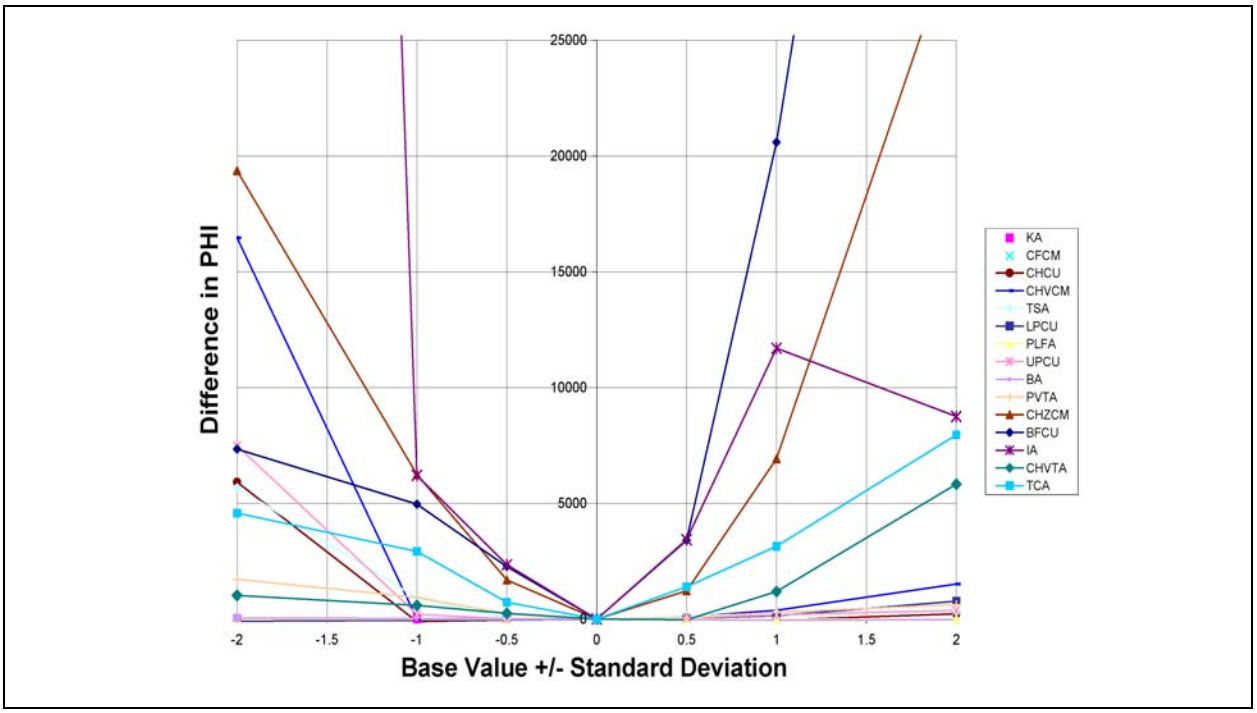

Figure 6-93
PHI Perturbation Results for Selected HSUs in BN-MME-SDA

Uncontrolled When Printed

Conceptually, the BFCU should be a sensitive HSU because it underlies most of Areas 19 and 20, separating the shallower volcanic HSUs from the PBRCM and BRA, as does the CFCU, and the correlation coefficient confirms that this relationship is true; the BFCU and CFCU permeabilities are strongly (greater than 0.95) negatively correlated (see Section 6.2.1.1), the effects of reducing the permeability in one can be offset by increasing the permeability in the other. The CHZCM, as previously noted, has sensitivity in the model because of the 23 observation wells completed in it. The IA is a thick rhyolite present near much calibration data but has no observation wells completed specifically in it. The IA does, however, connect with the CHZCM in a complex way, and this may be the reason for model sensitivity. Lastly, some of the remaining HSUs have relatively small-saturated extents, and the arrangement of the rest is concluded to be such as to not generate much effect. For instance, the TCA is nearly completely strata-bound by the LPCU and UPCU; changing its permeability has little effect because it is the lower permeability LPCU and UPCU that control the TCA ability to influence the flow system.

The Pahute Mesa HFMs, base and SCCC, incorporate a number of faults and other structural features (Appendix B assesses their likely properties in more detail). The Purse and Boxcar Fault systems have been previously identified as having sealing properties (Wolfsberg et al., 2002). Many others though, are unknown. The sensitivity analysis only revealed the Claim Canyon Caldera Structural Margin as a consistently sensitive feature due to its location on the southern edge of the model. Perturbation analysis showed the Hogback and the Rainier Mesa Caldera Structural Margin have a strong effect at a permeability multiplier of 100 (the response between 10 and 100 appears very nonlinear and shows little effect at 10). The Ribbon Cliff Structural Zone (fault 16) that runs east-west between Black Mountain and the Purse Fault is strongly sensitive at low values because it can restrict flow through the area, the North Timber Mountain Moat Structural Zone (Moat Fault, fault 15), Rainier Mesa Caldera Structural Margin, and Ammonia Tanks Caldera Structural Margin are sensitive for the same reason. Fault sensitivity tends to be one-sided; only lower values have any impact. Conceptually, this is sensible because a low (or high) permeability feature located in line with a flow path would have little obvious effect; the faults noted above all tend to lie across groundwater flow paths.

Oasis Valley and UGTA-regional model estimated boundary flow are used as a flow model calibration constraint. This use of boundary flows help further limit the inherent non-uniqueness in a

Uncontrolled When Printed

steady-state flow model with constant-head boundaries. Oasis Valley and western boundary flow are very sensitive to the DVCM, partly because the northern two-third or so of the western model boundary was treated as a no flow. If this conceptualization is revised, this conclusion may change to include additional HSUs, but because of the location of the DVCM near calibration data, it would likely still be sensitive even if the western boundary has a more extensive constant-head specified along its edge. The major inflow on the north is controlled by the LCCU1 at higher permeabilities and LPCU west of the Purse Fault at lower permeabilities. The LCCU1 effect is because at the higher permeability the high head near the Gold Meadows stock is easily propagated to the northern edge-creating outflow where the LCCU1 connects to the northern constant heads that are at lower potential than those near Gold Meadows stock. For the LPCU, at lower permeabilities it hinders flow through the "throat" between the lower permeability rocks in the Black Mountain caldera and the Purse Fault.

On the east, the PBRCM controls flow because it is connected to the boundary and of relatively large areal extent, with the LCA depth decay less important, but still contributing, because of its presence along the eastern edge of the model. The PCM is also sensitive in an analogous manner as the LCCU1, only oriented south, because it is connected to the boundary along the east and south edges. Finally, on the south, DVCM is important once again, presumably because whatever flow in excess of that supplied to Oasis Valley discharges through LCA3 directly to the south past Beatty. To some extent, the specific conclusions drawn are related only to the BN-MME-SDA alternative boundary flows examined via global sensitivity analysis; however, the broad conceptual understanding should still be transferable to the other cases.

6.3 HFM Uncertainty Analysis

It has been noted (Carrera and Neuman, 1986a and b) that inadequate model conceptualization is more detrimental to model predictive ability than parameter uncertainty. The Pahute Mesa CAIP (DOE/NV, 1999) recognizes this uncertainty and has propagated it by developing alternative geologic models for Pahute Mesa. The following section tests the major alternatives described by BN (2002) as summarized in Table 6-19 by implementing them in the FEHM flow model.

As previously described in Section 4.0, meshes for the base and SCCC HFMs were explicitly constructed. However, additional HFM alternatives were addressed using the mesh developed for the

Uncontrolled When Printed

base HFM. This is judged to be reasonable because all the alternatives were closer in initial conception to the base HFM than the SCCC HFM, and the base HFM had a slightly higher grid resolution. The base HFM also fully incorporated faults (as did the other alternatives), which were shown to be important in the previous sections. The procedure for approximating the alternative HFMs using the base HFM mesh is as follows:

- Identify the HSU for every node in the base HFM.
- Identify the HSU for every node in each alternative HFM.
- Using a relational database, find only the nodes in each alternative that are different from the base HFM.
- Construct FEHM input to change the nodes' HSU material type, and run FEHM.

The procedure is approximate because no consideration was (or can be) given to maintaining HSU continuity. Practically, it is more likely (but still unknown) that the uncertainty in actual HSU location in any alternative is greater than the error occurred in this approach, particularly when the depth of the changes is considered. For instance, in the raised Paleozoic (or pre-Tertiary) case, the uncertainty (thought to be large by BN [2002]) in the depth of basement rocks from gravity and well data was considered. Some units were shifted upward by as much as 800 m, with many areas raised 750 m.

In addition, BN (2002) suggested other possible modifications to the geologic model. Table 6-20 shows the suggestions and a brief comment on how they were or were not dealt with.

Uncontrolled When Printed

Table 6-20
Abridged List of Alternative Scenarios for the Pahute Mesa/Oasis Valley 3-D Hydrostratigraphic Model
(Page 1 of 10)

Alternative		Priority Group[a]	Comment
1.0	**HYDROSTRATIGRAPHY-RELATED ALTERNATIVES**		
1.1	**Alternatives to Simplify Hydrostratigraphy**		
1.1.1	Combine intra-caldera intrusives into a single HSU.	**D**	Are all the intra-caldera intrusives the same hydrologically? Can we combine the intrusives beneath the Ammonia Tanks and Rainier Mesa calderas?
	Response		The intrusives were assigned identical properties during calibration and their sensitivity investigated and found to be minimal.
1.1.2	Simplify HSUs above the water table.	**D**	Can HSUs in the unsaturated zone be lumped, simplified, or ignored?
	Response		The CAU model, by definition, is for the saturated zone only. HSUs in the unsaturated zone were ignored.
1.1.3	Decrease the depth of the model.	**D**	Is there any merit in raising the bottom of the model? Work on the regional model demonstrated that even after removing the lowest 2 km (1.2 mi) from the bottom of the model, there was no difference in the outcome compared to the original model. The elevation of the bottom of the framework model is now consistent with the regional model.
	Response		This was not investigated.
1.2	**Alternatives to Add Hydrostratigraphic Detail**		
1.2.1	Include all alluvium (AA) as mapped on USGS surface geologic maps.	**D**	In parts of the current base model, alluvium (typically, thin surficial deposits) is lumped with an underlying HSU. Thick deposits of AA, however are differentiated. Could this affect recharge (e.g., alluvium filling a wash or small structural valley)?
	Response		The effects of AA would have been apparent only in the USGS recharge estimates. MME does not consider soil texture, and DRI CMB masked the alluvium. These estimates were generated independently by the USGS, and it would be arbitrary to modify them.
1.2.2	Add collapse breccias along (within) caldera margins.	**D**	We do not know how permeable the breccias are, and we do not know exactly where they are located. Are they confining or conductive units? To explore this, collapse breccias would be added as another HSU. One way to do this is to symbolically add a wedge-shaped volume along the inside of the caldera.

Uncontrolled When Printed

Table 6-20
Abridged List of Alternative Scenarios for the Pahute Mesa/Oasis Valley 3-D Hydrostratigraphic Model
(Page 2 of 10)

Alternative		Priority Group[a]	Comment
	Response		This feature would require a fair amount of effort to modify the mesh because a digital geologic model was not created. This was not investigated further.
1.2.3	Subdivide the Fortymile Canyon composite unit (FCCM).	**A**	For example, this unit consists of lavas in the southeastern Timber Mountain moat area, but welded ash-flow tuffs become more common in the lower portion of the FCCM in Oasis Valley. These units may also become saturated in the deepest portion of the valley. A separate unit would allow more vertical resolution in the model.
	Response		As noted by BN (2002), category A items were implemented in the geologic models.
1.2.4	Differentiate units of the Twisted Canyon caldera.	**D**	The Twisted Canyon caldera (after Fridrich et al., 1999a) is relatively small and generally above the SWL. The Timber Mountain units are currently included with the detached volcanics composite units (DVCM) but could be differentiated to permit more detailed modeling.
	Response		The DVCM was found to be an important HSU in controlling flow in Oasis Valley. Further subdivision may have diluted this effect and was not considered further.
1.2.5	Subdivide the detached volcanics composite unit.	**A**	Is there enough information (e.g., in Fridrich et al., 1999a and b), and are the differences significant and/or predictable enough to warrant subdividing these units?
	Response		As noted by BN (2002), category A items were implemented in the geologic models.
1.2.6	Define areas of hydrothermal alteration.	**D**	Should we treat alteration as another HSU? This may be possible where there is evidence of alteration on the surface and in drill holes. Drill holes where hydrothermal alteration is documented include: ER-EC-1, ER-EC-6, PM-2 (deep), UE-20f (below 10,000 ft), UE-19w1 (shallowest; the hole cuts through Area 20 caldera margin, where the foot wall is hydrothermally altered but the hanging wall is not), ER-EC-7 and ER-EC-2A, all at various depths. To define hydrothermal alteration without evidence does not make sense. Are occurrences of hydrothermal alteration predictable?
	Response		It is not within the scope of the flow model to decide whether hydrothermal alteration is predictable. While it is a process, the sparse data do not lend themselves to generalization. This was not addressed.
1.2.7	Map caldera moat-filling units.	**D**	Differentiate moat gravels from other alluvium, though these units typically are not saturated.

Uncontrolled When Printed

Table 6-20
Abridged List of Alternative Scenarios for the Pahute Mesa/Oasis Valley 3-D Hydrostratigraphic Model
(Page 3 of 10)

Alternative		Priority Group[a]	Comment
	Response		Further mapping of geologic units is not in the flow model scope. The CAU flow model is for the saturated zone only.
1.2.8	Subdivide the Paintbrush composite unit (PCM) in the southern end of the model.	**C**	Though dominated by the Paintbrush Group, the PCM also includes remnants of the Rainier Mesa and Ammonia Tanks welded ash-flow tuffs and thin alluvium. In the north (the 1997 PM300 model area), the various Paintbrush tuffs are differentiated where drill hole data are available. We might be able to add more geologic detail, but we have almost no hydrologic data. Is the YMP information adequate to differentiate and map out various HSUs?
	Response		Assessment of YMP geologic data to refine HSUs is not in the scope of the flow model, and this was not addressed.
1.2.9	Subdivide the Kearsarge lavas identified in Well ER-EC-1.	**D**	The Kearsarge lava is a minor aquifer in the northwest corner of the model area and is currently modeled as the Kearsarge aquifer HSU. However, detailed petrographic analysis has identified the Kearsarge lava in Well ER-EC-1, farther south, which represents a newly recognized separate lobe of the lava. Currently, this lobe is lumped with the Crater Flat composite unit (CFCM), which contains lavas of uncertain thicknesses and extent.
	Response		This information is too sparse to be meaningfully addressed and was not considered further.
1.3 Alternatives to Develop Different Distributions for Pre-Tertiary HSUs			
1.3.1	LCCU in the southwestern portion of the model area.	**D**	Determine whether this outcrop is really LCCU (hydrologic “basement”) or LCCU1, with LCA beneath it
	Response		Additional mapping is beyond the scope of the flow model.
1.3.2	Outcrop of Paleozoic carbonate rocks west of Black Mountain.	**D**	It is currently modeled as LCA. Should it be LCA3?
	Response		LCA is assigned properties throughout the model domain, and those properties are adjusted as part of calibration. If the model had a systematic misfit in this area, then it may have been necessary to change properties, and identify geologic rationale. There are no head calibration data in this part of the model, and the need for this change could not be identified.
1.3.3	Continuity of LCA.	**D**	Model LCA as discontinuous from east to west across the model area. (Alternative 2.4.7 creates this geometry.)

Uncontrolled When Printed

Table 6-20
Abridged List of Alternative Scenarios for the Pahute Mesa/Oasis Valley 3-D Hydrostratigraphic Model
(Page 4 of 10)

Alternative		Priority Group[a]	Comment
	Response		Geometry addressed in HFM uncertainty analysis.
1.3.4	Basement subcrop.	**D**	Change the extent and thickness of LCA3 and LCCU1. Instead of only two small LCA3 subcrops in the southwestern corner, make a more extensive LCA3 plate(s)
	Response		Extensive geologic model alteration is beyond the scope of the flow model. Not addressed.
1.3.5	Vary the Paleozoic stratigraphy in the southern area.	**D**	Differentiate the LCA3 sandwiched between the two occurrences of UCCU, as in the YMP model.
	Response		The LCA3 was subdivided in the FEHM model into LCA3 and LCA3a to address this.
1.3.6	Vary the occurrence of the UCCU.	**A**	It was suggested to change the base model to have the western UCCU contact move eastward down along a line that goes through the middles of the calderas.
	Response		As noted by BN (2002), category A items were implemented in the geologic models.
1.3.7	LCCU1.	**A**	Depict as a continuous sheet in the southeastern portion of the model area.
	Response		As noted by BN (2002), category A items were implemented in the geologic models.
1.4 Other Hydrostratigraphy-Related Alternatives			
1.4.1	Intrusive confining unit beneath the Silent Canyon caldera.	**D**	Is this ICU different from that of the other resurgent calderas? What is the nature of this material? Can we define the hydrologic properties of a highly injected/altered rock mass?
	Response		It is beyond the scope of the flow model to address questions of volcanology. No data exist on the ICUs.
1.4.2	Composite units.	**D**	Change/divide composite units into aquifers and/or confining units.
	Response		The mesh is built using specific HSU geometries; thus, without a detailed geologic model describing such changes/divisions, a mesh was not constructed. Additional detailed geologic interpretation is beyond the scope of the flow model. This was not addressed further.
1.4.3	Pre-Belted Range composite unit (PBRCM).	**D**	Show PBRCM everywhere overlying the “basement.” Thin the younger units as necessary at basement highs to accommodate some added thickness of PBRCM.

Uncontrolled When Printed

Table 6-20
Abridged List of Alternative Scenarios for the Pahute Mesa/Oasis Valley 3-D Hydrostratigraphic Model
(Page 5 of 10)

Alternative		Priority Group[a]	Comment
	Response		The mesh is built using specific HSU geometries; thus, without a detailed geologic model describing such changes/divisions a mesh was not constructed. Additional detailed geologic interpretation is beyond the scope of the flow model. This was not addressed.
1.4.4	Mesozoic granite.	**D**	Make the Gold Meadows stock larger in the subsurface.
	Response		The stock is a low permeability feature, and no transport consequences of this change are apparent. Not addressed.
2.0 STRUCTURE-RELATED ALTERNATIVES			
2.1	Silent Canyon caldera alternative.	**B**	Develop an alternative based on McKee et al. (1999 and 2001) to explore a “structurally uncoupled” model for the SCCC.
	Response		This alternative was addressed in the SCCC HFM.
2.2	Simplify the model.	**D**	Omit all but the most profound structures and faults.
	Response		The SCCC HFM has fewer structures and faults, and partially addresses this.
2.3 Add More Structural Detail			
2.3.1	Faults and caldera margins.	**C**	Add width to these structures, modifying them from simple two-dimensional surfaces to a 3-D feature having some width. Can we predict where and why they might be a barrier and/or conduit to groundwater flow?
	Response		The numerical model requires that these features have a finite width. LANL reviewed the data and assessed whether individual faults may be barriers or conduits (see Appendix B).
2.3.2	Add more Tertiary faults or fault zones.	**D**	Perhaps begin by adding the mapped faults (shown on Slate et al. [1999] or the individual USGS quadrangle maps). Most reviewers thought that structurally the model contained the appropriate level of detail.
	Response		The mesh is built using specific HSU geometries; thus, without a detailed geologic model describing changes in faults such changes/divisions, revised conceptual model and mesh could not be constructed. Additional detailed geologic interpretation is beyond the scope of the flow model. This was not addressed.

Uncontrolled When Printed

Table 6-20
Abridged List of Alternative Scenarios for the Pahute Mesa/Oasis Valley 3-D Hydrostratigraphic Model
(Page 6 of 10)

Alternative		Priority Group[a]	Comment
2.3.3	Show several more older calderas.	**D**	Where is the source caldera for the Topopah Spring Tuff? If the gravity lows depicted on the USGS gravity maps are really older calderas, would it make any difference? Are they too deep to significantly affect groundwater flow?
	Response		Detailed geologic interpretation is not part of the scope of the flow model. This was not addressed further.
2.3.4	Add the CP thrust fault in the south.	**D**	The CP thrust is a poorly characterized, west-to-northwest-vergent thrust fault that appears to be mostly outside the boundaries of the model area. Do we really need to add this complexity to the southeastern margin of the model? Could the fault be elsewhere, too? The YMP geologic model includes the Calico Hills thrust, while the UGTA model shows a simpler variation without this thrust. Alternatively, the LCA3 might be more continuous in the southeast corner. In the southeast, there are potentially three versions of pre-Tertiary geometry: 1) As depicted in the current UGTA base model; 2) Alternative with LCA at the pre-Tertiary surface not covered with LCCU; 3) Base model with LCA3 as a continuous sheet, not as isolated islands.
	Response		The mesh is built using specific HSU geometries; thus, without a detailed geologic model describing such changes/divisions, a mesh was not constructed. Additional detailed geologic interpretation is beyond the scope of the flow model. This was not addressed further.
2.3.5	Juxtapose aquifers.	**C**	Deliberately juxtapose aquifer units across faults. See Alternative 2.5.3.
	Response		The mesh is built using specific HSU geometries; thus, without a detailed geologic model describing such changes/divisions, a mesh was not constructed. Additional detailed geologic interpretation is beyond the scope of the flow model. This was not addressed further.
2.4 Develop Different Structural Scenarios			
2.4.1	Vary fault dips.	**C**	The basin-and-range normal faults are modeled using an 80-degree dip. Varying fault dips would present more consequences in the source areas, where fault proximity to working points is important. This might be better addressed in sub-CAU-scale models.
	Response		The mesh is built using specific HSU geometries; thus, without a detailed geologic model describing such changes/divisions, a mesh was not constructed. Additional detailed geologic interpretation is beyond the scope of the flow model. This was not addressed.
2.4.2	Other fault variations.	**C**	Model faults as either present, a single plane, and/or a zone with multiple planes.

Uncontrolled When Printed

Table 6-20
Abridged List of Alternative Scenarios for the Pahute Mesa/Oasis Valley 3-D Hydrostratigraphic Model
(Page 7 of 10)

Alternative		Priority Group[a]	Comment
	Response		The numerical model requires that these features have a finite width and the mesh is specifically constructed to represent these features. It is not possible to modify fault geometries without a detailed digital geologic model and additional meshes. This was not addressed.
2.4.3	Vary the depth to basement rocks.	**B**	The uncertainty in depth to basement based on geophysical data is roughly 2,000 m (6,560 ft). This may not be geologically permissible in some areas. And where it is possible, what units would be thinned or thickened? Could the depth to the Ammonia Tanks and Rainier Mesa resurgent intrusive granites be raised or lowered?
	Response		This was addressed as the PZUP alternative.
2.4.4	Modify the shapes of calderas.	**D**	Do small differences in the shapes of calderas matter? Compare round vs. rectangular shapes; round the corners as a compromising geometry. The western and eastern lobes of the Timber Mountain caldera complex could be smaller, or extended. Separate the Rainier Mesa structural margin and the Ammonia Tanks structural margin in the north and south sides. Presently, the UGTA base model shows these structural margins merging together (the Ammonia Tanks margin as a reactivation of the Rainier Mesa margin) at those locations.
	Response		“Changes in caldera shape and HSUs were incorporated in the SCCC model.”
2.4.5	Explore variations of the Thirsty Canyon Lineament.	**B**	Because of its northeast trend and the short distance from testing areas on Pahute Mesa to Oasis Valley, if this lineament exists, it would be the most direct path for migration. Could it be a single (or zone of) north-northeast trending features or faults rather than a series of en echelon, more north-south-trending faults and caldera margins?
	Response		This was addressed as the Thirsty Canyon Lineament alternative.
2.4.6	Model a “trap-door” caldera geometry.	**D**	“Trap-door” type collapse of the Ammonia Tanks caldera (hinge at the south side) may be another interpretation to explain the gravity inversion data.
	Response		Revision of geologic interpretation is not part of the flow model scope. This was not addressed.

Uncontrolled When Printed

Table 6-20
Abridged List of Alternative Scenarios for the Pahute Mesa/Oasis Valley 3-D Hydrostratigraphic Model
(Page 8 of 10)

Alternative		Priority Group[a]	Comment
2.4.7	Vary the geometry/position of the BRT fault.	**B**	The current UGTA base model depicts the BRT as not deeply rooted. An alternative interpretation developed by the USGS depicts the BRT as a very deeply rooted and through going thrust. What latitude do we have in moving this feature (what does it do between outcrops?)? The BRT is modeled as a low-dip feature except where it ramps up, especially at the top of the pre-Tertiary surface (e.g., 40 degrees as per Jim Cole).
	Response		This was addressed as the deeply rooted thrust alternative.
2.4.8	Model Oasis Valley as an extensional basin.	**D**	The preferred interpretation, based on drill hole MyJo Coffer #1 and mapped units in the Transvaal Hills, shows Oasis Valley as part of the Timber Mountain caldera and not an extensional basin. Some disagree. Magnetic data do show north-south faults.
	Response		Revision of geologic interpretation is not part of the flow model scope. This was not addressed.
2.5 Other Structure-Related Alternatives			
2.5.1	Add structural detail in Oasis Valley.	**D**	Study structural features in the Oasis Valley discharge area. There are indications of north south trending faults. Is Chris Fridrich's structural model best?
	Response		Revision of geologic interpretation is not part of the flow model scope. This was not addressed.
2.5.2	"Smooth" versus "rough" HSU surface.	**D**	Computer idiosyncrasies have produced "hills" and "indentations" on HSU surfaces where none were intended. Does it matter? A rough surface might better approximate the effect of faulting.
	Response		The mesh is constructed from the digital geologic model. It is not possible to add this detail after the fact, and such changes are almost certainly minor with respect to overall HSU parameter uncertainty. This was not addressed.
2.5.3	Explore interconnected groundwater pathways.	**C**	Consider increasing or decreasing fault displacements so aquifers are juxtaposed across faults. Conversely, if aquifers are juxtaposed, adjust relative fault displacement to prevent aquifer-aquifer juxtaposition. This may best be handled with sub-CAU-scale models. See Alternative 2.3.5.
	Response		This can only be addressed by creating an alternative mesh for an associated geologic model that was not presented.

Uncontrolled When Printed

Table 6-20
Abridged List of Alternative Scenarios for the Pahute Mesa/Oasis Valley 3-D Hydrostratigraphic Model
(Page 9 of 10)

Alternative		Priority Group[a]	Comment
2.5.4	Consider defining basin/lows with faults.	**D**	The UGTA base model portrays many of the gravity lows as syncline-type structures and not half-grabens related to basin-and-range extension (e.g., northeast of the Black Mountain caldera). However, most reviewers and modelers seem to feel that the present fault detail is about right.
	Response		Revision of geologic interpretation is not part of the flow model scope. This was not addressed.
3.0 OTHER ALTERNATIVES			
3.1	Explore variations of the gravity ridge between the TMCC and the SCCC.	**B**	This feature appears as a gravity high between two calderas. Possible explanations include an intrusive resurgent-type body, a hydrothermally altered area, etc.
	Response		This is addressed in the Ridge alternative.
3.2	Reposition the topographic margins of calderas.	**D**	In some areas their placement seems strange, such as too far removed from the inferred structural margin or not recognizable at all.
	Response		Revision of geologic interpretation is not part of the flow model scope. This was not addressed.
3.3	Account for lower hydraulic heads at Wells ER-EC-4 and ER-EC-2A.	**D**	These two wells show a significant downward gradient.
	Response		This is a model calibration issue, not a geologic model alternative.
3.4	Maximize detail within 1,000 m (3,280 ft) of the water table.	**D**	Add the water table to the model. Will detail above the SWL affect the model? Will small differences at or just beneath the water table make big differences in the flow and transport modeling results (e.g., raise or lower an HSU, or, add or remove HSUs)?
	Response		The CAU model considers saturated flow only, and the mesh is truncated at the water table.
3.5	Add spring locations.	**A**	Add the locations of springs, particularly those near the TCL and the western margin of the TMCM.
	Response		The springs are considered in the flow model.

Uncontrolled When Printed

Table 6-20
Abridged List of Alternative Scenarios for the Pahute Mesa/Oasis Valley 3-D Hydrostratigraphic Model
(Page 10 of 10)

Alternative	Priority Group[a]	Comment

Source: Modified from BN, 2002

[a]**Group A** comprises changes to the UGTA base model recommended by the alternative scenario-working group, and are already implemented.
Group B comprises considered viable alternative scenarios that will be modeled.
Group C comprises proposed alternatives that would be better addressed during the hydrologic modeling phase, rather than as alternatives to the base model.
Group D comprises proposed alternatives that were deemed to be low priority (due to minimal consequences to groundwater flow and contaminant transport), not cost-effective, impractical (e.g., no data, too complex), or simply unnecessary to model at this time.

Uncontrolled When Printed

The remainder of this section describes the calibration of the five major alternate models (those for which EV models were constructed) to the MME recharge and boundary flow targets. The selected HSU depth-decay and anisotropy approach described in Section 5.6.2 was used in parameterizing the models beginning with the calibrated parameters as shown in Section 5.6.2. Calibration was stopped when the objective function was less than the worst calibrated model described in Section 5.0, a value of about 30,000. It is computationally infeasible to investigate these alternatives with the other parameterization approaches discussed in Section 5.6.

6.3.1 Thirsty Canyon Lineament Alternative (TCL-MME-SDA)

The Thirsty Canyon Lineament is a geophysically inferred structure. Because of its northwest trend, presence in Oasis Valley, and short distance from western Area 20 if this feature is caused by faulting it could be an enhanced flow path, although it may also be a barrier. This alternative places more permeable fractured rocks in the area. See Section 6.4 in BN (2002) for more information.

Plots of observed versus simulated values for the calibration wells, springs, Oasis Valley discharge, and boundary flows are shown in Figures 6-94 through 6-97. The scatter around the line of perfect agreement is generally random in Figure 6-94, until an observed head of 1,450 m is exceeded. At the very highest observed observation well heads, the model has a tendency toward undersimulation. The remaining errors above 1,450 m are all in far eastern Area 19, where data become very sparse and uncertainty increases. Figure 6-98 shows a histogram of weighted observation well residuals. The bulk of the weighted errors (about 95) are less than 10 m. The errors are very symmetrically distributed around zero. The total errors above +10 m and below -10 m appear to be about the same.

The Oasis Valley discharge and boundary flow components provide the water-balance constraint on the model. The total estimated Oasis Valley discharge in the CAU model domain; the simulated discharge, shown in Figure 6-96, is 209 kg/s. The total error is within one standard deviation (30 kg/s) as reported by Laczniak et al. (2001). The model trends the same as the data with some scatter, showing that the general representation of the area is correct. The boundary flows, estimated from regional model analysis, all trend the correct way (e.g., have the proper sign), with the largest relative misfit on the western edge.

Uncontrolled When Printed

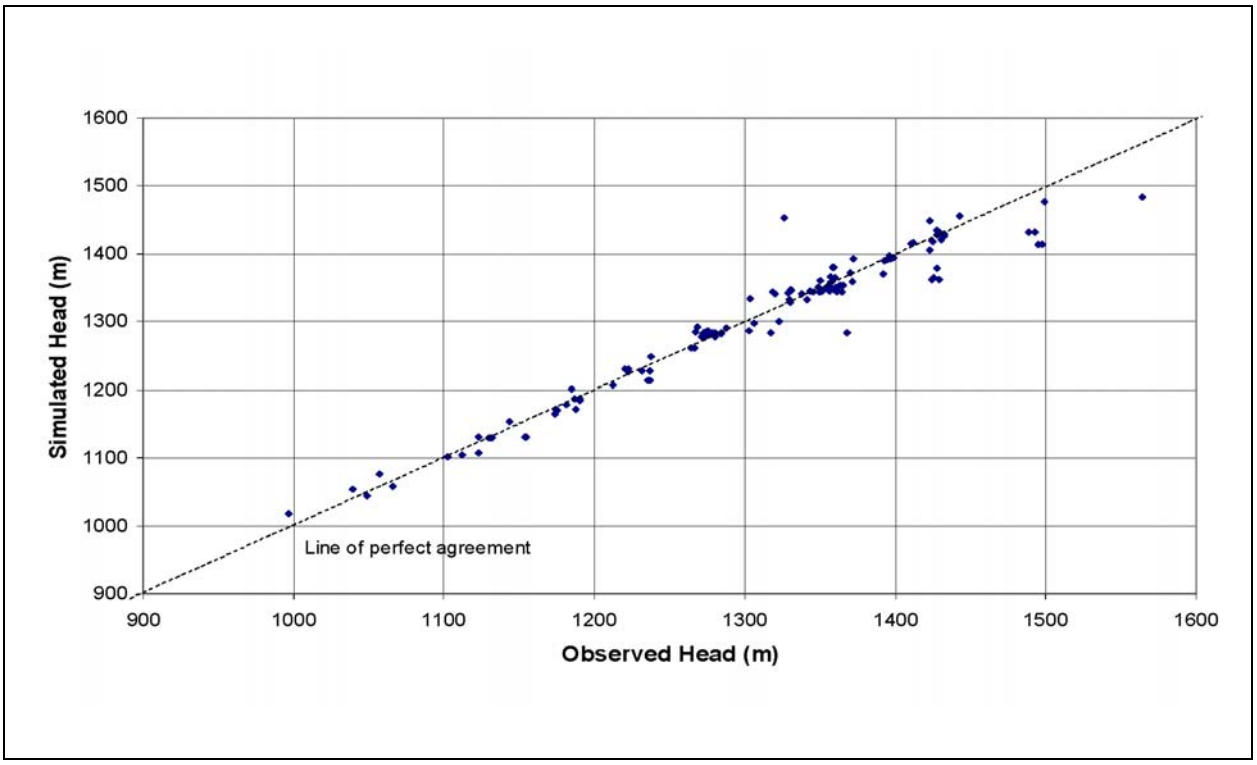

Figure 6-94
Observed Versus Simulated Observation Well Head for TCL-MME-SDA

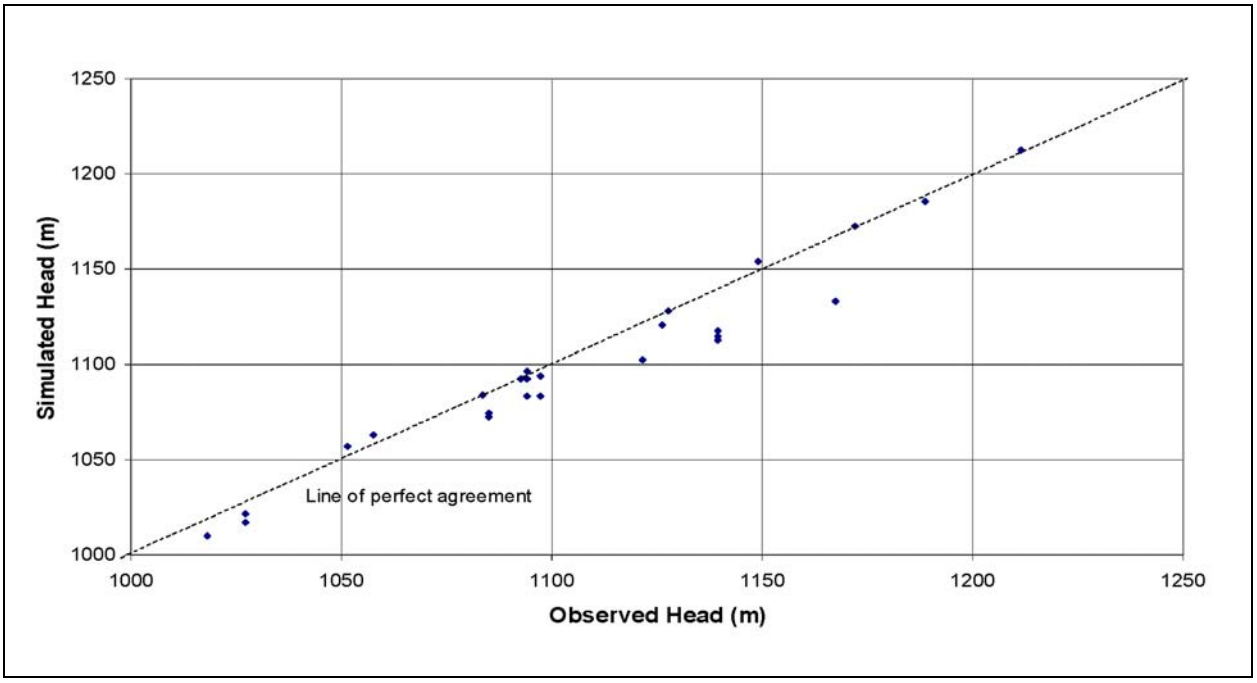

Figure 6-95
Observed Versus Simulated Spring Head for TCL-MME-SDA

Uncontrolled When Printed

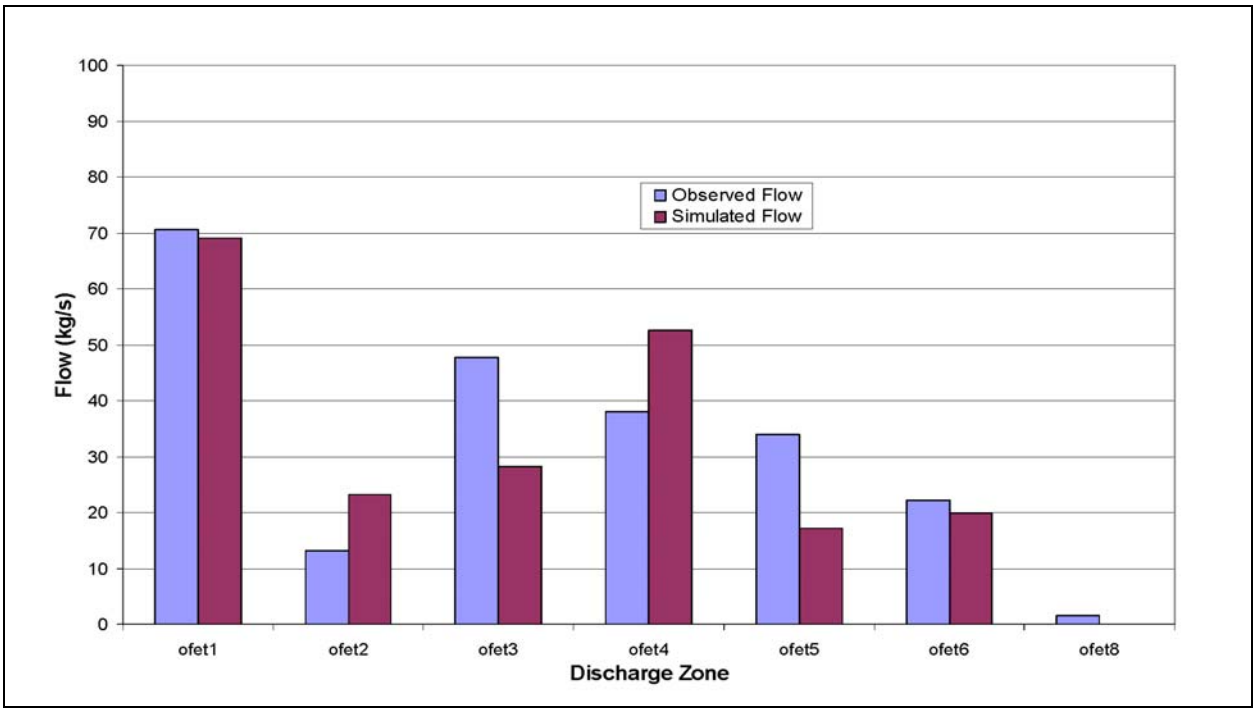

Figure 6-96
Observed and Simulated Oasis Valley Discharge for TCL-MME-SDA

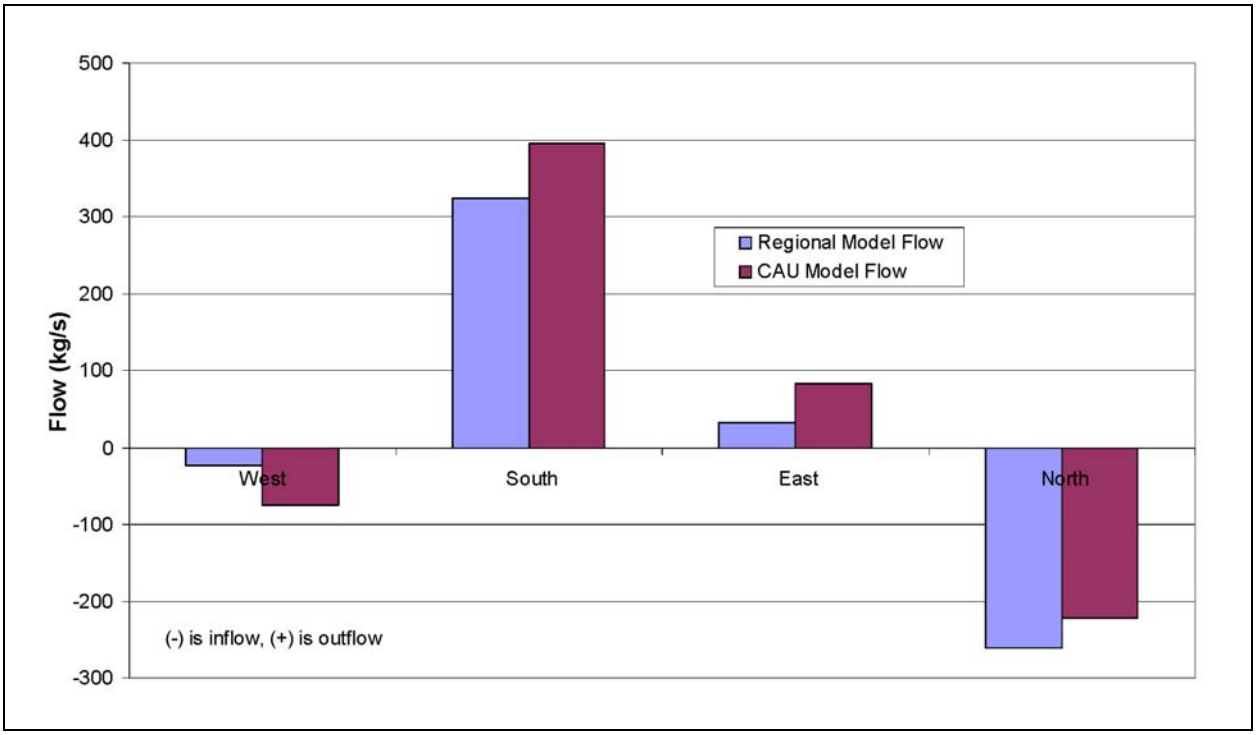

Figure 6-97
Observed and Simulated Boundary Flows for TCL-MME-SDA

Uncontrolled When Printed

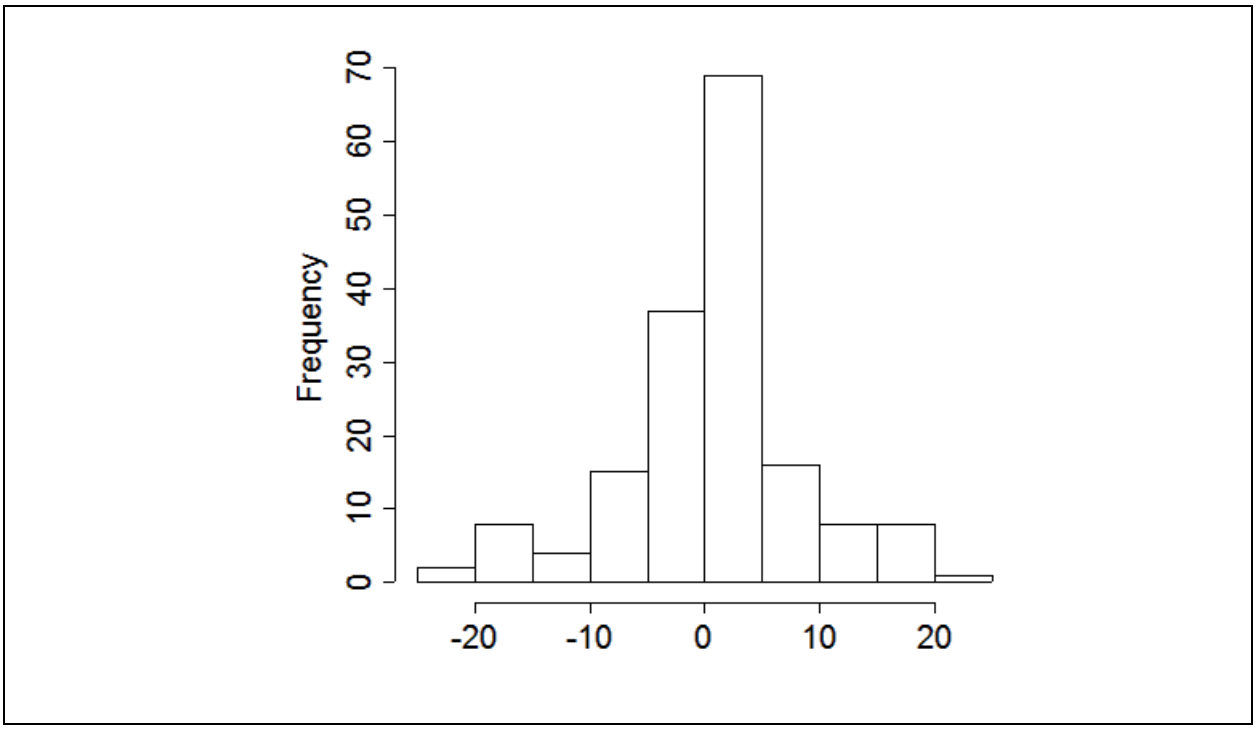

Figure 6-98
Histogram of Weighted Head Residuals for TCL-MME-SDA

The weighted head and spring errors are shown on Figure 6-99, color coded by value and sign. The driest, or undersimulated, well was U-19x. The single wettest well was UE-20n #1. In general, the errors are randomly distributed, although there is a slight dry bias in northern Area 20 at Easting and Northing of about 547,500 and 4,130,000 m, which includes Wells U-20i, UE-20e #1, U-20e, and U-20ar #1.

The quantitative measures of the model calibration are given by summary statistics shown in Table 6-21. These statistics alone are not used to judge model calibration; they are used to highlight errors in conjunction with the graphical approaches described previously. The mean error in well head is nearly zero (recall the symmetric residual histogram), a slight dry bias in the spring heads, with a slight overprediction bias for the flows. The total model objective function was 16,564; only 87 different than the base HFM (16,651). Table 6-22 shows the contribution of each data type to the total model goodness of fit.

Figure 6-100 shows the simulated water table for this model case. In the western part of Area 20, the influence of the Purse Fault is evident by the large offset in heads across it, with more subdued effects

Uncontrolled When Printed

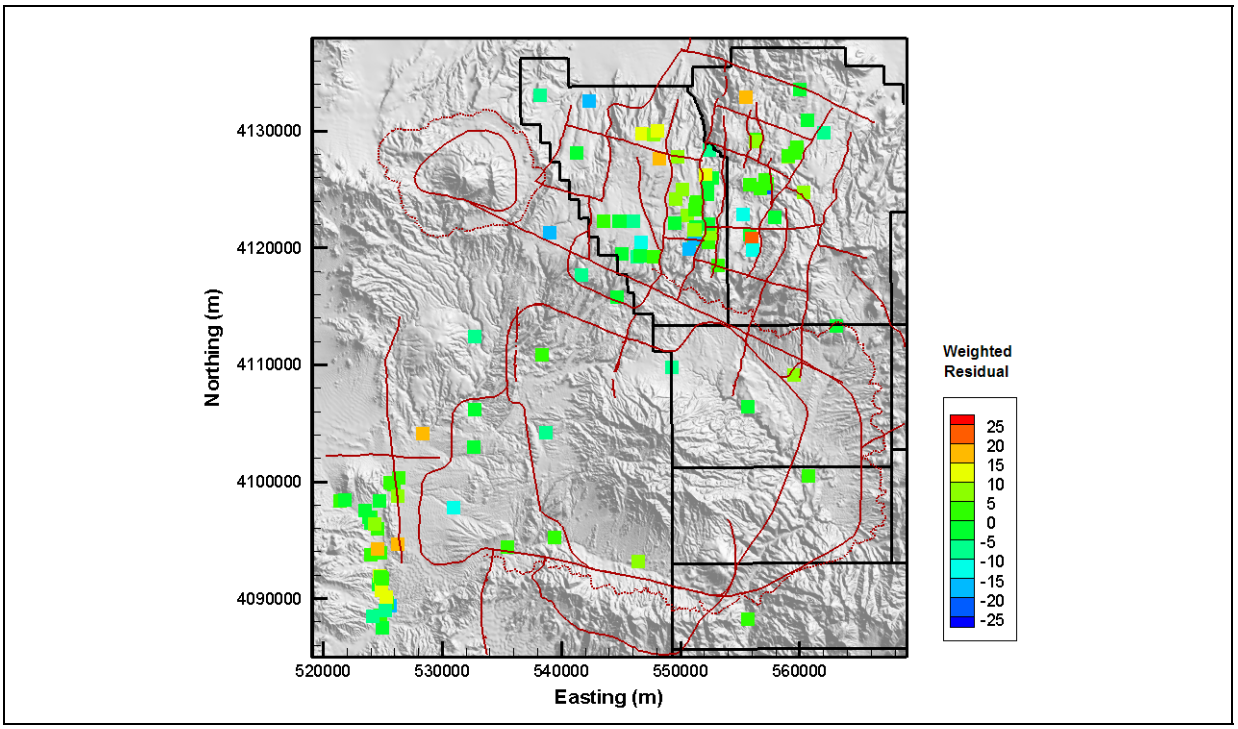

Figure 6-99
Post Plot of Weighted Well and Spring Head Residuals for TCL-MME-SDA

Table 6-21
Calibration Summary Statistics for TCL-MME-SDA

Calibration Data	Number of Data	Mean Weighted Error (m or kg/s)[a]	Maximum Weighted Residual	Minimum Weighted Residual	Error Standard Deviation (m or kg/s)
Well Head	152	-0.09	22 (U-19x)	-24 (UE-20n #1)	7.4
Spring Head	28	2.7	19 (Torrance Spring)	-5.5 (Spring id 159)	6.8
Oasis Valley Discharge	7	4.8	39 (Zone 3)	-29 (Zone 4)	24
Boundary Flow	4	-14	26 (West)	-35 (South)	27

[a]Positive sign is simulated less than target, negative is larger.

also present at West Boxcar Fault. Water flows from Areas 19 and 20 toward the southwest and Oasis Valley. Particle tracking (Figure 6-101) from each of the NTS wells shows the same generally noted flow paths as shown in Appendix A of the Pahute Mesa hydrologic data document (SNJV, 2004a).

Uncontrolled When Printed

Table 6-22
Contribution to Model Goodness of Fit by Data Type for TCL-MME-SDA

Data Type	Value (-)	Percent of Total
Well Head	8,342	50
Spring Head	1,285	8
Oasis Valley Discharge	3,966	24
Boundary Flow	2,971	18
Total	16,564	100

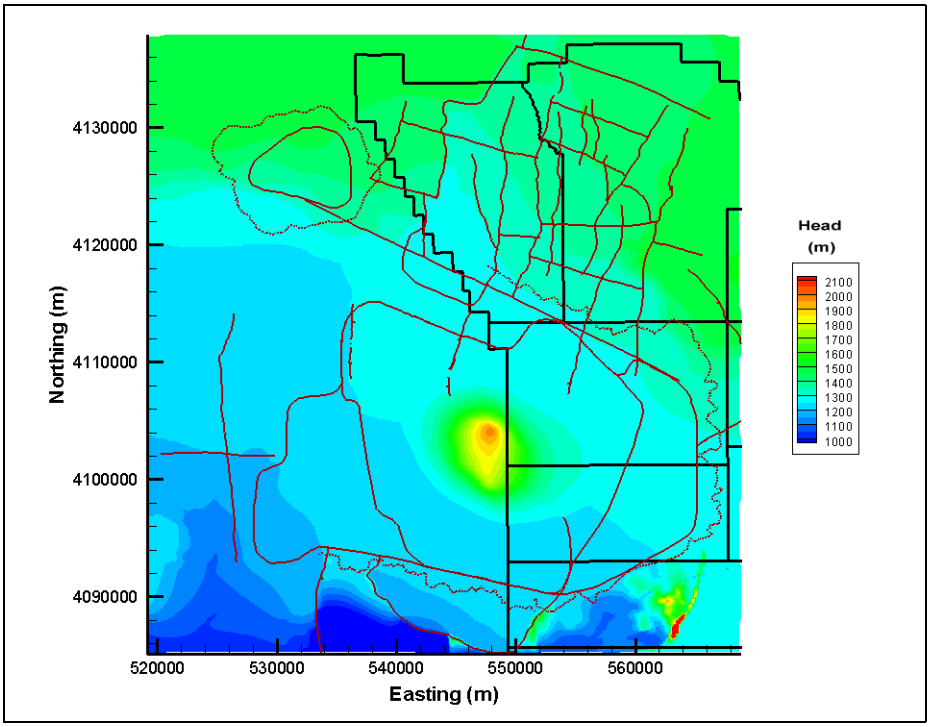

Figure 6-100
Simulated Water Table for TCL-MME-SDA

Relative to BN-MME-SDA, the particles exiting southern Area 20 near ER-EC-1 and ER-EC-6 dive a few hundred meters deeper and have a stronger tendency to discharge in southern Oasis Valley.

This alternative required no additional calibration; the BN-MME-SDA parameter values were mapped onto the HFM and the calibration shown obtained. With respect to flow, this alternative does not appear to be greatly different than the base HFM. The number of nodes that changed from the base HFM for this alternative, the HSU assigned in the base HFM and the changed HSU for the four

Uncontrolled When Printed

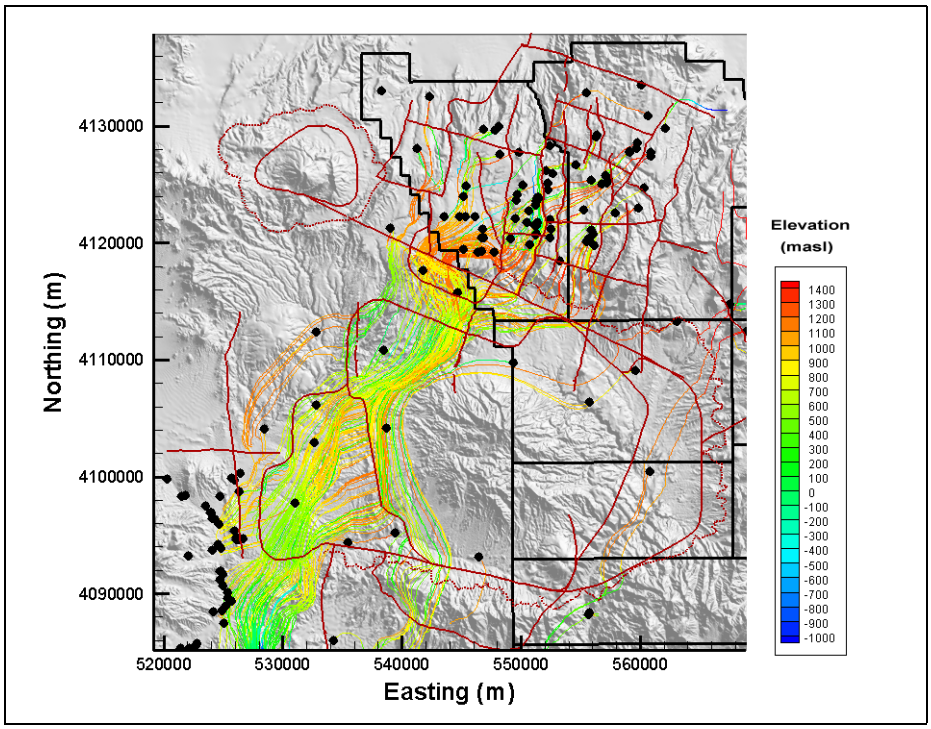

Figure 6-101
Particle Tracks for TCL-MME-SDA

largest node counts are shown in Table 6-23. Note that the change was generally from lower permeable to more permeable units. The total number of changed nodes was 49,013.

The properties used to parameterize this model are summarized in Section 6.3.6.

Table 6-23
Selected Node Changes for TCL HFM Alternative

Base HSU	Alternative HSU	Node Count
CHCU	TSA	4,878
CHCU	LPCU	2,217
LPCU	TCA	1,884
BFCU	CFCM	1,780

6.3.2 Basement Ridge Model Alternative (RIDGE-MME-SDA)

Water leaving the NTS from southwestern Area 20 tends to go southwest around the western edge of Timber Mountain. Data to define the bench between the Silent Canyon and Timber Mountain calderas are sparse. A higher gravity ridge has been measured in the area, which in the base model is

Uncontrolled When Printed

accounted for by LCA. This alternative distributes the BA, TCA, TSA, and CFCM further south so that they pinch out or truncate against the older, presumably less permeable units that form the bench, disrupting flow paths from Pahute Mesa. See Section 6.3 in BN (2002) for more information.

Plots of observed versus simulated values for the calibration wells, springs, Oasis Valley discharge, and boundary flows are shown in Figures 6-102 through 6-105. The scatter around the line of perfect agreement is generally random in Figure 6-102, until an observed head of 1,450 m is exceeded. At the very highest observed observation well heads, the model has a tendency toward undersimulation. On Figure 6-103, the line of perfect agreement is shown, and ideally the data would plot exactly onto this line. However, at the higher observed observation spring head, the model has a tendency toward undersimulation. The plot is not significantly different than those shown in Section 5.6.2. Figure 6-105 presents a plot of observed versus simulated values for boundary flows. Figure 6-106 shows a histogram of weighted observation well residuals. The bulk of the weighted errors (about 95) are less than ±10 m. The errors are not symmetrically distributed around zero, with larger oversimulated (negative sign) wells. The total errors above +10 m and below -10 m appear to be about the same.

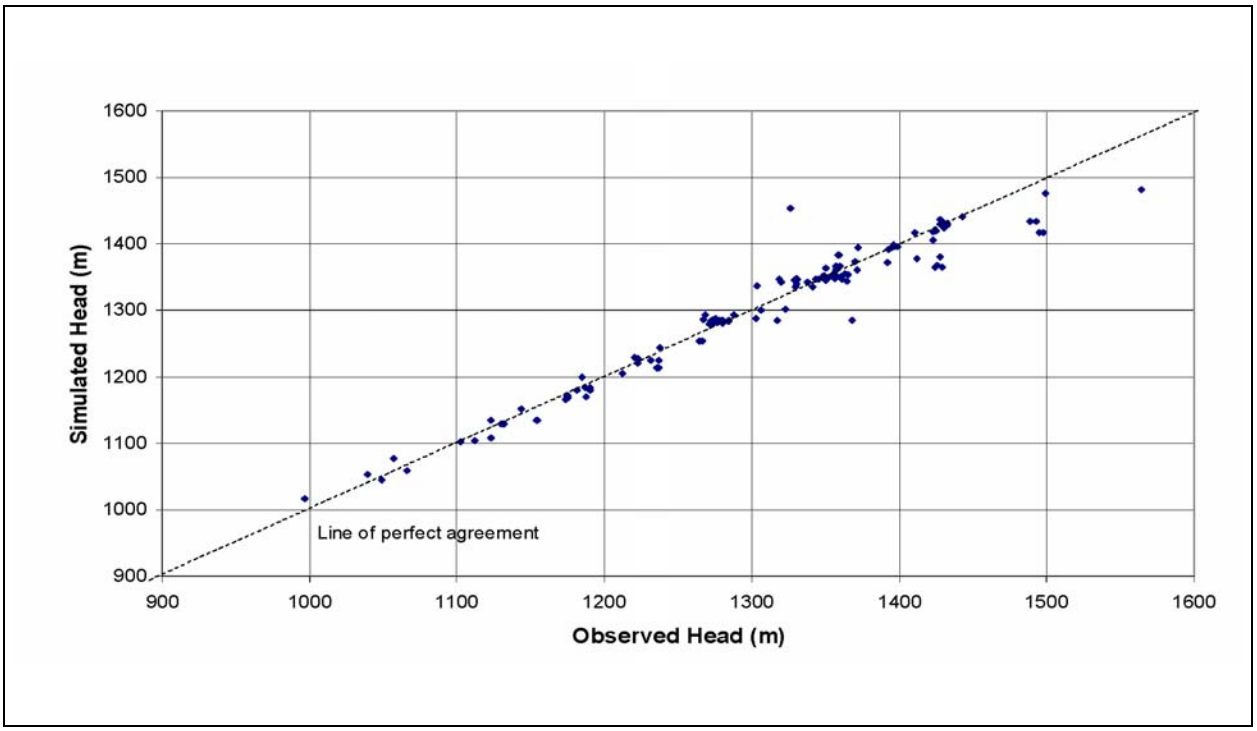

Figure 6-102
Observed Versus Simulated Observation Well Head for RIDGE-MME-SDA

Uncontrolled When Printed

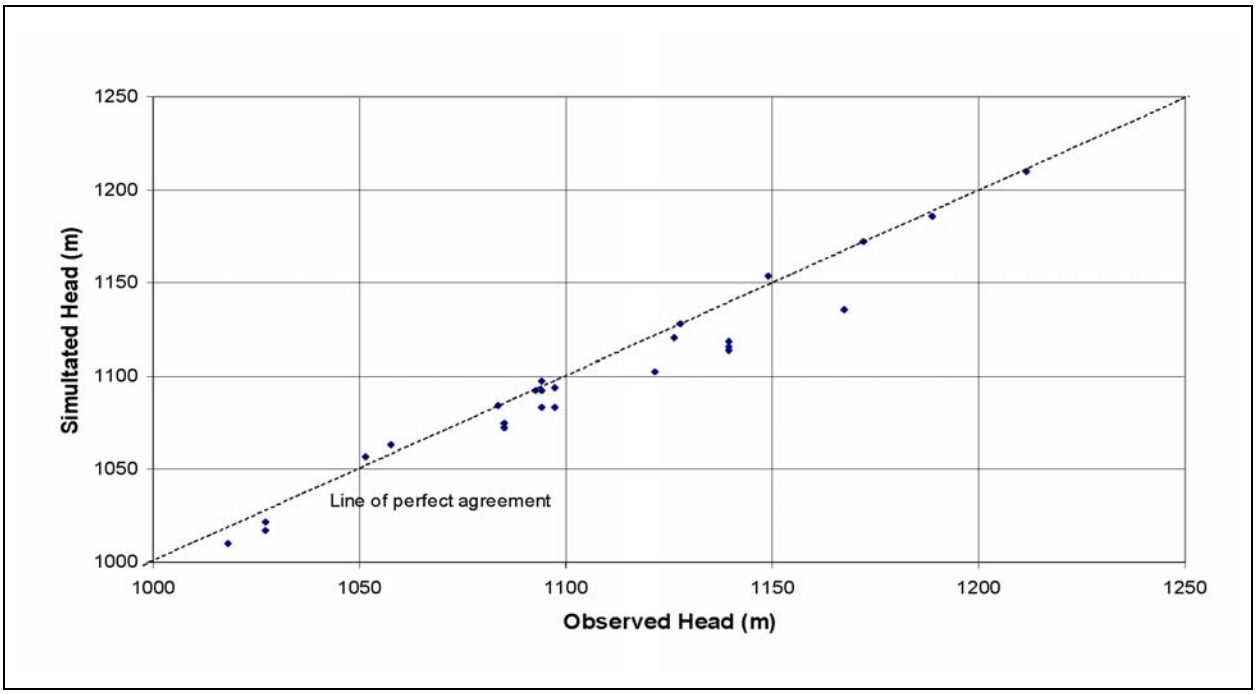

Figure 6-103
Observed Versus Simulated Spring Head for RIDGE-MME-SDA

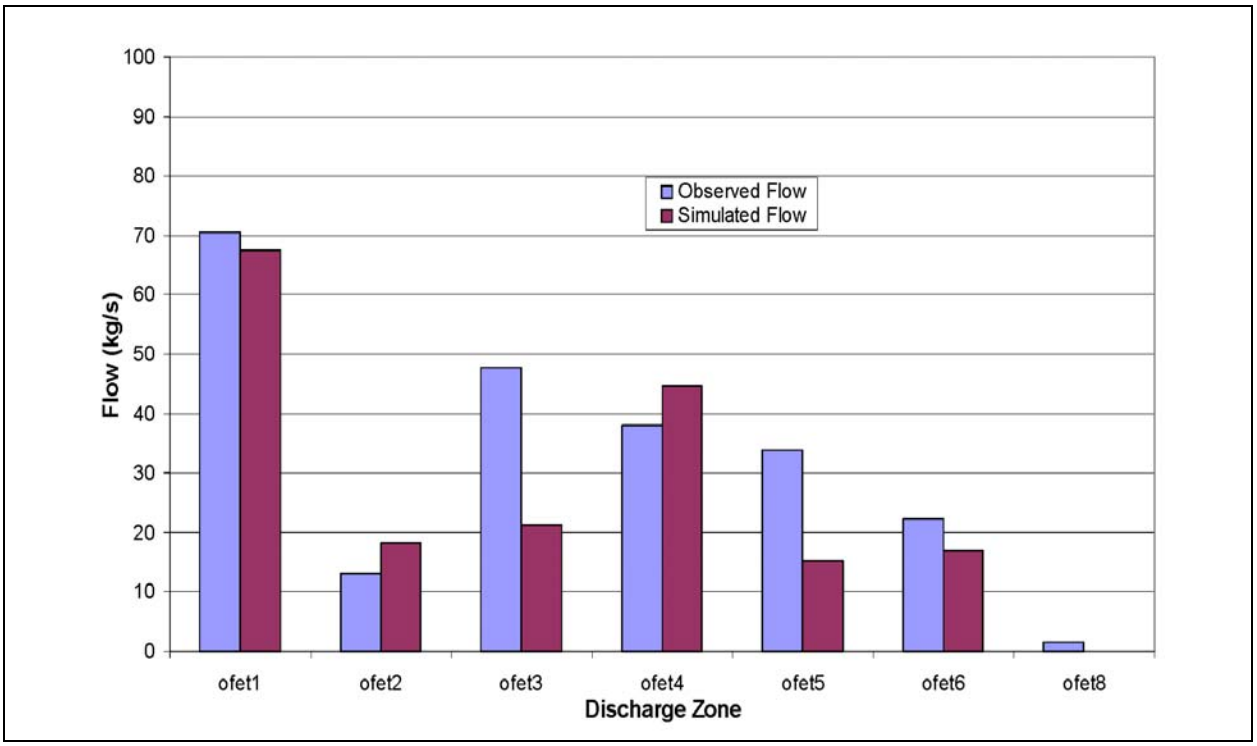

Figure 6-104
Observed and Simulated Oasis Valley Discharge for RIDGE-MME-SDA

Uncontrolled When Printed

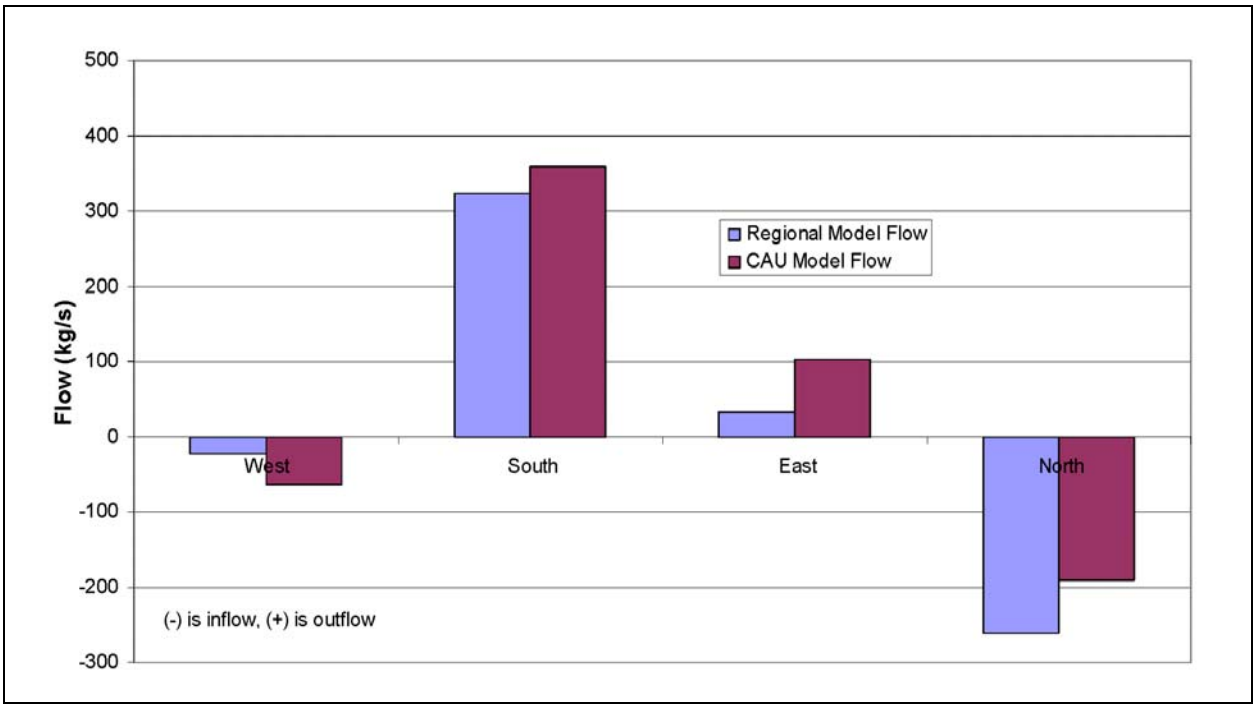

Figure 6-105
Observed and Simulated Boundary Flows for RIDGE-MME-SDA

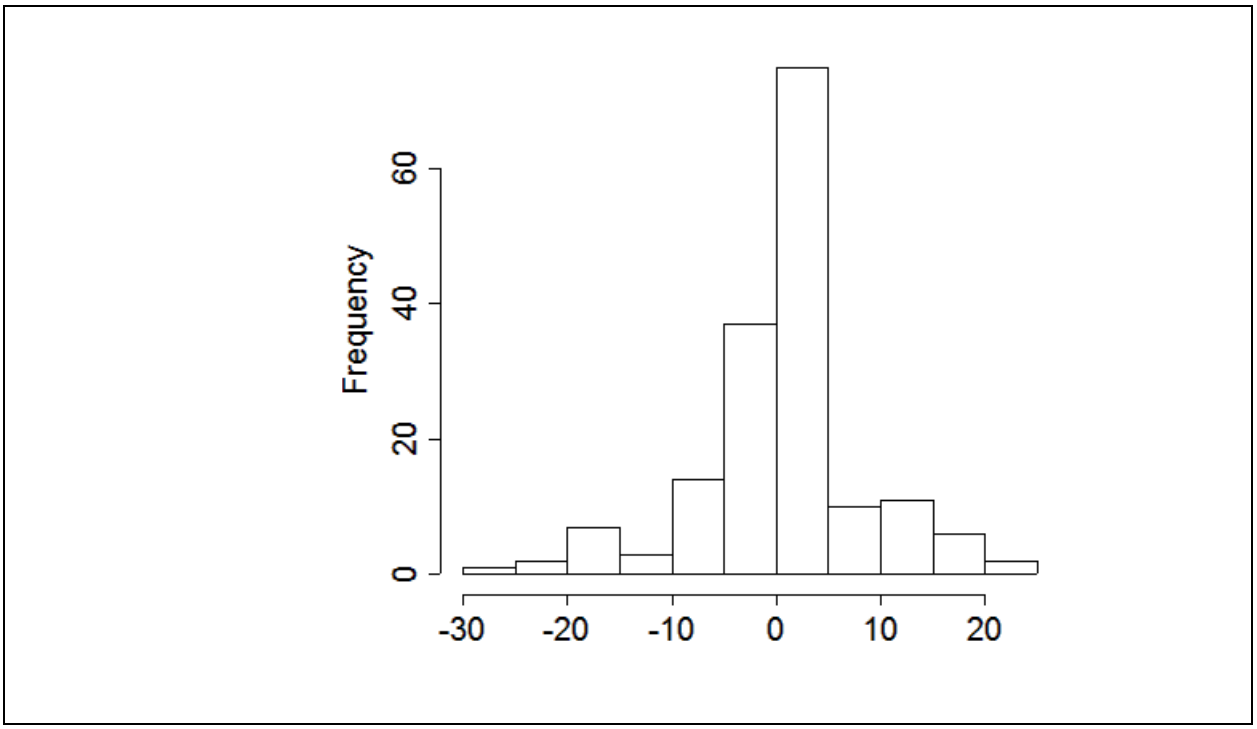

Figure 6-106
Histogram of Weighted Head Residuals for RIDGE-MME-SDA

Uncontrolled When Printed

The Oasis Valley discharge and boundary flow components provide the water-balance constraint on the model. The total estimated Oasis Valley discharge in the CAU model domain is 227 kg/s; the simulated discharge, shown in Figure 6-104, is 183 kg/s. This is about a 1.5 standard deviation less than the estimated value, which makes this model less good than most others in this regard. The model trends the same as the data with some scatter, showing that the general representation of Oasis Valley is correct. The boundary flows, estimated from regional model analysis, all trend the correct way (e.g., have the proper sign), with the largest relative misfit on the western edge.

The weighted head and spring errors are shown on Figure 6-107, color coded by value and sign. The driest, or undersimulated, well was U-20m. The most overpredicted head was at Well UE-20n #1. In general, the errors are randomly distributed, although there is a slight dry bias in northern Area 20 at Easting and Northing of about 547,500 and 4,130,000 m, which includes Wells U-20i, UE-20e #1, U-20e, and U-20ar #1.

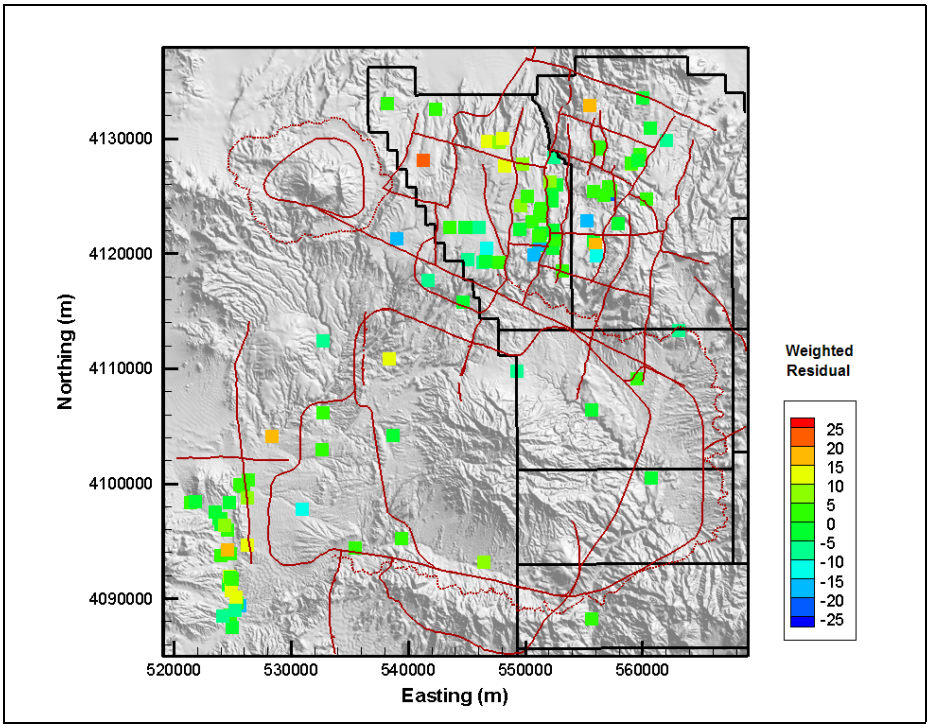

Figure 6-107
Post Plot of Weighted Well and Spring Head Residuals for RIDGE-MME-SDA

The quantitative measures of the model calibration are given by summary statistics shown in Table 6-24. There is a slight oversimulation bias for well heads. There is a slight dry bias in the

Uncontrolled When Printed

spring heads, with a slight overprediction bias for the flows. The total model objective function was 18,459, which is slightly worse than the best base HFM calibration (BN-MME-SDA). Table 6-25 shows the contribution of each data type to the total model goodness of fit.

Table 6-24
Calibration Summary Statistics for RIDGE-MME-SDA

Calibration Data	Number of Data	Mean Weighted Error (m or kg/s)[a]	Maximum Weighted Residual	Minimum Weighted Residual	Error Standard Deviation (m or kg/s)
Well Head	152	-0.07	23 (U-20m)	-27 (UE-20n #1)	7.8
Spring Head	28	2.8	19 (Torrance Spring)	-5.4 (Spring id 159)	6.8
Oasis Valley Discharge	7	12	53 (Zone 3)	-13 (Zone 4)	26
Boundary Flow	4	-17	20 (West)	-35 (East)	28

[a]Positive sign is simulated less than target, negative is larger.

Table 6-25
Contribution to Model Goodness of Fit by Data Type for RIDGE-MME-SDA

Data Type	Value (-)	Percent of Total
Well Head	9,351	51
Spring Head	1,289	7
Oasis Valley Discharge	4,665	25
Boundary Flow	3,154	17
Total	18,459	100

Figure 6-108 shows the simulated water table for this model case. In the western part of Area 20, the influence of the Purse Fault is evident by the large offset in heads across it, with more subdued effects also present at West Boxcar Fault. Particle tracking (Figure 6-109) from each of the NTS wells shows the same generally noted flow paths as shown by in Appendix A of the Pahute Mesa hydrologic data document (SNJV, 2004a). Relative to the base HFM calibration shown in Section 5.6.2, the particle tracks exit Area 20 further west and with a more even distribution. This is the effect of the truncation of BA, TCA, TSA, and CFCM against older, lower permeable units as described by BN (2002).

The parameters from BN-MME-SDA were mapped onto this HFM, and the calibration shown was obtained with no additional effort. Thus, the effects of this HFM on flow model metrics is modest.

Uncontrolled When Printed

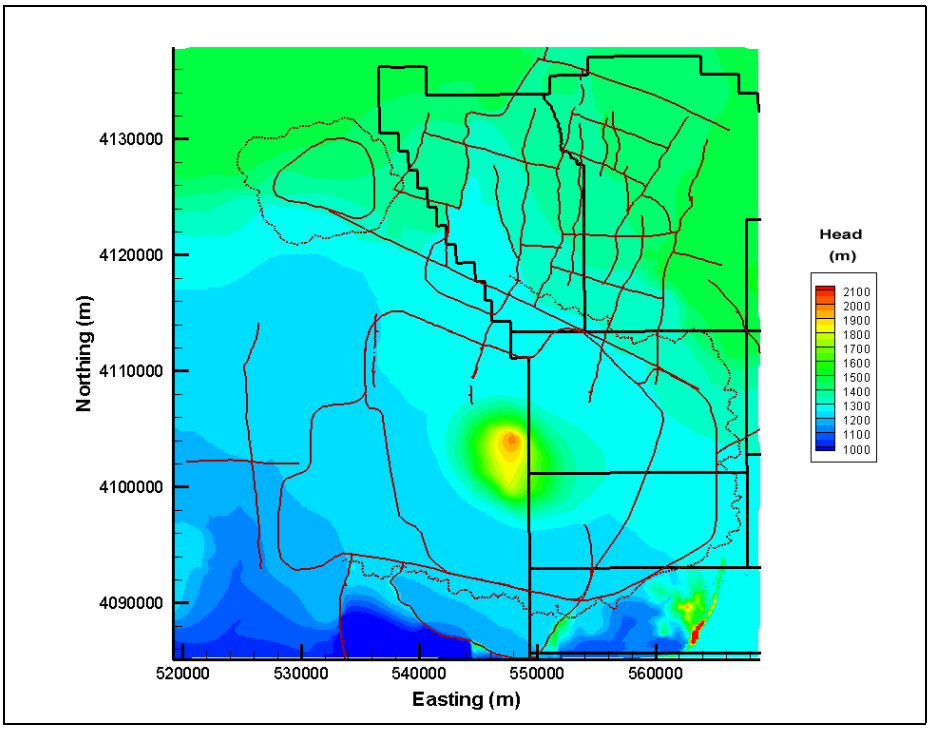

Figure 6-108
Simulated Water Table for RIDGE-MME-SDA

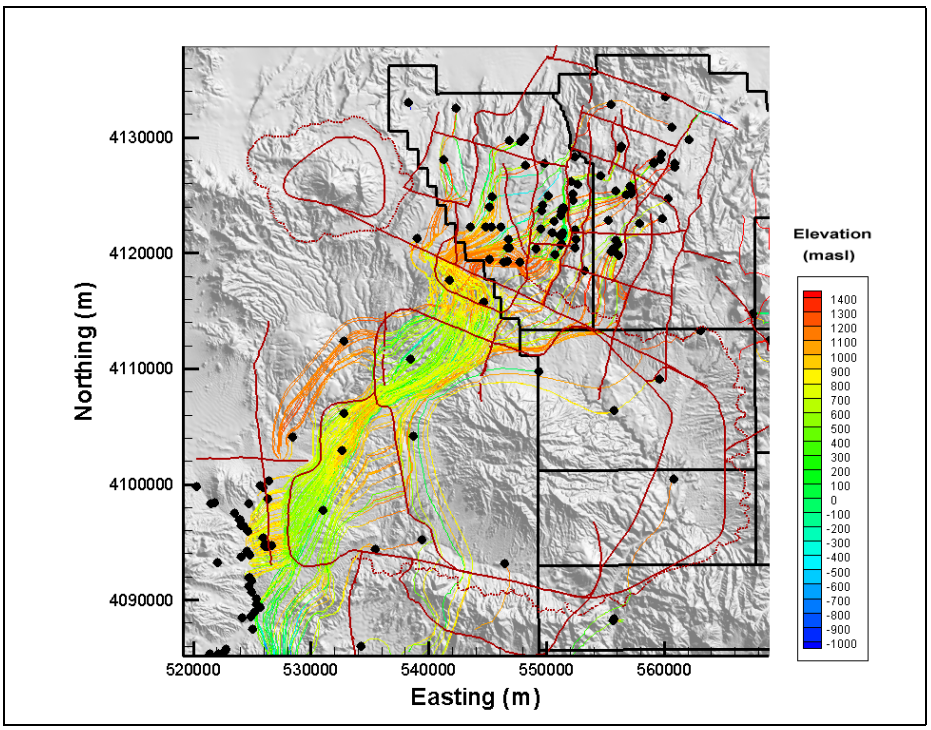

Figure 6-109
Particle Tracks for RIDGE-MME-SDA

Uncontrolled When Printed

The nodes that were changed from the base HFM for selected HSUs are summarized in Table 6-26. A total of 89,346 nodes were changed for RIDGE. The count is the largest of all the alternatives because this case makes changes in southern Pahute Mesa where the node spacing is relatively fine. The major change is from BA to FCCU; from high to low permeability. The TCA and TSA also change as described by BN (2002) and seen in Table 6-26 to less permeable HSUs. The properties used to parameterize this model are summarized in Section 6.3.6.

Table 6-26
Selected Node Changes for RIDGE HFM Alternative

Base HSU	Alternative HSU	Node Count
BA	FCCU	14,609
CHCU	CFCU	10,329
UPCU	CHCU	4,701
TCA	CHCU	4,568
TSA	CFCU	2,865

6.3.3 Raised Pre-Tertiary Surface Alternative (PZUP-MME-SDA)

The determination of depth to Paleozoic basement assumed a density/depth relation for gravity inversion. Two such distributions have been described for Pahute Mesa, which cause up to a 2-km variation in the position of the Paleozoic basement. This alternative raised the basement as much as possible and still remains in agreement with the hard data. The consequences were thought to be facilitation of groundwater flow around the eastern side of Timber Mountain. See Section 6.5 in BN (2002) for more information.

Plots of observed versus simulated values for the calibration wells, springs, Oasis Valley discharge, and boundary flows are shown in Figures 6-110 through 6-113. The scatter around the line of perfect agreement is generally random in Figure 6-110, until an observed head of 1,450 m is exceeded. At the very highest observed observation well heads, the model has a tendency toward undersimulation. On Figure 6-111, the line of perfect agreement is shown, and ideally the data would plot exactly onto this line. However, at the higher observed observation spring head, the model has a tendency toward undersimulation. The plot is not significantly different than those shown in Section 5.6.2. Figure 6-113 presents a plot of observed versus simulated values for boundary flows. Figure 6-114 shows a histogram of weighted observation well residuals. The bulk of the weighted errors (about 95)

Uncontrolled When Printed

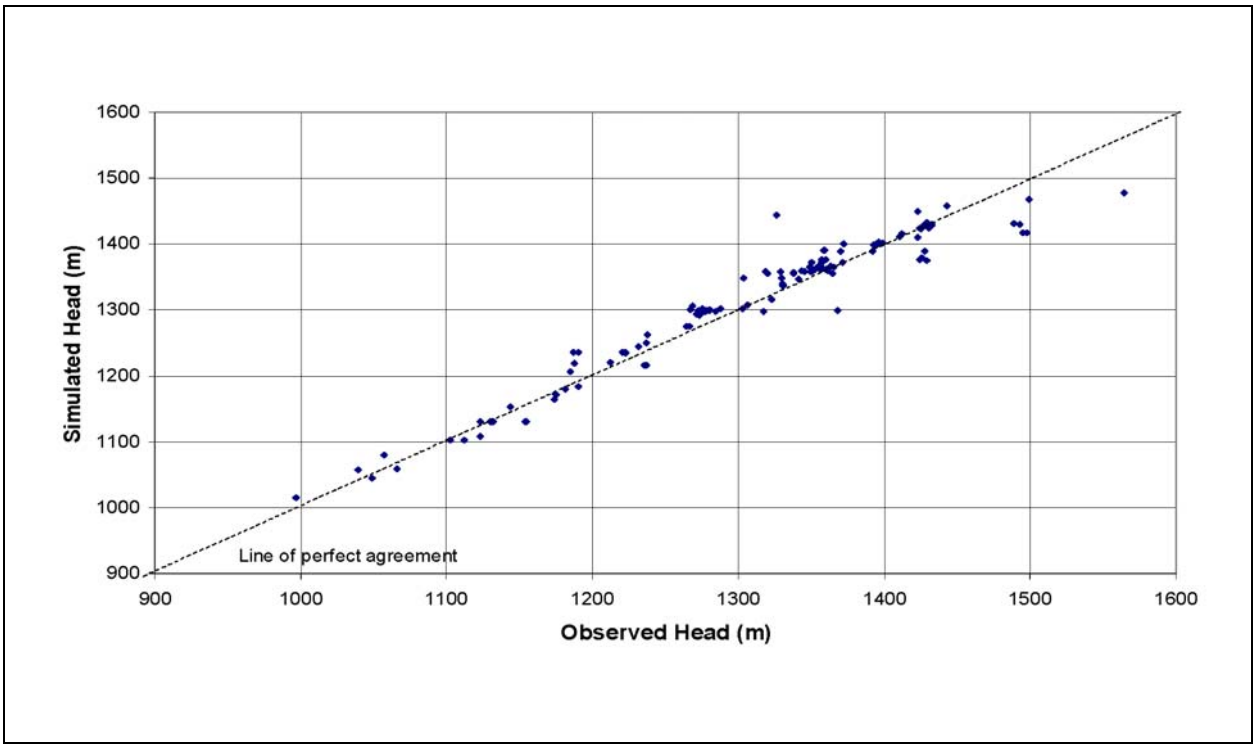

Figure 6-110
Observed Versus Simulated Observation Well Head for PZUP-MME-SDA

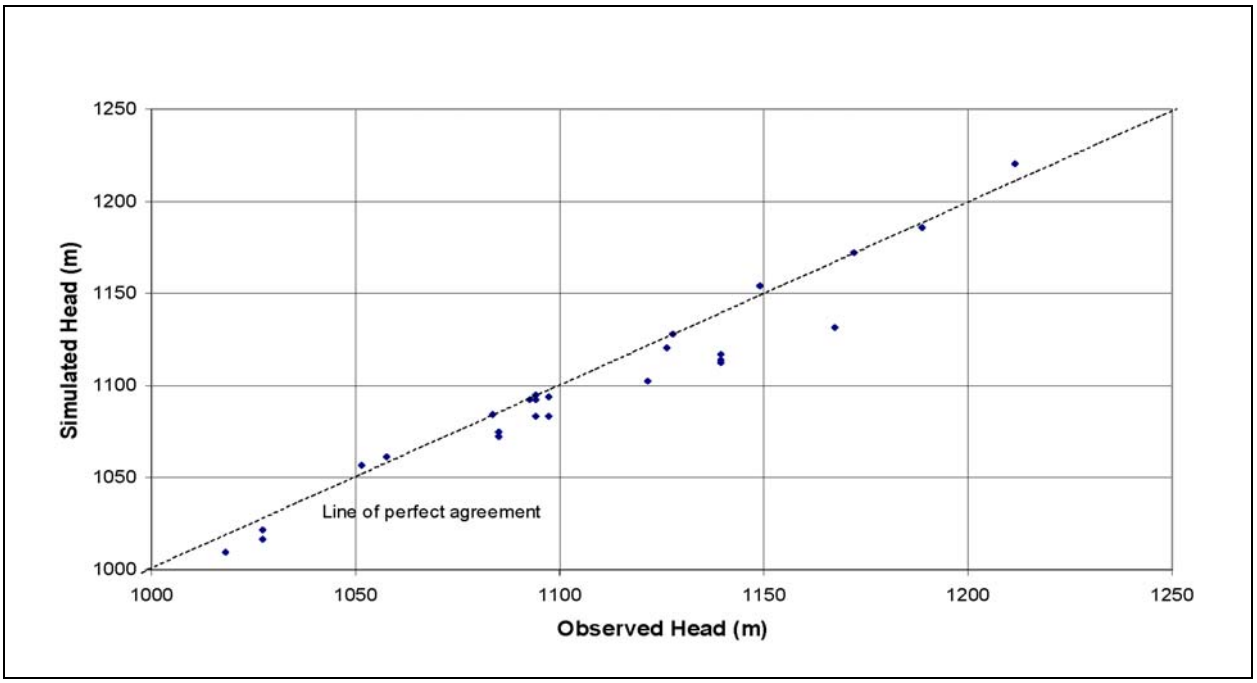

Figure 6-111
Observed Versus Simulated Spring Head for PZUP-MME-SDA

Uncontrolled When Printed

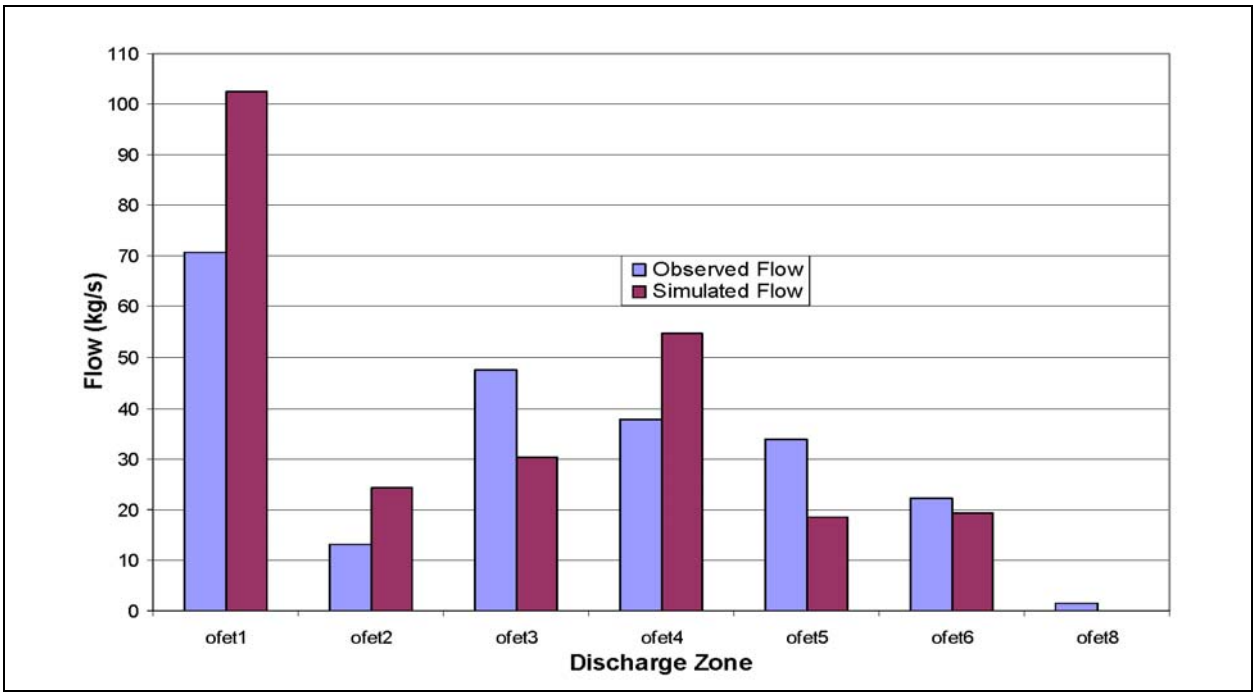

Figure 6-112
Observed and Simulated Oasis Valley Discharge for PZUP-MME-SDA

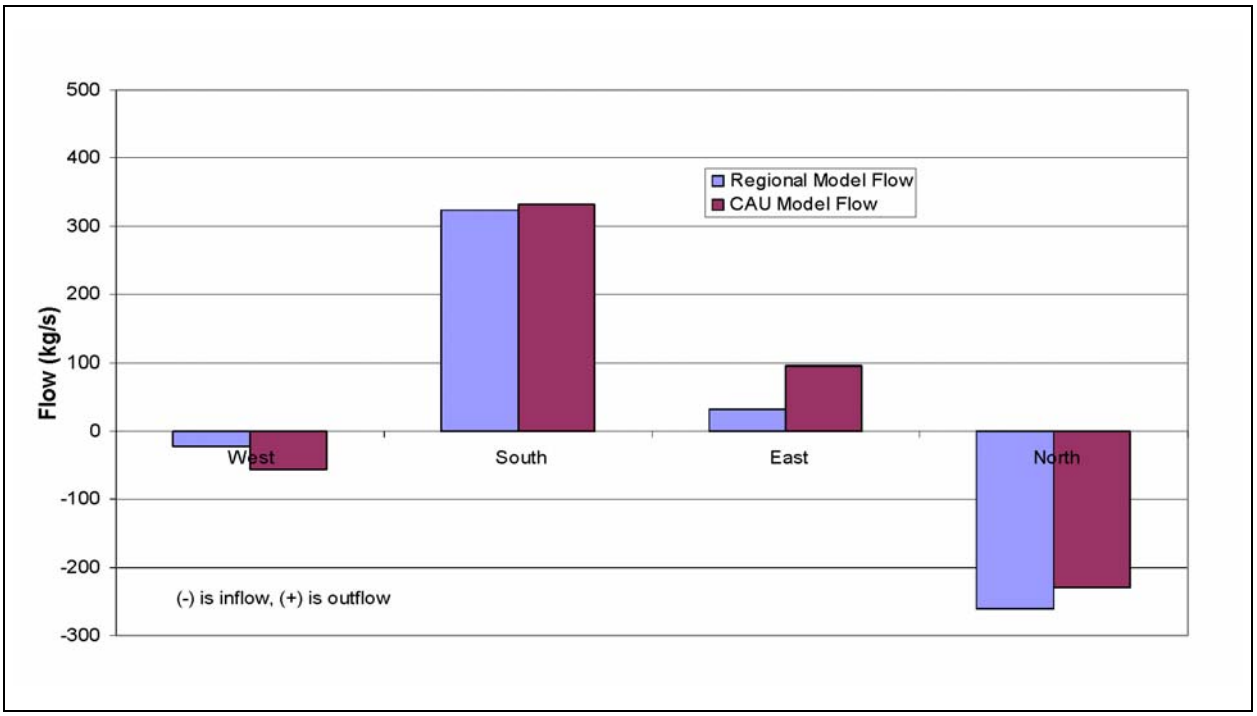

Figure 6-113
Observed and Simulated Boundary Flows for PZUP-MME-SDA

Uncontrolled When Printed

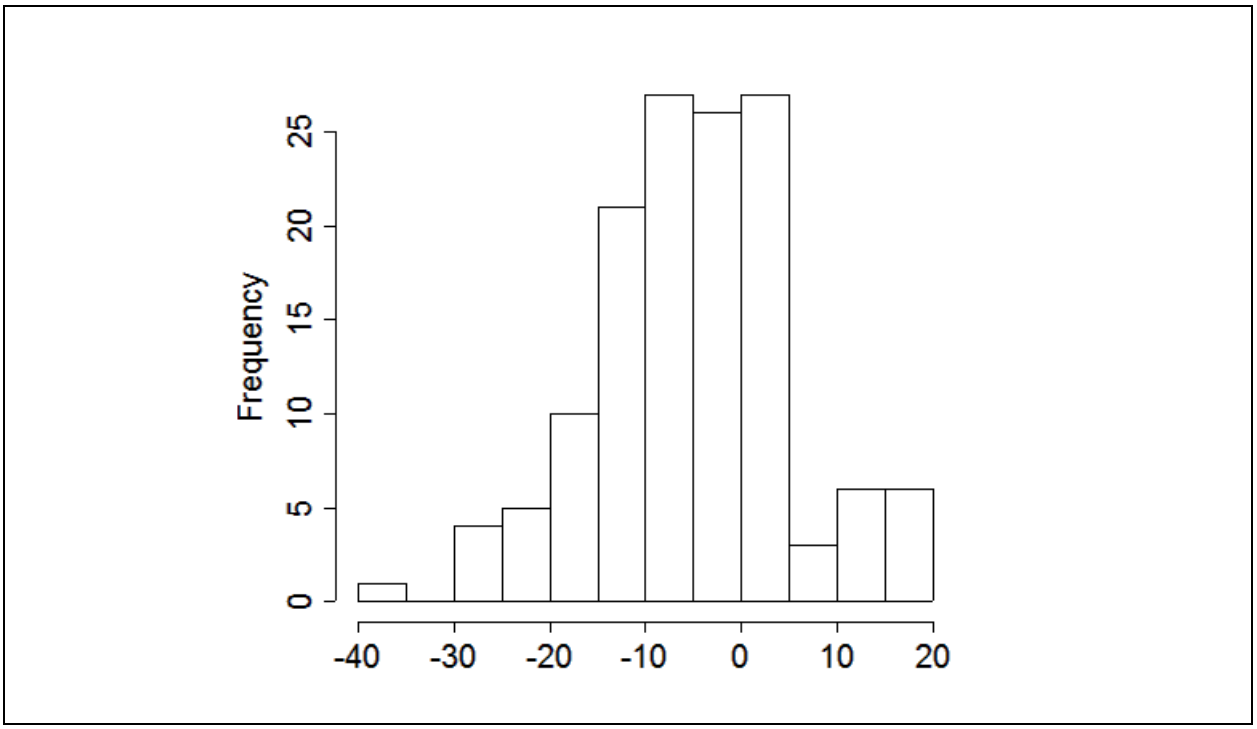

Figure 6-114
Histogram of Weighted Head Residuals for PZUP-MME-SDA

are less than ±10 m. The errors are not symmetrically distributed around zero, with a larger proportion of oversimulated (negative sign) wells.

The total estimated Oasis Valley discharge in the CAU model domain is 227 kg/s; the simulated discharge, shown in Figure 6-112, is 209 kg/s. The total error is within one standard deviation (30 kg/s) as reported by Laczniak et al. (2001). The model trends the same as the data with some scatter, showing that the general representation of the area is correct. The boundary flows, estimated from regional model analysis, all trend the correct way (e.g., have the proper sign), with the largest relative misfit on the western edge.

The weighted head and spring errors are shown on Figure 6-115, color coded by value and sign. There is a clear tendency to oversimulate heads, although this result is not associated with commensurate oversimulation of Oasis Valley discharge. The driest, or undersimulated, well was ER-OV-03a. The single wettest well was UE-20n #1.

Uncontrolled When Printed

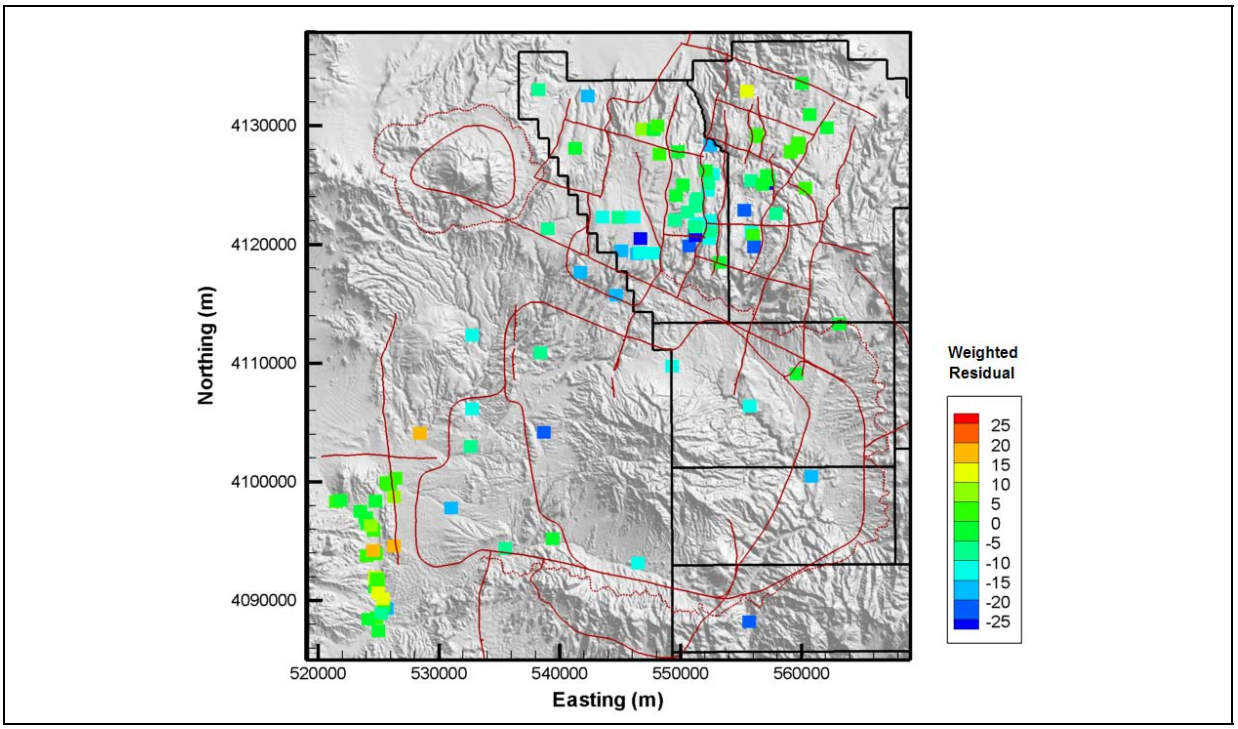

Figure 6-115
Post Plot of Weighted Well and Spring Head Residuals for PZUP-MME-SDA

The quantitative measures of the model calibration are given by summary statistics shown in Table 6-27. There is a slight dry bias in the spring heads, with a slight overprediction bias for the flows. The total model objective function was 22,513. Table 6-28 shows the contribution of each data type to the total model goodness of fit.

Figure 6-116 shows the simulated water table for this model case. In the western part of Area 20, the influence of the Purse Fault is evident by the large offset in heads across it, with more subdued effects also present at West Boxcar Fault. Water flows from Areas 19 and 20 toward the southwest and Oasis Valley. Particle tracking (Figure 6-117) from each of the NTS wells shows the same generally noted flow paths as shown in Appendix A of the Pahute Mesa hydrologic data document (SNJV, 2004a).

The initial results from this HFM were greatly different and required substantial effort to recalibrate. The number of changed nodes and associated HSUs for the four largest categories in this alternative are shown in Table 6-29. Notice that the changes are from higher permeability units to lower permeability units found at greater depth in the base HFM. Thus, the changes for this alternative are consistent with the intent of BN (2002) to raise the pre-Tertiary/Paleozoic contact and accentuate the

Uncontrolled When Printed

Table 6-27
Calibration Summary Statistics for PZUP-MME-SDA

Calibration Data	Number of Data	Mean Weighted Error (m or kg/s)[a]	Maximum Weighted Residual	Minimum Weighted Residual	Error Standard Deviation (m or kg/s)
Well Head	152	5.1	18 (U-19x)	-39 (ER-OV-03b)	10
Spring Head	28	2.6	19 (Torrance Spring)	-8.7 (Spring id 180)	6.9
Oasis Valley Discharge	7	-6.5	35 (Zone 3)	-64 (Zone 4)	34
Boundary Flow	4	-8.6	16 (West)	-31 (South)	19

[a]Positive sign is simulated less than target, negative is larger.

Table 6-28
Contribution to Model Goodness of Fit by Data Type for PZUP-MME-SDA

Data Type	Value (-)	Percent of Total
Well Head	16,416	61
Spring Head	1,337	5
Oasis Valley Discharge	7,865	29
Boundary Flow	1,500	5
Total	27,118	100

shallow flow system. The total number of changed nodes is 55,554. The properties used to parameterize this model are summarized in Section 6.3.6.

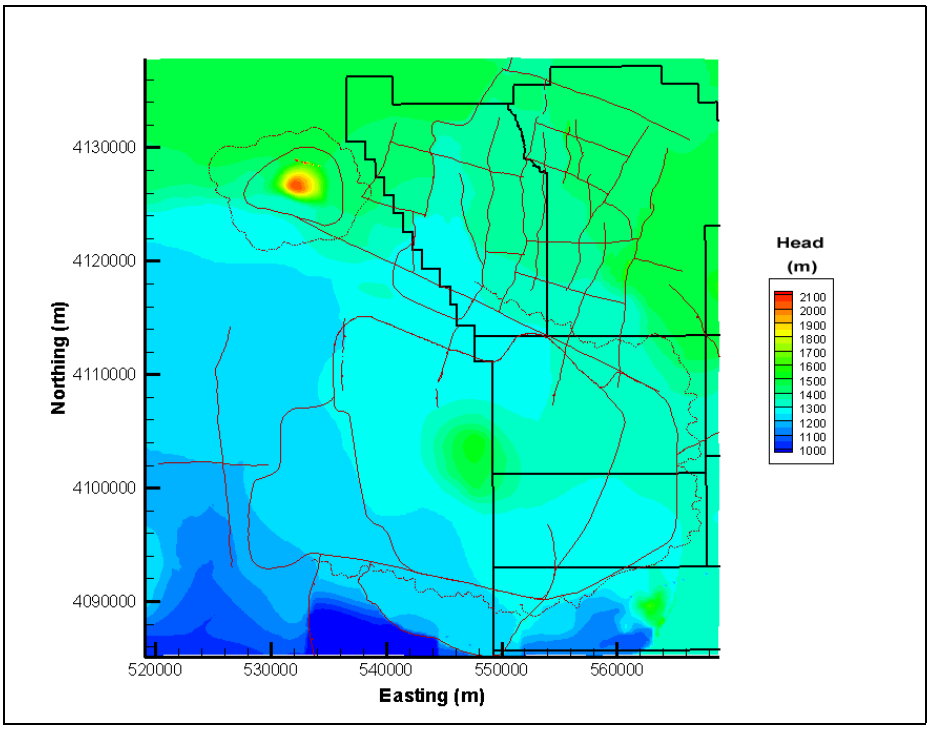

Figure 6-116
Simulated Water Table for PZUP-MME-SDA

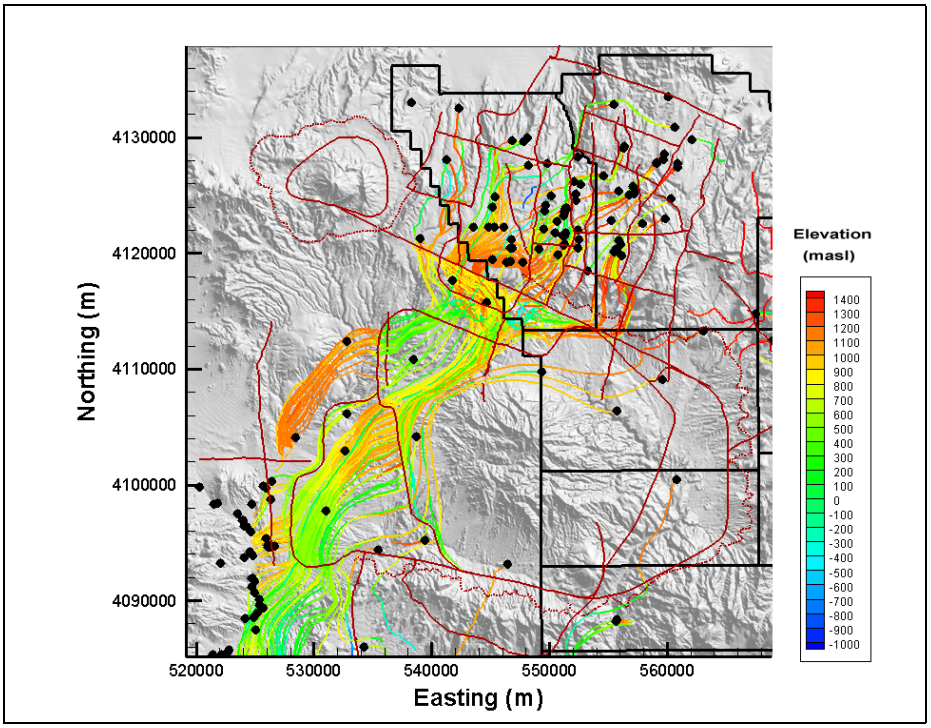

Figure 6-117
Particle Tracks for PZUP-MME-SDA

Uncontrolled When Printed

Table 6-29
Selected Node Changes for PZUP HFM Alternative

Base HSU	Alternative HSU	Node Count
TMCM	ATICU	10,637
PBRCM	LCA	9,576
TMCM	RMICU	5,388
PBRCM	LCCU1	5,188

6.3.4 Deeply Rooted Belted Thrust Fault Alternative (DRT-MME-SDA)

The Belted Range Fault is the principal pre-Tertiary structure in the model region and controls the distribution of pre-Tertiary rocks. The fault is poorly constrained over the model area, and an alternative was developed in which the fault extends deeper, resulting a thick sheet of LCCU over most of the model area. The anticipated consequence was the focusing of the flow system higher in the model from the reduction in the amount of permeable rocks, thus increasing flow velocity. See Section 6.7 in BN (2002) for more information.

Plots of observed versus simulated values for the calibration wells, springs, Oasis Valley discharge, and boundary flows are shown in Figures 6-118 through 6-121. The scatter around the line of perfect agreement is generally random in Figure 6-118, until an observed head of 1,450 m is exceeded. At the very highest observed observation well heads, the model has a tendency toward undersimulation. Moreover, on Figure 6-119, the line of perfect agreement is shown, and ideally the data would plot exactly onto this line. However, at the higher observed observation spring head, the model has a tendency toward undersimulation. The plot is not significantly different than those shown in Section 5.6.2. Figure 6-121 presents a plot of observed versus simulated values for boundary flows. Figure 6-122 shows a histogram of weighted observation well residuals. The bulk of the weighted errors (about 95) are less than ±10 m. The errors are not symmetrically distributed around zero, with a large proportion oversimulated (negative sign) wells and a single large (almost equal to 60 m) underprediction.

The total estimated Oasis Valley discharge in the CAU model domain is 227 kg/s; the simulated discharge, shown in Figure 6-120, is 214 kg/s. The total error is within one standard deviation (30 kg/s) as reported by Laczniak et al. (2001). The model trends the same as the data with some

Uncontrolled When Printed

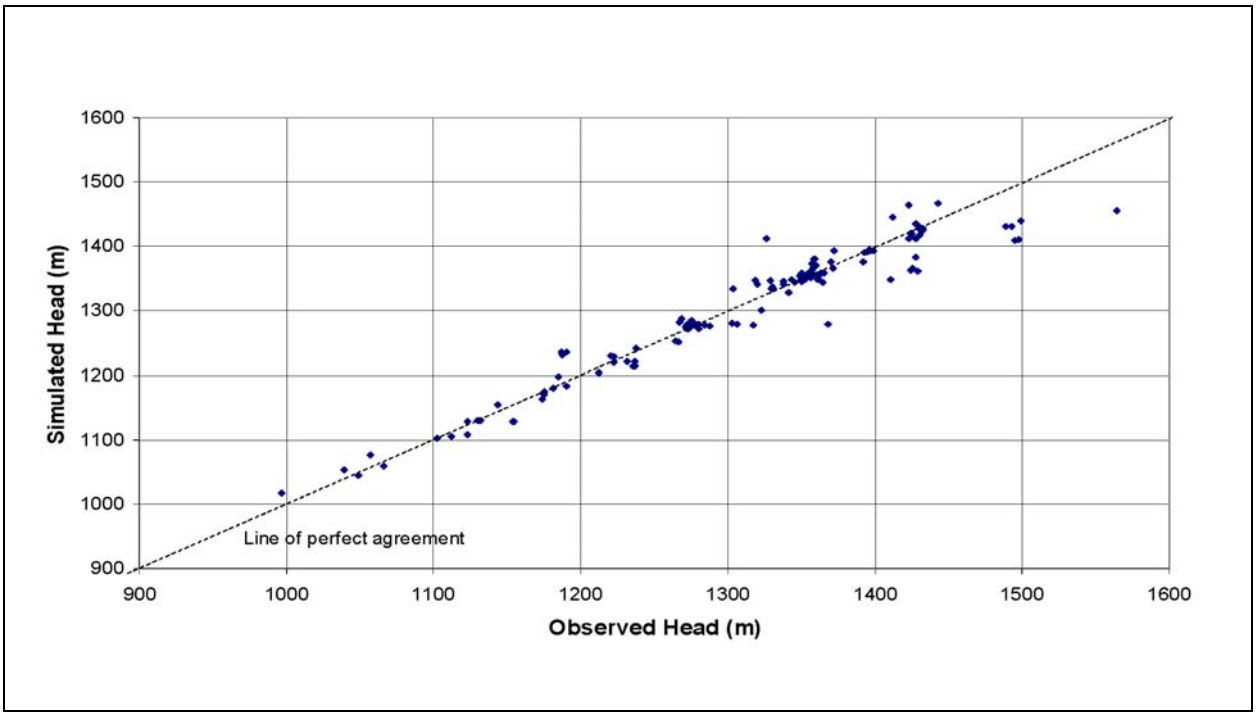

Figure 6-118
Observed Versus Simulated Observation Well Head for DRT-MME-SDA

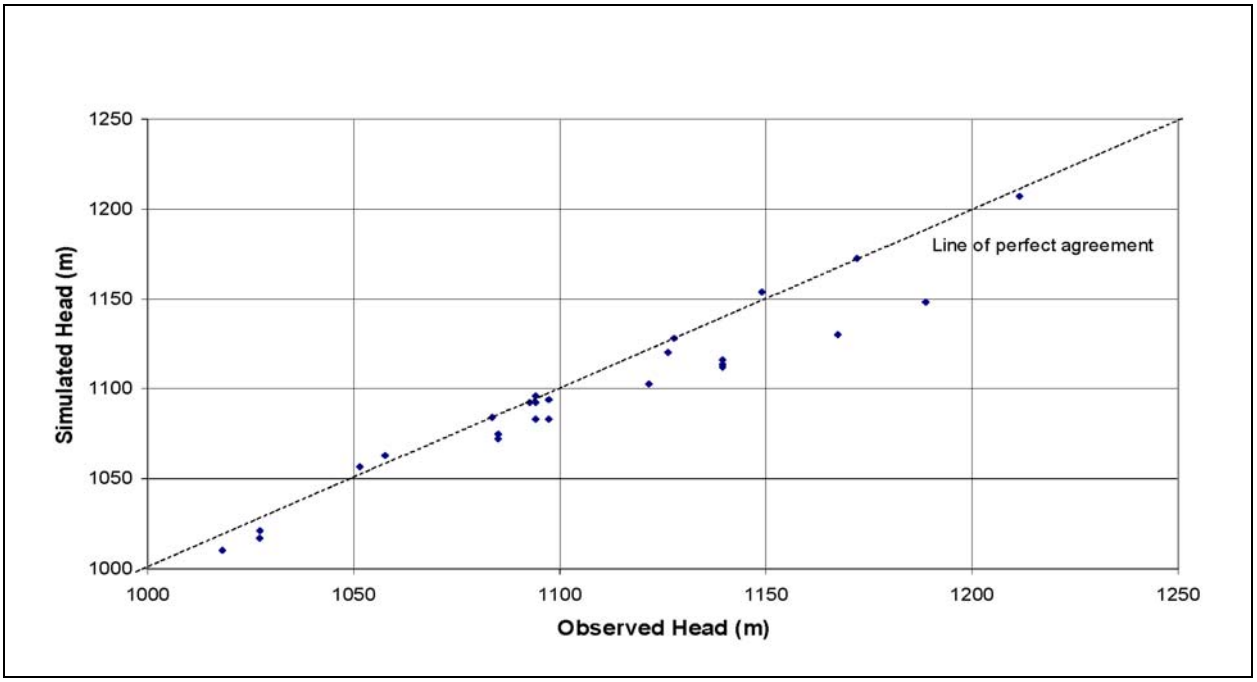

Figure 6-119
Observed Versus Simulated Spring Head for DRT-MME-SDA

Uncontrolled When Printed

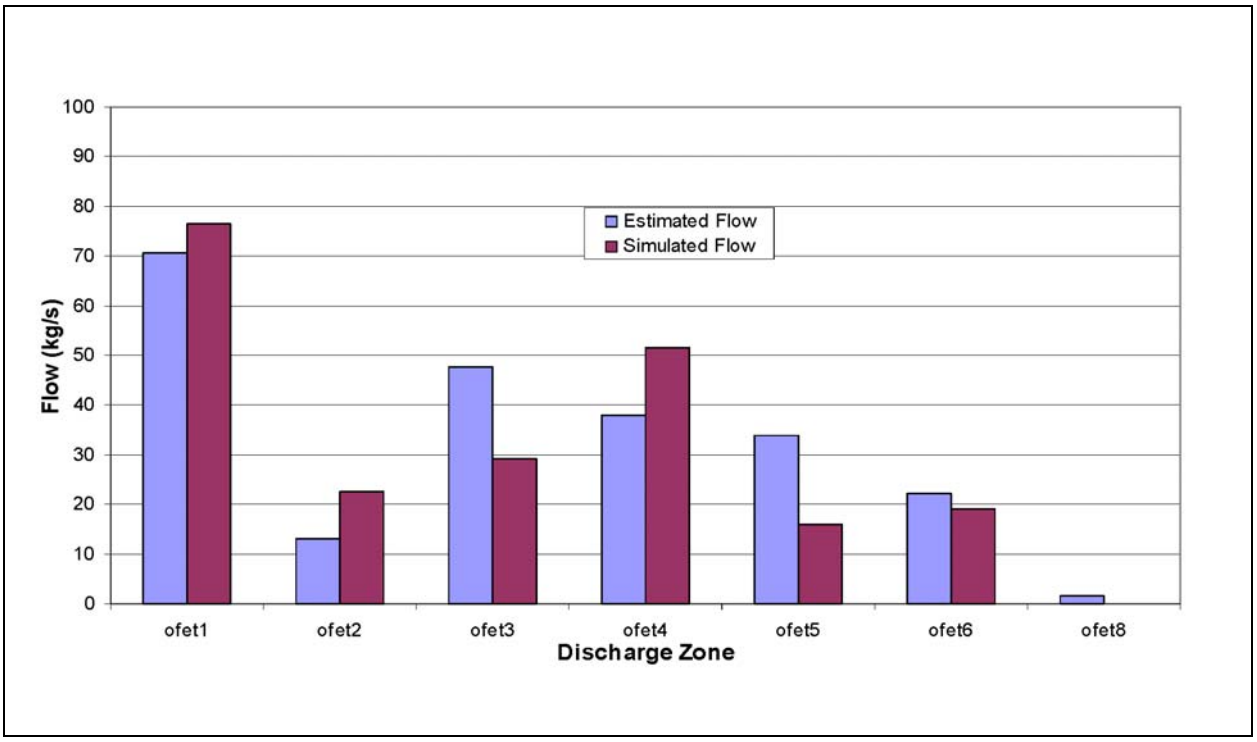

Figure 6-120
Observed and Simulated Oasis Valley Discharge for DRT-MME-SDA

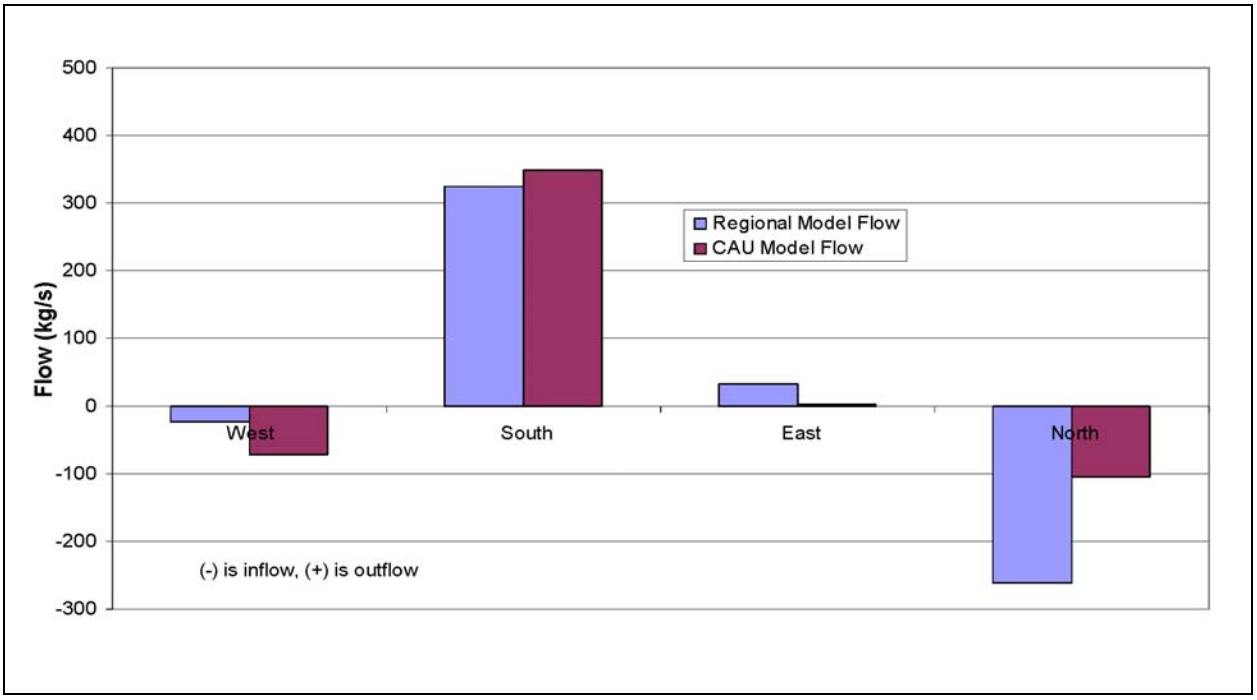

Figure 6-121
Observed and Simulated Boundary Flows for DRT-MME-SDA

Uncontrolled When Printed

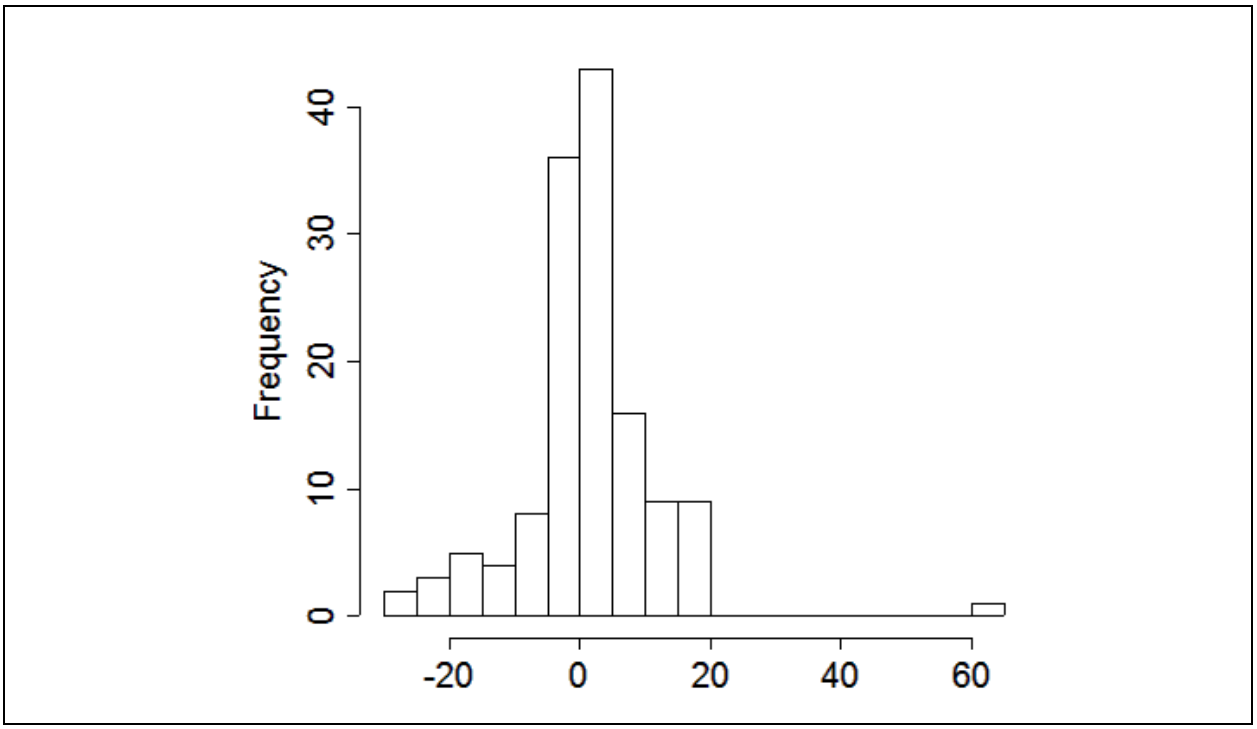

Figure 6-122
Histogram of Weighted Head Residuals for DRT-MME-SDA

scatter, showing that the general representation of the area is correct. The boundary flows, estimated from regional model analysis, all trend the correct way (e.g., have the proper sign), with the largest relative misfit on the eastern edge.

The weighted head and spring errors are shown on Figure 6-123, color coded by value and sign. The driest, or undersimulated, well was WW-8. The single wettest well was UE-20p. In general, the errors are randomly distributed, although there is a slight dry bias near WW-8 in the east-central model area, and an oversimulation bias in the north-central area (e.g., PM-2 and PM-3).

The quantitative measures of the model calibration are given by summary statistics shown in Table 6-30. The total model objective function was 26,240. Table 6-31 shows the contribution of each data type to the total model goodness of fit. Relative to other models in this section, the overall errors are clearly larger, but no worse than the SCCC HFM discussed in Section 5.7. While the model agreement with wells and boundary flow is clearly worse than the base HFM, the Oasis Valley discharge is only slightly affected. This may be because the deep-rooted thrust does not affect the units that control the flow of water into Oasis Valley.

Uncontrolled When Printed

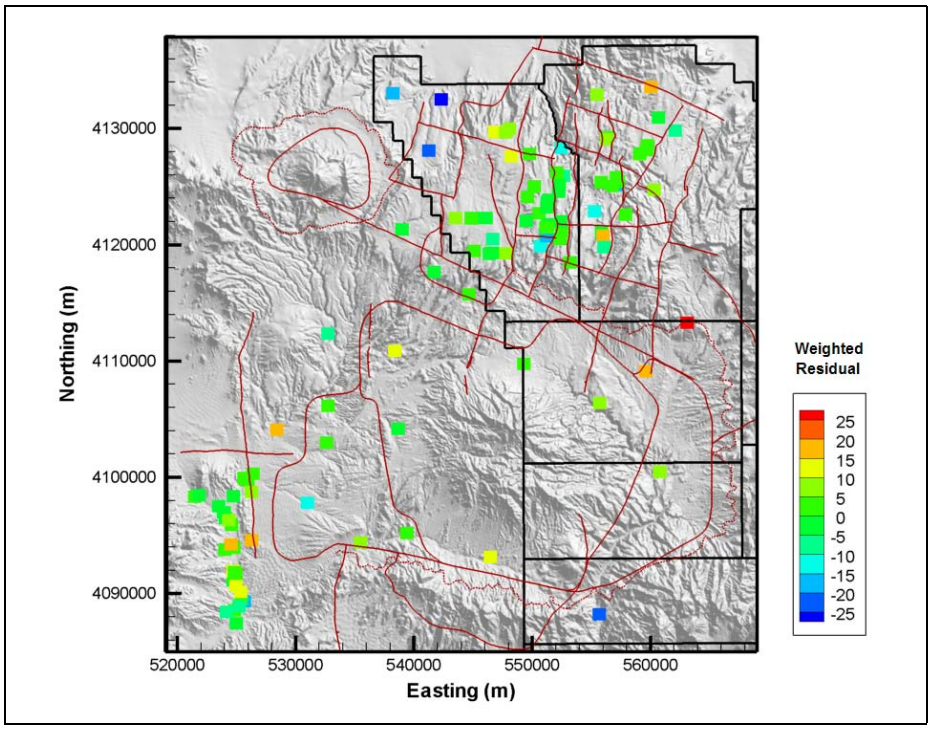

Figure 6-123
Post Plot of Weighted Well and Spring Head Residuals for DRT-MME-SDA

Table 6-30
Calibration Summary Statistics for DRT-MME-SDA

Calibration Data	Number of Data	Mean Weighted Error (m or kg/s)[a]	Maximum Weighted Residual	Minimum Weighted Residual	Error Standard Deviation (m or kg/s)
Well Head	152	0.27	61 (WW-8)	-27 (UE-20p)	9.6
Spring Head	28	2.9	19 (Torrance Spring)	-5.5 (Spring id 159)	6.8
Oasis Valley Discharge	7	3.5	37 (Zone 3)	-27 (Zone 4)	23
Boundary Flow	4	-13	24 (West)	-78 (North)	42

[a]Positive sign is simulated less than target, negative is larger.

Figure 6-124 shows the simulated water table for this model case. In the western part of Area 20, the influence of the Purse Fault is evident by the large offset in heads across it, with more subdued effects also present at West Boxcar Fault. Particle tracking (Figure 6-125) from each of the NTS wells shows the same generally noted flow paths as shown in Appendix A of the Pahute Mesa hydrologic data document (SNJV, 2004a).

Uncontrolled When Printed

Table 6-31
Contribution to Model Goodness of Fit by Data Type for DRT-MME-SDA

Data Type	Value (-)	Percent of Total
Well Head	13,886	53
Spring Head	1,301	5
Oasis Valley Discharge	3,946	15
Boundary Flow	7,106	27
Total	26,239	100

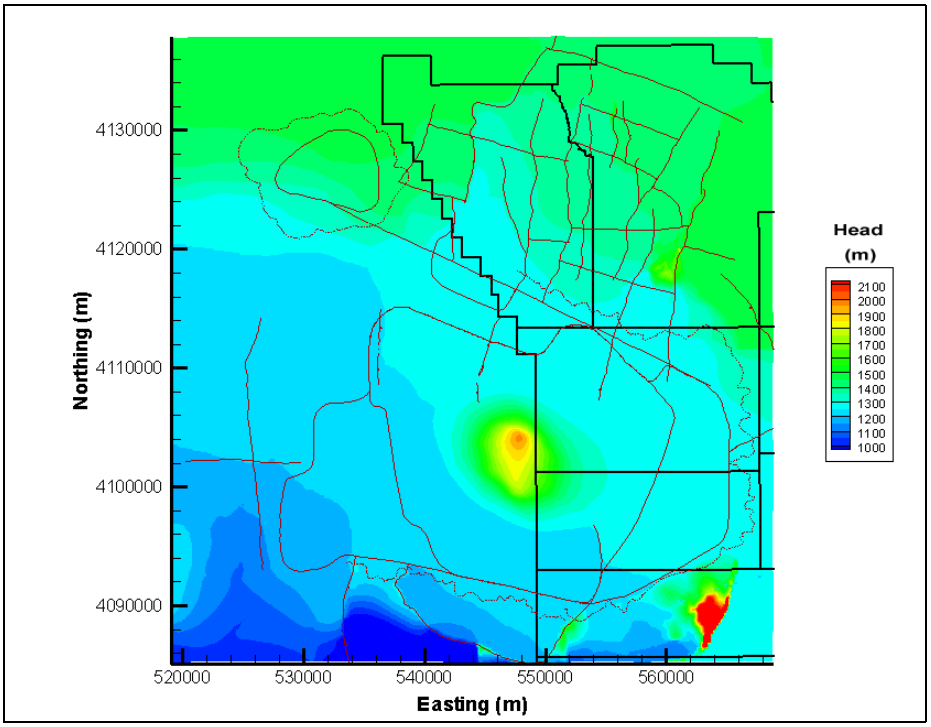

Figure 6-124
Simulated Water Table for DRT-MME-SDA

A summary of the major node HSU changes is shown in Table 6-32. The total node change count was 76,741. The changes are consistent with the propagation of the thrust westward as described by BN (2002). The properties used to parameterize this model are summarized in Section 6.3.6.

Uncontrolled When Printed

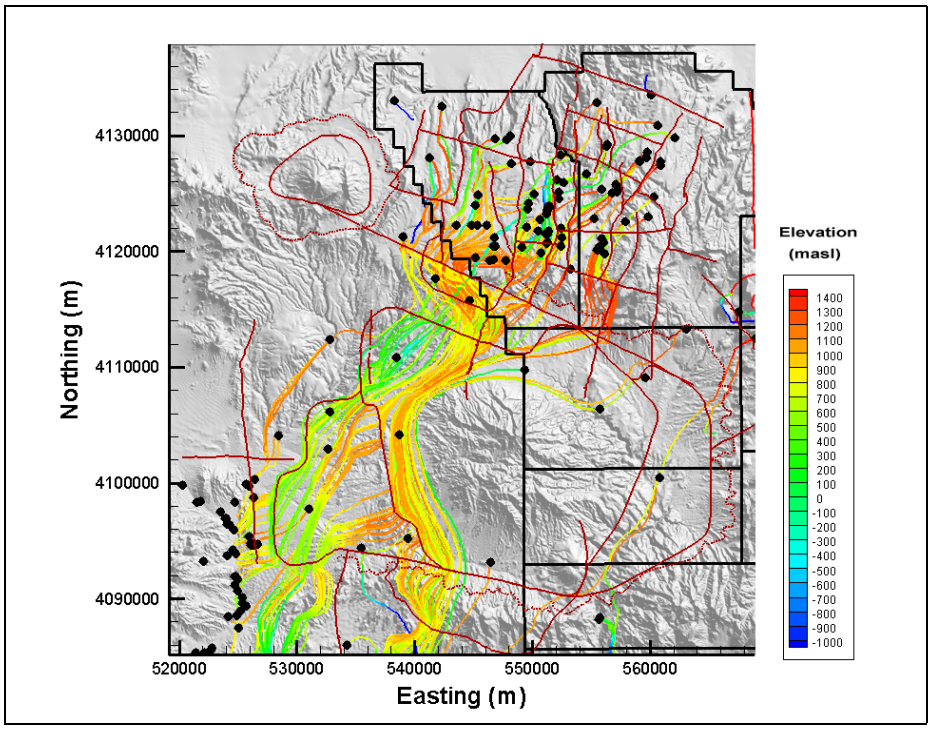

Figure 6-125
Particle Tracks for DRT-MME-SDA

Table 6-32
Selected Node Changes for DRT HFM Alternative

Base HSU	Alternative HSU	Node Count
LCA	LCA3	21,276
LCA	LCCU1	16,419
LCCU	LCCU1	10,165
UCCU	LCCU1	9,123

Uncontrolled When Printed

6.3.5 Contiguous Imbricate Thrust Sheet Alternative (SEPZ-MME-SDA)

In the eastern part of the model, an imbricate thrust fault is modeled that places LCA over UCCU. This relation is based on TW-1 and exposures east of the model area. A small surface exposure of the LCA occurs in this area that is thought to represent a small erosional remnant. This alternative explores the possibility that this feature is not a local remnant, but a continuous sheet. The expected consequence was to facilitate flow on the eastern side of Timber Mountain. See Section 6.6 in BN (2002) for more information.

Plots of observed versus simulated values for the calibration wells, springs, Oasis Valley discharge, and boundary flows are shown in Figures 6-126 through 6-129. The scatter around the line of perfect agreement is generally random in Figure 6-126, until an observed head of 1,450 m is exceeded. At the very highest observed observation well heads, the model has a tendency toward undersimulation. On Figure 6-127, the line of perfect agreement is shown, and ideally the data would plot exactly onto this line. However, at the higher observed observation spring head, the model has a tendency toward undersimulation. The plot is not significantly different than those shown in Section 5.6.2. Figure 6-129 presents a plot of observed versus simulated values for boundary flows. Figure 6-130 shows a histogram of weighted observation well residuals. The bulk of the weighted errors are less than ±10 m. The errors are not symmetrically distributed around zero, with a large proportion of oversimulated (negative sign) wells.

The Oasis Valley discharge and boundary flow components provide the water-balance constraint on the model. The total estimated Oasis Valley discharge in the CAU model domain is 227 kg/s; the simulated discharge, shown in Figure 6-128, is 210 kg/s. The total error is within one standard deviation (30 kg/s) as reported by Laczniak et al. (2001). The model trends the same as the data with some scatter, showing that the general representation of the area is correct. The boundary flows, estimated from regional model analysis, all trend the correct way (e.g., have the proper sign), with the largest relative misfit on the western edge.

The weighted head and spring errors are shown on Figure 6-131, color coded by value and sign. The two driest, or undersimulated, wells were ER-OV-06a and ER-OV-01. The single wettest well was U-19ad in northern Area 19. In general, the errors are randomly distributed, although there is a slight

Uncontrolled When Printed

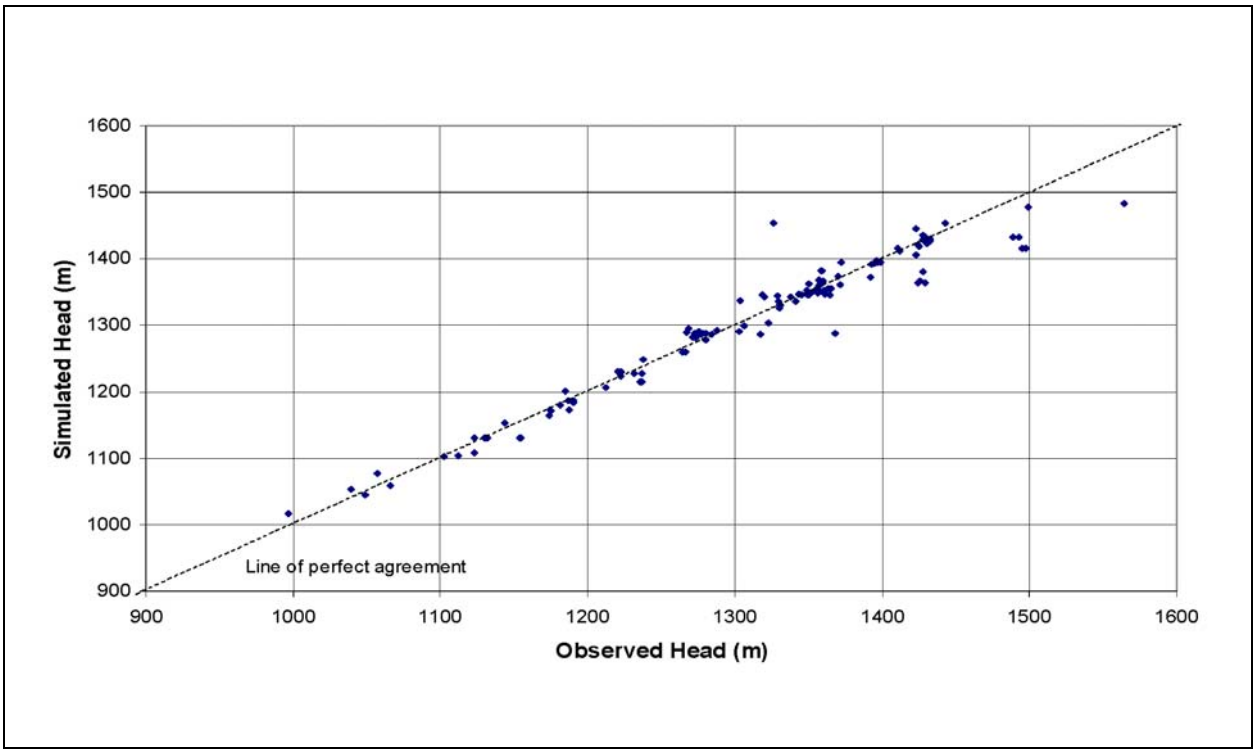

Figure 6-126
Observed Versus Simulated Observation Well Head for SEPZ-MME-SDA

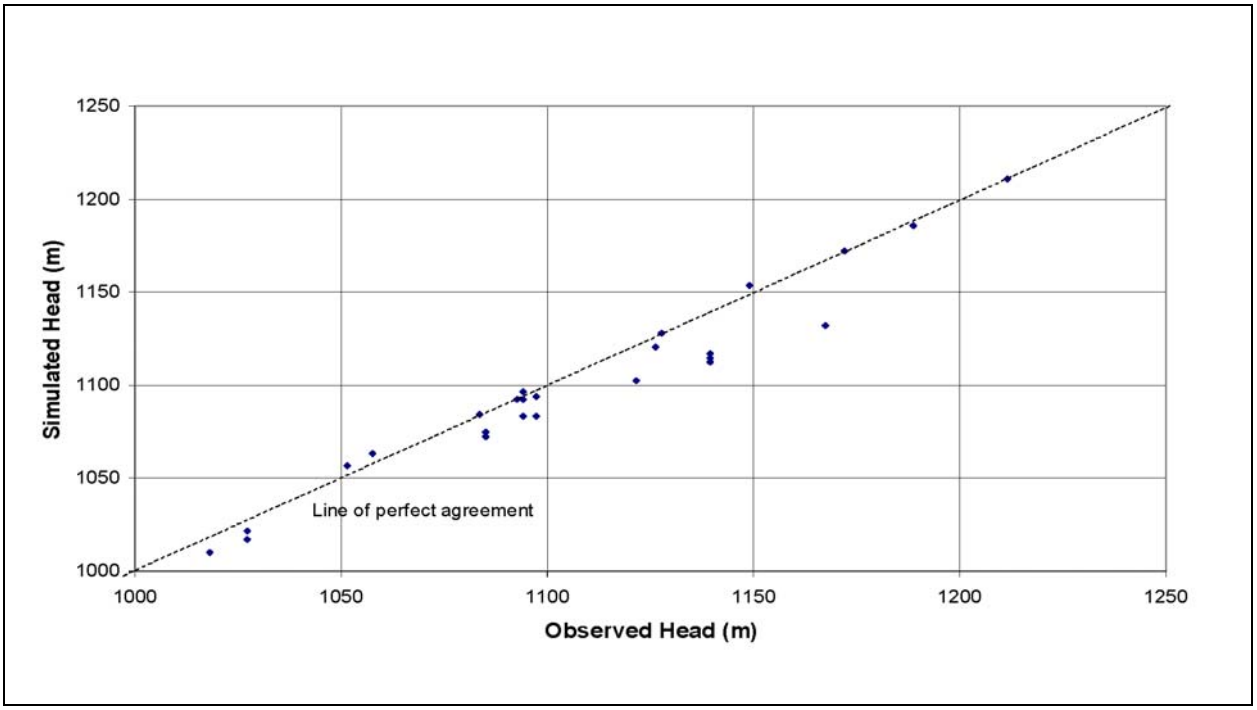

Figure 6-127
Observed Versus Simulated Spring Head for SEPZ-MME-SDA

Uncontrolled When Printed

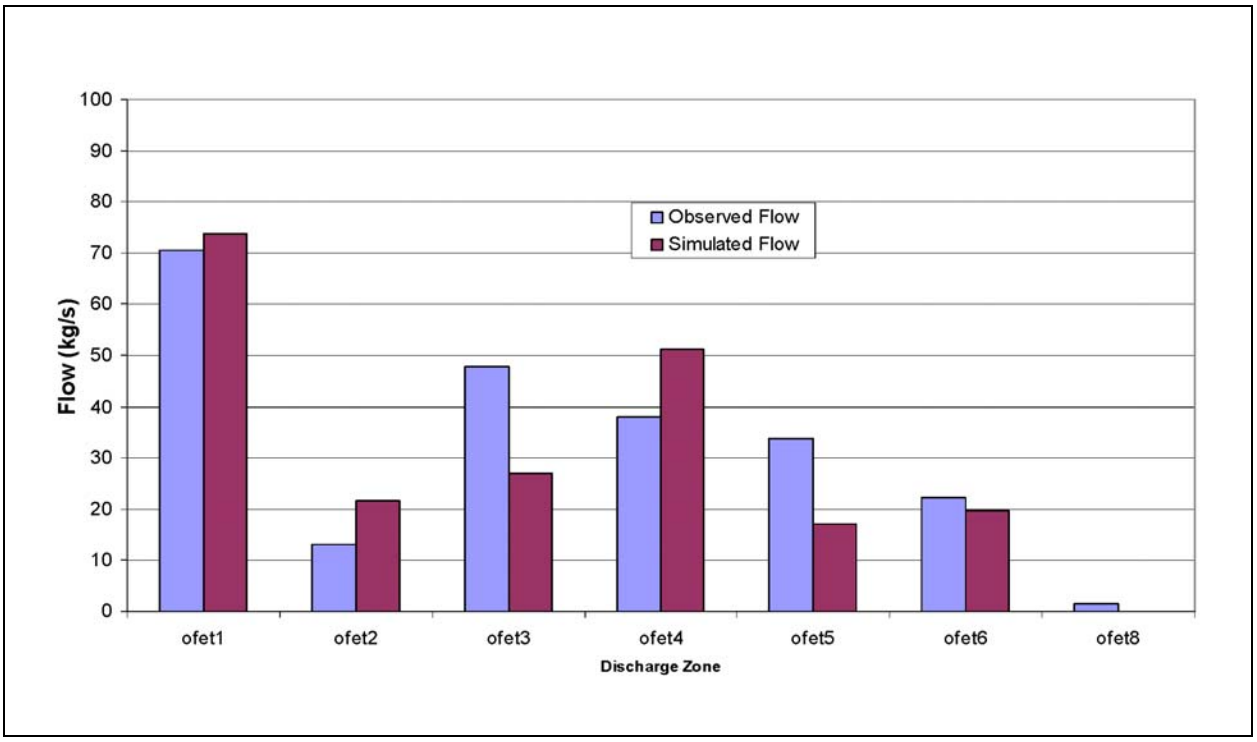

Figure 6-128
Observed and Simulated Oasis Valley Discharge for SEPZ-MME-SDA

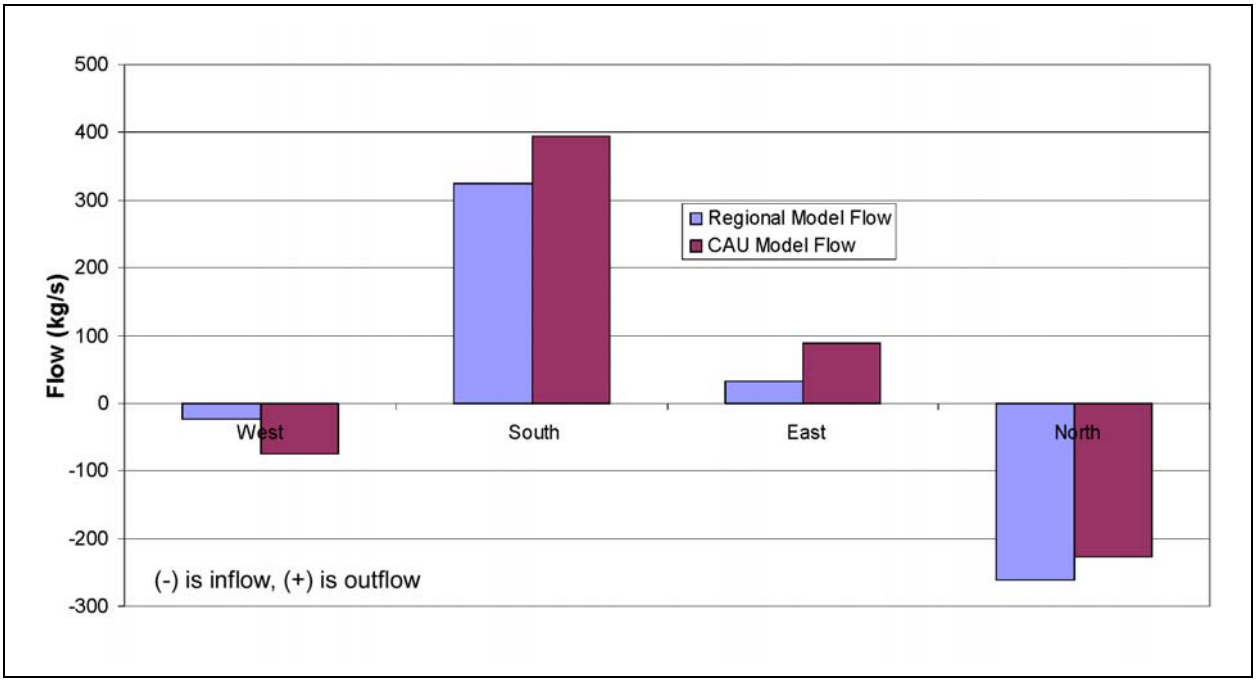

Figure 6-129
Observed and Simulated Boundary Flows for SEPZ-MME-SDA

Uncontrolled When Printed

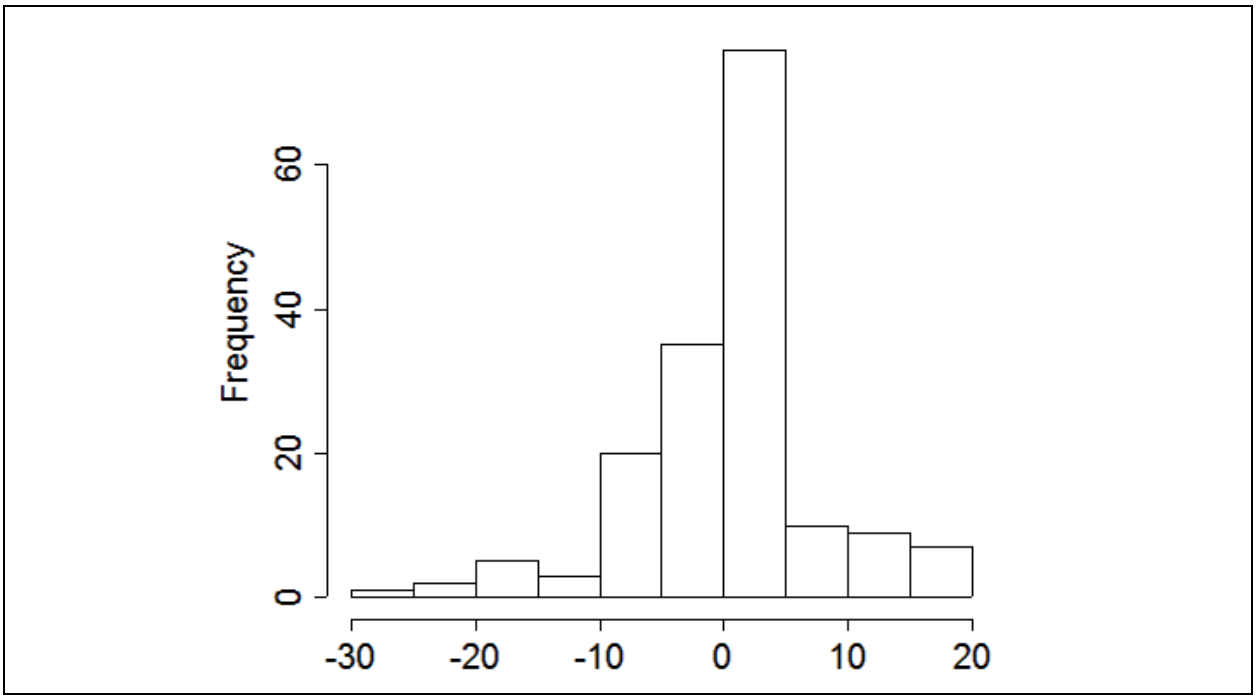

Figure 6-130
Histogram of Weighted Head Residuals for SEPZ-MME-SDA

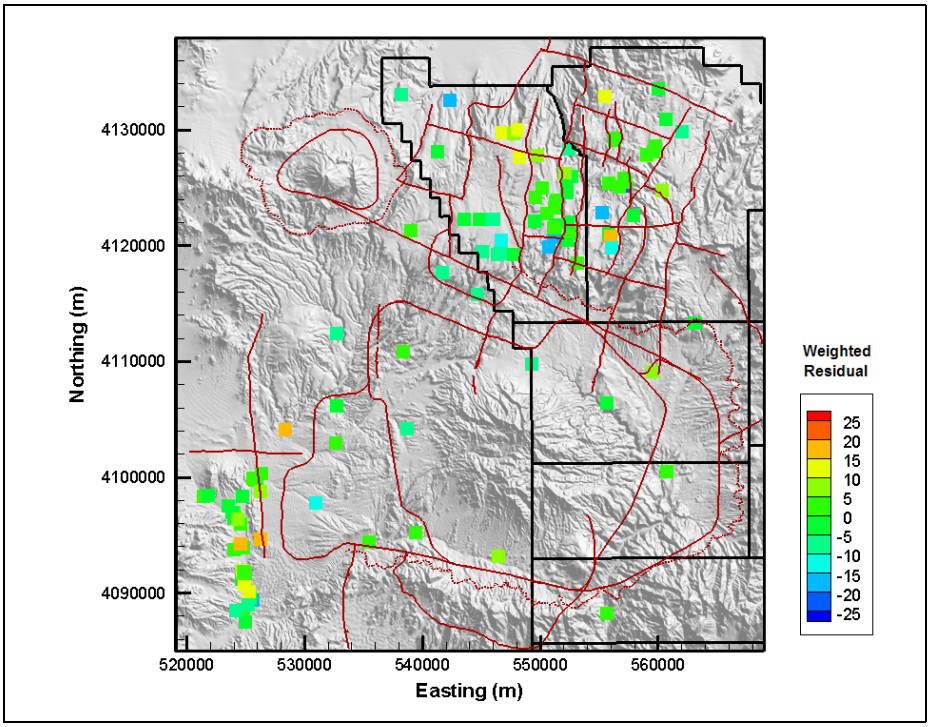

Figure 6-131
Post Plot of Weighted Well and
Spring Head Residuals for SEPZ-MME-SDA

Uncontrolled When Printed

dry bias in northern Area 20 at Easting and Northing of about 547,500 and 4,130,000 m, which includes Wells U-20i, UE-20e #1, U-20e, and U-20ar #1.

The quantitative measures of the model calibration are given by summary statistics shown in Table 6-33. These statistics are very similar to those shown in Section 5.6.2 for BN-MME-SDA. There is a slight dry bias in the spring heads, with a slight overprediction bias for the flows. The total model objective function was 16,159; slightly better than the best HFM calibration described in Section 5.6.2. Table 6-34 shows the contribution of each data type to the total model goodness of fit.

Table 6-33
Calibration Summary Statistics for SEPZ-MME-SDA

Calibration Data	Number of Data	Mean Weighted Error (m or kg/s)[a]	Maximum Weighted Residual	Minimum Weighted Residual	Error Standard Deviation (m or kg/s)
Well Head	152	-0.46	20 (U-19x)	-27 (UE-20n #1)	7.2
Spring Head	28	2.8	19 (Torrance)	-5.5 (Spring id 159)	6.8
Oasis Valley Discharge	7	4.6	41 (Zone 3)	-26 (Zone 4)	24
Boundary Flow	4	-13	26 (West)	-36 (South)	27

[a]Positive sign is simulated less than target, negative is larger.

Table 6-34
Contribution to Model Goodness of Fit by Data Type for SEPZ-MME-SDA

Data Type	Value (-)	Percent of Total
Well Head	7,979	49
Spring Head	1,284	8
Oasis Valley Discharge	3,898	24
Boundary Flow	2,999	19
Total	16,160	100

Figure 6-132 shows the simulated water table for this model case. In the western part of Area 20, the influence of the Purse Fault is still evident by the large offset in heads across it, with more subdued effects also present at West Boxcar Fault. Particle tracking (Figure 6-133) from each of the NTS wells shows the same generally noted flow paths as shown in Appendix A of the Pahute Mesa hydrologic data document (SNJV, 2004a).

Uncontrolled When Printed

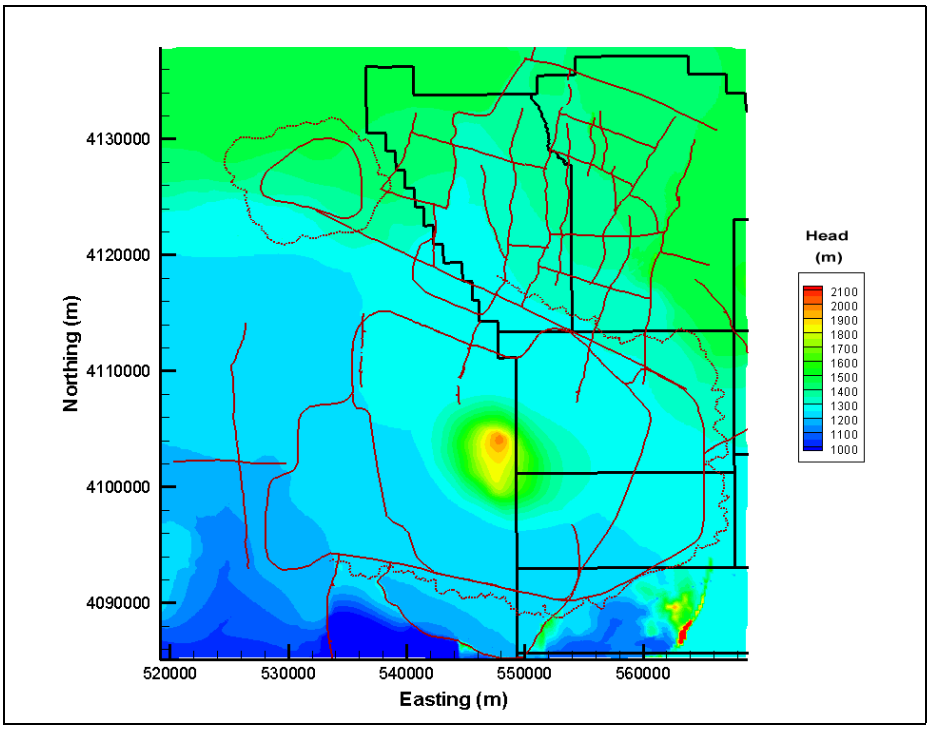

Figure 6-132
Simulated Water Table for SEPZ-MME-SDA

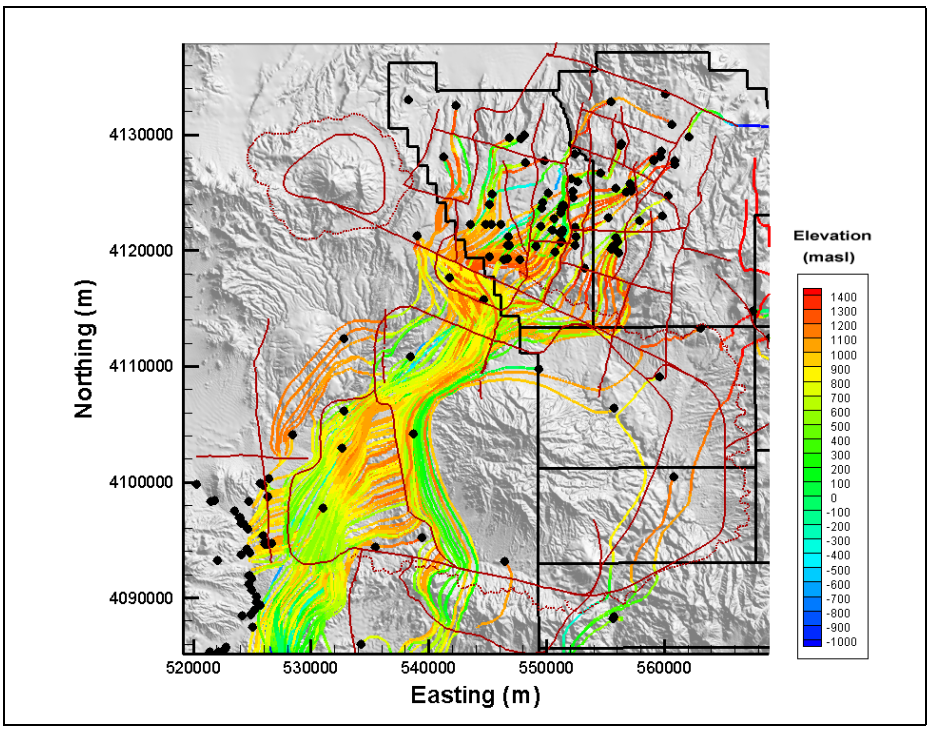

Figure 6-133
Particle Tracks for SEPZ-MME-SDA

Uncontrolled When Printed

The alternative HFM required no additional effort to recalibrate, and appears to have little impact on flow model metrics. A summary of the major node HSU changes is shown in Table 6-35. The total node change count was 8,425. The changes are consistent with increasing the continuity of the LCA in the southeast corner of the domain as described by BN (2002). The properties used to parameterize this model are summarized in Section 6.3.6.

Table 6-35
Selected Node Changes for SEPZ HFM Alternative

Base HSU	Alternative HSU	Node Count
UCCU	LCA3a	6,148
LCA	UCCU	2,277

6.3.6 HFM Uncertainty Analysis Summary

The calibrated HSU parameters for all five HFMs considered are shown in Table 6-36. In the case of TCL, RIDGE, and SEPZ alternatives, they are nearly identical to those used for the selected HSU depth-decay and anisotropy model (see Section 5.6.2) because the effects of the HSU changes required minimal parameter adjustment. However, DRT and PZUP caused dramatic changes in model output and required substantial effort to calibrate. A summary of flow model results for HFM uncertainty is presented in Table 6-37.

The estimates of HSU permeability used to guide the calibration were developed from the interpretation of hydraulic tests. As a qualitative model check, permeability from the model nodes associated with each test was extracted and arithmetically averaged in the case of a test zone with more than one associated node. These are shown in Figures 5-51 and 5-52 with the estimated values. Also shown is the mean permeability estimated for the test HSU as given by SNJV (2004a). Wells ER-EC-1, ER-EC-4, UE-19e, UE-19h, UE-20f, and UE-20h had noisy test data, and the estimated permeability should be considered to have larger uncertainty. The model calibrated permeabilities at the two observation wells from the BULLION FGE (ER-20-6 #1 and ER-20-6 #2) are about an order of magnitude and a half lower than the test values and lower than the value estimated (1.13×10^{-13} m^2) from model calibration by Wolfsberg et al. (2002) for the CHZCM, although within the range of uncertainty (at 2σ) estimated from the mean and standard deviation published by SNJV (2004a) between about 7×10^{-12} to 7×10^{-14} m^2. The permeability calibrated at UE-19h has the largest scatter among the HFMs, but the test value is fairly uncertain. There is some observed scatter that appears to be related to HFM. For instance, at ER-EC-7 the SCCC HFM has a permeability an order of magnitude and a half less than the base HFMs, which themselves are half an order of magnitude less than the estimated test value, but in good agreement with the estimated mean value. Similar results are also seen at Wells ER-EC-1 and ER-EC-6, and at ER 18-2 the SCCC HFM is actually quite a bit lower than the other data. However, no general conclusions can be drawn from the permeability comparison about the goodness of the HFMs because at Wells ER-EC-8, ER-EC-4, UE-19c, and UE-19gS the selected depth-decay and SCCC cases compare better to each other than the all depth-decay case (two different HFMs that were parameterized the same way).

All the alternative HFMs described here were parameterized with the selected HSU depth-decay and anisotropy approach (applied to the same HSUs as well) described in Section 5.6.2. They also were

Uncontrolled When Printed

Table 6-36
Calibrated HSU Parameters for All Five HFMs
(Page 1 of 3)

HSU	Notes log (k or k_0) (m^2)	BN-MME-SDA	TCL	SEPZ	RIDGE	DRT	PZUP
LCCU	k	-18	-25.00	-25.00	-25.00	-18.00	-25.00
LCA	**k_0**	**-14.20**	**-14.24**	**-14.24**	**-14.24**	**-14.24**	**-14.24**
UCCU	k	-16.78	-16.78	-16.78	-16.78	-16.78	-16.78
LCCU1	k	-12.43	-12.43	-12.43	-12.39	-15.54	-12.44
LCA3	**k_0**	**-13.38**	**-13.38**	**-13.38**	**-13.38**	**-13.38**	**-12.37**
MGCU	k	-18.38	-18.38	-18.38	-18.38	-18.38	-18.38
SCICU	k	-18.38	-18.38	-18.38	-18.38	-18.38	-18.38
CHICU	k	-18.38	-18.38	-18.38	-18.38	-18.38	-18.38
CCICU	k	-18.38	-18.38	-18.38	-18.38	-18.38	-18.38
RMICU	k	-18.38	-18.38	-18.38	-18.38	-18.38	-18.38
ATICU	k	-18.38	-18.38	-18.38	-18.38	-18.38	-18.38
BMICU	k	-18.38	-18.38	-18.38	-18.38	-18.38	-18.38
PBRCM Zone 13	**k_0**	**-11.91**	**-11.91**	**-11.91**	**-11.75**	**-13.15**	**-11.82**
BRA	**k_0**	**-11.51**	**-11.47**	**-11.47**	**-11.47**	**-11.47**	**-11.74**
BCU	k	-13.67	-13.80	-13.80	-13.80	-13.80	-13.80
KA	k	-11.78	-11.78	-11.78	-11.78	-11.78	-11.78
CFCU	k	-12.60	-12.60	-12.60	-12.60	-12.60	-12.60
CFCM	k	-15.07	-15.25	-15.25	-15.25	-15.39	-15.25
IA	k	-13.56	-13.48	-13.48	-13.48	-13.48	-13.48
CHCU	k	-14.61	-14.61	-14.61	-14.61	-14.61	-14.61
CHZCM	k	-13.49	-13.75	-13.75	-13.75	-14.22	-13.93
CHVCM	k	-13.39	-13.39	-13.39	-13.39	-13.39	-13.39
CHVTA	k	-11.81	-11.81	-11.81	-11.81	-11.81	-11.81
YMCFCM	**k_0**	**-14.54**	**-14.54**	**-14.54**	**-14.54**	**-14.54**	**-14.54**
TSA	k	-10.09	-10.26	-10.26	-10.26	-10.26	-10.26
LPCU	k	-13.04	-13.04	-13.04	-13.04	-13.04	-13.04
PLFA	k	-11.78	-11.78	-11.78	-11.78	-11.78	-11.78
TCA	k	-11.48	-11.48	-11.48	-11.48	-11.48	-11.48
UPCU	k	-15.33	-15.33	-15.33	-15.33	-15.33	-15.33
BA	k	-11.34	-11.34	-11.34	-11.34	-11.34	-11.34
PVTA	k	-12.33	-12.33	-12.33	-12.33	-12.33	-12.33
PCM	**k_0**	**-10.82**	**-10.82**	**-10.82**	**-10.88**	**-10.74**	**-11.00**

Table 6-36
Calibrated HSU Parameters for All Five HFMs
(Page 2 of 3)

HSU	Notes log (k or k_0) (m^2)	BN-MME-SDA	TCL	SEPZ	RIDGE	DRT	PZUP
LCA3a	**k_0**	**-14.03**	**-14.03**	**-14.03**	**-14.03**	**-14.03**	**-14.03**
FCCU	k	-12.98	-12.98	-12.98	-12.98	-12.98	-12.98
SCVCU	k	-16.28	-16.28	-16.28	-16.28	-16.28	-16.28
TMA	**k_0**	**-14.55**	**-14.53**	**-14.53**	**-14.53**	**-14.53**	**-14.31**
THCM	k	-12.88	-12.88	-12.88	-12.88	-12.88	-12.88
THLFA	k	-11.78	-11.78	-11.78	-11.78	-11.78	-11.78
TMCM	**k_0**	**-11.04**	**-11.04**	**-11.04**	**-11.04**	**-11.04**	**-11.04**
FCA	k	-11.50	-11.50	-11.50	-11.50	-11.50	-11.50
FCCM	k	-13.04	-13.04	-13.04	-13.04	-13.04	-13.04
DVA	k	-12.71	-12.71	-12.71	-12.85	-12.67	-12.66
DVCM	k	-13.23	-13.23	-13.23	-13.31	-13.25	-13.19
TCVA	**k_0**	**-10.65**	**-10.65**	**-10.65**	**-10.65**	**-10.65**	**-10.65**
YVCM	k	-10.08	-10.08	-10.08	-10.08	-10.08	-10.08
AA	k	-13.50	-13.50	-13.50	-13.50	-13.50	-13.50
LCA Zone 1	**k_0**	**-14.37**	**-14.37**	**-14.37**	**-14.37**	**-14.37**	**-14.37**
TCVA Zone 4	**k_0**	**-12.52**	**-10.65**	**-10.65**	**-10.65**	**-10.65**	**-10.65**
TCVA Zone 6	**k_0**	**-12.18**	**-12.52**	**-12.52**	**-12.52**	**-12.52**	**-12.03**
TMA Zone 4	**k_0**	**-10.42**	**-14.59**	**-14.59**	**-14.59**	**-14.59**	**-16.75**
TMA Zone 6	**k_0**	**-8.84**	**-12.18**	**-12.18**	**-12.18**	**-12.18**	**-12.33**
PBRCM Zone 80	**k_0**	**-11.30**	**-10.42**	**-10.42**	**-10.42**	**-10.42**	**-10.42**
PBRCM Zone 81	**k_0**	**-14**	**-8.84**	**-8.84**	**-8.84**	**-8.84**	**-8.84**
PBRCM Zone 82	**k_0**	**-11.49**	**-11.30**	**-11.30**	**-11.30**	**-11.30**	**-11.30**
PBRCM Zone 83	**k_0**	**-10.452**	**-13.10**	**-13.10**	**-13.10**	**-13.10**	**-13.10**
PBRCM Zone 84	**k_0**	**-11.26**	**-11.49**	**-11.49**	**-12.39**	**-11.07**	**-11.49**
PBRCM Zone 87	**k_0**	**-10.05**	**-10.45**	**-10.45**	**-10.45**	**-10.45**	**-8.58**
TMCM-ERM	**k_0**	**-11.05**	**-11.26**	**-11.26**	**-11.26**	**-11.26**	**-11.26**
TMCM-ATCW	**k_0**	**-11.94**	**-10.05**	**-10.05**	**-10.05**	**-10.05**	**-10.08**
TMCM-ATCE	**k_0**	**-10.76**	**-11.05**	**-11.05**	**-11.05**	**-11.05**	**-11.05**
TMCM-THS	**k_0**	**-12.5**	**-11.94**	**-11.94**	**-11.94**	**-11.94**	**-11.54**
TMCM-OV	**k_0**	**-9.40**	**-10.76**	**-10.76**	**-10.76**	**-10.76**	**-10.86**
TMCM-TMD	**k_0**	**-10.19**	**-12.50**	**-12.50**	**-12.50**	**-12.50**	**-12.00**
TMCM-NTMW	**k_0**	**-15.95**	**-9.40**	**-9.40**	**-9.40**	**-9.40**	**-9.42**

Uncontrolled When Printed

Table 6-36
Calibrated HSU Parameters for All Five HFMs
(Page 3 of 3)

HSU	Notes log (k or k_0) (m^2)	BN-MME-SDA	TCL	SEPZ	RIDGE	DRT	PZUP
TMCM-NTME	**k_0**	**-14.09**	**-10.19**	**-10.19**	**-10.19**	**-10.19**	**-9.95**
LPCU West of Purse Fault	k	**-10.80**	-15.95	-15.95	-15.95	-15.95	-15.95
UPCU West of Purse Fault	k	--	-14.09	-14.09	-14.09	-14.09	-14.09
BRA West of Purse Fault	k_0	--	-10.80	-10.80	-10.80	-10.80	-10.80

k = Permeability
k_0 = Reference permeability
See Table 4-1 for HSU descriptions.

Table 6-37
Summary of Flow Model Results for HFM Uncertainty Analysis

HFM	Water-Balance Condition	Calibration Observations Base HFM	Qualitative Flow Path Assessment Base HFM
TCL	MME	Almost identical calibration to BN. Required no additional effort to calibrate.	Particles go deeper near ER-EC-1 and ER-EC-6. Stronger tendency to go to Oasis Valley.
RIDGE	MME	Slightly poorer calibration than BN. Required no additional effort to recalibrate. Simulated low Oasis Valley discharge.	Particles exit Area 20 further west with a more even distribution than the base. Stronger tendency to go to Oasis Valley.
DRT	MME	Noticeably poorer calibration. Required substantial effort to recalibrate.	Fewer tracks go west into northern Oasis Valley. Tendency to exit at Easting 540,000 m.
PZUP	MME	Noticeably poorer calibration. Required substantial effort to recalibrate.	More particles go further west to exit at north Oasis Valley.
SEPZ	MME	Better calibration than base. Required no additional effort to recalibrate.	Very similar to base.

calibrated with the MME recharge map. Thus, a summary understanding can be developed of the relative HFM performance by considering the goodness of the respective calibrations. Figure 6-134 shows the objective function of each alternative HFM normalized by the results presented in Section 5.6.2. One alternative HFM (SEPZ) actually performed slightly better than the base HFM, with all of the improvement coming from a better agreement to the observation well data. The TCL alternative was nearly identical to the base HFM. The RIDGE case was mildly worse than the base HFM, primarily from increased misfit with the wells, although Oasis Valley flow was also noticeably

Uncontrolled When Printed

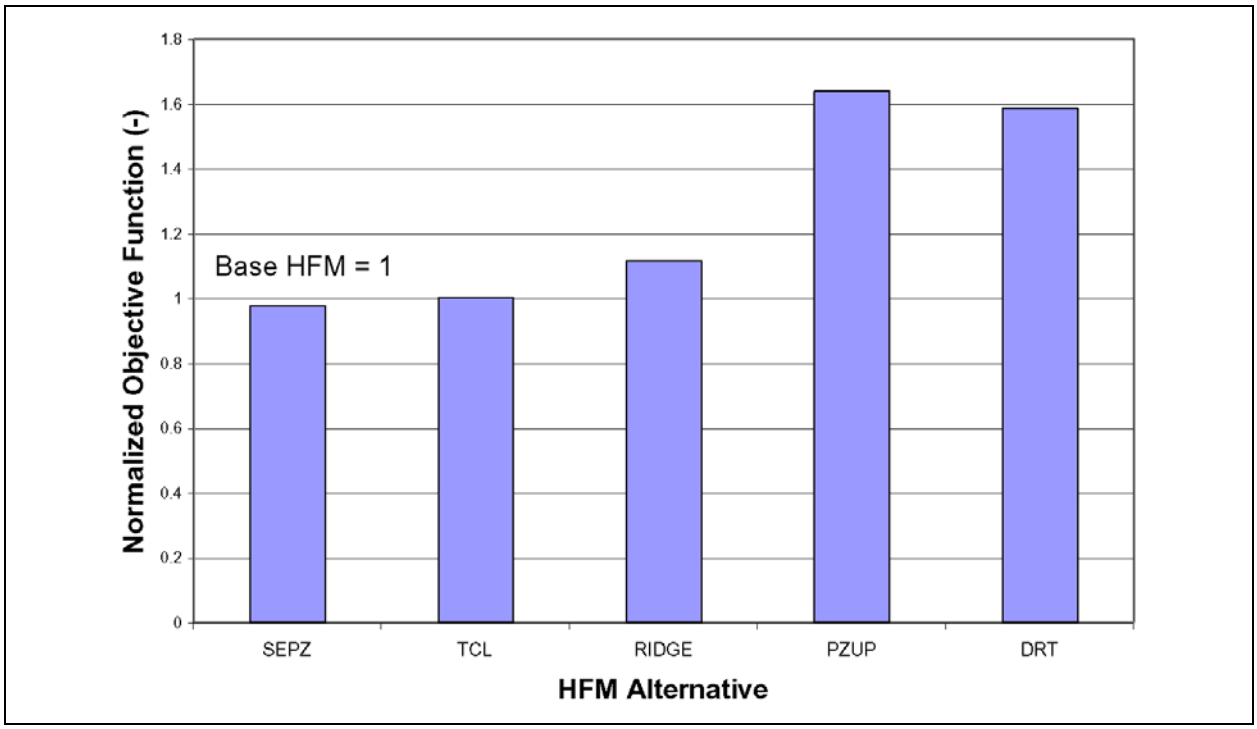

Figure 6-134
Normalized Objective Function of Alternative HFMs

undersimulated. The RIDGE case truncated the extent of VAs (BA, TCA, TSA) in southern Area 20 with older, lower permeability units. This results in more scatter in the model agreement with the observation well data, as shown by the increased error standard deviation in Table 6-24. Note that the mean error in Table 6-24 is improved over the base HFM, which if taken without the context of the error standard deviation would lead to the erroneous conclusion that the RIDGE-MME model was the better calibrated of the two models. The PZUP and DRT alternatives give far and away the most different results in comparison to the base HFM calibration, which relative to the degree of HFM changes is reasonable. The DRT alternative has significant misfit on the boundary flows because the large section of LCCU1 extending westward and northward into the model greatly reduces transmissivity along the northern boundary.

Relative to the prediction of radionuclide migration (the ultimate goal of the project), it is the differences in flow paths that is relevant. The SEPZ alternative, for instance, is so like the base HFM in all regards that it does not appear to provide any estimate of uncertainty useful to radionuclide migration. The PZUP alternative, however, has more particles exiting in the northern part of Oasis Valley, which is an issue of concern. The TCL and RIDGE alternatives have a tendency for more

Uncontrolled When Printed

particles to discharge in Oasis Valley, also a qualitative concern. Particle paths in the DRT alternative focus more along the western flank of Timber Mountain, a result that may be important to the ultimate delineation of the contaminant boundary, but is not readily identifiable as a risk to the biosphere.

6.4 Water-Balance Uncertainty Analysis

The Pahute Mesa CAIP (DOE/NV, 1999) states that boundary condition uncertainty must be considered in the flow model analysis, and that the two sources of boundary condition uncertainty are the recharge distribution and the model boundary flow derived from the regional model. These two factors control the water balance of the CAU-scale model, which in turns has a direct bearing on the overall flow rate, and hence groundwater velocity, through the model domain. This section briefly reviews the approach used to address water-balance uncertainty, and presents results for the base HFM and the SCCC HFM alternative.

6.4.1 Recharge Uncertainty

In arid systems with deep groundwater it is generally acknowledged that accurate estimation of recharge is difficult. There are some water-balance constraints for the entire regional flow system (e.g., discharge at Ash Meadows, Oasis Valley, Death Valley) but there is no perennial surface water flow in the Oasis Valley area that could be used to directly balance local inflow and outflow as is possible in other areas of the country.

In order to bound the possible recharge volumes, three recharge models were used. They are the chloride mass-balance approach of Russell and Minor (2002) (referred to as the DRI model hereafter), the MME empirical method (referred to as the MME hereafter) presented in the UGTA regional model (DOE/NV, 1997, IT, 1996a through f; IT, 1997a and b), and the distributed parameter watershed (referred to as the USGS hereafter) model of Hevesi et al. (2003). The chloride mass-balance recharge estimate was further subdivided to remove recharge in the alluvium (DRIA) and in the alluvium and below an elevation of 1,237 m (DRIAE). The distributed parameter watershed model had versions with (USGSD) and without runoff (USGSND) and run-on. The areal distribution and mass flows associated with these recharge models are shown in Section 4.3 and Table 4-5.

The base and SCCC HFMs were previously calibrated with the MME recharge model (see Sections 5.6 and 5.7). The DRI and USGS recharge models were then applied and the models recalibrated.

6.4.2 Lateral-Flow Uncertainty

The Pahute Mesa CAU flow model domain cannot be considered independently of the regional groundwater flow system. The inflow and outflows along the model edges are estimated from the regional model, but some uncertainty exists in these flows because they cannot be observed directly, and there are only large-scale constraints on the flow system.

In order to address the lateral-flow component of uncertainty, different combinations of recharge model and boundary flow are considered. It is possible to combine recharge models with boundary flows derived from using other recharge models in the regional model. For instance, the DRI recharge model could be used in conjunction with the boundary flows estimated using the USGS recharge model. However, the appropriateness of such combinations is difficult to interpret. The approach taken was to use a given recharge model with the regional model boundary flows derived from the same recharge model in the regional model. These combinations can be more readily interpreted to bound water-balance uncertainty as follows:

- The DRI recharge model has the highest mass flow and results in the highest CAU model boundary flows. Using these two datasets together results in a flow system with higher flow (and hence velocity) than the MME and USGS recharge models.
- The USGS model tends toward the lower range of recharge estimates. The overall flow of water through the system tends to be less than the MME or DRI models.

The base and SCCC HFMs were calibrated with the MME recharge model derived boundary flows in Sections 5.6 and 5.7, respectively; hence, this part of the analysis has already been completed. For the water-balance uncertainty analysis, the recharge model was changed, and then the flow model was recalibrated with the boundary flows that correspond to the same recharge model and regional model boundary flow.

Uncontrolled When Printed

6.4.3 Base Geologic Model Water-Balance Uncertainty Analysis

The base HFM with the selected HSU depth decay and anisotropy (BN-SDA) parameterization as described in Section 5.6.2 was used as the basis for analyzing water-balance uncertainty. Four combinations of recharge model and boundary flows are considered as follows:

1. DRIA recharge and boundary flow
2. DRIAE recharge and boundary flow
3. USGSD recharge and USGSND boundary flow (boundary flows with the USGSD recharge model were not calculated from the UGTA regional model)
4. USGSND recharge and USGSND boundary flow

In addition, the LCCU1 variation described in Section 6.2.4.2 is also investigated.

6.4.3.1 DRI Recharge Model

The base HFM - selected HSU depth-decay and anisotropy was calibrated with the DRIA and DRIAE recharge and boundary flows. Tables 6-38 and 6-39 summarize the calibration statistics for DRIAE and DRIA, respectively. The objective function is nearly the same, 21,407 versus 20,716. The results shown in Tables 6-38 and 6-39 are very similar, and only the DRIA recharge model will be carried for further analyses because it tends to spread recharge around the domain to a greater extent and the elevation screen only affects lower elevations.

Table 6-38
Calibration Summary Statistics for BN-DRIAE-SDA

Calibration Data	Number of Data	Mean Weighted Error (m or kg/s)	Maximum Weighted Residual	Minimum Weighted Residual	Error Standard Deviation (m or kg/s)
Well Head	152	-1.8	20 (ER-OV-03a)	-32 (UE-20n #1 1,005.84 m)	8.1
Spring Head	28	3.1	19 (Torrance Spring)	-5.4 (Spring id 159)	6.9
Oasis Valley Discharge	7	2.0	41 (Zone 3)	-18 (Zone 4)	21
Boundary Flow	4	-24	23 (West)	-60 (North)	42

[a]Positive sign is simulated less than target, negative is larger.

Uncontrolled When Printed

Table 6-39
Calibration Summary Statistics for BN-DRIA-SDA

Calibration Data	Number of Data	Mean Weighted Error (m or kg/s)[a]	Maximum Weighted Residual	Minimum Weighted Residual	Error Standard Deviation (m or kg/s)
Well Head	152	-1.5	20 (ER-OV-03a)	-31 (UE-20n #1 1,005.84 m)	7.9
Spring Head	28	3.1	19 (Torrance Spring)	-5.3 (Ute Springs Culvert)	6.9
Oasis Valley Discharge	7	3.1	42 (Zone 3)	-18 (Zone 4)	21
Boundary Flow	4	-23	23 (West)	-58 (North)	41

[a]Positive sign is simulated less than target, negative is larger.

Figure 6-135 shows the posted weighted residuals; there is a perceptible bias to oversimulate heads that is also suggested by the mean error. Simulated Oasis Valley discharge is 219 kg/s (versus an estimated discharge of 227 kg/s). Figure 6-136 shows the simulated water table, and Figure 6-137 shows the simulated flow paths from NTS wells. The water table and flow paths have the same general character seen in all the simulations, but there is an intensified flow path out to the south at Easting of about 540,000 m. The DVCM, PCM, BRA, and YMCFCM permeabilities (including k_0) all increased between a quarter and half an order of magnitude over the values used to calibrate the MME recharge in order to bleed off the additional recharge (nearly double that of the MME) imposed by the DRIA recharge model. This increase in permeability causes the increased flow across the southern boundary through the PCM and YMCFCM that is seen in the simulated flow paths.

The reduced LCCU1 permeability alternative variation of the model (Section 6.2.4.2) was also investigated with the DRIA recharge map. Table 6-40 shows the summary calibration statistics; the objective function is 27,712.

Figure 6-138 shows the posted weighted residuals; the error appears random with a slight oversimulation bias. Simulated Oasis Valley discharge is 216 versus 227 kg/s estimated. Figure 6-139 shows the simulated water table, and Figure 6-140 shows the simulated flow paths from NTS wells.

Uncontrolled When Printed

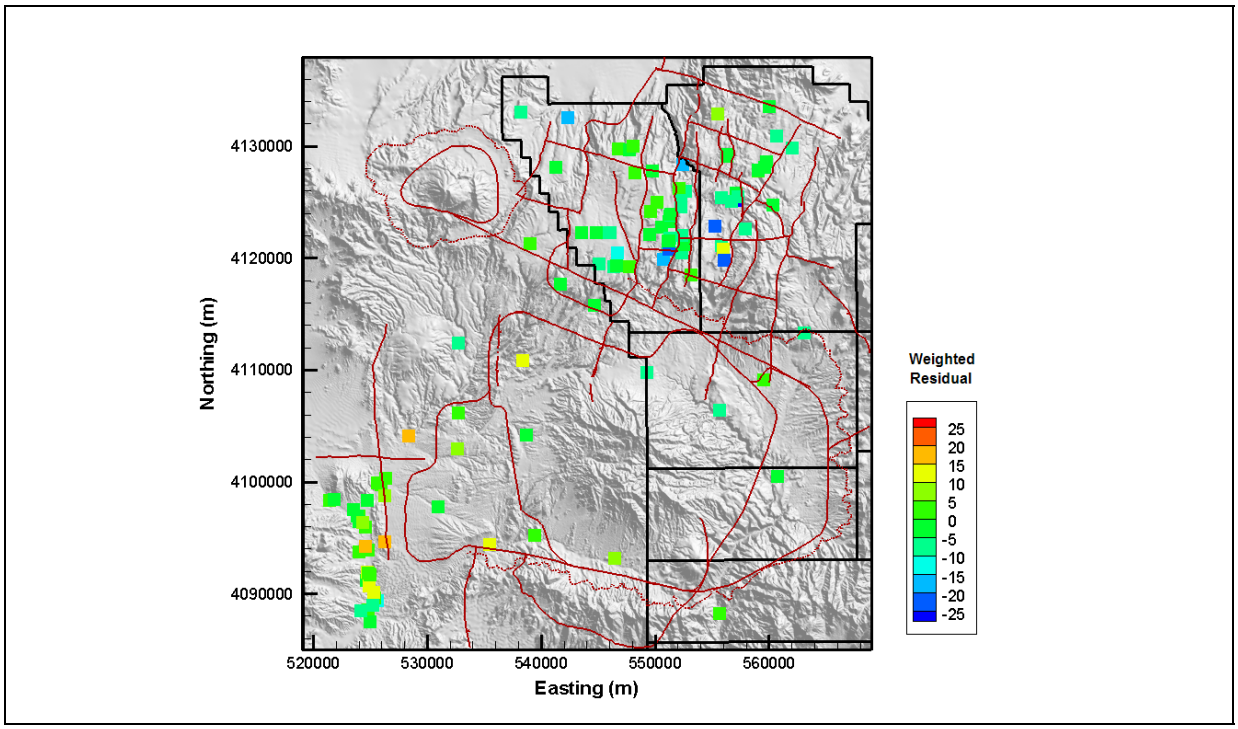

Figure 6-135
Posted Weighted Residuals for BN-DRIA-SDA

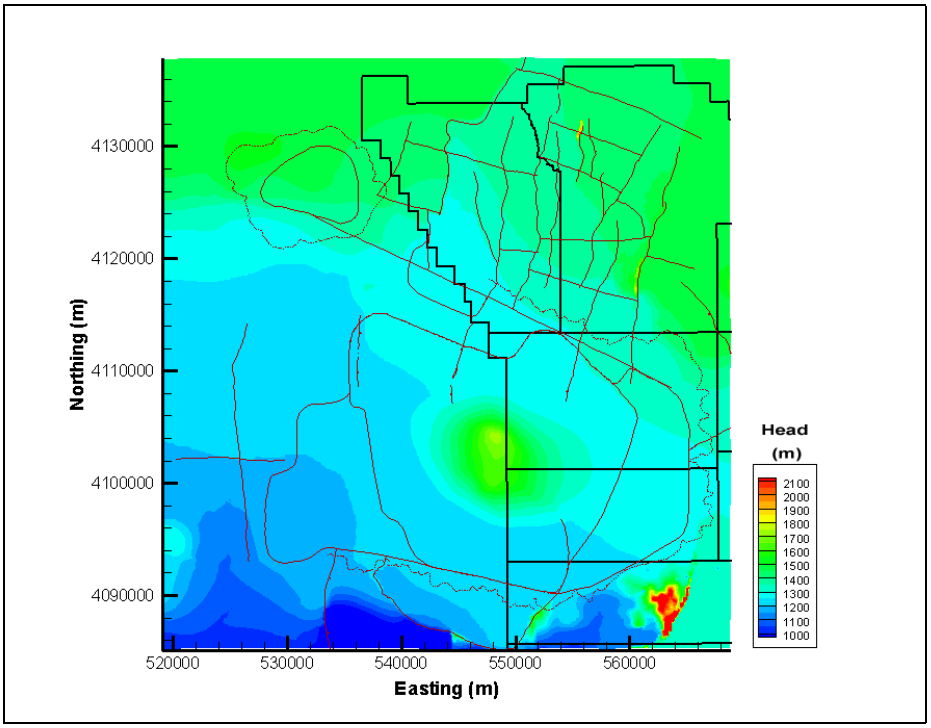

Figure 6-136
Simulated Water Table for BN-DRIA-SDA

Uncontrolled When Printed

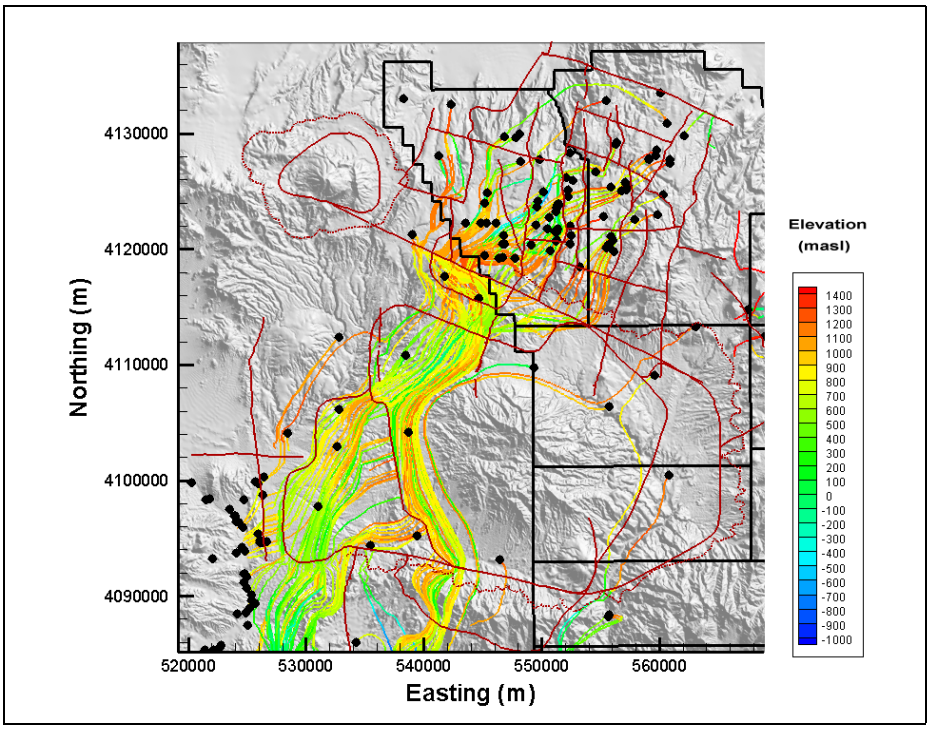

Figure 6-137
Particle Tracks for BN-DRIA-SDA

Table 6-40
Calibration Summary Statistics for BN-DRIA-SDA Reduced LCCU1 Permeability Alternative

Calibration Data	Number of Data	Mean Weighted Error (m or kg/s)[a]	Maximum Weighted Residual	Minimum Weighted Residual	Error Standard Deviation (m or kg/s)
Well Head	152	1.4	76 (WW-8)	-24 (UE-20n #1 1,005.84 m)	9.6
Spring Head	28	3.1	19 (Torrance Spring)	-6.0 (Spring id 159)	6.9
Oasis Valley Discharge	7	2.9	41 (Zone 3)	-19 (Zone 4)	20
Boundary Flow	4	-23	22 (East)	-70 (South)	49

[a]Positive sign is simulated less than target, negative is larger.

Uncontrolled When Printed

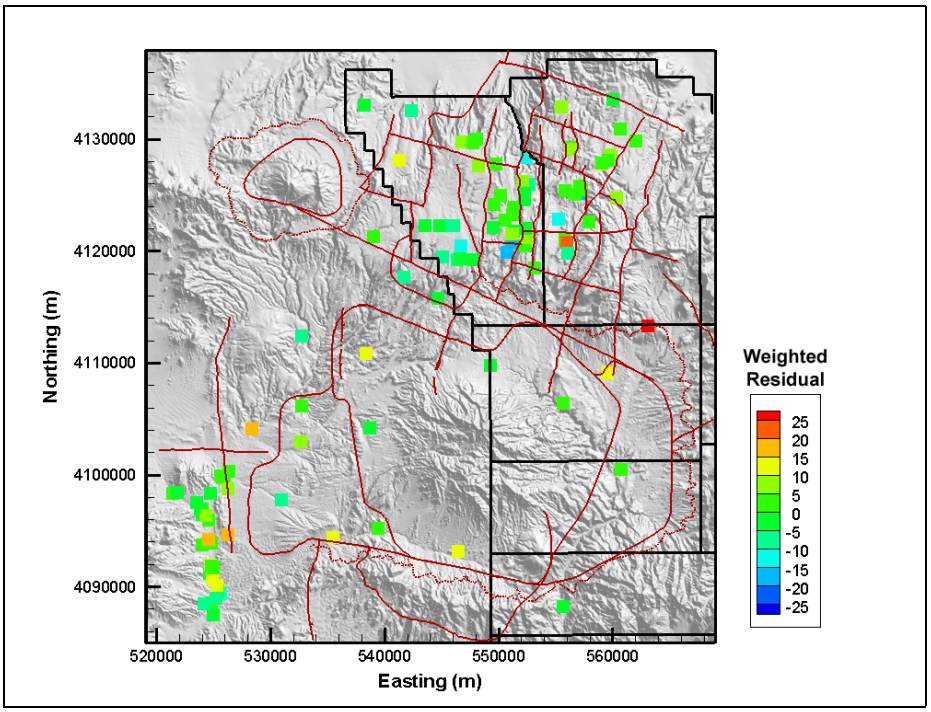

Figure 6-138
Post Plot of Weighted Well and Spring Head Residuals for BN-DRIA-SDA Reduced LCCU1 Permeability Alternative

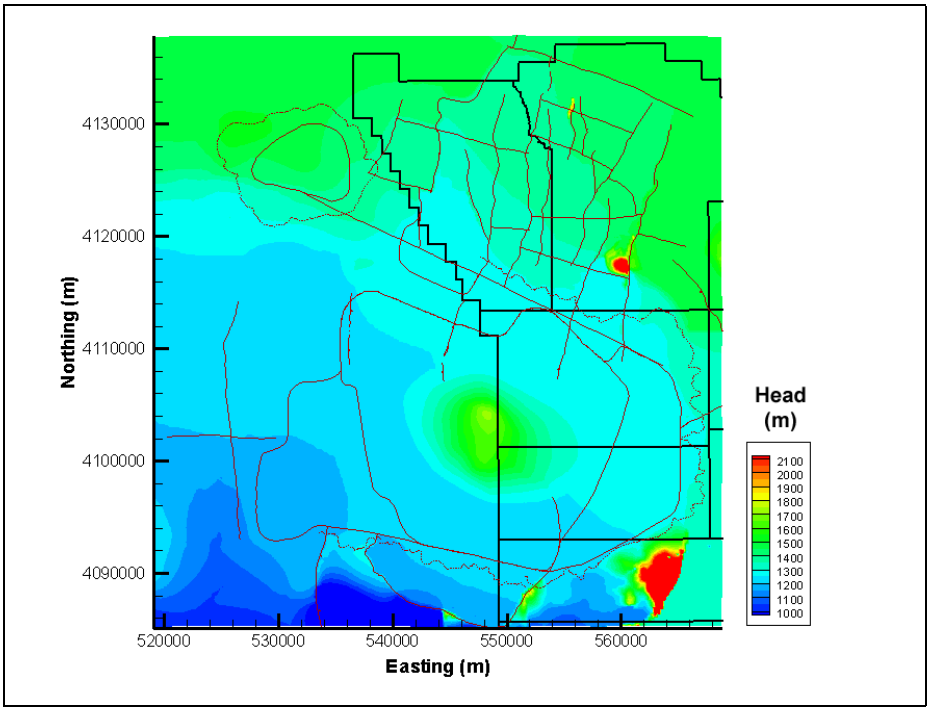

Figure 6-139
Simulated Water Table for BN-DRIA-SDA Reduced LCCU1 Permeability Alternative

Uncontrolled When Printed

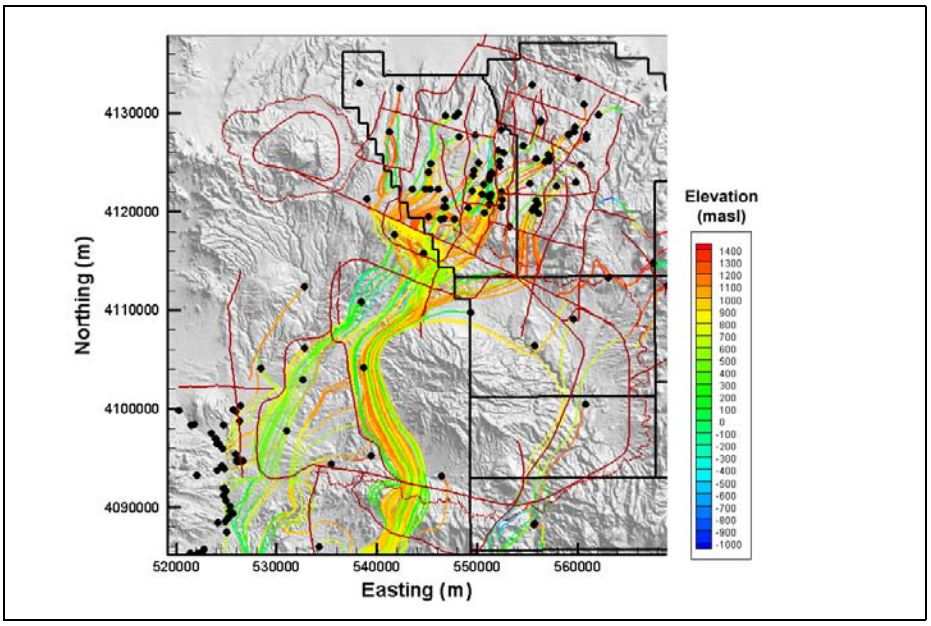

Figure 6-140
Particle Tracks for BN-DRIA-SDA Reduced LCCU1 Permeability Alternative

The clear change between the base calibrated HFM and lower reduced LCCU1 permeability alternative for both the MME and DRI recharge models is the poor matching of WW-8. It does seem not conceptually reasonable that the LCCU1 should support the hydraulic head in this area via its connection to the higher boundary heads, but again, there is no information as to the properties of the LCCU1.

6.4.3.2 USGS Recharge Model

The summary calibration statistics for the base HFM with the USGSND and USGSD recharge models are shown in Tables 6-41 and 6-42. The objective functions are 11,615 and 14,054, respectively. The USGSND model has the lowest recharge volume of all the alternatives and the best objective function. In general, the USGS recharge models calibrate far better than the MME and DRI recharge models. This is because the lower recharge results in fewer local changes in head from recharge accretion. The USGSND recharge model calibrates better than the USGSD model for similar reasons. However, conceptually it does not seem reasonable to neglect the basic watershed processes of runoff and run-on in estimating recharge; thus, the USGSND recharge model is not considered further. Furthermore, goodness of calibration is not the sole metric on which models should be judged.

Uncontrolled When Printed

Table 6-41
Calibration Summary Statistics for BN-USGSND-SDA

Calibration Data	Number of Data	Mean Weighted Error (m or kg/s)[a]	Maximum Weighted Residual	Minimum Weighted Residual	Error Standard Deviation (m or kg/s)
Well Head	152	0.42	19 (ER-OV-03a)	-24 (UE-20n #1 1,005.84 m)	6.2
Spring Head	28	2.8	19 (Torrance Spring)	-5.3 (Ute Springs Culvert)	6.7
Oasis Valley Discharge	7	7.9	43 (Zone 3)	-19 (Zone 4)	23
Boundary Flow	4	5.2	26 (West)	-5.8 (South)	14

[a]Positive sign is simulated less than target, negative is larger.

Table 6-42
Calibration Summary Statistics for BN-USGSD-SDA

Calibration Data	Number of Data	Mean Weighted Error (m or kg/s)[a]	Maximum Weighted Residual	Minimum Weighted Residual	Error Standard Deviation (m or kg/s)
Well Head	152	-1.9	18 (ER-OV-03a)	-30 (UE-20n #1 1,005.84 m)	7.0
Spring Head	28	2.7	19 (Torrance Spring)	-5.3 (Ute Springs Culvert)	6.8
Oasis Valley Discharge	7	3.2	42 (Zone 3)	-23 (Zone 1)	25
Boundary Flow	4	-1.7	26 (West)	-14 (East)	16

[a]Positive sign is simulated less than target, negative is larger.

Post plots of weighted well and spring head residuals are shown in Figures 6-141 and 6-142 for the USGSND and USGSD recharge models, respectively. The USGSND results show a more uniform degree of error, but there is a slight bias in central Area 20 to undersimulated heads. In contrast, the USGSD recharge model shows a systematic, but small, bias to oversimulated heads. The difference is entirely caused by differences in the recharge maps because the same set of hydraulic parameters was used for both cases. Figures 6-143 and 6-144 show the simulated water tables, which are very similar and show the broad features of the flow system correctly. Simulated Oasis Valley discharge is 199 and 215 kg/s for the USGSND and USGSD recharge models, respectively.

Uncontrolled When Printed

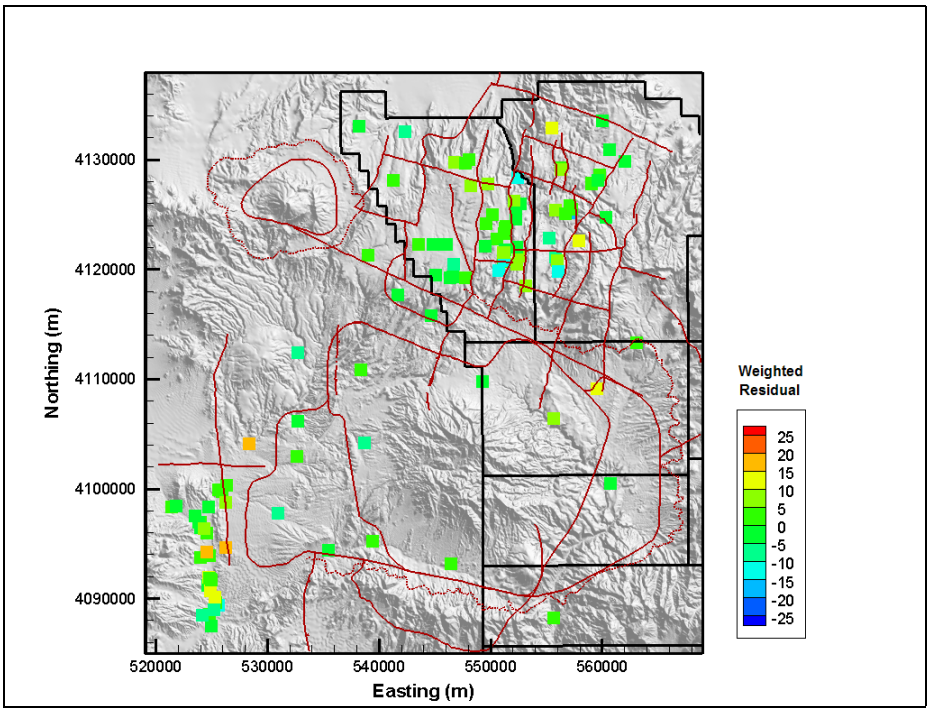

Figure 6-141
Post Plot of Weighted Well and Spring Head Residuals for BN-USGSND-SDA

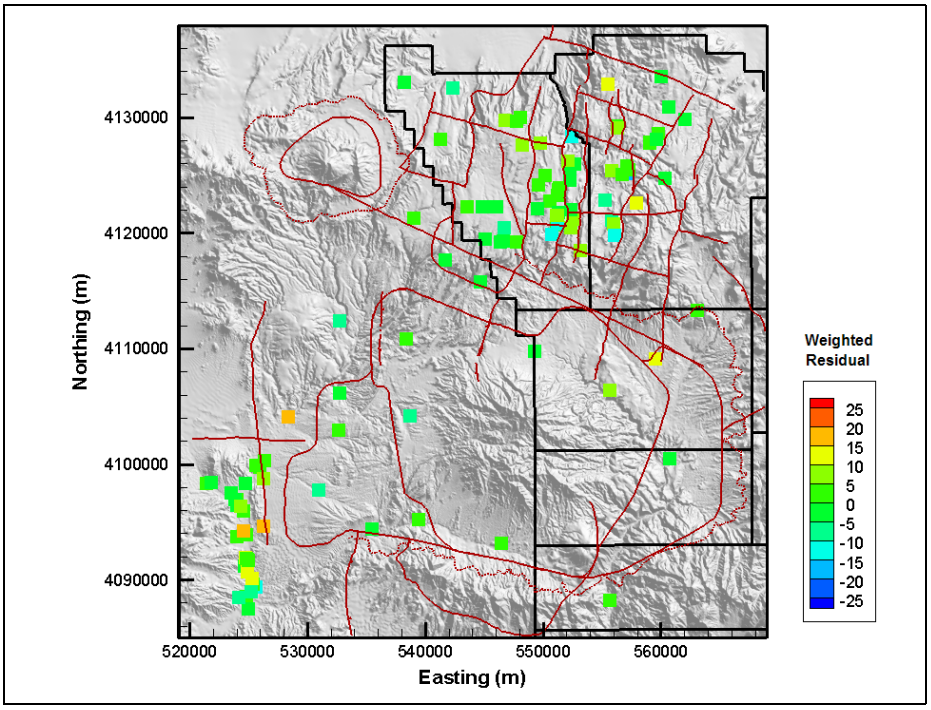

Figure 6-142
Post Plot of Weighted Well and Spring Head Residuals for BN-USGSD-SDA

Uncontrolled When Printed

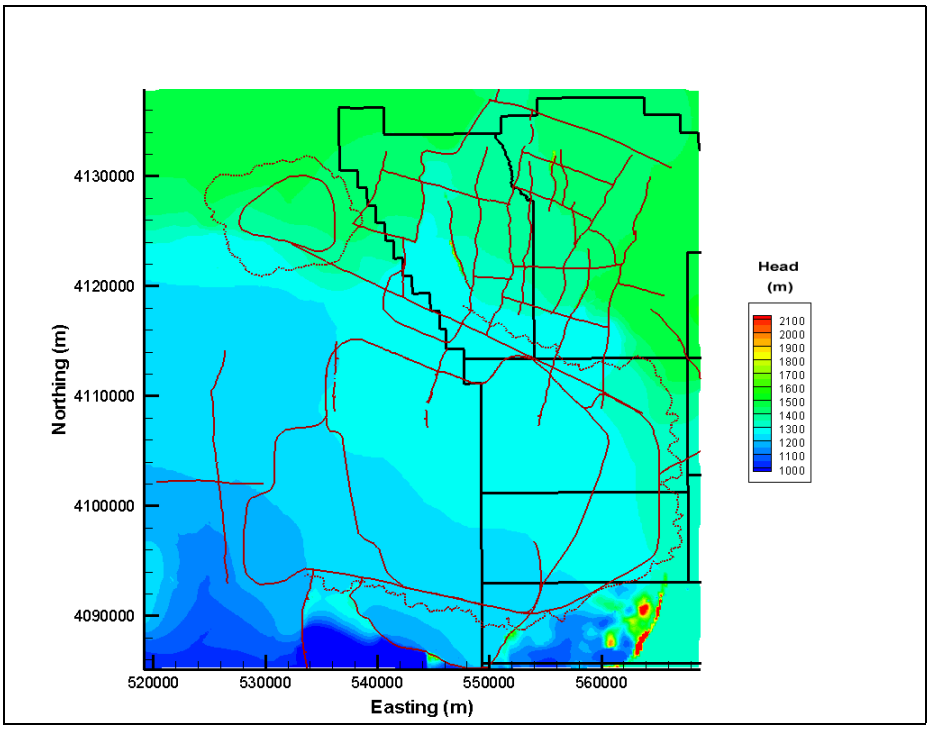

Figure 6-143
Simulated Water Table for BN-USGSND-SDA

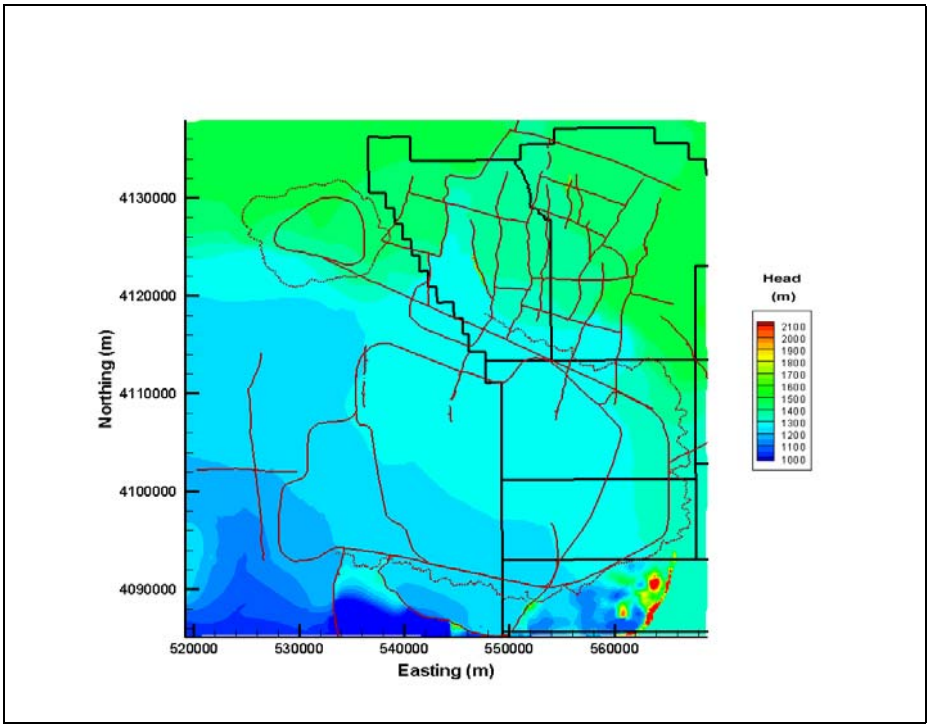

Figure 6-144
Simulated Water Table for BN-USGSD-SDA

Uncontrolled When Printed

Figures 6-145 and 6-146 show the simulated flow paths for the USGSND and USGSD recharge models. The simulated flow paths are very similar in trajectory. The main perceptible difference is in northeastern Area 19 where a few paths go to the northeast with the USGSD recharge versus west in the USGSND case. This difference is interpreted to arise from influence of local accretion of recharge on the flow paths. Table 6-43 shows the calibration summary statistics for the reduced LCCU1 permeability alternative case with the USGSD recharge model. The objective function is 10,304, the best of all the models presented in this report. The error standard deviation is markedly lower compared to the results of the DRIA simulations, and somewhat lower than the MME simulations. Simulated Oasis Valley discharge is 208 versus 227 kg/s estimated.

A post plot of weighted residuals for the reduced LCCU1 permeability alternative case shows a relatively homogenous scatter of error with the exception of UE-18t and ER-18-2, which are undersimulated (Figure 6-147). Figure 6-148 shows the simulated water table. The simulated flow paths (Figure 6-149) are very similar to the USGSD and USGSND results previously presented in this section. The major difference is more flow paths go down Fortymile Canyon (e.g., from ER-18-2 and UE-18t). A few particles exit deep along the southern boundary at about Easting 538,000 m that exit at Oasis Valley for the other cases.

The HSU permeabilities that changed the most between the MME and USGS recharge models are the BFCU, CFCM, IA, and CHZCM, which reduced by about an order of magnitude, three-quarters of an order of magnitude, two orders of magnitude, and one order of magnitude, respectively. Thus, the effect of dropping recharge rate was to require permeability to decrease in order to enhance the effect of the lower recharge in maintaining head. The two order of magnitude decrease in IA properties takes its permeability to the lowest bound thought plausible. The other reductions, particularly in the BFCU, appear reasonable.

Uncontrolled When Printed

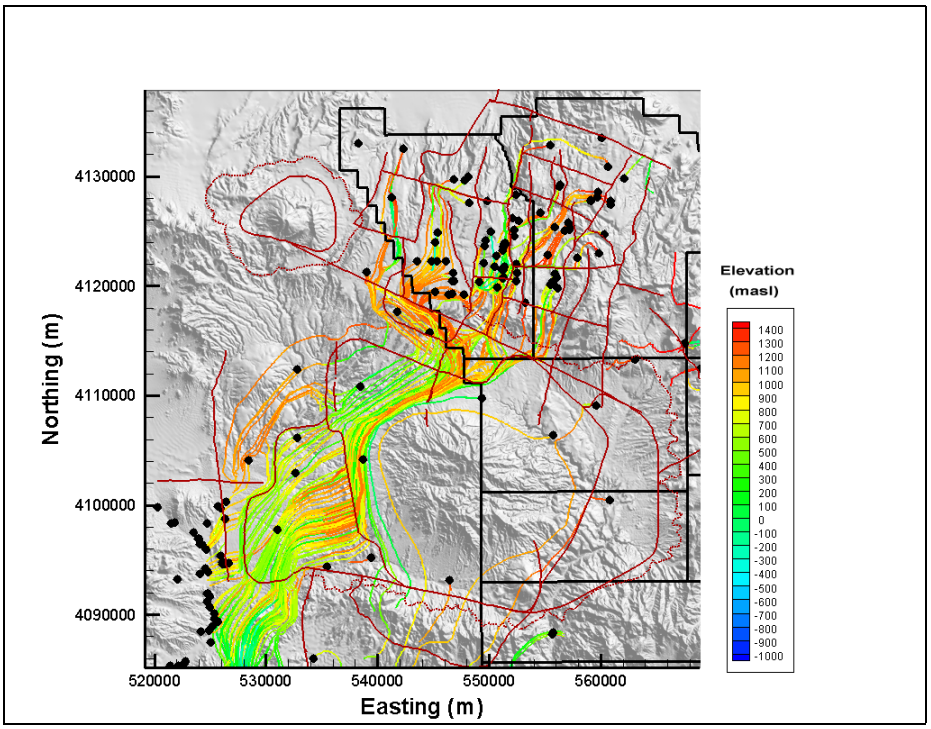

Figure 6-145
Particle Tracks for BN-USGSND-SDA

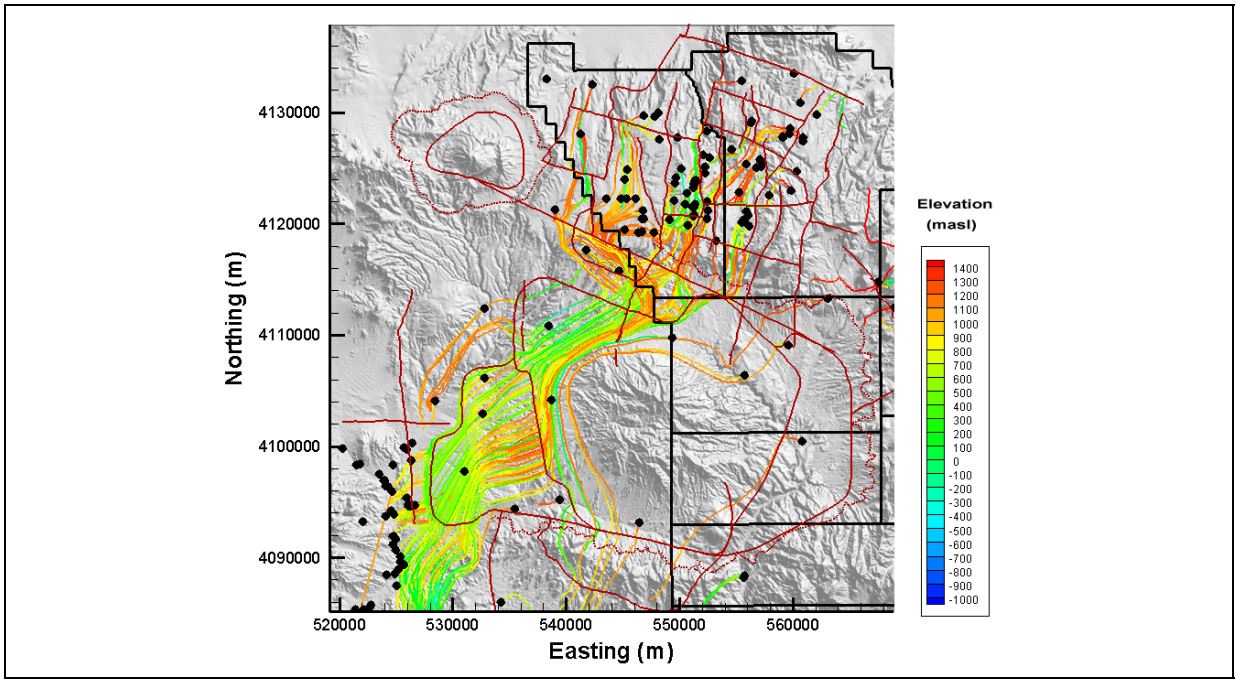

Figure 6-146
Particle Tracks for BN-USGSD-SDA

Table 6-43
Calibration Summary Statistics for BN-USGSD-SDA Reduced LCCU1 Permeability Alternative

Calibration Data	Number of Data	Mean Weighted Error (m or kg/s)[a]	Maximum Weighted Residual	Minimum Weighted Residual	Error Standard Deviation (m or kg/s)
Well Head	152	0.33	18 (ER-OV-06a)	-24 (UE-20n #1 1,005.84 m)	6.0
Spring Head	28	2.7	19 (Torrance Spring)	-7.2 (Spring id 159)	6.9
Oasis Valley Discharge	7	5.3	45 (Zone 3)	-18 (Zone 4)	21
Boundary Flow	4	5.1	21 (West)	-4.4 (North)	11

[a]Positive sign is simulated less than target, negative is larger.

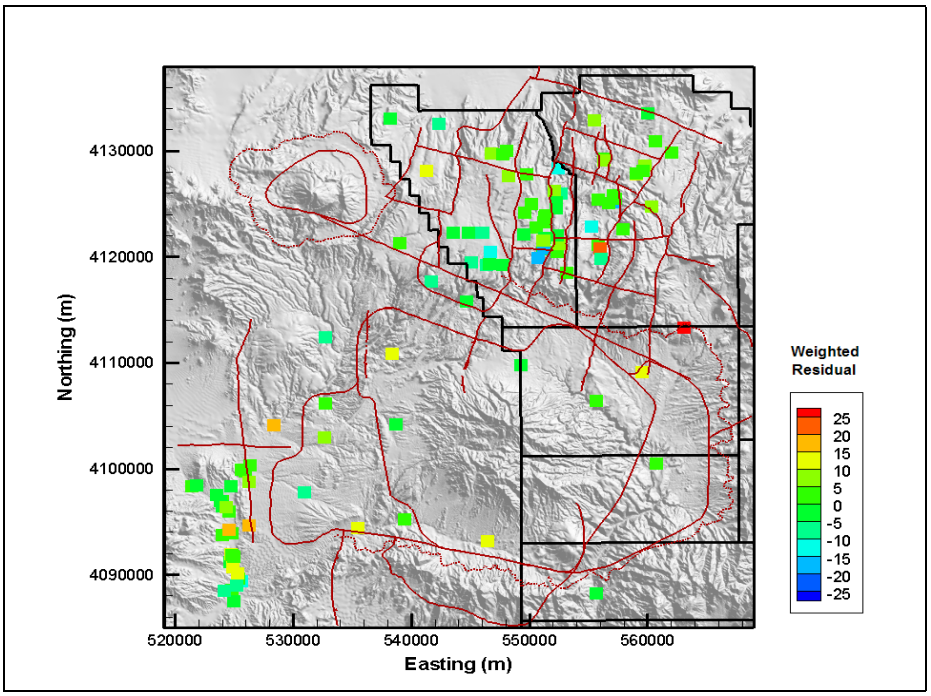

Figure 6-147
Post Plot of Weighted Well and Spring Head Residuals for BN-USGSD-SDA Reduced LCCU1 Permeability Alternative

Uncontrolled When Printed

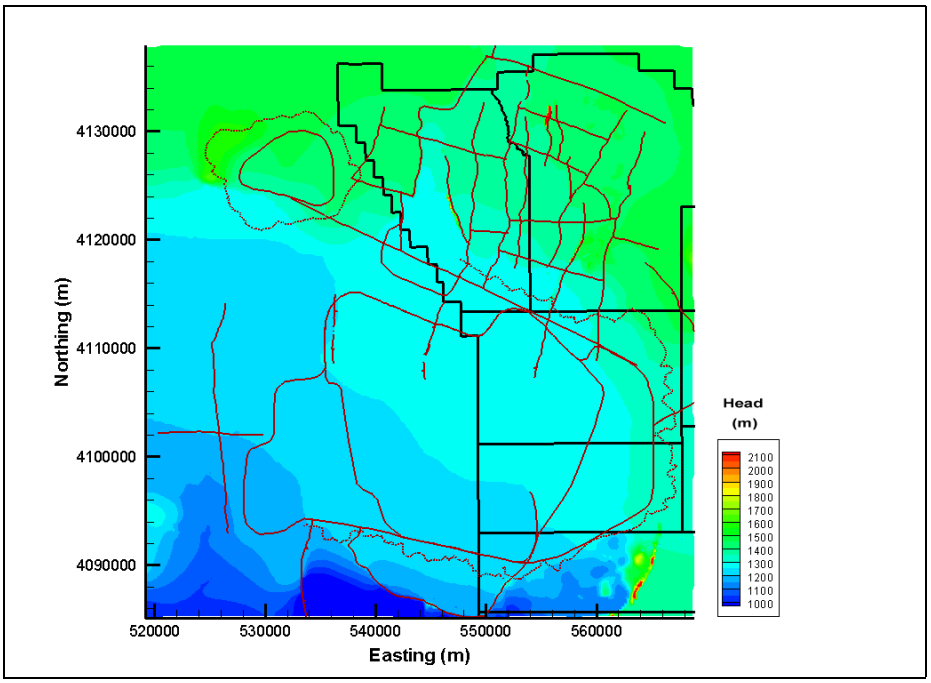

Figure 6-148
Simulated Water Table for BN-USGSD-SDA
Reduced LCCU1 Permeability Alternative

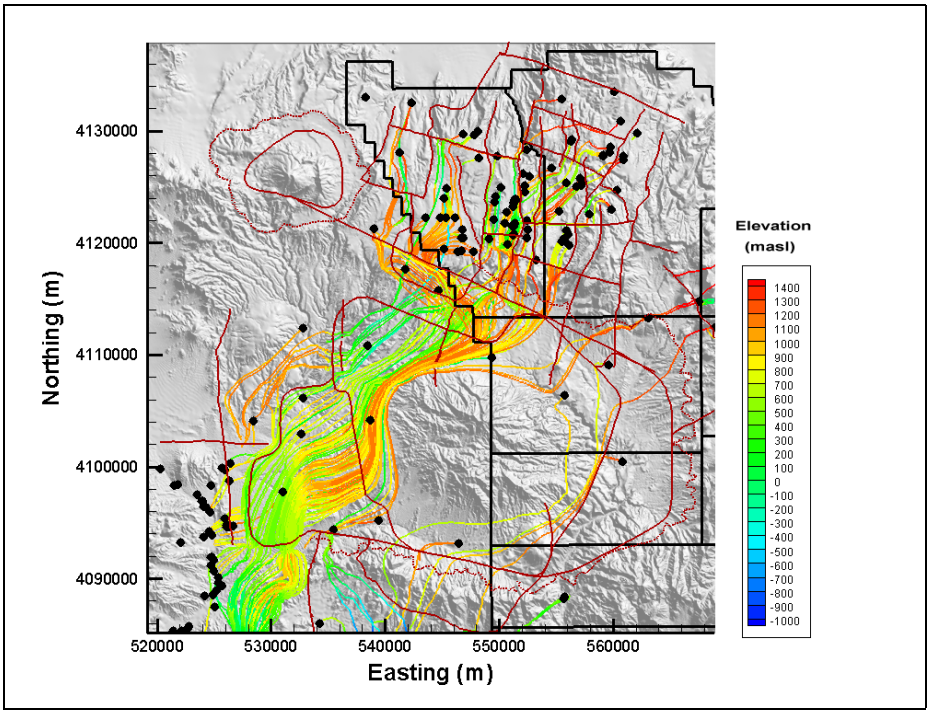

Figure 6-149
Particle Tracks for BN-USGSD-SDA
Reduced LCCU1 Permeability Alternative

6.4.4 SCCC Geologic Model Water-Balance Uncertainty Analysis

The SCCC HFM as described in Section 5.7 was used as the basis for analyzing water-balance uncertainty. Based on the results of Section 6.4.3, only two combinations of recharge model and boundary flows are considered as follows:

1. DRIA recharge and boundary flow
2. USGSD recharge and USGSND boundary flow

6.4.4.1 DRI Recharge Model

Calibration summary statistics for the SCCC HFM with the DRIA recharge model (SCCC-DRIA) are shown in Table 6-44. In spite of the high recharge associated with this map, the simulated observation well data are biased slightly low. The error standard deviations are slightly higher than those for the MME recharge calibration shown in Section 5.6. The model objective function is 31,086 versus 31,800 for calibration with the MME recharge model.

Table 6-44
Calibration Summary Statistics for SCCC-DRIA-SDA

Calibration Data	Number of Data	Mean Weighted Error (m or kg/s)[a]	Maximum Weighted Residual	Minimum Weighted Residual	Error Standard Deviation (m or kg/s)
Well Head	152	2.2	33 (PM-3 Piezometer 2)	-30 (U-20c)	11
Spring Head	28	2.5	19 (Torrance Spring)	-45 (Spring id 163)	11
Oasis Valley Discharge	7	9.0	42 (Zone 5)	-28 (Zone 4)	26
Boundary Flow	4	-27	-38 (North)	-64 (West)	35

[a]Positive sign is simulated less than target, negative is larger.

Uncontrolled When Printed

Figure 6-150 shows the posted weighted residuals; there is a strong underprediction in the east-central part of the model including Wells WW-8, ER-30-1, UE-18t, and ER-18-2 that is also suggested by the mean error. Wells WW-8 and PM-3 were undersimulated in the MME calibration as well, and this error is thus a consequence of the HFM, not the recharge model. Simulated Oasis Valley discharge is 195 kg/s. Figure 6-151 shows the simulated water table, and Figure 6-152 shows the simulated flow paths from NTS wells. The water table and flow paths have the same general character seen in all the simulations, but there is a large number of paths simulated as flowing around the eastern side of Timber Mountain. In the MME calibration, flow paths exit southern Area 20 on a nearly due south trajectory and then turn west around Timber Mountain. Slight shifts in head gradient were induced in the recalibration to the DRIA recharge model that caused a large amount of flow paths to go down Fortymile Canyon instead of into Oasis Valley. The parameter that changed the most was the permeability of the Calico Hills unit (recall that five HSUs from the base HFM were lumped into one Calico Hills HSU in the SCCC HFM), which increased nearly an order of magnitude. The PCM k_0 also increased by about half an order of magnitude. Sensitivity analysis showed that the PCM affected heads in the domain by controlling flow out to the south. The PCM increased permeability in this high recharge case is interpreted as being necessary in order to reduce heads elevated by the additional recharge in the DRIA recharge model. The TCVA and DVCM permeabilities also increased slightly. The increase in the DVCM permeability compensates for more flow apparently going down Fortymile Canyon by allowing more inflow from the west to maintain Oasis Valley discharge. This interpretation is supported by the result that the oversimulation of ET discharge Zone 4 is larger in this case than most others, and that Zone 5 in the southern part of Oasis Valley (which does not appear in any other model variation as a large error) has too low a discharge. This combination of HFM and recharge model does not appear to be reasonable.

Uncontrolled When Printed

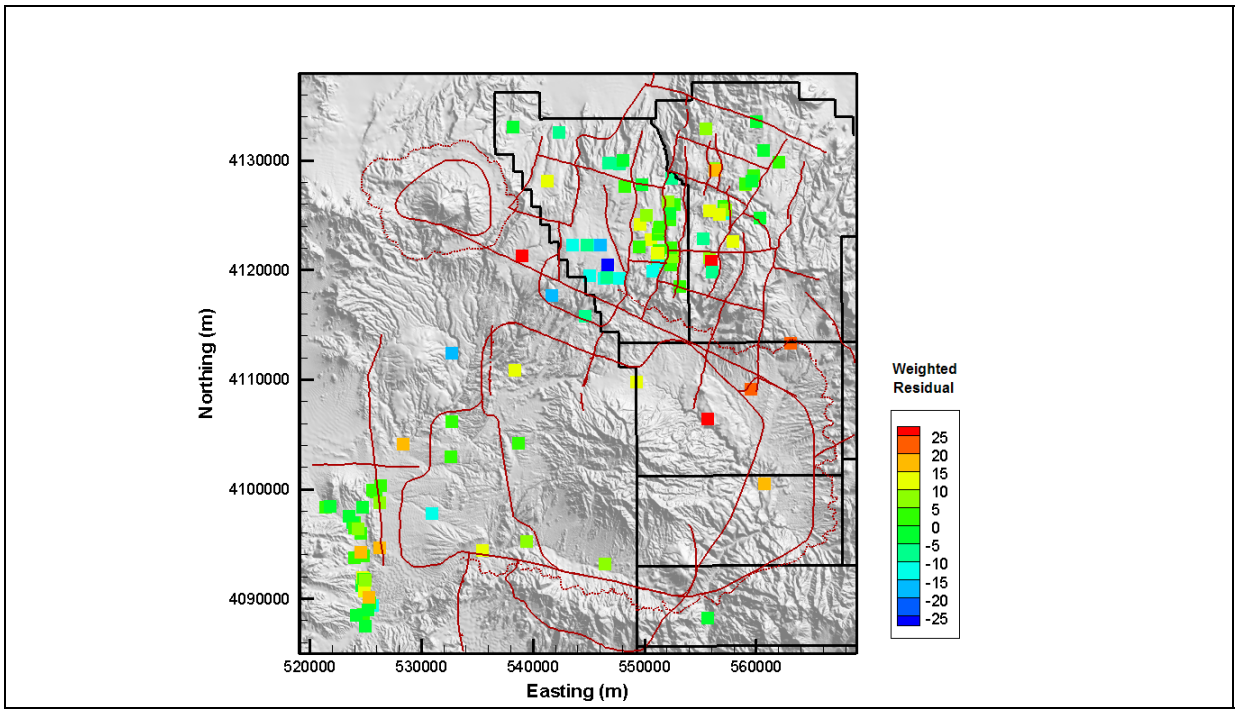

Figure 6-150
Post Plot of Weighted Well and Spring Head Residuals for SCCC-DRIA-SDA

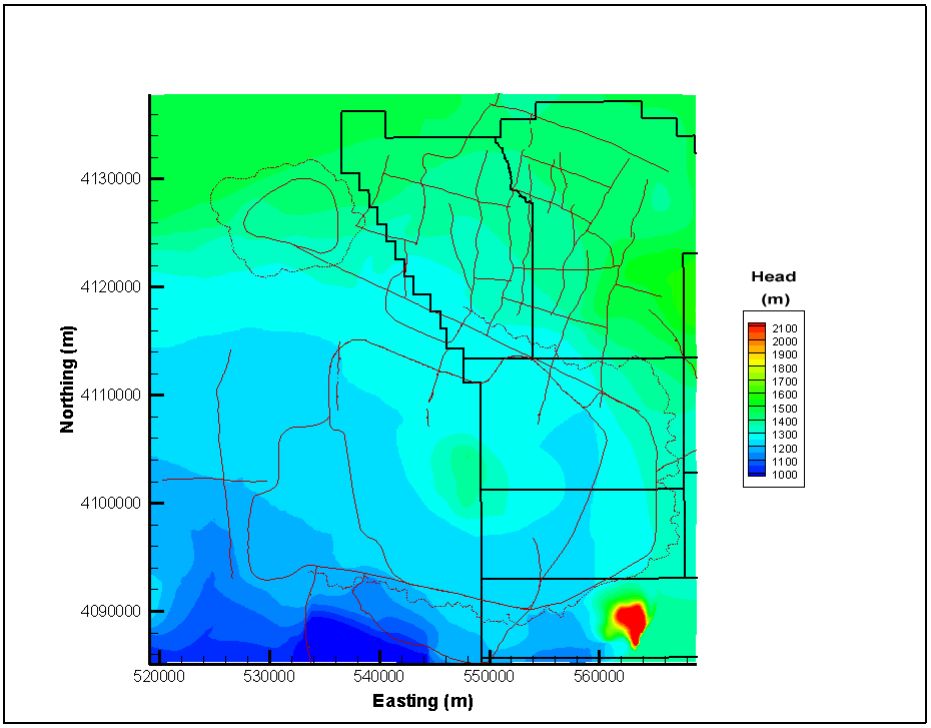

Figure 6-151
Simulated Water Table for SCCC-DRIA-SDA

Uncontrolled When Printed

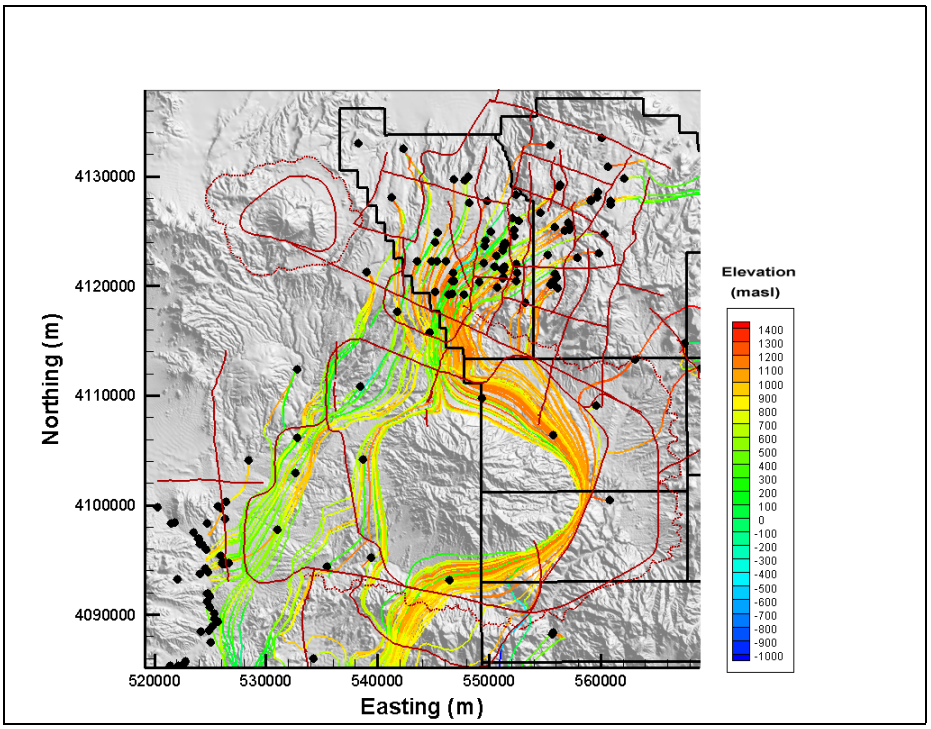

Figure 6-152
Particle Tracks for SCCC-DRIA-SDA

6.4.4.2 USGS Recharge Model

The calibration summary statistics for the SCCC HFM with the USGSD recharge model are shown in Table 6-45. The model objective function is 32,254 versus 31,800 for calibration with the MME recharge model.

Figure 6-153 shows the posted weighted residuals; there is a strong underprediction including WW-8 and PM-3 (which were also undersimulated in the MME calibration shown in Section 5.7). There is a bias to undersimulation in east-central Area 19. Simulated Oasis Valley discharge is 220 kg/s. Figure 6-154 shows the simulated water table, and Figure 6-155 shows the simulated flow paths from NTS wells. The water table and flow paths have the same general character seen in all the simulations, but there are more simulated flow paths around the eastern side of Timber Mountain, down Fortymile Canyon, and back around the southern part of Timber Mountain than with the MME recharge. The flow paths for the USGS recharge model are more like the DRIA recharge flow paths than the MME, which is surprising given that these two recharge models are at the opposite end of the spectrum of values. The parameters that changed the most in calibrating the SCCC HFM with the

Uncontrolled When Printed

Table 6-45
Calibration Summary Statistics for SCCC-USGSD-SDA

Calibration Data	Number of Data	Mean Weighted Error (m or kg/s)[a]	Maximum Weighted Residual	Minimum Weighted Residual	Error Standard Deviation (m or kg/s)
Well Head	152	-0.20	31 (U-19x)	-44 (U-20c)	12
Spring Head	28	2.7	19 (Torrance Spring)	-44 (Spring id 163)	11
Oasis Valley Discharge	7	1.9	34 (Zone 3)	-34 (Zone 4)	23
Boundary Flow	4	16	37 (East)	-14 (North)	25

[a]Positive sign is simulated less than target, negative is larger.

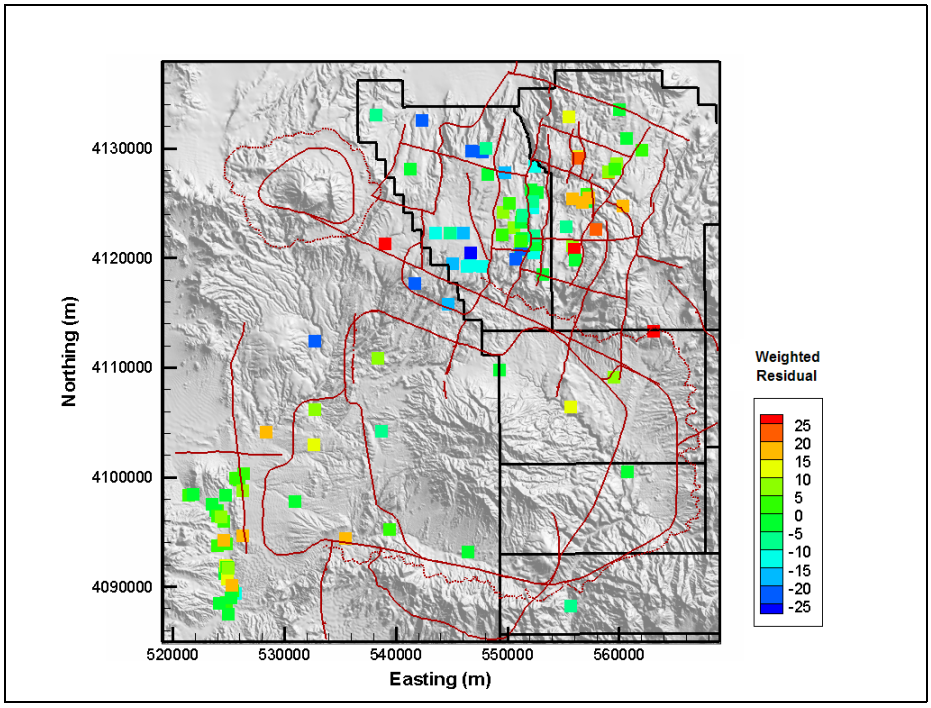

Figure 6-153
Post Plot of Weighted Well and Spring Head Residuals for SCCC-USGSD-SDA

USGSD recharge map include the permeability of the PBRCM, FCCM, DVCM, Calico Hills, LCA3, and PCM. The PBRCM permeability increased by an order of magnitude, with lesser increases in the PCM and DVCM, and LCA3. Physically, this is interpreted as being necessary to allow more flow in

Uncontrolled When Printed

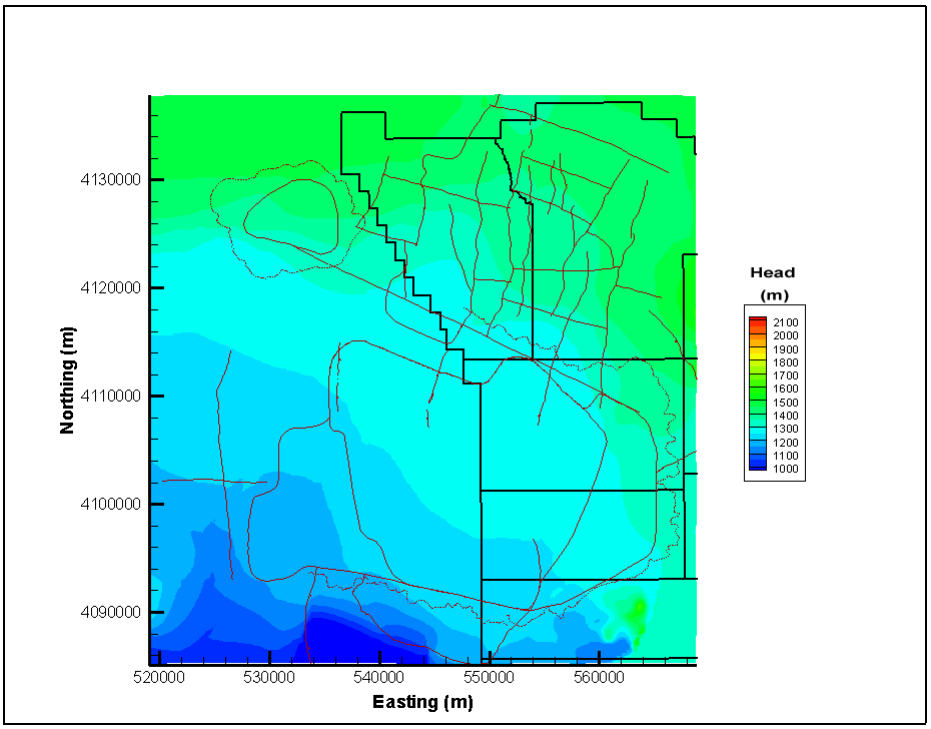

Figure 6-154
Simulated Water Table for SCCC-USGSD-SDA

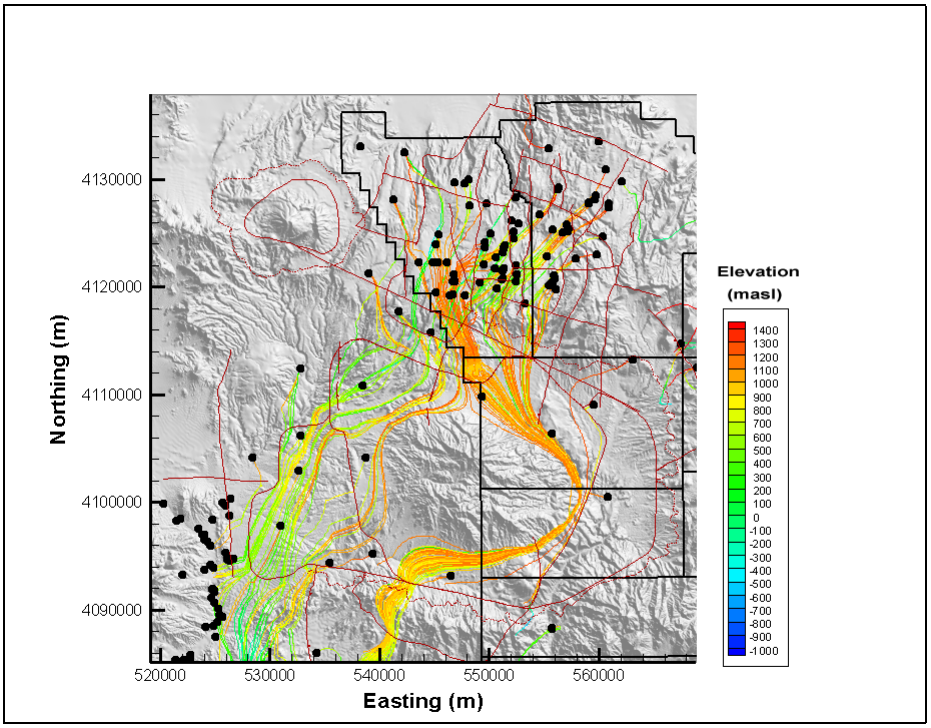

Figure 6-155
Particle Tracks for SCCC-USGSD-SDA

Uncontrolled When Printed

on the north and east model edges (through PBRCM and LCA3) and support the heads, and to allow more inflow from the west to maintain flow in Oasis Valley (through DVCM), and to balance out the increased flow and heads in the northern domain (through PCM). Because of the decreased recharge the FCCM permeability, which rings Timber Mountain, had to decrease to hold heads up, as did the Calico Hills permeability.

6.4.5 Summary of Water-Balance Uncertainty Analysis

Recalibrating the base and SCCC HFMs to a suite of recharge models and boundary flows addresses the water-balance component of flow model uncertainty. A total of eight combinations of recharge model, boundary flow, and HFM were considered (Table 6-46). Alternative recharge models included the two variations of the USGS distributed parameter model and two variations of the DRI chloride mass-balance model. In addition, a sub-variation of the base HFM with reduced LCCU1 permeability alternative was also considered. The boundary flows developed from the UGTA regional model (DOE/NV, 1997) analysis for the corresponding recharge models were used in conjunction with each respective recharge model. For example, the DRIA recharge model was used along with the UGTA regional model boundary flows resulting from the DRIA recharge model. In general, reducing recharge via the USGS recharge model had the effect of dropping permeability, with the converse resulting from the DRI recharge model. This is expected behavior in a steady-state model. Some of the downward changes, notably the IA for the USGS recharge model cases, are to the lower limit of estimated parameter uncertainty. No such issue was noted on the estimated upper end of parameter uncertainty with the DRI recharge model.

In general, all the combinations of HFM, recharge models, and boundary flows could be as well calibrated as with the MME recharge and boundary flow. This recalibration, however, can result in a few marginal parameter values as noted for the IA. The poorest-performing HFM considered under all recharge models was the SCCC alternative, as was also noted in Section 5.8. The lack of deep faults, particularly along the Purse Fault, limits the degree of freedom necessary to give a reasonable calibration. The SCCC HFM also showed the greatest sensitivity of simulated flow paths to recharge model, with significantly more flow paths down Fortymile Canyon for the DRIA and the USGSD recharges than for the MME recharge, or any other HFM and recharge combination. The combination of HFM and water-balance uncertainty is further addressed in Section 6.5.

Uncontrolled When Printed

Table 6-46
Summary of Flow Model Results for Water-Balance Uncertainty

HFM	Water-Balance Condition	Calibration Issues	Qualitative Flow Path Assessment
BN	DRIA	Slight oversimulation bias in Area 19	Fewer particles go west into northern Oasis Valley
BN	DRIAE	Slight oversimulation bias in Area 19	Fewer particles go west into northern Oasis Valley
BN	USGSD	Third-best calibration Slight oversimulation bias	Particles go deeper along northeastern Timber Mountain, but stay shallower after crossing Moat Fault than in base
BN	USGSND	Second-best calibration	Particles go deeper along northeastern Timber Mountain, but stay shallower after crossing Moat Fault than in base
BN Reduced LCCU1 Permeability Alternative	DRIA	Worst BN DRI calibration	Particle tracks concentrated on western flank of Timber Mountain, fewer go to Oasis Valley than in base
BN Reduced LCCU1 Permeability Alternative	USGSD	Best calibration	Very similar to base
SCCC	DRIA	Little change from MME	Particle tracks mainly go down Fortymile Canyon
SCCC	USGSD	Little change from SCCC with MME	Particle tracks mainly go down Fortymile Canyon

The particle paths, with the notable exception of the SCCC HFM, tend to behave similarly across all recharge alternatives, suggesting that HFM uncertainty plays a greater role than recharge uncertainty.

6.5 Combining HFM and Water-Balance Uncertainty

The Pahute Mesa CAIP (DOE/NV, 1999) requires that HFM and boundary condition uncertainty be considered in the flow model analysis. This section presents the approach used to address the joint effects of HFM and water-balance uncertainty and the results of the analysis.

Table 6-1 in Section 6.1.2 shows the matrix of HFM, recharge, and boundary flow uncertainties. Section 6.3 addresses HFM uncertainty by evaluating five alternative HFMs (in addition to base and SCCC) with the MME recharge model and associated boundary flows, and Section 6.4 addresses water-balance uncertainty by evaluated the USGSD, USGSND, DRIA, and DRIAE recharge models with the base and SCCC HFMs. The final assessment is the conjunction of HFM and water-balance uncertainty.

Uncontrolled When Printed

The first component of this assessment is the selection of alternative HFMs for evaluation. The SCCC HFM, the major alternative, has already been considered in Section 6.4, and its calibration is discussed in Section 5.7. The five alternative HFMs derived from the base HFM that were considered in Section 6.3 are also candidates for this evaluation. Of the five alternative HFMs considered in Section 6.3 two are distinctly different: the PZUP and DRT alternatives. Other, subtler differences were noticed between the remaining alternatives, but PZUP and DRT had pronounced differences. Therefore, the PZUP and DRT HFMs are chosen for additional water-balance uncertainty analysis.

The water-balance uncertainty was bounded by considering the DRIA and USGSD recharge models and associated UGTA regional boundary flows. The DRIAE and USGSND were assessed in Section 6.4, and it was decided that DRIA and USGSD have physical characteristics that make them desirable and that these two recharge alternates are sufficient to bound uncertainty. The areal distribution and mass flows associated with these recharge models is shown in Section 4.3.1.

The PZUP and DRT HFMs were calibrated with the MME recharge model in Section 6.3. The DRIA and USGSD recharge models were applied and the models recalibrated; the results are described in the following sections.

6.5.1 Raised Pre-Tertiary Surface (PZUP) HFM

The PZUP HFM with the selected HSU depth-decay and anisotropy (PZUP-MME-SDA) parameterization as described in Section 5.6.2 was used as the basis for analyzing the joint effects of HFM and water-balance uncertainty. Based on the results of Section 6.4.3, only two combinations of recharge model and boundary flows are considered as follows:

1. DRIA recharge and boundary flow
2. USGSD recharge and USGSND boundary flow

6.5.1.1 DRIA Recharge Model

Table 6-47 summarizes the calibration statistics. It is interesting to note that the mean head error is slightly positive, but with this high recharge model and potentially reduced transmissivity, the opposite result would be expected. The scatter of error as shown by the high error standard deviation in fitting the boundary flows is the worst of all models considered; MME recharge with this HFM

Uncontrolled When Printed

Table 6-47
Calibration Summary Statistics for PZUP-DRIA-SDA

Calibration Data	Number of Data	Mean Weighted Error (m or kg/s)[a]	Maximum Weighted Residual	Minimum Weighted Residual	Error Standard Deviation (m or kg/s)
Well Head	152	0.45	31 (USW UZ-N91)	-25 (UE-20n #1 1,005.84 m)	7.4
Spring Head	28	2.8	19 (Torrance Spring)	-5.3 (Spring id 159)	6.7
Oasis Valley Discharge	7	-17	27 (Zone 3)	-47 (Zone 1)	30
Boundary Flow	4	-34	59 (West)	-93 (East)	67

[a]Positive sign is simulated less than target, negative is larger.

also had some of the larger boundary flow errors. The increased volume of mainly lower permeability rocks limits the ability of this model to move water across the boundaries. The objective function is 33,713. Relative to the calibration with MME recharge this calibration is worse, but not greatly so.

Figure 6-156 shows the posted weighted residuals; there is a slight bias to undersimulate heads that is also suggested by the mean error. The visual impression of the residuals shows more scatter to high and low values than most other results. Simulated Oasis Valley discharge is 286 kg/s (versus 227 kg/s estimated), one of the highest simulated Oasis Valley discharges of all models. This is nearly two standard deviations above the estimated value (e.g., the upper 95 percent confidence limit on Oasis Valley discharge). This is interpreted as arising from the larger accretion of recharge that must move through shallower high-permeability HSUs, which can still satisfy Oasis Valley discharge while the boundary flows are otherwise more poorly matched than in other cases. Figure 6-157 shows the simulated water table, and Figure 6-158 shows the simulated flow paths. The water table and flow paths have the same general character seen in all the simulations. The mound under Black Mountain is from the substitution of TCVA with low permeability BMICU. The DVCM, BRA, LCA Zone 1, CHZCM, and YMCFCM permeabilities (including k_0) all increased between a quarter and an order of magnitude over the values used to calibrate the MME recharge in order to bleed off the additional recharge (nearly double that of the MME) imposed by the DRIA recharge model.

Uncontrolled When Printed

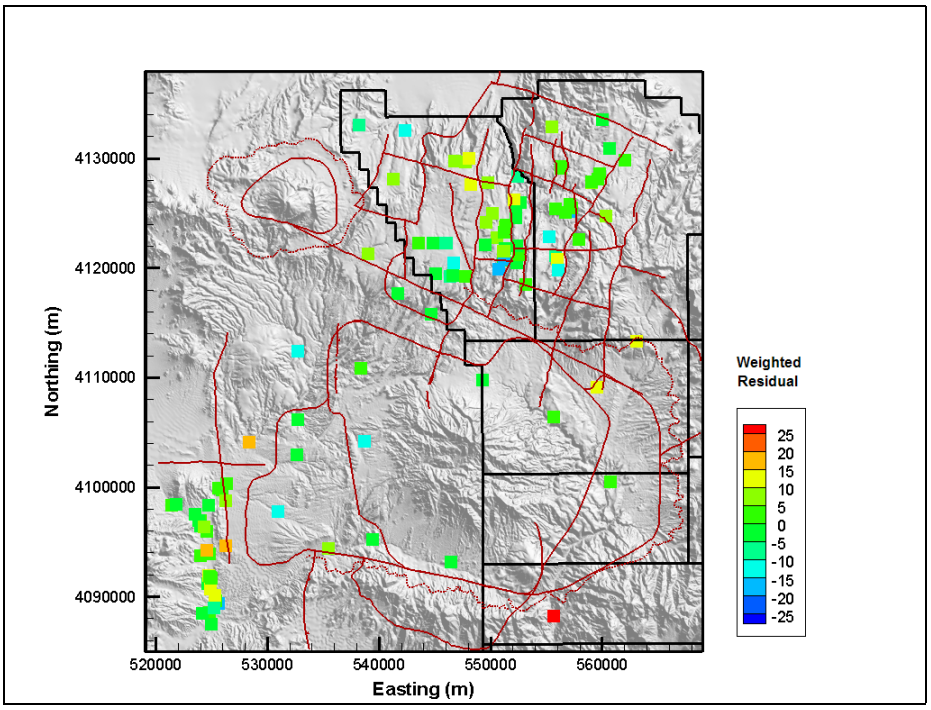

Figure 6-156
Post Plot of Weighted Well and Spring Head Residuals for PZUP-DRIA-SDA

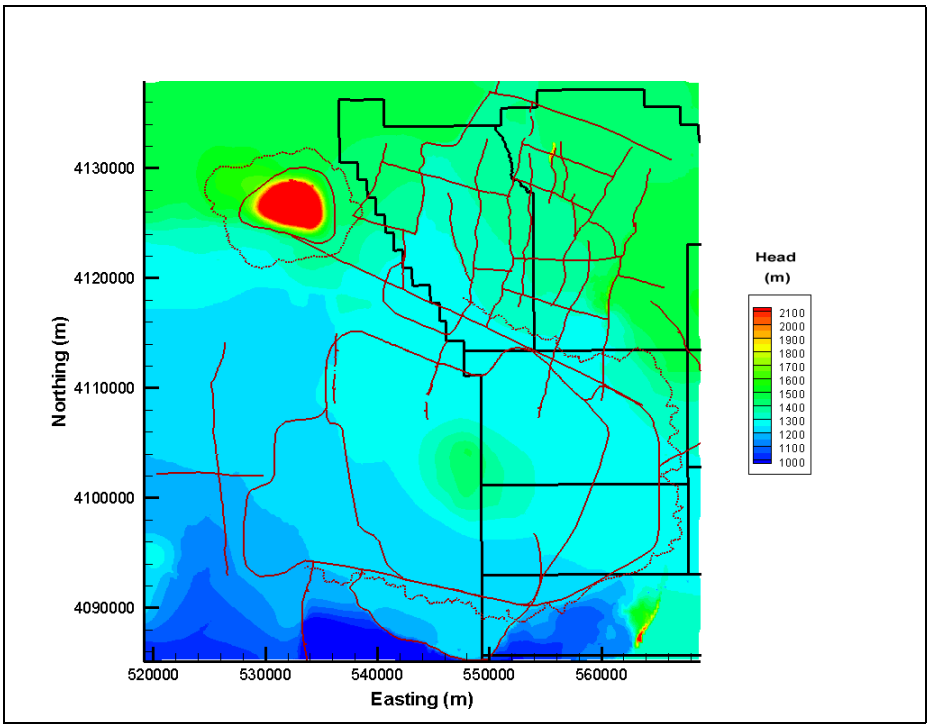

Figure 6-157
Simulated Water Table for PZUP-DRIA-SDA

Uncontrolled When Printed

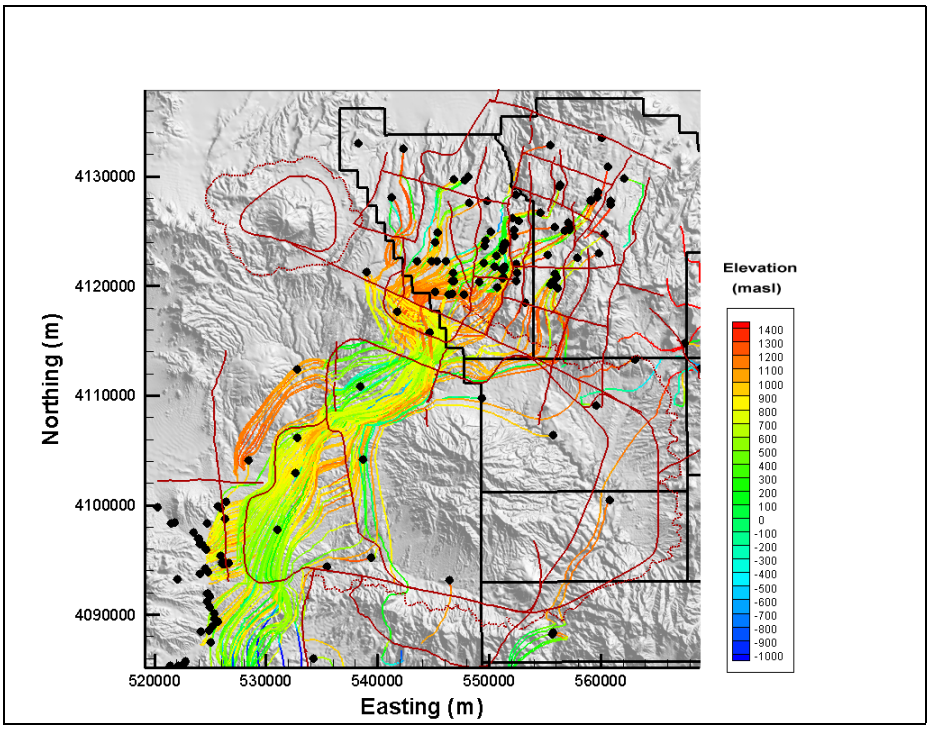

Figure 6-158
Particle Tracks for PZUP-DRIA-SDA

6.5.1.2 USGSD Recharge Model

The summary calibration statistics for the PZUP HFM and USGSD recharge model and USGSND boundary flows are shown in Table 6-48. There is a definite bias to undersimulate observation well heads. The objective function is 29,666, slightly worse than the calibration with the MME recharge model, but marginally better than the DRIA calibration.

Post plots of weighted well and spring head residuals are shown in Figure 6-159 for the USGSD recharge model. There is definite bias to undersimulate heads by 20 to 25 m in central Pahute Mesa that is also seen in the mean error. However, the boundary flows are matched well with an error standard deviation less than with both the MME and DRIA recharge models, although some of this effect may be artificial because the boundary flows for this recharge model are the lowest in magnitude. Figure 6-160 shows the simulated water table, which appears to show the broad features of the flow system correctly. Simulated Oasis Valley discharge is 208 kg/s. Thus, the controlling factor for Pahute Mesa head is not entirely the same as that which controls Oasis Valley discharge (which was noted in the sensitivity analysis as well). Figure 6-161 show the simulated flow paths,

Uncontrolled When Printed

Table 6-48
Calibration Summary Statistics for PZUP-USGSD-SDA

Calibration Data	Number of Data	Mean Weighted Error (m or kg/s)[a]	Maximum Weighted Residual	Minimum Weighted Residual	Error Standard Deviation (m or kg/s)
Well Head	152	5.8	42 (U-19x)	-17 (ER-OV-04a)	13
Spring Head	28	3.0	19 (Torrance Spring)	-5.3 (Ute Springs Culvert)	6.7
Oasis Valley Discharge	7	5.3	37 (Zone 3)	-26 (Zone 4)	23
Boundary Flow	4	6.0	15 (West)	-5.9 (East)	9.9

[a]Positive sign is simulated less than target, negative is larger.

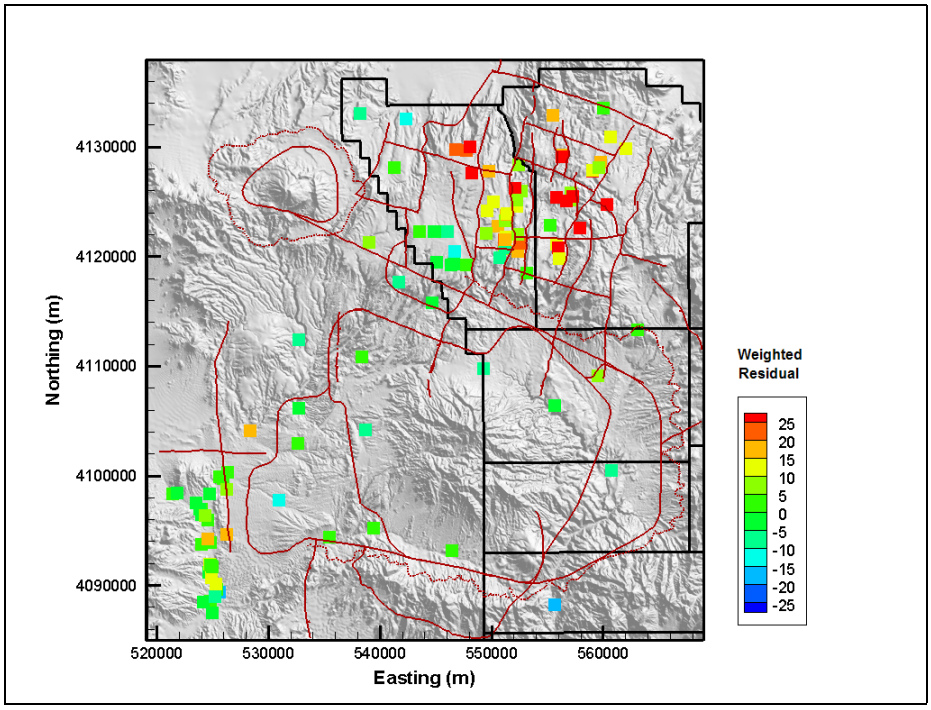

Figure 6-159
Post Plot of Weighted Well and Spring Head Residuals for PZUP-USGSD-SDA

which, in spite of the bias in head, show flow paths that appear quite reasonable. Hence, the overall direction of the hydraulic gradient is still reasonable in this case.

Uncontrolled When Printed

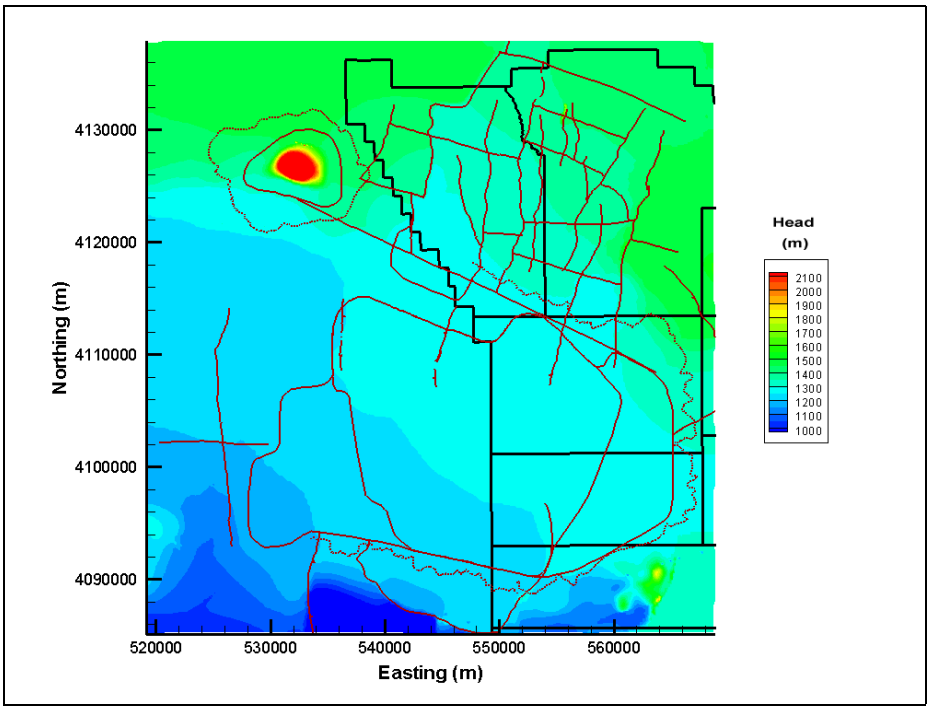

Figure 6-160
Simulated Water Table for PZUP-USGSD-SDA

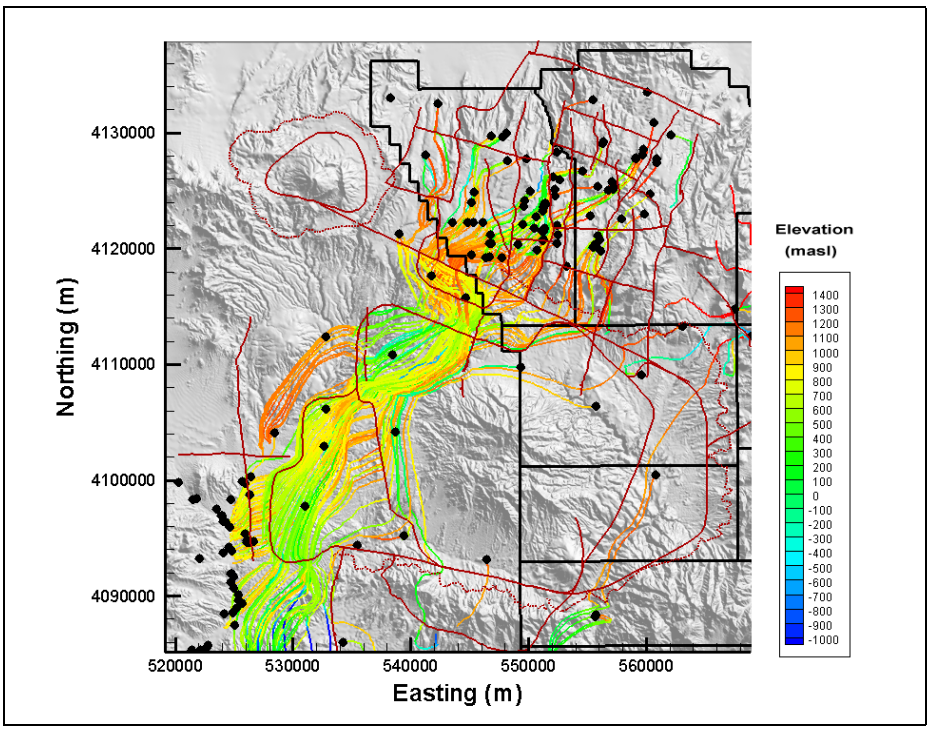

Figure 6-161
Particle Tracks for PZUP-USGSD-SDA

Uncontrolled When Printed

The HSU permeabilities that changed the most between the MME and USGS recharge models are the LCA3, PCM, TMA, and the various TMCM HSUs, all of which had modest decreases (a quarter an order of magnitude or less). Thus, the effect of dropping the recharge rate was to require permeability to decrease in order to enhance the effect of the lower recharge in maintaining head.

6.5.2 Deeply Rooted Belted Thrust Fault (DRT) HFM

The DRT HFM as described in Section 2.0 and Section 6.3 was also used for analyzing joint HFM and water-balance uncertainty. Based on the results of Section 6.4.3, only two combinations of recharge model and boundary flows are considered as follows:

1. DRIA recharge and boundary flow
2. USGSD recharge and USGSND boundary flow

6.5.2.1 DRIA Recharge Model

Calibration summary statistics for the DRT HFM with the DRIA recharge model are shown in Table 6-49. The error standard deviations are noticeably higher than those for the MME recharge calibration shown in Section 6.3. The scatter on boundary flows is comparable to the PZUP HFM and DRIA combination; this is because the LCCU1 is propagated extensively throughout the model and its low permeability makes it difficult to move water in and out of the model (similarly to the PZUP HFM). The model objective function is 37,630 versus 26,240 for calibration with the MME recharge model.

Figure 6-162 shows the posted weighted residuals; there is a strong underprediction at WW-8, although UE-18t and ER-18-2, which are often undersimulated when WW-8 is undersimulated, are reasonably matched. This is because of the higher recharge that applies more water locally that can correct bias. Simulated Oasis Valley discharge is 236 kg/s, one of the larger values from the suite of models tested, although not as large as the PZUP HFM and DRIA recharge. Figure 6-163 shows the simulated water table, and Figure 6-164 shows the simulated flow paths from NTS wells. The water table and flow paths have the same general character seen in all the simulations, but there is shift in flow paths such that many exit along the southern boundary at about 540,000 m Easting. This result is also noted in Section 6.3; thus, it is concluded that the shift in flow paths is due to the HFM and not the recharge model.

Uncontrolled When Printed

Table 6-49
Calibration Summary Statistics for DRT-DRIA-SDA

Calibration Data	Number of Data	Mean Weighted Error (m or kg/s)[a]	Maximum Weighted Residual	Minimum Weighted Residual	Error Standard Deviation (m or kg/s)
Well Head	152	-0.88	69 (WW-8)	-35 (U-19ad)	10
Spring Head	28	2.6	19 (Torrance Spring)	-6.0 (Spring id 159)	6.9
Oasis Valley Discharge	7	-2.8	45 (Zone 5)	-44 (Zone 4)	30
Boundary Flow	4	-40	6.6 (West)	-85 (South)	58

[a]Positive sign is simulated less than target, negative is larger.

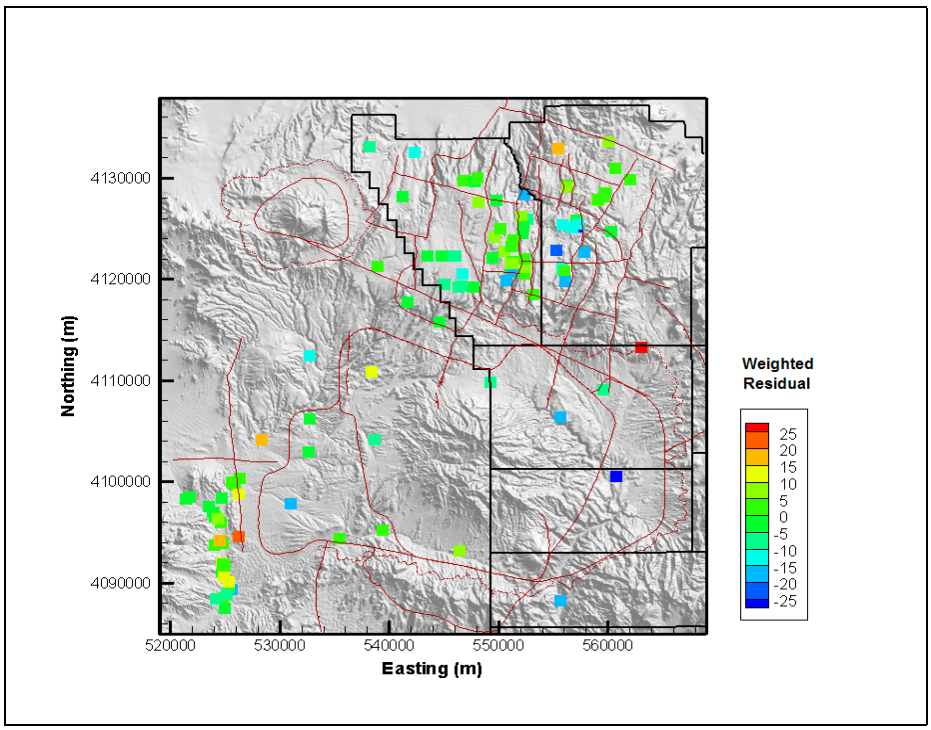

Figure 6-162
Post Plot of Weighted Well and Spring Head Residuals for DRT-DRIA-SDA

The HSU permeabilities that changed the most in calibrating the DRT HFM between the MME and DRIA recharge models include those of the CHZCM (an increase of just over an order of magnitude), DVCM (a slight decrease), LCA3 (an order of magnitude increase), CFCM (order of magnitude increase), PCM (slight increase), PBRCM Zone 84 (this zone controls flow from the north into Oasis

Uncontrolled When Printed

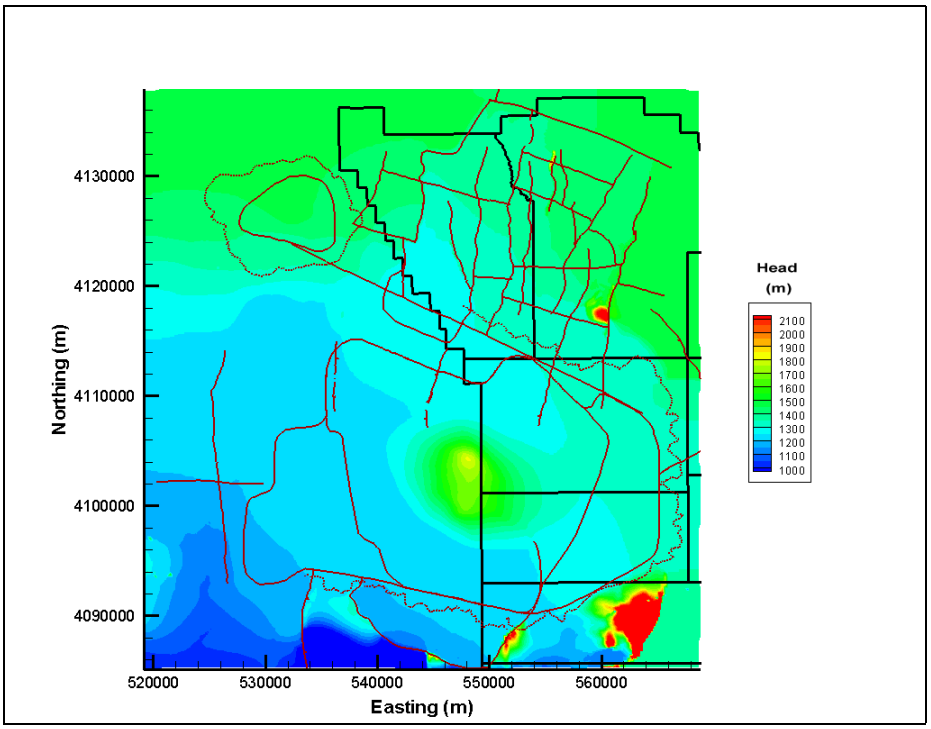

Figure 6-163
Simulated Water Table for DRT-DRIA-SDA

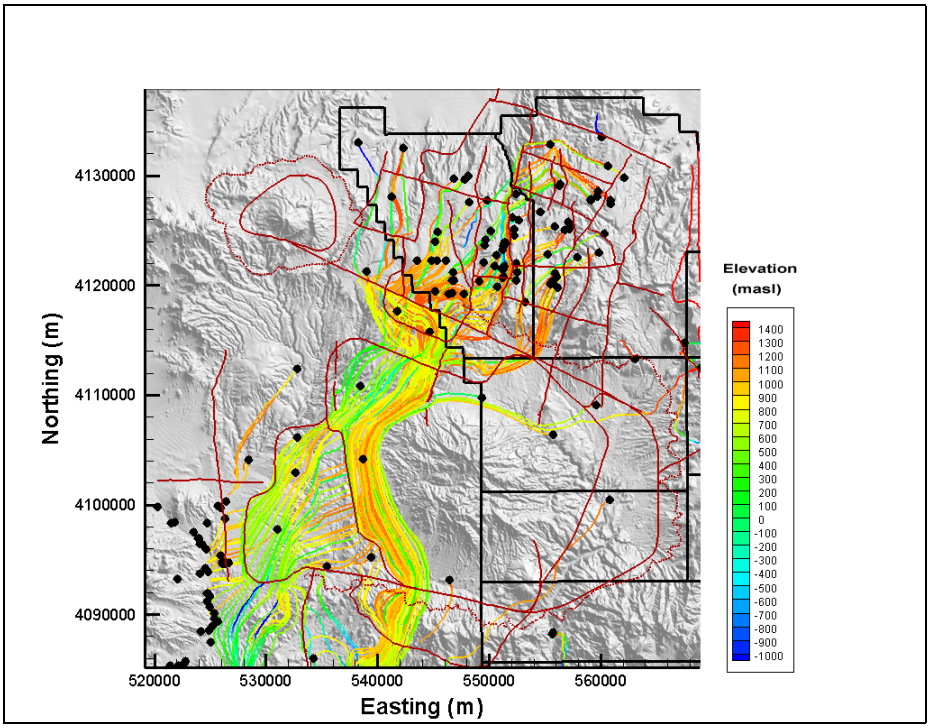

Figure 6-164
Particle Tracks for DRT-DRIA-SDA

Uncontrolled When Printed

Valley, about half an order of magnitude decrease). The interpretation of these changes is that the CHZCM and CFCM increased in permeability in order to move water out of Areas 19 and 20. Sensitivity analysis showed that PCM has a strong effect on average head in the domain, and its increased permeability is interpreted to be necessary to bleed off head by moving more water out of the system. The PBRCM Zone 84 and DVCM became tighter to limit flow to Oasis Valley from the north and west boundaries, respectively, because so much more is available from recharge accretion.

6.5.2.2 USGSD Recharge Model

The calibration summary statistics for the DRT HFM with the USGSD recharge model are shown in Table 6-50. The model objective function is 19,043 versus 26,240 for calibration with the MME recharge model. The calibration of this HFM and recharge model is much better than with the DRIA recharge model.

Table 6-50
Calibration Summary Statistics for DRT-USGSD-SDA

Calibration Data	Number of Data	Mean Weighted Error (m or kg/s)[a]	Maximum Weighted Residual	Minimum Weighted Residual	Error Standard Deviation (m or kg/s)
Well Head	152	1.3	37 (WW-8)	-32 (USW UZ-N91)	9.0
Spring Head	28	2.6	19 (Torrance Spring)	-6.3 (Spring id 159)	6.8
Oasis Valley Discharge	7	6.8	39 (Zone 3)	-21 (Zone 4)	22
Boundary Flow	4	-3.9	20 (West)	-33 (North)	23

[a]Positive sign is simulated less than target, negative is larger.

Figure 6-165 shows the posted weighted residuals; there is a strong underprediction including wells WW-8, UE-18t, and ER-18-2. There appears to be a modest bias to undersimulate heads in north-central Area 20, in central Area 19, and in the east-central area near the head of Fortymile Canyon. Simulated Oasis Valley discharge is 203 kg/s. Figure 6-166 shows the simulated water table, and Figure 6-167 shows the simulated flow paths from NTS wells. Flow paths are more concentrated with this recharge model than with the DRIA, and flow paths are also shallower than with the DRIA recharge model. This is interpreted as a consequence of the reduced permeabilities

Uncontrolled When Printed

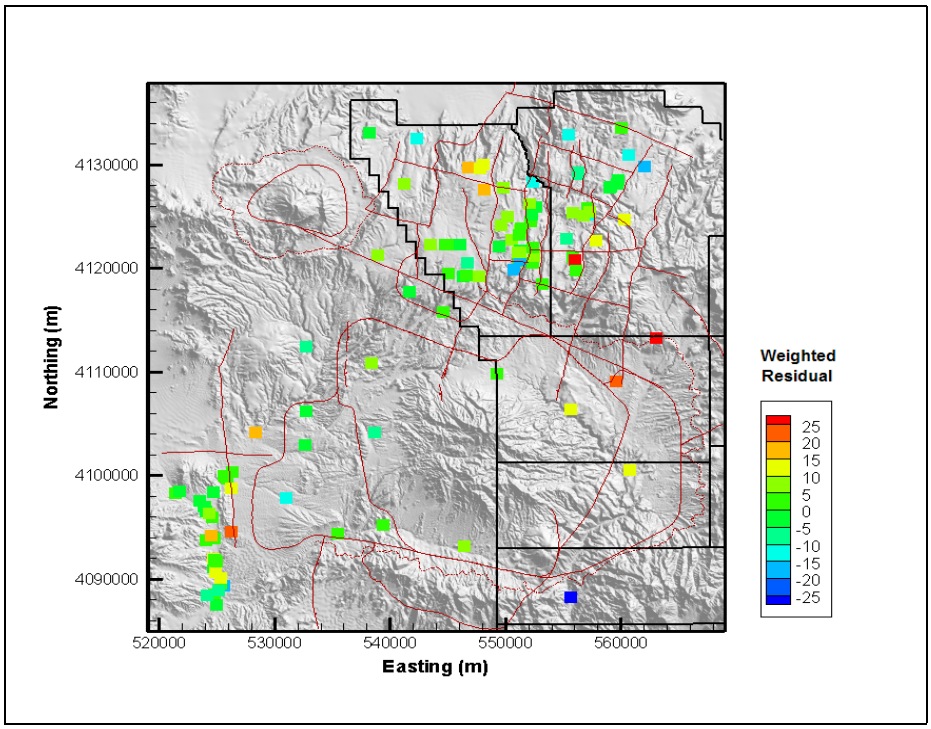

Figure 6-165
Post Plot of Weighted Well and Spring Head Residuals for DRT-USGSD-SDA

required to hold up model heads. The flow paths also show (like DRT-DRIA) a strong component of flow exiting the model at about Easting 540,000 m. In conclusion this is a function of HFM, not the recharge model.

The HSU permeabilities that changed between the DRIA and MME recharge models are the CFCU (two order of magnitude reduction), CFCM (one order of magnitude reduction), BRA (half an order of magnitude reduction), and CHZCM (one-quarter order of magnitude reduction). All these reductions are compensation for the reduced recharge in the USGSD model versus the MME model.

Uncontrolled When Printed

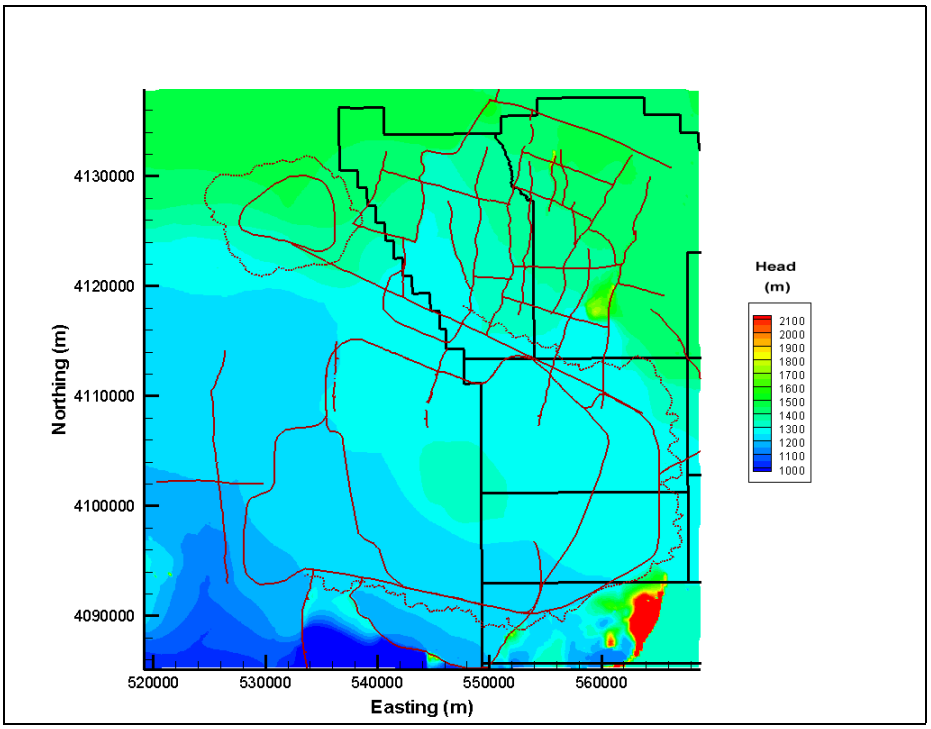

Figure 6-166
Simulated Water Table for DRT-USGSD-SDA

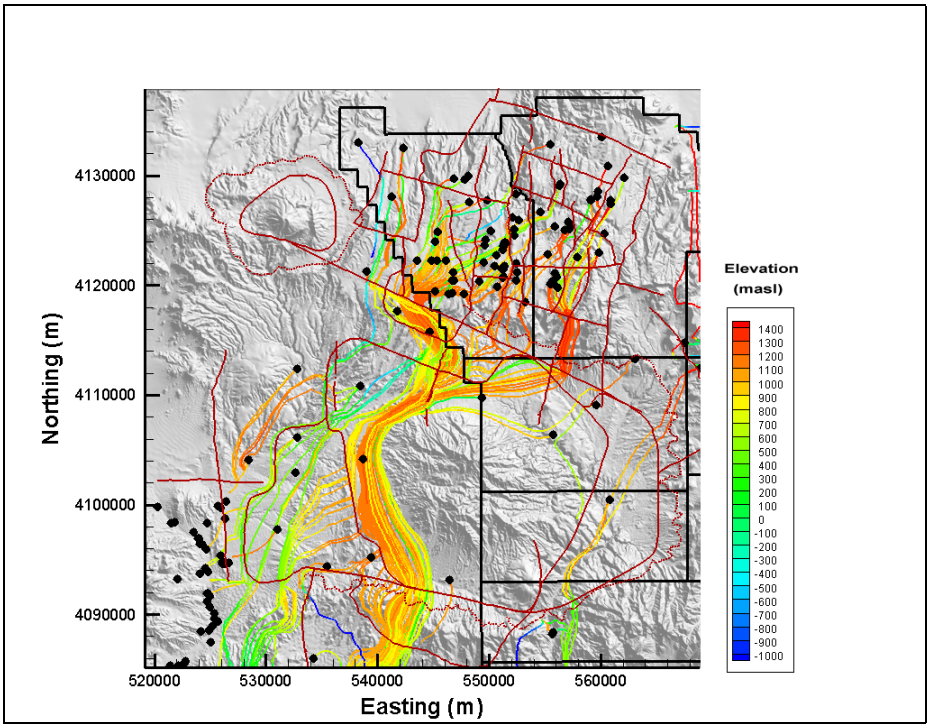

Figure 6-167
Particle Tracks for DRT-USGSD-SDA

Uncontrolled When Printed

6.5.3 Summary of HFM and Water-Balance Uncertainty Analysis

The two alternative HFMs most distinctly different than the base HFM (the DRT and PZUP cases) were combined with the DRIA and USGSD recharge models to further bound flow-system uncertainty. Both the DRT and PZUP HFMs have, by design, increased volumes of low permeability rock, although this is a consequence of the different conceptual models. Not surprisingly, both these alternatives do not perform well in matching boundary flows with the high volume (relative to the USGS and MME recharge models) DRIA recharge model simply because they do not have sufficient system transmissivity to move enough water across the boundaries. The simulated Oasis Valley flows tend to be on the high side, but not unreasonably so, and the heads are matched with a slight oversimulation bias. With respect to the boundary flows, these HFMs do perform reasonably with the USGSD recharge model, which is a direct consequence of the larger amount of lower permeability rocks in each HFM. However, there is a bias, modest for DRT and severe for PZUP, to undersimulate observation well head.

There are differences in the simulated flow paths, although not as great as might be expected. For instance, the PZUP HFM with the USGSD recharge model has a severe bias to undersimulate head on Pahute Mesa, but qualitatively the flow paths still appear reasonable. This is because the bias is ubiquitous; thus, the flow direction is maintained. The DRT HFM, in all cases, simulates a focused flow path that seems counterintuitive to the conceptual model of flow from Pahute Mesa to Oasis Valley, but still can match Oasis Valley discharge. With changing recharge models, the main simulated flow paths do not change in the DRT HFM, but at the highest recharge (DRIA) distinctly more paths exit in Oasis Valley than with the lowest recharge (USGSD). Thus, the large changes in flow paths from the DRT HFM are generated by the HFM itself, not the variation in recharge models. Conversely, the goodness of the calibrations varies in the PZUP case, but the flow paths show relatively minor variations. In both cases it appears that the HFM uncertainty dominates the recharge model uncertainty, although the models show different calibration pathologies.

It is clear from the results presented in this section that the combinations of HFM and recharge models do not perform similarly. Table 6-51 summarizes pertinent observations with respect to the flow model results. Section 7.0 explores these flow fields further in a more quantitative framework with respect to the observed geochemistry.

Table 6-51
Summary of Flow Model Results for HFM and Water-Balance Uncertainty

HFM	Water-Balance Condition	Calibration Issues	Qualitative Flow Path Assessment
PZUP	DRIA	Highest Oasis Valley discharge	Similar to MME
PZUP	USGSD	Approximately 20 m bias in Areas 19 and 20 Highest head undersimulation Largest residual standard deviation	Similar to MME
DRT	DRIA	WW-8 poorly matched Higher Oasis Valley discharge	Concentration of flow paths exiting at Easting 540,000 m
DRT	USGSD	Head undersimulation bias Poor fit in east-central model	Concentration of flow paths exiting at Easting 540,000 m

Uncontrolled When Printed

7.0 GEOCHEMICAL VERIFICATION

7.1 Approach

The calibrated flow models described in Sections 5.0 and 6.0 are evaluated with respect to independently developed groundwater mixing targets determined from geochemical analyses. The purpose of these comparisons is to determine whether the sources of groundwater at certain wells within the domain, as modeled, are consistent with the geochemical interpretation. In the comparisons, the sources of groundwater in the models are determined with reverse-particle simulations. In reverse mode, when a particle leaves the groundwater flow system, its location is documented. The top of the model has been discretized into eight separate recharge zones and the side boundaries have been discretized into seven separate inflow zones for a total of 15 unique source zones (Figure 7-1). With this method, the fraction of water from each of the recharge and boundary inflow zones that is present in the groundwater at the mixing target wells is computed. These fractions are compared with the mixing ratios estimated by interpreting geochemical compositions (Kwicklis et al., 2005).

The structure of Section 7.0 is such that after the methods are described in Section 7.1, substantial text is devoted to documenting the different behavior of each of the different flow models for each of the different geochemistry target wells (Sections 7.2 and 7.3). The quantitative comparison ranking all of the models does not come until Section 7.5. For a summary of the model comparison and ranking, the reader can skip to Section 7.5 after completing Section 7.1, and then return to the details of Sections 7.2 and 7.3 as needed.

7.1.1 Review of Verification Target Study Results

In an independent study, Kwicklis et al. (2005) estimated mixing ratios of water types at multiple boreholes in the Pahute Mesa CAU model domain. The specific objective conducted by Kwicklis et al. (2005) was to develop geochemical mixing targets for the CAU flow model. That report describes

Uncontrolled When Printed

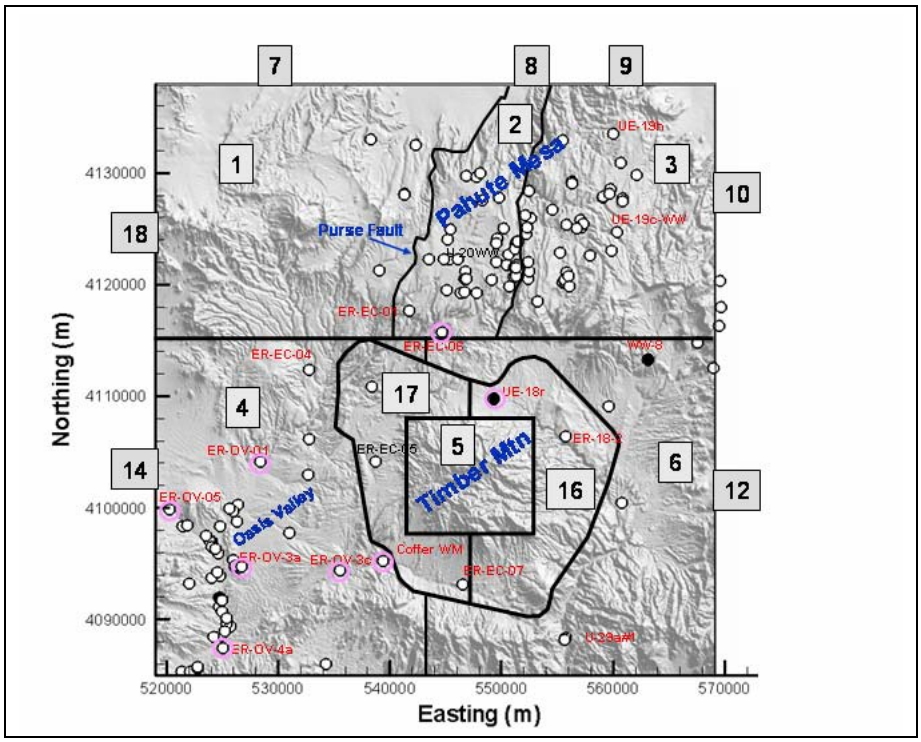

Figure 7-1
Zones Used To Identify Sources of Recharge and Inflow

in detail the methods and data that were used to estimate groundwater mixing ratios at target wells. This subsection provides a brief summary of that study.

7.1.1.1 Inverse Modeling Method

The inverse mixing model seeks to determine sources of water and their relative abundance in samples collected in various wells. The sources are identified as water types found in upgradient wells that are different from one another. The assessed mixing occurs as a result of dispersive interaction along flow pathways and through capture (and mixing) in a well, possibly from different depths.

Kwicklis et al. (2005) report that three distinct groundwater types can be identified in the Pahute Mesa/Oasis Valley flow system on the basis of their Cl^-, SO_4^{2-}, δD, and $\delta^{18}O$ compositions. Groundwaters in the northernmost Thirsty Canyon area, typified by groundwater samples from Wells ER-EC-1 and ER-EC-4, are characterized by relatively light δD and $\delta^{18}O$ compositions and high Cl^- and SO_4^{2-} concentrations compared to most other groundwaters in the flow system. Groundwaters in

Uncontrolled When Printed

Areas 19 and 20 of Pahute Mesa, typified by groundwaters at wells U-20WW, UE-19h and UE-19cWW, also have relatively light δD and $\delta^{18}O$ compositions, but have relatively low Cl^- and SO_4^{2-} concentrations compared to the northernmost Thirsty Canyon samples. Groundwater from Rainier Mesa, typified by groundwater from Well U-12s, and groundwater from the upper Fortymile Wash area, typified by groundwater from Wells UE-29a #1 and UE-29a #2 HTHs, are characterized by relatively low Cl^- and SO_4^{2-} concentrations and heavy δD and $\delta^{18}O$ compositions. Kwicklis et al. (2005) then add some additional distinctions such as identifying recharge on Timber Mountain as a water type represented by the composition of water found in Well ER-EC-7.

The wells whose sampled compositions are used to represent upgradient sources in the inverse modeling are ER-EC-1, ER-EC-4, Tolicha Peak, UE-29a #2, ER-EC-7, U-20 WW, UE-18r, UE-19h, UE-19 WW, Cedar Pass, WW-8, and ER-18-2 (see Figure 7-1). Their spatial relevance will be discussed in the next section. The wells at which mixing ratios of water represented by these upgradient sources are computed include UE-18r, ER-EC-6, ER-OV-05, ER-OV-01, ER-OV-04a, ER-OV-03a, and Coffer Windmill Well (see Figure 7-1). These wells, which help identify approximate flow paths, provide a counterclockwise sweep around the north flank of Timber Mountain, through Oasis Valley, and around to the southwest flank of Timber Mountain.

The geochemistry inverse modeling is conducted with the PHREEQC code (Parkhurst and Appelo, 1999) and described in detail by Kwicklis et al. (2005). The method seeks to identify optimal fractions of source water types in a mixed sample. Mathematically, PHREEQC seeks to optimize the following set of simultaneous algebraic equations:

$$C^j_{mixture} = f_1C^j_1 + f_2C^j_2 + \ldots. + f_nC^j_n \tag{7-1}$$

$$f_1 + f_2 + \ldots. + f_n = 1 \tag{7-2}$$

where C are the concentrations, j is the measured constituent (e.g., Cl^-, SO_4^{2-}, δD, and $\delta^{18}O$), and f_i are the volumetric fractions from the unique upgradient source types.

Mathematically, to identify n values of f_i, j must be equal to n-1. So, if only four non-reactive tracer concentrations are used, then only four upgradient source types can be used. Therefore, Kwicklis

et al. (2005) considered multiple different combinations in the simulations and they limited the process by requiring hydrologic plausibility between upgradient and downgradient sources.

7.1.1.2 Results at Boreholes Considered

At each of the target boreholes considered, several different plausible mixing ratios for source constituents were often simulated with PHREEQC. These different results provide ranges in uncertainty for the comparison with model results. The ranges are often quite large indicating significantly different plausible mixing compositions. The ranges of uncertainty reported by Kwicklis et al. (2005) indicate the differences between plausible models, but not the uncertainty associated with any given model or the data.

The results of the inverse mixing models are presented by Kwicklis et al. (2005, Tables 4 through 13, and 21 through 23). The key summary tables used for comparison with the flow models are reproduced in Section 7.2 as appropriate for the boreholes considered. Notes identify their number in the original document. The values in the tables provide input to the graphic comparisons between geochemistry analysis and flow model simulations.

Kwicklis et al. (2005) developed a series of figures based upon the mixing compositions and ranges of uncertainty to show the evolution of groundwater from different source areas (Kwicklis et al., 2005, Figures 12 through 17). For example, Figure 7-2 shows the sources and mixing ratio ranges for water at ER-OV-01. Along the path, water from the northwest (ER-EC-1) mixes with water from north-central Pahute Mesa (U-20 WW) to create a nearly equal mix at ER-EC-6. These components continue to be factored into ratios at downstream wells for which ER-EC-6 helps define the composition and mixing. Similarly, Figures 7-3 and 7-4 show the evolution and mixing source waters on Paths 4 and 6 (as defined by Kwicklis et al., 2005) with final targets in Oasis Valley or along the southwest flank of Timber Mountain.

Finally, a set of plausible flow paths that honor the mixing models are drawn. These are shown in Figure 7-5. For comparison, Figure 7-6 shows the simulated pathlines of particles originating within open screened intervals of the wells in the model domain in the base-case calibrated flow model. Qualitatively, this comparison shows great similarity between the two sets of flow paths.

Uncontrolled When Printed

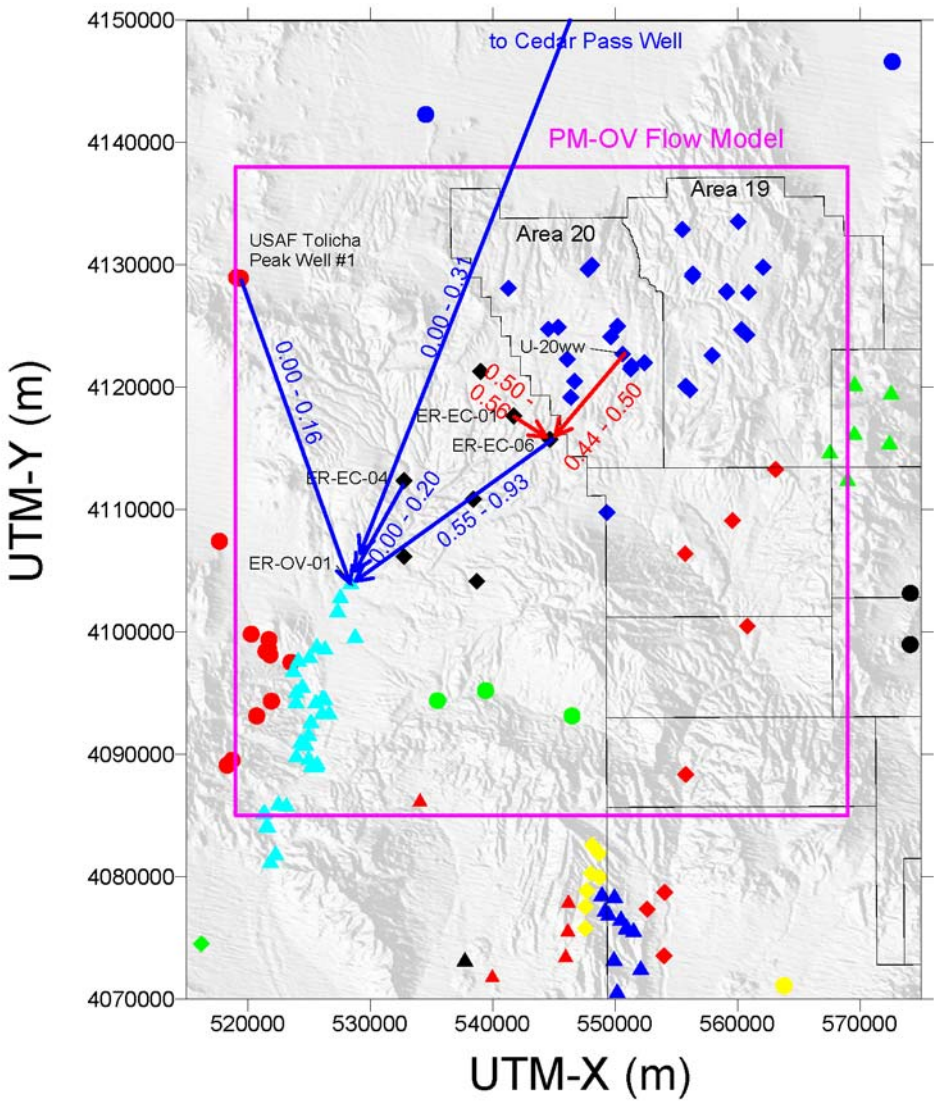

Figure 7-2
Schematic of Mixing Ratios from Upstream Source Wells Along Path 1 Toward ER-OV-01(from Kwicklis et al., 2005, Figure 13)

Uncontrolled When Printed

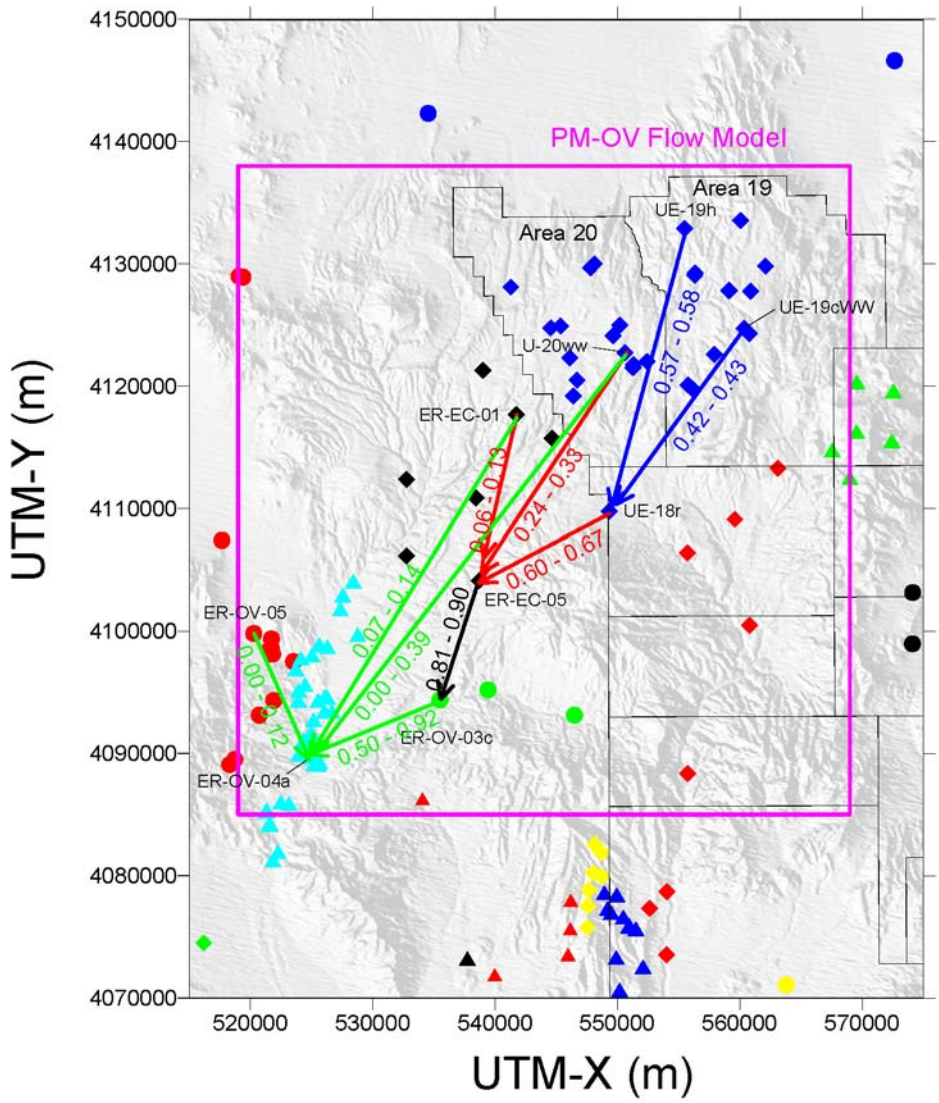

Figure 7-3
Schematic of Mixing Ratios from Upstream Source Wells Along Path 4 Toward ER-OV-04a (from Kwicklis et al., 2005, Figure 15)

Uncontrolled When Printed

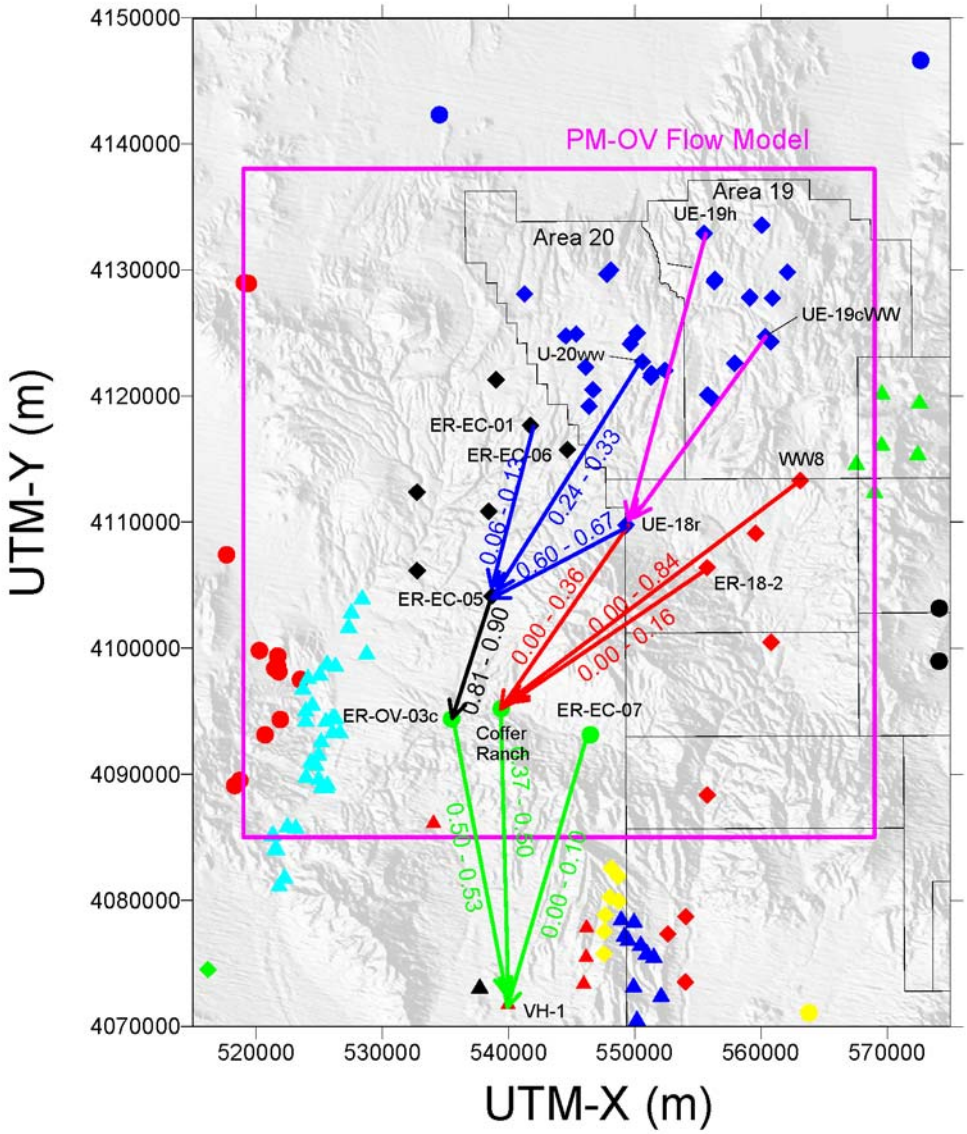

Figure 7-4
Schematic of Mixing Ratios from Upstream Source Wells Along Path 6 Toward Coffer Windmill Well (from Kwicklis et al., 2005, Figure 13)

Uncontrolled When Printed

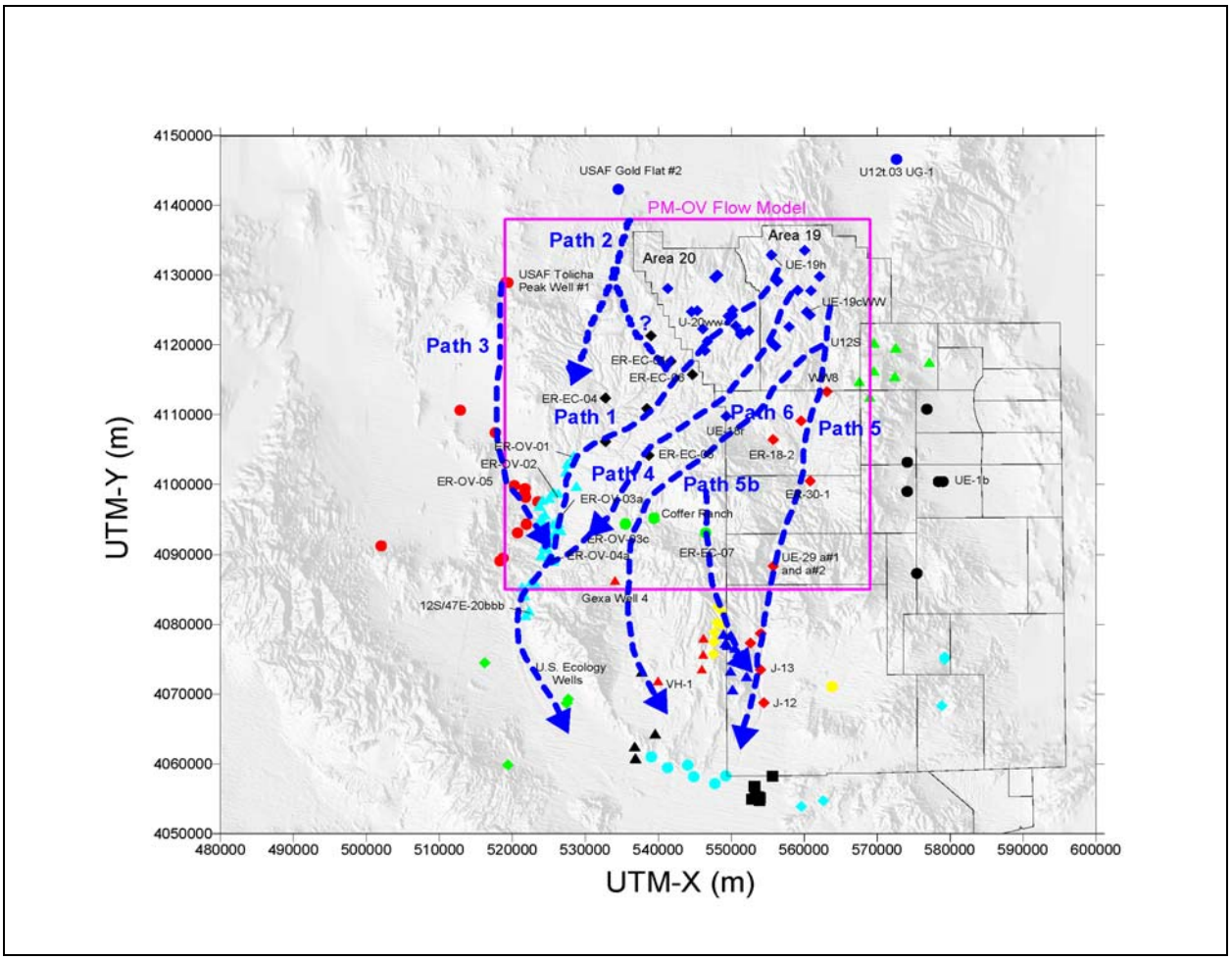

Figure 7-5
Flow Paths Estimated by Kwicklis et al. (2005) Based on Mixing Models

7.1.2 Reverse-Particle-Tracking Method

To compare the calibrated flow models with the mixing compositions quantitatively, reverse-particle tracking is used to identify fractions of water from different geographic source locations that are found at the target wells. In the reverse-particle-tracking method, the flow field in a calibrated steady-state flow model is simply reversed so particles released at a well of interest move upgradient and eventually leave the model at locations where water actually enters the model as either recharge or boundary flow.

In FEHM, two different particle-tracking algorithms are available. They are (a) the residence time transfer function particle-tracking method, PTRK (Robinson, 2004), and (b) the conventional streamline-particle-tracking method, SPTR, which is based on the standard method of Pollock (1988).

Uncontrolled When Printed

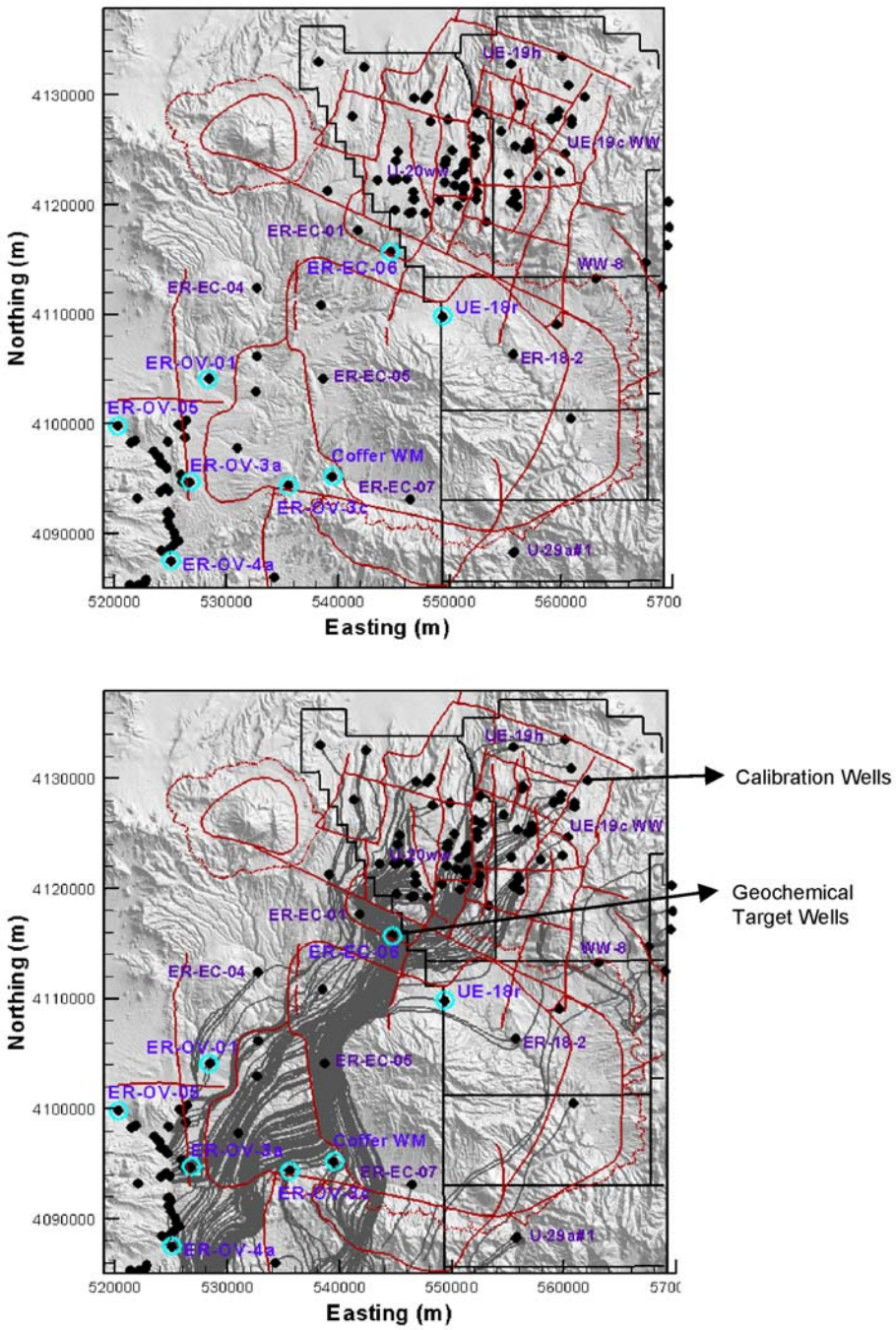

Figure 7-6
Locations of Flow Model Calibration Wells (black circles), Geochemical Target Wells (blue circles), and Pathlines for Forward SPTR Particles Originating in Open Screened Intervals of Wells in Model Domain

Uncontrolled When Printed

For mapping out the spatial origins of water in steady-state flow models, PTRK is used here due to its efficiency. In PTRK, particles simply move from cell to cell in proportion to the flux distribution across the different faces of the cell. Its efficiency comes from the algorithm in which no velocity interpolations are required. Thus, more particles can be simulated quickly with PTRK. The tradeoff is that lateral numerical dispersion is greater in PTRK than in SPTR due to the assumption of complete mixing in each cell. Whereas the SPTR method interpolates velocities within a cell to map out high-resolution pathways, the width of a PTRK pathway is no less than the width of a control volume in the model, and spreading occurs in all directions in which there is any flow out of a cell. However, for the purpose here of identifying the upgradient origin of groundwater in large geographic areas, that error is not considered to be of great importance. By contrast, the lateral dispersion associated with PTRK in a forward solute-transport simulation may not be acceptable because the point concentrations simulated at downstream wells of interest might be too dilute.

Figure 7-7 provides a comparison between the PTRK and SPTR particle-tracking models when used in reverse mode. This figure is particularly important because SPTR particles released from a small volume tend to find the diverse set of flow paths that converge and provide mixing at Well ER-OV-03a. Had all of the SPTR particles remained closely grouped together and exited the model in approximately the same location, there would have been greater cause for concern about the PTRK lateral dispersion. Instead, however, this comparison demonstrates that flow paths originating from geographically different upstream zones are identifiable. For the statistical comparison, PTRK is a more desirable methodology because 10 million particles can be easily tracked. As they spread to the different upstream source zones (see Section 7.1.3), a statistically significant number of particles are available for calculating the fractions originating in the different zones (Figure 7-1). Therefore, PTRK is used for all reverse transport modeling in Section 7.0.

7.1.3 Recharge and Inflow Zone Definitions

For comparison between the model results and the geochemical interpretations, groundwater source zones in the model domain are defined based on the location of the upgradient source wells used by Kwicklis et al. (2005). These groundwater source zones are used to bin the reverse-particle exit locations and calculate the fractions of groundwater at the target wells that originate in different areas of the model. These zones, listed in Table 7-1, are shown in Figure 7-1. Table 7-1 provides the

Uncontrolled When Printed

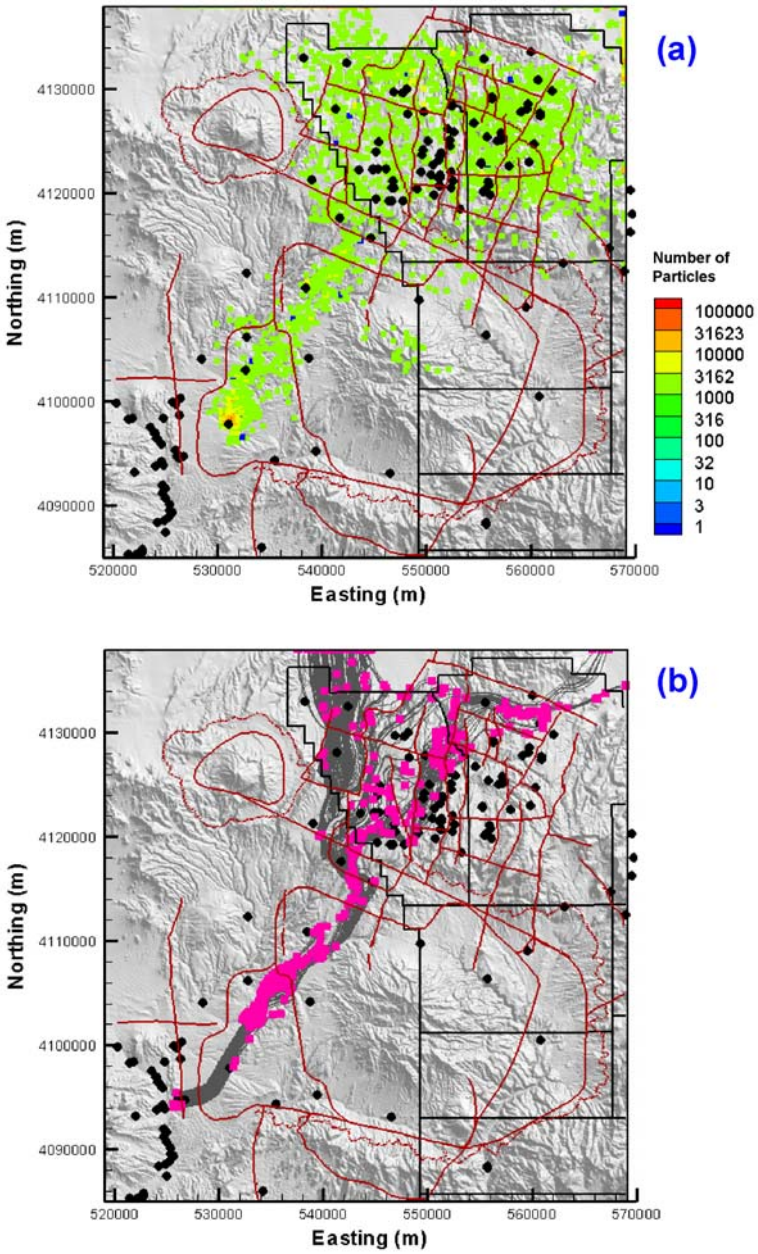

Figure 7-7
Comparison of Reverse PTRK and SPTR Particle-Tracking Methods for Particles Originating at Well ER-OV-03a

Figure (a) shows the exit locations and numbers (indicated by color scale) for 10 million PTRK particles. Figure (b) shows the reverse SPTR paths (grey lines) and exit locations (red squares) for 1,000 SPTR particles. The SPTR simulation is conducted with no dispersion. Black circles in both figures are wells in the domain.

Uncontrolled When Printed

Table 7-1
Spatial Association of Geochemistry Source Wells

Zone	ID Letter	Geochemistry Well	Model Zone
Northwest	A	ER-EC-1, Tolicha Peak, ER-EC-4	1, 7, 18
Recharge-washes	B	Local Recharge	17, 4
Recharge - TM	B	ER-EC-7	5
North Central	C	U-20 WW	2,8
Northeast	D	UE-18r, UE-19h, UE-19c WW, Cedar Pass	3,9
Southeast	E	WW-8	6,12
East (boundary flow)	E	WW-8	10
East (TM)	F	ER-18-2	16

spatial correlation between upstream source wells used in the geochemistry analysis and the recharge and boundary zones used in the reverse-particle-tracking simulations.

7.1.4 Method for Comparing Model Results to Targets

7.1.4.1 Comparison Zones

Starting with a calibrated steady-state flow model, the flow field is reversed and 10 million particles are released at the node or nodes representing the open interval of UE-18r, ER-EC-6, ER-OV-04a, ER-OV-05, ER-OV-01, ER-OV-03a, ER-OV-03c, and Coffer Windmill Well (a separate run is done for each well). The particles move upgradient and then leave the flow system. The number of particles exiting each zone, as identified in Figure 7-1 and Table 7-1, is documented for each simulation. These are then used to compute the mixing ratios by dividing the number of particles leaving each zone by 10 million. The model zones through which particles leave are combined, per Table 7-1, to represent eight geographic source zones. A few items in Table 7-1 require additional clarification. First, the geochemistry at ER-EC-1 and Tolicha Peak are different (Kwicklis et al., 2005), indicating that inflow across the northern boundary for this model domain is different from recharge in the northwest quadrant of the model domain. The purpose of the A grouping is to identify waters that are entirely different from those entering the model domain as recharge to the east of the Purse Fault, which is why they are grouped as such. Second, the Cedar Pass well source water is grouped in D. The actual flow path from Cedar Pass into the model domain is not known, particularly

Uncontrolled When Printed

whether it enters to the east or west of the Purse Fault intersection with the northern boundary. As will be shown later, this issue only applies at one of the nine target wells, ER-OV-01, and is relatively minor there. Comparisons between the model results and the mixing source wells are then made graphically as described below.

7.1.4.2 Explanation of Comparison Plots

For each target well in each flow field, a plot of the form in Figure 7-8 is created. The vertical lines represent the range of uncertainty in the fraction of groundwater from the indicated upgradient well that is present at the target well, as calculated by the geochemical model. The upgradient wells are grouped by geographic location (Table 7-1) and are color coded in the legend of the plots. For example, the northwest source zone can be represented by water types from ER-EC-1, Tolicha Peak, and/or ER-EC-4. In the model, the northwest source zone is represented by Zones 1 and 7. For each of the model zones, the symbol on the legend facilitates comparison with source wells. Thus, ER-EC-1, Tolicha Peak, and ER-EC-4 are followed by the model symbol for northwest source of groundwater (A), and so on for the other zones.

When multiple wells are present within a single source zone, the process of determining the geochemical ranges is somewhat more complicated. For the case where two source wells fall within the same zone, the target range is determined as the minimum and maximum of the combined fractions of the two wells in all plausible PHREEQC models. Figure 7-9 shows the 16 plausible mixing models developed for this example. The blue line shows the sum of NW1 and NW2 waters for each model. The range for the NW zone, then, is defined as the minimum and maximum values on the blue curve. In the comparison figure (b), the total possible range of all wells in this zone (0.14 to 0.37) is represented by adjacent lines for the individual wells, but each line spans the entire range.

7.2 Geochemical Verification Results for BN-MME-SDA

This section compares the base model results with the geochemistry mixing targets. The base model includes the BN HFM, the MME recharge map selected HSU depth decay and anisotropy, and lateral boundary fluxes from the regional model calibrated with the MME recharge map over the entire region (Section 4.2). This section provides a template for geochemical comparison results associated

Uncontrolled When Printed

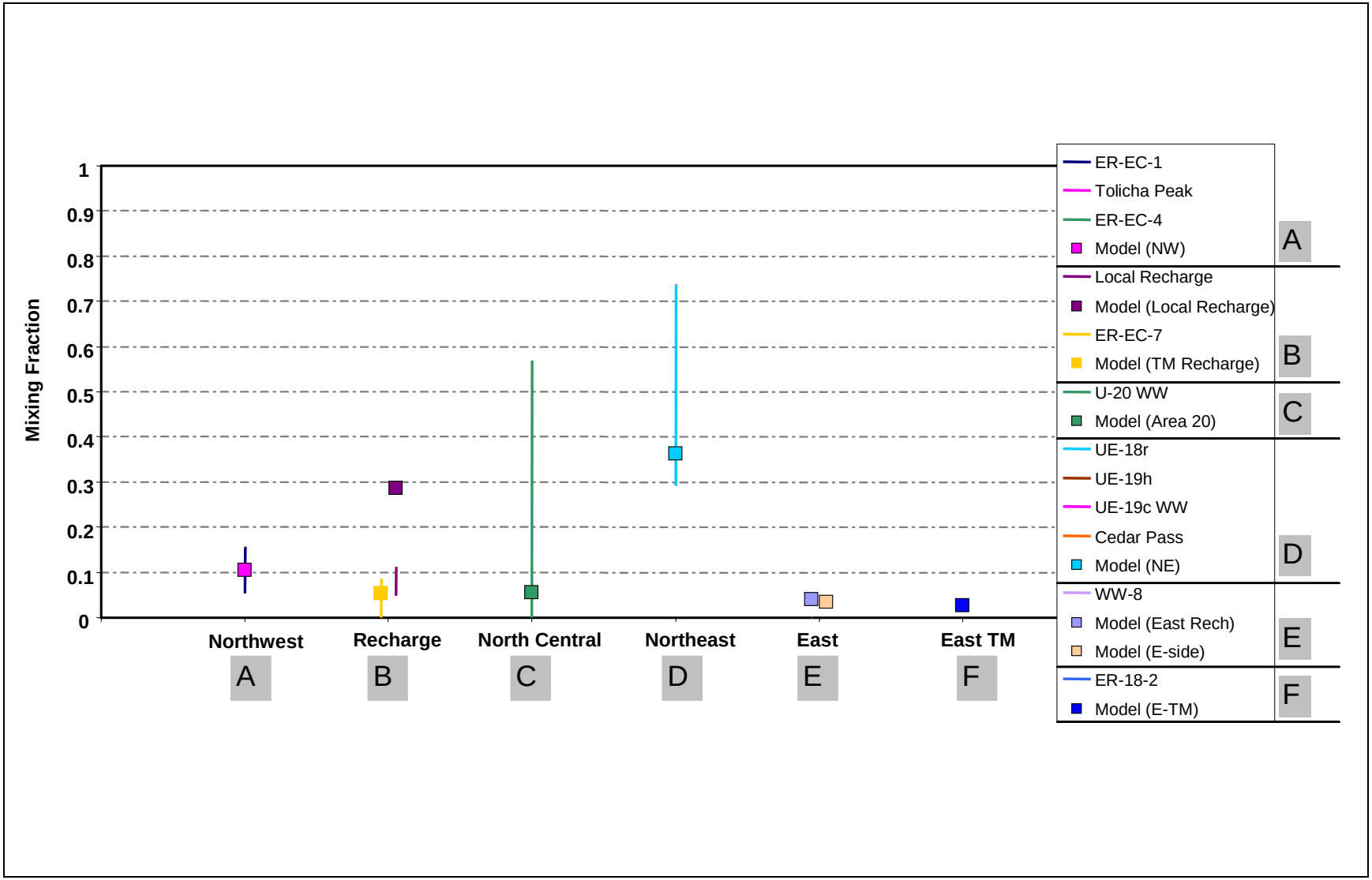

Figure 7-8
Example of Geochemistry Comparison Plot

Vertical lines represent mixing target uncertainties, and symbols represent model results.

Uncontrolled When Printed

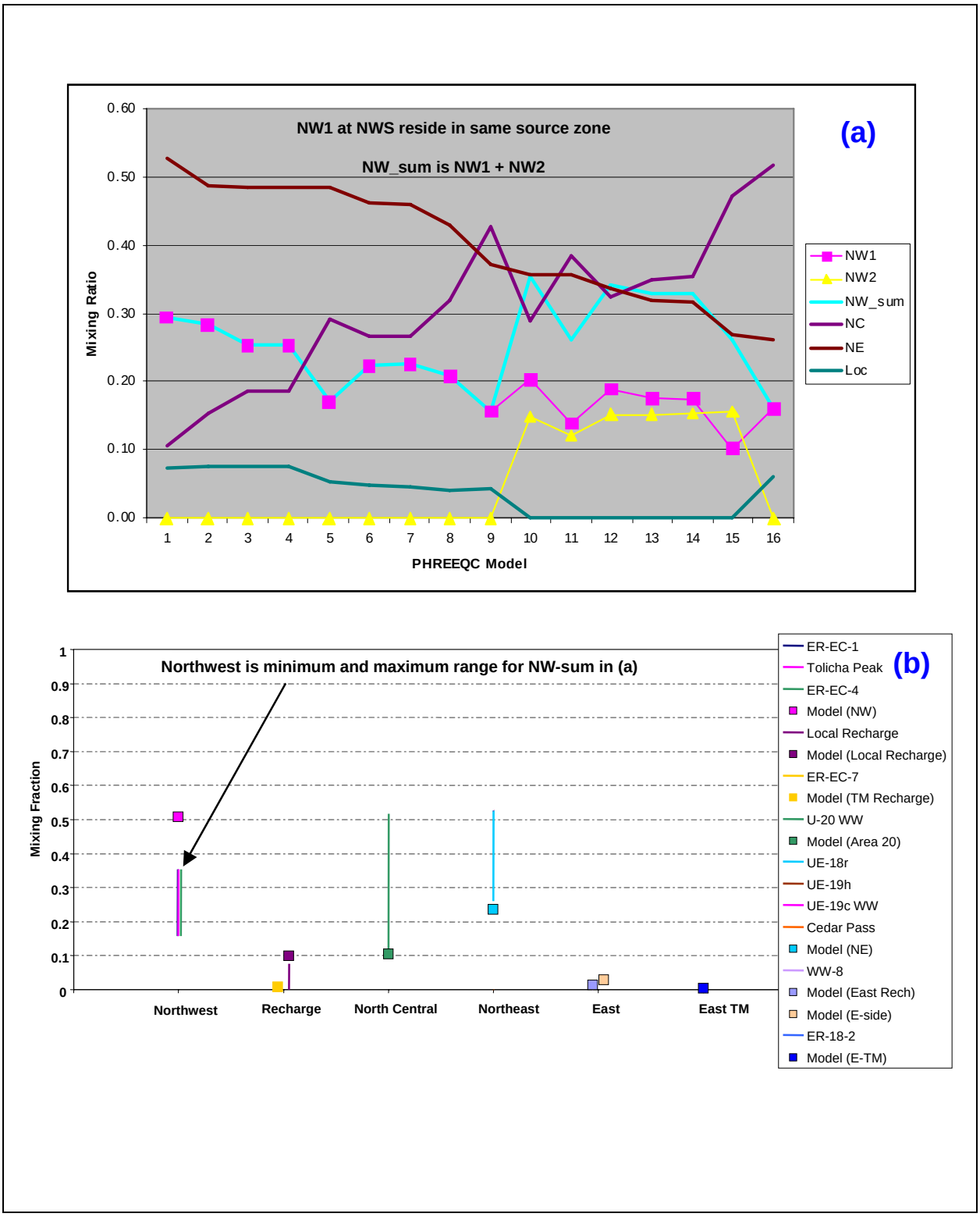

Figure 7-9
Example of PHREEQC and PTRK Results Comparison

Figure (a) shows 16 PHREEQC model results for mixing at a well. Figure (b) shows PTRK results.

Uncontrolled When Printed

with alternative HFMs and alternative recharge maps as listed in Table 6-1. Figure 7-6 shows the pathlines of particles originating at wells in the model domain as well as the locations and identities of the eight wells at which comparisons are made. The comparisons are made for target wells in the following order: UE-18r, ER-EC-6, ER-OV-05, ER-OV-01, ER-OV-03a, ER-OV-04a, ER-OV-03c, and Coffer Windmill Well. The sequence follows a somewhat counterclockwise path around Timber Mountain, sampling the different pathways described by Kwicklis et al. (2005).

7.2.1 UE-18r

Sitting just north of Timber Mountain, possible modeled source locations for water at UE-18r are from Areas 19 and 20 of Pahute Mesa, from Timber Mountain, and from the flow into the model across the eastern boundary. Figure 7-10 shows the flow paths for the BN-MME-SDA with forward particle paths (SPTR) colored in grey and the source locations for water at this well identified by reverse-particle-tracking (PTRK) exit densities (colored symbols), and the comparison between the model and the geochemistry mixing targets (b), developed from the data in Table 7-2. The two parts of this figure need to be considered together. The reverse-particle-tracking simulation shows a high density of particle exit locations in red along the eastern model boundary. In fact, in this model, 85 percent of all reverse PTRK particles originating at UE-18r leave the model along the eastern model boundary, as is shown in (b). In contrast, the geochemical interpretation (Table 7-2) suggests that most water at UE-18r is similar to that of the Area 19 wells with a small component resembling water in ER-18-2.

7.2.1.1 Simulated Rainier Mesa Recharge at UE-18r

This comparison raises the question of whether flow across the eastern model boundary at Gold Meadows Stock (near the water table) could be geochemically similar to the Area 19 wells. Kwicklis et al. (2005) determined that WW-8 type water and HTH-1-type water are not possible at UE-18r. Their analysis shows a small component of ER-18-2 water at UE-18r, but that ER-18-2 water indicates a source of old, deep origin, possibly from the regional carbonate aquifer. It does not represent local recharge as might occur in upper Fortymile Canyon (Kwicklis et al., 2005). Therefore, there is no geochemical evidence that would suggest the feasibility of shallow groundwater flow from Rainier Mesa recharge arriving at UE-18r.

Uncontrolled When Printed

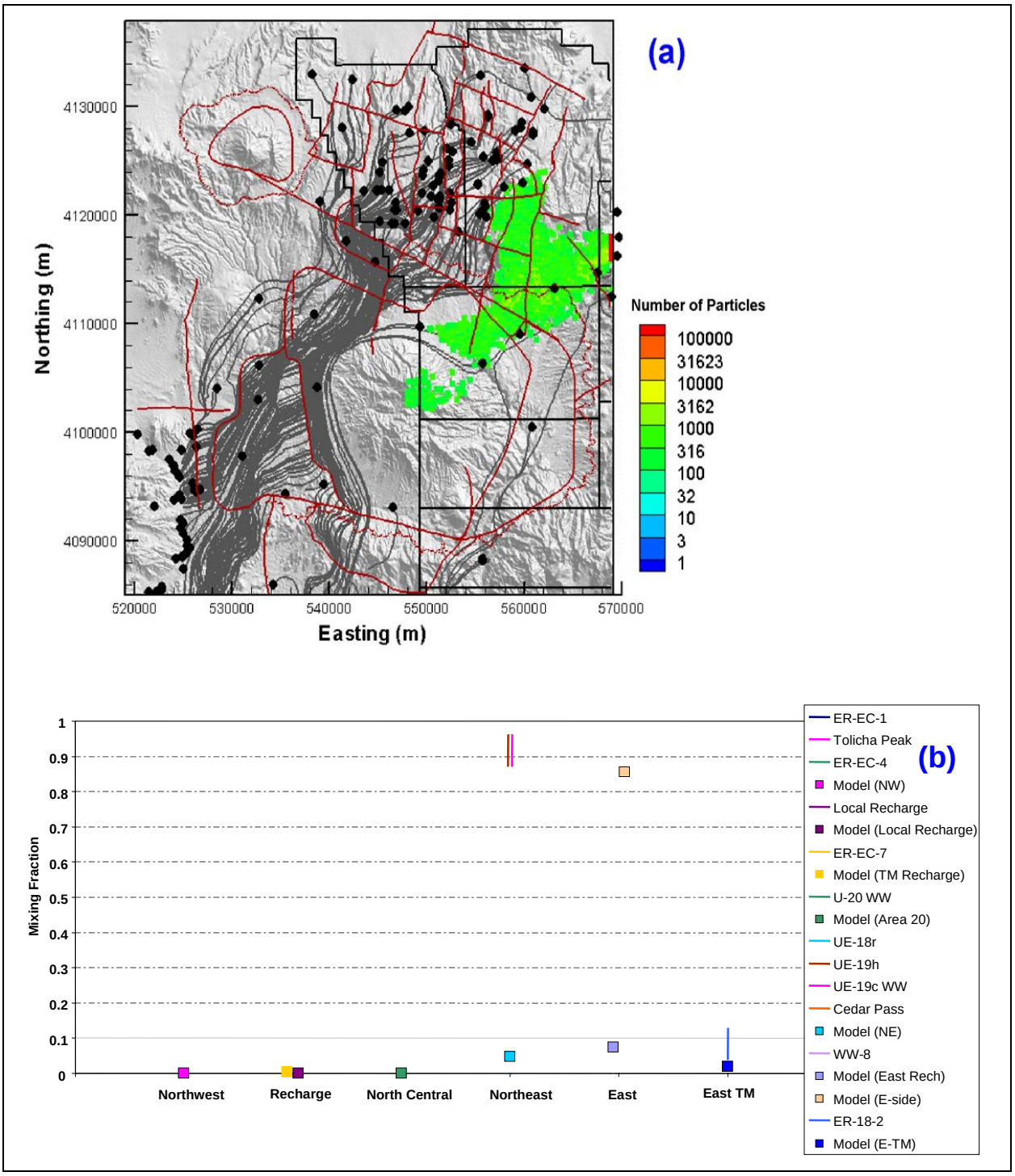

Figure 7-10
Comparison of Flow Model with Geochemical Mixing Targets at UE-18r for BN-MME-SDA

Figure (a) shows the flow paths as mapped by forward SPTR particles originating at wells (grey lines) and the source recharge locations identified by reverse PTRK particle tracking (colored squares). Figure (b) shows the model comparison with geochemical mixing target ranges.

Uncontrolled When Printed

Table 7-2
Fractions of Groundwater from Various Upgradient Wells Present in Groundwater at Well UE-18r

Mixing Component	Minimum Fraction	Maximum Fraction
ER-18-2	0.087	0.122
ER-EC-7	0.000	0.000
WW-8	0.000	0.000
Test Well #1	0.000	0.000
UE-19h	0.370	0.429
UE-19c WW	0.484	0.543

Note: Shallow groundwater from Well UE-29a #2 was used to represent local recharge from ephemeral surface runoff. Groundwater from ER-EC-7 was used to represent recharge from infiltration at Timber Mountain. See Kwicklis et al. (2005) for discussion of uncertainty tolerances and rock water reactions for the calculations represented in this specific table.

In some of the model simulations, highly localized, large flows across the eastern boundary at Gold Meadows near the water table are clearly due to the high fixed boundary heads at Gold Meadows coupled with relatively large calibrated LCCU1 permeabilities (see Sections 6.2 and 6.2.4.4). With a high boundary head and a high-permeability conduit, it is not surprising that significant simulated flow enters the model domain at this location. These flows do not adversely affect the head and flux calibrations, but they do result in unsupportable geochemical sources at UE-18r. Thus, this analysis serves to identify and quantify this error, as discussed in Section 7-5.

7.2.1.2 BN-MME-SDA Reduced LCCU1 Permeability Alternative

In the first alternative model, the LCCU1 permeability was fixed at about one order of magnitude lower than in the base case before recalibration of other HSU permeabilities, resulting in substantially less flow across the eastern boundary at Gold Meadows. For comparison, Figure 7-11 shows the reverse-particle-tracking simulation and the zone comparison to the geochemistry mixing targets for the BN-MME-SDA with reduced LCCU1 permeability alternative (described in Section 6.2.4.4). In this model, the reverse particles from UE-18r leave the system within the model domain in areas of high recharge in Area 19. Approximately 60 percent of the water at UE-18r originates within the northeast quadrant of the flow model domain in this simulation, but to the southeast of Wells UE-19h and UE-19c WW. In the absence of groundwater chemistry data in the area where the simulated recharge occurs (southeastern Area 19), it is assumed that the groundwater chemical composition is

Uncontrolled When Printed

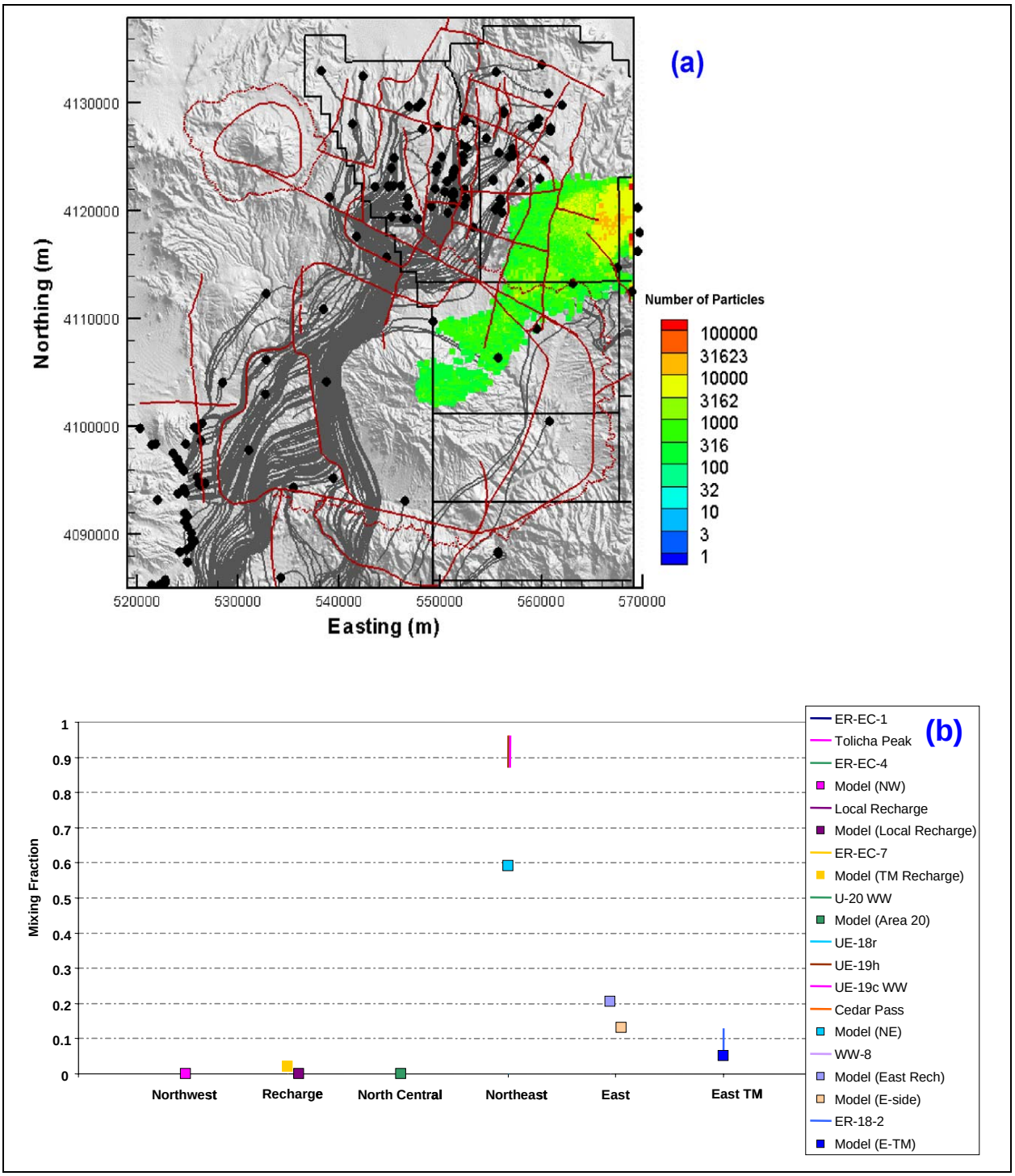

Figure 7-11
Comparison of Flow Model with Geochemical Mixing Targets at UE-18r in the Reduced LCCU1 Permeability Alternative

Figure (a) shows the flow paths as mapped by forward SPTR particles originating at wells (grey lines) and the source recharge locations identified by reverse PTRK particle tracking (colored squares). Figure (b) shows the model comparison with geochemical mixing target ranges.

Uncontrolled When Printed

similar to that of UE-19h and UE-19c WW. Further, Kwicklis et al. (2005) do not distinguish whether the source water identified by UE-19h and UE-19c WW originates as recharge within the model domain or as flow across the model boundary from the north. Another 20 percent of the mixed water (East) originates in Zone 6 (Figure 7-1). From Figure 7-11, it is clear that this component is all recharge from the northernmost portion of Zone 6, which may not be geochemically distinguishable from Zone 3. Also 13 percent (rather than 85 percent as in the base case, BN-MME-SDA) of the water at UE-18r in this model comes across the model boundary from the Gold Meadows. For comparison, Figure 7-12 shows the reverse-particle exit locations along the eastern boundary for the BN-MME-SDA and reduced LCCU1 permeability alternative models. Significantly more particles exit the eastern model boundary along a very short zone at the water table in the HSU LCCU1 in (a) compared to (b). It is important to note that the water in UE-18r does not resemble the water in WW-8 (Kwicklis et al., 2005), which could be along potential pathways from Rainier Mesa to UE-18r.

The geochemistry indicates that at UE-18r, there should be between 4 and 13 percent water with a signature like that found in ER-18-2. In the reduced LCCU1 permeability simulation, 5 percent of water found in UE-18r originates in Zone 16. However, considering that ER-18-2 water resembles deep, old groundwater rather than local recharge, the spatial correlation of BN-MME-SDA reduced LCCU1 permeability alternative particle exit locations to ER-18-2 is not significant. In the original BN-MME-SDA simulation, virtually no water originates from Zone 16. Further, the water entering the model as flow across the east boundary is shallow and therefore would not resemble ER-18-2 water.

7.2.1.3 UE-18r Summary

Summarizing the UE-18r comparison, the geochemistry indicates that most of the water should originate in the northeast with a small component resembling a deep source found in ER-18-2 on the east flank of Timber Mountain. The reduced LCCU1 permeability alternative simulations are consistent with this interpretation, whereas the BN-MME-SDA simulations are plagued with large volumes of flow into the model from Gold Meadows. The source of the water arriving at UE-18r in the reduced LCCU1 permeability alternative is consistent with specified boundary conditions on the model. Namely, the MME recharge prescribes a zone of high recharge where the source of the

Uncontrolled When Printed

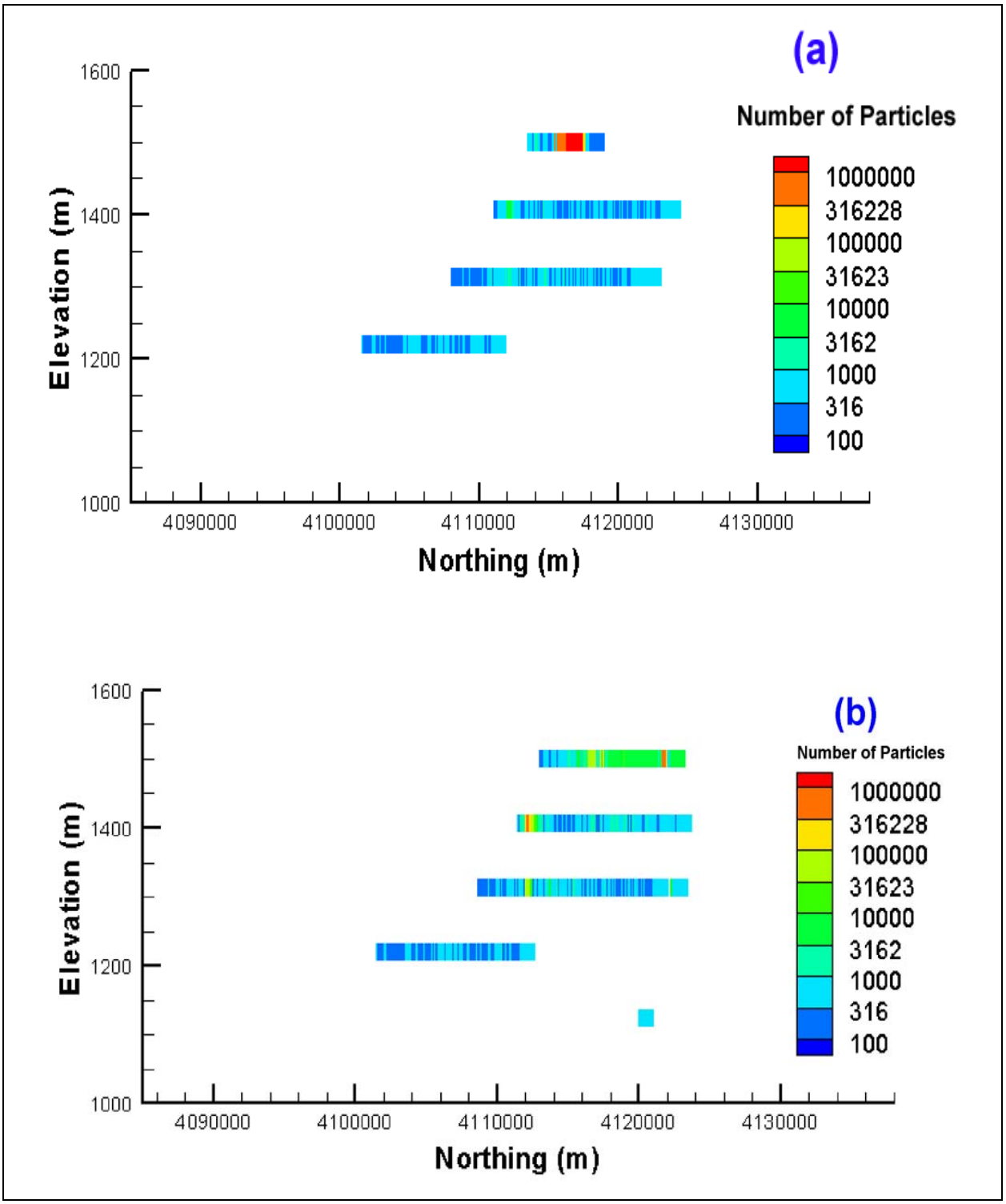

Figure 7-12
Particle Exit Locations on Model East Face for (a) BN-MME-SDA and (b) for BN-MME-SDA Reduced LCCU1 Permeability Alternative

Note the high density of exiting particles in (a) occurs within the LCCU1 HSU.

Uncontrolled When Printed

majority of water arriving at UE-18r is identified (Area 19 recharge zones). The combination of recharge occurring in Zones 3 and 6 is approximately in the range of Area 19-type water implied by the geochemistry. Kwicklis et al. (2005) do not distinguish whether the source water identified by UE-19h and UE-19c WW originates as recharge within the model domain or as flow across the model boundary from the north. The 13 percent of flow across the eastern boundary results from the boundary conditions reflecting the regionally high head at Gold Meadows Stock and, hence, large gradient into the Pahute Mesa CAU flow model domain, but is significantly less than the 85 percent flow from the east in BN-MME-SDA due to reduced LCCU1 permeability in this alternative.

7.2.2 ER-EC-6

Moving counterclockwise around Timber Mountain and away from the eastern boundary, the differences between BN-MME-SDA results and the reduced LCCU1 permeability alternative become far less differentiable; results for the two models are often nearly indistinguishable.

Well ER-EC-6 is just south of the termination of the Purse Fault; possible source locations for water at ER-EC-6 are from areas north on either side of the Purse Fault. The geochemistries of water from these two different zones are distinctly different (Kwicklis et al., 2005). The simulated flow paths in this region of the model domain are very complex as flow paths from the northwest and northeast converge in upper Thirsty Canyon (Figures 7-13 and 7-14).

The geochemical interpretation (Table 7-3) suggests that there should be approximately equal ratios of water from either side of the Purse Fault mixing at ER-EC-6. By comparison, the simulation results in Figures 7-13 and 7-14 for BN-MME-SDA and the reduced LCCU1 permeability alternative show that between 80 and 90 percent of the water source at ER-EC-6 is from west of the Purse Fault (although the plan view figures show approximately equal distribution of recharge from either side of the fault (a), most of the source water at ER-EC-6 is simulated to have originated as inflow along the northern boundary, which cannot be seen in the plan view).

The discrepancy between either of the flow model results and the geochemistry interpretation must be considered with regard to the structure of the flow paths at ER-EC-6. In this area, significant convergence of flow for highly different source areas occurs, as indicated by the geochemistry. In the model, at the exact location of ER-EC-6, most of the water is arriving from the northwest. However,

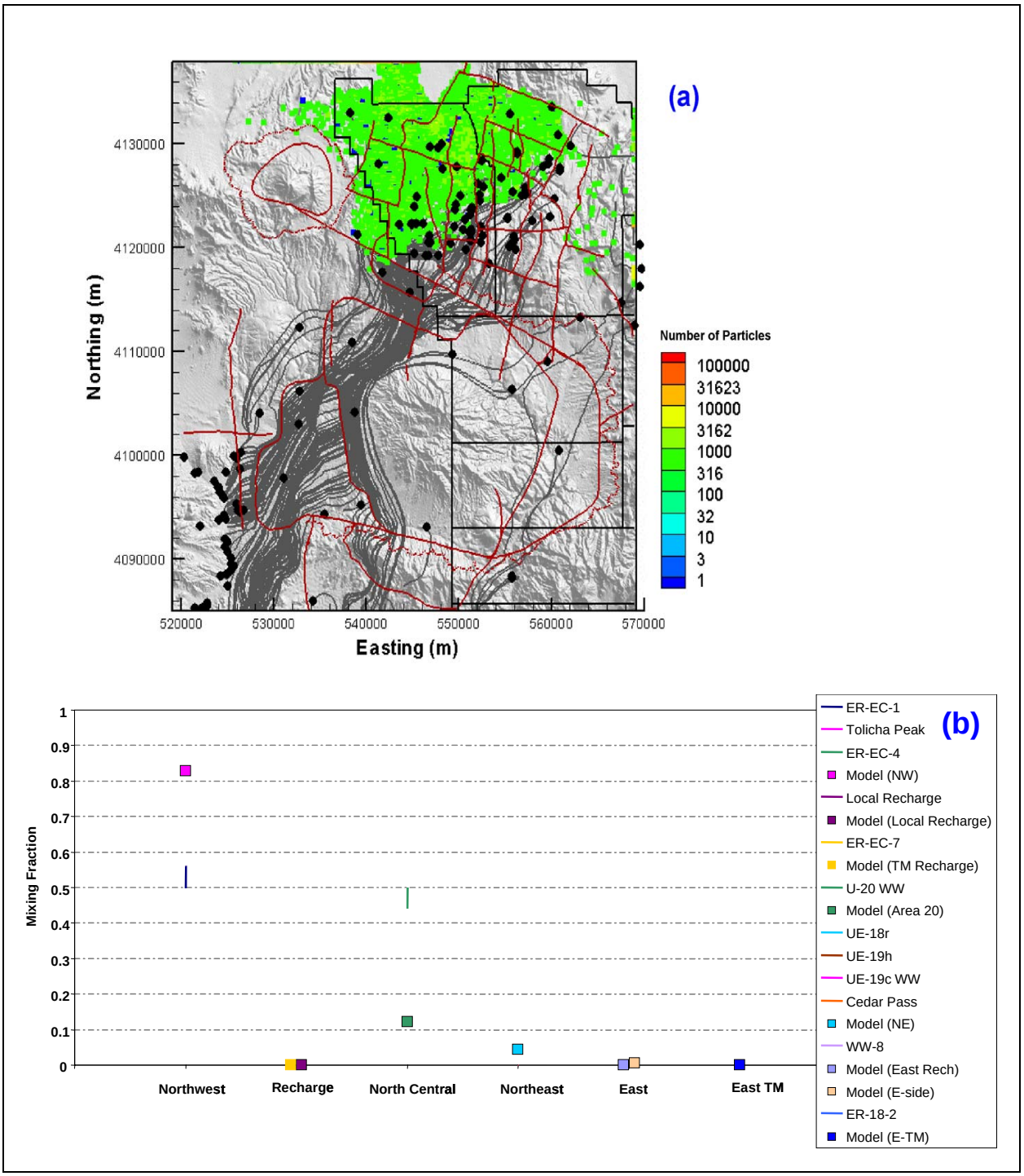

Figure 7-13
Comparison of Flow Model with Geochemical Mixing Targets at ER-EC-6 for BN-MME-SDA

Figure (a) shows the flow paths as mapped by forward SPTR particles originating at wells (grey lines) and the source recharge locations identified by reverse PTRK particle tracking (colored squares). Figure (b) shows the model comparison with geochemical mixing target ranges.

Uncontrolled When Printed

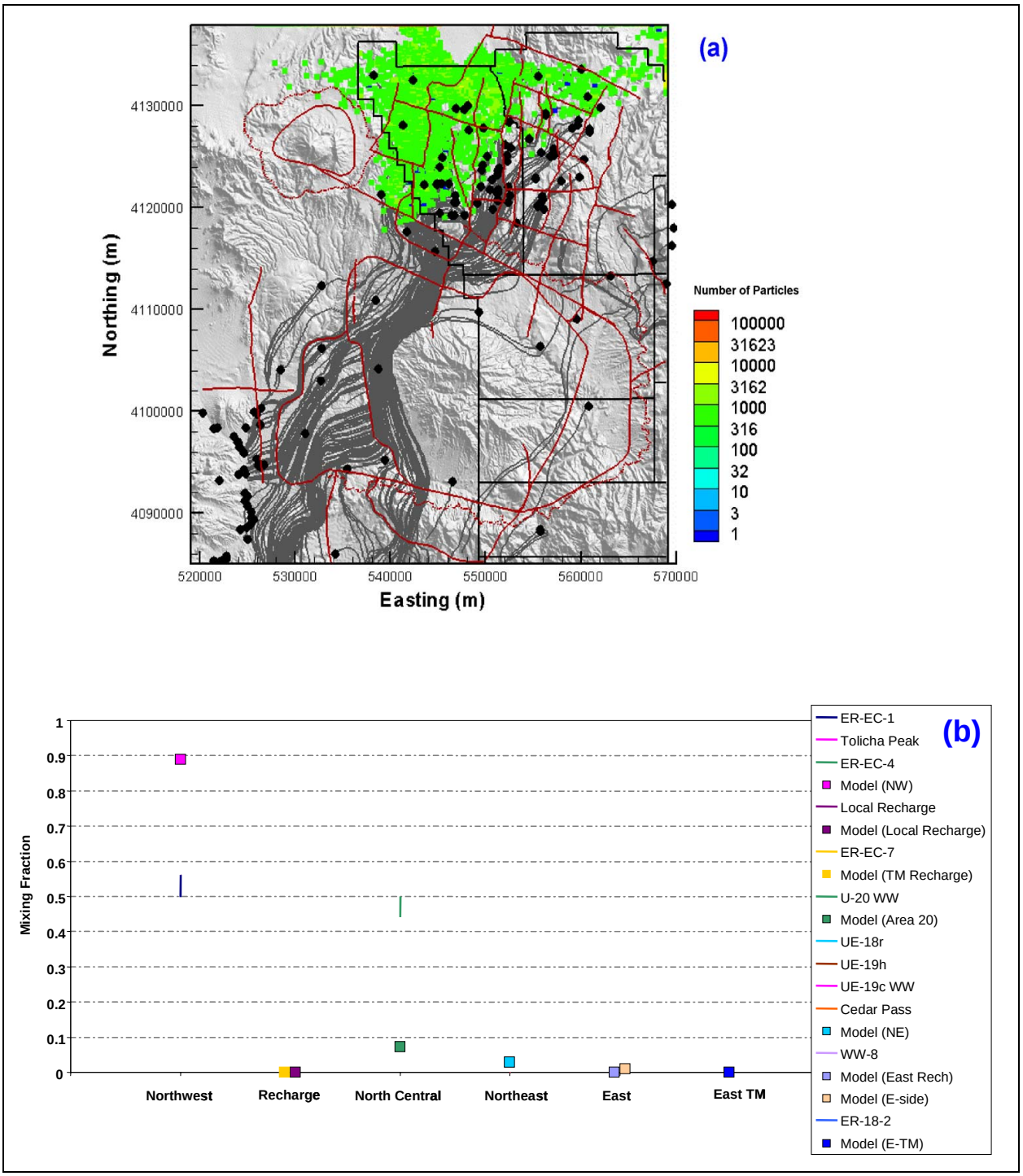

Figure 7-14
Comparison of Flow Model with Geochemical Mixing Targets at ER-EC-6 in the Reduced LCCU1 Permeability Alternative

Figure (a) shows the flow paths as mapped by forward SPTR particles originating at wells (grey lines) and the source recharge locations identified by reverse PTRK particle tracking (colored squares). Figure (b) shows the model comparison with geochemical mixing target ranges.

Uncontrolled When Printed

Table 7-3
Fractions of Groundwater from Various Upgradient Wells Present in Groundwater at Well ER-EC-6

Mixing Component	Minimum Fraction	Maximum Fraction
ER-EC-1	0.498	0.561
U-20 WW	0.440	0.502
UE-19h	0.000	0.000
Cedar Pass Well	0.000	0.000
UE-29a #2	0.000	0.000

Table 6 from Kwicklis et al. (2005). Note: Belted Range Aquifer minerals from Table 2 were used for this set of models. Shallow groundwater from Well UE-29a #2 was used to represent local recharge.

the figure shows that only a short distance to the east of ER-EC-6, the flow paths from the northeast enter this zone of convergence in upper Thirsty Canyon. Thus, although the quantitative comparison has discrepancies, the trend of the modeled flow paths and the geochemically inferred mixing are consistent.

A second explanation for the large ratio of northwest source water at ER-EC-6 in the simulations may be related to the no-flow conditions on the northern half of the western boundary. Eliminating the ability of water entering the system on the northern boundary from exiting on the western boundary could lead to translated flow paths to east. This explanation may hold for the mixing at ER-OV-01 as well.

This analysis highlights an additional consideration: Does too much water enter the model domain on the western half of the northern boundary? Data controls (basically nil) in this portion of the domain are not as good as to the east of the Purse Fault. If the head and subsequent gradient on the western northern boundary were lower, then inflow on that boundary would be less, and more flow from the northeast would mix at ER-EC-6. However, lowering the northern boundary heads would result in much poorer matches to internal model heads at wells west of the Purse Fault such as PM-2 and PM-3.

Uncontrolled When Printed

7.2.3 ER-OV-01

Well ER-OV-01 is in the transition zone from lower Thirsty Canyon into upper Oasis Valley. This is the target well where Cedar Pass Well source water plays a role in comparing the model results with the geochemical mixing targets. As mentioned previously, Cedar Pass Well source water is lumped with the other sources in the northeast, rather than the inflows from the northwest. Given how the source zones were defined, it is actually not clear whether water with Cedar Pass Well chemistry enters the model domain as inflow to the east or west of the Purse Fault. However, because there are greater differences in water chemistry between Cedar Pass and ER-EC-1 than UE-19h, Cedar Pass-type water inflows have been included with those coming into the model east of the Purse Fault. Well ER-OV-01 is the only target well where this distinction matters. For the analyses of ER-OV-01 water in this section, the Cedar Pass contribution (0 to 0.308) in the geochemical mixing targets is included with northeast waters for comparison with the model results. However, it can also be considered in the comparison with northwest source water. As will be shown later, the impact of this assignment on the comparisons is minor relative to other distinguishing differences for the different calibrated flow models.

The northwest contribution could be between 35 and 60 percent, the north-central component between 25 and 55 percent, and the northeast component as much as 30 percent (assuming Cedar Pass water can be associated with this zone). There is also a small contribution from local recharge of up to 6 percent. These target ranges are derived from Table 7-4. The model results for both BN-MME-SDA and the LCCU1 alternative show about a 60/40 split of source water between the northwest quadrant and recharge in Thirsty Canyon, with virtually no source water from the north-central or northeast zones (Figures 7-15 and 7-16). As with ER-EC-6 for these flow models, the flow paths from Areas 20 and 19 east of the Purse Fault do not extend quite as far west as the well. In these simulations, the impact of flow (or lack of flow) across the eastern boundary at Gold Meadows is not evident at this well dominated by northwestern flows.

One reason the northeast and north-central flow paths do not intersect this well in the simulation is that local recharge in Thirsty Canyon pushes those flow paths southeast, as shown in Figure 7-16. In the simulations, more than 30 percent of the source water at ER-OV-01 originates as recharge in Thirsty Canyon. However, the geochemical interpretation (Kwicklis et al., 2005) indicates that less than 10 percent of the water in the ER-OV-01 samples should be from local recharge. Considering

Uncontrolled When Printed

Table 7-4
Fractions of Groundwater from Various Upgradient Wells Present in Groundwater at Well ER-OV-01

Mixing Component	Minimum Fraction	Maximum Fraction
USAF Tolicha Peak #1	0.000	0.163
ER-EC-4	0.000	0.198
ER-EC-1	0.274	0.523
U-20 WW	0.242	0.468
Cedar Pass Well	0.000	0.308
UE-29 a #2	0.000	0.062

Table 22 from Kwicklis et al. (2005). Note: Paintbrush Aquifer minerals from Table 2 (Kwicklis et al., 2005) were used for this set of models. Shallow groundwater from Well UE-29 a #2 was used to represent local recharge. Minimum and maximum mixing fractions for Wells ER-EC-1 and U-20 WW were calculated by multiplying the minimum and maximum fractions of groundwater from these wells at ER-EC-6 (Table 6 in Kwicklis et al., 2005) by the minimum and maximum fractions of groundwater from Well ER-EC-6 at Well ER-OV-01 (Table 5 in Kwicklis et al., 2005).

the Thirsty Canyon recharge as shown in the flux map used in these base-case simulations (Figure 4-14), the fraction of local recharge at ER-OV-01 in the simulations is not surprising.

Another reason the northeast flow paths do not intersect ER-OV-01 may be due to the no-flow conditions on the northern half of the western boundary. That condition may force flow paths from the north to effectively push paths from the northeast away from this well. Finally, had Cedar Pass Well water been used in the target for northwest rather than northeast water, the differences between model and targets would have been slightly different. The model results would have been within range for northwest water, where they are slightly higher now. And, the northeast model results would be good because they are zero. However, this difference is relatively small and does not play a significant role in the model comparisons later in Section 7.3.3. Also, these models still underpredict flow from the north-central zone.

Summarizing the comparison, simulated flow paths from north-central and northeastern Pahute Mesa are east of ER-OV-01. The flow paths come close, but are pushed to the southeast by local recharge in Thirsty Canyon and possibly by high flow into the model along the western half of the northern boundary as indicated in the ER-EC-6 analysis. Qualitatively, the flow paths match those estimated from the geochemistry well, but quantitatively, the well is at least several kilometers west of the flow paths originating in eastern Area 20 and Area 19.

Uncontrolled When Printed

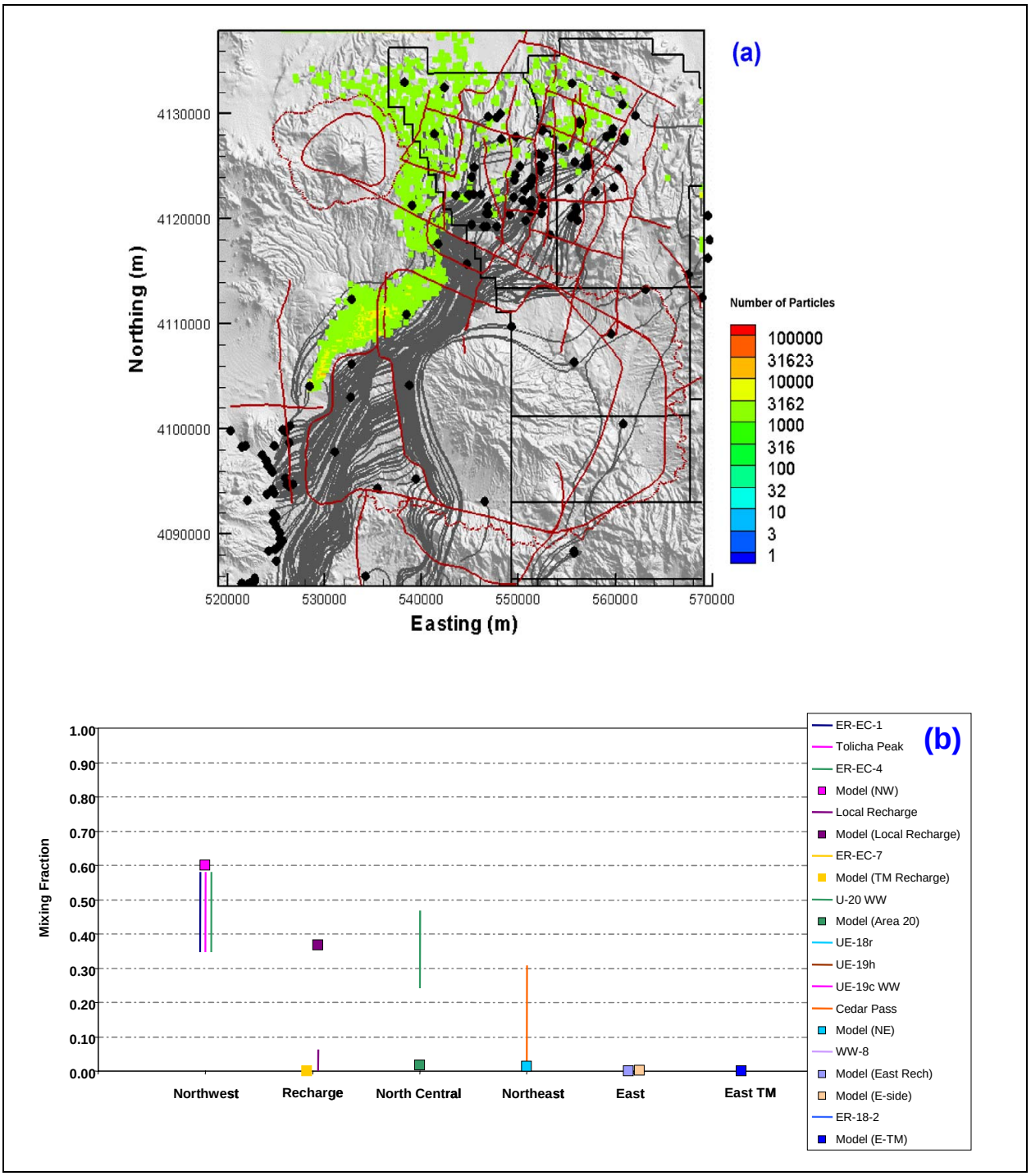

Figure 7-15
Comparison of Flow Model with Geochemical Mixing Targets at ER-OV-01 for BN-MME-SDA

Figure (a) shows the flow paths as mapped by forward SPTR particles originating at wells (grey lines) and the source recharge locations identified by reverse PTRK particle tracking (colored squares). Figure (b) shows the model comparison with geochemical mixing target ranges.

Uncontrolled When Printed

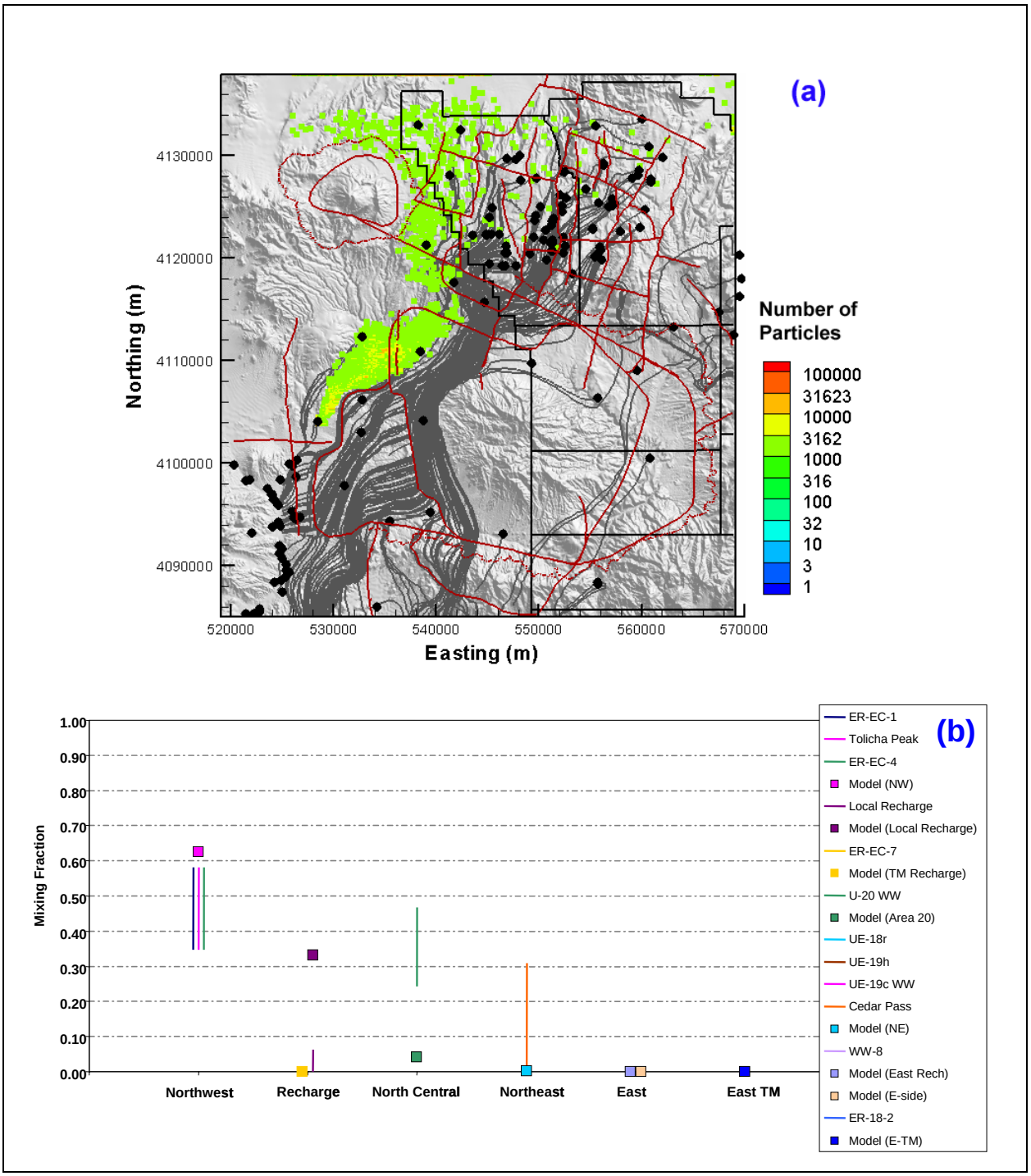

Figure 7-16
Comparison of Flow Model with Geochemical Mixing Targets at ER-OV-01 in the Reduced LCCU1 Permeability Alternative

Figure (a) shows the flow paths as mapped by forward SPTR particles originating at wells (grey lines) and the source recharge locations identified by reverse PTRK particle tracking (colored squares). Figure (b) shows the model comparison with geochemical mixing target ranges.

Uncontrolled When Printed

7.2.4 ER-OV-05

Well ER-OV-05 is in Oasis Valley near the western boundary of the model. The geochemistry and flow model simulations are consistent with each other, indicating the source of water found at the well is entirely from the northwest quadrant of the model domain (Table 7-5; Figures 7-17 and 7-18).

Table 7-5
Fractions of Groundwater from Various Upgradient Wells Present in Groundwater at Well ER-OV-05

Mixing Component	Model 2 Mean (Min, Max)
USAF Tolicha Peak	0.720 (0.717, 0.726)
Cedar Pass Well	0.000
ER-EC-4	0.280 (0.274, 0.283)
UE-29a #2	0.000

Table 7 from Kwicklis et al. (2005). Note: To obtain convergent models for this set of wells, it was necessary to increase the uncertainty tolerance on aluminum to 0.0001 moles/L or approximately 2.6 mg/L. Belted Range aquifer minerals from Table 2 were used for this set of models. Shallow groundwater from Well UE-29a #2 was used to represent local recharge. Only Model 2 from Kwicklis et al. (2005) is considered here. Model 1 is less certain due to the Cedar Pass water component, which cannot be accurately assigned to a specific zone in this domain. However, if it is assumed that Cedar Pass water enters this model domain on the western half of the northern boundary, then the two models are virtually identical.

There is virtually no difference between BN-MME-SDA and the LCCU1 alternative. It is interesting to note that the water of Tolicha Peak well and ER-OV-05 are nearly identical in chemical composition. In the geochemical mixing model, this water is also nearly a perfect mix of local recharge-type water (UE-29a #2) and ER-EC-1 water. Thus, this suggests an even split of local recharge in the northwest and flow into the model across the western half of the northern boundary.

7.2.5 ER-OV-04a

The geochemistry of ER-OV-04a, south and a little east of ER-OV-05, indicates a reduced component of the source originating in the northwest and increasing components from the north-central and northeast zones (Table 7-6). The BN-MME-SDA and the reduced LCCU1 permeability alternative flow model simulations follow this trend, as shown in Figures 7-19 and 7-20.

In the BN-MME-SDA model, the simulated northwest component is just slightly above its target, and the simulated fractions of the mixed water from the north central and northeast are at the low ends of the ranges suggested by the geochemistry. Most interesting is that there is a 9 percent contribution

Uncontrolled When Printed

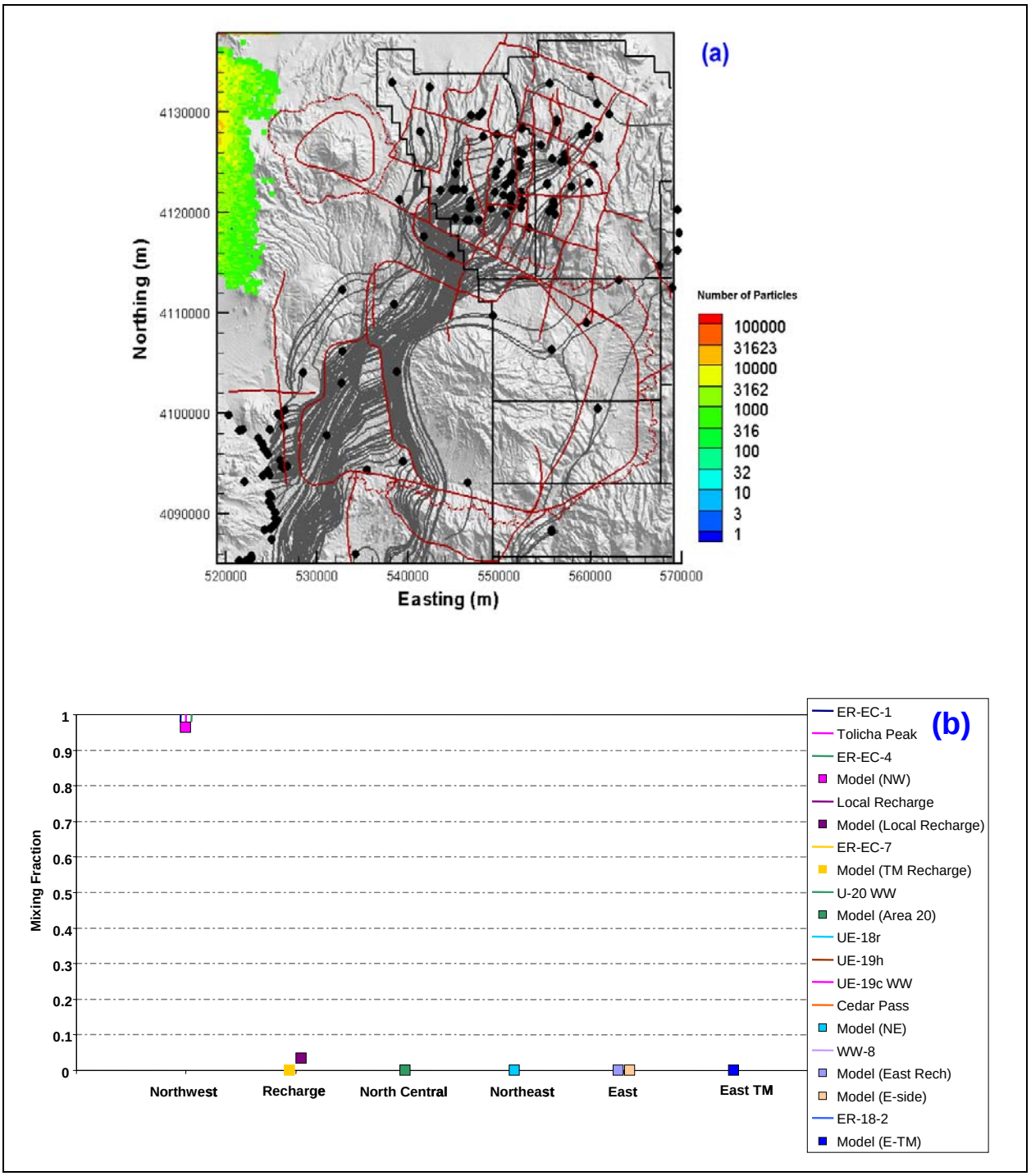

Figure 7-17
Comparison of Flow Model with Geochemical Mixing Targets at ER-OV-05 for BN-MME-SDA

Figure (a) shows the flow paths as mapped by forward SPTR particles originating at wells (grey lines) and the source recharge locations identified by reverse PTRK particle tracking (colored squares). Figure (b) shows the model comparison with geochemical mixing target ranges.

Uncontrolled When Printed

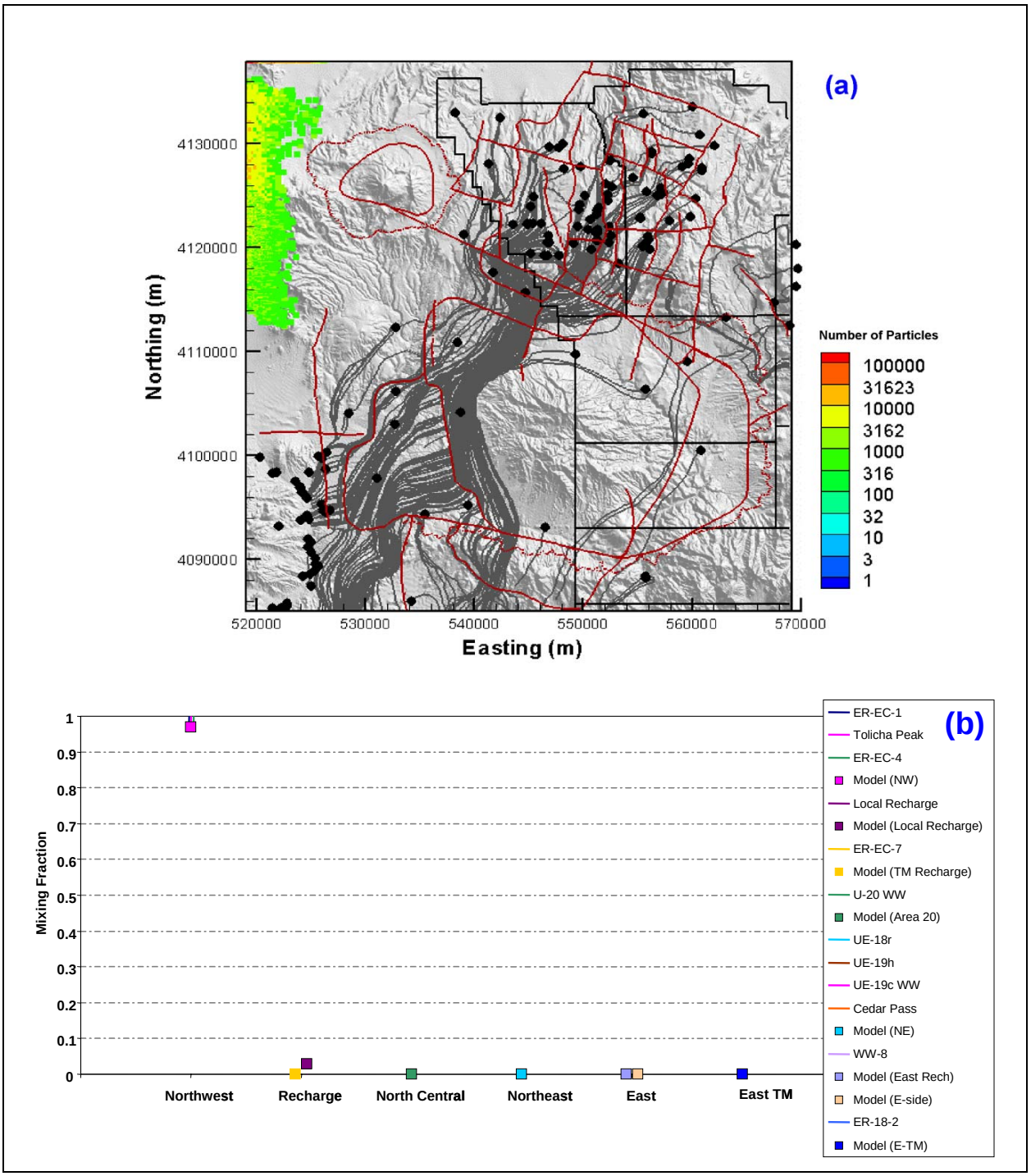

Figure 7-18
Comparison of Flow Model with Geochemical Mixing Targets at ER-OV-05 in the Reduced LCCU1 Permeability Alternative

Figure (a) shows the flow paths as mapped by forward SPTR particles originating at wells (grey lines) and the source recharge locations identified by reverse PTRK particle tracking (colored squares). Figure (b) shows the model comparison with geochemical mixing target ranges.

Uncontrolled When Printed

Table 7-6
Fractions of Groundwater from Various Upgradient Wells Present in Groundwater at Well ER-OV-04a

Mixing Component	Minimum Fraction	Maximum Fraction
U-20 WW	0.219	0.419
ER-EC-1	0.145	0.253
UE-18r	0.280	0.455
USAF Tolicha Peak	0.000	0.113
Cedar Pass Well	0.000	0.071
ER-EC-4	0.000	0.070
UE-29a #2	0.000	0.129

Table 23 from Kwicklis et al. (2005). Note: Timber Mountain Aquifer minerals from Table 2 were used for this set of models. Shallow groundwater from Well UE-29a #2 was used to represent local recharge. Note that the minimum fractions for the components from USAF Tolicha Peak, Cedar Pass and ER-EC-4 wells were determined by noting that the minimum contribution from Well ER-OV-05 in Table 13 is 0.00. The maximum component for these wells in Table 22 was determined by multiplying their maximum contributions in Table 7 by the maximum ER-OV-05 component in Table 13 (0.156). The UE-29a #2 contribution in Table 13 was augmented by 0.076 based on similar reasoning.

from inflow across the eastern boundary. Figure 7-19 shows that this inflow comes into the model at the high boundary head zone at Gold Meadows. Thus, the inflow that dominated the UE-18r water type in the base-case model is now showing up again in the southwest portion of the domain.

In the reduced LCCU1 permeability alternative, the low LCCU1 permeability reduces inflow to the model on the eastern boundary at Gold Meadows. The result at ER-OV-04a, by comparison to BN-MME-SDA results, is that there is a slight increase in northwest inflow contribution to the mixing ratio and a reduction in east boundary inflow. Comparison of Figures 7-19 and 7-20 along the eastern boundary clearly shows the location of high inflow for the base model.

Considering the complexity of flow paths and distances from source zones, the trend for either model, as compared with ER-OV-05 and ER-OV-03a, is encouraging in that the flow model results tend to track the changes suggested by the geochemistry in different areas of the model domain.

7.2.6 ER-OV-03a

Well ER-OV-03a is in lower Beatty Wash, east of ER-OV-03a, north of ER-OV-04a, and east of ER-OV-05; relative to groundwater at ER-OV-05, its source water as estimated by Kwicklis et al.

Uncontrolled When Printed

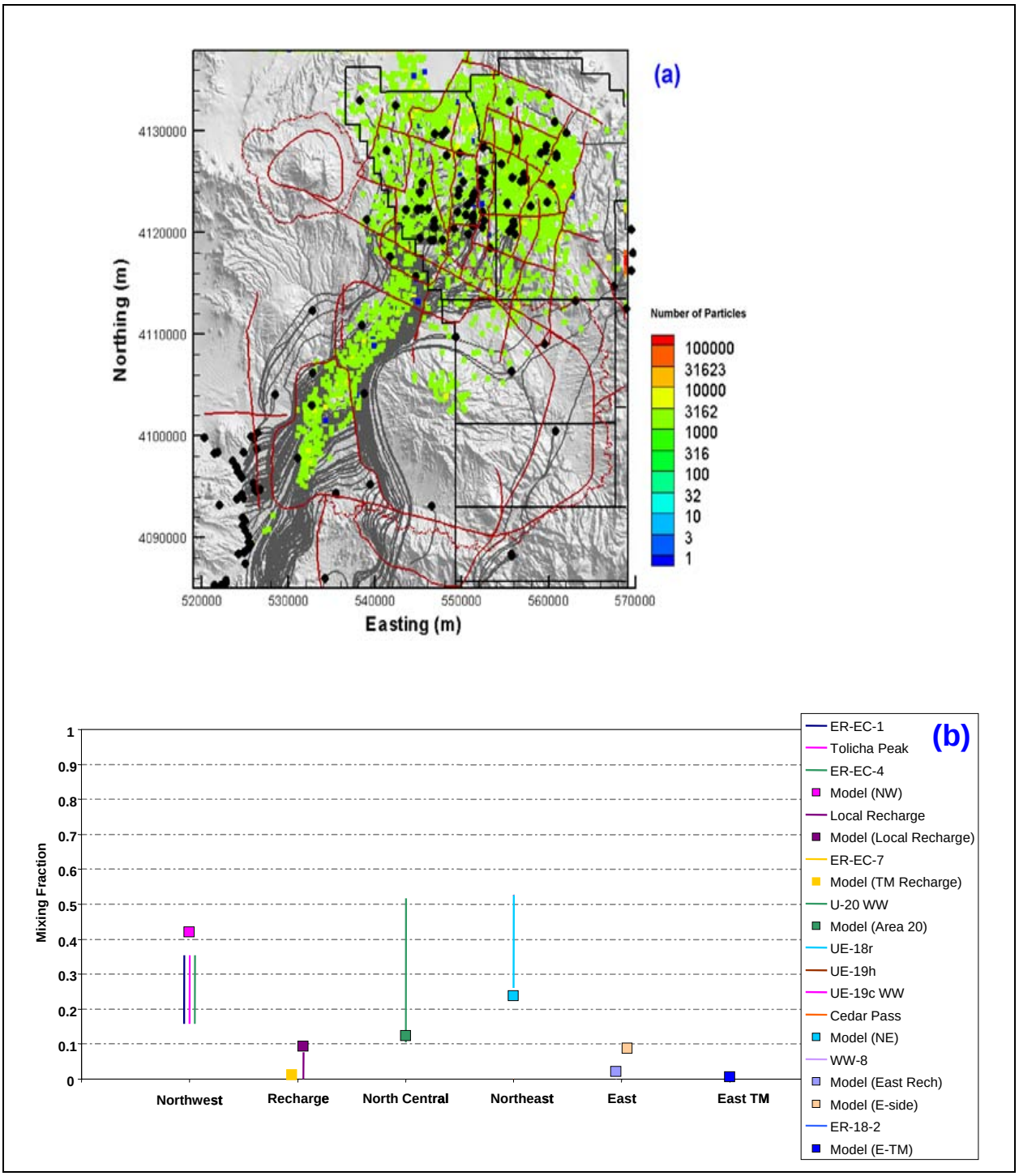

Figure 7-19
Comparison of Flow Model with Geochemical Mixing Targets at ER-OV-04a for BN-MME-SDA

Figure (a) shows the flow paths as mapped by forward SPTR particles originating at wells (grey lines) and the source recharge locations identified by reverse PTRK particle tracking (colored squares). Figure (b) shows the model comparison with geochemical mixing target ranges.

Uncontrolled When Printed

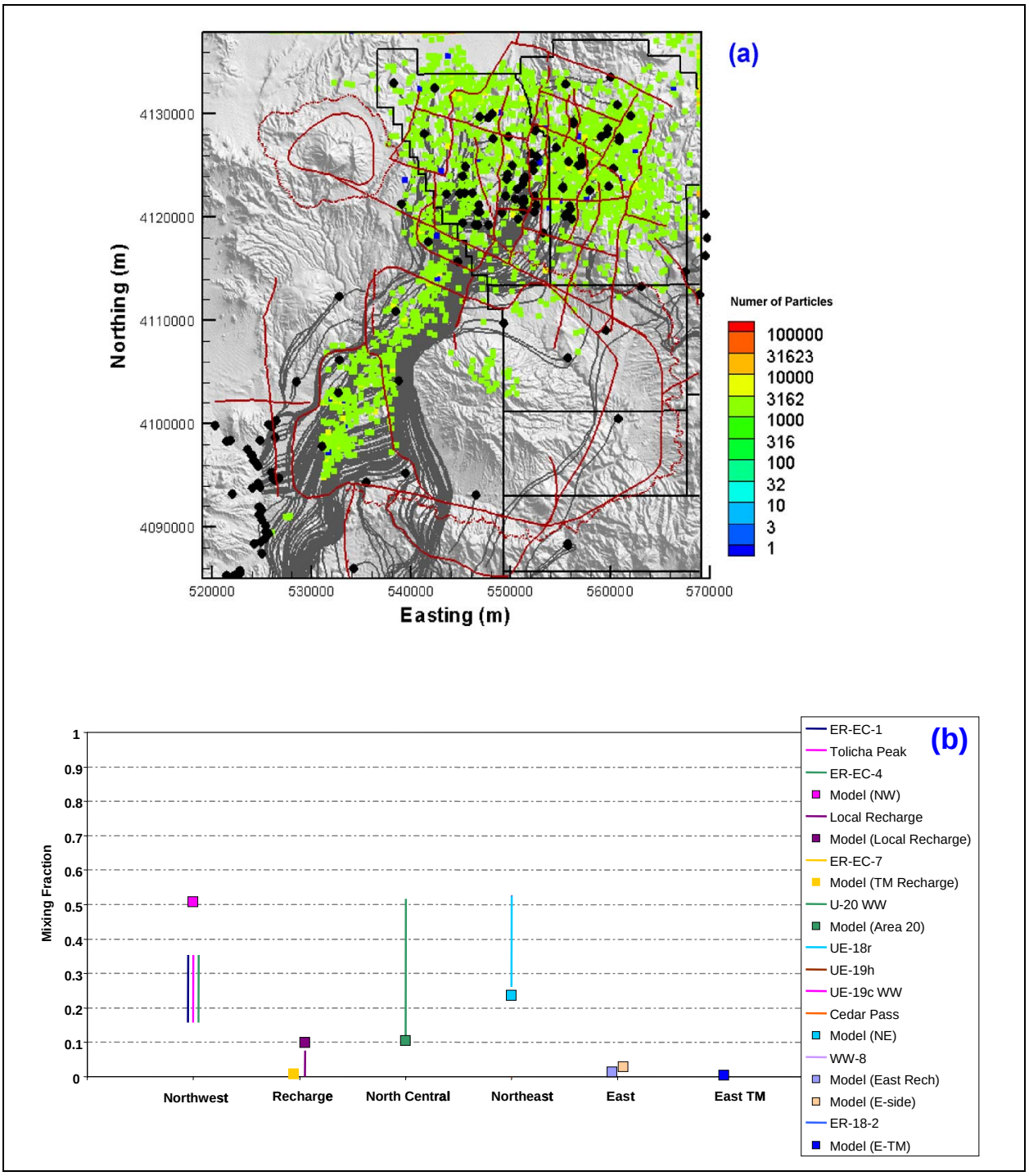

Figure 7-20
Comparison of Flow Model with Geochemical Mixing Targets at ER-OV-04a in the Reduced LCCU1 Permeability Alternative

Figure (a) shows the flow paths as mapped by forward SPTR particles originating at wells (grey lines) and the source recharge locations identified by reverse PTRK particle tracking (colored squares). Figure (b) shows the model comparison with geochemical mixing target ranges.

Uncontrolled When Printed

(2005) includes decreasing components from the northwest and increasing components from north-central and northeast Pahute Mesa (Table 7-7). The base-case flow model captures this change, with source fractions generally within the ranges estimated in the geochemistry analysis (Figure 7-21). As the source component from the northwest decreases in the simulations, the source component from the north-central and northeast zones increases. The only discrepancies between the flow model and the geochemistry for ER-OV-03a are that (a) the flow model estimates a slightly larger fraction of local recharge, as can be seen in the cluster of yellow exit counts in the reverse-particle-tracking figure, and (b) there is a small (less than 5 percent) contribution from the eastern model boundary at Gold Meadows. The component of recharge source is consistent with the specified local recharge flux in the MME map (Figure 4-14), and can be compared with results using different recharge maps later in this section. The east boundary source (Gold Meadows) is small but persistent and geochemically unexplainable.

Table 7-7
Fractions of Groundwater from Various Upgradient Wells Present in Groundwater at Well ER-OV-03a

Mixing Component	Minimum Fraction	Maximum Fraction
U-20 WW	0.000	0.482
UE-19h	0.145	0.648
ER-EC-1	0.289	0.469
UE-29a #2	0.000	0.081

Table 4 from Kwicklis et al. (2005). Note: Paintbrush Aquifer minerals from Table 2 were used for this set of models. Shallow groundwater from Well UE-29a #2 was used to represent local recharge.

The LCCU1 alternative (Figure 7-22) shows some interesting differences when compared to the base case. The small contribution from the eastern boundary to ER-OV-03a is gone in this model. Surprisingly, however, the northwest contribution has decreased, too, and the local recharge component has increased. This highlights the local and large-scale complexities in these simulated flow systems. With less inflow from the east in the LCCU1 alternative model, there is less westward flow to “push” local recharge away from ER-OV-03a, resulting in the increased local recharge component. Examination of the flow pathlines (grey) in the two figures shows the differences in flow direction relative to the same sources in these two models.

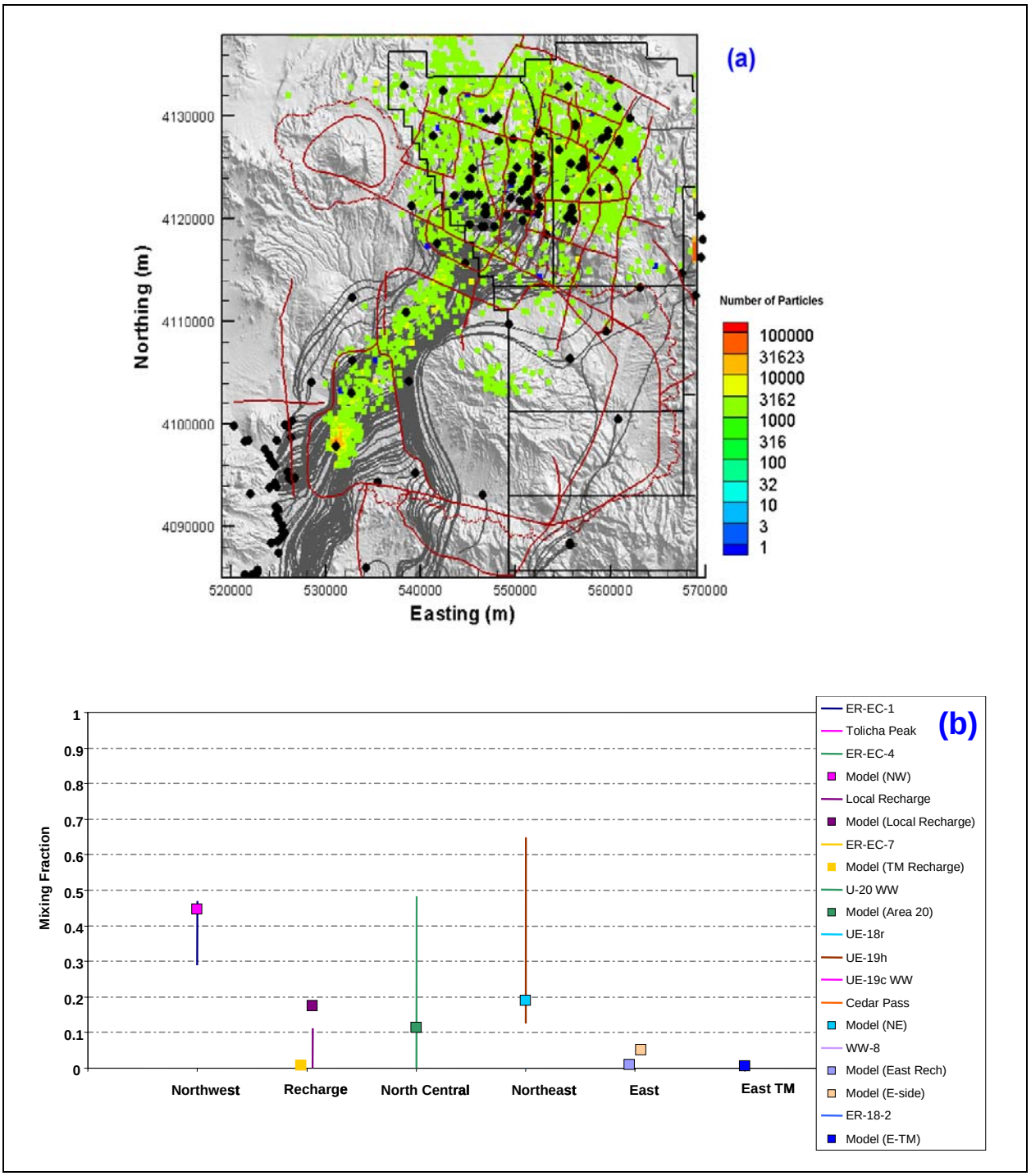

Figure 7-21
Comparison of Flow Model with Geochemical Mixing Targets at ER-OV-03a for BN-MME-SDA

Figure (a) shows the flow paths as mapped by forward SPTR particles originating at wells (grey lines) and the source recharge locations identified by reverse PTRK particle tracking (colored squares). Figure (b) shows the model comparison with geochemical mixing target ranges.

Uncontrolled When Printed

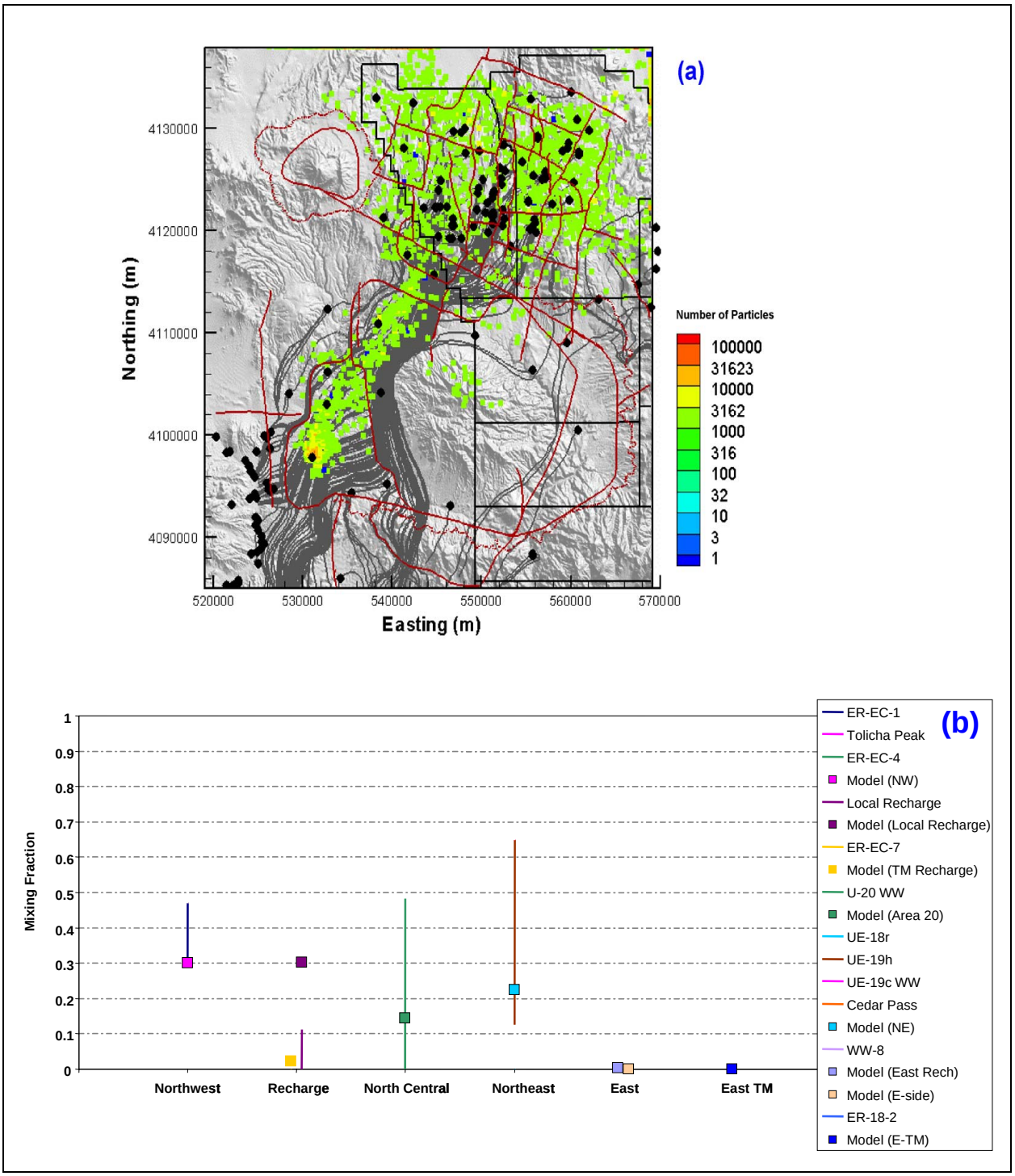

Figure 7-22
Comparison of Flow Model with Geochemical Mixing Targets at ER-OV-03a in the Reduced LCCU1 Permeability Alternative

Figure (a) shows the flow paths as mapped by forward SPTR particles originating at wells (grey lines) and the source recharge locations identified by reverse PTRK particle tracking (colored squares). Figure (b) shows the model comparison with geochemical mixing target ranges.

Uncontrolled When Printed

7.2.7 ER-OV-03c

Moving further east toward Timber Mountain, Well ER-OV-03c is in lower Beatty Wash. By comparison with the three previous wells, the geochemical analysis suggests a decreasing component of groundwater from the northwest, the appearance of a small amount of Timber Mountain recharge, some local recharge in the wash, and increasing source contributions from north-central and northeast Pahute Mesa (Table 7-8). As the geochemical interpretations indicate the presence of a larger groundwater component from the northeast, so does the simulation trend (Figure 7-23). However, the base-case model (a) substantially overpredicts local recharge from Beatty Wash, (b) underpredicts contributions from the northeast, and (c) has about a 15 percent contribution from the east boundary at Gold Meadows. With regard to (a), the model is consistent with the recharge map for this base case, which prescribes a considerable recharge flux into the model in the wash.

Table 7-8
Fractions of Groundwater from Various Upgradient Wells Present in Groundwater at Well ER-OV-03c, Including Sources for Groundwater at ER-EC-5

Mixing Component	Minimum Fraction	Maximum Fraction
ER-EC-1	0.054	0.157
U-20 WW	0.000	0.568
UE-18r	0.292	0.736
ER-EC-7	0.000	0.086
UE-29a #2	0.047	0.113

Table 11 from Kwicklis et al. (2005). Note: The uncertainty tolerance for aluminum was set to 0.00002 moles/kg or about 1 mg/L to reduce convergence problems. Timber Mountain aquifer minerals from Table 2 were used for this set of models. Shallow groundwater from Well UE-29a #2 was used to represent local recharge.

The reduced LCCU1 permeability alternative (Figure 7-24) shows good improvement on all three discrepancies listed for BN-MME-SDA listed above. The local recharge component is reduced from more than 40 percent to less than 30 percent. The northeast contribution increases to within the target range, and the east boundary contribution reduces to less than 3 percent. Further, the northwest component increases to the middle of the target range. Thus, for Well ER-EC-3c, the LCCU1 alternative appears to provide better matches to the targets than BN-MME-SDA.

Uncontrolled When Printed

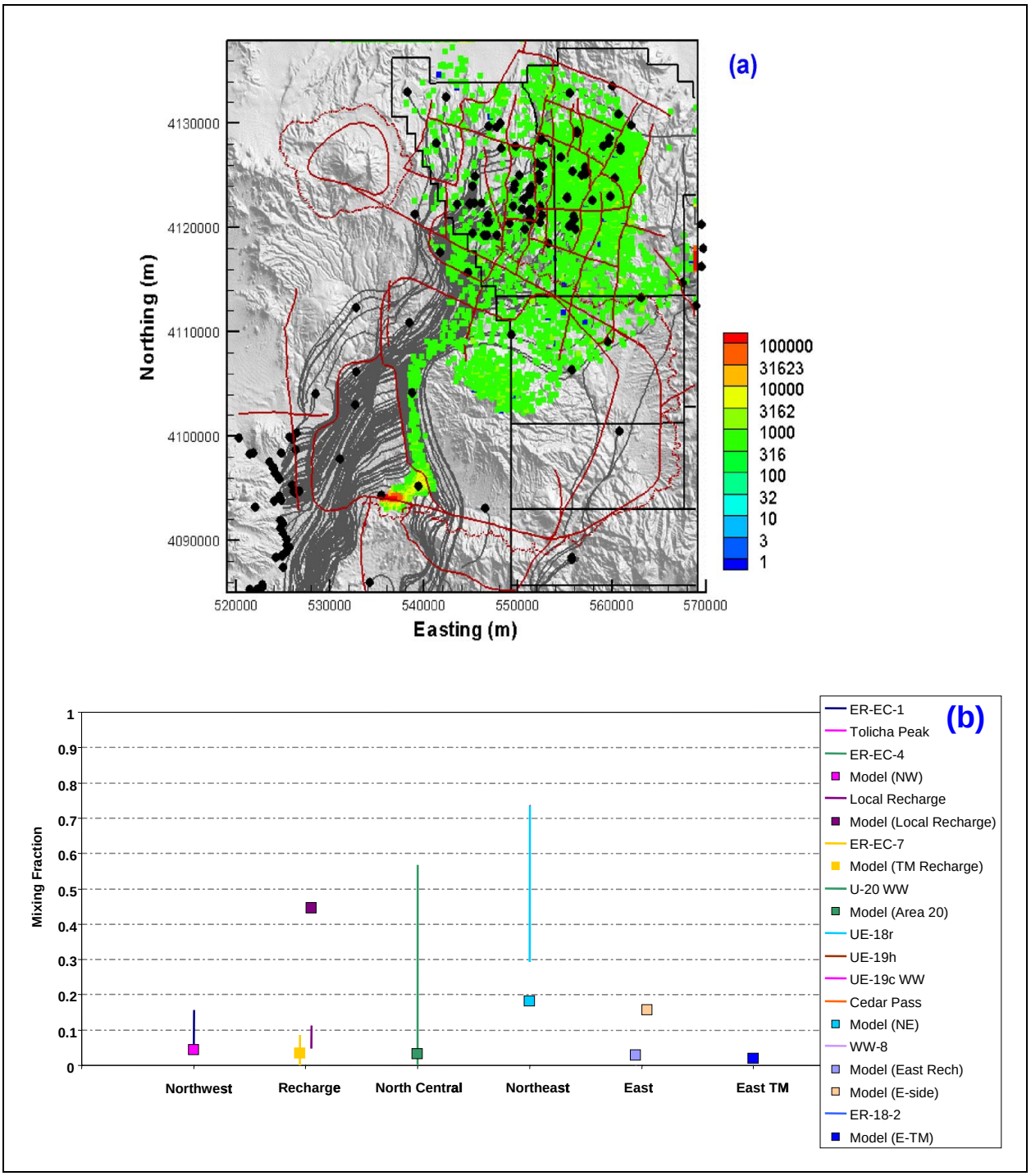

Figure 7-23
Comparison of Flow Model with Geochemical Mixing Targets at ER-OV-03c for BN-MME-SDA

Figure (a) shows the flow paths as mapped by forward SPTR particles originating at wells (grey lines) and the source recharge locations identified by reverse PTRK particle tracking (colored squares). Figure (b) shows the model comparison with geochemical mixing target ranges.

Uncontrolled When Printed

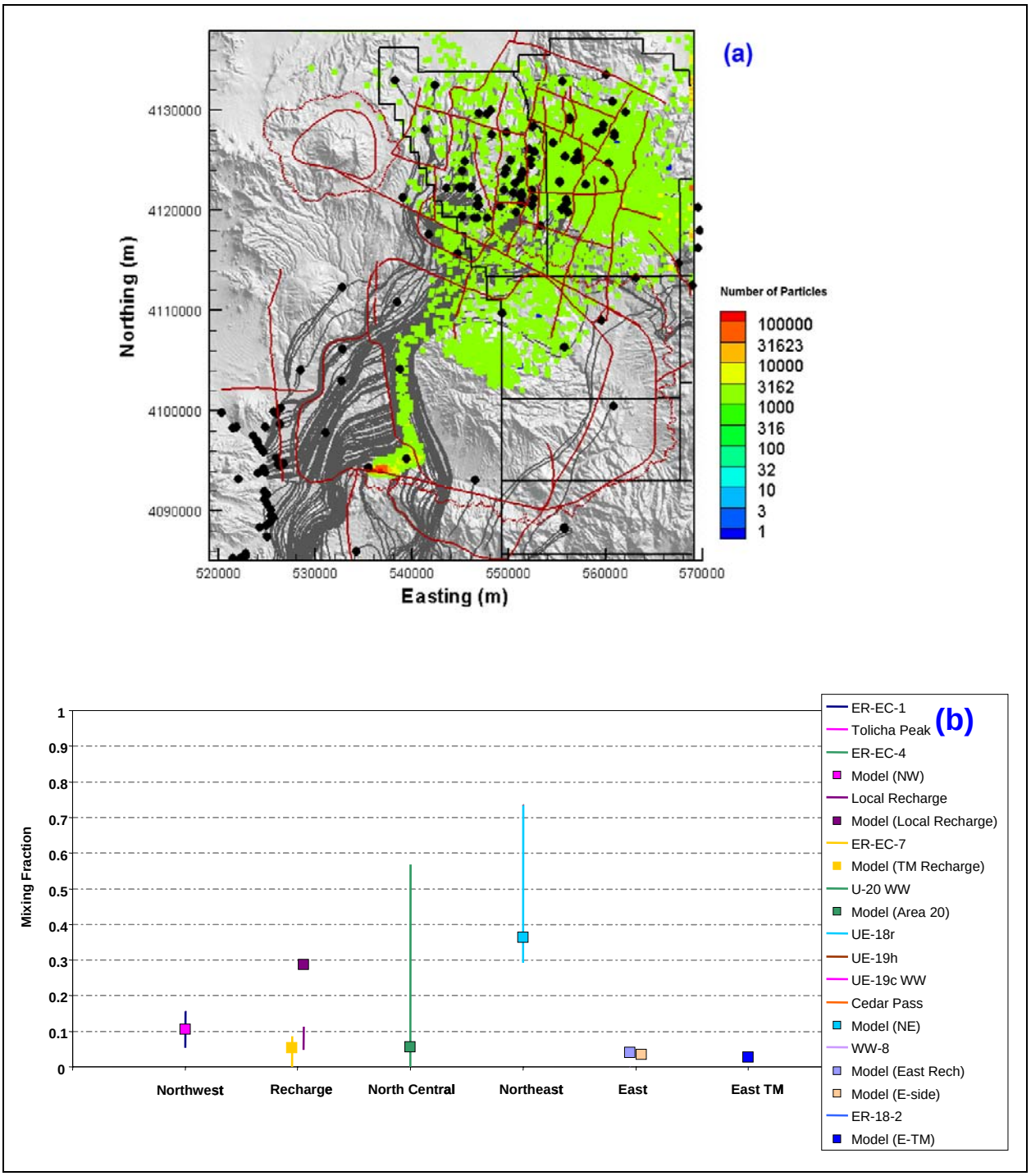

Figure 7-24
Comparison of Flow Model with Geochemical Mixing Targets at ER-OV-03c in the Reduced LCCU1 Permeability Alternative

Figure (a) shows the flow paths as mapped by forward SPTR particles originating at wells (grey lines) and the source recharge locations identified by reverse PTRK particle tracking (colored squares). Figure (b) shows the model comparison with geochemical mixing target ranges.

Uncontrolled When Printed

7.2.8 Coffer Windmill Well

Moving yet further east, the Coffer Windmill Well is on the southwest flank of Timber Mountain. Compared to nearby ER-OV-03c, the geochemical analysis suggests a marked difference in the source of water (Table 7-9). Not surprisingly, the component from Timber Mountain recharge can

Table 7-9
Fractions of Groundwater from Various Upgradient Wells Present in Groundwater at the Coffer Windmill Well

Mixing Component	Minimum Fraction	Maximum Fraction
UE-18r	0.000	0.357
ER-18-2	0.000	0.157
WW-8	0.000	0.843
ER-EC-7	0.000	0.643
UE-29a #2	0.000	0.000

Table 21 from Kwicklis et al. (2005). Note: Timber Mountain minerals from Table 2 were used for this set of models. Shallow groundwater from Well UE-29a #2 represents local recharge from stream-channel runoff in these models.

increase (represented by ER-EC-7). The northwest and north-central source components vanish and the potential northeast component decreases slightly. However, there could be a component from the east (upper Fortymile Canyon), with a signature like that found in WW-8. The large ranges suggest that these different sources must swap for each other in the PHREEQC model, which is confirmed in Figure 7-25. One possibility is a mixture of WW-8 and ER-18-2 waters, suggesting significant flow from Rainier Mesa. This is the only geochemical target well showing a potential Rainier Mesa signature, if WW-8 represents flow into Fortymile Canyon from the east rather than from Pahute Mesa to the north. However, UE-18r waters (Pahute Mesa source) and local recharge from Timber Mountain are equally likely. The BN-MME-SDA model shows a result intermediate to the two end members. Most of the source water is from the northeast or from local recharge, but 20 percent is from the east boundary at Gold Meadows (Figure 7-26). The reduced LCCU1 permeability alternative produces a match similar to one of the end members with no contribution from WW-8-type water (Figure 7-27).

In both models, the recharge occurs near the well rather than from the top of Timber Mountain. The geochemical control is likely not sufficient to rule this out, but it is important to note that UE-29a #2

Uncontrolled When Printed

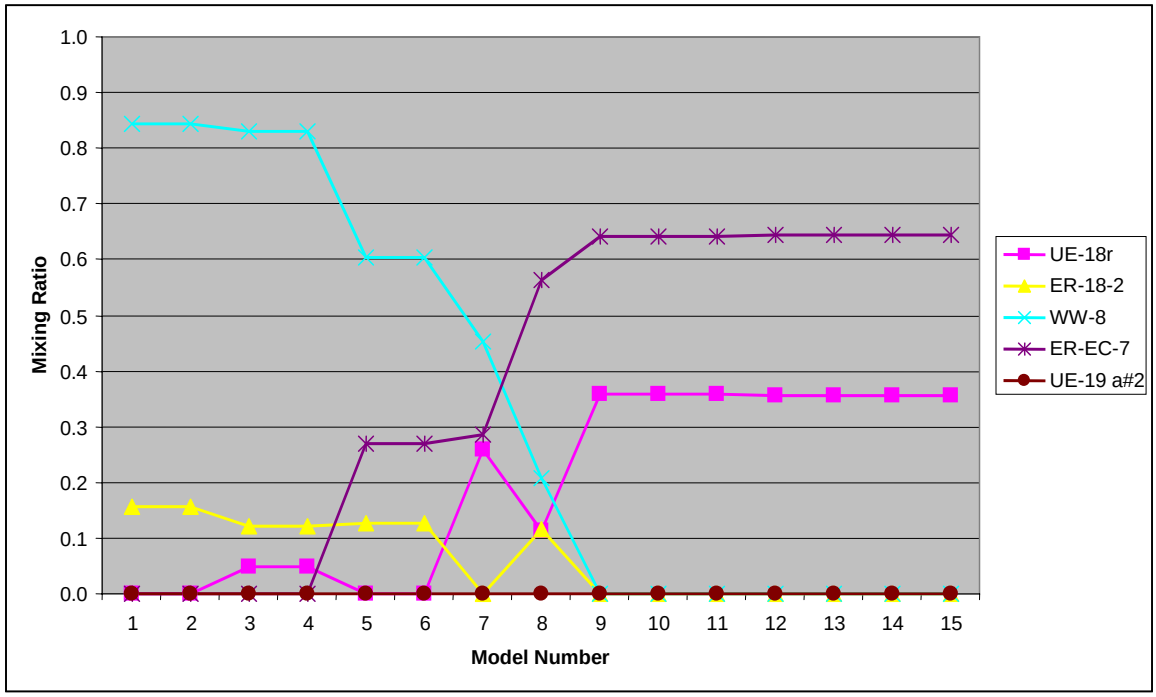

Figure 7-25
PHREEQC Models for Coffer Windmill Well

type water is not modeled to be present in the Coffer Windmill Well. The representative water for Timber Mountain is ER-EC-7, which could actually be a result of overland flow or interflow. Further, the MME map (Figure 4-14) explicitly redistributes water into washes and canyons. Thus, it is not surprising to have water from Timber Mountain recharging in the washes on the flanks in the simulation. The simulated northwest component of water at Coffer Windmill Well enters the model across the northern boundary. Its presence may be indicative of high inflows along that boundary resulting from the head boundary condition there.

The BN-MME-SDA model has a non-trivial component from Gold Meadows and has a large (38 percent) contribution from local recharge in washes instead of the top of Timber Mountain. The reduced LCCU1 permeability alternative model slightly overestimates the contribution from the northeast, has a large (25 percent) contribution from local recharge in washes instead from the top of Timber Mountain, and has an 11 percent contribution from the northwest, the latter of which is inconsistent with the geochemistry.

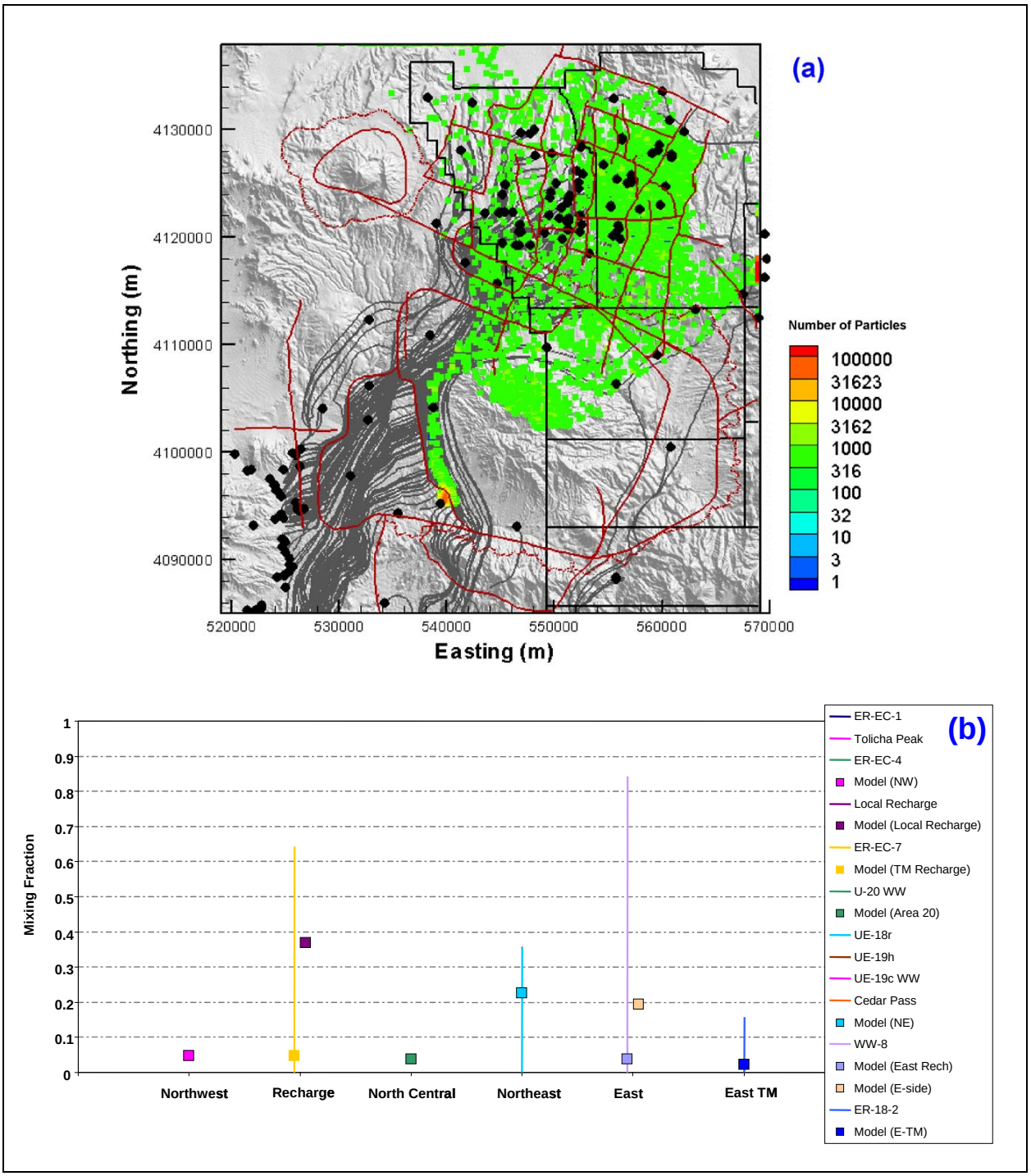

Figure 7-26
Comparison of Flow Model with Geochemical Mixing Targets at Coffer Windmill Well for BN-MME-SDA

Figure (a) shows the flow paths as mapped by forward SPTR particles originating at wells (grey lines) and the source recharge locations identified by reverse PTRK particle tracking (colored squares). Figure (b) shows the model comparison with geochemical mixing target ranges.

Uncontrolled When Printed

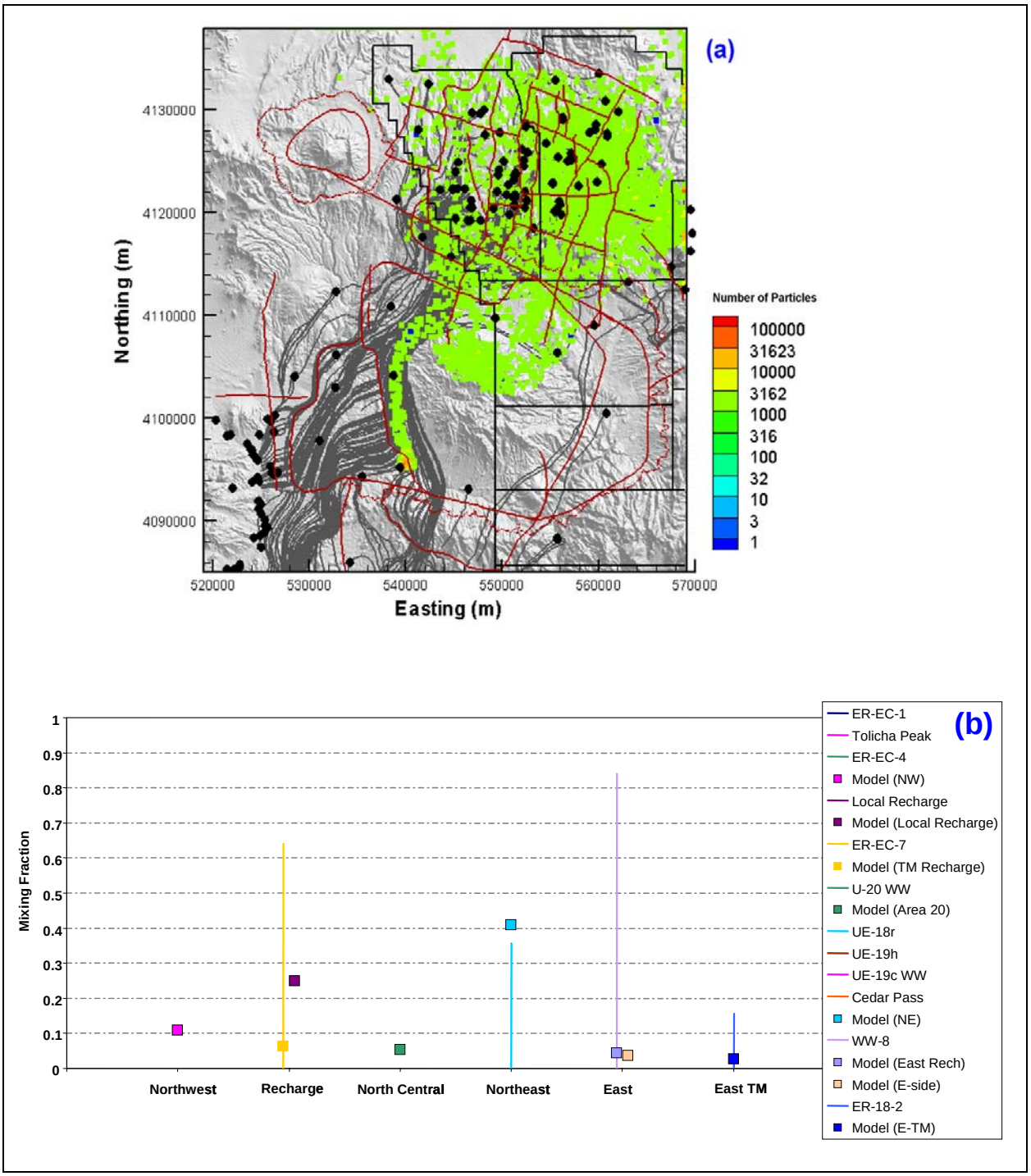

Figure 7-27
Comparison of Flow Model with Geochemical Mixing Targets at Coffer Windmill Well in the Reduced LCCU1 Permeability Alternative

Figure (a) shows the flow paths as mapped by forward SPTR particles originating at wells (grey lines) and the source recharge locations identified by reverse PTRK particle tracking (colored squares). Figure (b) shows the model comparison with geochemical mixing target ranges.

Uncontrolled When Printed

7.3 Geochemical Verification Results: Comparing Alternative Uncertain Models

In this section, the geochemical verification approach is applied for calibrated models with alternative water-balance conditions and alternative HFMs. The two alternative water-balance conditions include (a) the USGSD recharge map and associated boundary flux targets and (b) the DRIA recharge map and associated boundary flux targets. These two alternatives are described in detail in Section 4.3.1.

The alternative HFMs evaluated include SCCC, PZUP, DRT, RIDGE, TCL, and SEPZ as described in Table 2-5. For purposes of comparison, these are evaluated with the MME recharge map and associated boundary flux targets. Alternative water-balance conditions are also evaluated for PZUP and DRT.

Each of the water-balance alternatives and HFM alternatives represent conceptual model uncertainty. Therefore, they are compared with each other and to the BN-MME-SDA results described in the previous section for each of the target geochemical mixing wells. In each case, the alternative water-balance condition results are shown first followed by the alternative HFM results. As in the previous section, the comparison follows a counterclockwise tracking of target wells within the model domain, starting with UE-18r. For each target well considered, the geochemical mixing targets are shown graphically with the model results. The tables from Kwicklis et al. (2005) from which the graphic results are based are presented for each well discussed in Section 7.2.

In this section, different models for which results are compared at each target well are listed in Table 7-10. With this many different flow models, the primary purpose of this subsection is to provide visual comparison of the different model behaviors at each of the seven target wells.

Table 7-10
Hydrostratigraphic Models and Water-Balance Conditions Evaluated with Respect to Chemical Mixing Targets

HFM and Parameterization	Water-Balance Condition
BN-SDA reduced LCCU1 permeability alternative	MME
	USGSD
	DRIA
BN-SDA	MME
	USGSD
	DRIA
BN-ADA	MME
SCCC-SDA	MME
	USGSD
	DRIA
PZUP	MME
DRT	MME
RIDGE	MME
TCL	MME
SEPZ	MME
PZUP	USGSD
	DRIA
DRT	USGSD
	DRIA

Uncontrolled When Printed

7.3.1 UE-18r

7.3.1.1 Alternative Water-Balance Conditions, BN HFM

Figures 7-28 and 7-29 show the model results for the recalibrated flow models using the USGSD and DRIA alternative recharge maps, respectively, on the base HFM with reduced LCCU1 permeability alternative. The difference at first looks substantial. However, the sources of water at UE-18r, as estimated with reverse particles, for these two different recharge maps are actually quite similar, as shown in part (b) of the two figures. Most water comes from southeast Area 19, where high recharge is specified. The remaining sources are from the eastern flank of Timber Mountain (Zone 16) and the eastern model boundary at Gold Meadows. Slightly more water at UE-18r comes from Gold Meadows in the USGSD model (10 percent) than in the DRIA model (6 percent), probably because the gradient into the BN-USGSD model is greater due to lower total recharge flux. However, all HSU permeabilities are recalibrated in each model, leading to complex flow paths. The total component from Zones 10 and 16 is about similar for both models.

By comparison, model results for the BN-SDA (higher LCCU1 permeability alternative) with the USGSD and DRIA water-balance conditions lead to only small contributions from recharge within the model domain and 75 to 90 percent flow contributions from Gold Meadows on the eastern model boundary, respectively (Figure 7-30). Finally, the BN-MME-ADA model (Figure 7-31) shows a nearly even split between recharge within the model domain and simulated boundary flow from Gold Meadows at UE-18r. Section 7.5 addresses the differences between model results and geochemical target ranges and uses them to quantitatively rank the different flow models.

7.3.1.2 SCCC Alternative HFM

For the MME water-balance conditions and the SCCC alternative HFM, Figure 7-32 shows the forward pathlines for particles originating at wells (grey), the reverse-particle exits (colored), and the zone comparison for the mixing ratios between the model and the geochemistry targets. This model is substantially different from the base HFM and water-balance alternatives presented earlier in this section. Here, the source of water at UE-18r is from central and northern Area 19, with no contribution from anywhere near the eastern model boundary. The result is a very good fit to the geochemistry targets. However, the small component resembling ER-18-2 water is missing. Well

Uncontrolled When Printed

ER-18-2 water, however, is difficult to categorize in this spatial analysis. It is located on the eastern flank of Timber Mountain, but its chemistry is that of a deep groundwater, possibly from the carbonate aquifer. It is not representative of modern recharge.

The reason for the prominent difference between the SCCC model and other models based on the BN HFM is that there is a much stronger north-to-south flow component in Area 19, leading to greater flows into upper Fortymile Canyon. The southeast flow paths away from UE-18r beg the question of whether sufficient Area 19 water will be simulated in southwest wells, which will be addressed sequentially in this section.

The USGSD and DRIA water-balance conditions were also applied in calibrations of the SCCC model. In both of these alternatives, an unexplainable large component of the UE-18r water is simulated to originate in the northwest; on the other side of the Purse Fault (Figure 7-33), such results are not supported by any chemical mixing models for UE-18r, making those models suspect.

7.3.1.3 PZUP, DRT, RIDGE, TCL, and SEPZ Alternative HFMs

The other alternative HFMs with MME water-balance conditions are considered in this section with the quantitative comparisons in Figures 7-34 through 7-36. These can be broken into two groups with regard to their results at UE-18r. In the first group, PZUP and DRT both provide good matches at UE-18r, with most water originating in Area 19 and less than 20 percent coming from Zones 6 and 16, essentially on the east flank of Timber Mountain. In both of these cases, the inflow from Gold Meadows is very small. In the second group, RIDGE, TCL, and SEPZ show the primary contribution at UE-18r coming from Gold Meadows (east model boundary) and virtually no source anywhere in Area 19 within the model domain. Flow models with substantial inflow to the model at Gold Meadows with a path directly to UE-18r represent unlikely groundwater flow pathways as determined by Kwicklis et al. (2005). The geochemical mismatches between the model and verification targets for Gold Meadows inflow are quantified as errors in Section 7.5.

Alternative water-balance models USGSD and DRIA were also considered for the PZUP and DRT HFMs (Figures 7-37 and 7-38). For the PZUP model, both water-balance alternatives led to significantly more Gold Meadows source water at UE-18r than is simulated with the MME water balance. For DRT, however, the USGSD water-balance produces nearly identical results to the MME

Uncontrolled When Printed

water-balance model. The DRIA water-balance model with the DRT HFM, interestingly, simulates a majority of the source water at UE-18r originating as recharge within the model domain, thus avoiding the Gold Meadows inflow errors.

7.3.1.4 Summary: UE-18r

The most important issue at UE-18r is whether the simulated source of groundwater is from recharge within the model domain or from the eastern model boundary at Gold Meadows. The geochemistry analysis of Kwicklis et al. (2005) indicates that it is improbable for the source of water at UE-18r to originate at Rainier Mesa, east of the model domain. Table 7-11 separates the models based on this specific indicator.

Uncontrolled When Printed

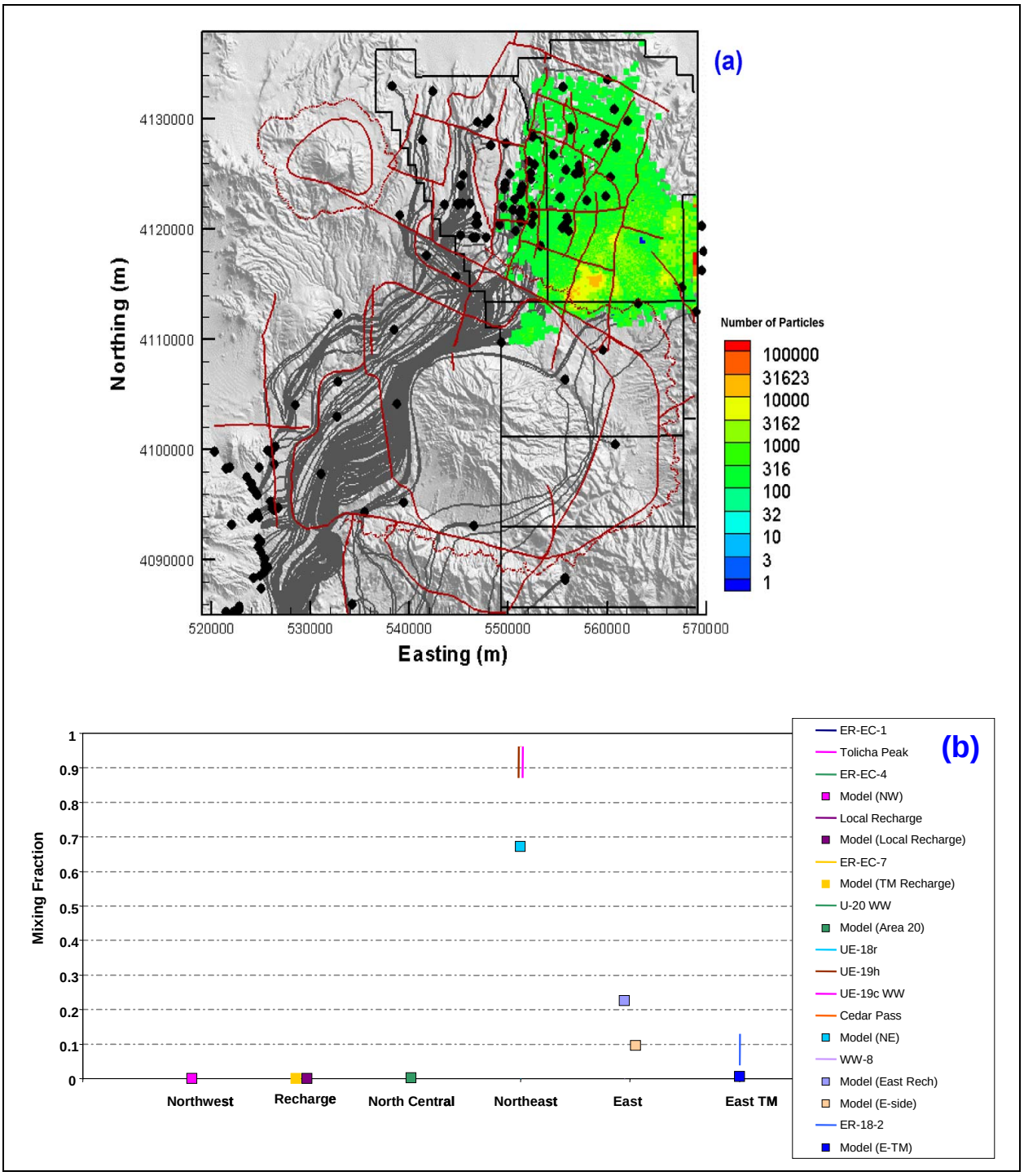

Figure 7-28
Comparison of Flow Model with Geochemical Mixing Targets at UE-18r for BN-USGSD-SDA in the Reduced LCCU1 Permeability Alternative

Figure (a) shows the flow paths as mapped by forward SPTR particles originating at wells (grey lines) and the source recharge locations identified by reverse PTRK particle tracking (colored squares). Figure (b) shows the model comparison with geochemical mixing target ranges.

Uncontrolled When Printed

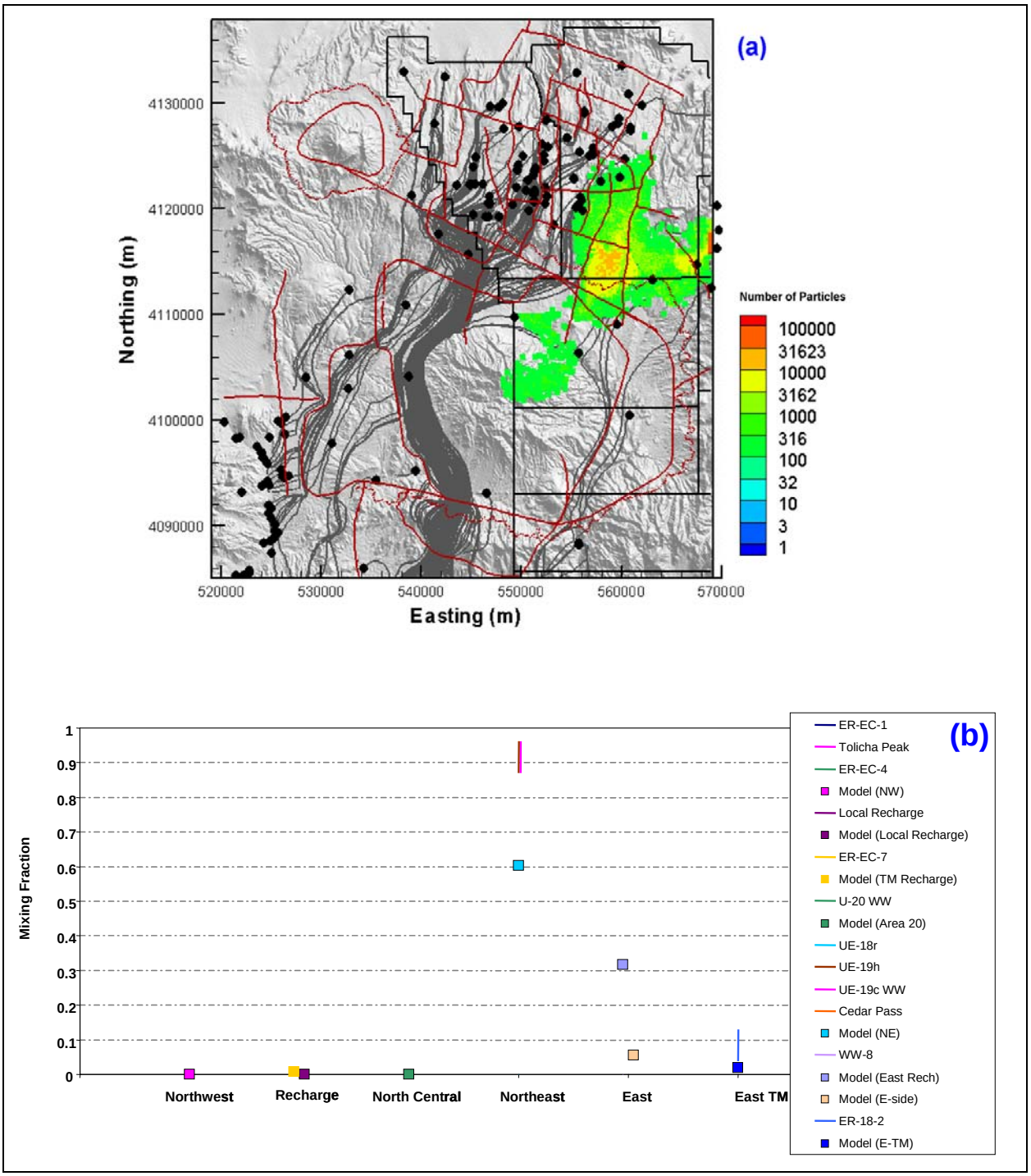

Figure 7-29
Comparison of Flow Model with Geochemical Mixing Targets for UE-18r for BN-DRIA-SDA in the Reduced LCCU1 Permeability Alternative

Figure (a) shows the flow paths as mapped by forward SPTR particles originating at wells (grey lines) and the source recharge locations identified by reverse PTRK particle tracking (colored squares). Figure (b) shows the model comparison with geochemical mixing target ranges.

Uncontrolled When Printed

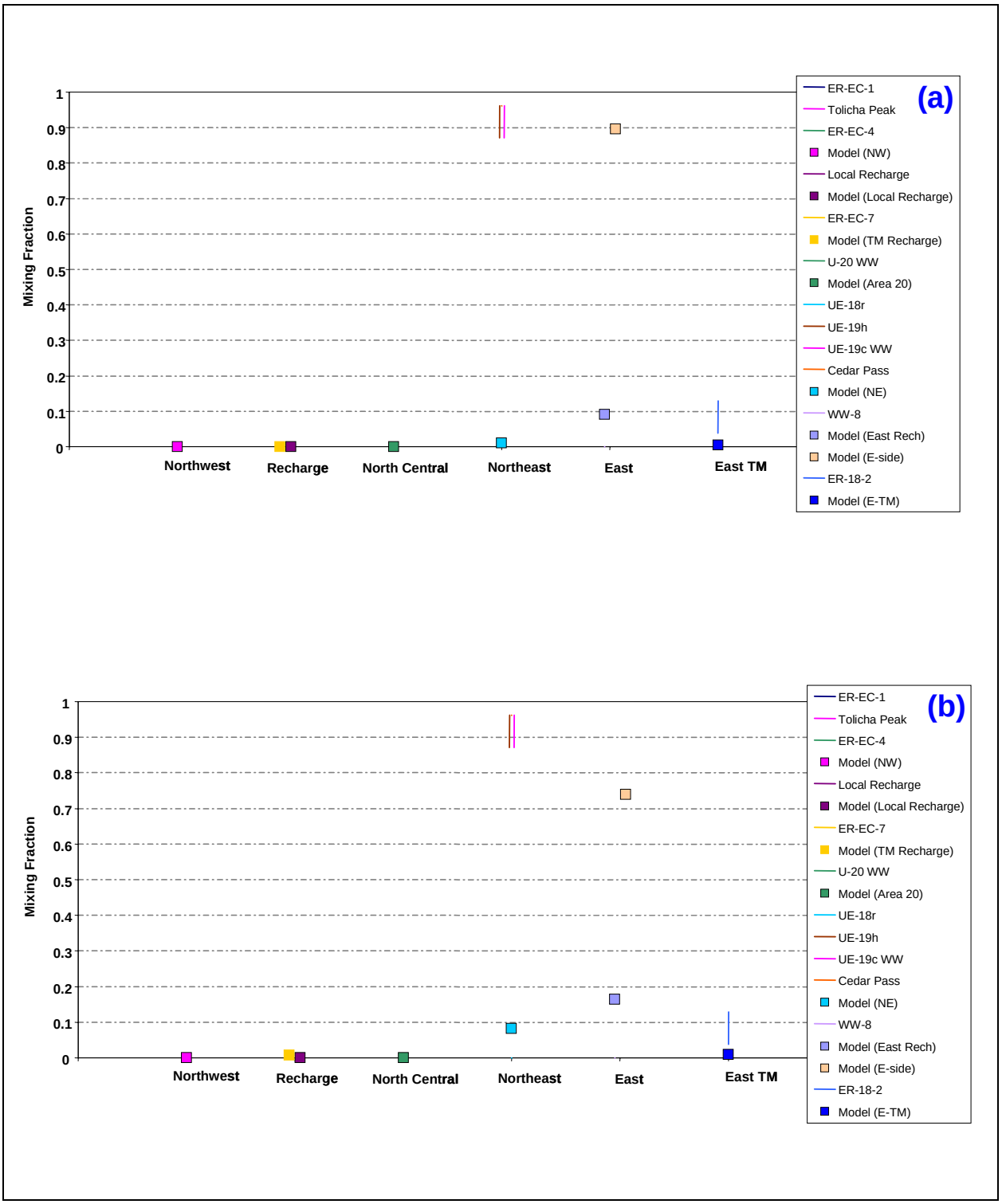

Figure 7-30
Quantitative Geochemical Comparison at UE-18r for
(a) BN-USGSD-SDA and (b) BN-DRIA-SDA

Uncontrolled When Printed

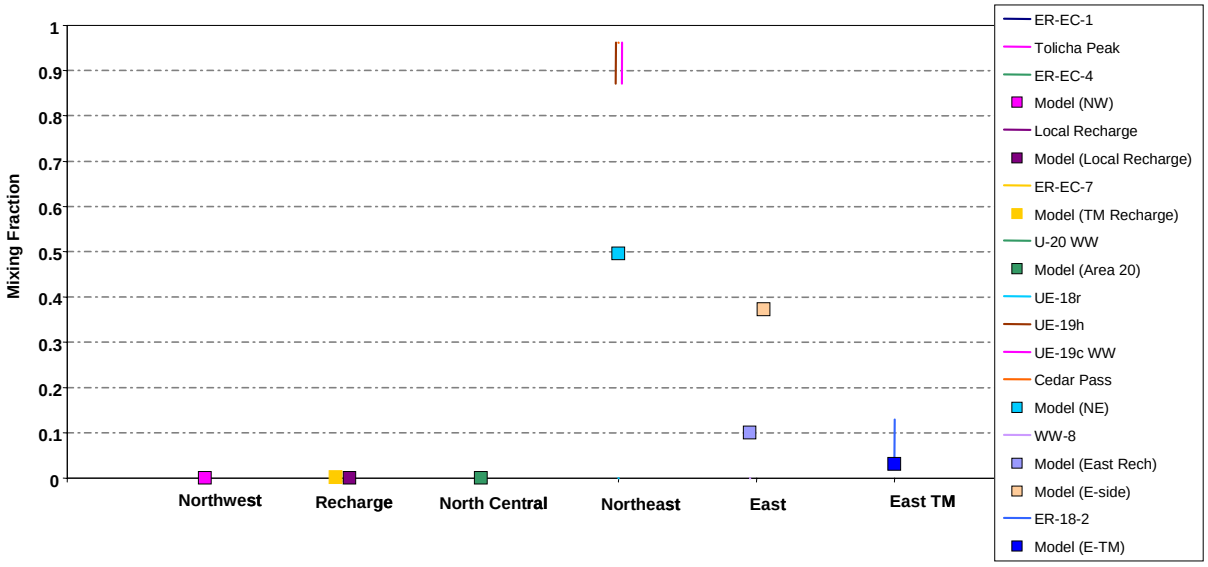

Figure 7-31
Comparison of Flow Model Geochemical Mixing Targets at UE-18r for BN-MME-ADA

Uncontrolled When Printed

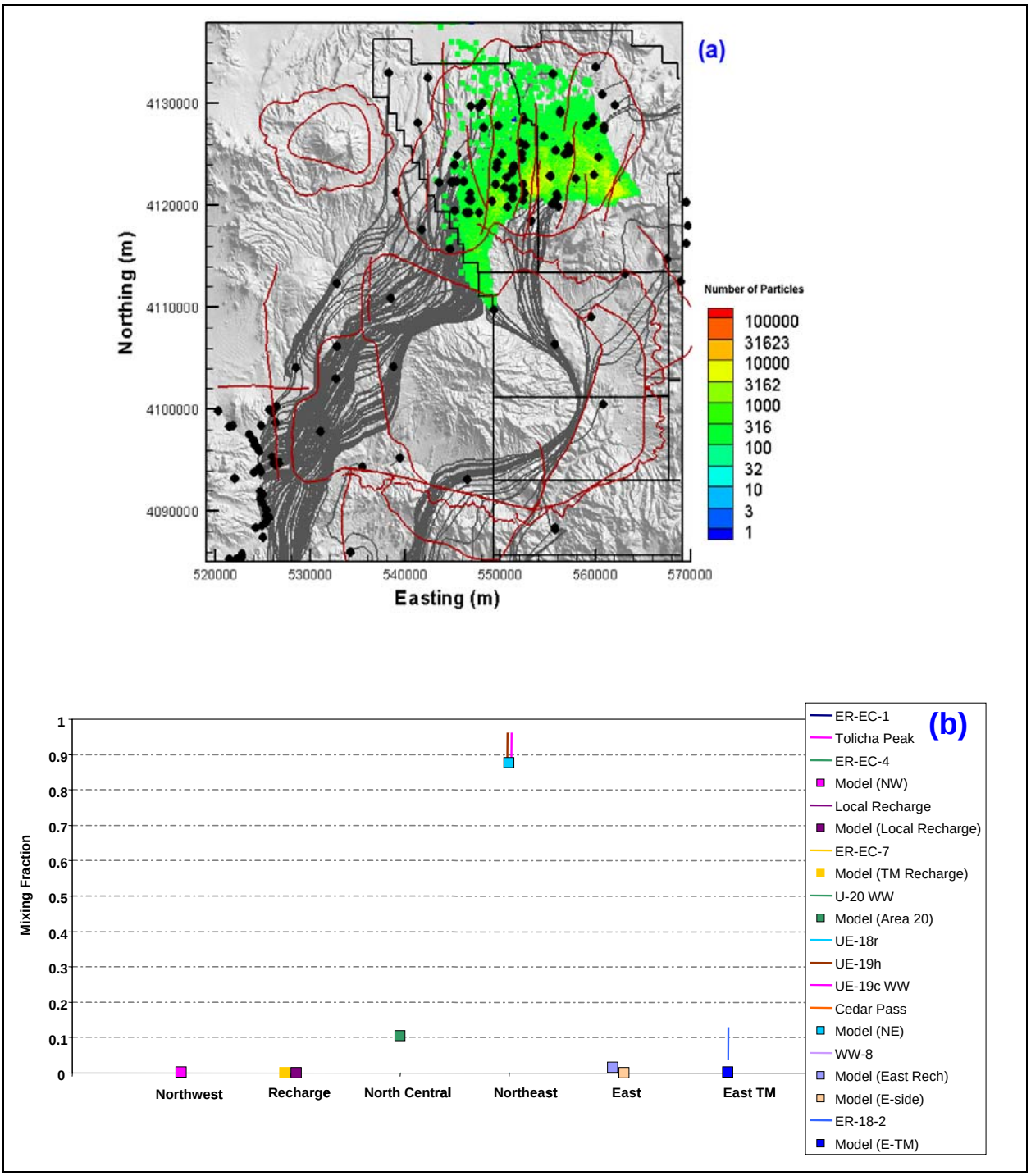

Figure 7-32
Comparison of Flow Model with Geochemical Mixing Targets at UE-18r for SCCC-MME-SDA

Figure (a) shows the flow paths as mapped by forward SPTR particles originating at wells (grey lines) and the source recharge locations identified by reverse PTRK particle tracking (colored squares). Figure (b) shows the model comparison with geochemical mixing target ranges.

Uncontrolled When Printed

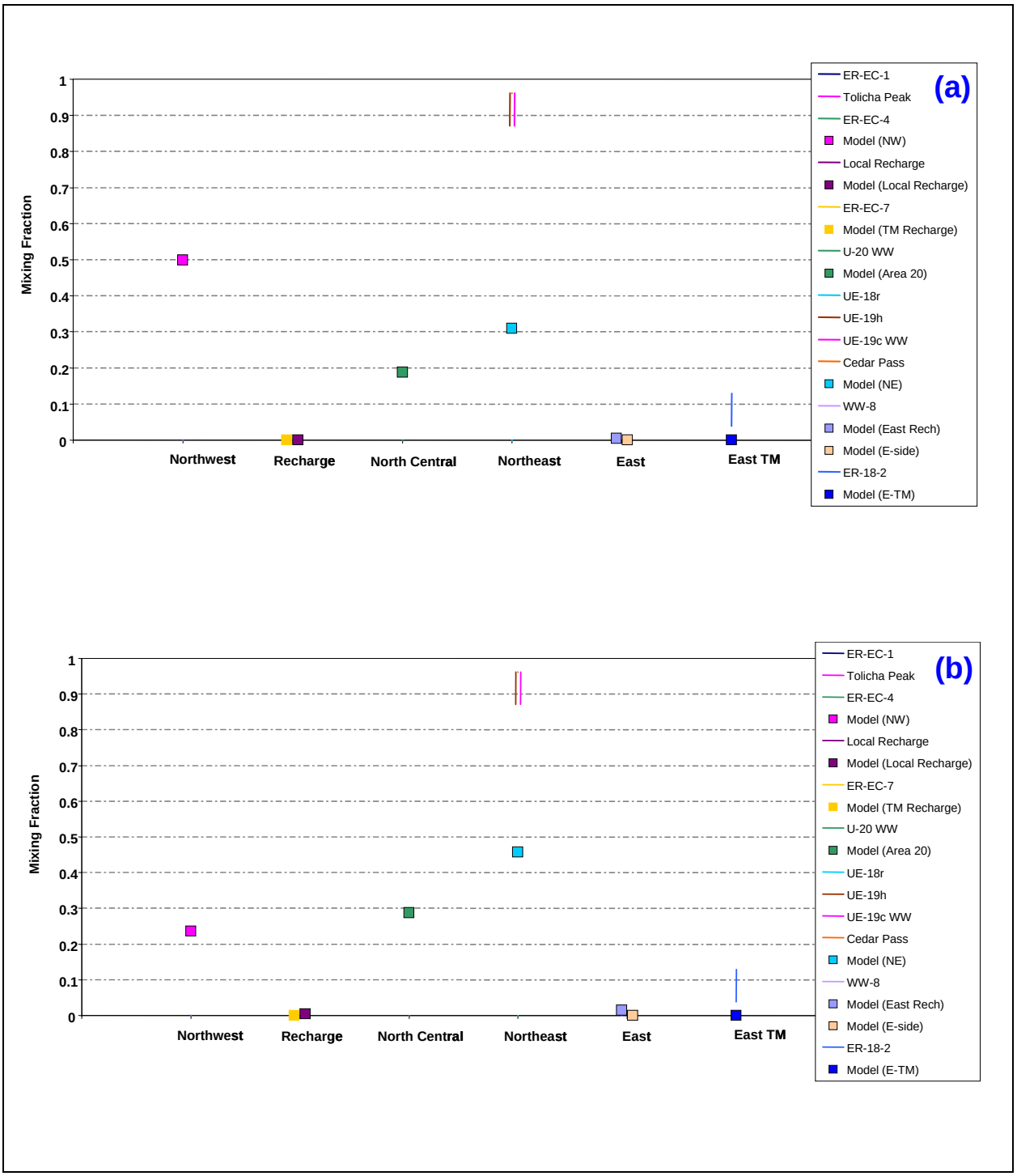

Figure 7-33
Quantitative Geochemical Comparisons at UE-18r for (a) SCCC-USGSD-SDA and (b) SCCC-DRIA-SDA

Uncontrolled When Printed

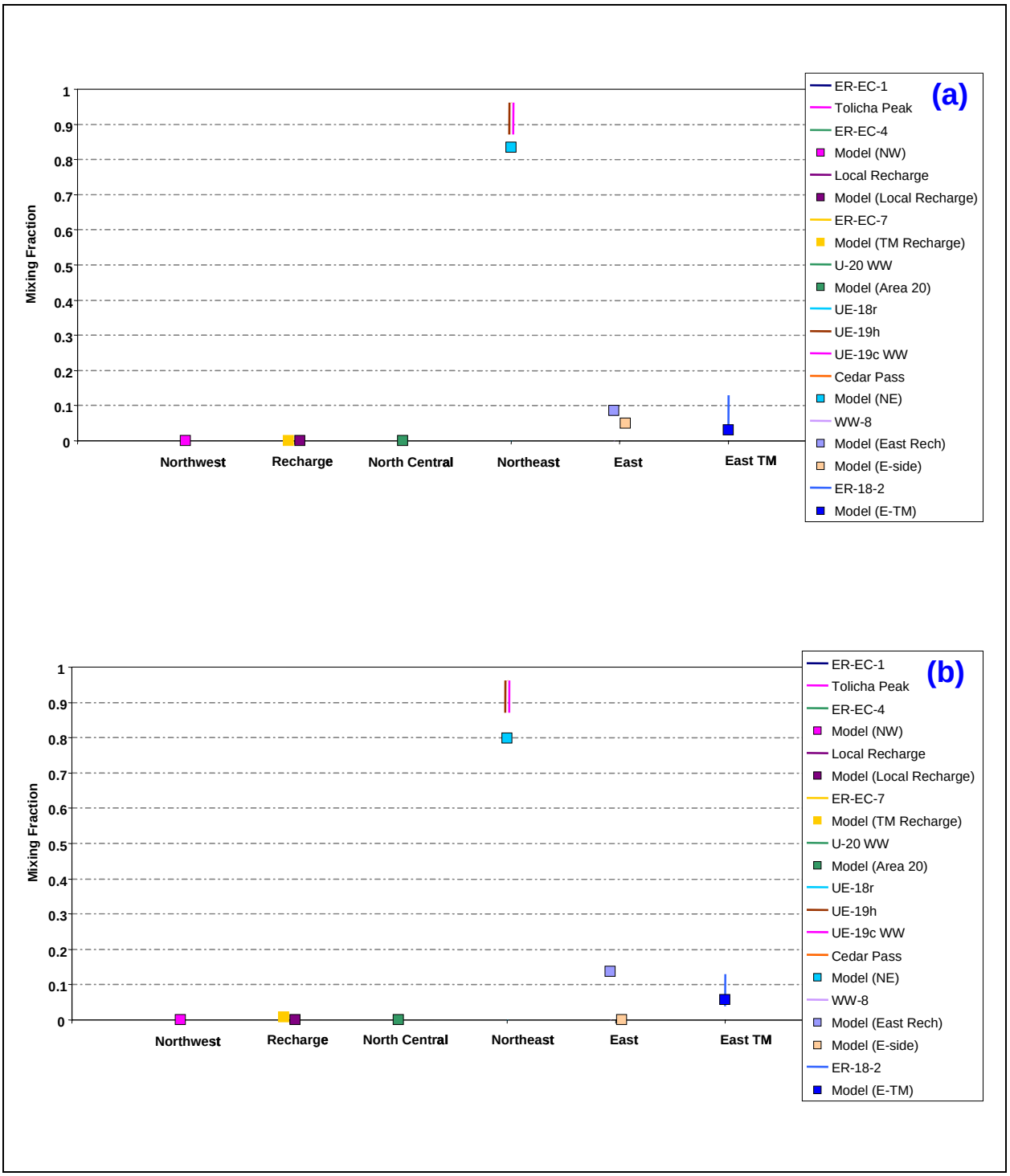

Figure 7-34
Quantitative Geochemical Comparisons at UE-18r for
(a) PZUP-MME-SDA and (b) DRT-MME-SDA

Uncontrolled When Printed

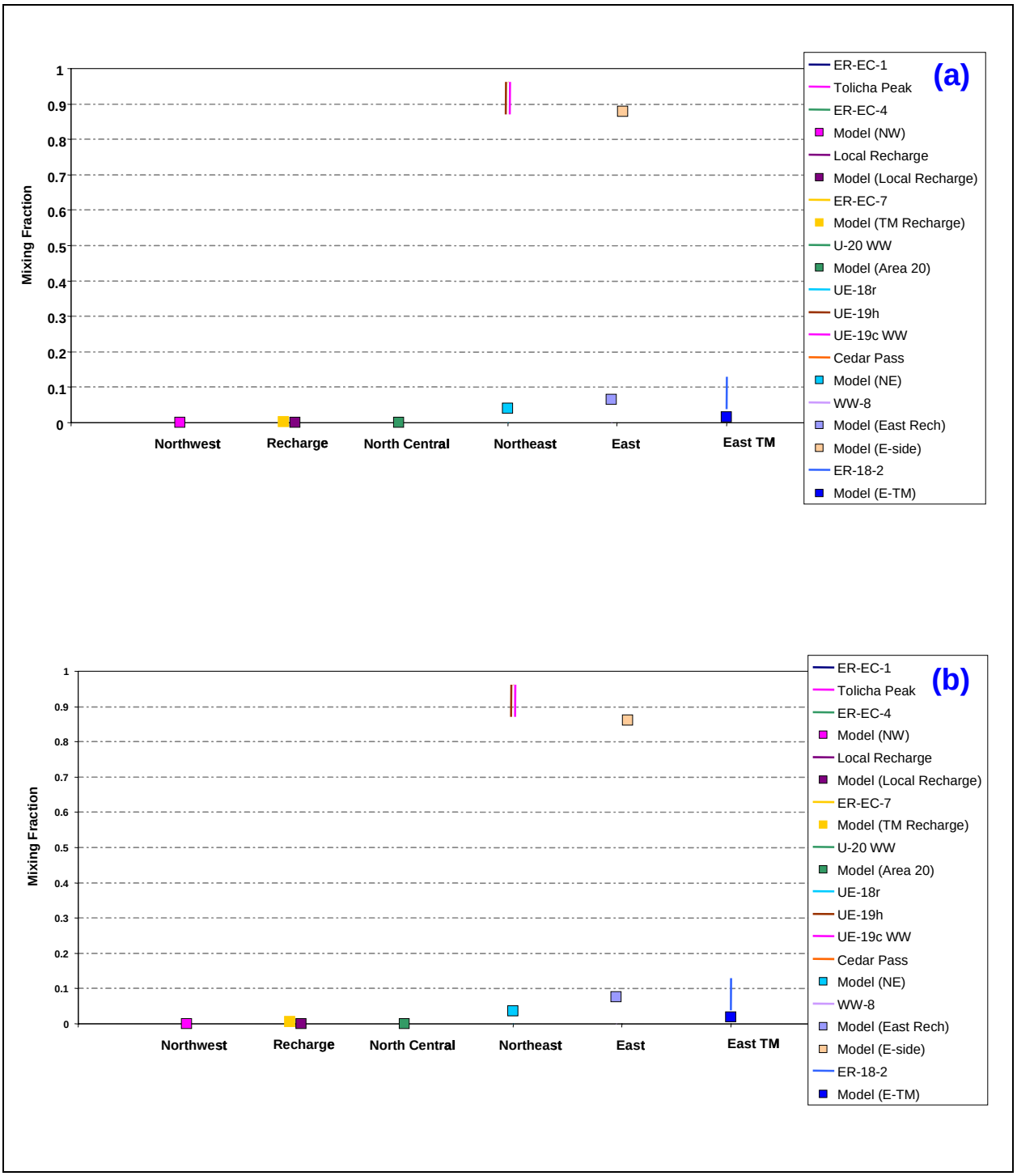

Figure 7-35
Quantitative Geochemical Comparisons at UE-18r for
(a) RIDGE-MME-SDA and (b) TCL-MME-SDA

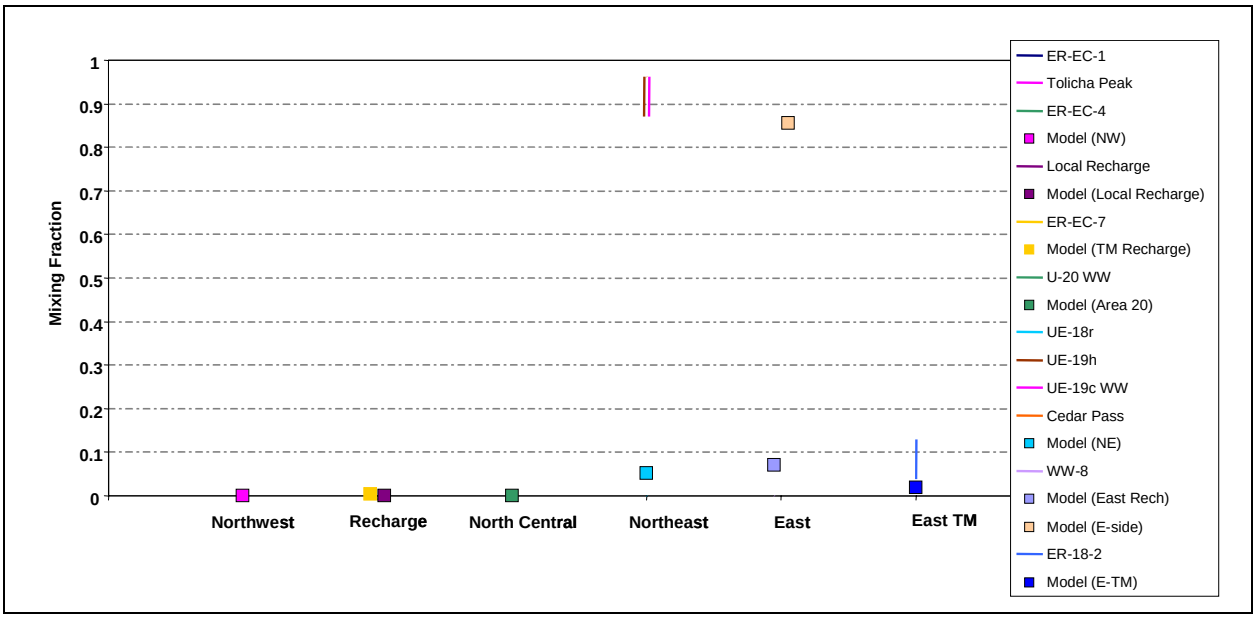

Figure 7-36
Quantitative Geochemical Comparison at UE-18r for SEPZ-MME-SDA

Uncontrolled When Printed

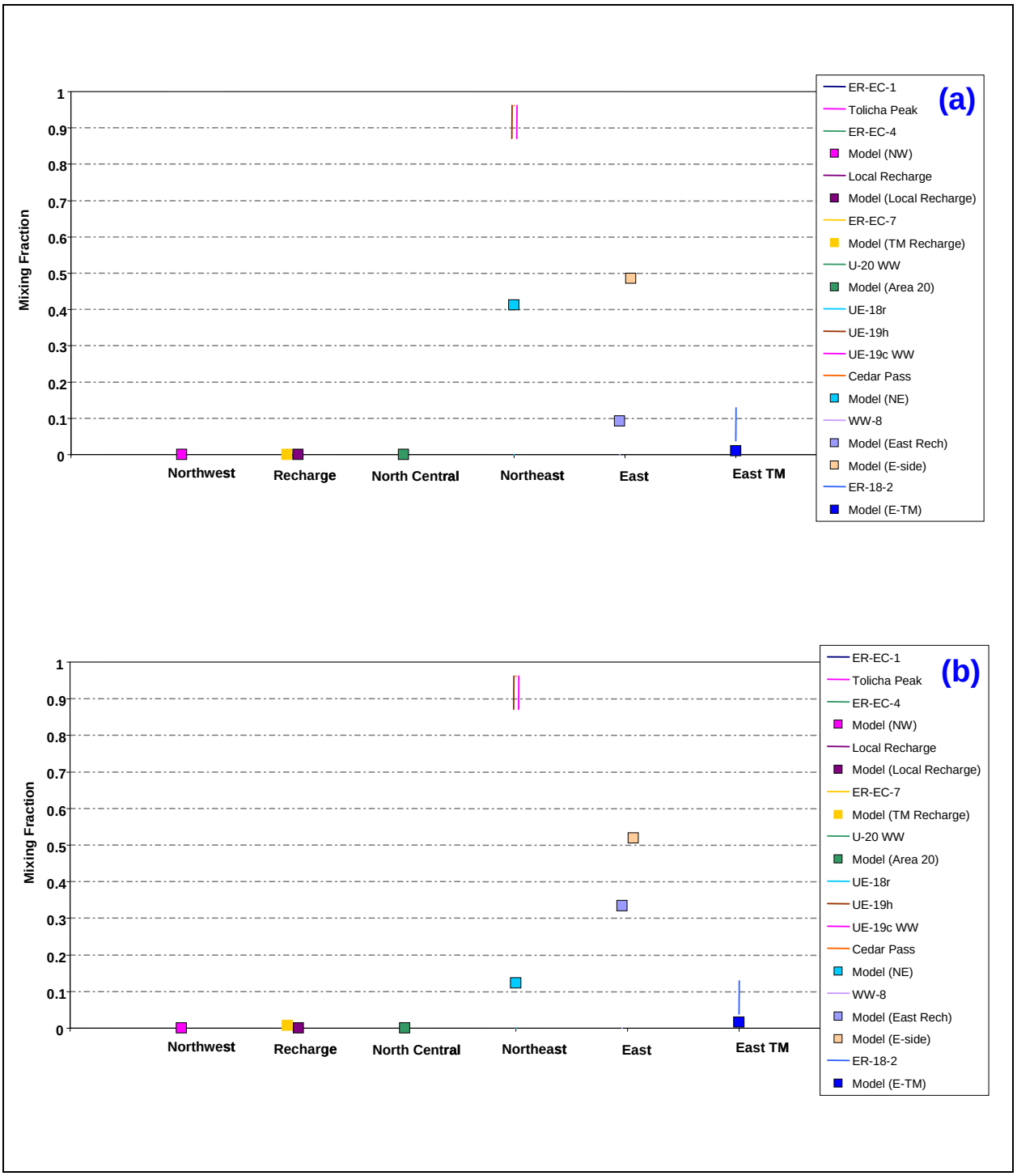

Figure 7-37
Quantitative Geochemical Comparisons at UE-18r for
(a) PZUP-USGSD-SDA and (b) PZUP-DRIA-SDA

Uncontrolled When Printed

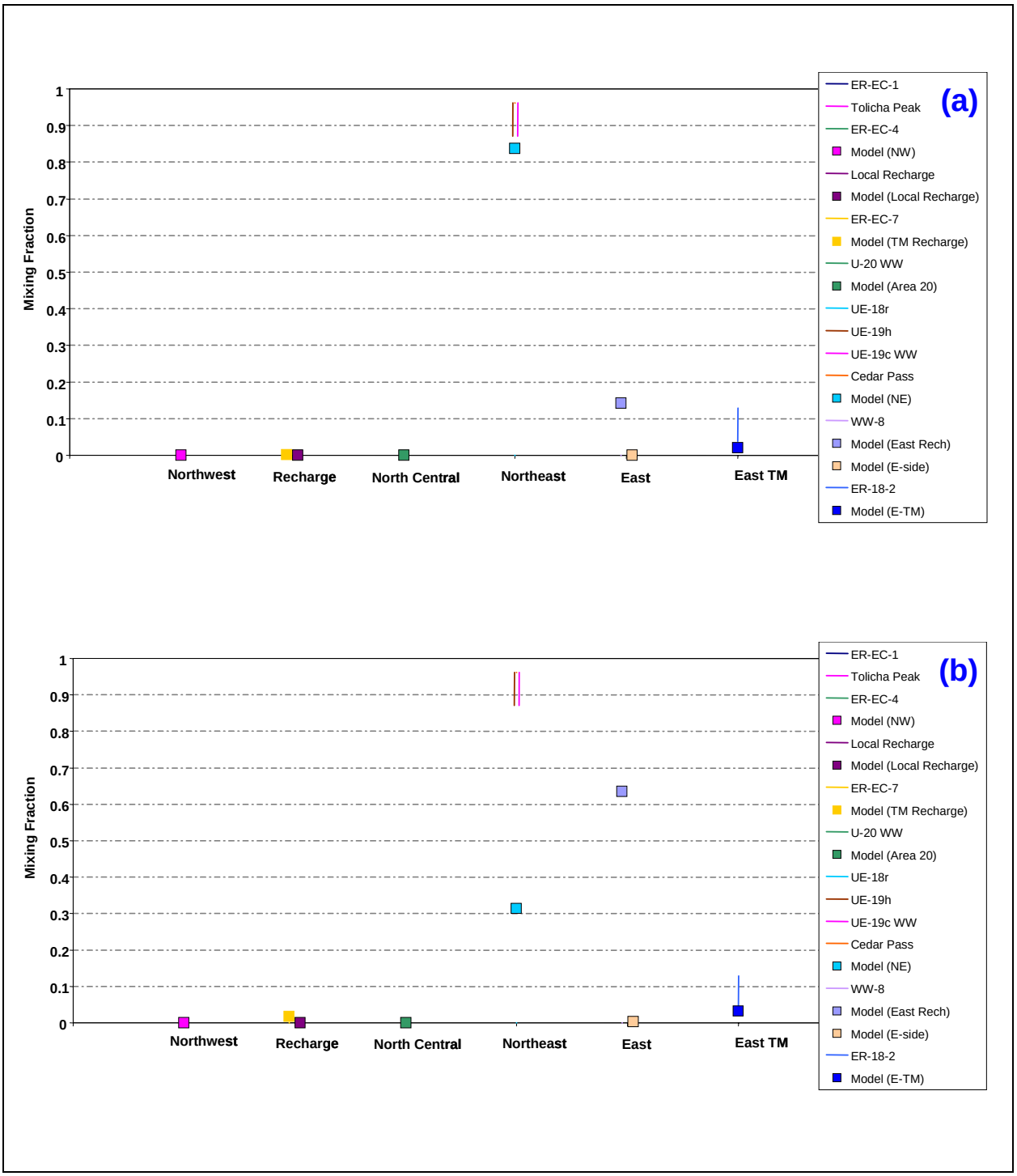

Figure 7-38
Quantitative Geochemical Comparisons at UE-18r for (a) DRT-USGSD-SDA and (b) DRT-DRIA-SDA

Uncontrolled When Printed

Table 7-11
Comparison of Alternative Models at UE-18r

HFM	Water-Balance Condition	Inflow from Gold Meadows?	Other Problems
BN-SDA reduced LCCU1 permeability alternative	MME		
	USGSD		
	DRIA		
BN-SDA	MME	X	
	USGSD	X	
	DRIA	X	
BN-ADA	MME		
SCCC-SDA	MME		
	USGSD		X
	DRIA		X
PZUP	MME		
DRT	MME		
RIDGE	MME	X	
TCL	MME	X	
SEPZ	MME	X	
PZUP	USGSD		
	DRIA	X	
DRT	USGSD		
	DRIA		

Uncontrolled When Printed

7.3.2 ER-EC-6

7.3.2.1 Alternative Water-Balance Conditions, BN HFM

Figures 7-39 and 7-40 show the model results for the recalibrated flow models using the USGSD and DRIA alternative recharge maps, respectively, on the reduced LCCU1 permeability alternative. For each recharge scenario, the simulated source of water at ER-EC-6 is primarily from the northwest. For the DRIA case, which is the "high" recharge flux scenario, about 15 percent of the ER-EC-6 source is from the recharge zone in Areas 20 and 19. For the USGSD case, recharge in the north-central and northeast areas is not large enough to produce a southwestward flow direction to ER-EC-6. However, as described in the base-case analysis, ER-EC-6 is in a highly complex local area where mixing from the northwest mixes with north-central and northeast water. Although the later sources do not show up in significant quantities in these simulations, they do mix with the northwest water at the top of Thirsty Canyon, not far from ER-EC-6.

Model results for BN-USGSD-SDA and BN-DRIA-SDA show an interesting difference (Figure 7-41). The USGSD model shows the entire source of water at ER-EC-6 coming from the northwest. By comparison, the DRIA model nearly matches the even split target between sources west and east of the Purse Fault, which is an improvement over the DRIA model with reduced LCCU1 permeability alternative. Finally, BN-MME-ADA (Figure 7-42) shows nearly all of ER-EC-6 water arriving from the northwest.

7.3.2.2 SCCC Alternative HFM

Given the way the Purse Fault is represented in the SCCC model, it was expected that ER-EC-6 would be dominated by northwest water. However, the SCCC-MME-SDA, as calibrated, produces a nearly perfect match to the geochemistry targets at ER-EC-6 (Figure 7-43). Flow to ER-EC-6 comes almost perfectly from the north. Because the well is due south of the Purse Fault, the mixing from either side of the fault is nearly even. The contribution from the northeast is not troubling because that water is so similar to the north-central water when compared with northwest water (Kwicklis et al., 2005).

Uncontrolled When Printed

The SCCC model calibrated with the DRIA water-balance conditions leads to a slight deterioration in the simulated mixing at ER-EC-6 from the MME water-balance conditions. Then, with the USGSD conditions, the mixing is lost as the entire source is from the northwest (Figure 7-44).

7.3.2.3 PZUP, DRT, RIDGE, TCL, and SEPZ Alternative HFMs

The other alternative HFMs with MME water-balance conditions are considered in this section with the quantitative comparisons in Figures 7-45 through 7-47. As with UE-18r, these can be broken into two groups with regard to their results at ER-EC-6. In the first group, PZUP, DRT, and SEPZ show a tendency similar to the base case, in which most water at ER-EC-6 arrives from the northwest. The SEPZ shows a further east source, although small, similar to BN-DRIA and SCCC.

In the second group, RIDGE-MME-SDA and TCL-MME-SDA show a drastic decrease in northwest source at ER-EC-6, with more than 80 percent coming from the north-central and northeast zones combined. This indicates the northwest inflow and recharge must be well to the west of ER-EC-6. Whereas all other models except the SCCC alternative HFM err on the side of too much northwest-type water at ER-EC-6, RIDGE-MME-SDA and TCL-MME-SDA err in the other direction with not enough northwest-type water.

The USGSD and DRIA alternative water-balance models were also considered for the PZUP and DRT HFMs (Figures 7-48 and 7-49). For both models, the USGSD water-balance alternative led to a nearly complete northwest source at ER-EC-6. The DRIA alternative, however, leads to an almost perfect mix of source water from either side of the Purse Fault. The BN-MME-ADA falls into the category of models with most source water at ER-EC-6 being to the northwest.

7.3.2.4 Summary: ER-EC-6

Nearly every model is unable to provide a 50/50 mix of water from west and east of the Purse Fault at ER-EC-6. This may be explainable by the complex zone of mixing near ER-EC-6 and the impact of the no-flow western boundary. The results may be acceptable in that the mixing generally does occur, just not right at ER-EC-6. Table 7-12 shows which models provide better estimates of the mixing right at ER-EC-6.

Uncontrolled When Printed

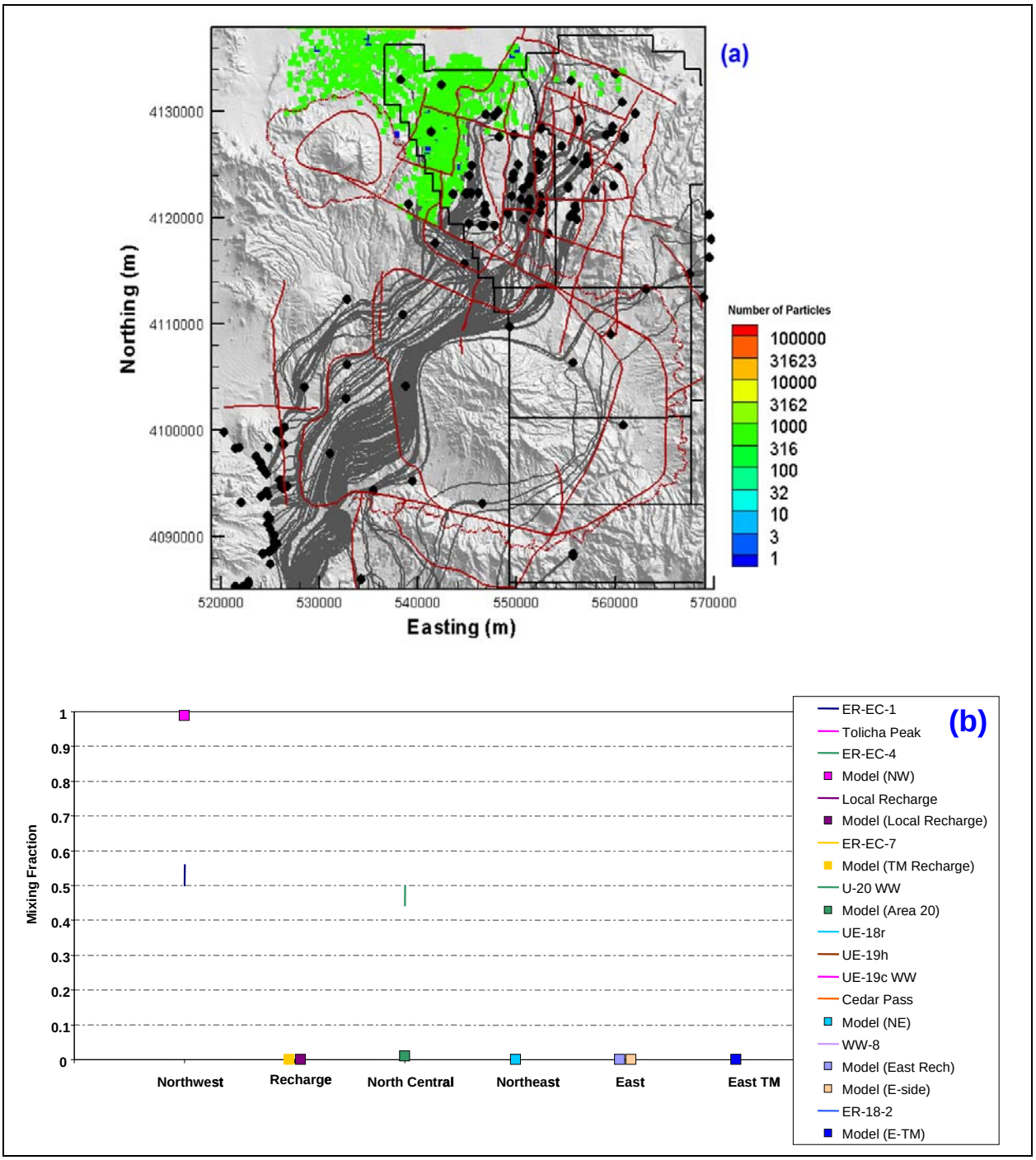

Figure 7-39
Comparison of Flow Model with Geochemical Mixing Targets at ER-EC-6 for BN-USGSD-SDA in the Reduced LCCU1 Permeability Alternative

Figure (a) shows the flow paths as mapped by forward SPTR particles originating at wells (grey lines) and the source recharge locations identified by reverse PTRK particle tracking (colored squares). Figure (b) shows the model comparison with geochemical mixing target ranges.

Uncontrolled When Printed

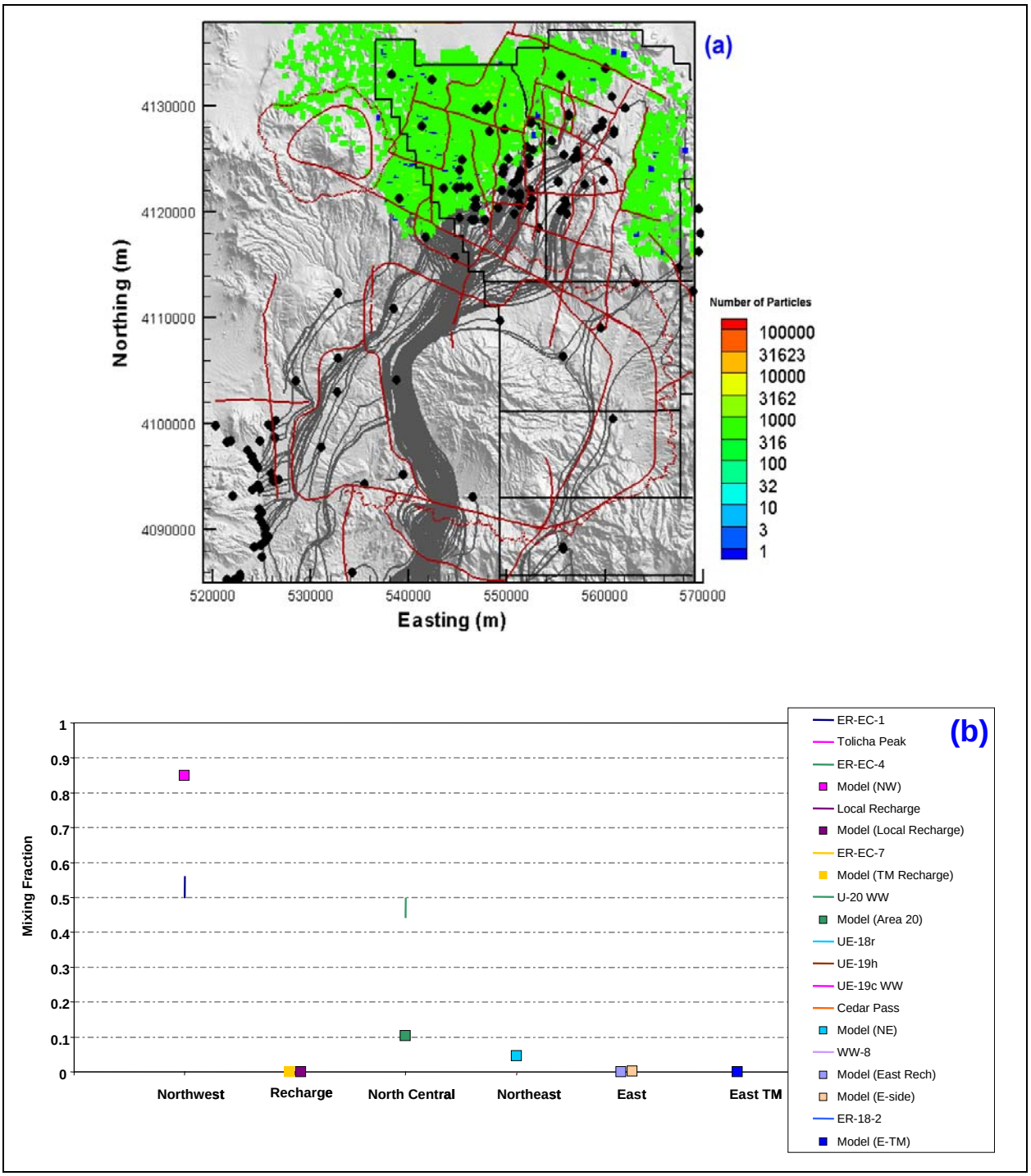

Figure 7-40
Comparison of Flow Model with Geochemical Mixing Targets at ER-EC-6 for BN DRIA-SDA in the Reduced LCCU1 Permeability Alternative

Figure (a) shows the flow paths as mapped by forward SPTR particles originating at wells (grey lines) and the source recharge locations identified by reverse PTRK particle tracking (colored squares). Figure (b) shows the model comparison with geochemical mixing target ranges.

Uncontrolled When Printed

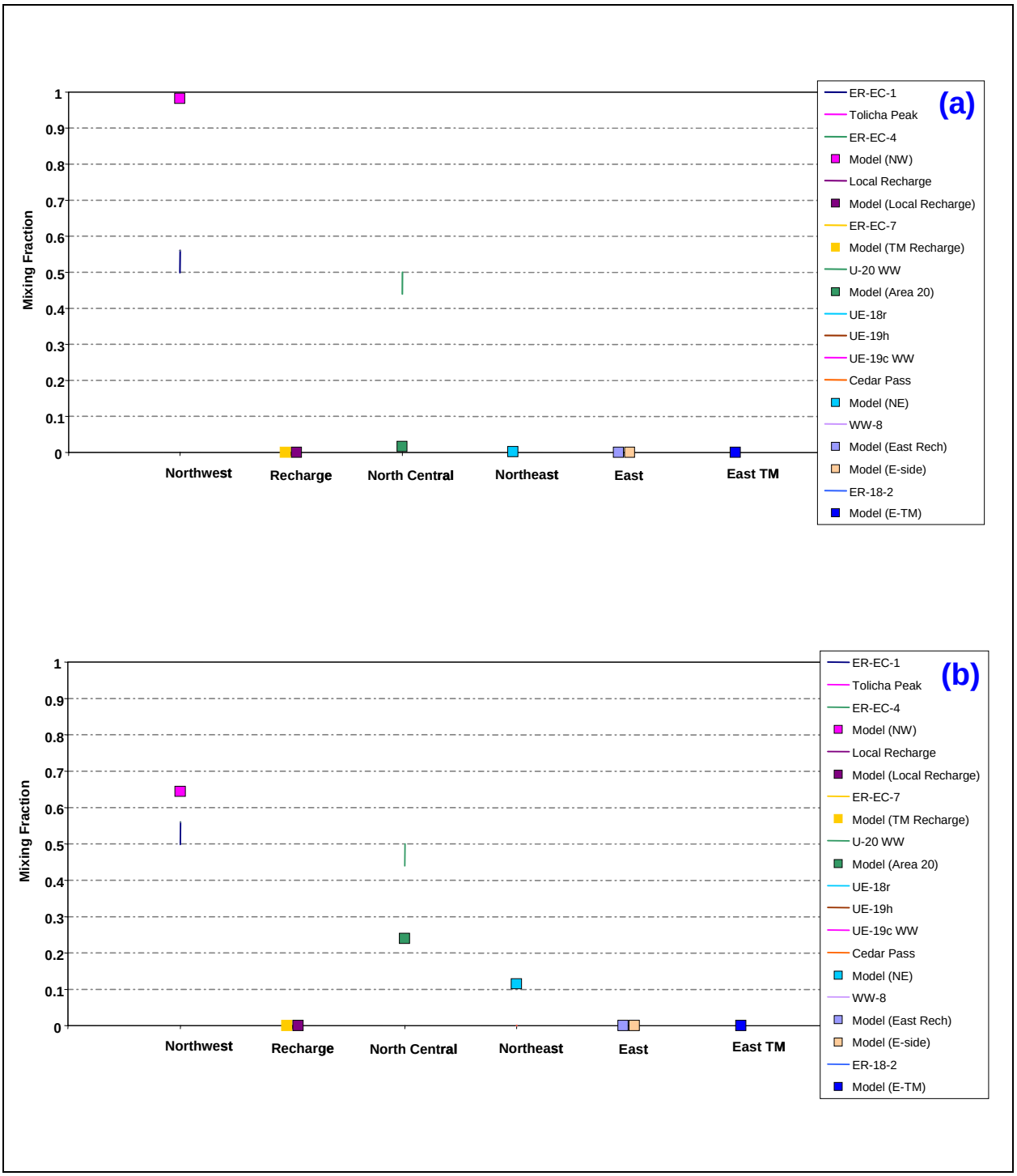

Figure 7-41
Quantitative Geochemical Comparison at ER-EC-6 for
(a) BN-USGSD-SDA and (b) BN-DRIA-SDA

Uncontrolled When Printed

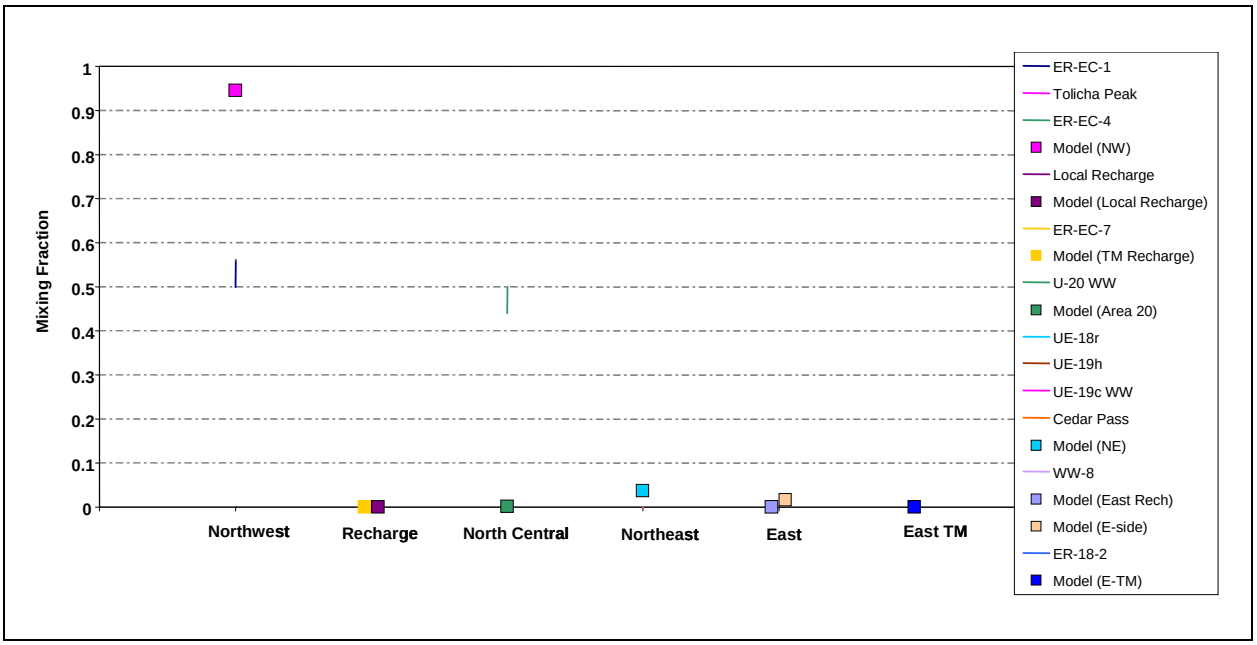

Figure 7-42
Comparison of Flow Model with Geochemical Mixing Targets at ER-EC-6 for BN-MME-ADA

Uncontrolled When Printed

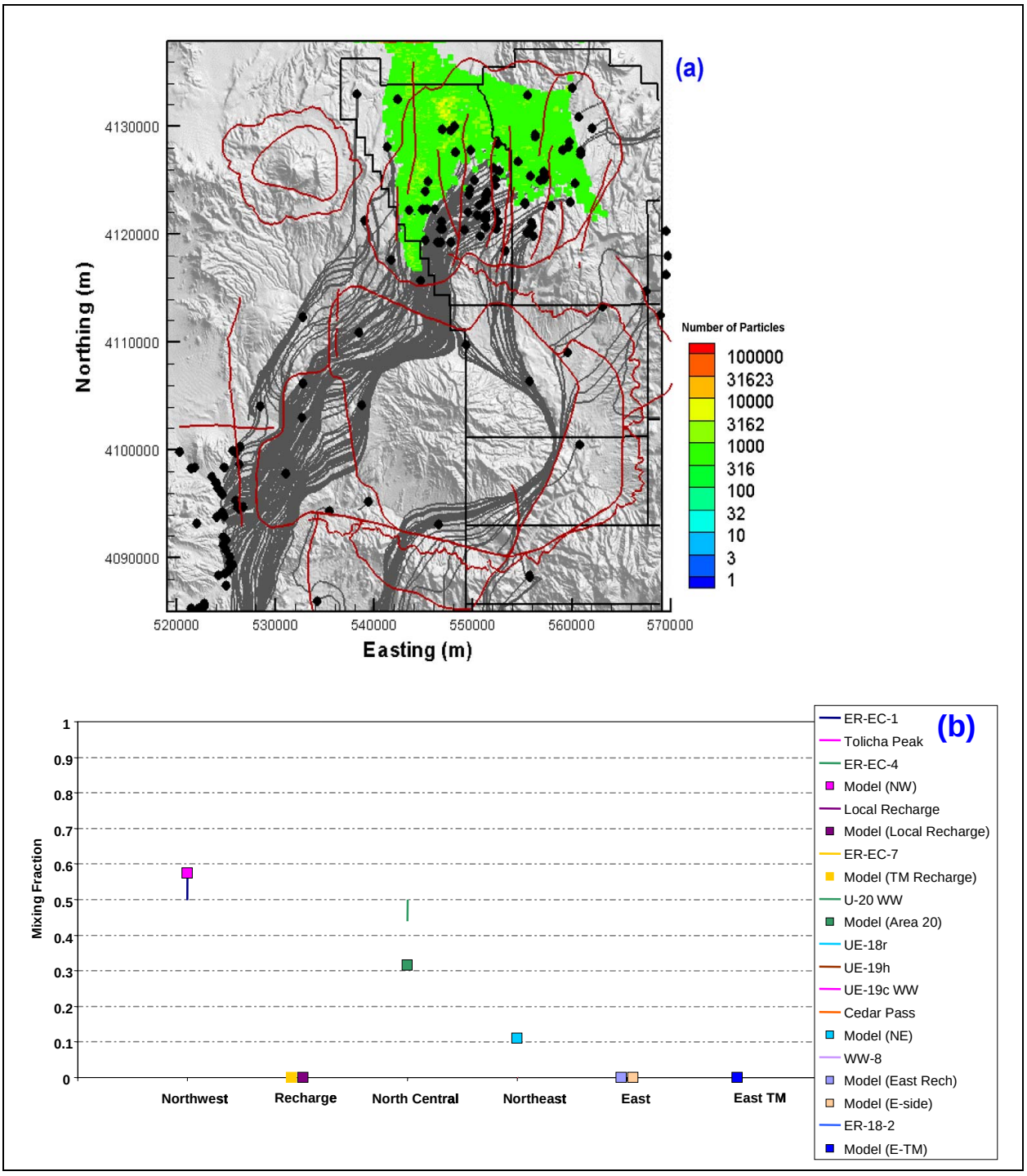

Figure 7-43
Comparison of Flow Model with Geochemical Mixing Targets at ER-EC-6 for SCCC-MME-SDA

Figure (a) shows the flow paths as mapped by forward SPTR particles originating at wells (grey lines) and the source recharge locations identified by reverse PTRK particle tracking (colored squares). Figure (b) shows the model comparison with geochemical mixing target ranges.

Uncontrolled When Printed

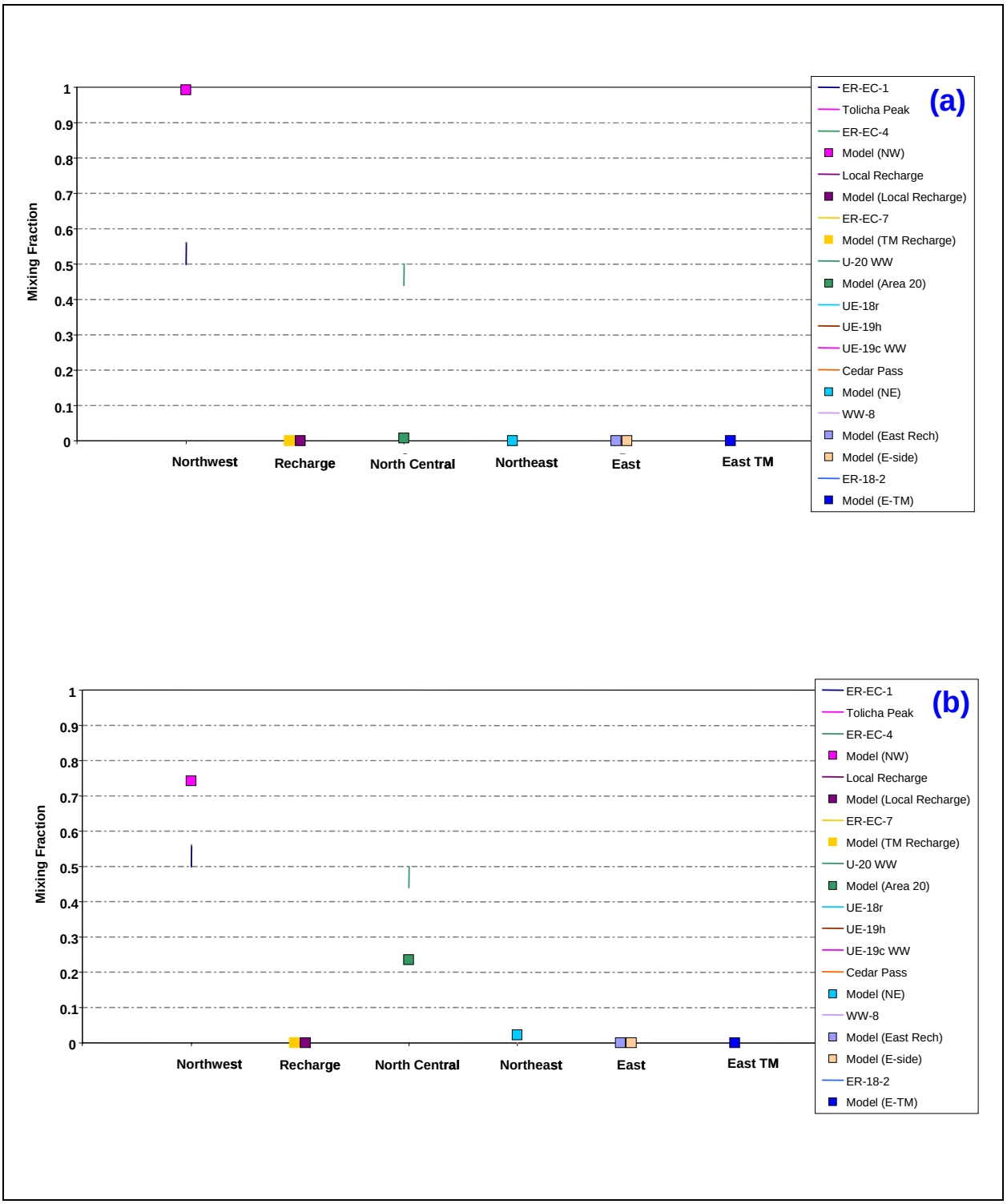

Figure 7-44
Quantitative Geochemical Comparisons at ER-EC-6 for (a) SCCC-USGSD-SDA and (b) SCCC-DRIA-SDA

Uncontrolled When Printed

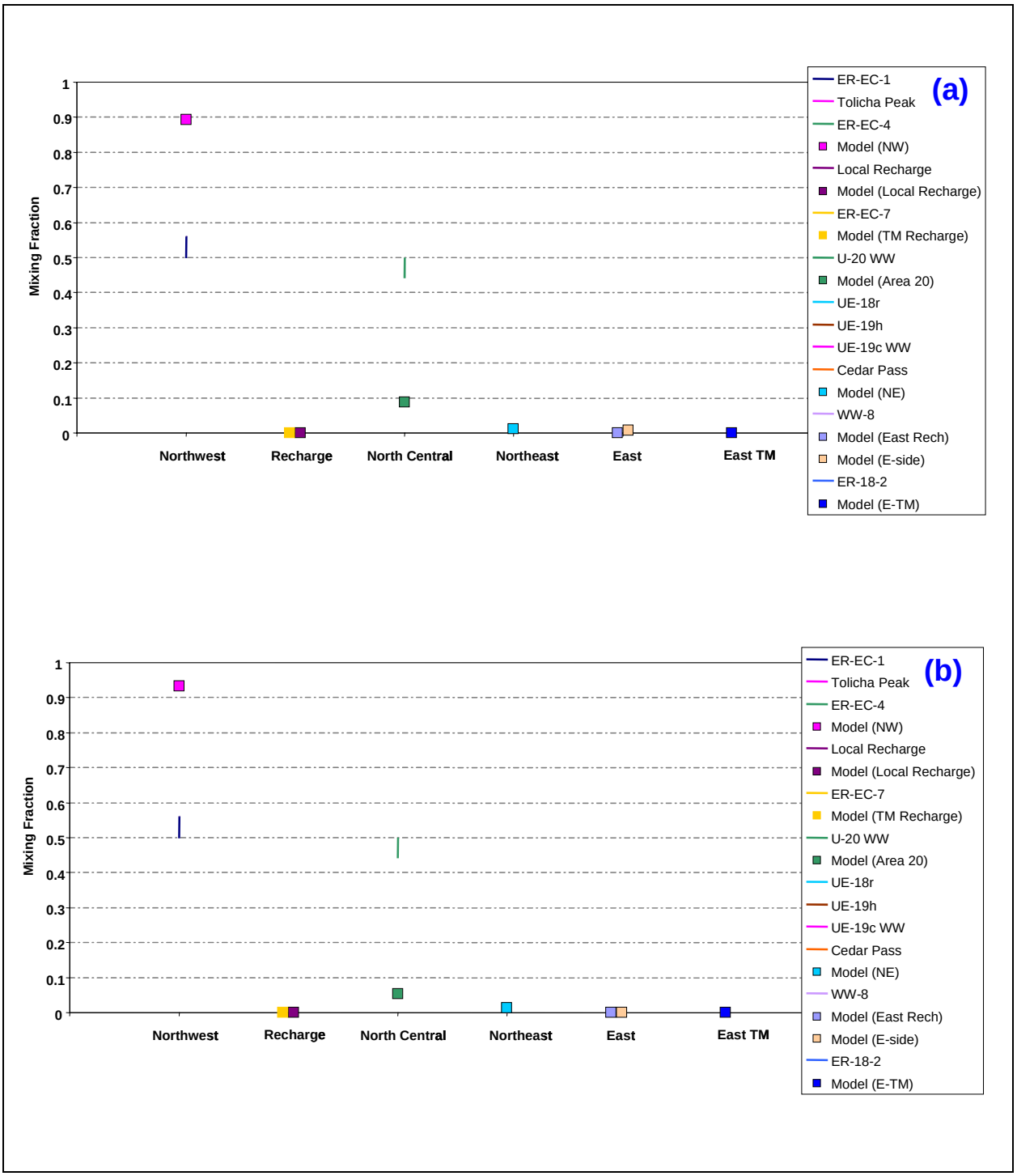

Figure 7-45
Quantitative Geochemical Comparisons at ER-EC-6 for
(a) PZUP-MME-SDA and (b) DRT-MME-SDA

Uncontrolled When Printed

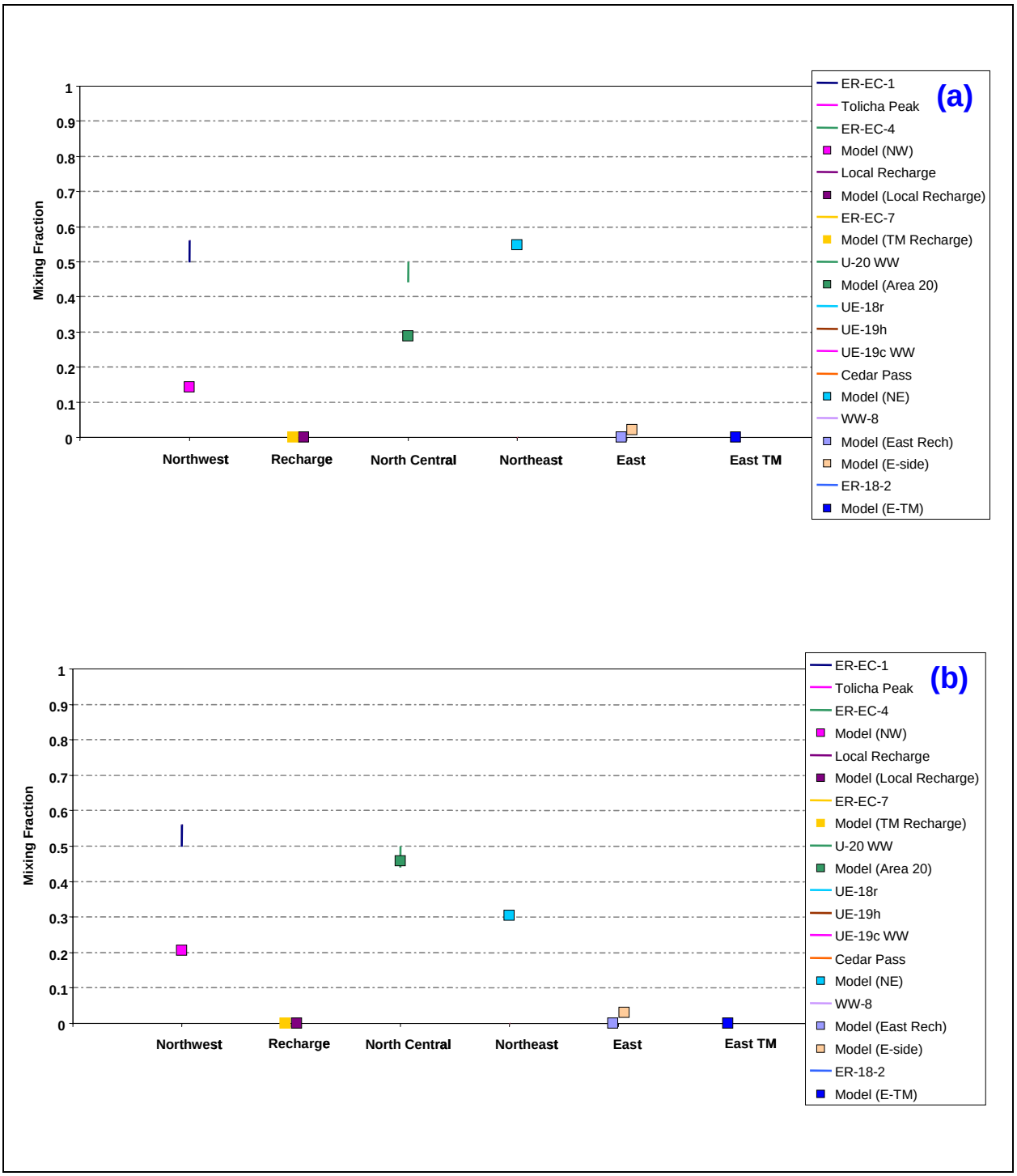

Figure 7-46
Quantitative Geochemical Comparison at ER-EC-6 for
(a) RIDGE-MME-SDA and (b) TCL-MME-SDA

Uncontrolled When Printed

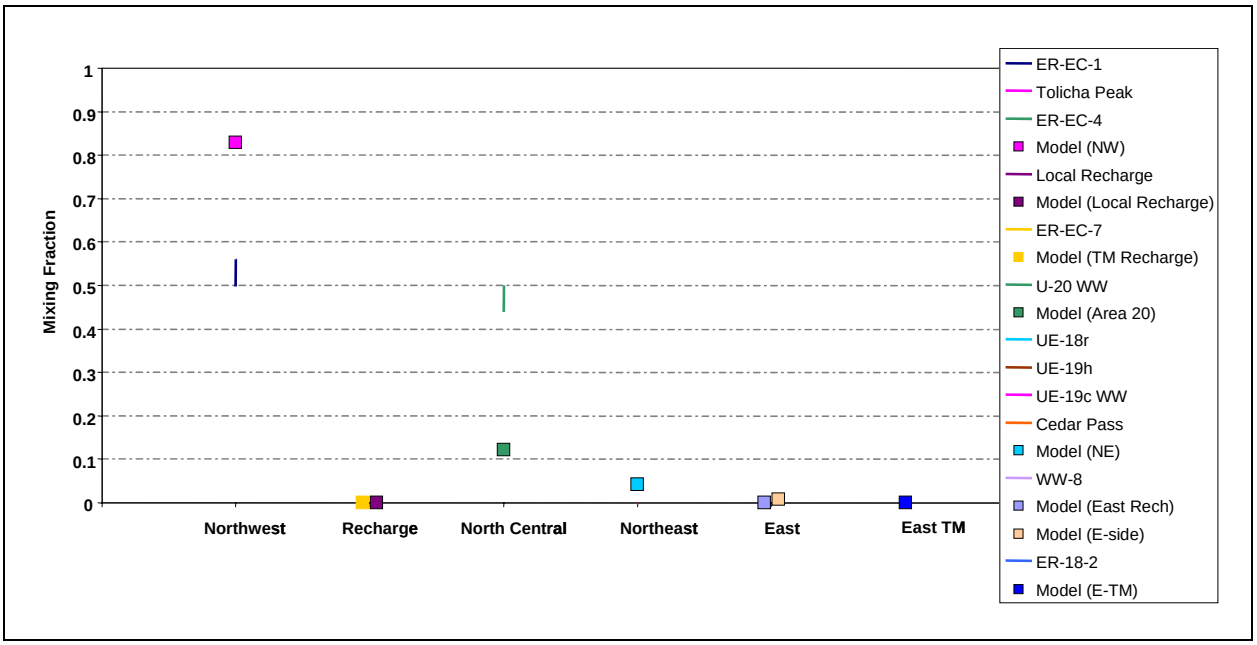

Figure 7-47
Comparison of Flow Model with Geochemical Mixing Targets at ER-EC-6 for SEPZ-MME-SDA

Uncontrolled When Printed

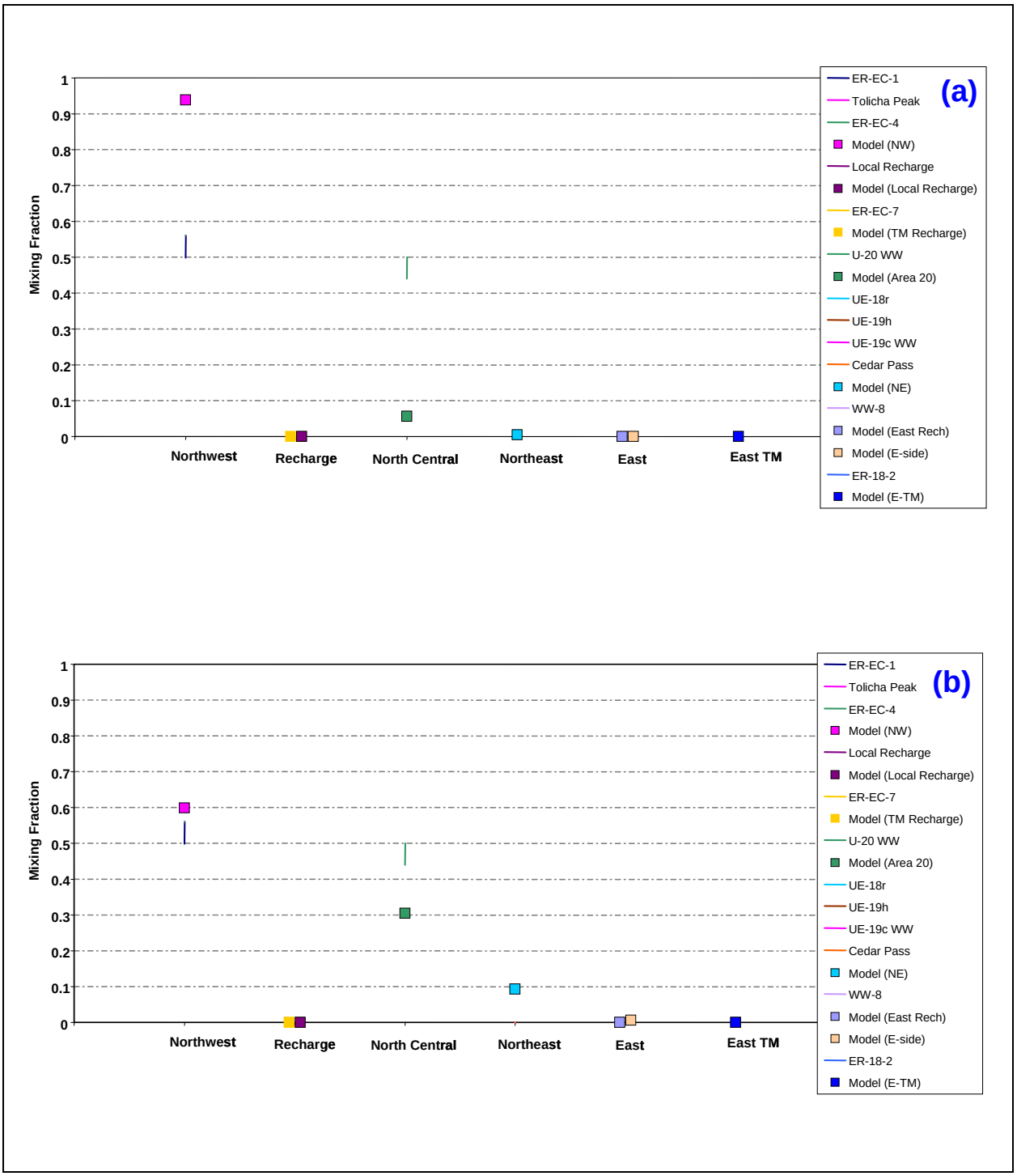

Figure 7-48
Quantitative Geochemical Comparisons at ER-EC-6 for
(a) PZUP-USGSD-SDA and (b) PZUP-DRIA-SDA

Uncontrolled When Printed

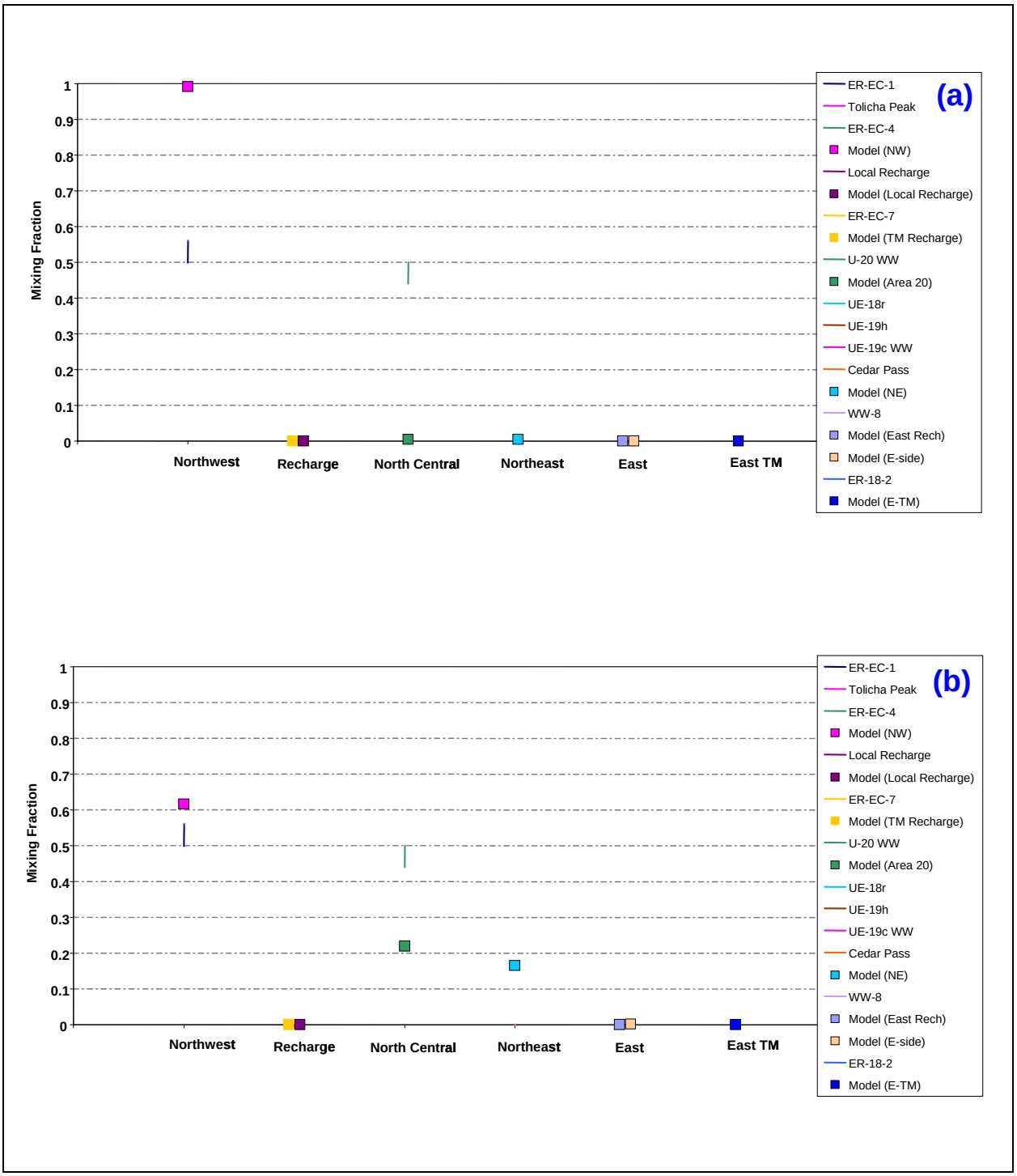

Figure 7-49
Quantitative Geochemical Comparisons at ER-EC-6 for
(a) DRT-USGSD-SDA and (b) DRT-DRIA-SDA

Uncontrolled When Printed

Table 7-12
Comparison of Alternative Models at ER-EC-6

HFM	Water-Balance Condition	Overpredicts the Northwest Source Component	Other Issues
BN-SDA reduced LCCU1 permeability alternative	MME	X	
	USGSD	X	
	DRIA	X	
BN-SDA	MME	X	
	USGSD	X	
	DRIA		
BN-ADA	MME	X	
SCCC-SDA	MME		
	USGSD	X	
	DRIA	X	
PZUP	MME	X	
DRT	MME	X	
RIDGE	MME		X
TCL	MME		X
SEPZ	MME	X	
PZUP	USGSD	X	
	DRIA		
DRT	USGSD	X	
	DRIA		

Uncontrolled When Printed

7.3.3 ER-OV-01

7.3.3.1 Alternative Water-Balance Conditions, BN HFM

The simulated mixing at ER-OV-01 in the USGSD and DRIA recharge alternatives with the BN HFM with reduced LCCU1 permeability alternative is primarily between northwest water and local recharge, with little contribution from the north central and northeast (Figures 7-50 and 7-51). Whereas the northwest source overprediction was greater for the USGSD alternative at ER-EC-6, it is worse for the DRIA alternative here at ER-OV-01, where virtually no north-central or northeast contributions are simulated, yet again highlighting the complex mixing occurring along the Thirsty Canyon flow path. For both of these models, more local recharge is simulated than is called for by the geochemistry analysis, highlighting the impact of independent redistribution of flow into washes and canyons in the recharge map.

Model results for the BN HFM with the USGSD and DRIA water-balance conditions are nearly identical to each other and to the USGSD water balance with the reduced LCCU1 permeability alternative model described above (Figure 7-52). The BN-MME-ADA matches the northwest source component better than the alternative water-balance models, but at the expense of greater errors in local recharge estimates (Figure 7-53).

7.3.3.2 SCCC Alternative HFM

As with the BN models, the SCCC models also overpredict either local recharge or northwest sources at ER-OV-01, and they underpredict the component of north-central and northeast sources. The SCCC alternative HFM with MME water-balance conditions has the greatest local recharge overpredictions, but the northwest source component is nearly within the geochemical target range (Figure 7-54). Both the USGSD and DRIA water-balance conditions for this HFM lead to good local recharge estimates but very large overpredictions of the northwest source (Figure 7-55).

7.3.3.3 PZUP, DRT, RIDGE, TCL, and SEPZ Alternative HFMs

The other alternative HFMs with MME water-balance conditions are considered in this section with the quantitative comparisons in Figures 7-56 through 7-58. These five alternatives perform similarly and reasonably well with respect to the northwest source component, but they all overestimate the

Uncontrolled When Printed

local recharge and they underestimate the north-central and northeast source components, with the exception of RIDGE-MME-ADA. This model is notable because 20 percent of the sources for ER-OV-01 are from east of the Purse Fault. Due to the similarities of Area 20 and Area 19 water, this result can be interpreted as almost within range of the targets if the north-central and northeast zones are combined.

At ER-OV-01, the USGSD and DRIA water-balance conditions for PZUP calibrations both lead to small overestimates of the northwest source and local recharge, but they have favorable results for the north-central and northeast source components (Figure 7-59). The DRIA model produces the closest match to the north-central and northeast contributions, which is particularly interesting because that is where many of the calibrated models discussed thus far fail.

The DRT HFM model calibrated with both USGSD and DRIA water-balance conditions overestimates both the northwest source and the local recharge, and it has no source contribution from the north-central or northeast zones (Figure 7-60). The MME water-balance conditions for this HFM led to closer matches to the northwest component but worse matches to the local recharge.

7.3.3.4 Summary: ER-OV-01

Nearly every model is unable to provide a source from the north-central and northeast zones at ER-OV-01. This is due to high recharge in Thirsty Canyon forcing those pathlines to the east and possibly due to the no-flow western boundary. In the Table 7-13 comparison, model results that provide some northwest and north-central groundwater at ER-OV-01 are highlighted. Uppercase Xs indicate the issue is worse than lowercase x symbols.

Uncontrolled When Printed

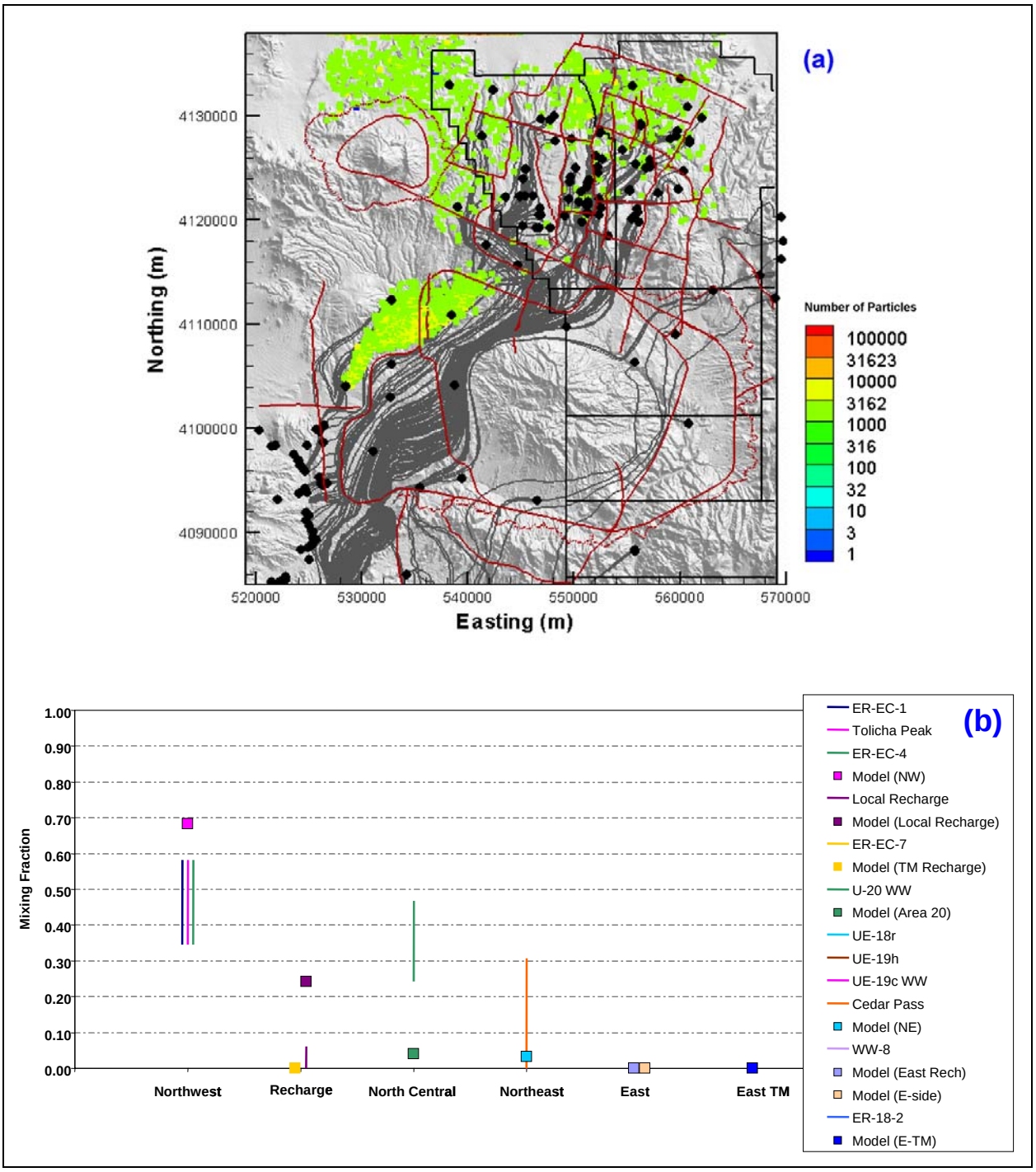

Figure 7-50
Comparison of Flow Model with Geochemical Mixing Targets at ER-OV-01 for BN-USGSD-SDA in the Reduced LCCU1 Permeability Alternative

Figure (a) shows the flow paths as mapped by forward SPTR particles originating at wells (grey lines) and the source recharge locations identified by reverse PTRK particle tracking (colored squares). Figure (b) shows the model comparison with geochemical mixing target ranges.

Uncontrolled When Printed

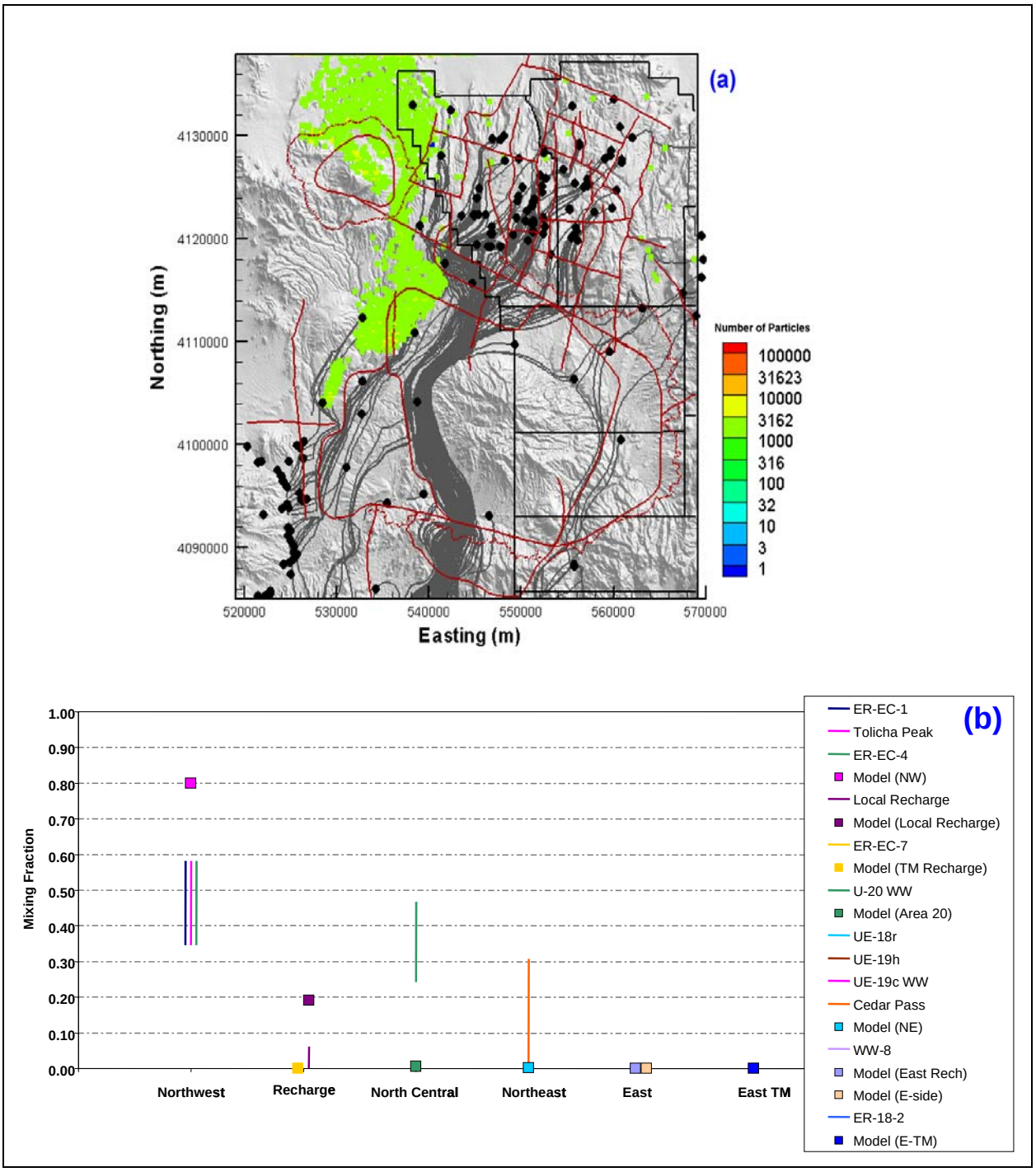

Figure 7-51
Comparison of Flow Model with Geochemical Mixing Targets at ER-OV-01 for BN-DRIA-SDA in the Reduced LCCU1 Permeability Alternative

Figure (a) shows the flow paths as mapped by forward SPTR particles originating at wells (grey lines) and the source recharge locations identified by reverse PTRK particle tracking (colored squares). Figure (b) shows the model comparison with geochemical mixing target ranges.

Uncontrolled When Printed

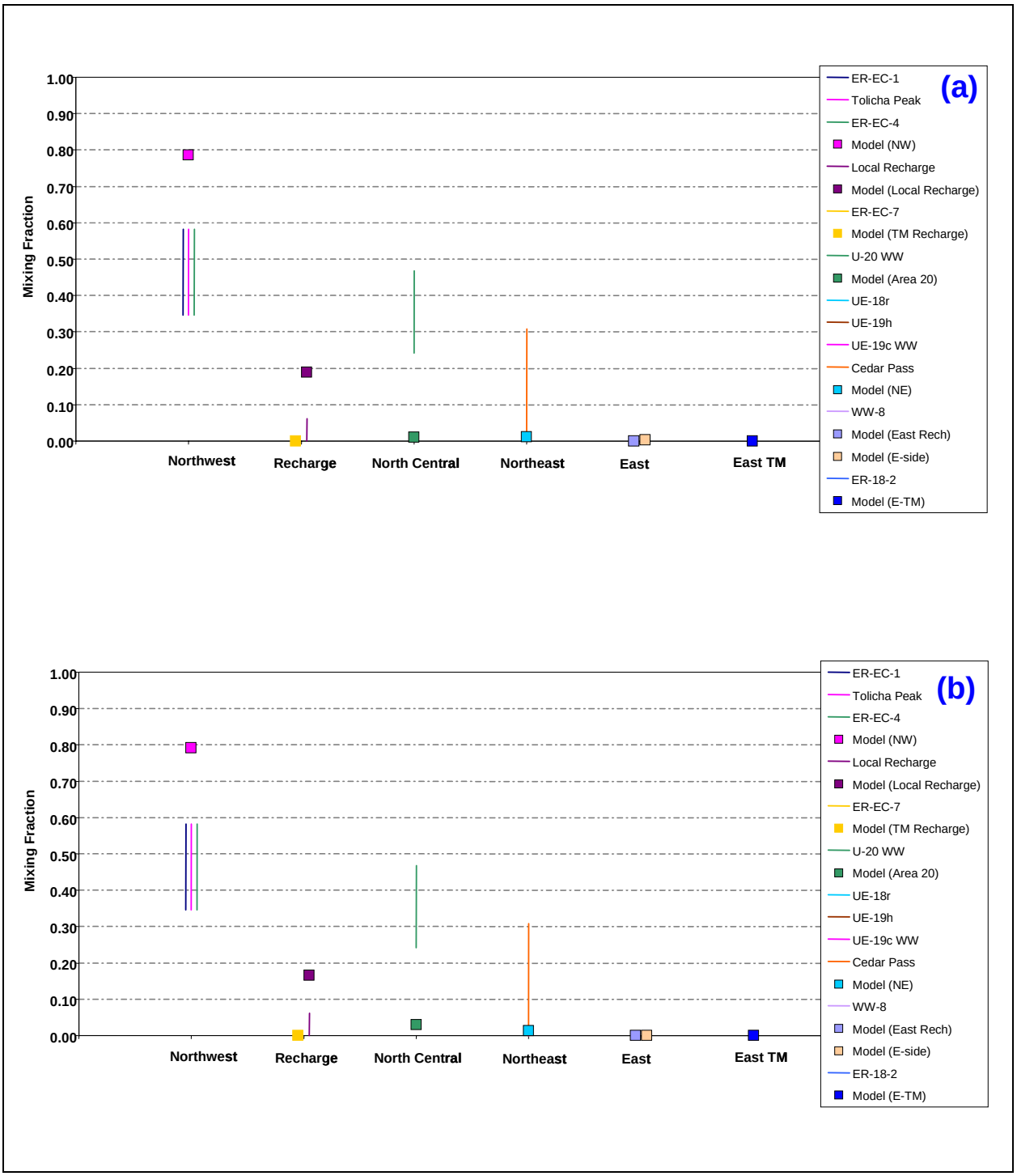

Figure 7-52
Quantitative Geochemical Comparison at ER-OV-01 for
(a) BN-USGSD-SDA and (b) BN-DRIA-SDA

Uncontrolled When Printed

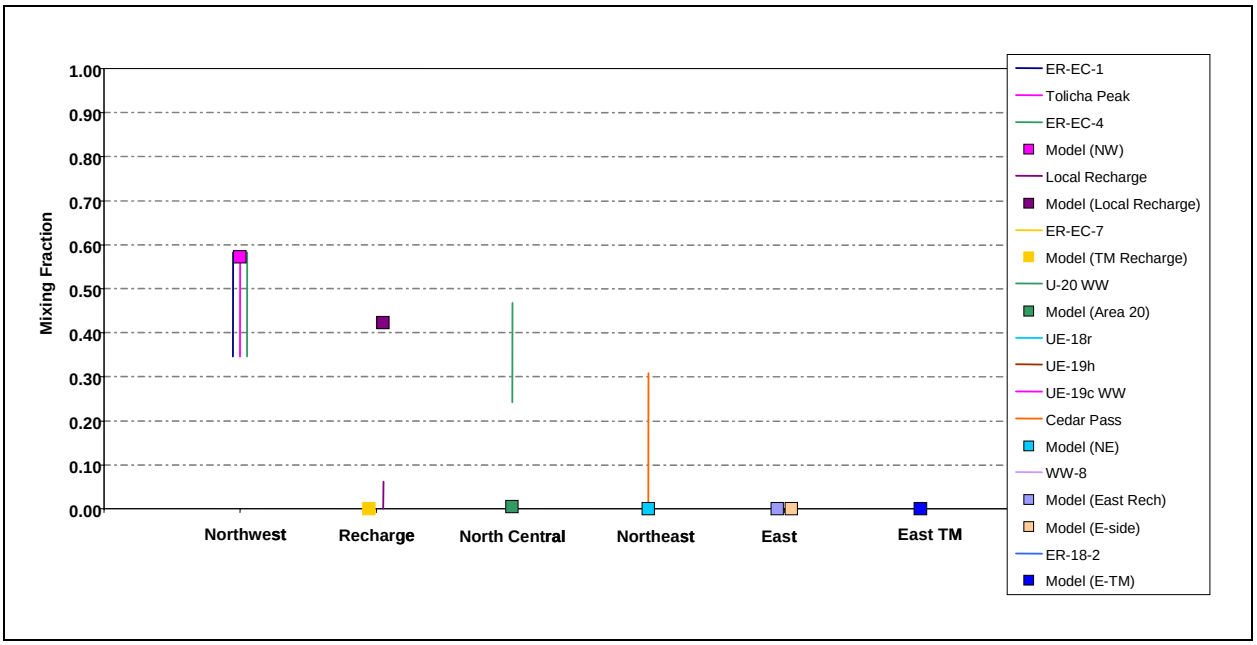

Figure 7-53
Comparison of Flow Model with Geochemical Mixing Targets at ER-OV-01 for BN-MME-ADA

Uncontrolled When Printed

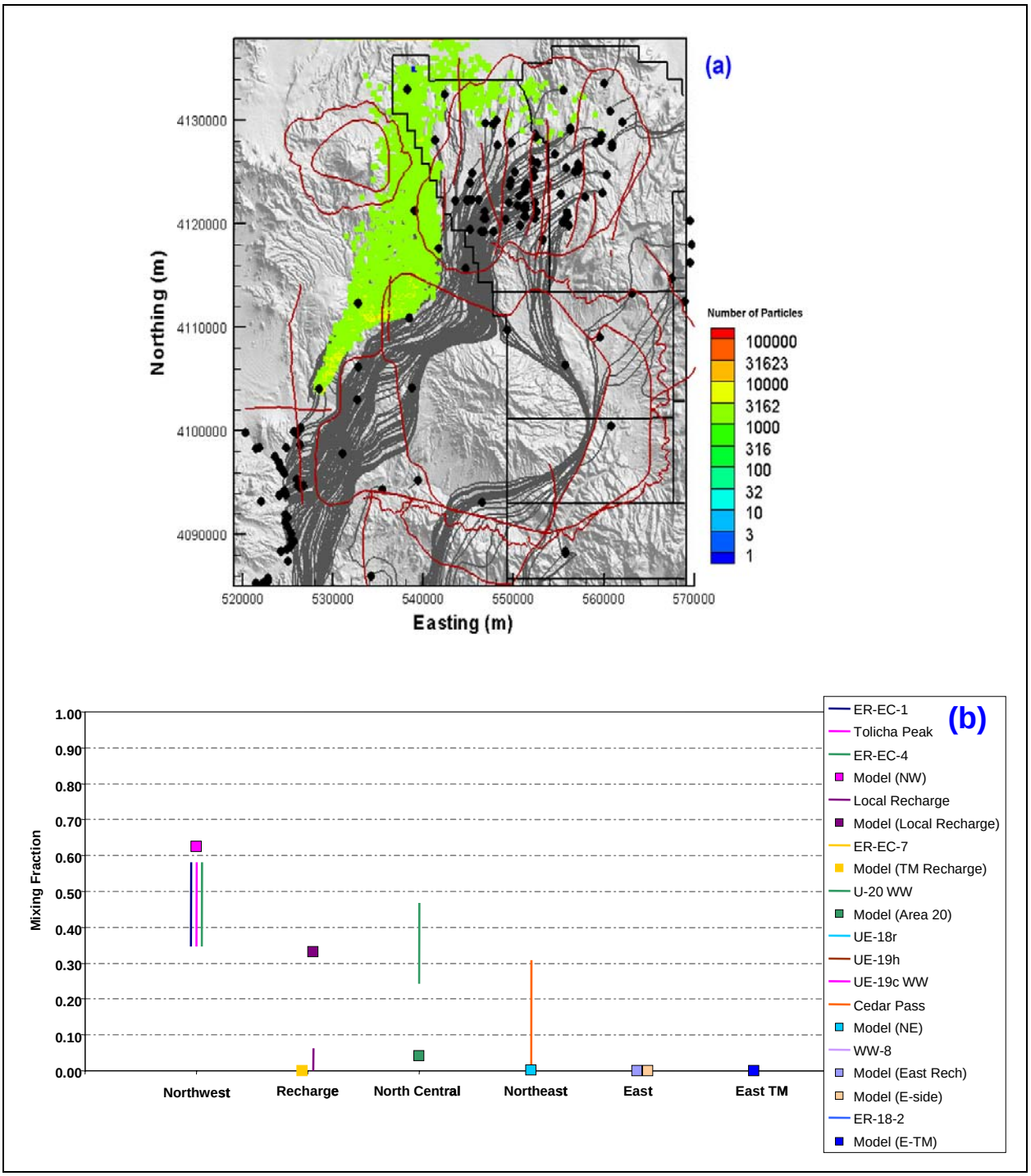

Figure 7-54
Comparison of Flow Model with Geochemical Mixing Targets at ER-OV-01 for SCCC-MME-SDA

Figure (a) shows the flow paths as mapped by forward SPTR particles originating at wells (grey lines) and the source recharge locations identified by reverse PTRK particle tracking (colored squares). Figure (b) shows the model comparison with geochemical mixing target ranges.

Uncontrolled When Printed

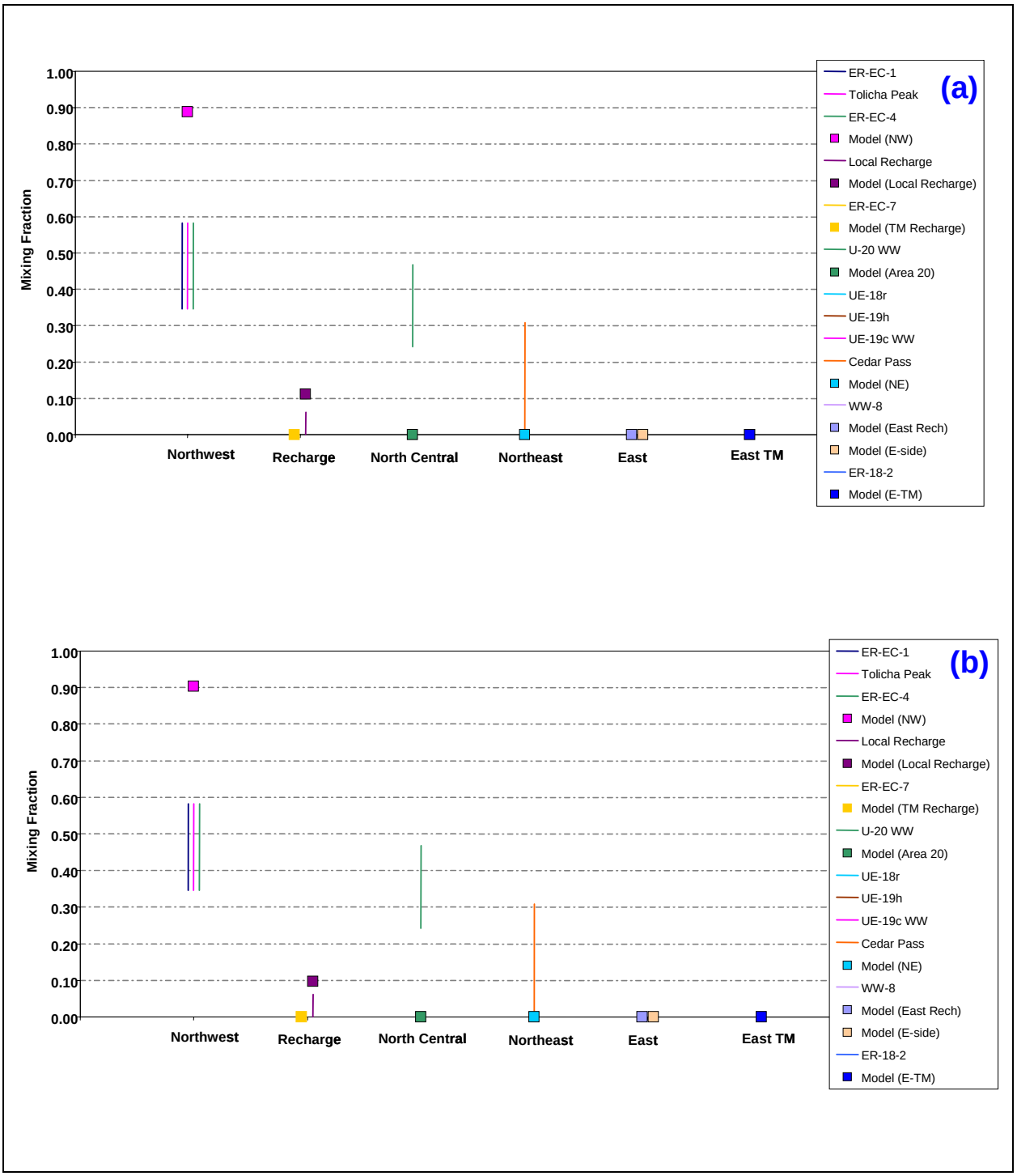

Figure 7-55
Quantitative Geochemical Comparisons at ER-OV-01 for (a) SCCC-USGSD-SDA and (b) SCCC-DRIA-SDA

Uncontrolled When Printed

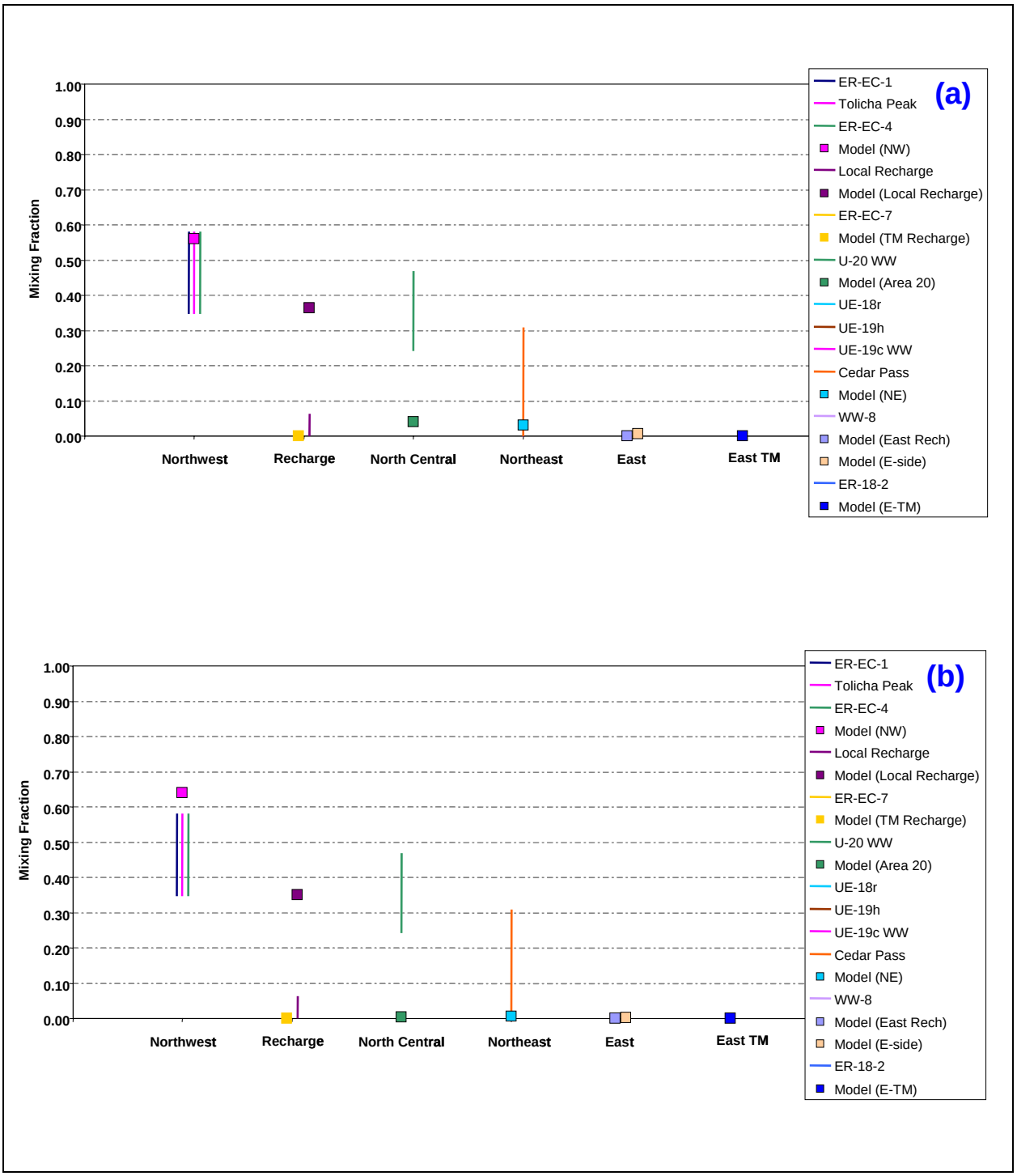

Figure 7-56
Quantitative Geochemical Comparison at ER-OV-01 for
(a) PZUP-MME-SDA and (b) DRT-MME-SDA

Uncontrolled When Printed

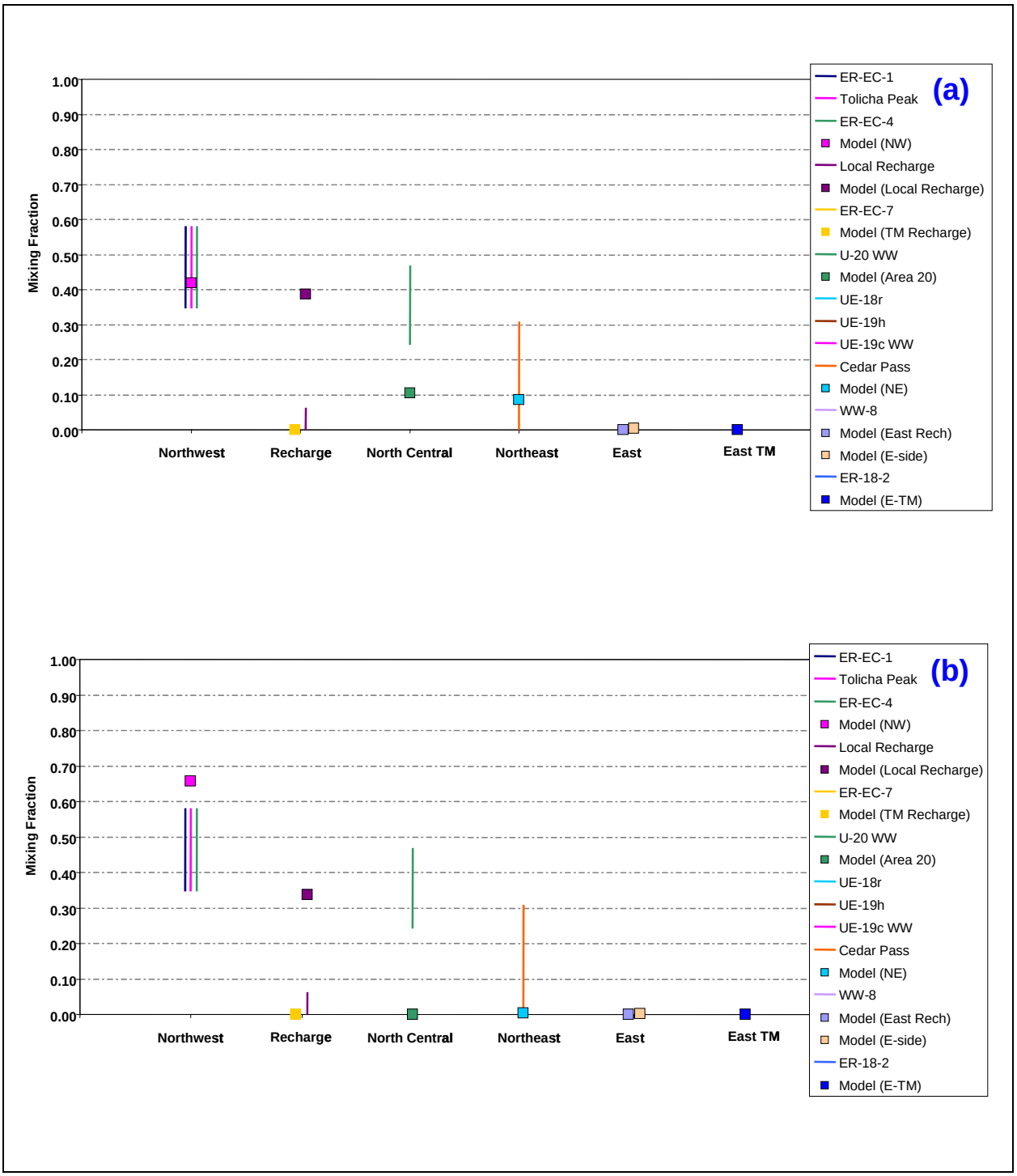

Figure 7-57
Quantitative Geochemical Comparisons at ER-OV-01 for
(a) RIDGE-MME-SDA and (b) TCL-MME-SDA

Uncontrolled When Printed

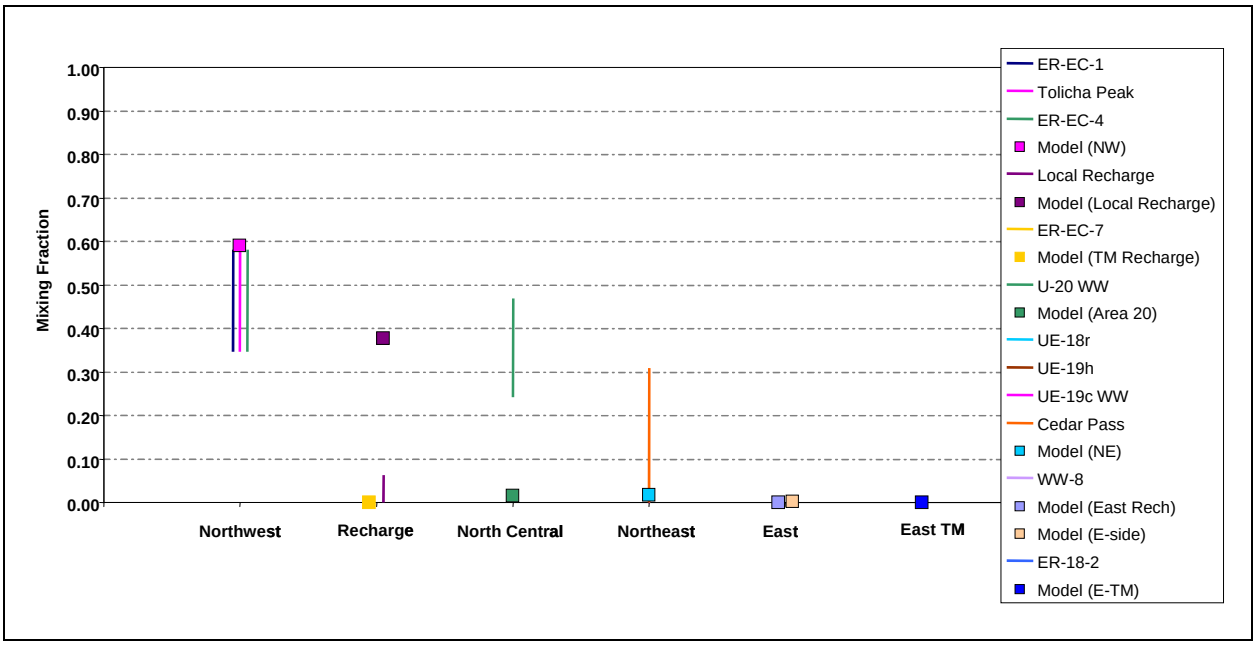

Figure 7-58
Comparison of Flow Model with Geochemical Mixing Targets at ER-OV-01 for SEPZ-MME-SDA

Uncontrolled When Printed

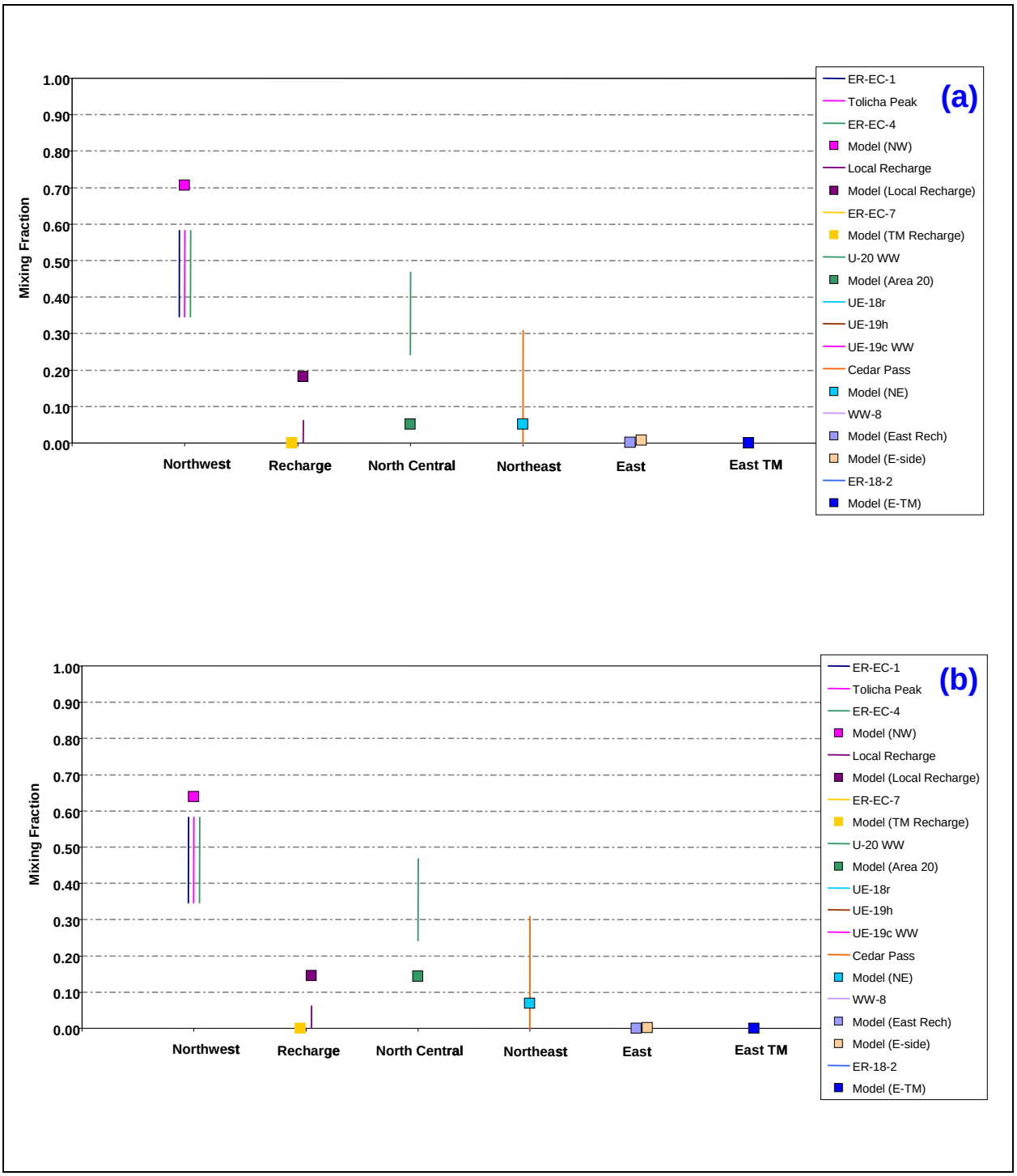

Figure 7-59
Quantitative Geochemical Comparisons at ER-OV-01 for (a) PZUP-USGSD-SDA and (b) PZUP-DRIA-SDA

Uncontrolled When Printed

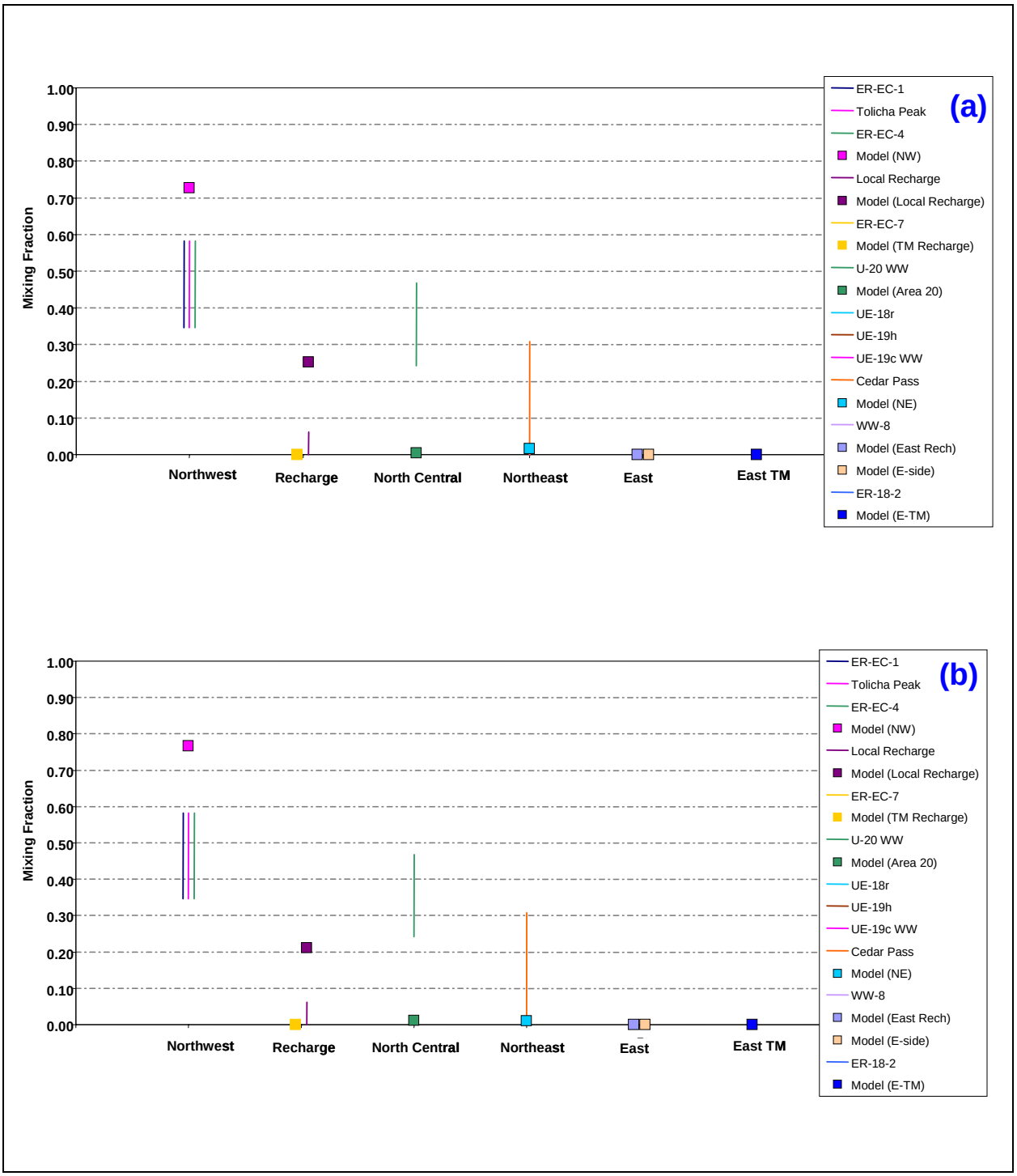

Figure 7-60
Quantitative Geochemical Comparisons at ER-OV-01 for
(a) DRT-USGSD-SDA and (b) DRT-DRIA-SDA

Uncontrolled When Printed

Table 7-13
Comparison of Alternative Models at ER-OV-01

HFM	Water-Balance Condition	Underpredicts North-Central and/or Northeast Source	Overpredicts the Northwest Source	Overpredicts Local Recharge
BN-SDA reduced LCCU1 permeability alternative	MME	X		x
	USGSD	X	x	x
	DRIA	X	X	x
BN-SDA	MME	X		X
	USGSD	X	X	x
	DRIA	X	X	x
BN-ADA	MME	X		X
SCCC-SDA	MME	X		X
	USGSD	X	X	
	DRIA	X	X	
PZUP	MME	X		X
DRT	MME	X		X
RIDGE	MME			X
TCL	MME	X		X
SEPZ	MME	X		X
PZUP	USGSD		x	x
	DRIA			
DRT	USGSD	X	x	x
	DRIA	X	x	x

Uncontrolled When Printed

7.3.4 ER-OV-05

7.3.4.1 Alternative Water-Balance Conditions, BN HFM

As with the BN-MME-SDA reduced LCCU1 permeability alternative, the simulated mixing at ER-OV-05 for the USGSD and DRIA water-balance conditions match the targets well with a simple flow path from the northwest to the target well (Figures 7-61 and 7-62). It is interesting to note the effects of the different recharge maps, as represented by the locations and densities of reverse particles leaving the two different models. Not surprisingly, the BN-MME-SDA (high LCCU1 permeability) with both USGSD and DRIA water-balance conditions and the BN-MME-ADA model estimate the northwest source well (Figures 7-63 and 7-64).

7.3.4.2 SCCC Alternative HFM

Due to the boundary conditions and lack of HFM complexity on the west side of the model, flow is predominantly north to south. Thus, the SCCC alternative HFM model results with MME water-balance conditions are not significantly different from the BN HFM models (Figure 7-65). The only notable aspect of the alternative water-balance model calibrations with the SCCC HFM (Figure 7-66) is that when DRIA is used, a significant component of the mixing source is from local recharge. However, considering data control in this portion of the domain and the arbitrary boundaries for the different zones leads one to simply note that the recharge source for water at ER-OV-05 in this model is somewhat further south than in most other models.

7.3.4.3 PZUP, DRT, RIDGE, TCL, and SEPZ Alternative HFMs

As with all ER-OV-05a cases described thus far, there are no substantial differences between the alternative HFM and MME water-balance scenarios (Figures 7-67 through 7-69). When considering the alternative water-balance conditions for PZUP and DRT (Figures 7-70 and 7-71), the only notable features is that the location of some of the local recharge for the DRIA models is further south than the other water-balance condition models.

7.3.4.4 Summary: ER-OV-05

All of the models considered for ER-OV-05a produce reasonable results. There are no discriminating features in the geochemistry target matching that were identified for this well.

Uncontrolled When Printed

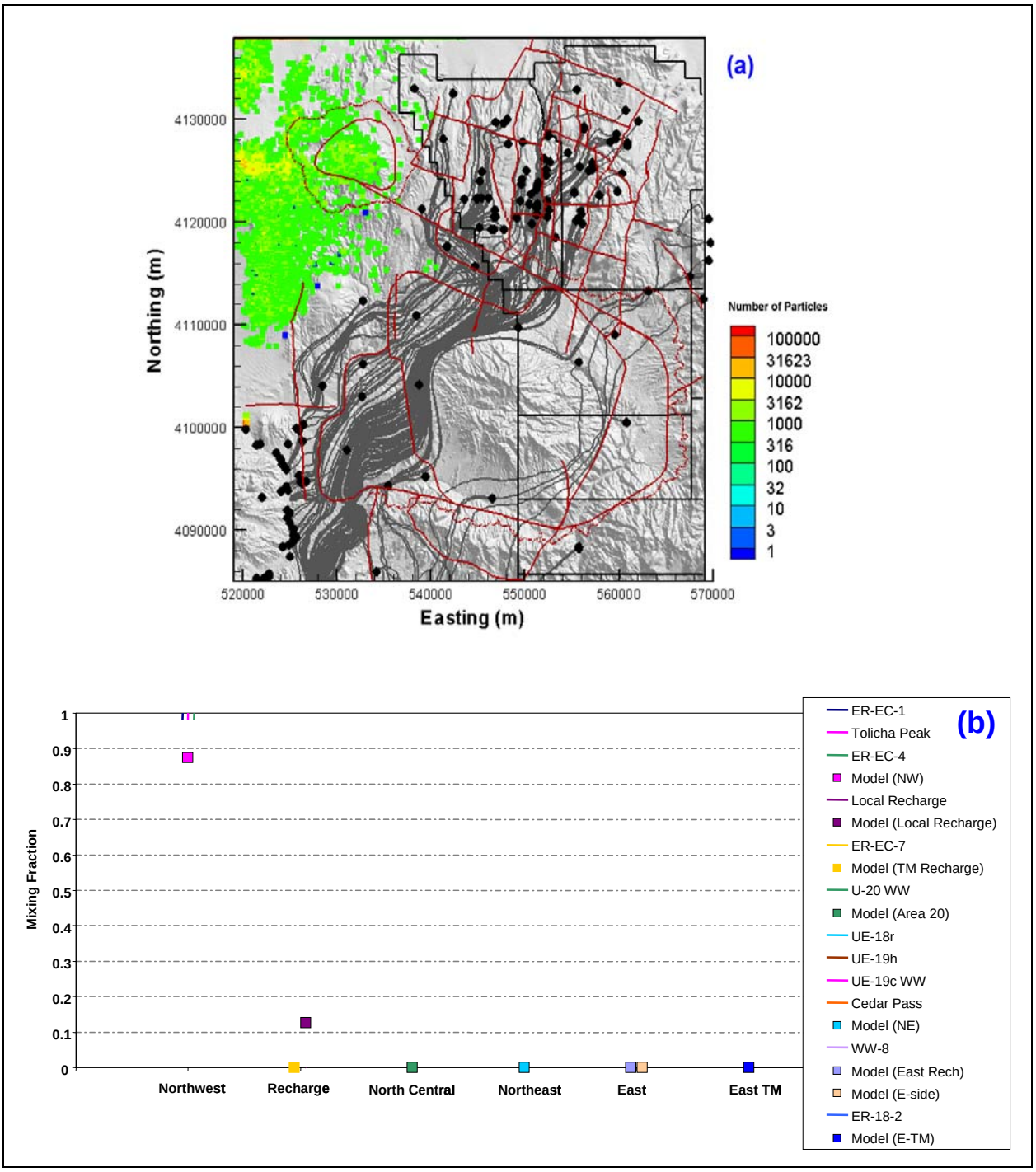

Figure 7-61
Comparison of Flow Model with Geochemical Mixing Targets at ER-OV-05 for BN-USGSD-SDA in the Reduced LCCU1 Permeability Alternative

Figure (a) shows the flow paths as mapped by forward SPTR particles originating at wells (grey lines) and the source recharge locations identified by reverse PTRK particle tracking (colored squares). Figure (b) shows the model comparison with geochemical mixing target ranges.

Uncontrolled When Printed

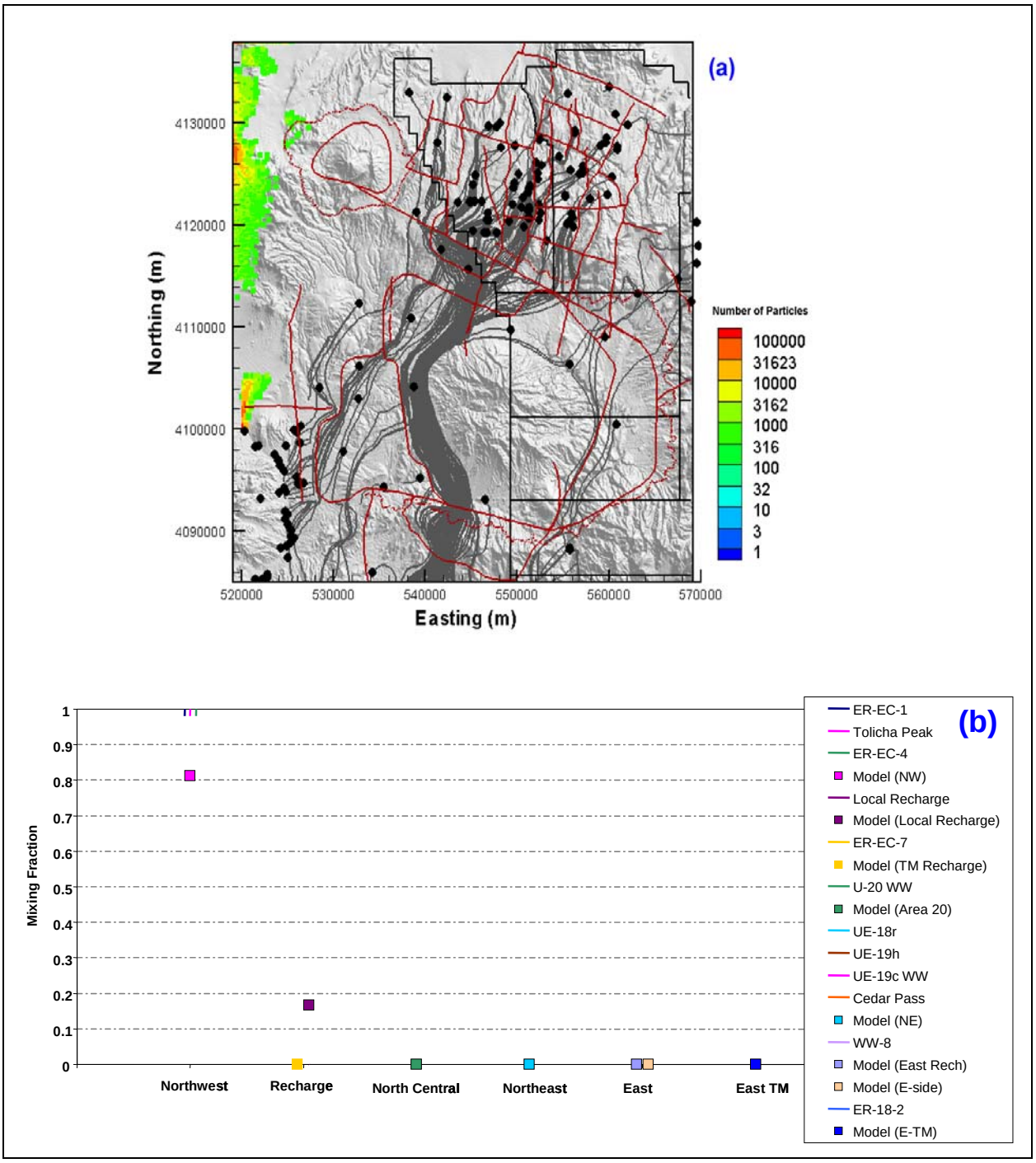

Figure 7-62
Comparison of Flow Model with Geochemical Mixing Targets at ER-OV-05 for BN-DRIA-SDA in the Reduced LCCU1 Permeability Alternative

Figure (a) shows the flow paths as mapped by forward SPTR particles originating at wells (grey lines) and the source recharge locations identified by reverse PTRK particle tracking (colored squares). Figure (b) shows the model comparison with geochemical mixing target ranges.

Uncontrolled When Printed

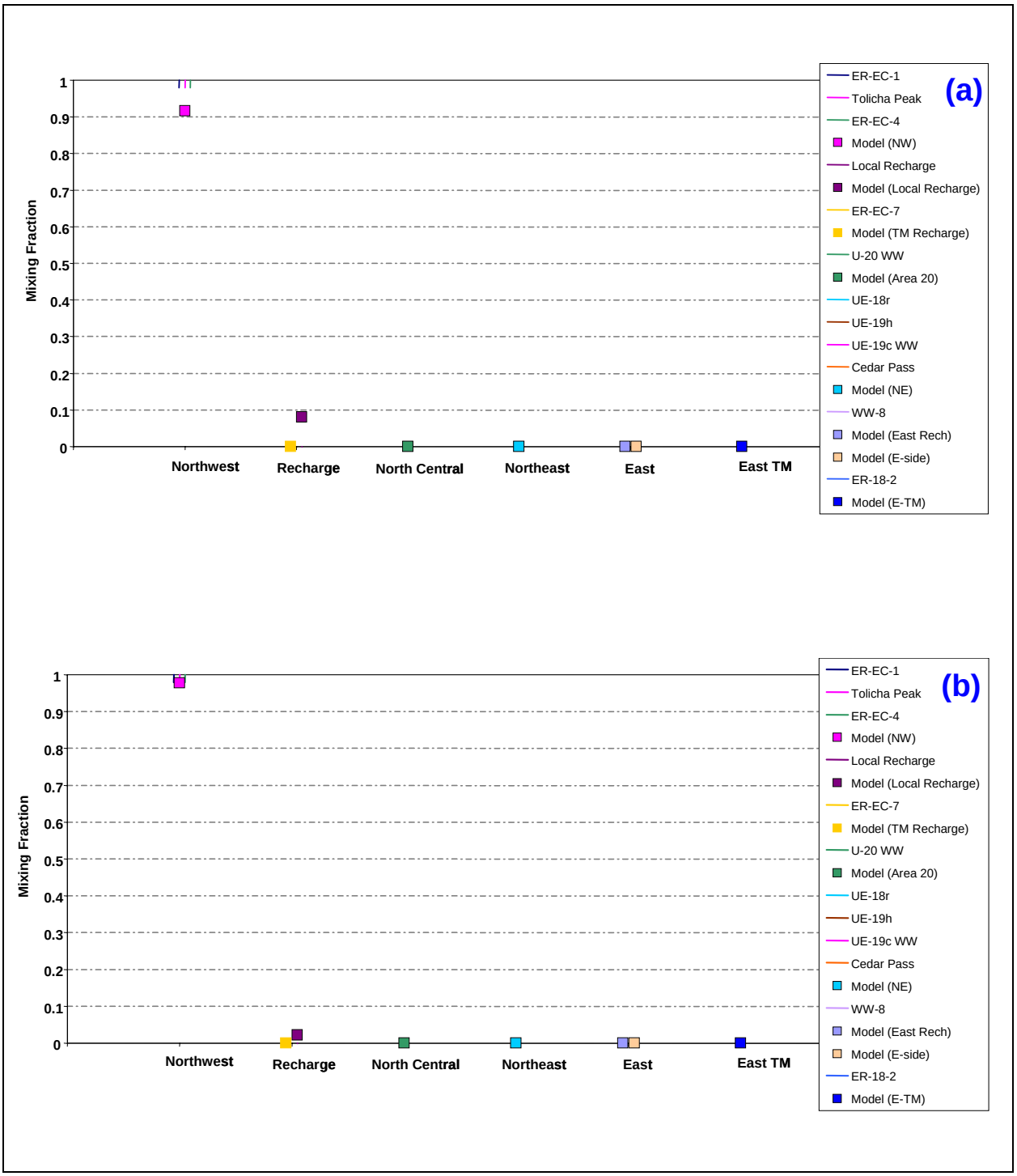

Figure 7-63
Quantitative Geochemical Comparisons at Well ER-OV-05 for (a) BN-USGSD-SDA and (b) BN-DRIA-SDA

Uncontrolled When Printed

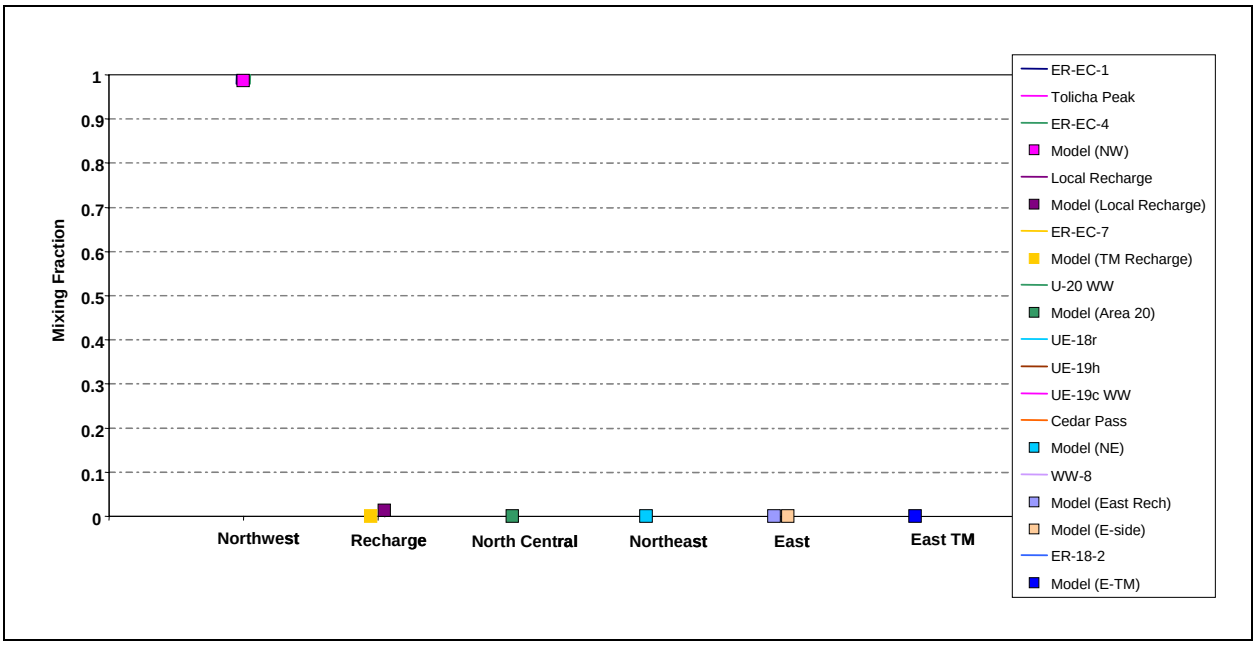

Figure 7-64
Comparison of Flow Model with Geochemical Mixing Targets at ER-OV-05 for BN-MME-ADA

Uncontrolled When Printed

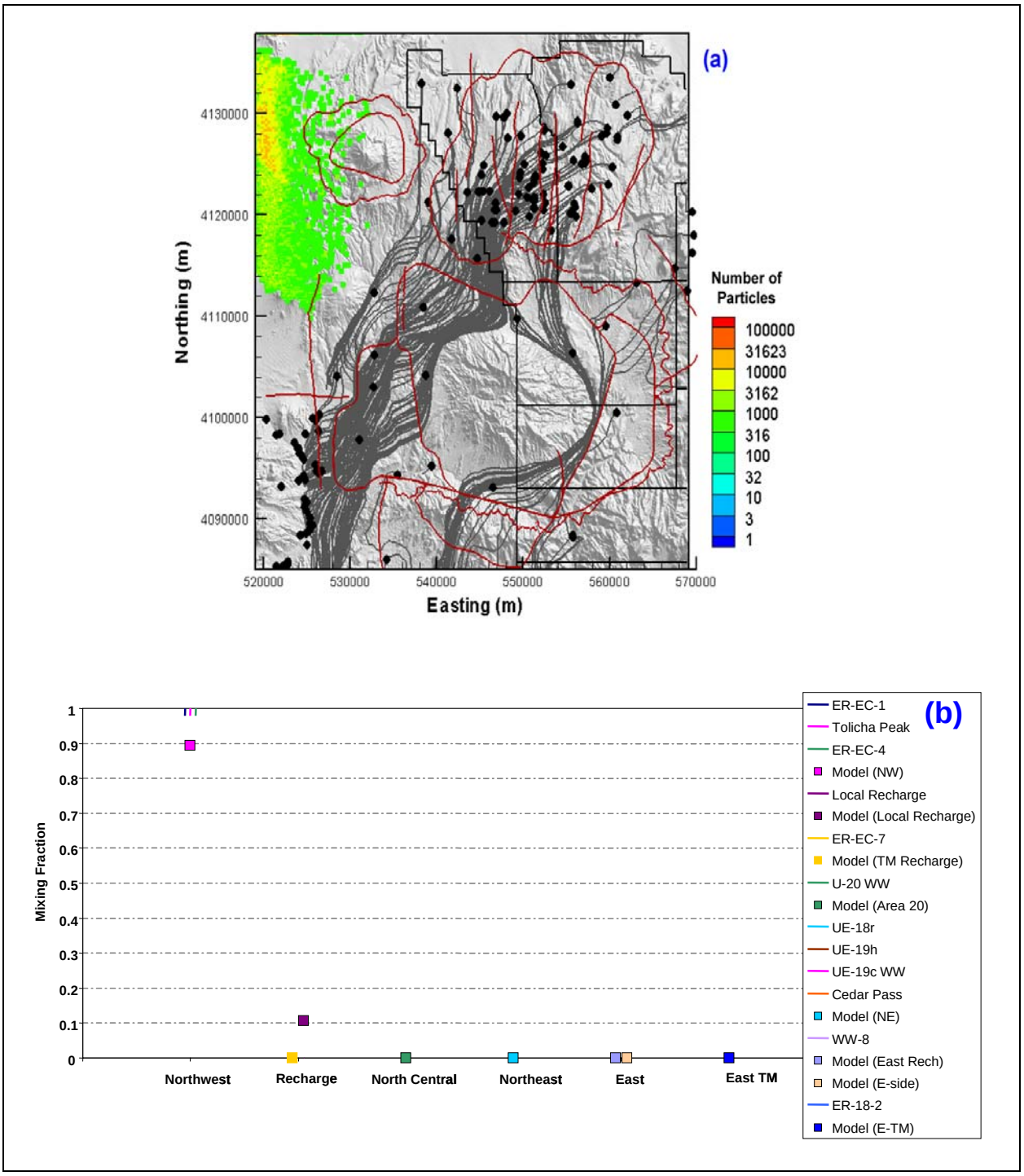

Figure 7-65
Comparison of Flow Model with Geochemical Mixing Targets at ER-OV-05 for SCCC-MME-SDA

Figure (a) shows the flow paths as mapped by forward SPTR particles originating at wells (grey lines) and the source recharge locations identified by reverse PTRK particle tracking (colored squares). Figure (b) shows the model comparison with geochemical mixing target ranges.

Uncontrolled When Printed

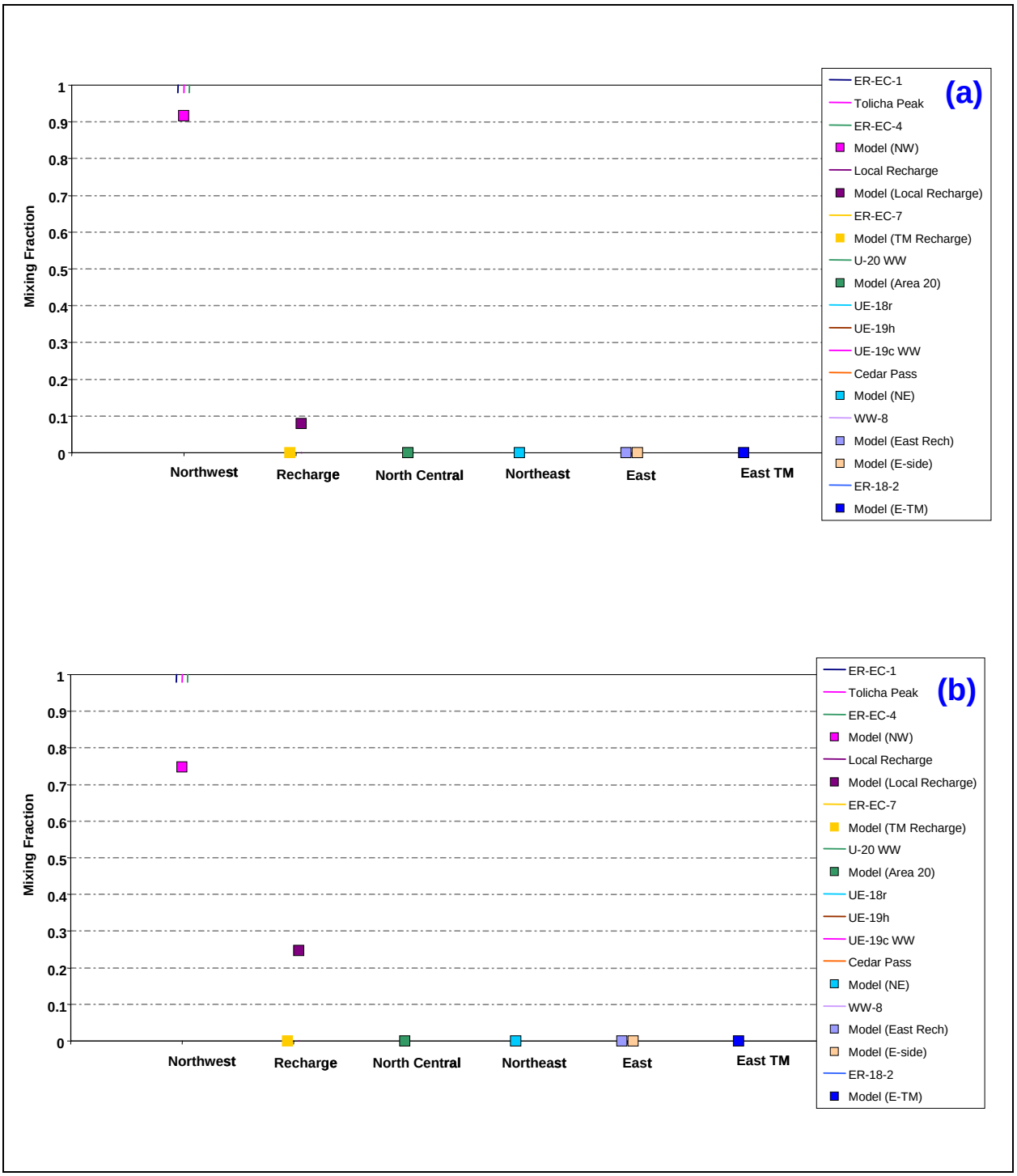

Figure 7-66
Quantitative Geochemical Comparisons at ER-OV-05 for (a) SCCC-USGSD-SDA and (b) SCCC-DRIA-SDA

Uncontrolled When Printed

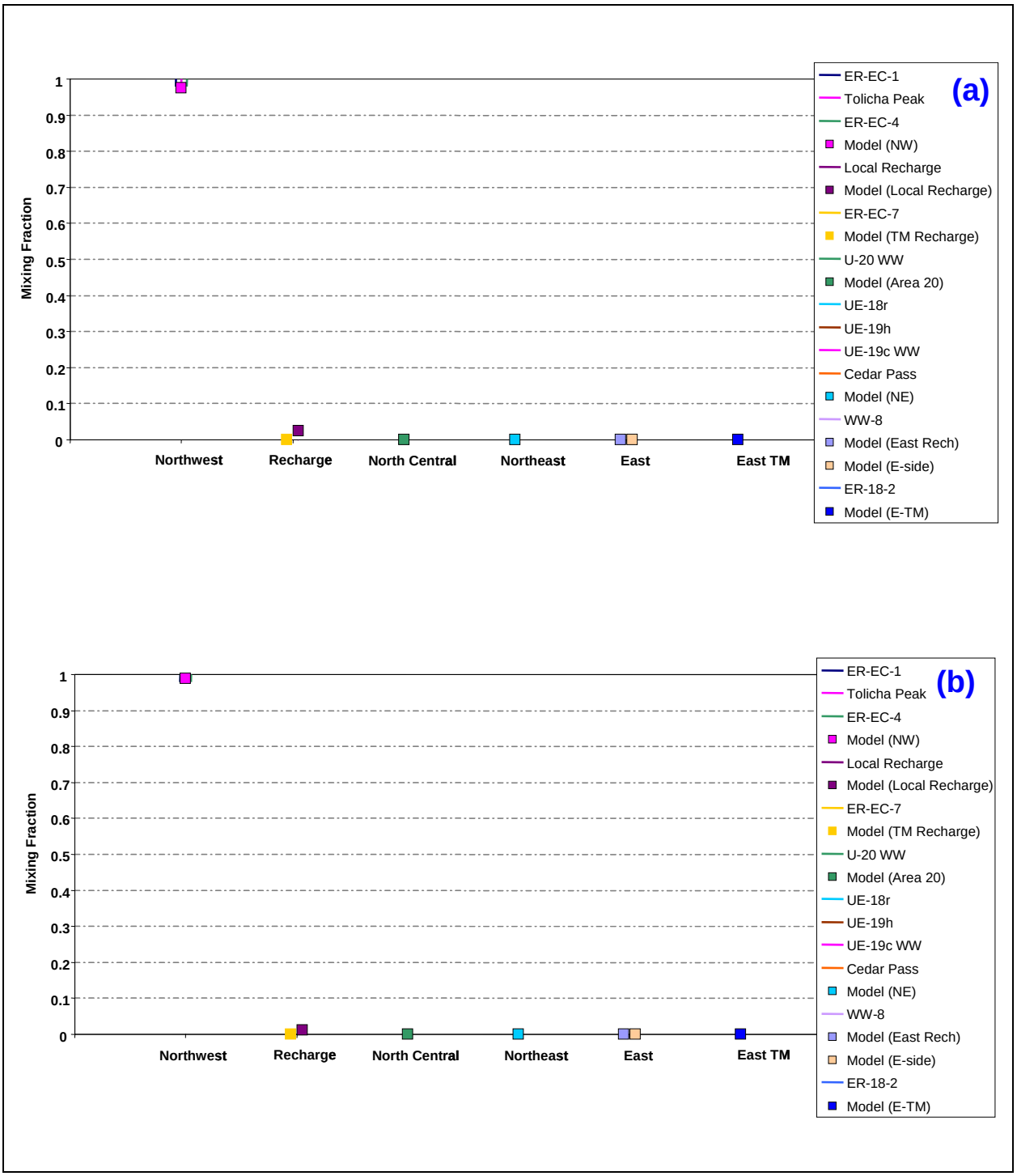

Figure 7-67
Quantitative Geochemical Comparison at ER-OV-05 for
(a) PZUP-MME-SDA and (b) DRT-MME-SDA

Uncontrolled When Printed

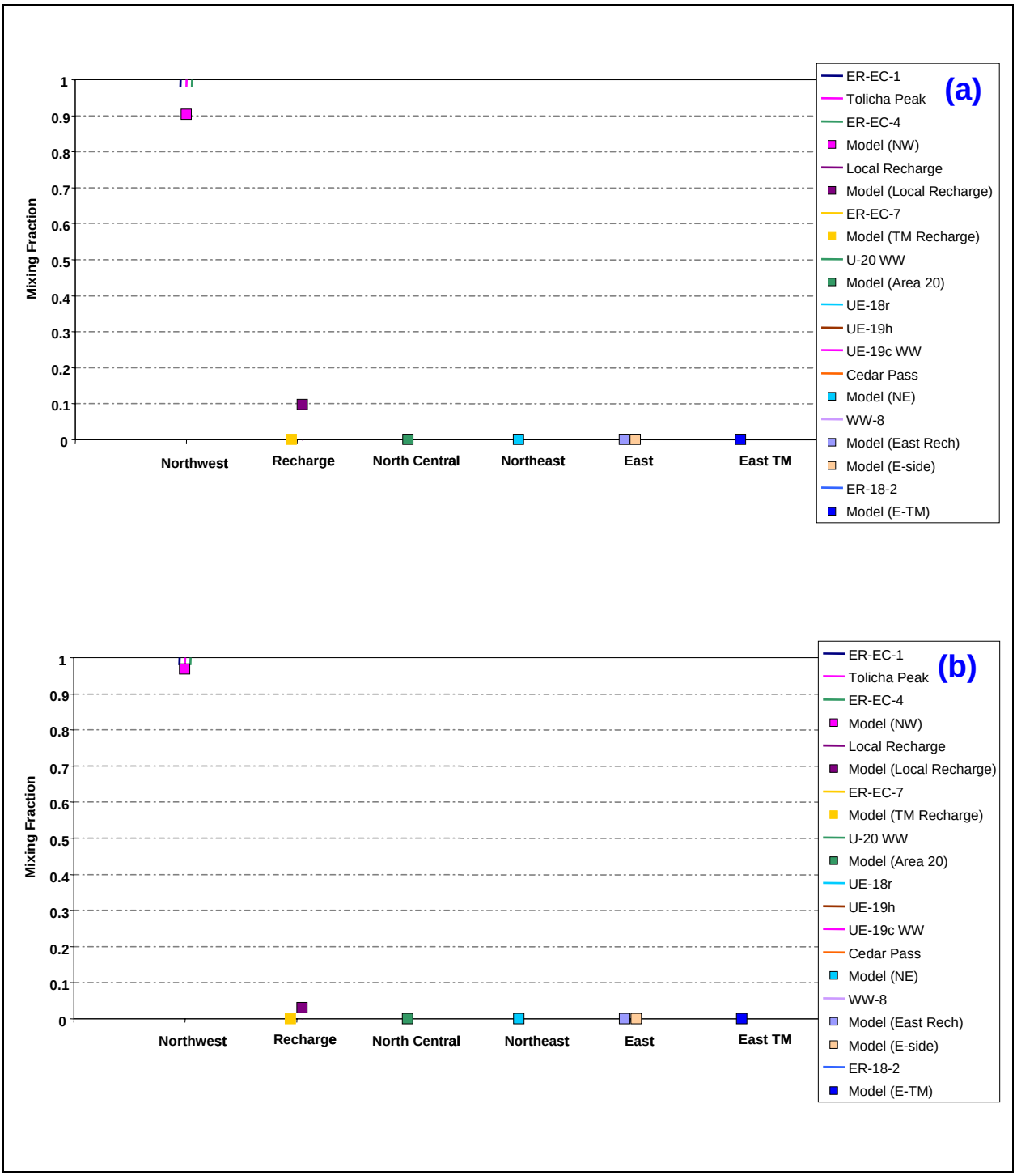

Figure 7-68
Quantitative Geochemical Comparisons at ER-OV-05 for
(a) RIDGE-MME-SDA and (b) TCL-MME-SDA

Uncontrolled When Printed

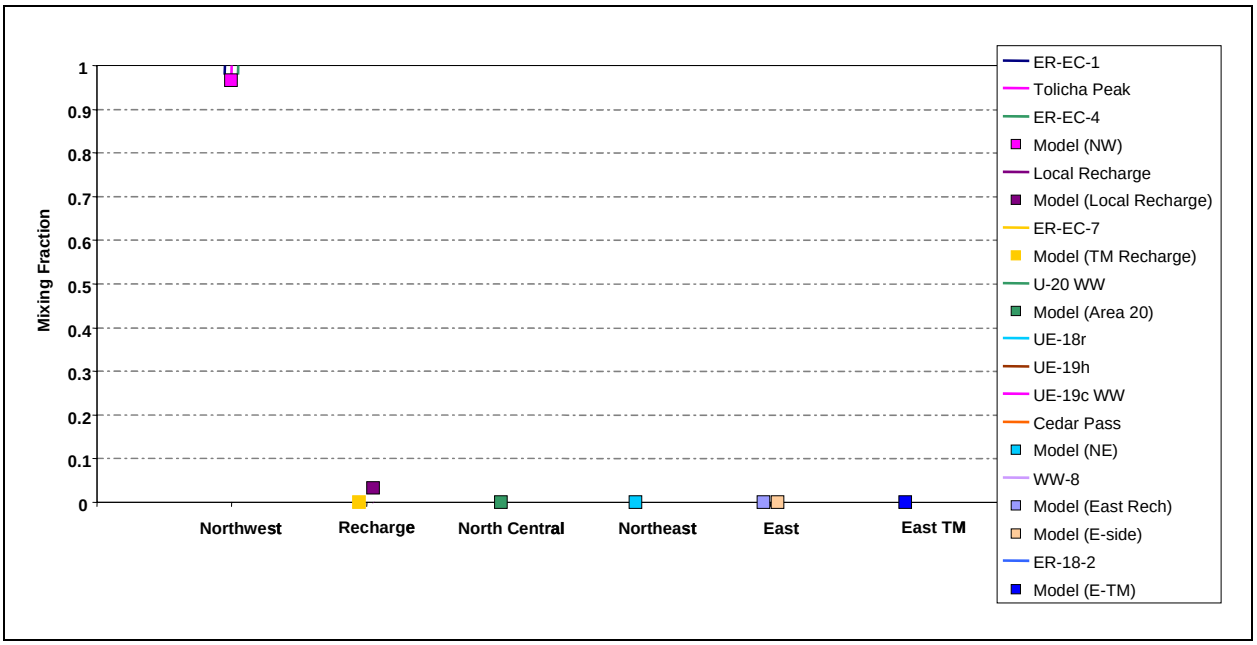

Figure 7-69
Comparison of Flow Model with Geochemical Mixing Targets at ER-OV-05 for SEPZ-MME-SDA

Uncontrolled When Printed

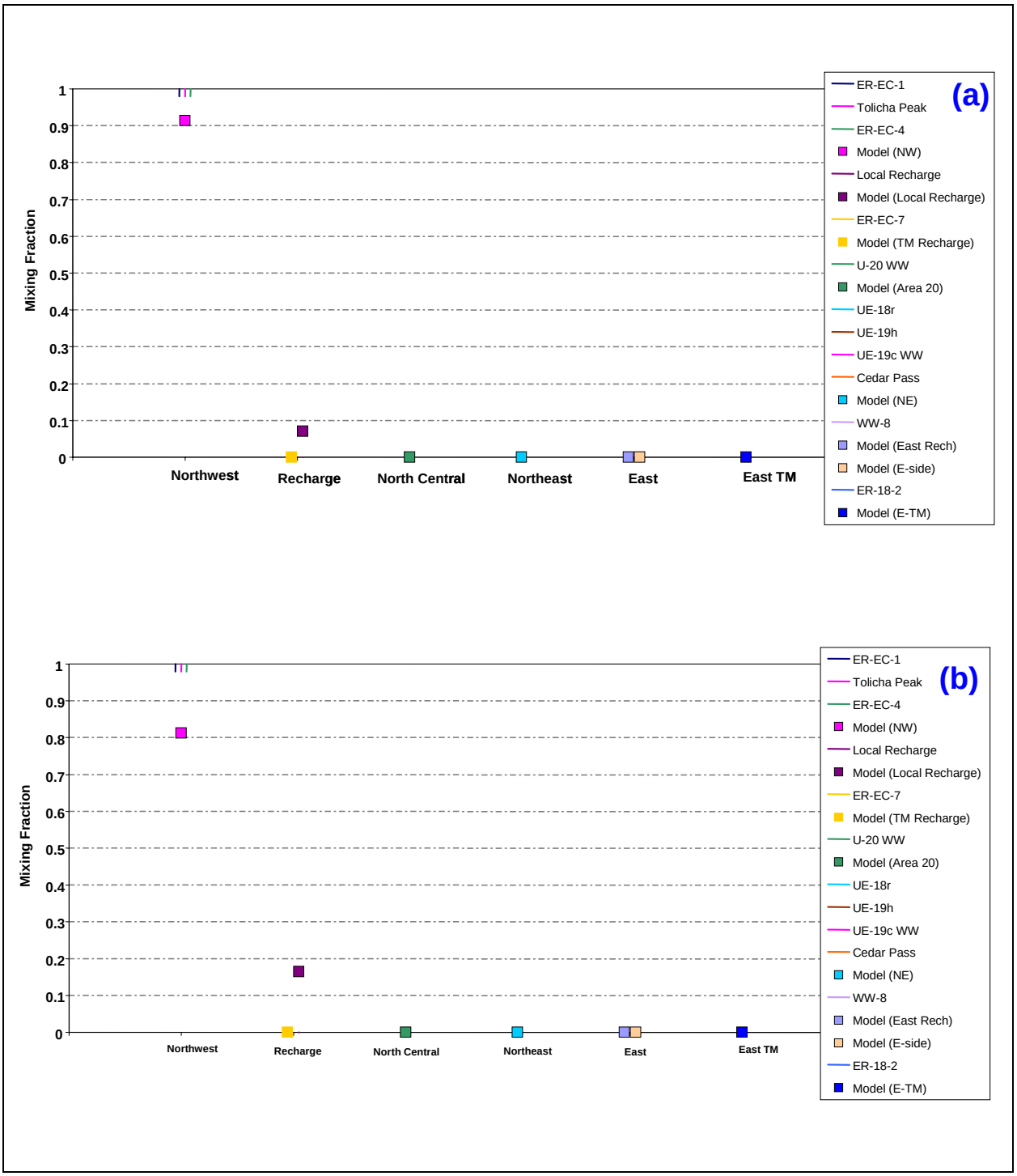

Figure 7-70
Quantitative Geochemical Comparisons at ER-OV-05 for (a) PZUP-USGSD-SDA and (b) PZUP-DRIA-SDA

Uncontrolled When Printed

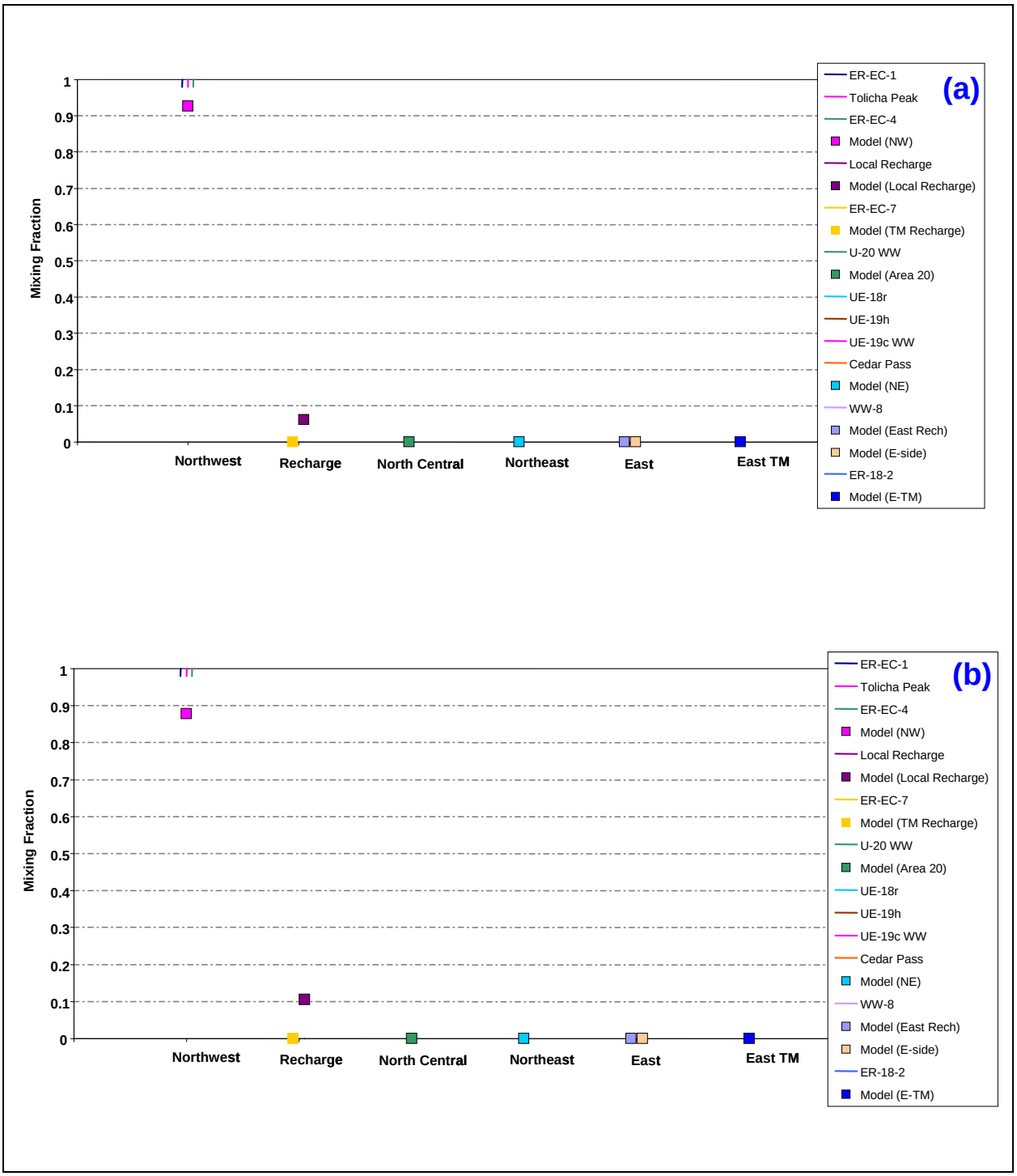

Figure 7-71
Quantitative Geochemical Comparisons at ER-OV-05 for
(a) DRT-USGSD-SDA and (b) DRT-DRIA-SDA

Uncontrolled When Printed

7.3.5 ER-OV-04a

7.3.5.1 Alternative Water-Balance Conditions, BN HFM

Moving from ER-OV-05 to ER-OV-04a, the predominance of northwest source water at the target well decreases as more mixing occurs with water originating east of the Purse Fault. The greater total flux DRIA water-balance model does not capture the mixing trend as well, with excessive source water coming from the northwest and local recharge and almost no source water from east of the Purse Fault (Figure 7-72). The BN-USGSD-SDA reduced LCCU1 permeability alternative captures this trend well, but with an overestimation of northwest source water (Figure 7-73).

Examination of results at ER-OV-04a for the base HFM (with higher LCCU1 permeability) model with alternative water-balance conditions in Figure 7-74 shows that the USGSD model captures the trend well, with the exception of nearly 30 percent source contribution from Gold Meadows across the eastern model boundary. The DRIA model does not show the east boundary component, but does result in a greater overestimate of northwest source water. The DRIA model for the BN HFM is a significant improvement over the DRIA model for the reduced LCCU1 permeability alternative. Finally, the BN-MME-ADA model shows a very good match to the trend, but with a substantial overestimate of local recharge as a result of the MME recharge map (Figure 7-75).

7.3.5.2 SCCC Alternative HFM

The SCCC alternative HFM model produces a flow field that captures the geochemistry mixing trend quite well, with a slight overestimate of local recharge and a small contribution of Timber Mountain recharge not estimated in the geochemistry (Figure 7-76). Contrary to the MME model results with the SCCC HFM, both the USGSD and DRIA conditions lead to models with overestimates of either northwest sources or local recharge and no north-central or northeast components at ER-OV-04a (Figure 7-77).

Uncontrolled When Printed

7.3.5.3 PZUP, DRT, RIDGE, TCL, and SEPZ Alternative HFMs

The remaining alternative HFM scenarios with MME water-balance conditions show the mixing reasonably well (Figures 7-78 through 7-80), although some perform better with regard to inflow from the east model boundary and/or local recharge as listed below:

- PZUP – overall good match, similar to SCCC with slight overestimate of local recharge and Timber Mountain source.
- DRT – overestimates the northwest component and underestimates the northeast component, thus missing the dominant mixing trend, but matches local recharge well.
- RIDGE – matches the north-central and northeast components, but troublesome east model boundary inflow offsets underestimate of northwest component. Local recharge estimated well.
- TCL – overall good match, east model boundary component seems to offset underestimate of north-central component.
- SEPZ – very good match, but with slight east boundary component and slight northwest overestimate.

The PZUP model with USGSD and DRIA water-balance conditions also matches the geochemistry well, although the USGSD model shows a 20 percent contribution from the east model boundary at Gold Meadows and the DRIA model overestimates local recharge to this well (Figure 7-81). The DRT-USGSD models shows substantial overestimation of northwest inflow, whereas the DRI recharge map on DRT corrects that error at the expense of excessive local infiltration (Figure 7-82).

7.3.5.4 Summary: ER-OV-04a

At ER-OV-04a, there are four different, but often related, mismatches between the model simulations and the geochemistry targets. They are (a) overestimation of source groundwater from the northwest, (b) underestimation of source groundwater from the north central and northeast, (c) overestimation of source water from the eastern model boundary, and (d) overestimation of local recharge. In general, one would expect the overestimation of local recharge to be a function of the water-balance conditions. However, that is not necessarily the case. The inflow from the eastern model boundary is often related to the HFM. Table 7-14 identifies the mismatch issues for each simulation. Only those with more than a 10 percent mismatch are identified.

Uncontrolled When Printed

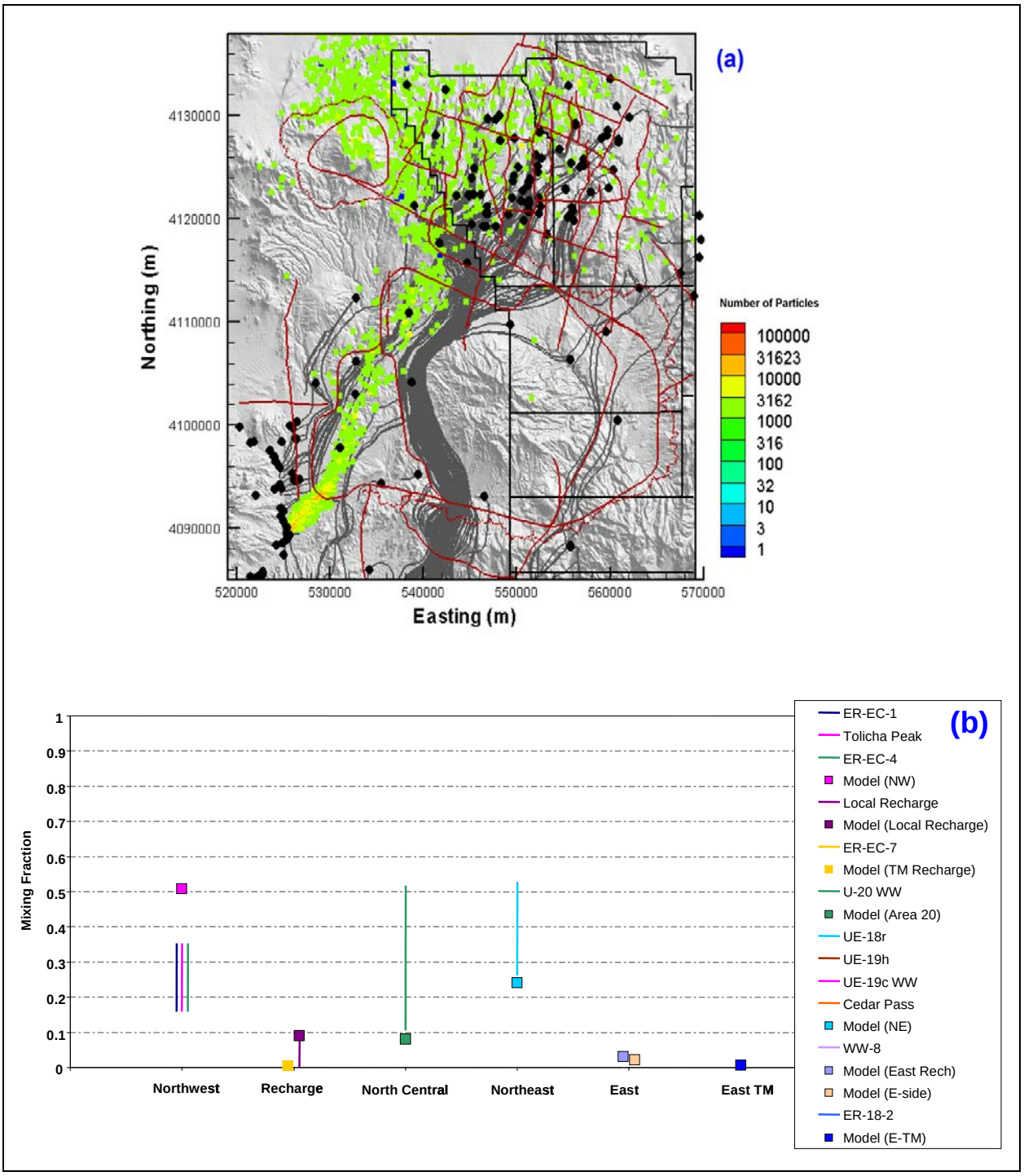

Figure 7-72
Comparison of Flow Model with Geochemical Mixing Targets at ER-OV-04a for BN-DRIA-SDA in the Reduced LCCU1 Permeability Alternative

Figure (a) shows the flow paths as mapped by forward SPTR particles originating at wells (grey lines) and the source recharge locations identified by reverse PTRK particle tracking (colored squares). Figure (b) shows the model comparison with geochemical mixing target ranges.

Uncontrolled When Printed

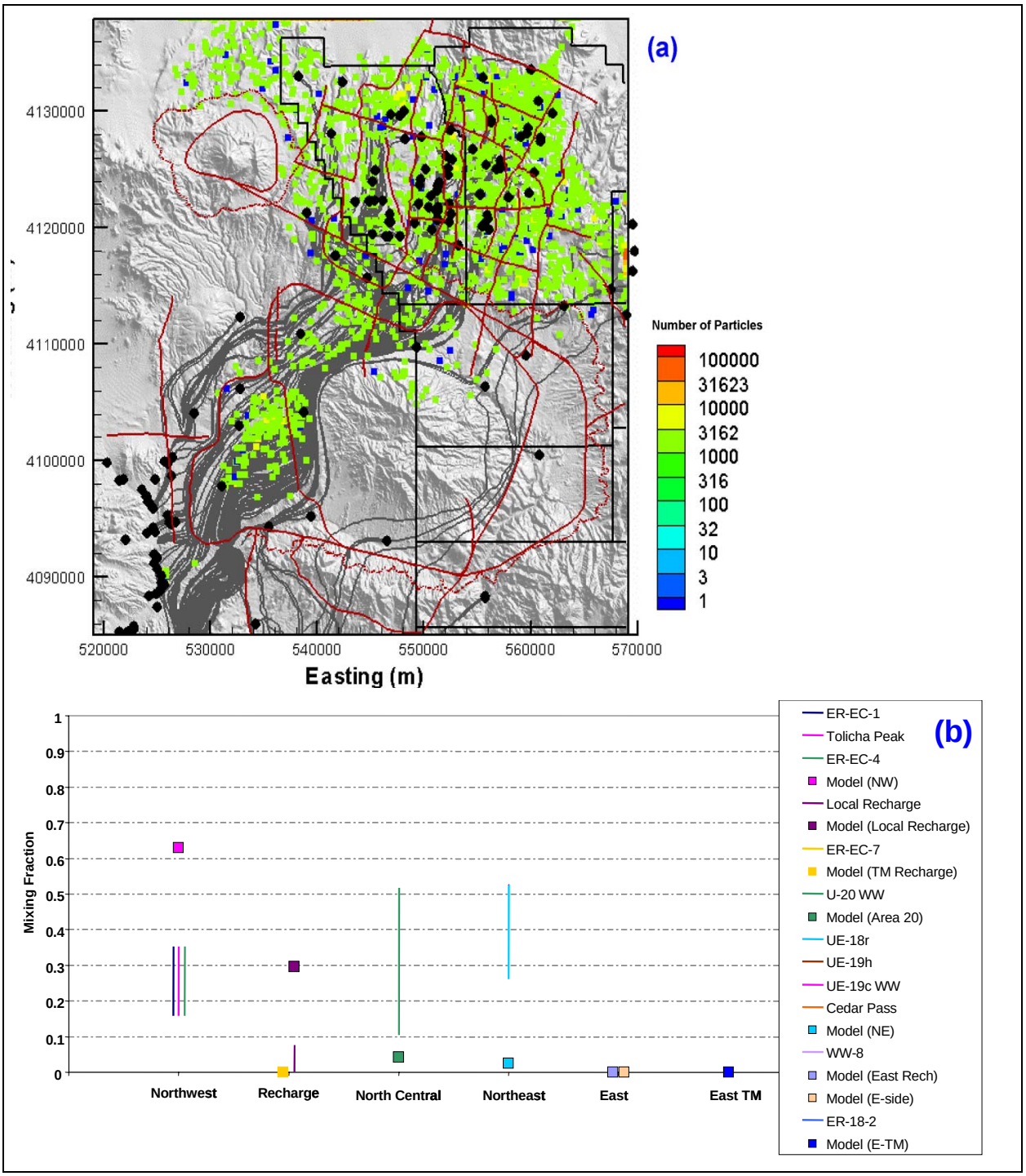

Figure 7-73
Comparison of Flow Model with Geochemical Mixing Targets at ER-OV-04a for BN-USGSD-SDA in the Reduced LCCU1 Permeability Alternative

Figure (a) shows the flow paths as mapped by forward SPTR particles originating at wells (grey lines) and the source recharge locations identified by reverse PTRK particle tracking (colored squares). Figure (b) shows the model comparison with geochemical mixing target ranges.

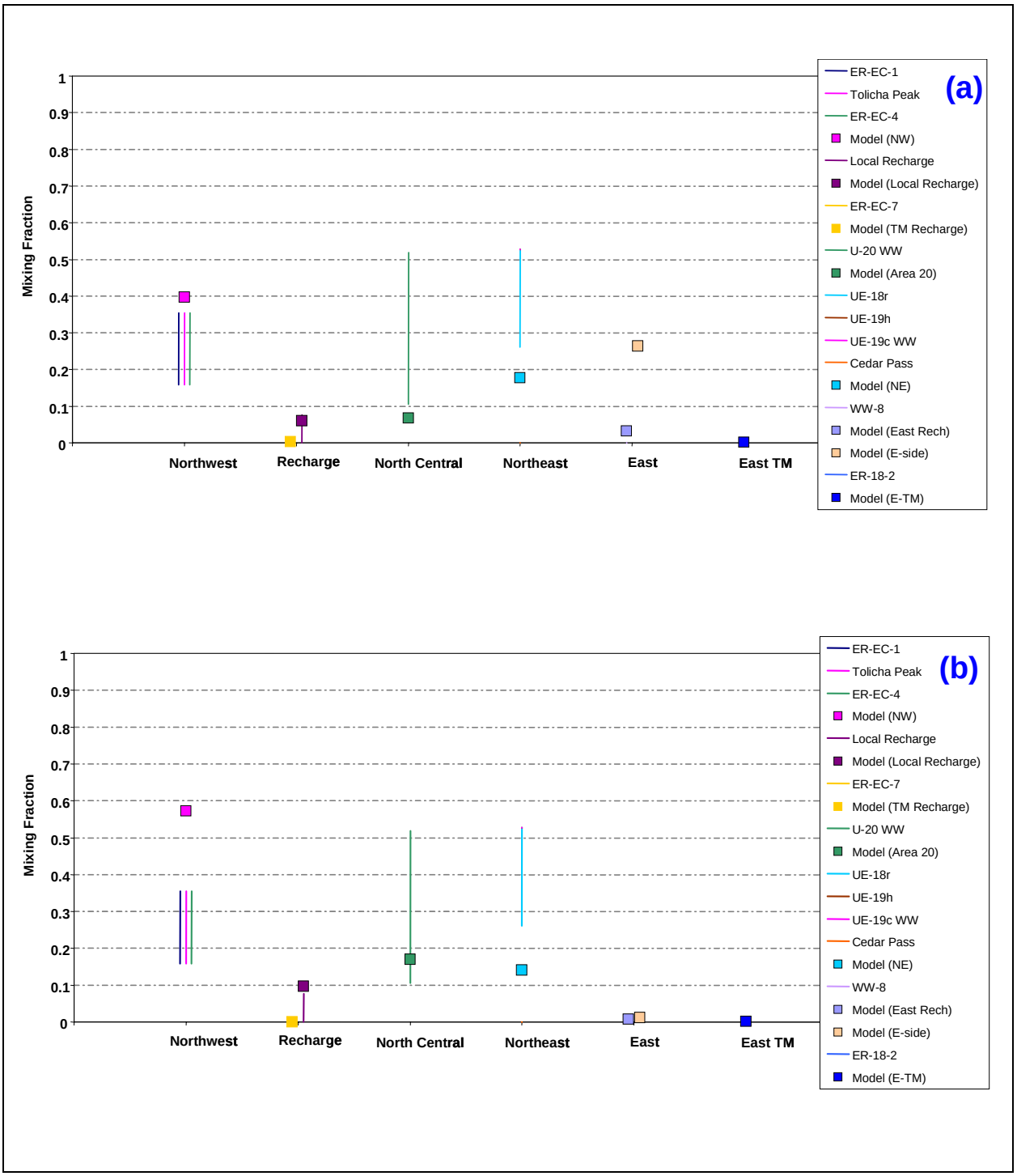

Figure 7-74
Quantitative Geochemical Comparison at ER-OV-04a for (a) BN-USGSD-SDA and (b) BN-DRIA-SDA

Uncontrolled When Printed

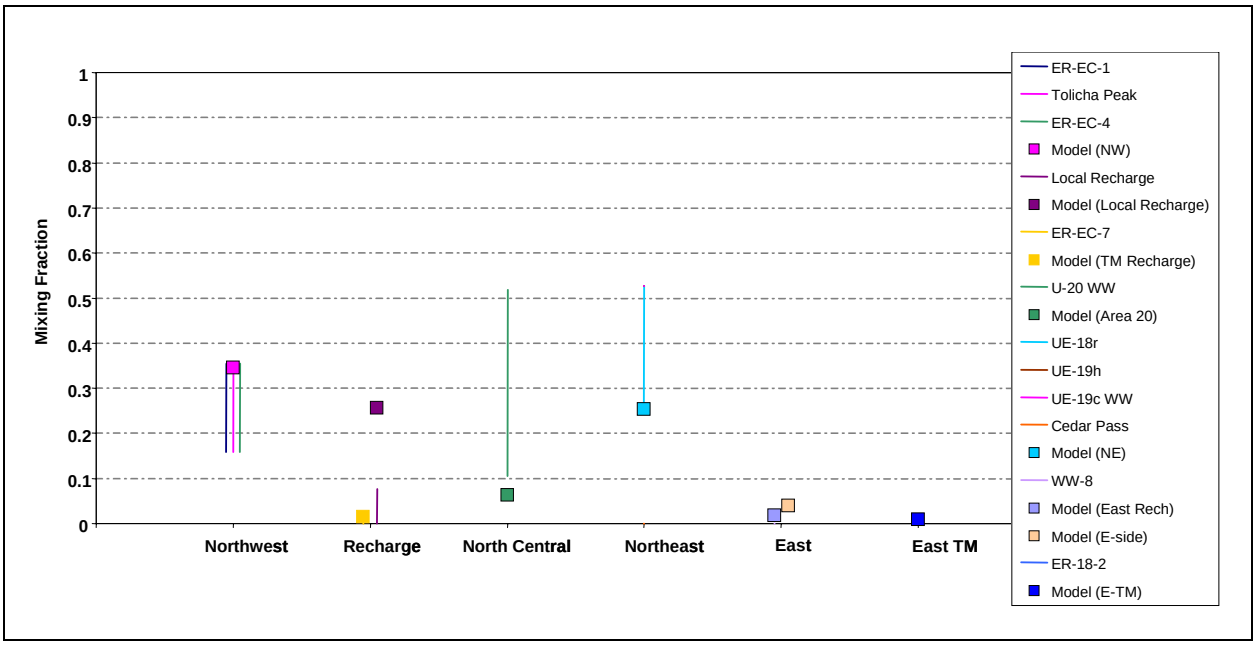

Figure 7-75
Comparison of Flow Model with Geochemical Mixing Targets at ER-OV-04a for BN-MME-ADA

Uncontrolled When Printed

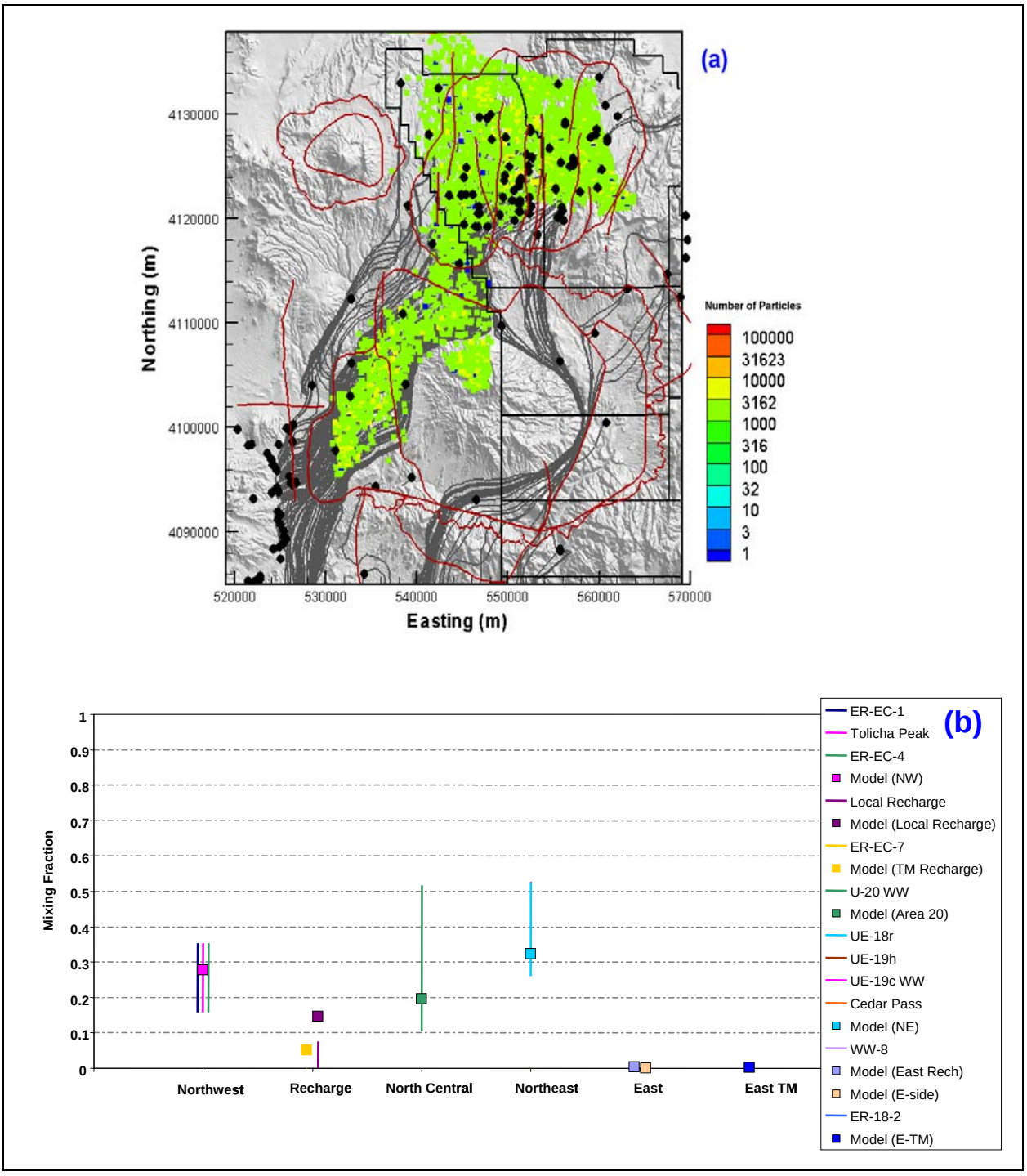

Figure 7-76
Comparison of Flow Model with Geochemical Mixing Targets at ER-OV-04a for SCCC-MME-SDA

Figure (a) shows the flow paths as mapped by forward SPTR particles originating at wells (grey lines) and the source recharge locations identified by reverse PTRK particle tracking (colored squares). Figure (b) shows the model comparison with geochemical mixing target ranges.

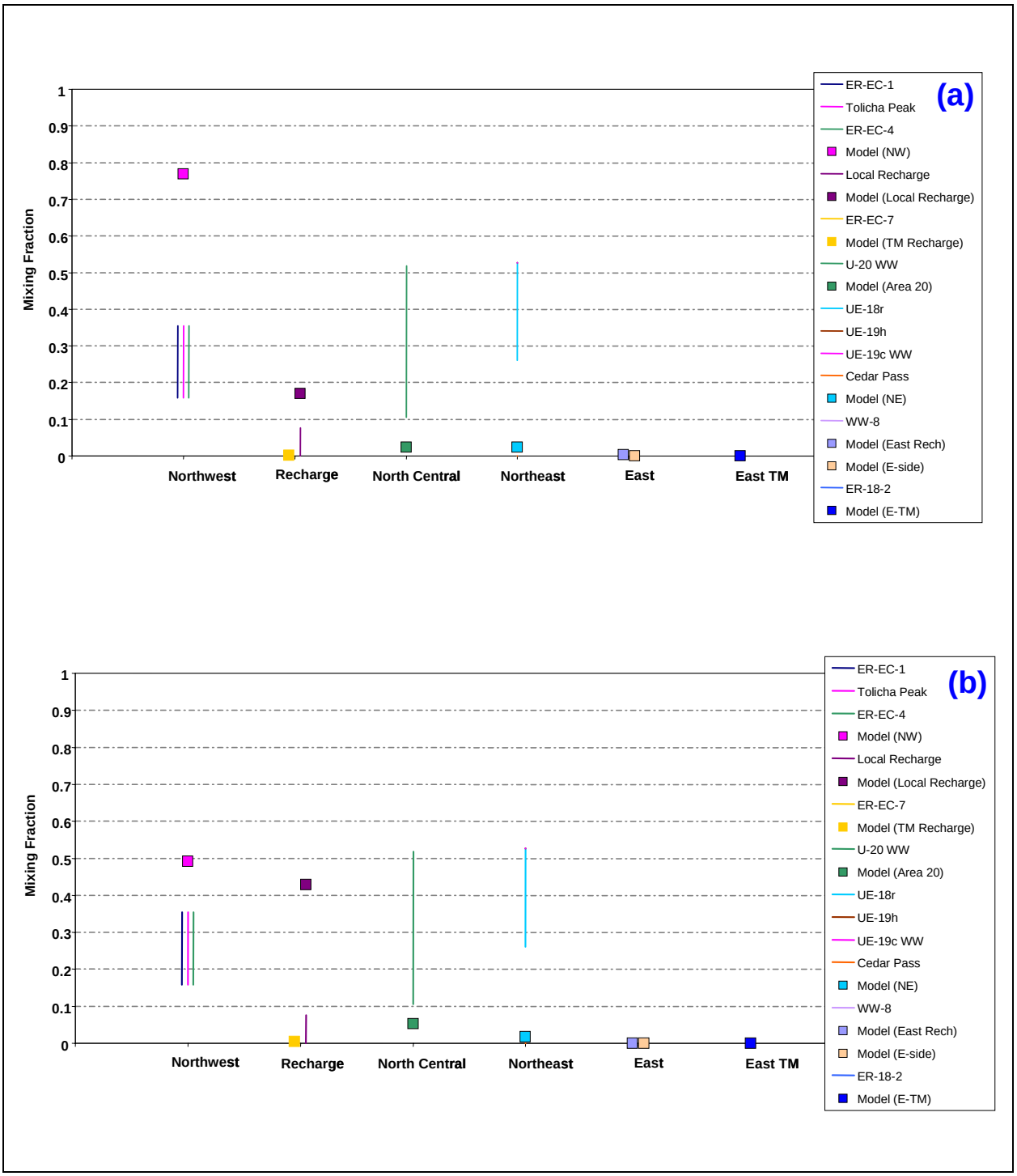

Figure 7-77
Quantitative Geochemical Comparisons at ER-OV-04a for (a) SCCC-USGSD-SDA and (b) SCCC-DRIA-SDA

Uncontrolled When Printed

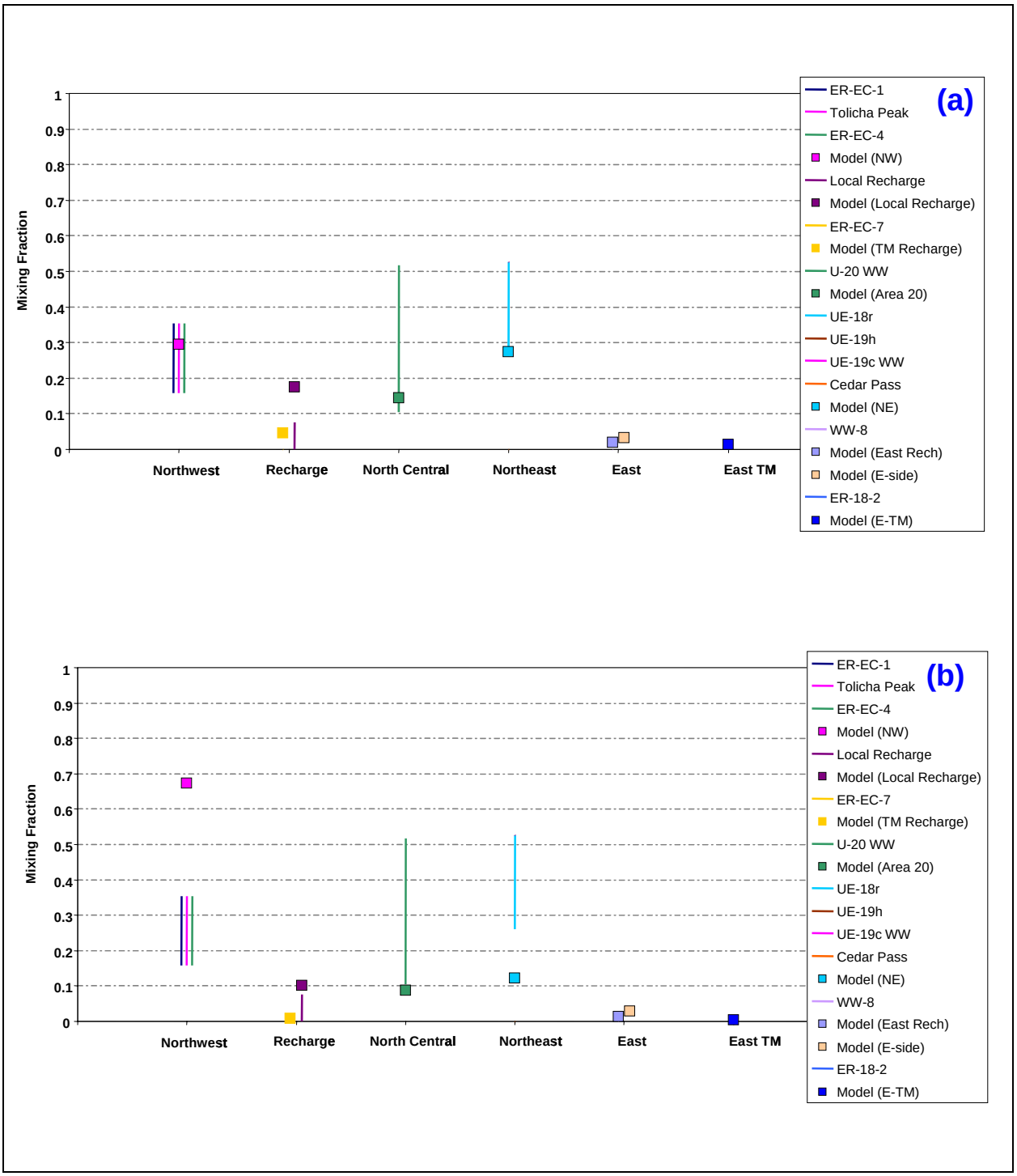

Figure 7-78
Quantitative Geochemical Comparisons at ER-OV-04a for (a) PZUP-MME-SDA and (b) DRT-MME-SDA

Uncontrolled When Printed

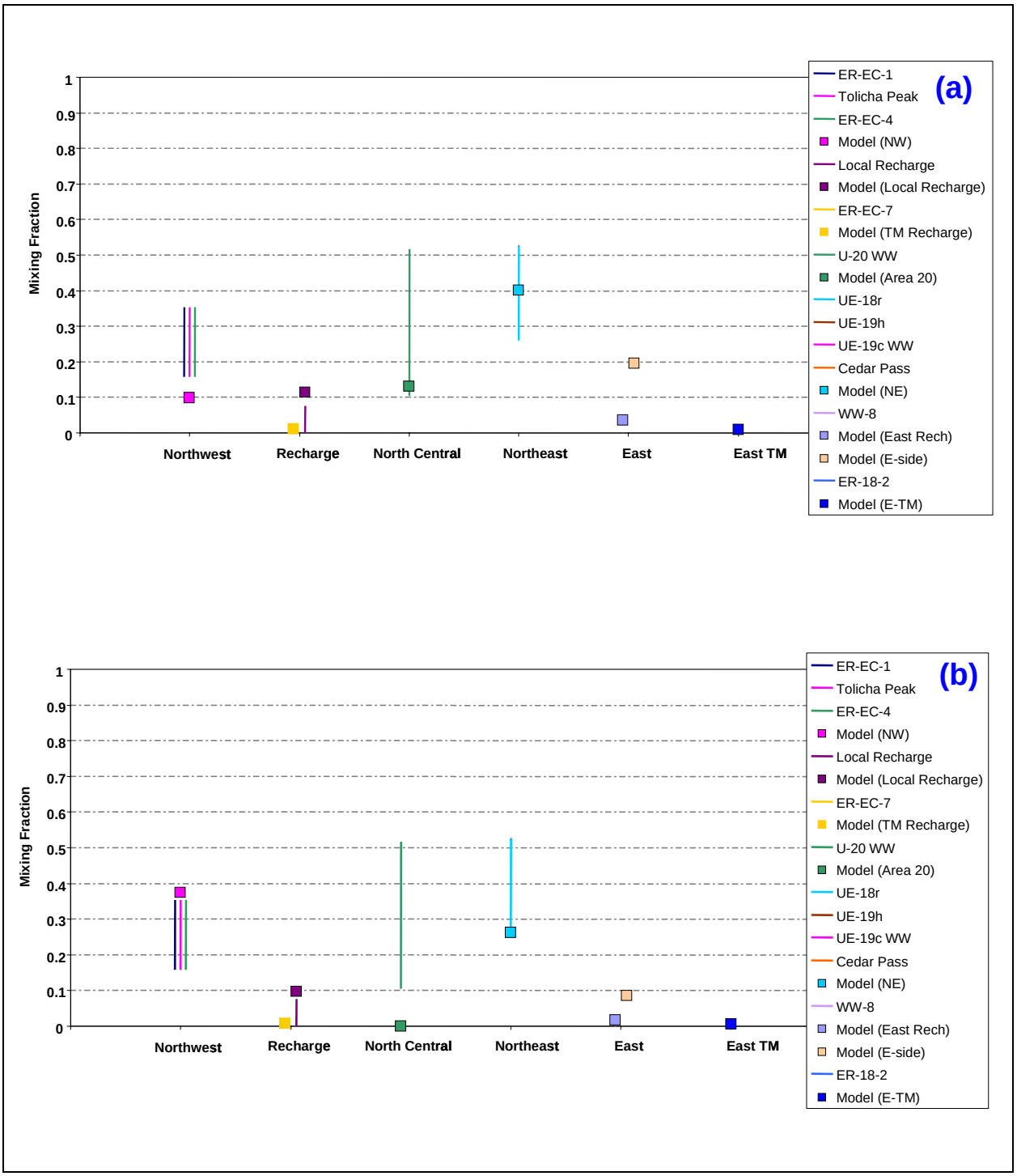

Figure 7-79
Quantitative Geochemical Comparisons at ER-OV-04a for
(a) RIDGE-MME-SDA and (b) TCL-MME-SDA

Uncontrolled When Printed

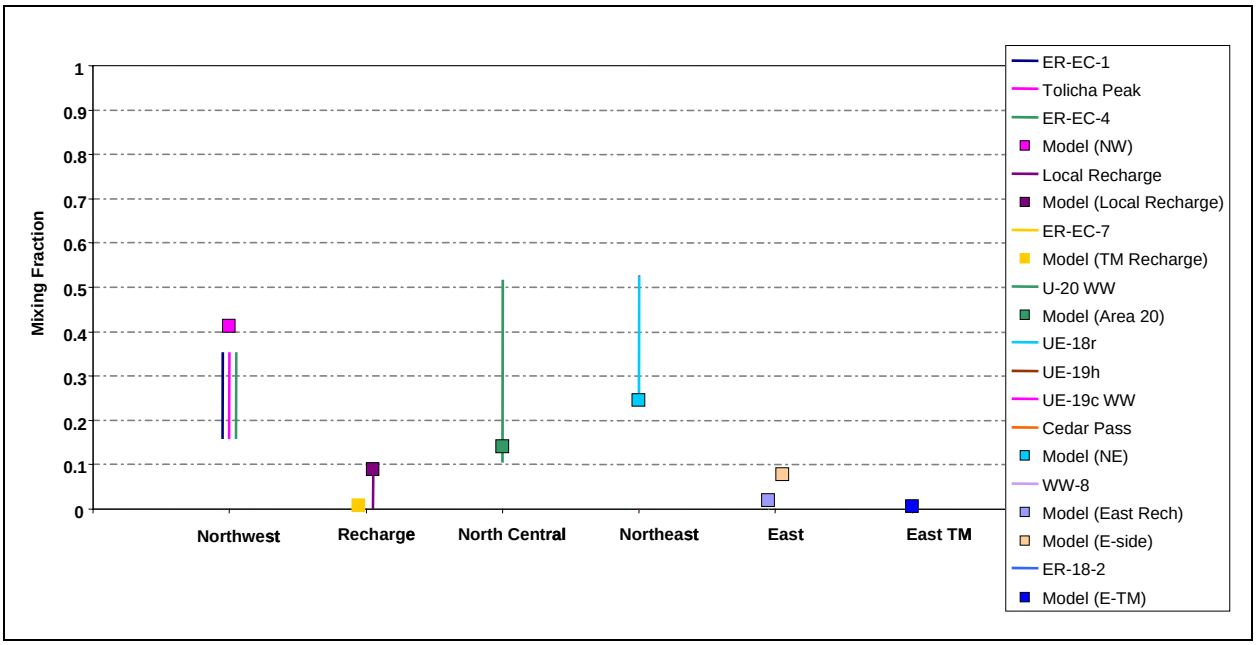

Figure 7-80
Comparison of Flow Model with Geochemical Mixing Targets at ER-OV-04a for SEPZ-MME-SDA

Uncontrolled When Printed

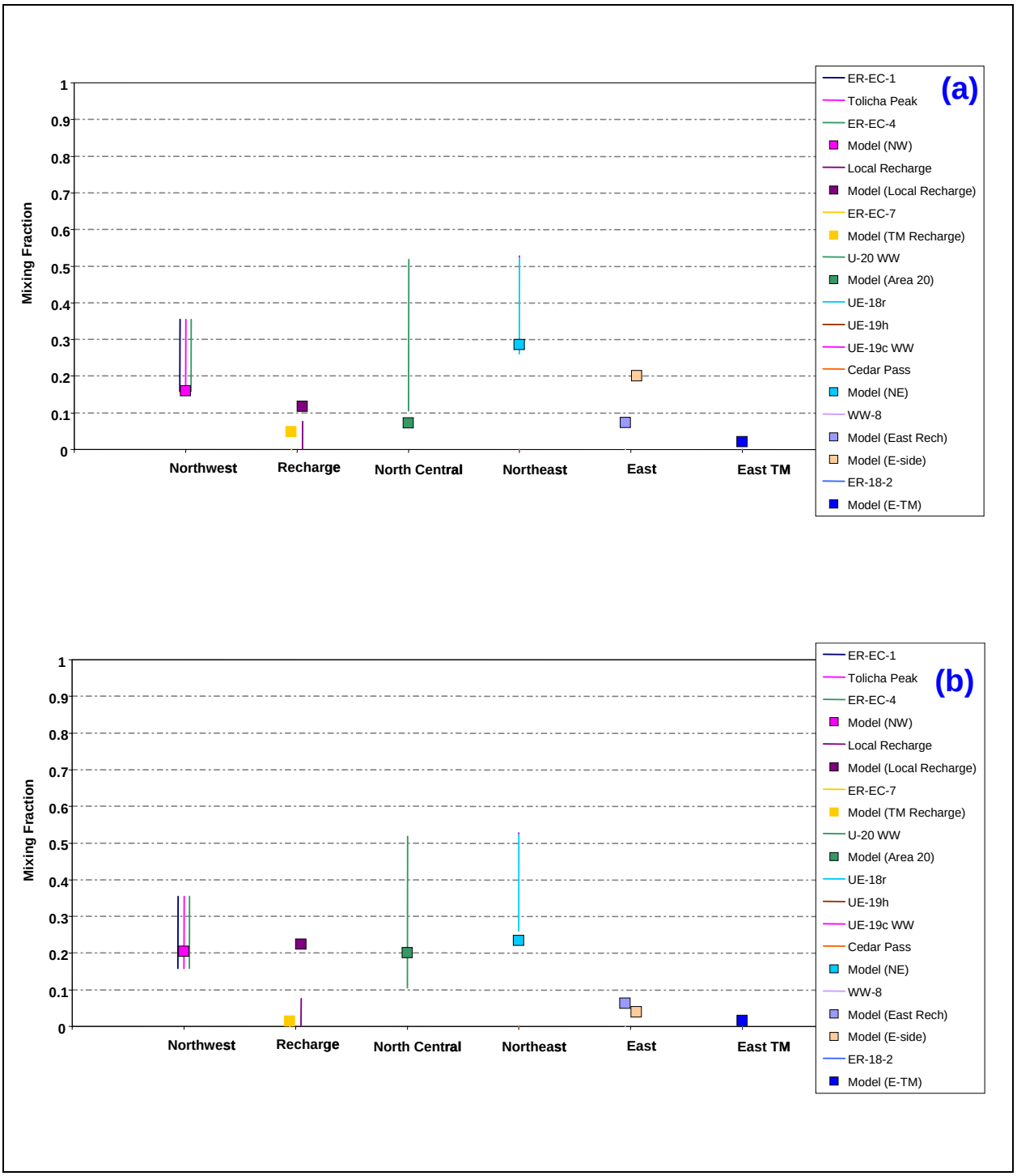

Figure 7-81
Quantitative Geochemical Comparisons at ER-OV-04a for (a) PZUP-USGSD-SDA and (b) PZUP-DRIA-SDA

Uncontrolled When Printed

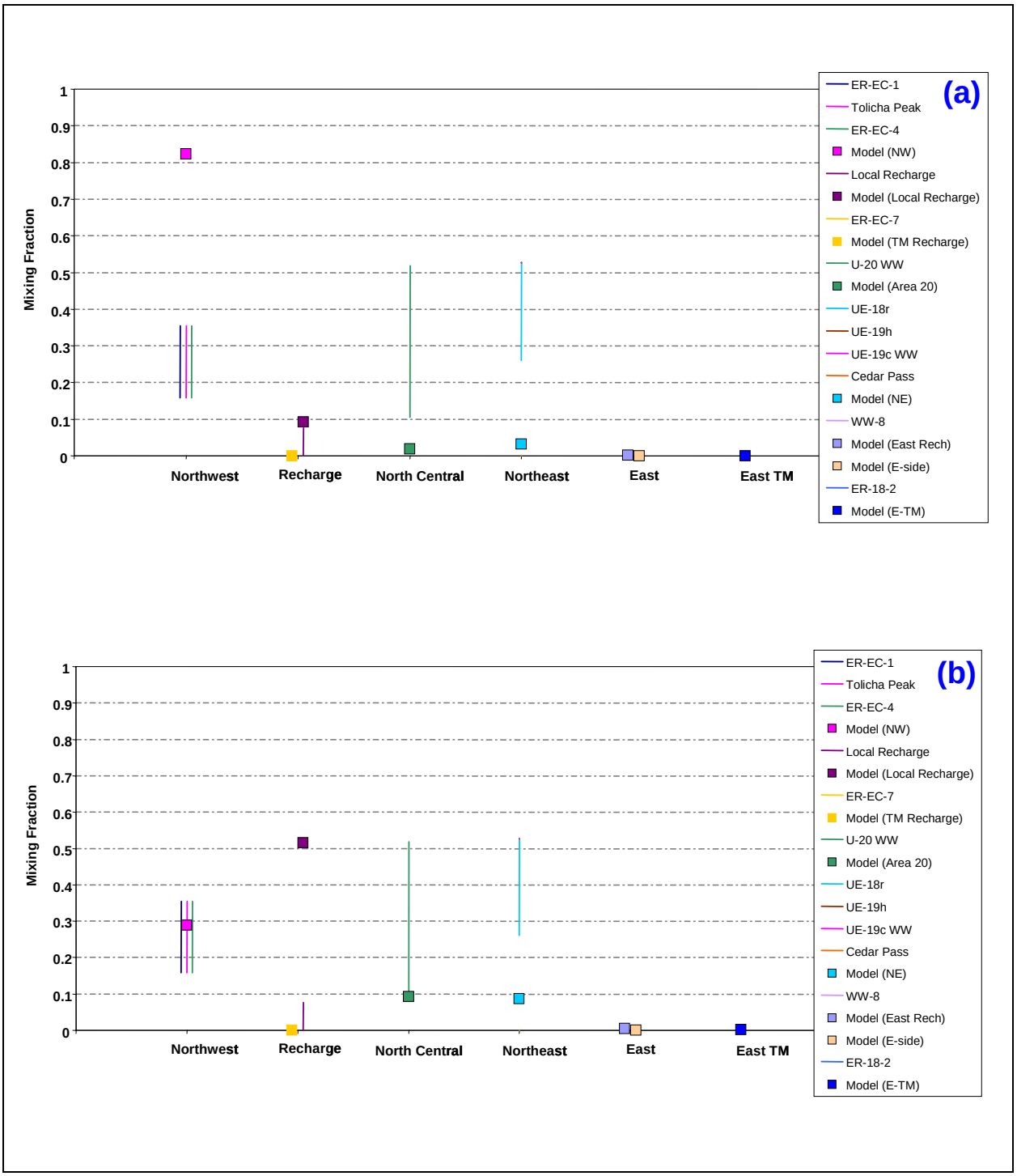

Figure 7-82
Quantitative Geochemical Comparisons at ER-OV-04a for (a) DRT-USGSD-SDA and (b) DRT-DRIA-SDA

Uncontrolled When Printed

Table 7-14
Comparison of Alternative Models at ER-OV-04a

HFM	Water-Balance Condition	Overestimation of Northwest Source	Underestimation of North-Central and Northeast Source	Overestimation of East Boundary Source	Overestimation of Local Recharge
BN-SDA reduced LCCU1 permeability alternative	MME	X			
	USGSD	X			
	DRIA	X	X		X
BN-SDA	MME				
	USGSD			X	
	DRIA	X	X		
BN-ADA	MME				X
SCCC-SDA	MME				
	USGSD	X	X		
	DRIA	X	X		X
PZUP	MME				
DRT	MME	X	X		
RIDGE	MME			X	
TCL	MME				
SEPZ	MME				
PZUP	USGSD			X	
	DRIA				X
DRT	USGSD	X	X		
	DRIA		X		X

Uncontrolled When Printed

7.3.6 ER-OV-03a

7.3.6.1 Alternative Water-Balance Conditions, BN HFM

The mixing ratios at ER-OV-03a for the BN-USGSD-SDA reduced LCCU1 permeability alternative case are similar to those of ER-OV-04a, although with somewhat larger uncertainty ranges. The USGSD simulation matches the targets very well, with only a small overestimate of source water from the northwest (Figure 7-83). By comparison, the BN-DRIA-SDA reduced LCCU1 permeability alternative simulation retains the same problem it had at ER-OV-04a; the only sources for ER-OV-03a water are from the northwest and from local recharge in Oasis Valley and Thirsty Canyon (Figure 7-84).

Similar to ER-OV-04a, the BN-USGSD-SDA (high LCCU1 permeability) matches the chemistry targets well at ER-OV-03a, with the exception of a 20 percent contribution from Gold Meadows (Figure 7-85). Results at ER-OV-03a for BN-DRIA-SDA are better than for the reduced LCCU1 permeability alternative because they match contributions from the north central, northeast, and northwest, but they overestimate the local recharge source. The BN-MME-ADA model also provides a good match at this well, with the exception of an overestimate in local recharge that is expected with the MME water-balance conditions (Figure 7-86).

7.3.6.2 SCCC Alternative HFM

The SCCC alternative HFM model produces a flow field that captures the geochemistry mixing trend quite well, but with an overestimation of local recharge and a small contribution of Timber Mountain recharge not estimated in the geochemistry (Figure 7-87).

Unlike the SCCC model calibrated with MME conditions, the USGSD and DRIA models produce mixing results with no sources from the north central or northeast (Figure 7-88). The USGSD model overestimates the northwest source and the DRIA model overestimates local recharge.

Uncontrolled When Printed

7.3.6.3 PZUP, DRT, RIDGE, TCL, and SEPZ Alternative HFMs

The remaining alternative HFM scenarios with MME water-balance conditions show the mixing reasonably well (Figures 7-89 through 7-91), although some perform better with regard to inflow from the east model boundary and/or local recharge as listed below:

- PZUP – very good match.
- DRT – overestimates the northwest component and local recharge, resulting in slight underestimation of the northeast source component.
- RIDGE – underestimates northwest source, which is offset by Gold Meadows Source Component.
- TCL – overall good match, but with slight east boundary component.
- SEPZ – overall good match, but with slight east boundary component and recharge overestimate.

Figures 7-92 and 7-93 show the comparisons for PZUP and DRT with alternative water-balance conditions. The PZUP with USGSD water-balance conditions provides a good match at ER-OV-03a, but with 12 percent source from Gold Meadows. The DRIA also provides a good match to targets; the overestimate in local recharge can likely be grouped with the underestimate of northwest source water to make a reasonable chemical match.

The DRT with USGSD water-balance conditions far overshoots the estimate for northwest groundwater sources and predicts almost none from the north central and northeast. These errors are corrected substantially with DRIA water-balance conditions, but the local recharge is then overestimated.

7.3.6.4 Summary: ER-OV-03a

At ER-OV-03a, there are four different, but often related, mismatches between the model simulations and the geochemistry targets. They are (a) overestimation of source groundwater from the northwest, (b) underestimation of source groundwater from the north central and northeast, (c) overestimation of source water from the eastern model boundary, and (d) overestimation of local recharge. Table 7-15 identifies the mismatch issues for each simulation. Only those with more than a 10 percent mismatch are identified.

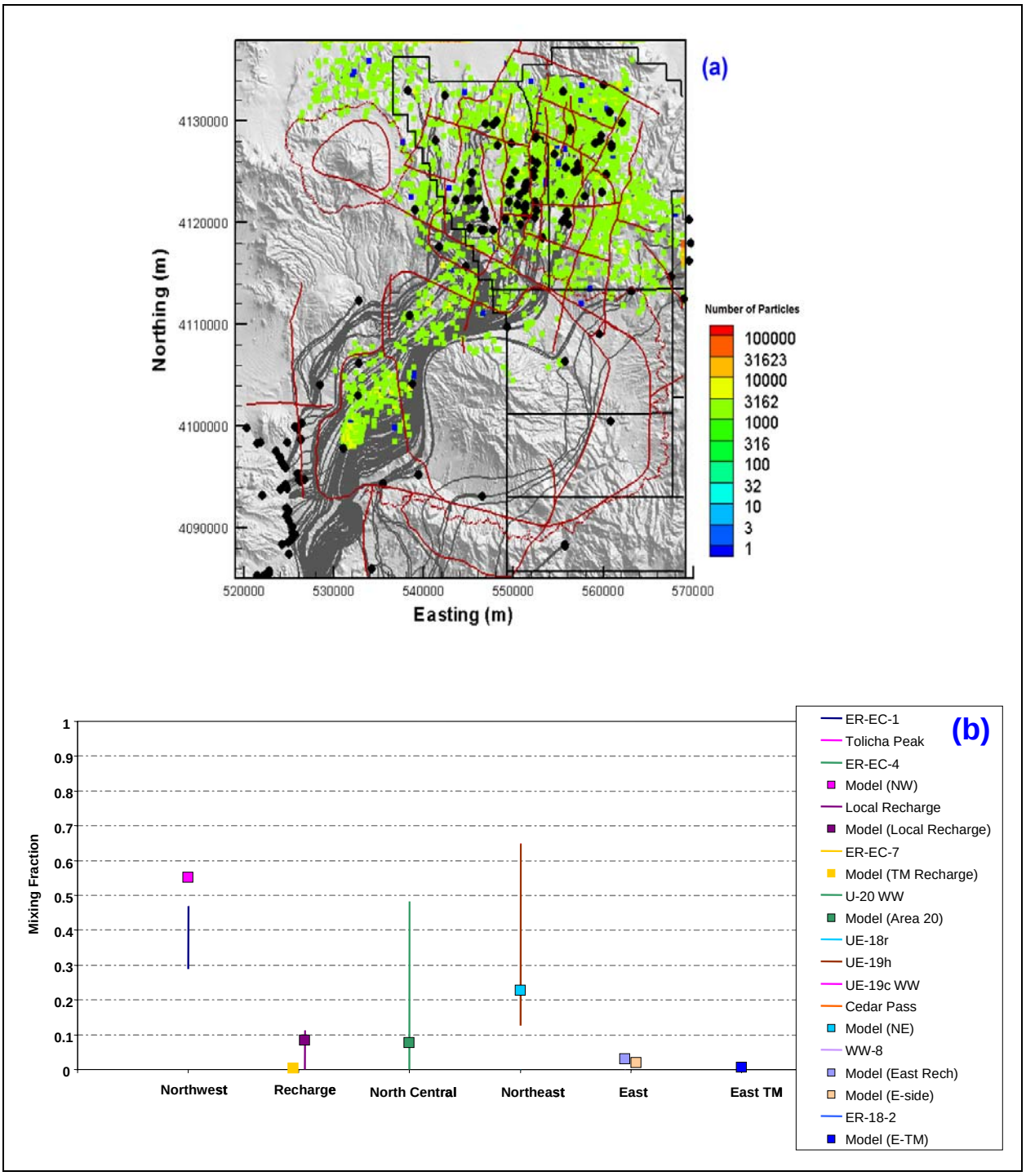

Figure 7-83
Comparison of Flow Model with Geochemical Mixing Targets at ER-OV-03a for BN-USGSD-SDA in the Reduced LCCU1 Permeability Alternative

Figure (a) shows the flow paths as mapped by forward SPTR particles originating at wells (grey lines) and the source recharge locations identified by reverse PTRK particle tracking (colored squares). Figure (b) shows the model comparison with geochemical mixing target ranges.

Uncontrolled When Printed

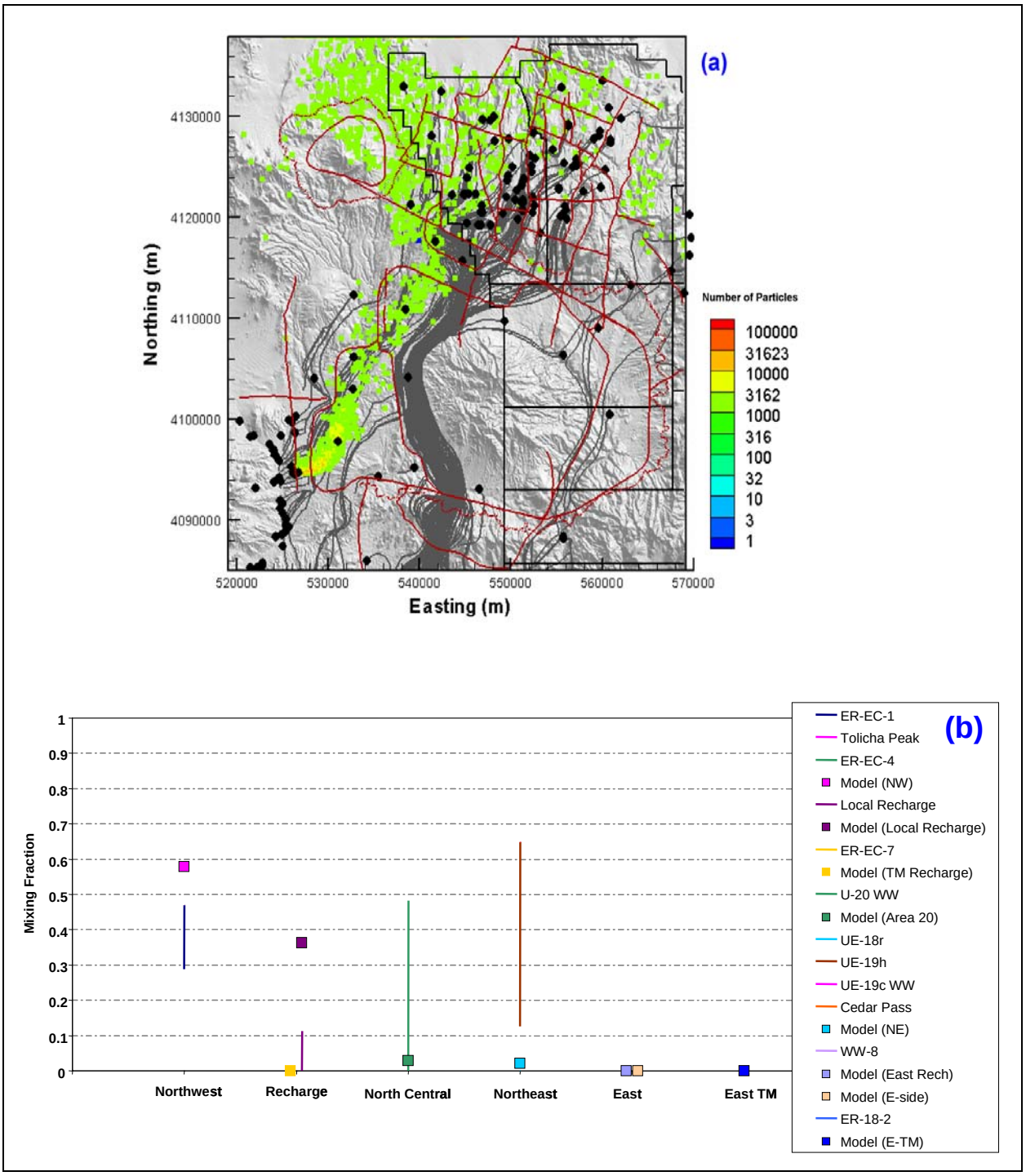

Figure 7-84
Comparison of Flow Model with Geochemical Mixing Targets at ER-OV-03a for BN-DRIA-SDA in the Reduced LCCU1 Permeability Alternative

Figure (a) shows the flow paths as mapped by forward SPTR particles originating at wells (grey lines) and the source recharge locations identified by reverse PTRK particle tracking (colored squares). Figure (b) shows the model comparison with geochemical mixing target ranges.

Uncontrolled When Printed

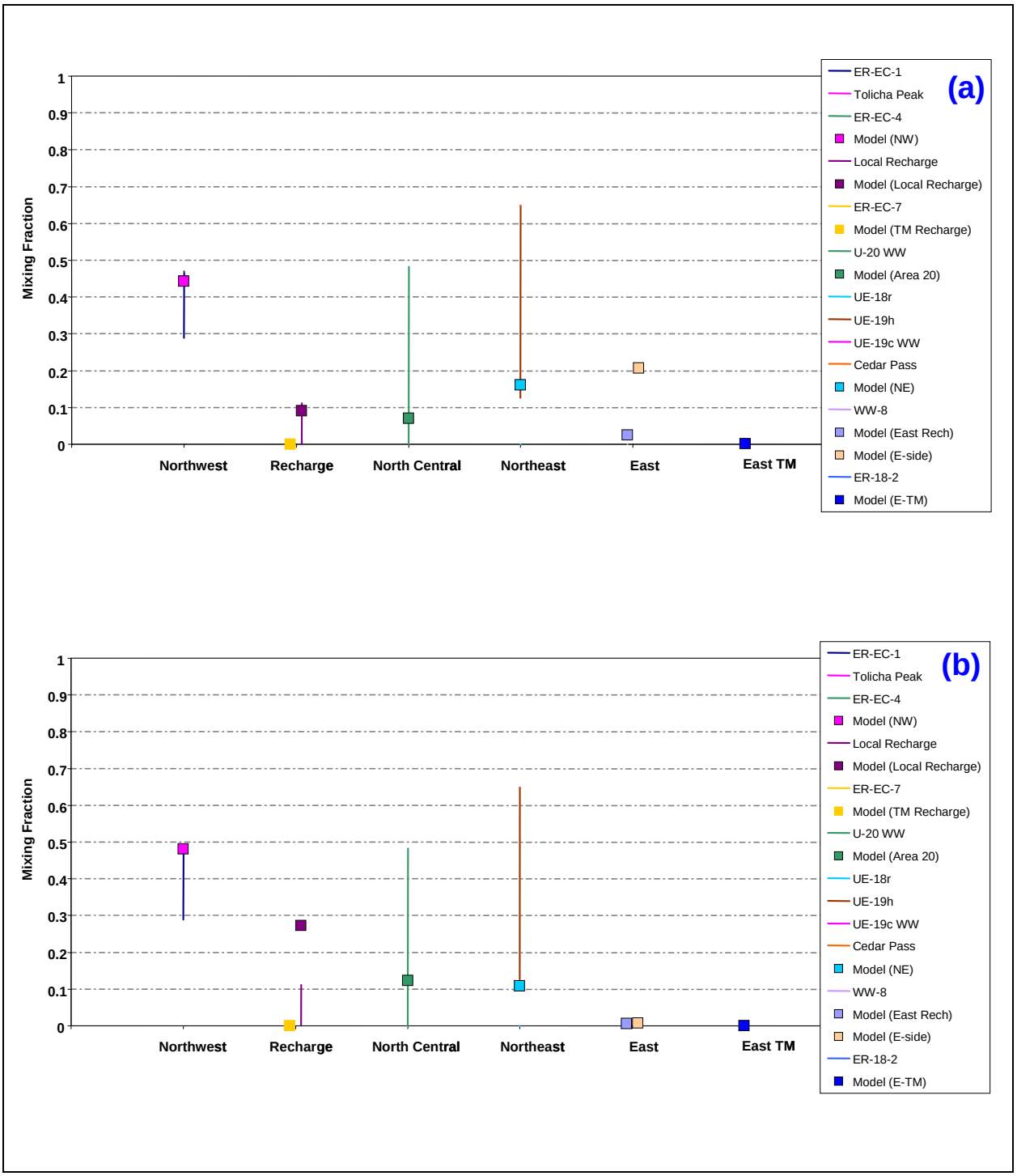

Figure 7-85
Quantitative Geochemical Comparisons at ER-OV-03a for (a) BN-USGSD-SDA and (b) BN-DRIA-SDA

Uncontrolled When Printed

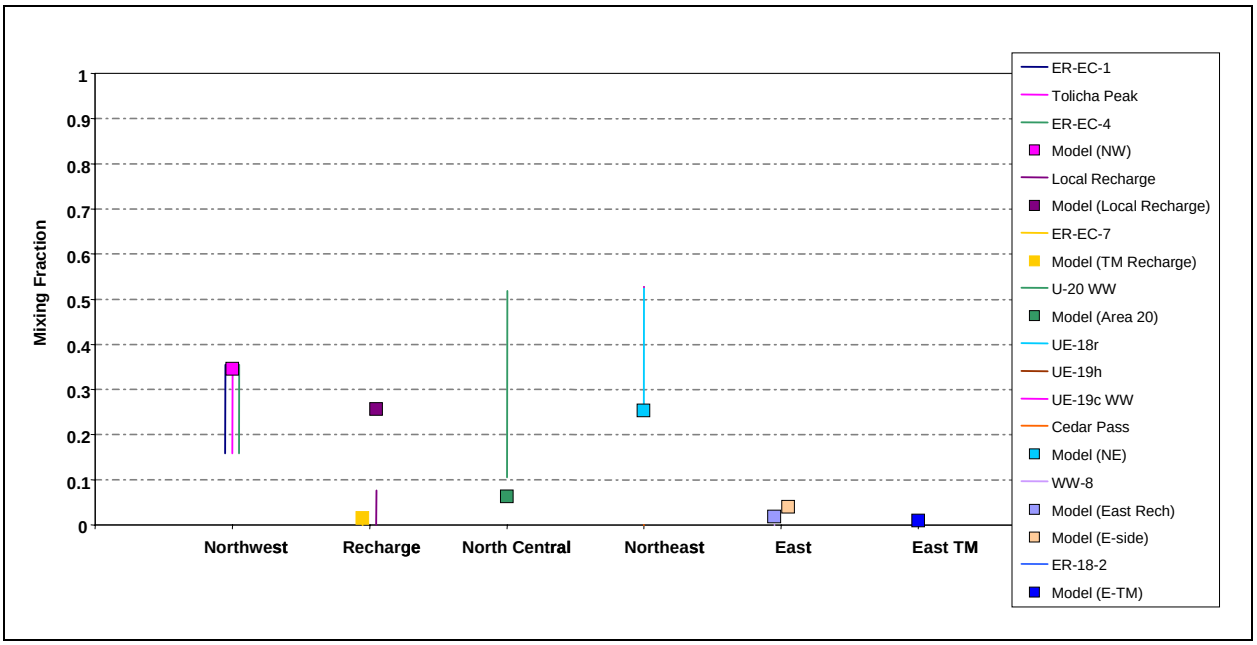

Figure 7-86
Comparison of Flow Model with Geochemical Mixing Targets at ER-OV-03a for BN-MME-ADA

Uncontrolled When Printed

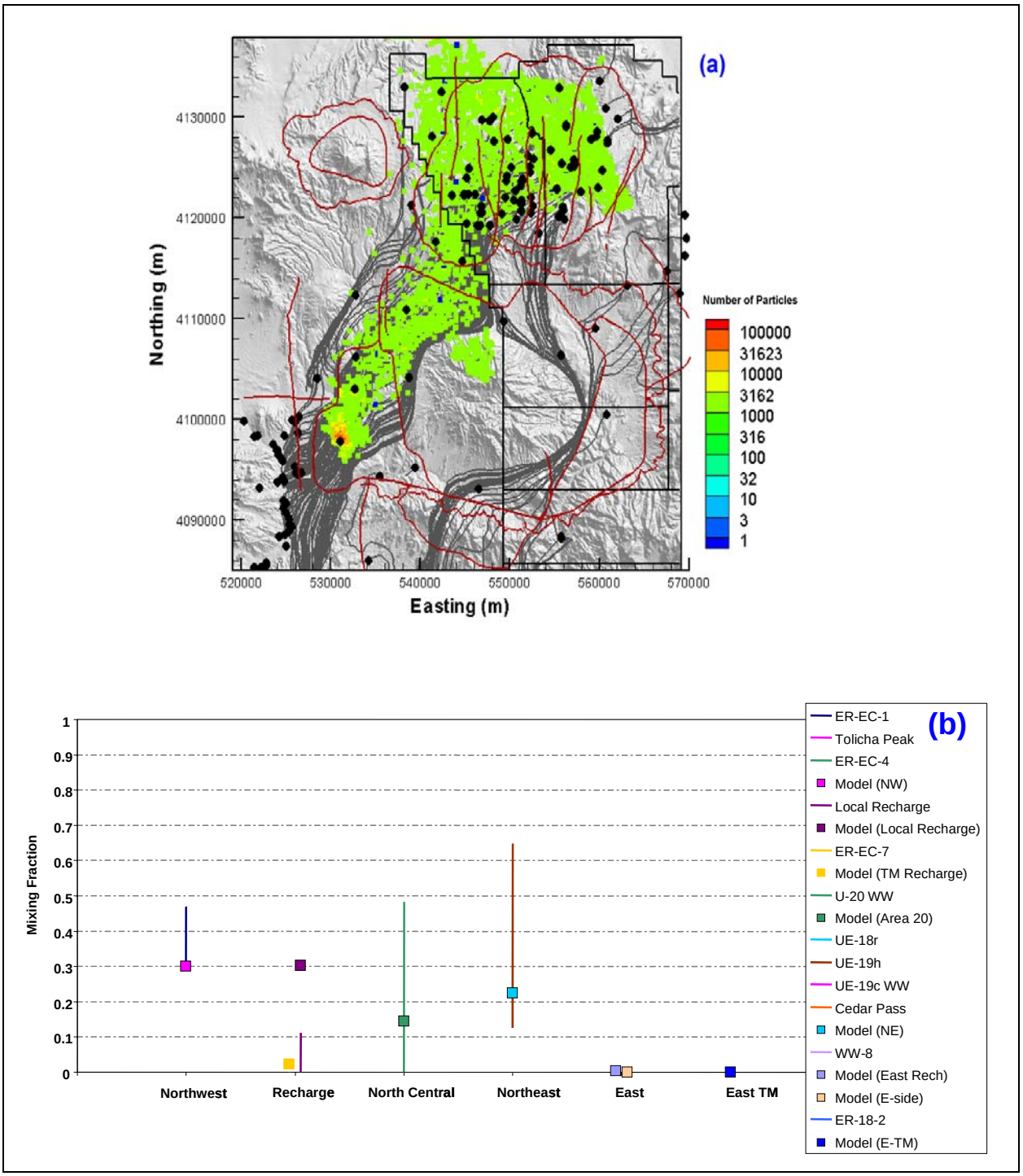

Figure 7-87
Comparison of Flow Model with Geochemical Mixing Targets at ER-OV-03a for SCCC-MME-SDA

Figure (a) shows the flow paths as mapped by forward SPTR particles originating at wells (grey lines) and the source recharge locations identified by reverse PTRK particle tracking (colored squares). Figure (b) shows the model comparison with geochemical mixing target ranges.

Uncontrolled When Printed

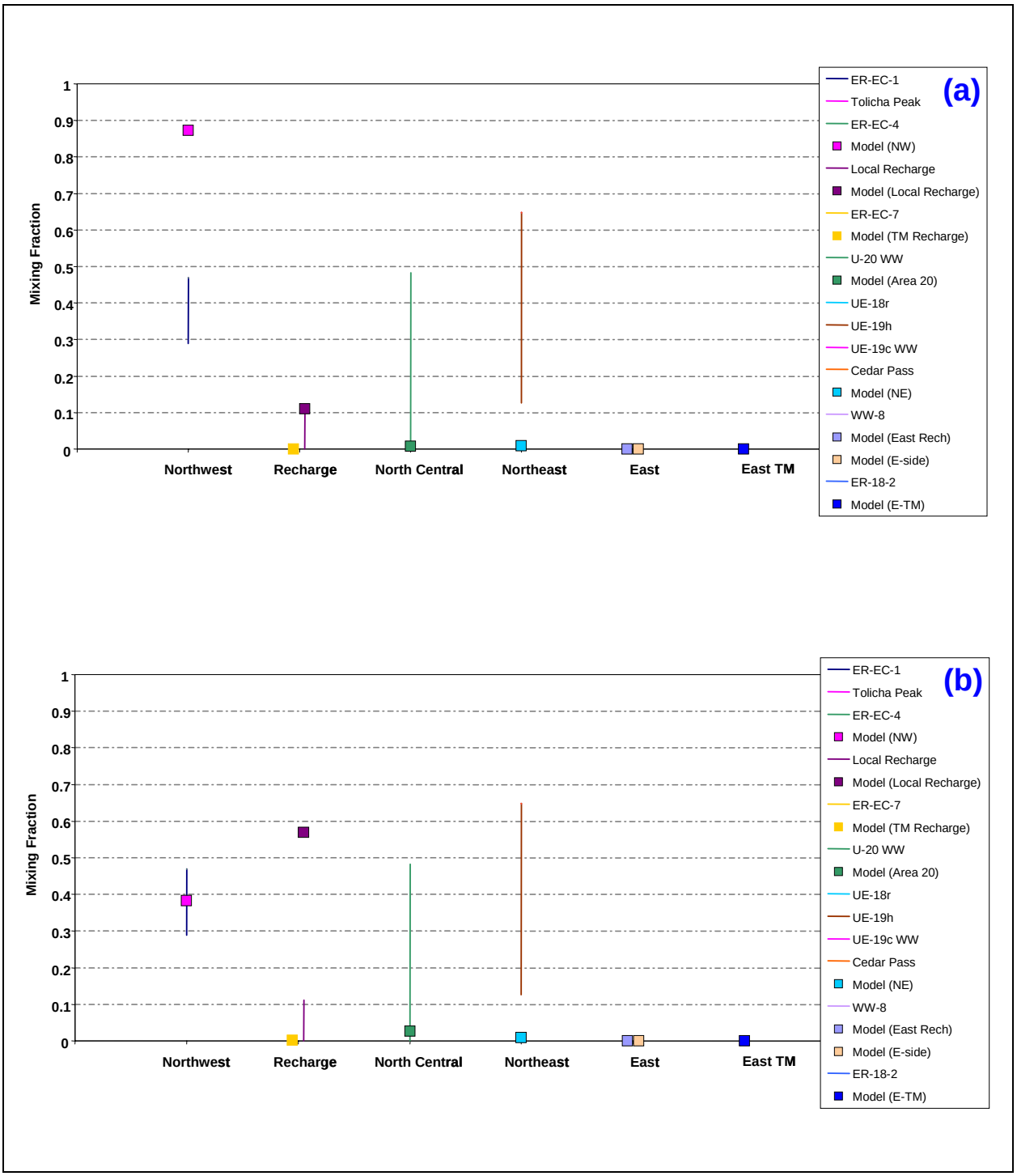

Figure 7-88
Quantitative Geochemical Comparisons at ER-OV-03a for (a) SCCC-USGSD-SDA and (b) SCCC-DRIA-SDA

Uncontrolled When Printed

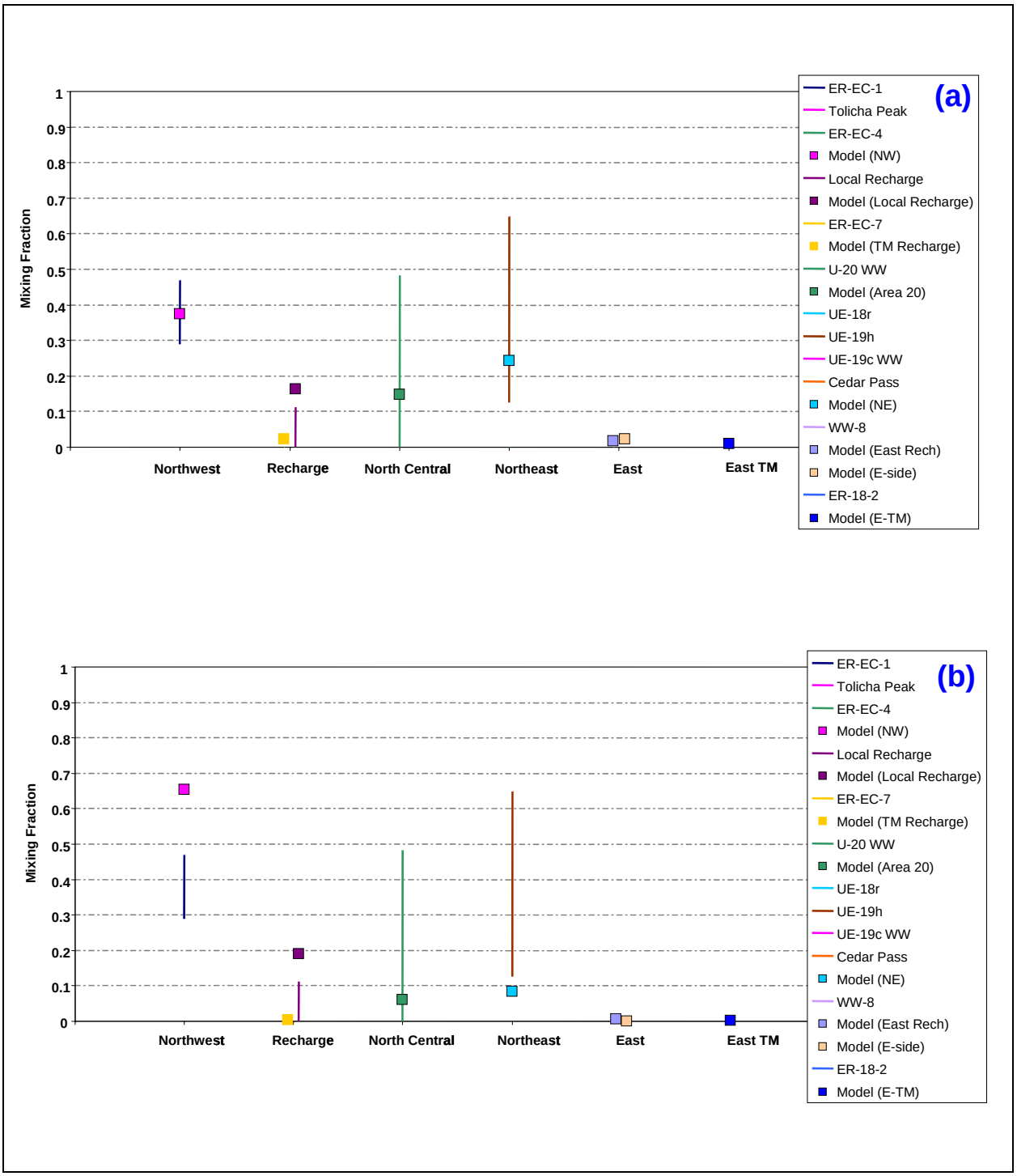

Figure 7-89
Quantitative Geochemical Comparisons at ER-OV-03a for (a) PZUP-MME-SDA and (b) DRT-MME-SDA

Uncontrolled When Printed

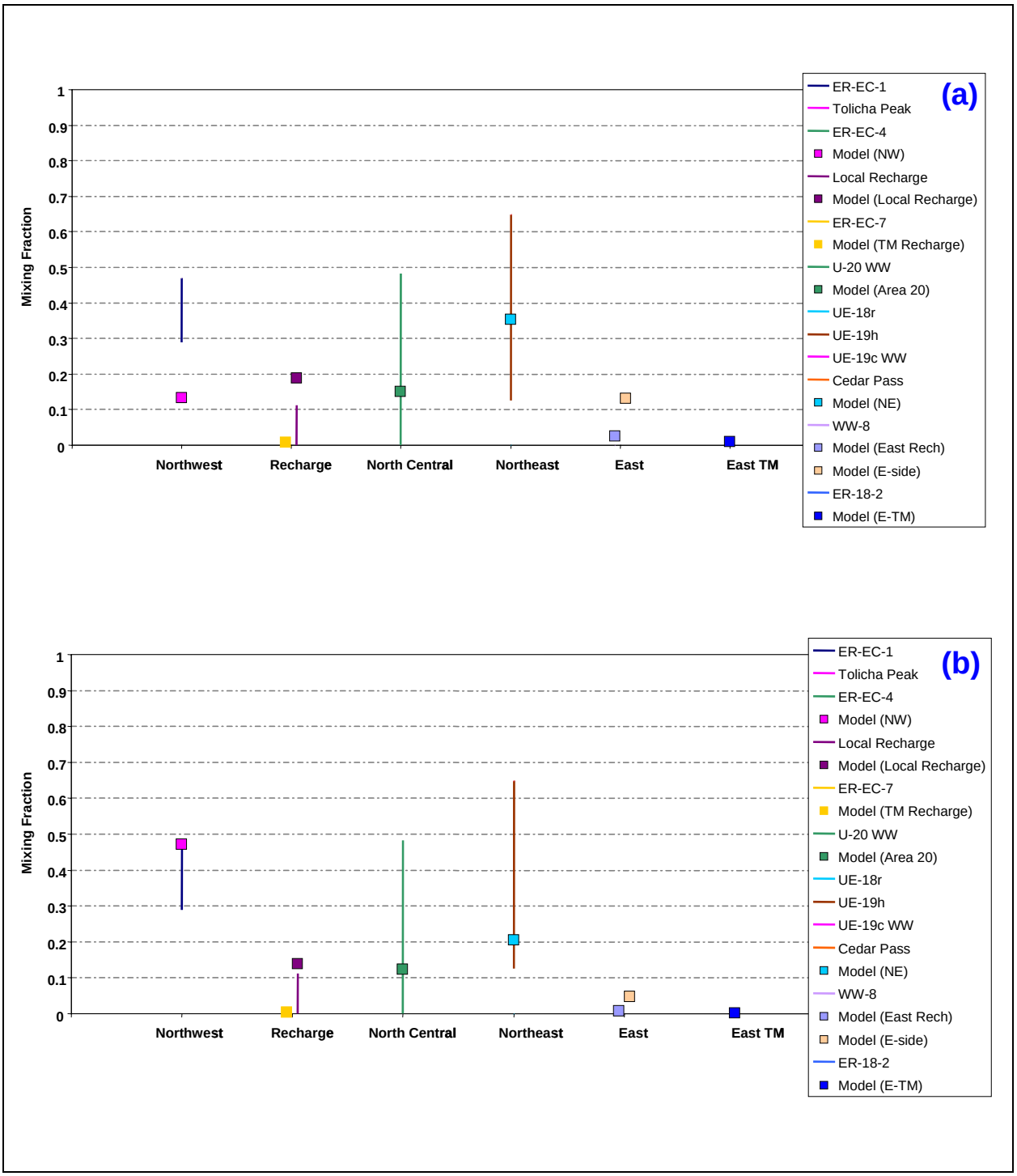

Figure 7-90
Quantitative Geochemical Comparisons at ER-OV-03a for
(a) RIDGE-MME-SDA and (b) TCL-MME-SDA

Uncontrolled When Printed

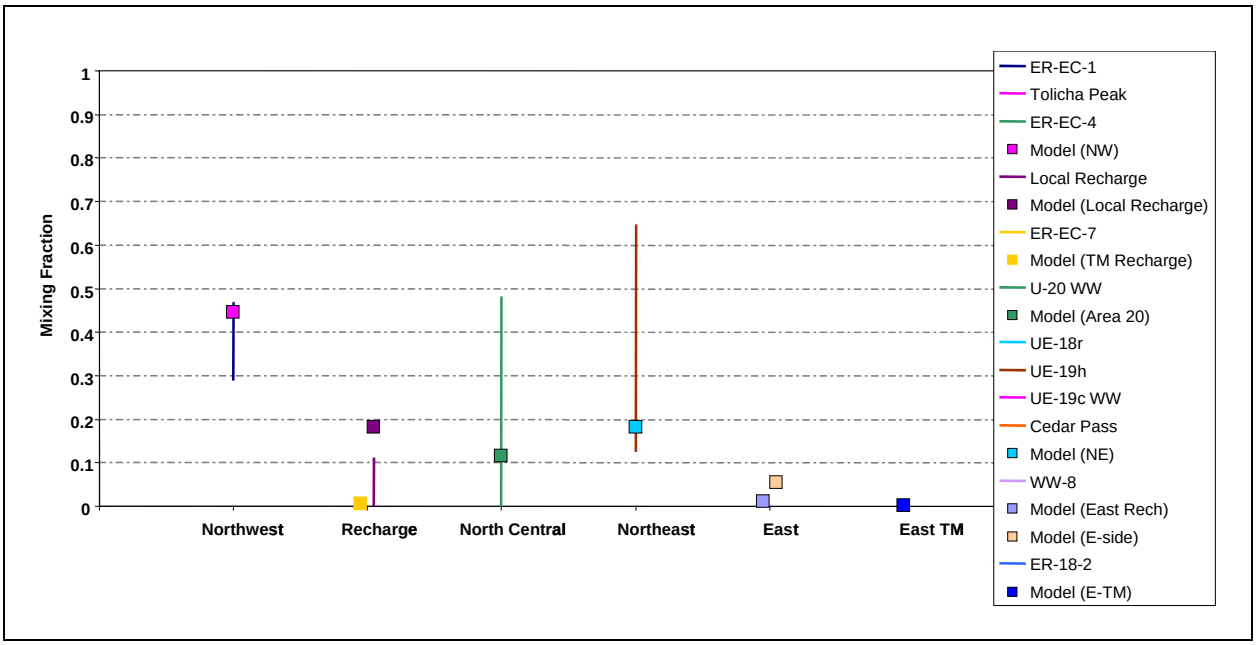

Figure 7-91
Comparison of Flow Model with Geochemical Mixing Targets at ER-OV-03a for SEPZ-MME-SDA

Uncontrolled When Printed

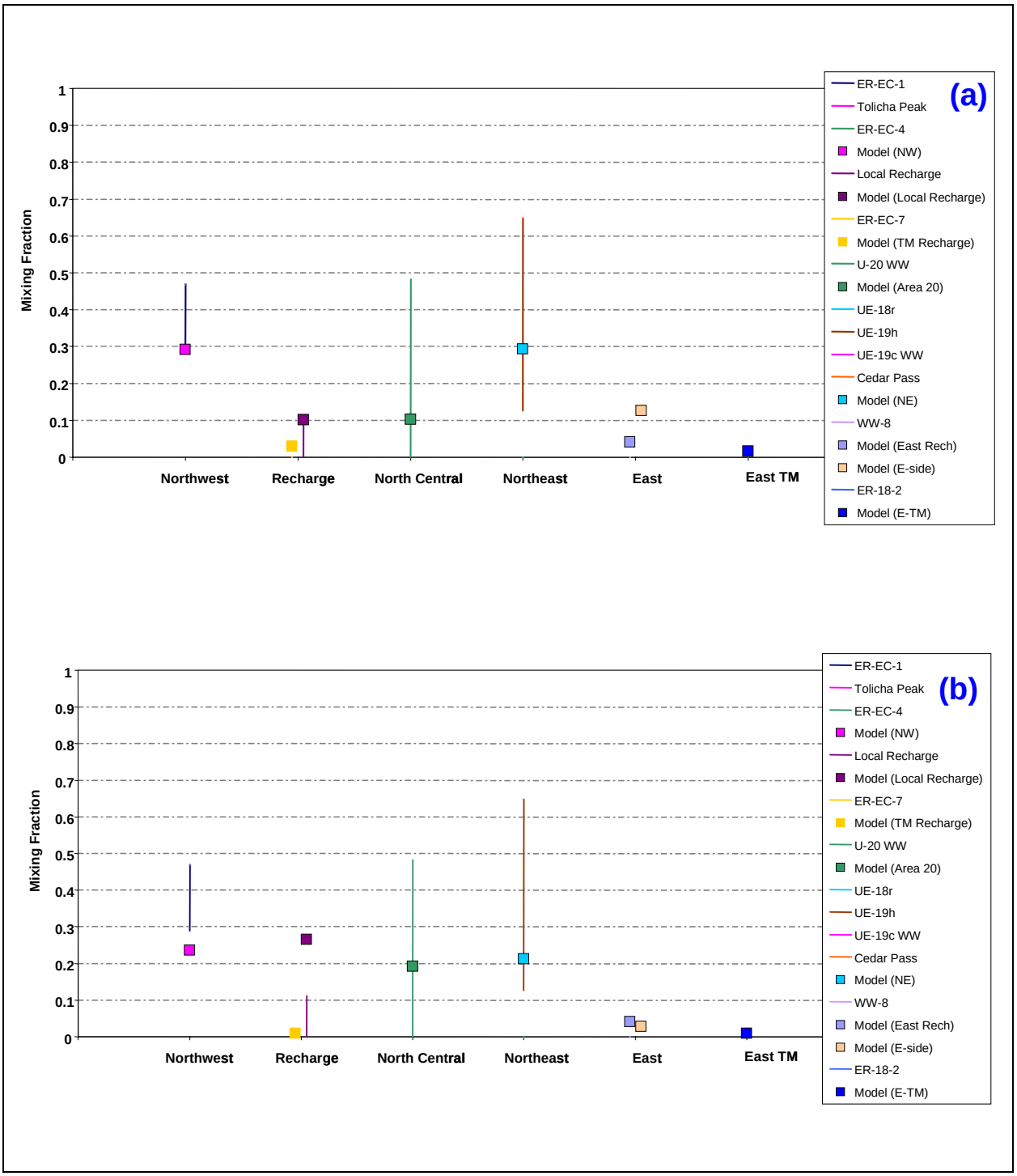

Figure 7-92
Quantitative Geochemical Comparisons at ER-OV-03a for (a) PZUP-USGSD-SDA and (b) PZUP-DRIA-SDA

Uncontrolled When Printed

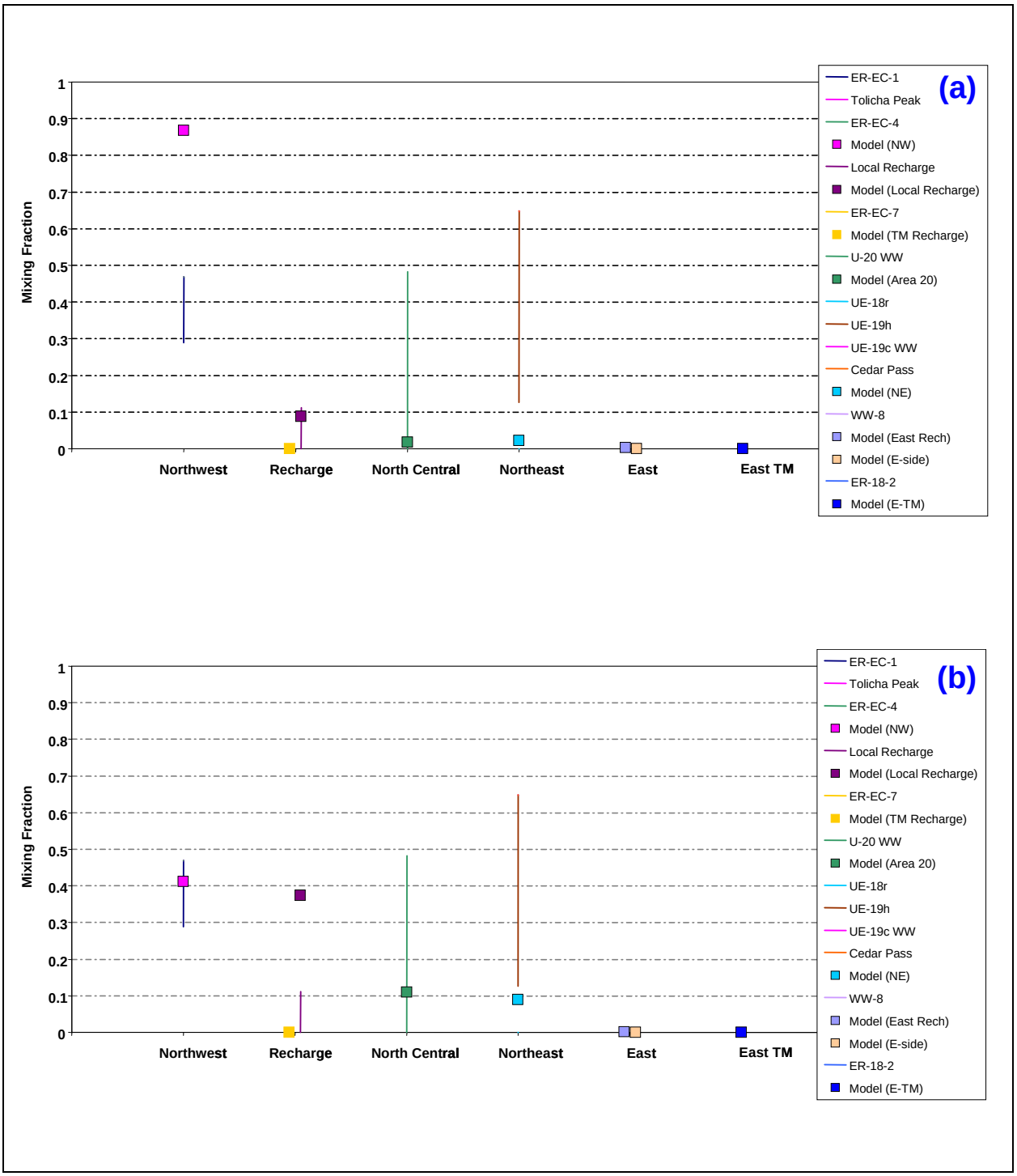

Figure 7-93
Quantitative Geochemical Comparisons at ER-OV-03a for (a) DRT-USGSD-SDA and (b) DRT-DRIA-SDA

Uncontrolled When Printed

Table 7-15
Comparison of Alternative Models at ER-OV-03a

HFM	Water-Balance Condition	Overestimation of Northwest Source	Underestimation of North-Central and Northeast Source	Overestimation of East Boundary Source	Overestimation of Local Recharge
BN-SDA reduced LCCU1 permeability alternative	MME				X
	USGSD				
	DRIA	X	X		X
BN-SDA	MME				
	USGSD			X	
	DRIA				X
BN-ADA	MME				X
SCCC-SDA	MME				X
	USGSD	X	X		
	DRIA		X		
PZUP	MME				
DRT	MME	X			
RIDGE	MME	-X[a]		X	
TCL	MME				
SEPZ	MME				
PZUP	USGSD			X	
	DRIA				X
DRT	USGSD	X	X		
	DRIA				X

[a]The actual discrepancy for this model is underestimation of northwest source.

7.3.7 ER-OV-03c

7.3.7.1 Alternative Water-Balance Conditions, BN HFM

The mixing ratios at ER-OV-03c show a reduction in northwest source water and an increase in source from the northeast. The results for the BN-USGS-SDA in the reduced LCCU1 permeability alternative nearly matches the targets, but with overestimates in Timber Mountain recharge and the east boundary at Gold Meadows (Figure 7-94). The DRIA calibration shows a very different picture with no Timber Mountain recharge, no problems with flow across the east model boundary, but an overestimate in northwest source water and local recharge, and an underprediction of northeast source water (Figure 7-95).

For the BN-USGSD-SDA (high LCCU1 permeability), an overestimate in east boundary flow leads to a reduction in sources at ER-OV-03c from the north central and northeast (Figure 7-96). The same model with DRIA conditions (Figure 7-96) shows a marked improvement on the inflow from Gold Meadows, but at the expense of increased local recharge. The BN-MME-ADA shows good agreement with targets, but with a small overestimate in east model boundary source water and local recharge (Figure 7-97).

7.3.7.2 SCCC Alternative HFM

The SCCC alternative HFM model (Figure 7-98) with MME water-balance conditions produces a flow field that captures the geochemistry mixing trend quite well at ER-OV-03c, but with an overestimate of local recharge in Beatty Wash as is expected with the MME recharge map. Figure 7-99 shows that the USGSD conditions for the model lead to poor results with no north-central or northeast sources and with overestimates in northwest, Timber Mountain, and local recharge sources. The DRIA model for SCCC suffers the same problem, with only a small increase in north-central source contribution (Figure 7-99).

7.3.7.3 PZUP, DRT, RIDGE, TCL, and SEPZ Alternative HFMs

The remaining alternative HFM scenarios with MME water-balance conditions show the similar results at ER-OV-03c (Figures 7-100 through 7-102), with the primary difference being the size of the local recharge and east boundary source overpredictions. The largest local recharge overprediction is

Uncontrolled When Printed

with DRT (60 percent) and the smallest is with PZUP (39 percent). The largest east boundary source estimate is with RIDGE (23 percent) and the smallest is with DRT (0 percent).

When the USGSD water-balance condition is used with PZUP, the east boundary flow contribution shoots up at the expense of the northwest and north-central components, which are pushed to the west of ER-OV-03c (Figure 7-103). The DRIA condition on the PZUP model maintains a northeast component at ER-OV-03c, but about 40 percent of the source comes from the east boundary and southeast quadrant of the model domain (Figure 7-103).

The DRT model with USGSD overestimates the northwest source and local recharge at the expense of underestimating the northeast source (Figure 7-104). With DRIA, the DRT model matches the target trend well, but with smaller northwest and local recharge source overestimates (Figure 7-104).

7.3.7.4 Summary: ER-OV-03c

As with the other wells southwest of Timber Mountain, at ER-OV-03c, there are four different mismatches between the model simulations and the geochemistry targets. They are (a) overestimation of source groundwater from the northwest, (b) underestimation of source groundwater from the north central and northeast, (c) overestimation of source water from the eastern model boundary, and (d) overestimation of local recharge. Table 7-16 identifies the mismatch issues for each simulation. Only those with more than a 10 percent mismatch are identified. Numerical quantification and comparison of this and all other target wells is presented in Section 7.5.

Uncontrolled When Printed

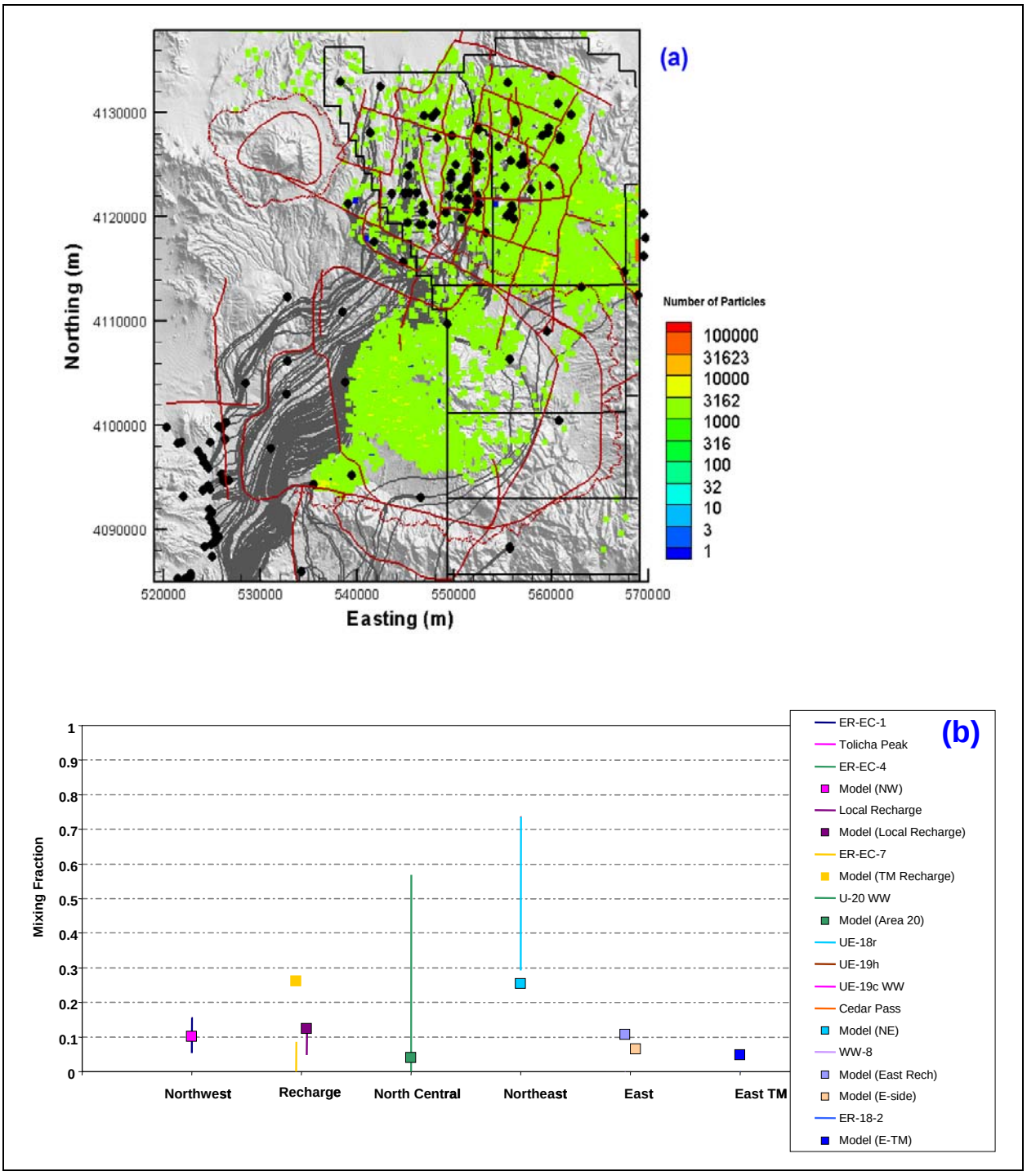

Figure 7-94
Comparison of Flow Model with Geochemical Mixing Targets at ER-OV-03c for BN-USGSD-SDA in the Reduced LCCU1 Permeability Alternative

Figure (a) shows the flow paths as mapped by forward SPTR particles originating at wells (grey lines) and the source recharge locations identified by reverse PTRK particle tracking (colored squares). Figure (b) shows the model comparison with geochemical mixing target ranges.

Uncontrolled When Printed

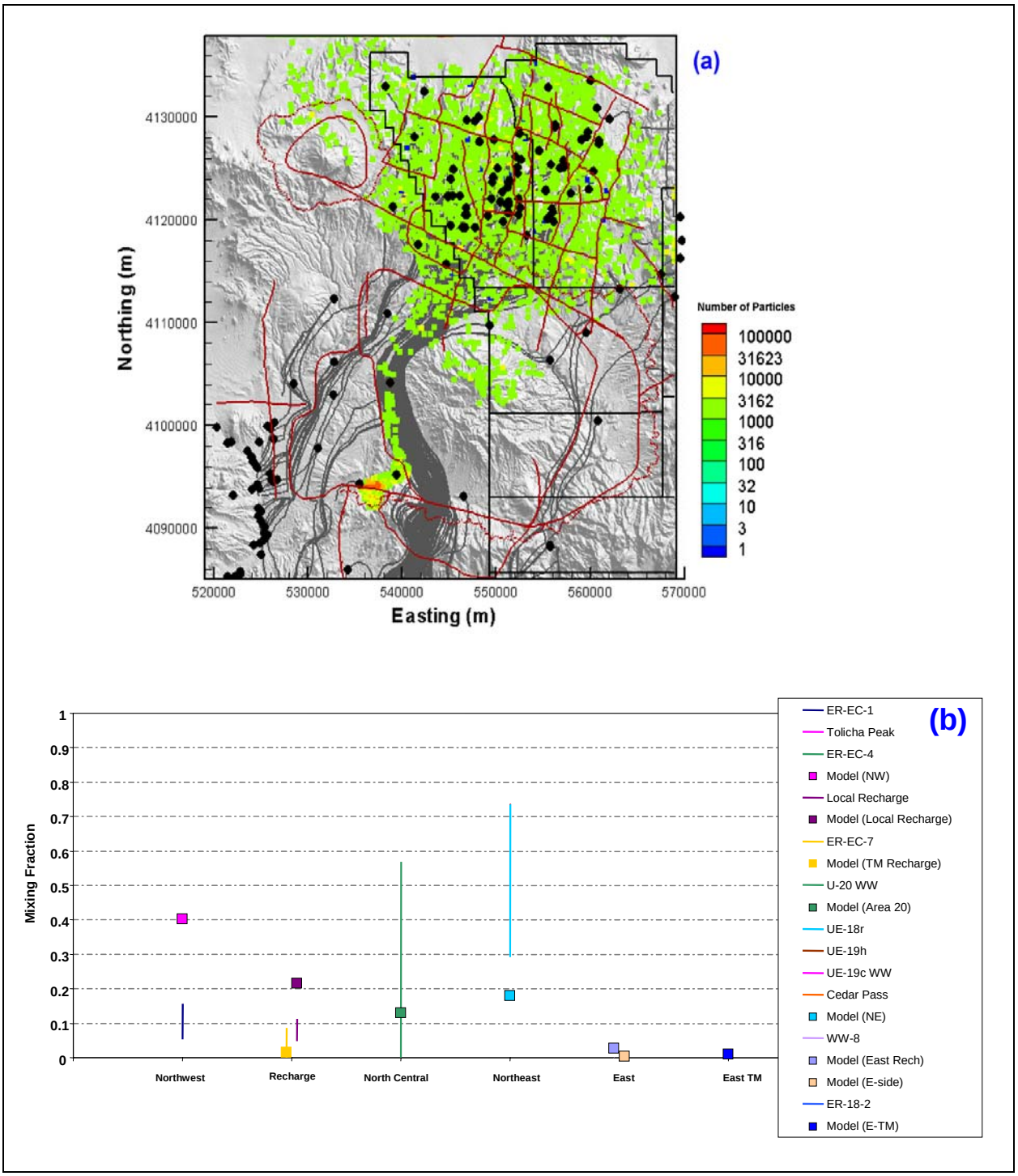

Figure 7-95
Comparison of Flow Model with Geochemical Mixing Targets at ER-OV-03c for BN-DRIA-SDA in the Reduced LCCU1 Permeability Alternative

Figure (a) shows the flow paths as mapped by forward SPTR particles originating at wells (grey lines) and the source recharge locations identified by reverse PTRK particle tracking (colored squares). Figure (b) shows the model comparison with geochemical mixing target ranges.

Uncontrolled When Printed

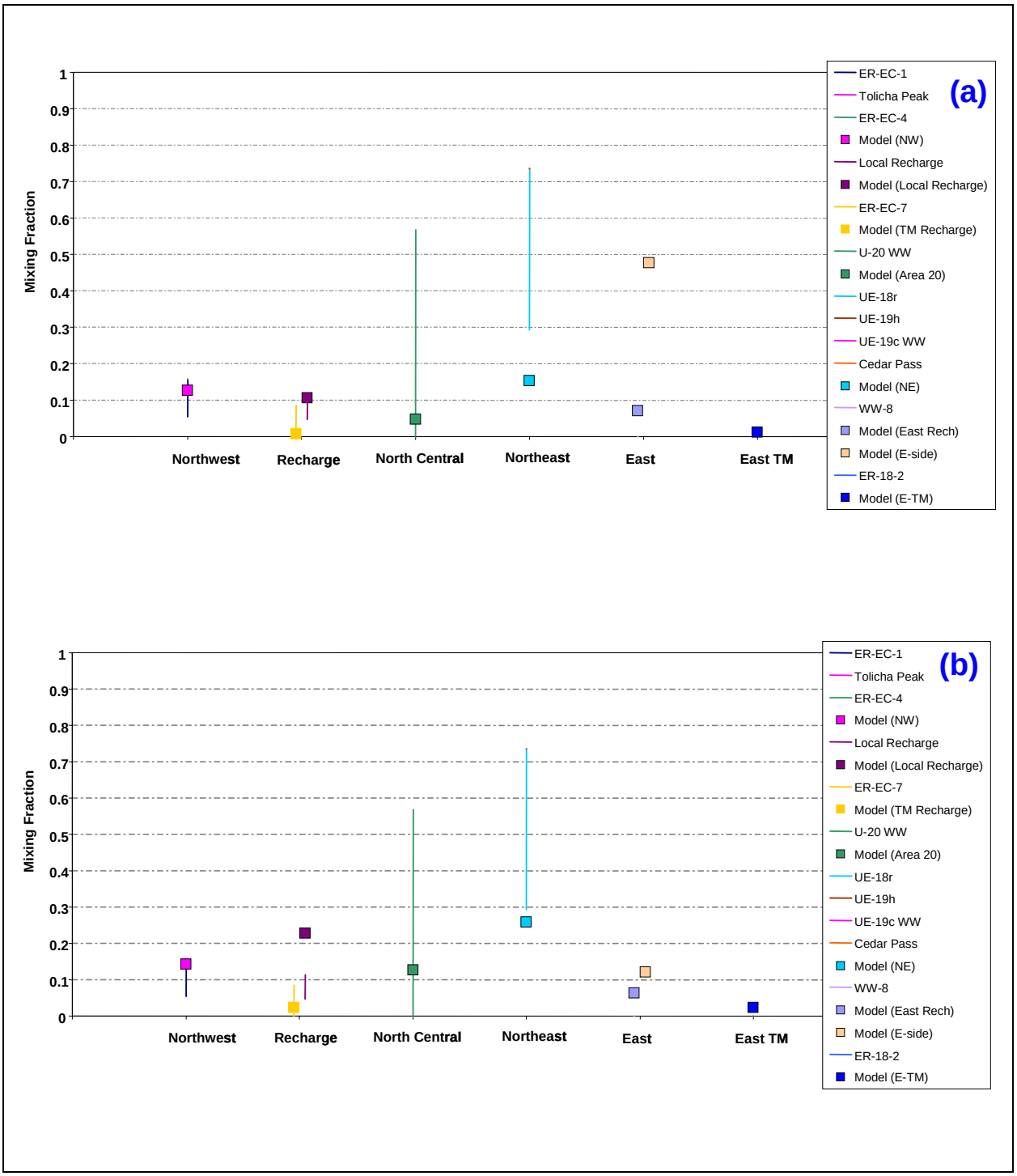

Figure 7-96
Quantitative Geochemical Comparisons at ER-OV-03c for (a) BN-USGSD-SDA and (b) BN-DRIA-SDA

Uncontrolled When Printed

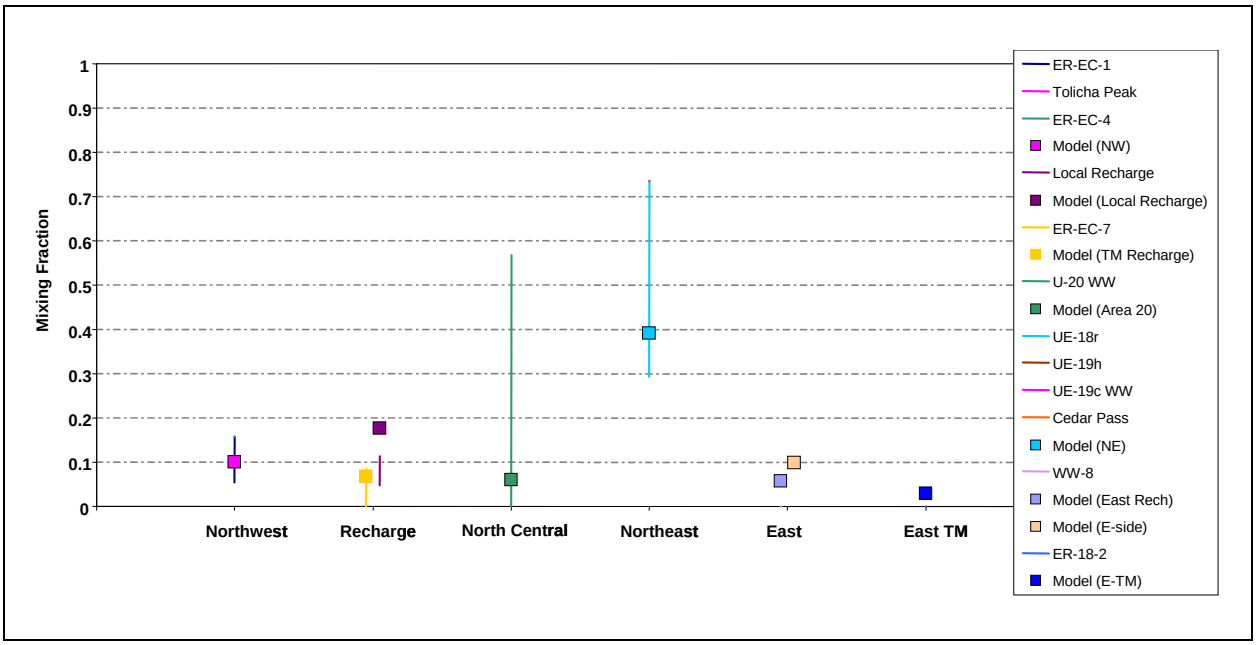

Figure 7-97
Comparison of Flow Model with Geochemical Mixing Targets at ER-OV-03c for BN-MME-ADA

Uncontrolled When Printed

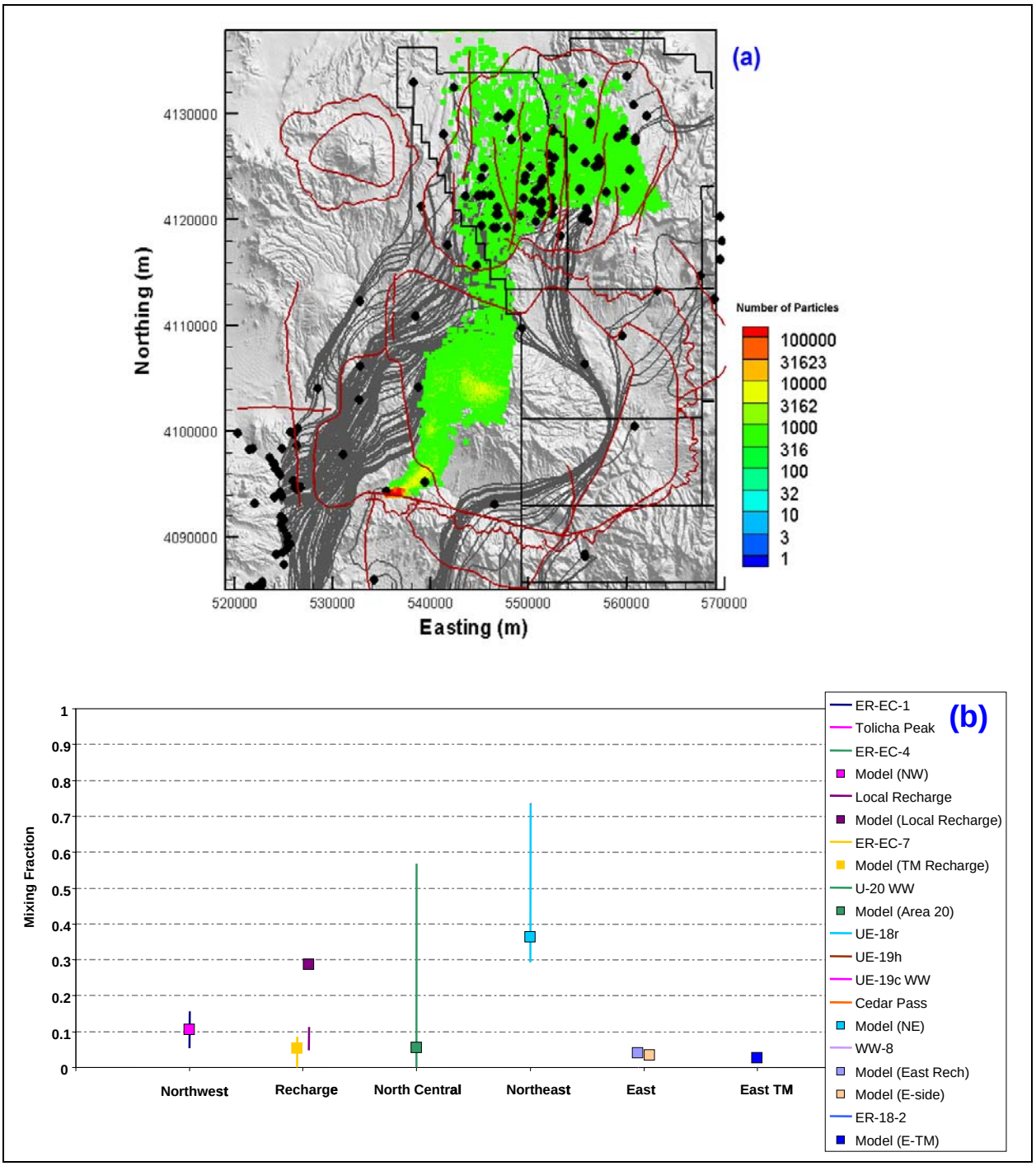

Figure 7-98
Comparison of Flow Model with Geochemical Mixing Targets at ER-OV-03c for SCCC-MME-SDA

Figure (a) shows the flow paths as mapped by forward SPTR particles originating at wells (grey lines) and the source recharge locations identified by reverse PTRK particle tracking (colored squares). Figure (b) shows the model comparison with geochemical mixing target ranges.

Uncontrolled When Printed

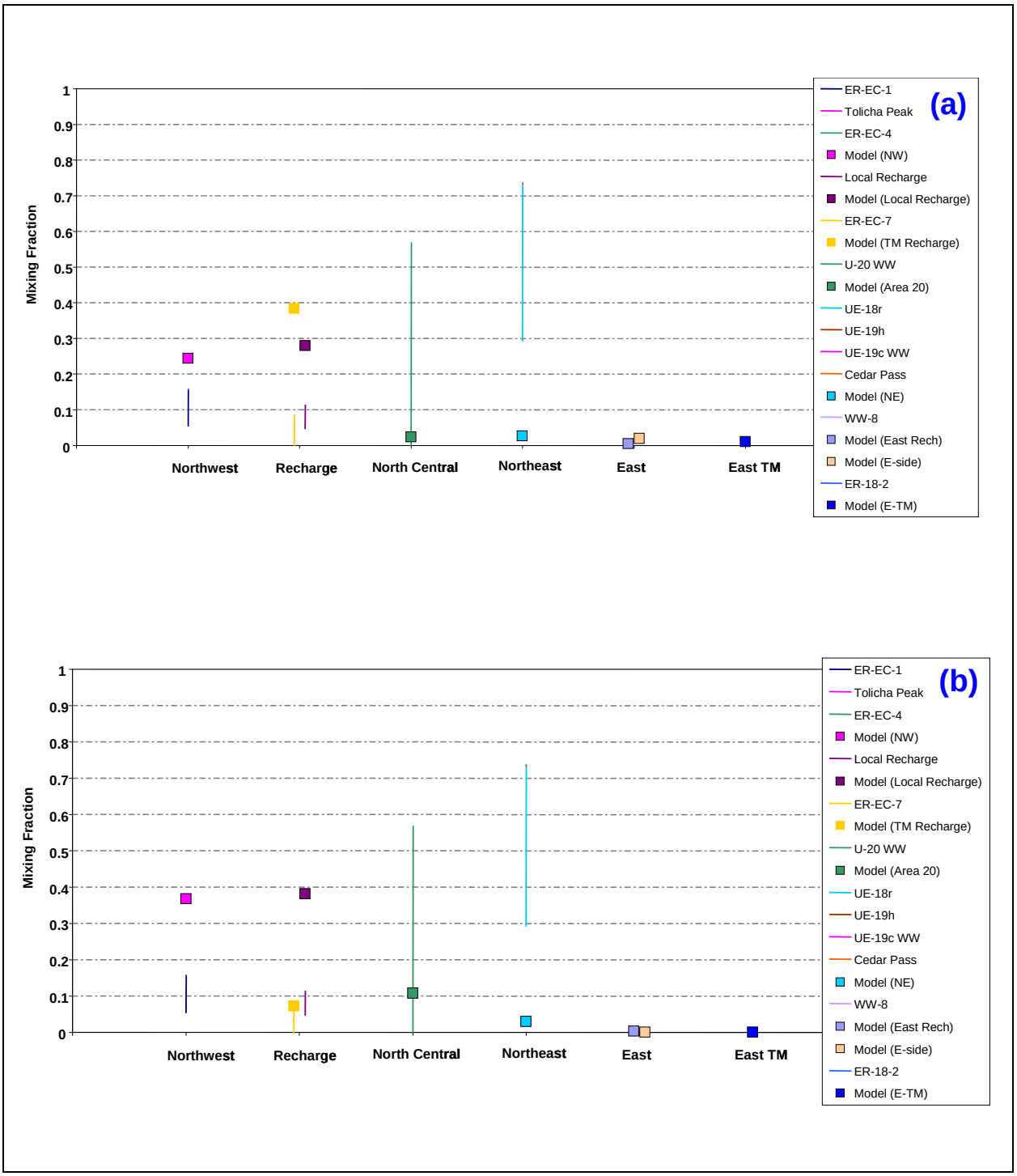

Figure 7-99
Quantitative Geochemical Comparisons at ER-OV-03c for (a) SCCC-USGSD-SDA and (b) SCCC-DRIA-SDA

Uncontrolled When Printed

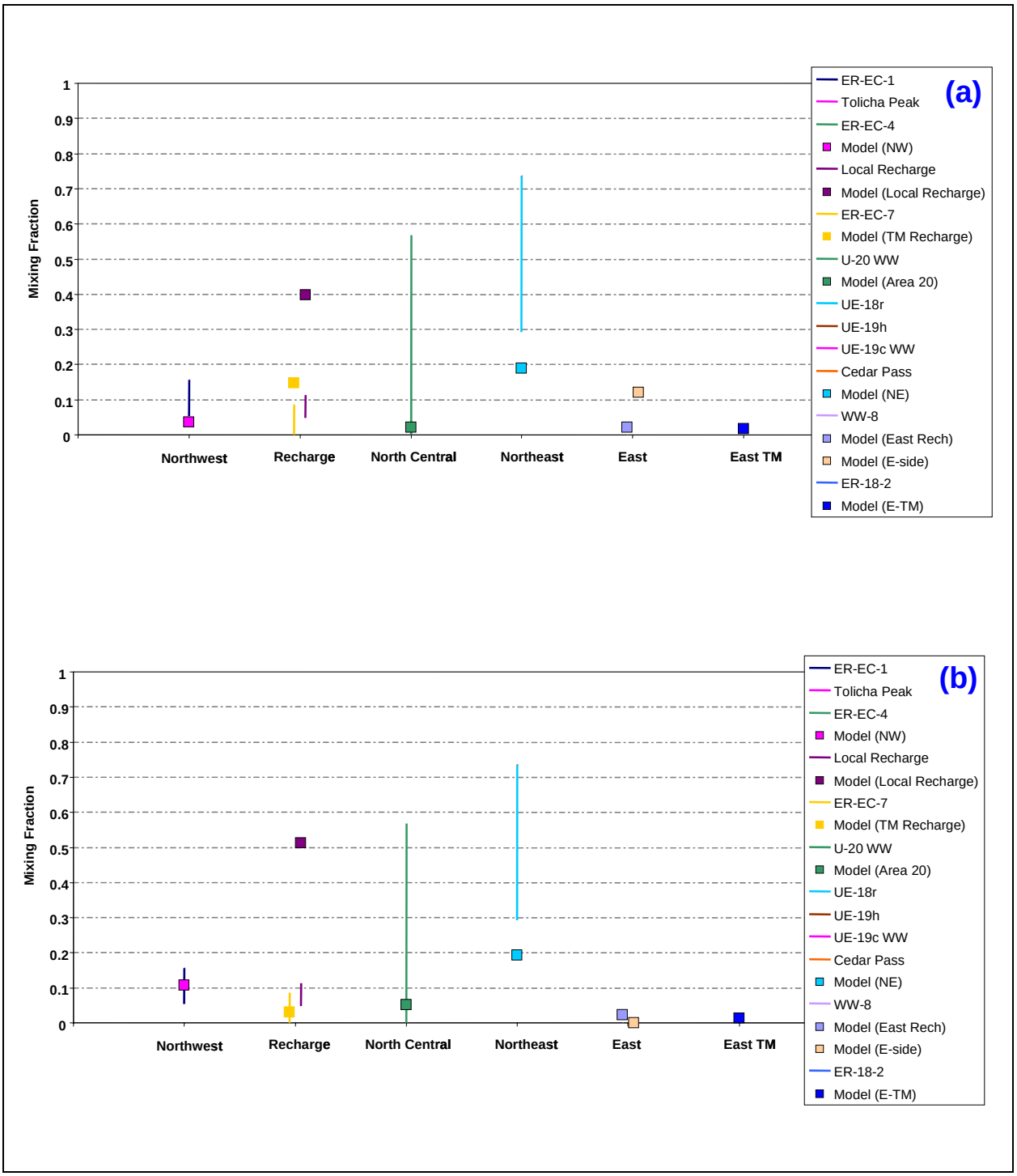

Figure 7-100
Quantitative Geochemical Comparisons at ER-OV-03c for
(a) PZUP-MME-SDA and (b) DRT-MME-SDA

Uncontrolled When Printed

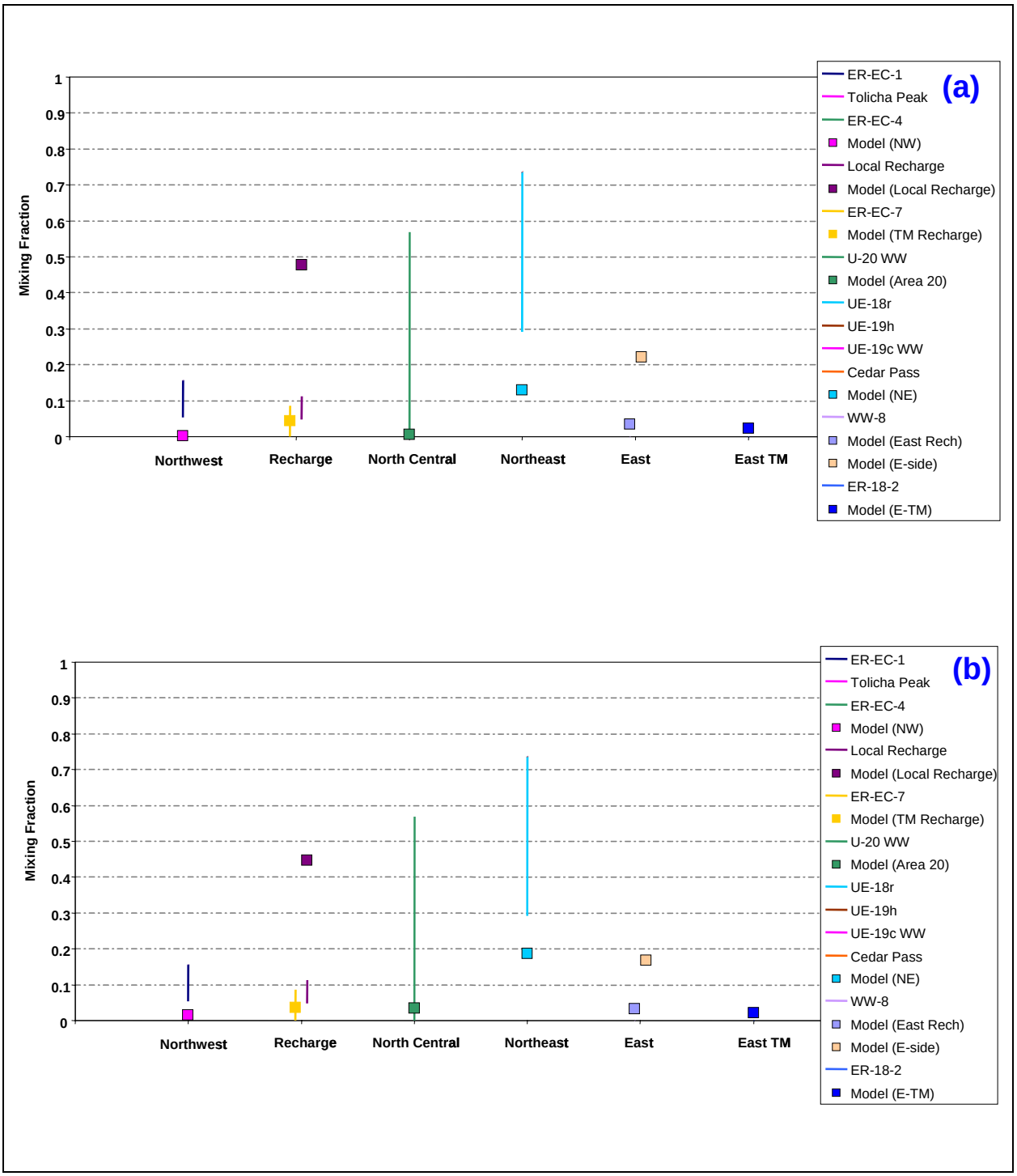

Figure 7-101
Quantitative Geochemical Comparisons at ER-OV-03c for
(a) RIDGE-MME-SDA and (b) TCL-MME-SDA

Uncontrolled When Printed

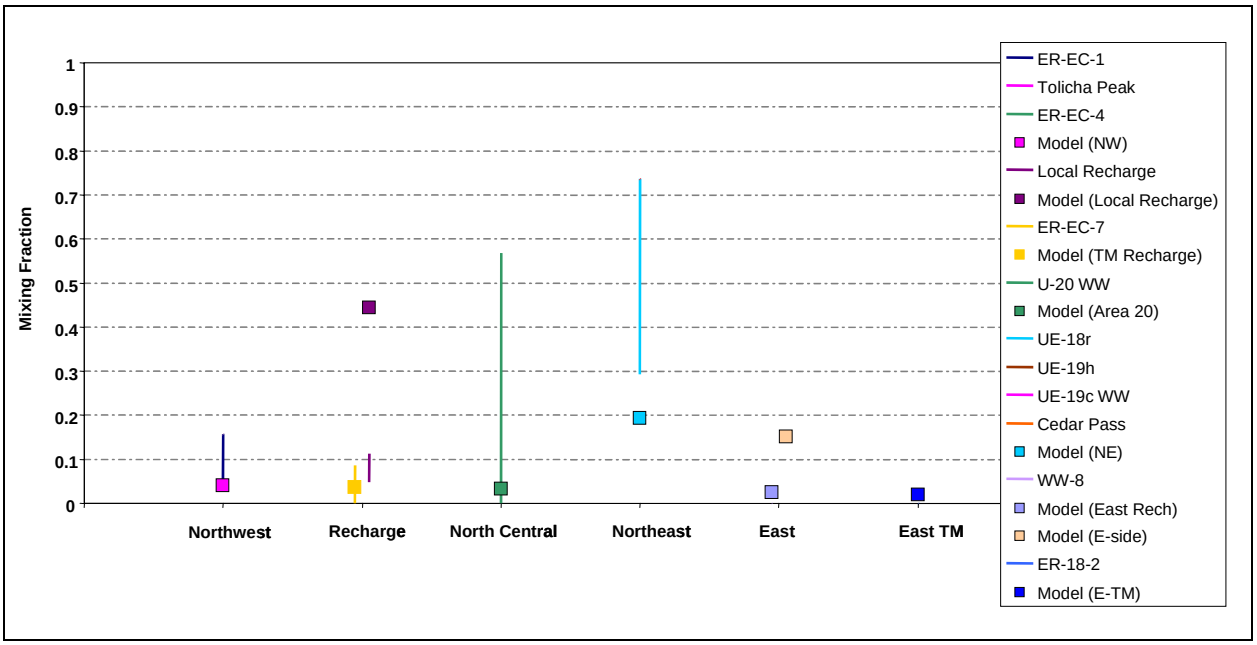

Figure 7-102
Comparison of Flow Model with Geochemical Mixing Targets at ER-OV-03c for SEPZ-MME-SDA

Uncontrolled When Printed

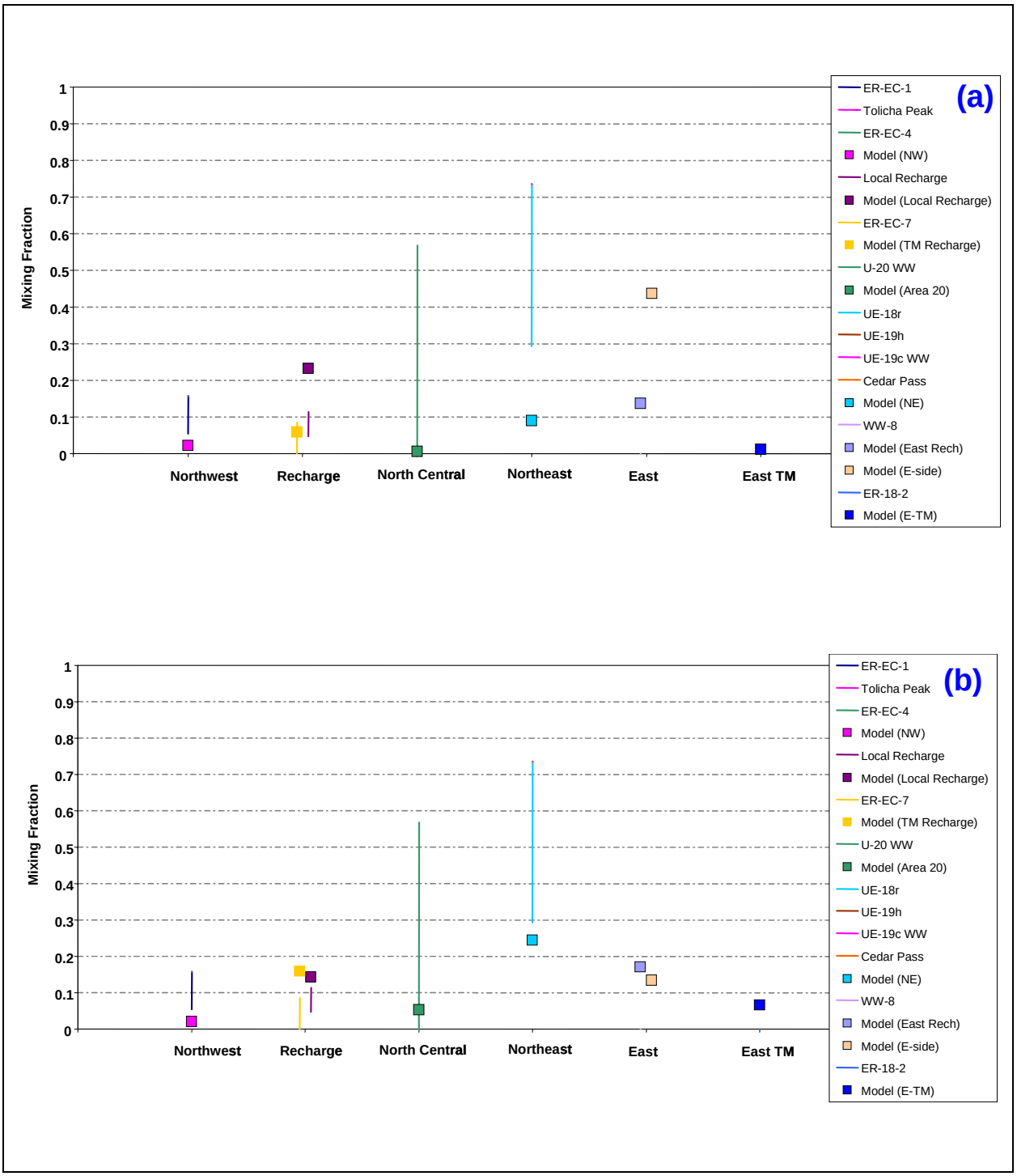

Figure 7-103
Quantitative Geochemical Comparisons at ER-OV-03c for
(a) PZUP-USGSD-SDA and (b) PZUP-DRIA-SDA

Uncontrolled When Printed

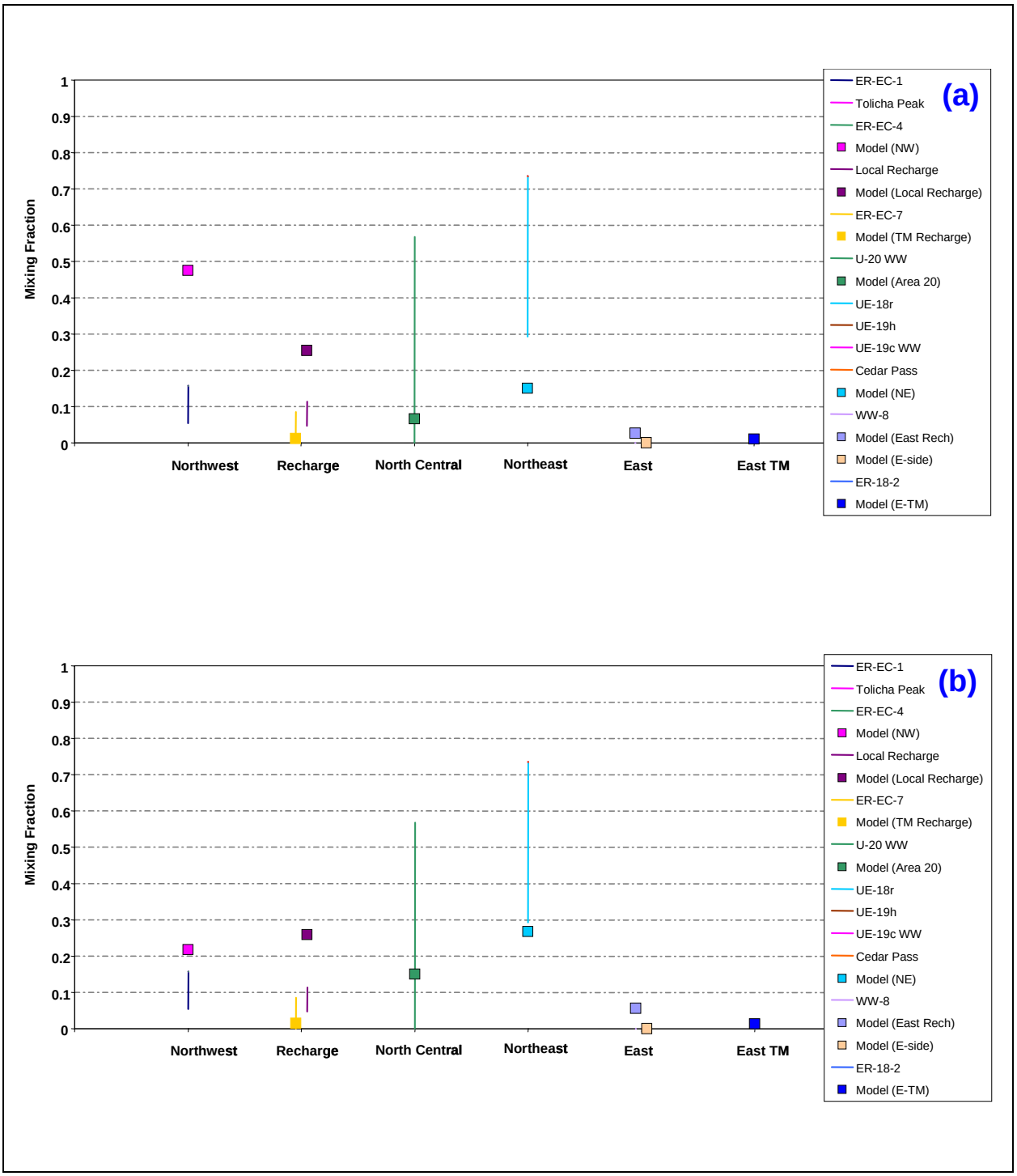

Figure 7-104
Quantitative Geochemical Comparisons at ER-OV-03c for
(a) DRT-USGSD-SDA and (b) DRT-DRIA-SDA

Uncontrolled When Printed

Table 7-16
Comparison of Alternative Models at ER-OV-03c

HFM	Water-Balance Condition	Overestimation of Northwest Source	Underestimation of North-Central and Northeast Source	Overestimation of East Boundary Source	Overestimation of Local Recharge
BN-SDA reduced LCCU1 permeability alternative	MME				X
	USGSD				X (TM)
	DRIA	X			
BN-SDA	MME		X	X	X
	USGSD		X	X	
	DRIA			X	
BN-ADA	MME				
SCCC-SDA	MME				X
	USGSD		X		X
	DRIA	X	X		X
PZUP	MME			X	X
DRT	MME				X
RIDGE	MME		X	X	X
TCL	MME		X	X	X
SEPZ	MME		X	X	X
PZUP	USGSD		X	X	X
	DRIA			X	
DRT	USGSD	X	X		
	DRIA				X

7.3.8 Coffer Windmill Well

At the Coffer Windmill Well, the source of water has shifted to include greater contributions from either the northeast or even the eastern model boundary, as discussed in Section 7.2. As with the other seven target wells considered in this section, Figures 7-105 through 7-115 show the model comparisons with the geochemistry mixing targets for each alternative water balance and/or HFM considered. Because of the wide range in uncertainty for the sources of water at this well (Figure 7-25), the primary concern in comparing the models is whether too much northwest or local recharge source is simulated. These are clearly compared in Table 7-17.

7.3.8.1 Summary: Coffer Windmill Well

As described in Section 7.2, Coffer Windmill Well has a wide range of uncertainty in the chemical mixing targets. The groundwater looks like a mix of WW-8 and ER-18-2 water, like a mix of Timber Mountain Recharge (ER-EC-7) and Area 19 water (UE-18r), or some combination in between. Because WW-8 water is so similar to Rainier Mesa water in HTH-1 (Kwicklis et al., 2005), they are considered as equally possible in this comparison. Likewise, because it is unclear how different upper Beatty Wash recharge is from ER-EC-7 water they are both considered as equally possible local recharge, but their combination is considered with regard to the total local recharge estimate. Thus, the mismatches of greatest concern are (a) overestimation of source groundwater from the northwest and (b) overestimation of local recharge (e.g., no source water from the north-central, northeast or eastern zones). Table 7-17 identifies the mismatch issues for each simulation. Only those with more than a 10 percent mismatch are identified.

Uncontrolled When Printed

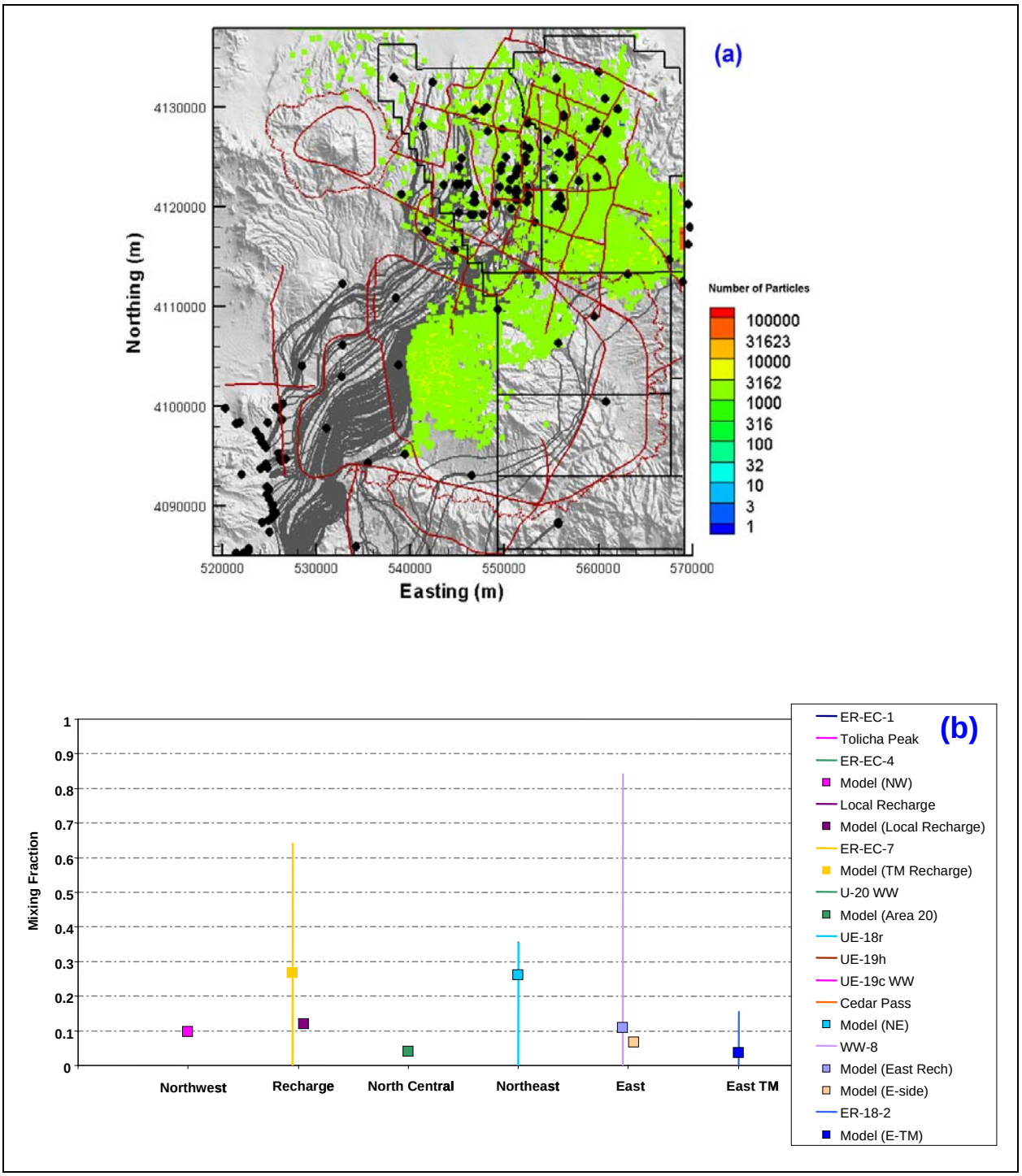

Figure 7-105
Comparison of Flow Model with Geochemical Mixing Targets at Coffer Windmill Well for BN-USGSD-SDA in the Reduced LCCU1 Permeability Alternative

Figure (a) shows the flow paths as mapped by forward SPTR particles originating at wells (grey lines) and the source recharge locations identified by reverse PTRK particle tracking (colored squares). Figure (b) shows the model comparison with geochemical mixing target ranges.

Uncontrolled When Printed

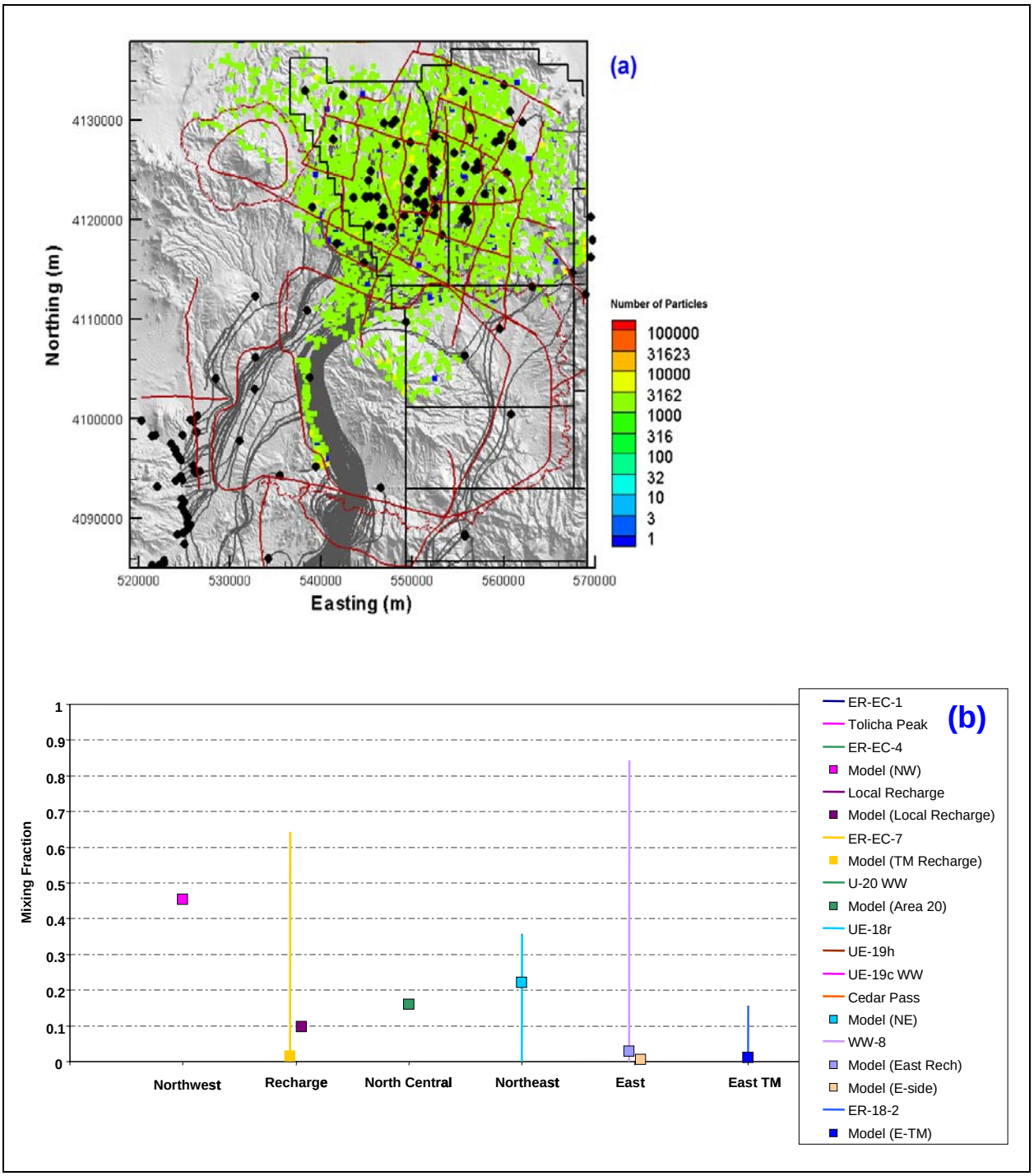

Figure 7-106
Comparison of Flow Model with Geochemical Mixing Targets at Coffer Windmill Well for BN-DRIA-SDA in the Reduced LCCU1 Permeability Alternative

Figure (a) shows the flow paths as mapped by forward SPTR particles originating at wells (grey lines) and the source recharge locations identified by reverse PTRK particle tracking (colored squares). Figure (b) shows the model comparison with geochemical mixing target ranges.

Uncontrolled When Printed

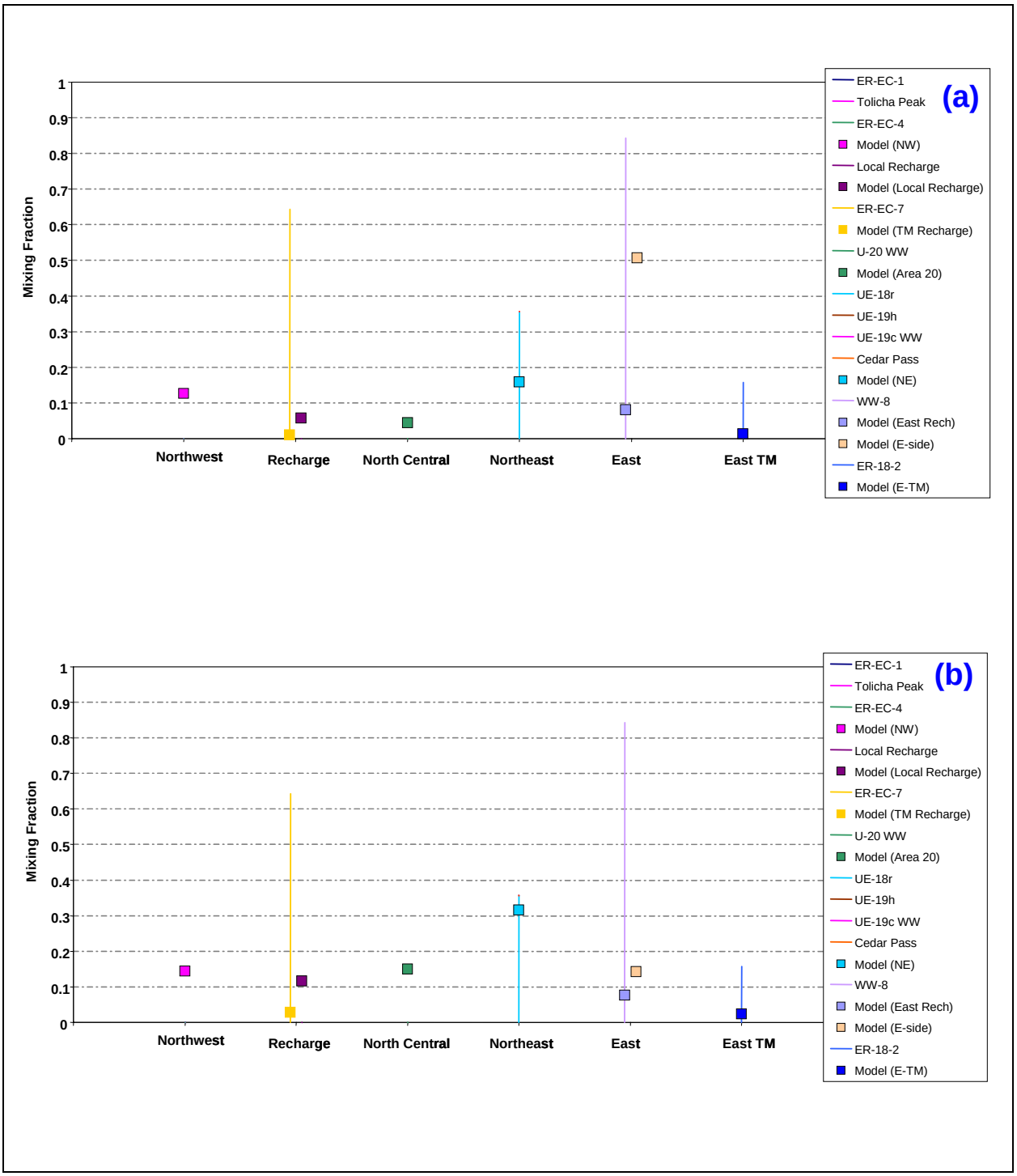

Figure 7-107
Quantitative Geochemical Comparisons at Coffer Windmill Well for (a) BN-USGSD-SDA and (b) BN-DRIA-SDA

Uncontrolled When Printed

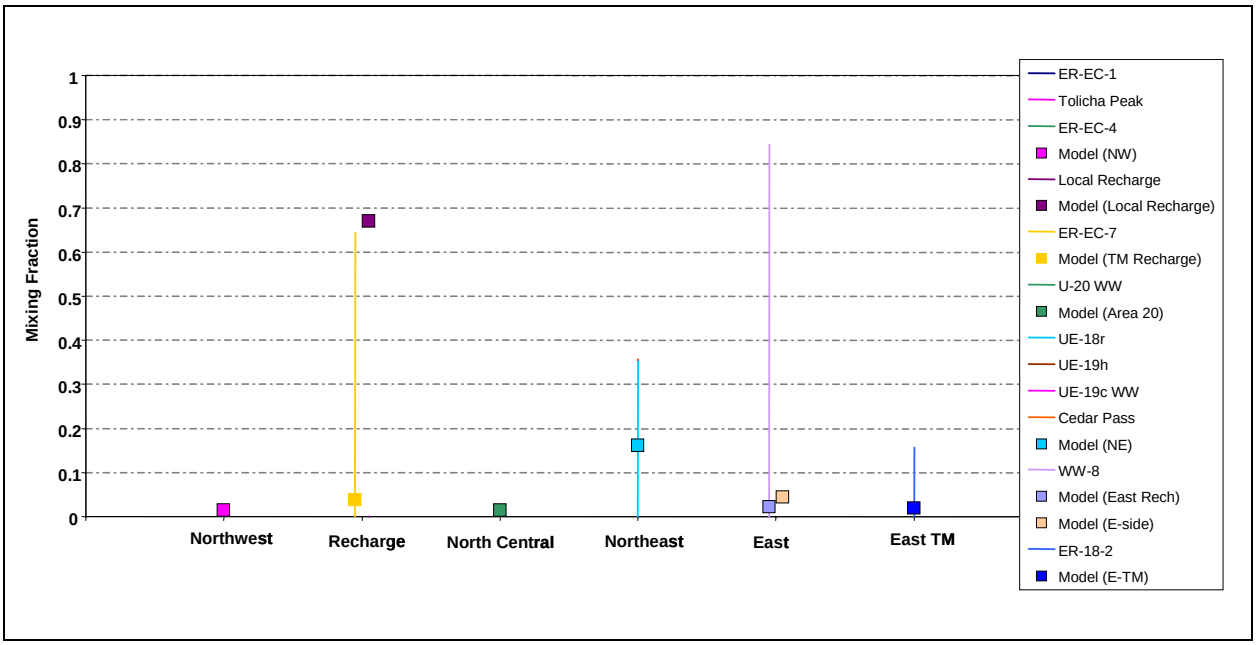

Figure 7-108
Comparison of Flow Model with Geochemical Mixing Targets at Coffer Windmill Well for BN-MME-ADA

Uncontrolled When Printed

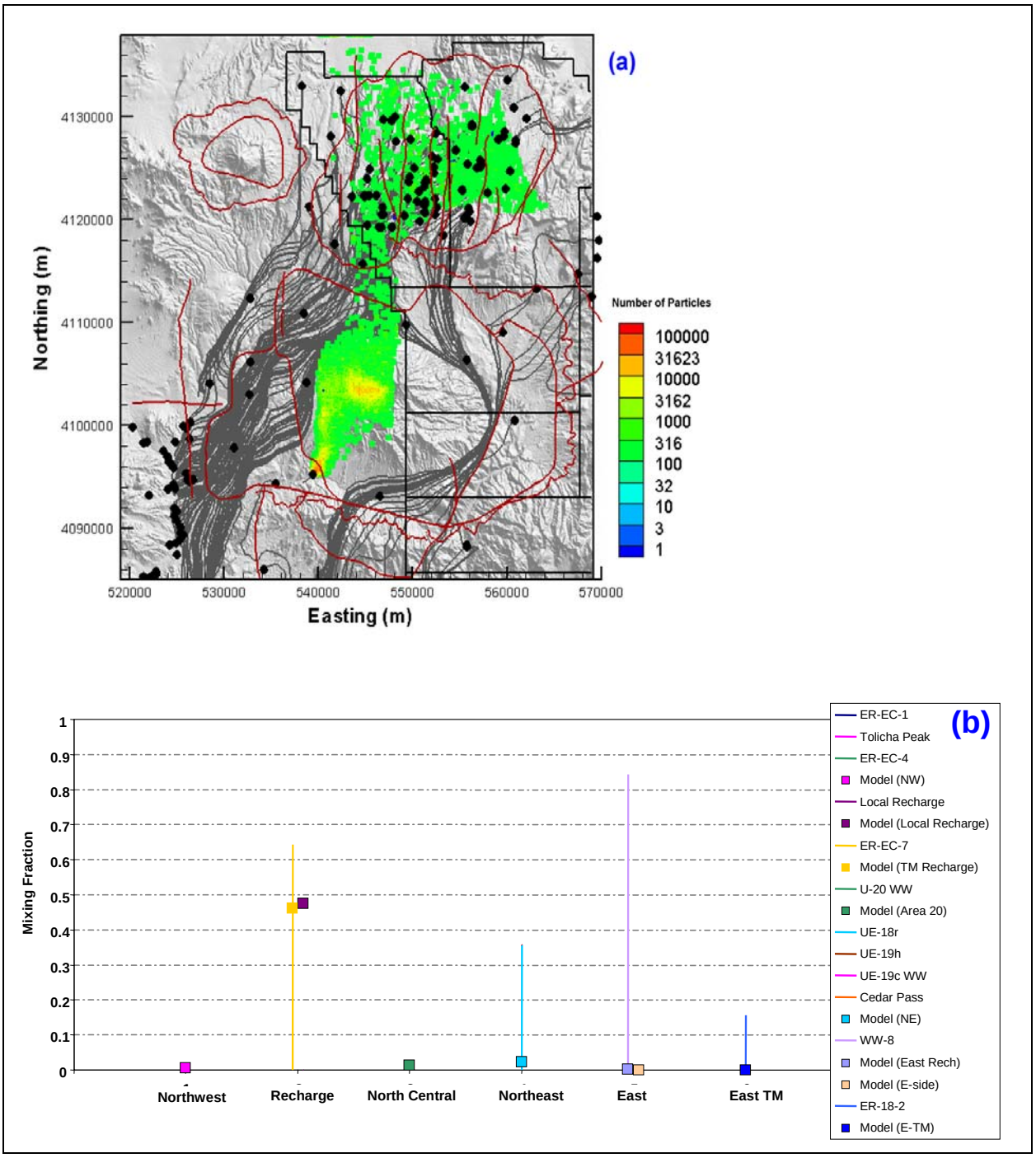

Figure 7-109
Comparison of Flow Model with Geochemical Mixing Targets at Coffer Windmill Well for SCCC-MME-SDA

Figure (a) shows the flow paths as mapped by forward SPTR particles originating at wells (grey lines) and the source recharge locations identified by reverse PTRK particle tracking (colored squares). Figure (b) shows the model comparison with geochemical mixing target ranges.

Uncontrolled When Printed

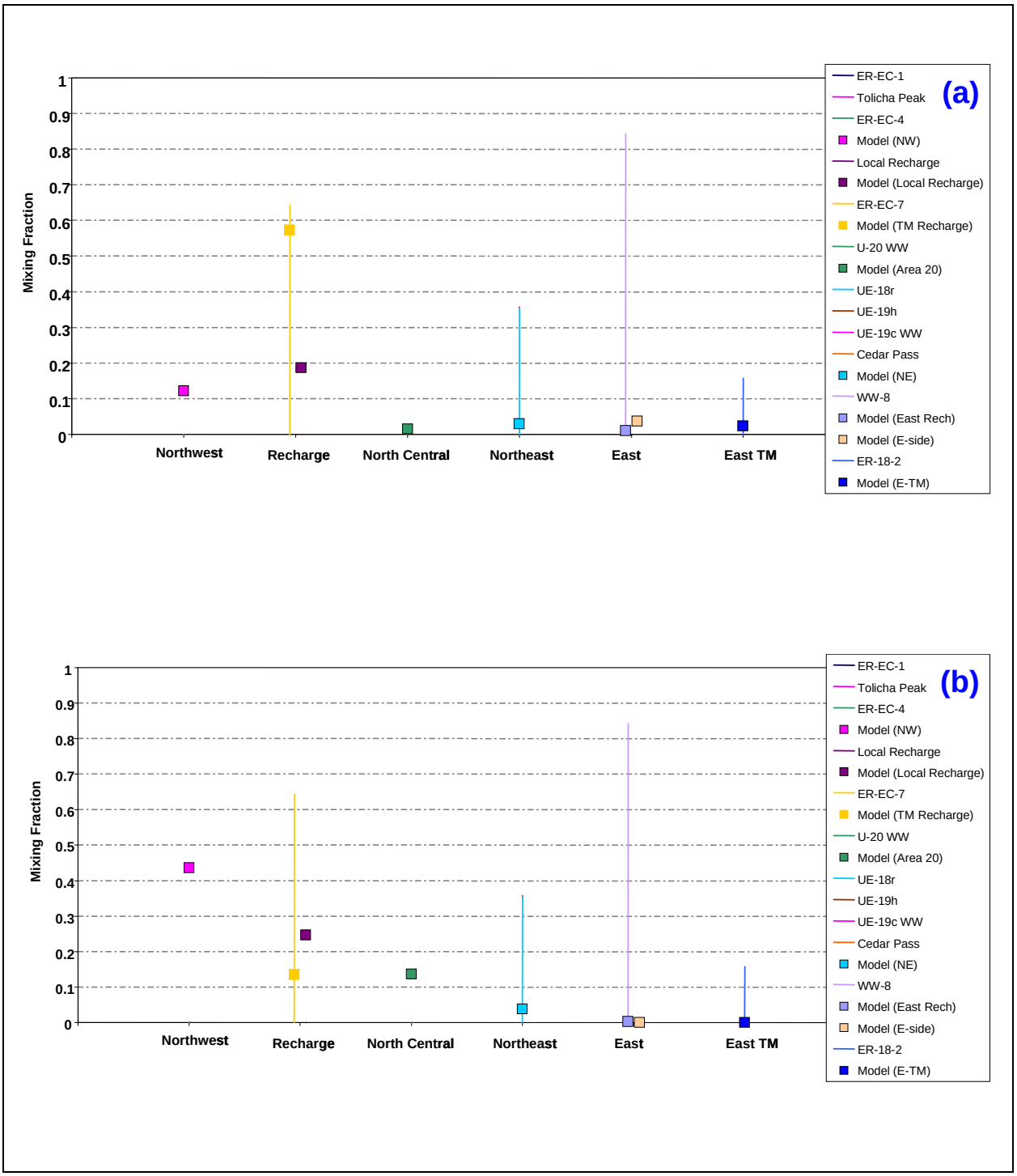

Figure 7-110
Quantitative Geochemical Comparisons at Coffer Windmill Well for (a) SCCC-USGSD-SDA and (b) SCCC-DRIA-SDA

Uncontrolled When Printed

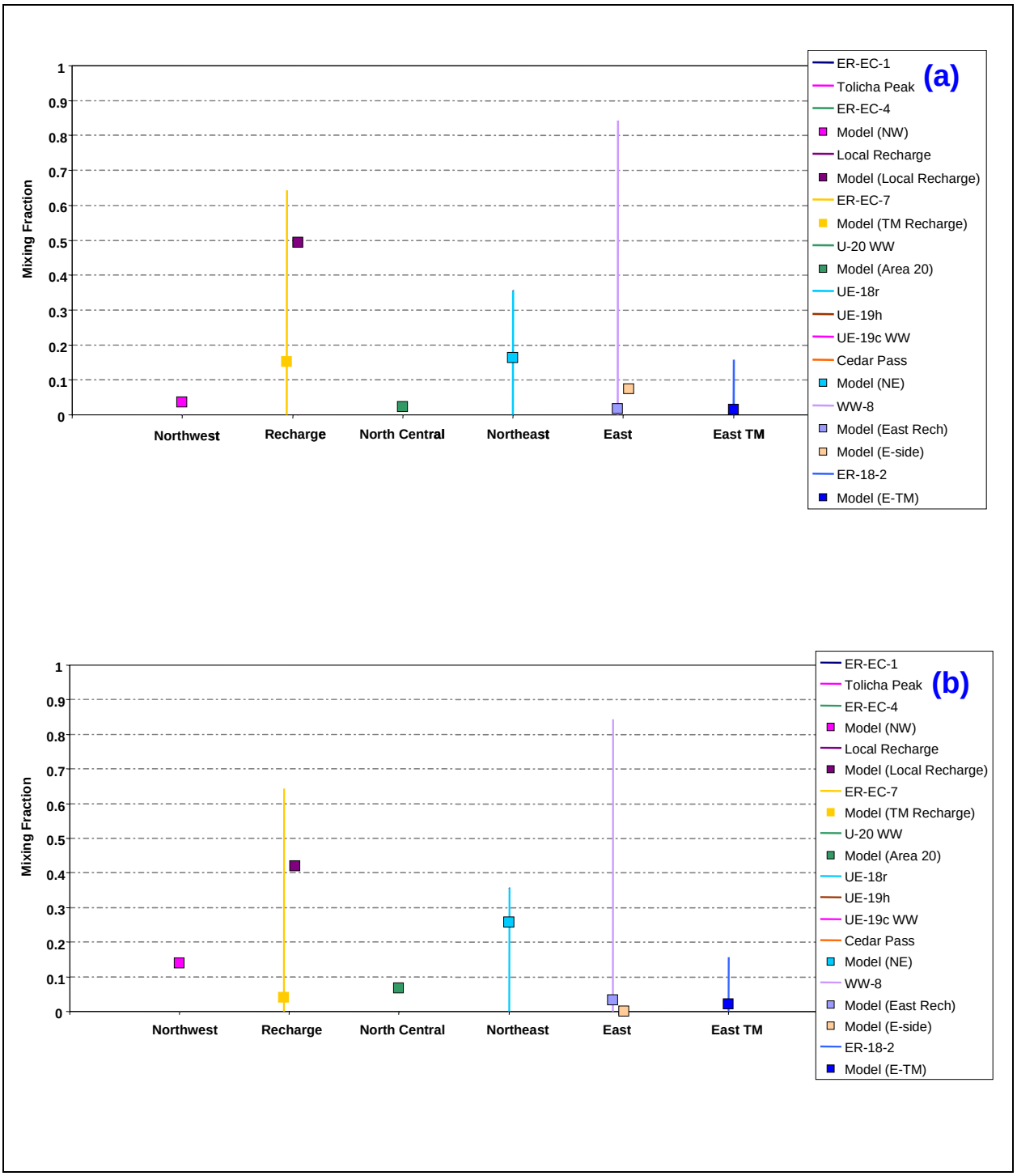

Figure 7-111
Quantitative Geochemical Comparisons at Coffer Windmill Well for (a) PZUP-MME-SDA and (b) DRT-MME-SDA

Uncontrolled When Printed

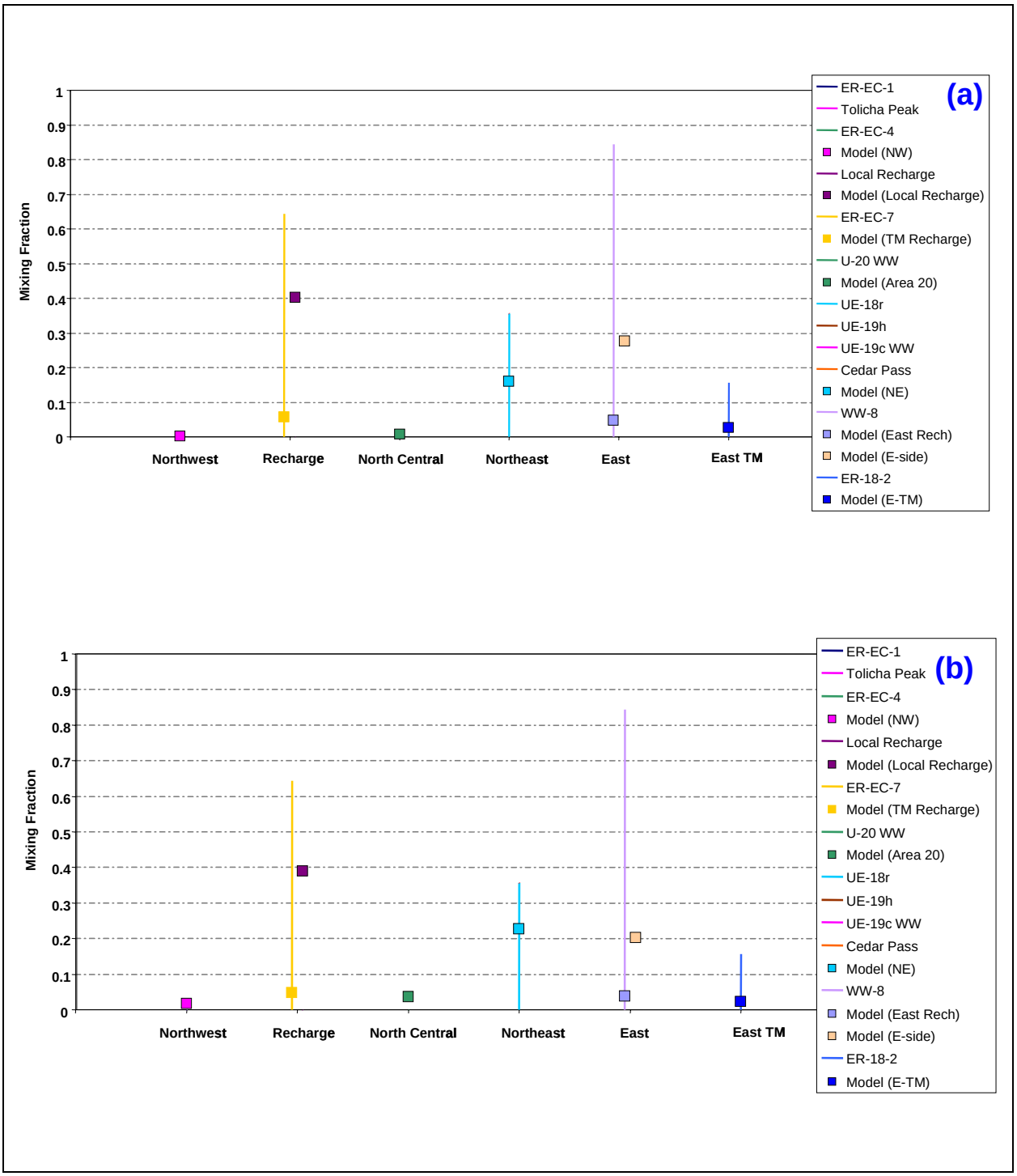

Figure 7-112
Quantitative Geochemical Comparisons at Coffer Windmill Well for (a) RIDGE-MME-SDA and (b) TCL-MME-SDA

Uncontrolled When Printed

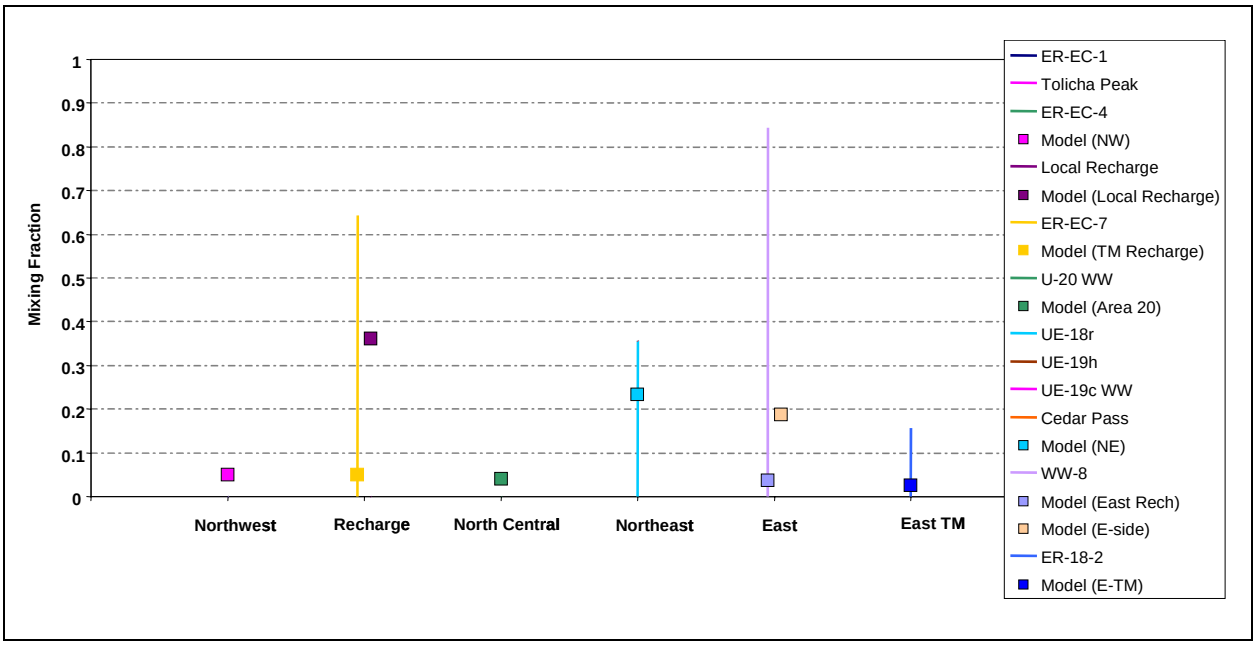

Figure 7-113
Comparison of Flow Model with Geochemical Mixing Targets at Coffer Windmill Well for SEPZ-MME-SDA

Uncontrolled When Printed

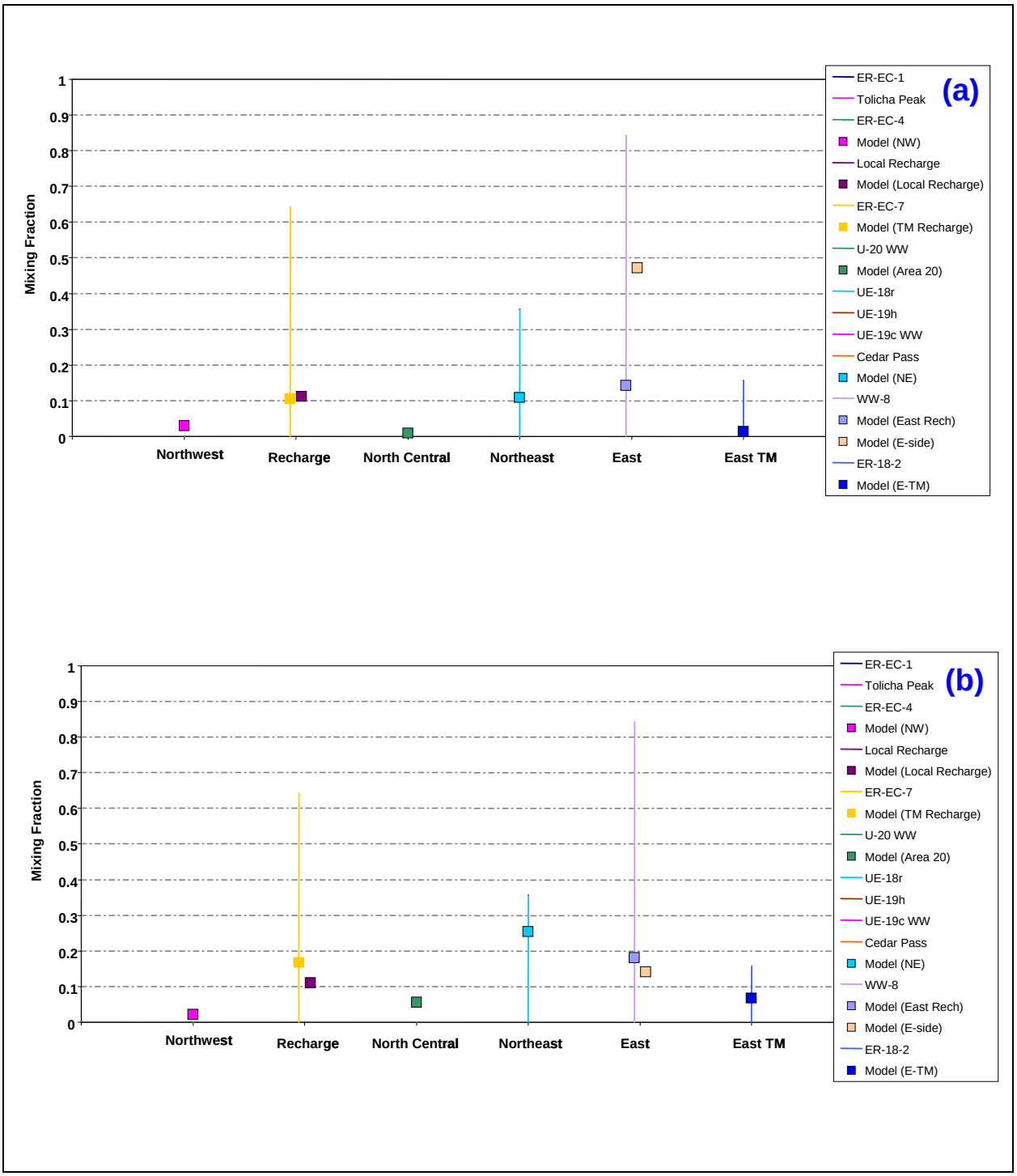

Figure 7-114
Quantitative Geochemical Comparisons at Coffer Windmill Well for (a) PZUP-USGSD-SDA and (b) PZUP-DRIA-SDA

Uncontrolled When Printed

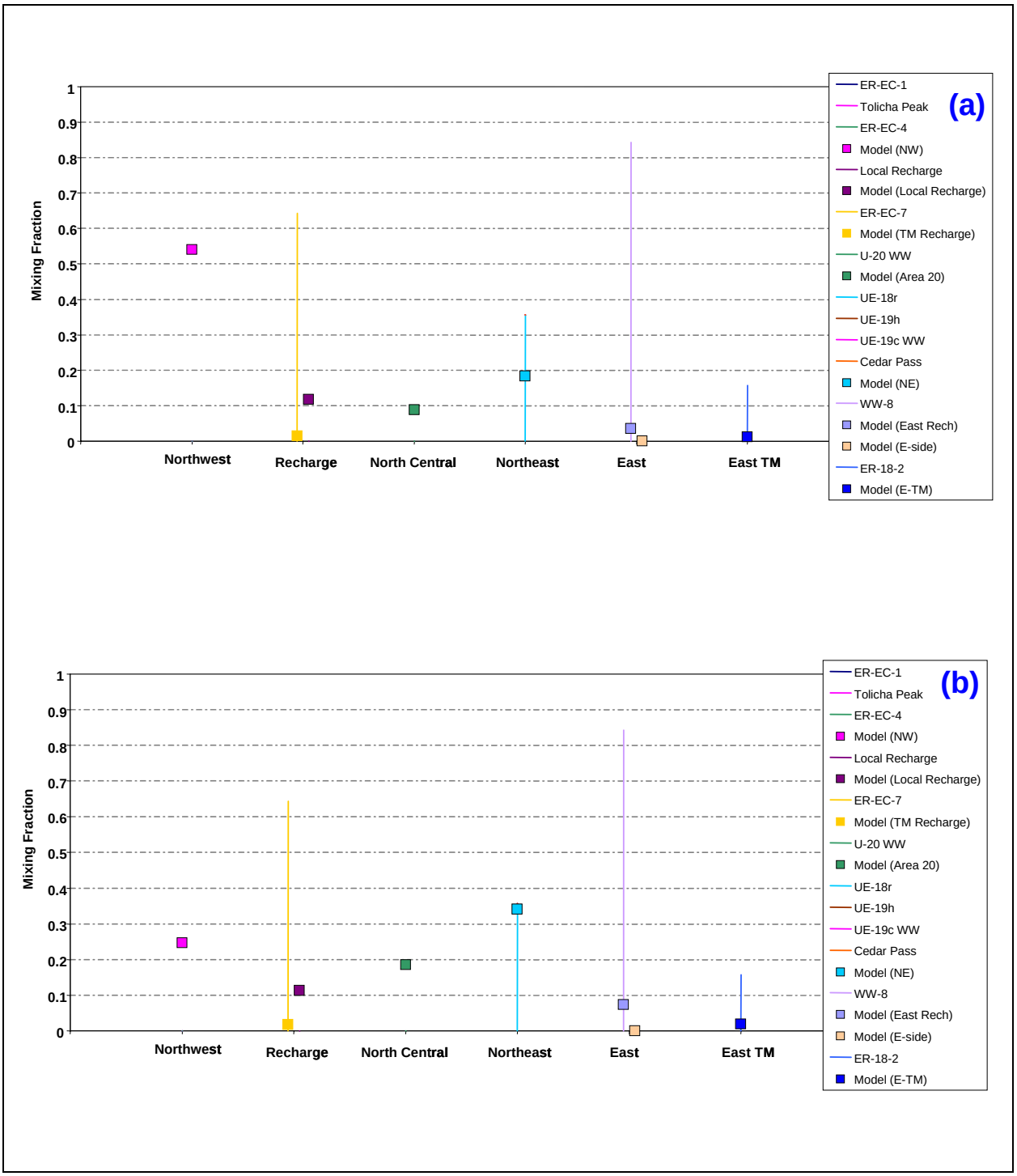

Figure 7-115
Quantitative Geochemical Comparisons at Coffer Windmill Well for (a) DRT-USGSD-SDA and (b) DRT-DRIA-SDA

Uncontrolled When Printed

Table 7-17
Comparison of Alternative Models at Coffer Windmill Well

HFM	Water-Balance Condition	Overestimation of Northwest Source	Overestimation of Local Recharge
BN-SDA reduced LCCU1 permeability alternative	MME	X	
	USGSD		
	DRIA	X	
BN-SDA	MME		
	USGSD	X	
	DRIA	X	
BN-ADA	MME		
SCCC-SDA	MME		
	USGSD	X	
	DRIA	X	
PZUP	MME		
DRT	MME	X	
RIDGE	MME		
TCL	MME		
SEPZ	MME		
PZUP	USGSD		
	DRIA		
DRT	USGSD	X	
	DRIA	X	

Uncontrolled When Printed

7.4 Geochemistry Performance of the Fortymile Canyon Alternate

One of the sensitivity simulations discussed in Section 6.2.4 involved manual intervention of a calibration to force a high permeability pathway southward along Fortymile Canyon. By increasing the permeabilities of the TMCM and reducing the LCCU1 permeability alternative and then recalibrating the flow model, a reasonable objective function was obtained, and the amount of flow originating on Pahute Mesa and flowing to the east of Timber Mountain was increased. Figure 7-116 shows the simulated pathlines highlighting the increased southward flow to the east of Timber Mountain. The quality of the comparison to geochemical mixing targets of this model decreases substantially from those discussed previously in this section. Figure 7-117 shows that nearly 80 percent of the source water for UE-18r in this simulation is from the northwest. However, the chemistry analysis indicates that there is no water source at UE-18r with such a signature. Figures 7-118 through 7-121 show a systematic error in overprediction of northwest source water at the Oasis Valley wells. This results from the northeast source water moving southward and to the east of Timber Mountain, rather than to Oasis Valley, where the geochemical analysis indicates it should be present.

The geochemistry verification study for this flow model, coupled with the calibration results, indicate that this flow model is not a good representation of the PM/OV flow system. Water from the northeast that should arrive in Oasis Valley moves southward below Fortymile Canyon instead. The increased permeabilities that make such flow possible in the model produce systematic errors in the calibration as well (Figure 6-76). The simulated heads along the east side of Timber Mountain are uniformly below observations, indicating at large-scale problem with the parameters and their impacts in groundwater flow.

Uncontrolled When Printed

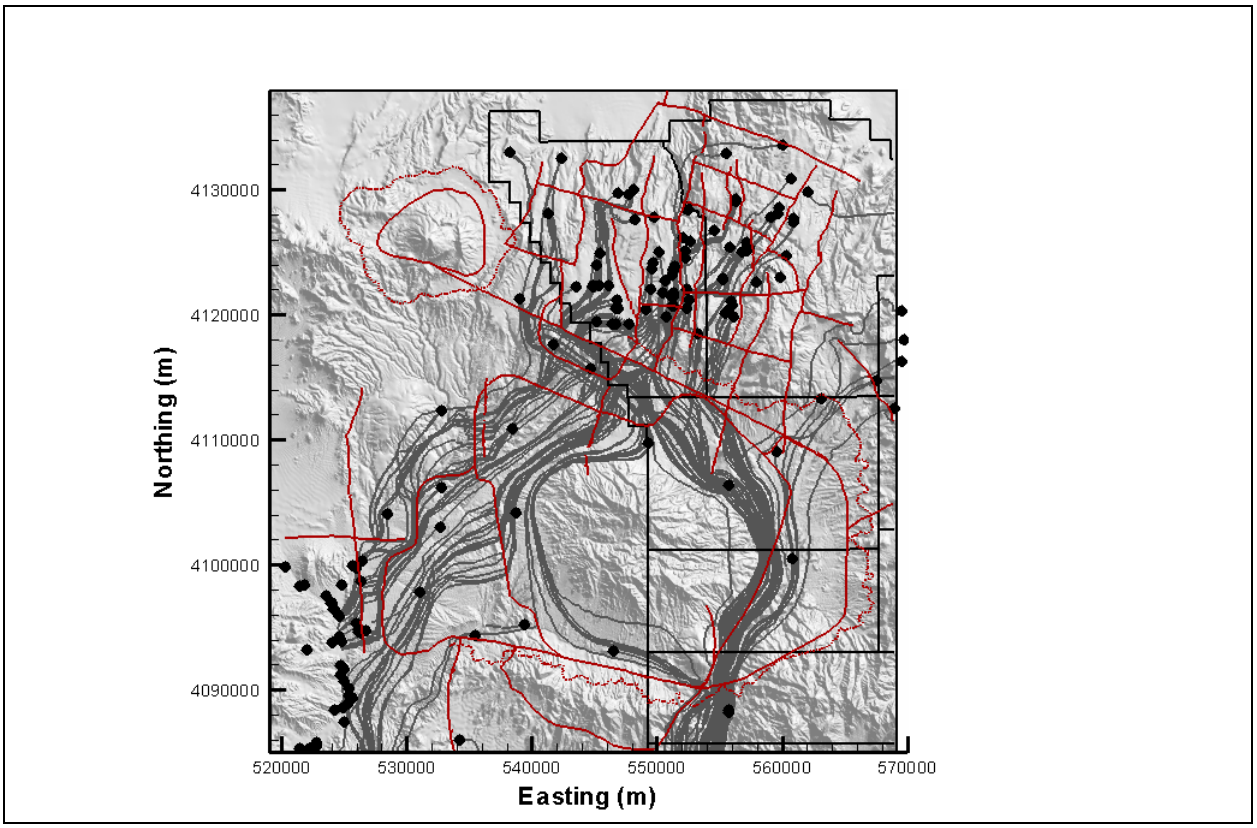

Figure 7-116
Paths of Particles Released in Wells for BN-USGSD-FMC Calibrated Flow Model

Uncontrolled When Printed

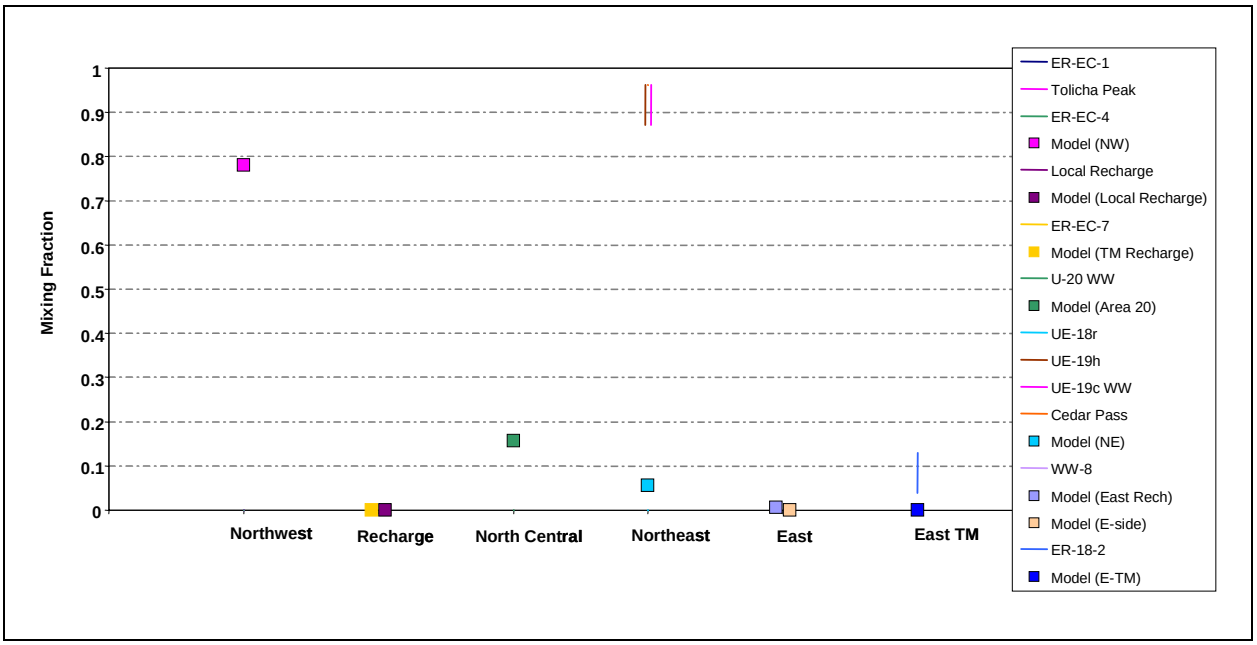

Figure 7-117
Comparison of Flow Model with Geochemical Mixing Targets for UE-18r with the BN-USGSD-FMC Flow Model

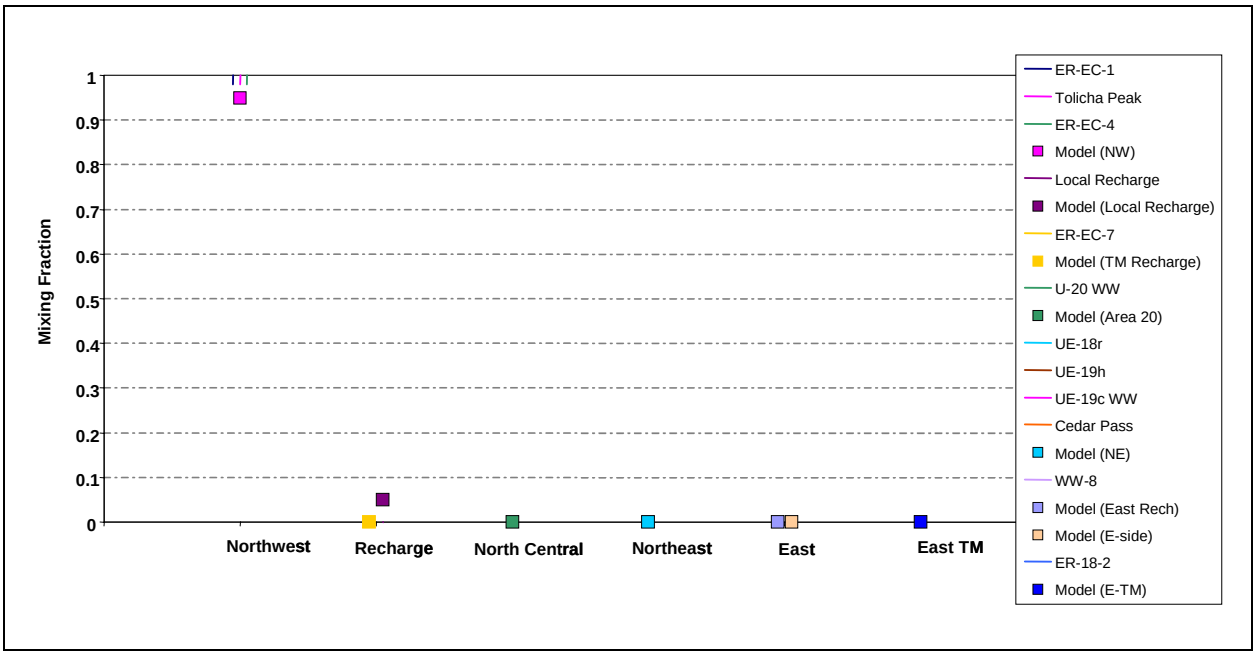

Figure 7-118
Comparison of Flow Model with Geochemical Mixing Targets for ER-OV-04a with the FMC-USGSD-SDA Flow Model

Uncontrolled When Printed

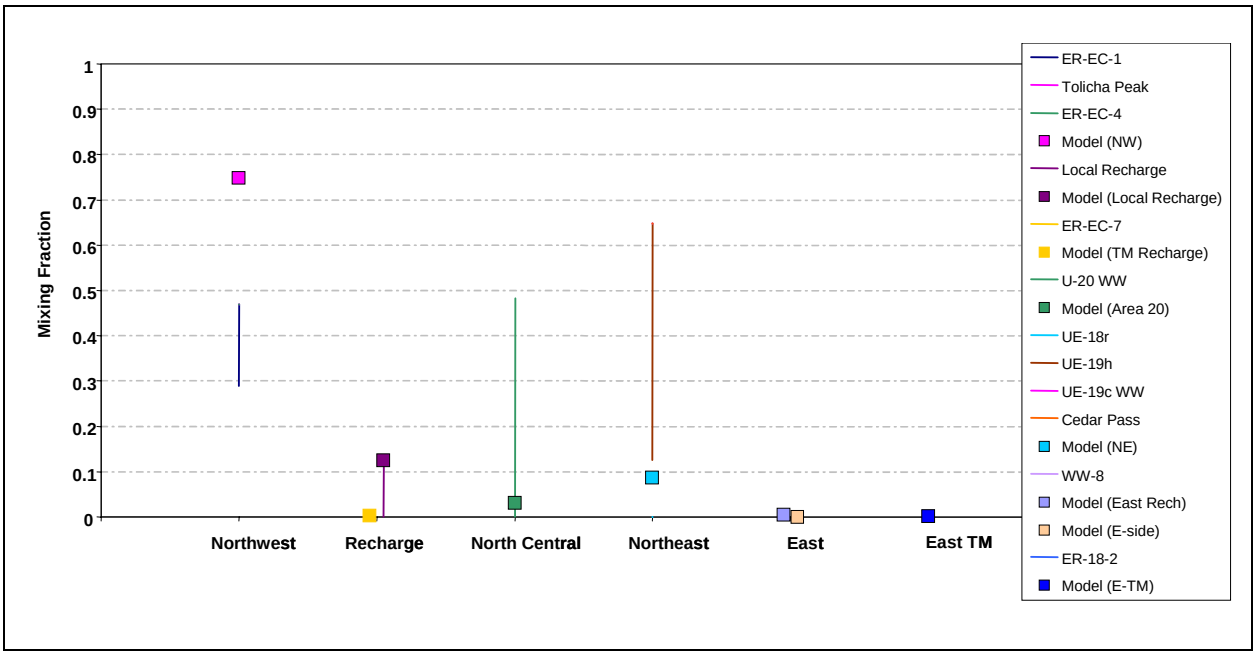

Figure 7-119
Comparison of Flow Model with Geochemical Mixing Targets for ER-OV-03a with the FMC-USGSD-SDA Flow Model

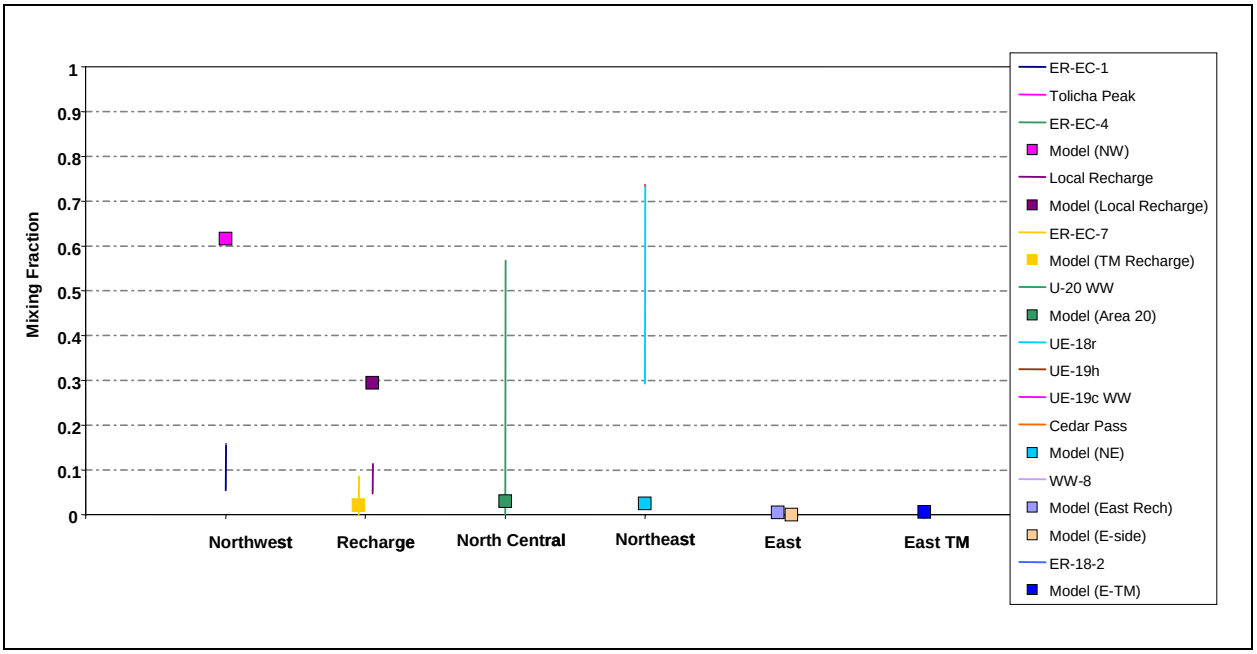

Figure 7-120
Comparison of Flow Model with Geochemical Mixing Targets for ER-OV-03c with the FMC-USGSD-SDA Flow Model

Uncontrolled When Printed

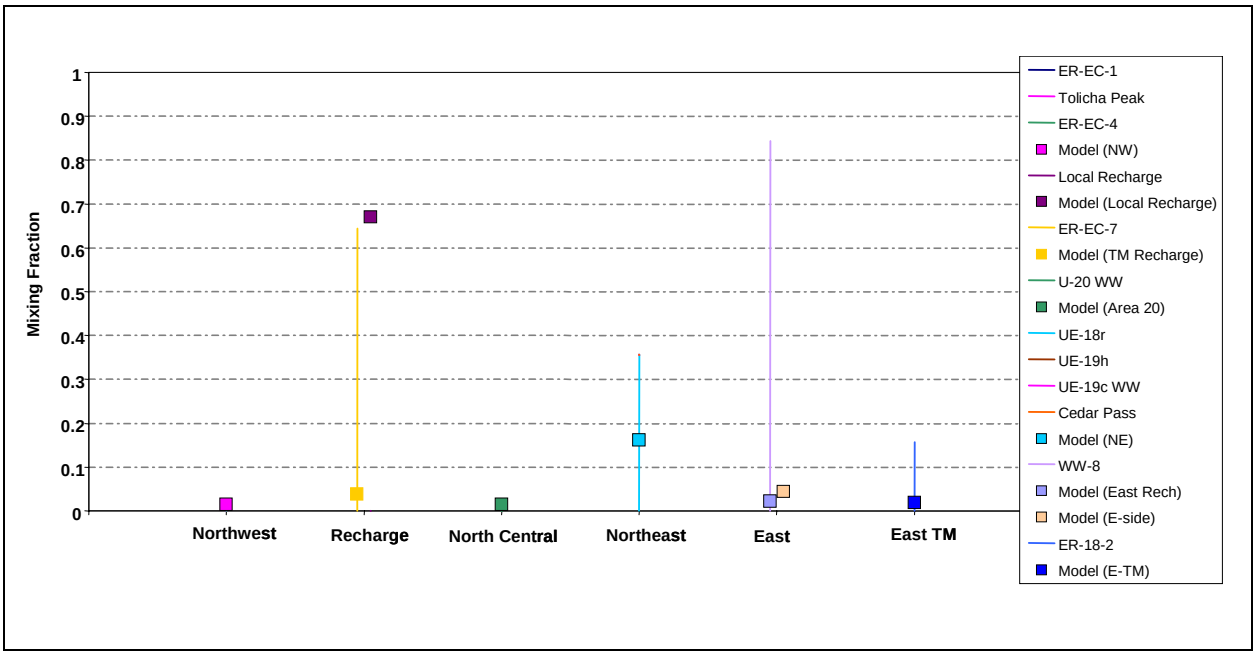

Figure 7-121
Comparison of Flow Model with Geochemical Mixing Targets for Coffer Windmill Well with the FMC-USGSD-SDA Flow Model

Uncontrolled When Printed

7.5 Quantitative Analysis and Ranking of Flow Models Based on Geochemistry

7.5.1 Quantifying the Flow Models

In Sections 7.2 and 7.3, each flow model was evaluated for each geochemical mixing target, graphically showing the ranges of source contributions from recharge/inflow zones in the domain as estimated by Kwicklis et al. (2005) (lines) compared with the fractions simulated with the reverse transport model (symbols), as shown in Figure 7-8. The geochemical residual for each recharge/inflow zone in the figures is the difference between the target range and the simulated fraction. However, visual inspection of figures in Sections 7.2 and 7.3 does not provide the quantitative analysis necessary to assess the performance of the different flow models.

For all target wells in each of the calibrated flow models, there are four potential types of error identified by the comparison of model results with geochemical mixing targets. These are:

- **RM:** Too much inflow across the eastern boundary from Rainier Mesa. Although the gradients suggest such flow might be possible, the geochemistry rules it out at all target wells except Coffer Windmill Well.
- **NW:** Too much inflow across the northern boundary west of the Purse Fault (Figure 7-1).
- **NCNE:** Not enough flow from the north-central and northeast areas east of the Purse Fault.
- **Rech:** Too much local recharge (lower Thirsty Canyon and Oasis Valley).

Eighteen of these residual types result at the target wells, forming the basis for a comparison and ranking of 19 different flow models. For example, UE-18r_RM is the error of too much inflow across the eastern model boundary (RM is notation for Rainier Mesa) as identified by differences between the geochemical target and model results at UE-18r. Its value is the difference between the symbol (model value) and the top of the line (geochemical mixing target range) in the first column of figures such as Figure 7-8. Another example is ER-OV-04a_Rech, which is excessive local recharge at ER-OV-04a. Apparent similarities in the errors among various models motivate a formal cluster analysis seeking to identify models with similar geochemical residuals. The clusters are developed with the objective of minimizing the intervariance within each cluster and maximizing the intervariance between different clusters. The analysis is achieved with a k-means clustering

Uncontrolled When Printed

algorithm, which is an iterative process for assigning models to different clusters and then testing the objective. This analysis highlights four distinct clusters of the 19 models considered (Table 7-18).

Table 7-18
k-Means Clusters of Flow Models Based on Geochemical Residuals

Cluster	1	2	3	4
Models	SCCC-DRIA SCCC-USGSD DRT-USGSD BN-DRIA-LCCU1	PZUP-USGSD BN-DRIA PZUP-DRIA BN-MME-ADA	BN-USGSD RIDGE-MME SEPZ-MME BN-MME TCL-MME	DRT-MME DRT-DRIA BN-MME-LCCU1 PZUP-MME BN-USGSD-LCCU1 SCCC-MME

Figure 7-122 shows the mean cluster value for each of the 18 geochemical residuals for each of the four clusters of the 19 models. The nomenclature for the residuals is such that the target well is listed first, followed by one of the four types of error listed above. Figure 7-123 shows the individual residual components of the total geochemical residual for each model, grouped by cluster. The four clusters can be summarized as follows:

- **Cluster 4:** Continuous problems with too much inflow from NW.
- **Cluster 3:** Substantial inflow from Rainier Mesa at UE-18r, ER-OV-04a, ER-OV-03a, and ER-OV-03c. Additional problems with local recharge at ER-OV-01 and ER-OV-03c
- **Cluster 2:** Inflow from Rainier Mesa, but not as bad as Cluster 3, particularly at UE-18r.
- **Cluster 1:** Local recharge issues at ER-OV-03a, ER-OV-03c, and ER-OV-01, however, not substantially different than other models at those locations.

The analysis in Figure 7-124 shows strong correspondence between the total geochemical residual and the type of model error(s) associated with the four clusters. Cluster 1 shows the strongest performance in total geochemical residual because these models are not plagued with NW inflow issues or Rainier Mesa inflow issues. The problems with local recharge in Cluster 1 are most indicative of local errors in the specified recharge models and less of the global flow solution. Generally, the recharge modes seem to apply more recharge in the washes than is consistent with the geochemisty. Cluster 4 models are characterized by incorrect assessment of inflow from the northwest and Cluster 3 models are characterized by excessive inflows from Rainier Mesa

Uncontrolled When Printed

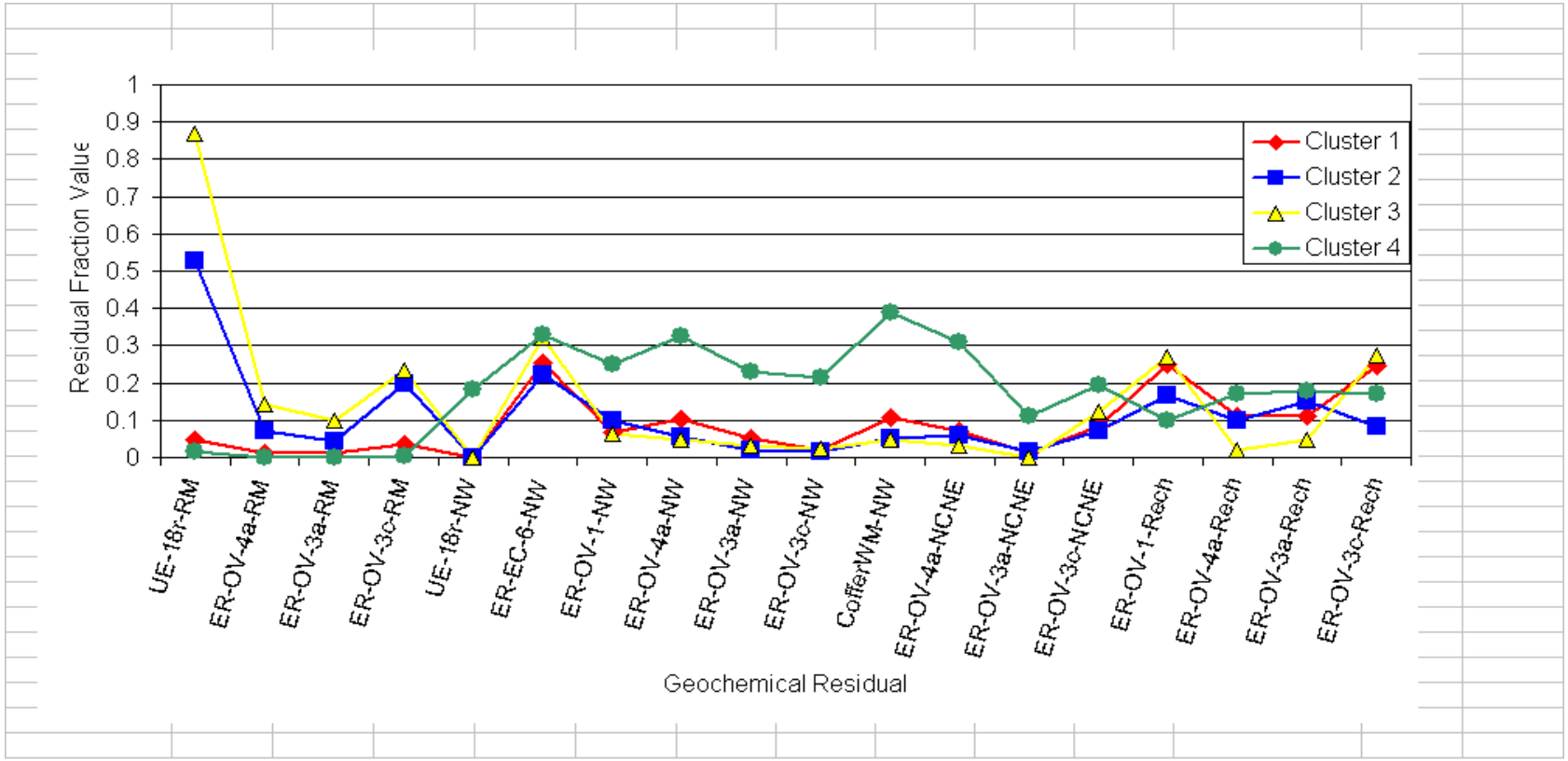

Figure 7-122
Geochemical Residual Means for Each Cluster

The residuals are defined as Well_name-Error_type and grouped by error type to highlight differences between the clusters.

Uncontrolled When Printed

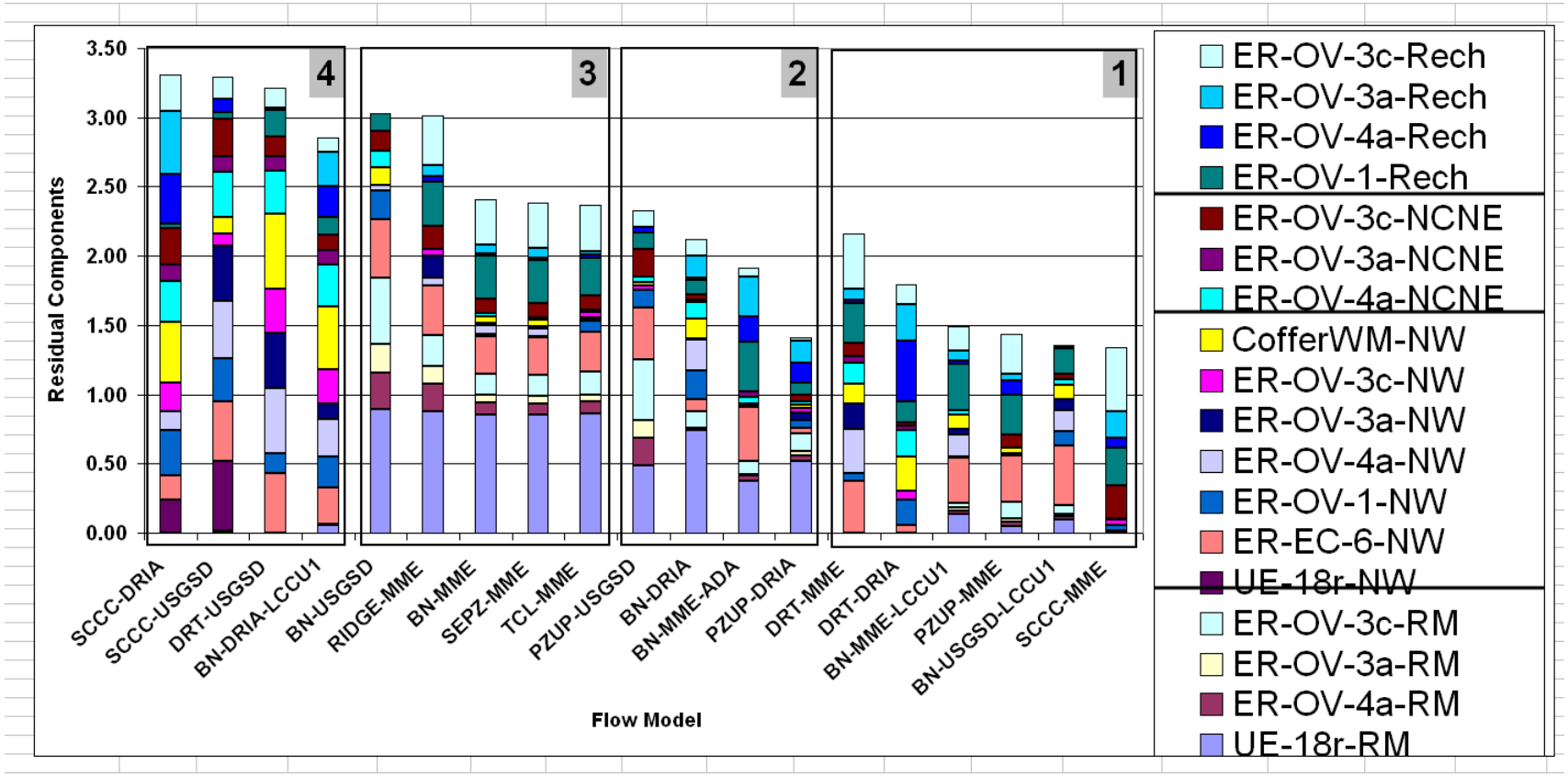

Figure 7-123
Components of the Total Geochemical Residual for Each Model

The models are grouped by the four clusters and the residuals are grouped by error type.

Uncontrolled When Printed

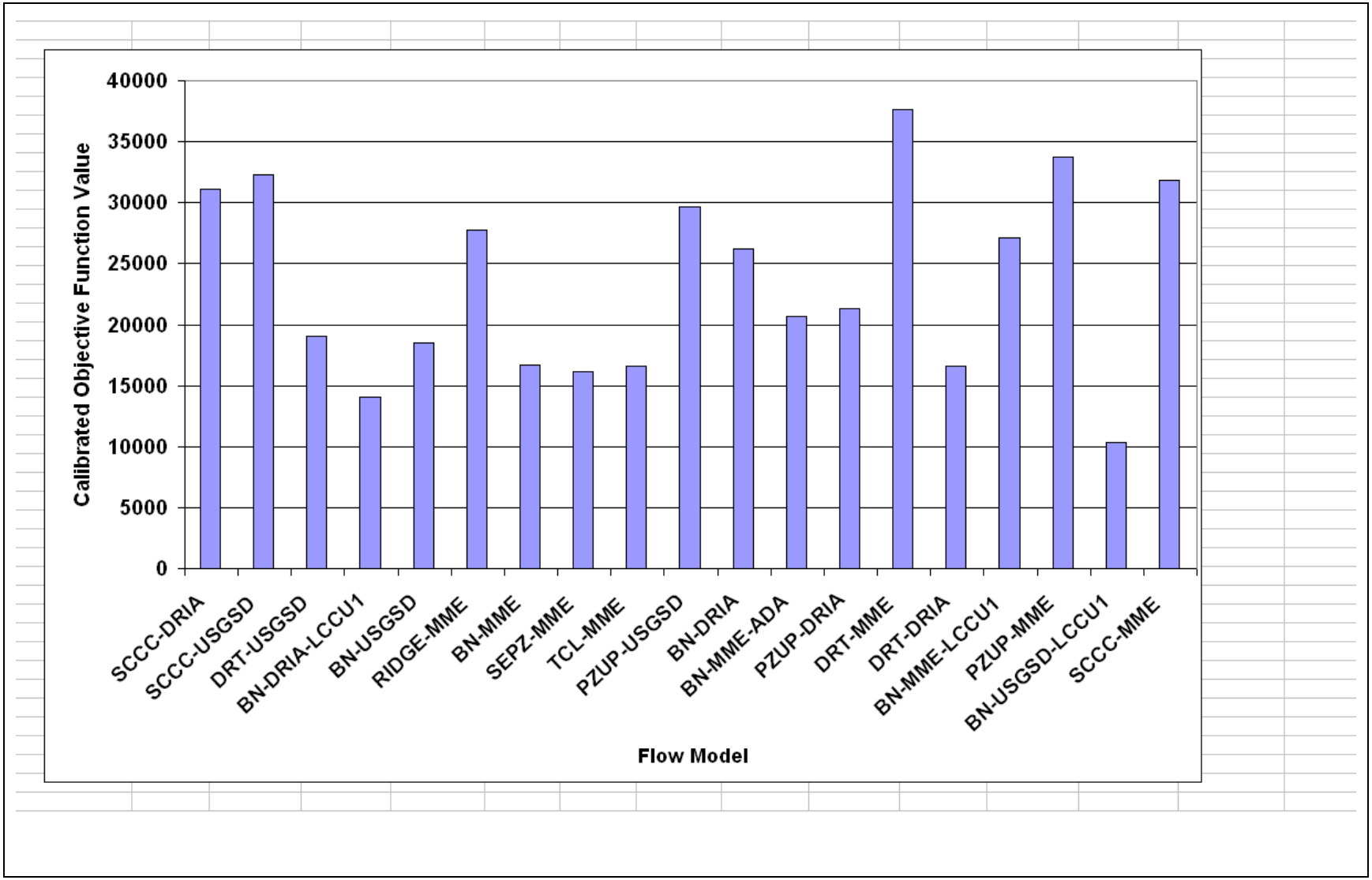

Figure 7-124
Flow Model Calibration Objective Functions, Sorted To Compare with Geochemical Residuals in Figure 7-123

Uncontrolled When Printed

(Gold Meadows to the east of the model domain). Cluster 2 models perform very well in all regards other than Rainier Mesa inflow, and they represent the better half of the models with Rainier Mesa inflow problems, the worse half being Cluster 3. It is also instructive to note that the total geochemical residual does not correspond with the final objective function of the head/flux calibrations (Figure 7-124). This is not surprising because the flow models were all calibrated by substantially reducing the flow/flux objective function from initial values more than an order of magnitude higher, with the assessment that they were all reasonably calibrated and ready for comparison.

7.5.2 Ranking the Flow Models

The total geochemical residual can be used to rank the quality of flow models relative to how well they represent inflow sources at downgradient wells (not their contaminant transport prediction capability). But first, flow models that do not perform well with regard to the verification data need to be eliminated from further consideration. Clusters 4 and 3 have systematic errors that are in direct conflict with the global flow system interpretation based on geochemistry. They have irreconcilably excessive inflows from the northwest at Gold Flat (Cluster 4) or from Gold Meadows on the eastern boundary (Cluster 3). Thus, they can be eliminated. At the other end of this analysis, the Cluster 1 models generally do not have such global flow errors. The Cluster 1 errors are dominated by excessive local infiltration as a direct result of the specified infiltration maps; these errors are similar in all four clusters. The impacts on flow and transport are local and generally downgradient from the sources, thus, they are far less significant than those errors in Clusters 3 and 4 when considering contaminant migration at the CAU scale. The Cluster 2 models have the Rainier Mesa inflow problems that characterize Cluster 3, but they are not as severe. They also have better performance than Cluster 1 models in almost all other regards. The PZUP-DRIA flow model in Cluster 2 has a total geochemical residual lower than all but one of the Cluster 1 models, and the remaining Cluster 2 models have total geochemical residuals similar to the worst two models in Cluster 1 (Figure 7-123). Thus, it is recommended, that these models be considered during transport modeling, at least in sensitivity analysis.

Uncontrolled When Printed

7.6 Summary

Multiple groundwater flow models were calibrated to minimize differences between simulated and observed heads as well as simulated and estimated boundary fluxes for the Pahute Mesa CAU at the NTS (Section 5.0 and Section 6.0). These models represent alternative conceptualizations for both geologic structure (faults and material thickness and extent), and water-balance conditions (recharge and boundary flux). Although all of the flow models are calibrated to minimize the residuals between simulated and target heads and fluxes, the resulting flow systems are different.

Kwicklis et al. (2005) developed an independent geochemical verification dataset with which to assess the various calibrated flow models. The geochemical analysis provides mixing ratios at wells within the domain, identifying the fractions of source water from upgradient zones present in groundwater samples collected at the target wells. Based upon the geochemical mixing targets, the calibrated flow models are interrogated with reverse transport simulations to identify how well they match the verification data in their predictions of mixing different upgradient sources.

Section 7.0 summarized the geochemical analysis, the reverse transport simulation methodology, and the quantitative comparison and ranking of the alternative flow model calibrations that are available for use in future assessments of contaminant migration.

Uncontrolled When Printed